PERGAMON MATERIALS SERIES
SERIES EDITOR: R.W. CAHN

UNDERNEATH THE BRAGG PEAKS
Structural Analysis of Complex Materials

by

T. EGAMI
and S.J.L. BILLINGE

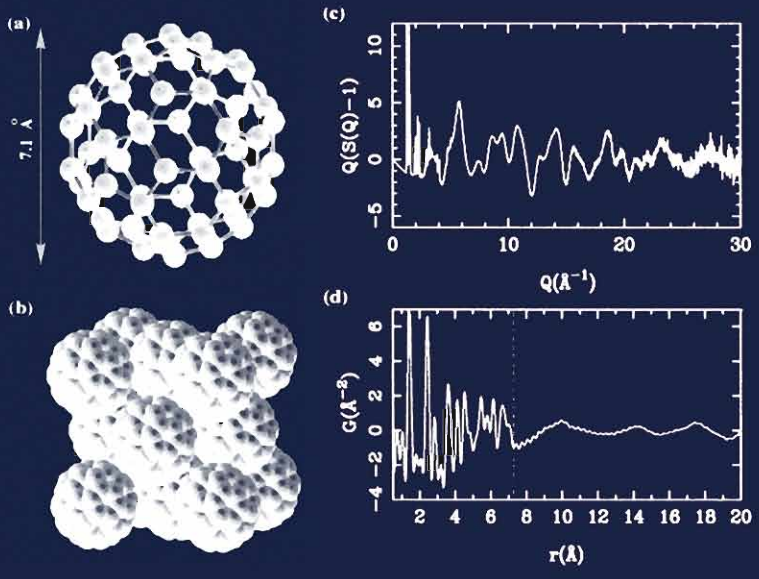

Pergamon

PERGAMON MATERIALS SERIES
VOLUME 7

UNDERNEATH THE BRAGG PEAKS
Structural Analysis of Complex Materials

PERGAMON MATERIALS SERIES

Series Editor: Robert W. Cahn FRS
Department of Materials Science and Metallurgy, University of Cambridge, Cambridge, UK

Vol. 1 **CALPHAD** by N. Sauders and A. P. Miodownik
Vol. 2 **Non-Equilibrium Processing of Materials** edited by C. Suryanarayana
Vol. 3 **Wettability at High Temperatures** by N. Eustathopoulos, M. G. Nicholas and B. Drevet
Vol. 4 **Structural Biological Materials** edited by M. Elices
Vol. 5 **The Coming of Materials Science** by R .W. Cahn
Vol. 6 **Multinuclear Solid-State NMR of Inorganic Materials** by K. J. D. MacKenzie and M. E. Smith
Vol. 7 **Underneath the Bragg Peaks: Structural Analysis of Complex Materials** by T. Egami and S. J. L. Billinge.

A Selection of forthcoming titles in this series:

Phase Transformations in Titanium-and Zirconium-Based Alloys
by S. Banerjee and P. Mukhopadhyay
Thermally Activated Mechanisms in Crystal Plasticity
by D. Caillard and J. -L. Martin
Nucleation by A. L. Greer and K. F. Kelton
Non-Equilibrium Solidification of Metastable Materials from Undercooled Melts
by D. M. Herlach and B. Wei
The Local Chemical Analysis of Materials
by J. W. Martin
Synthesis of Metal Extractants
by C. K. Gupta
Structure of Materials
by T. B. Massalski and D. E. Laughlin
Intermetallic Chemistry
by R. Ferro and A. Saccone

PERGAMON MATERIALS SERIES

UNDERNEATH THE BRAGG PEAKS
Structural Analysis of Complex Materials

by

Takeshi Egami*

Department of Materials Science and Engineering,
University of Pennsylvania, Philadelphia, PA 19104, USA

*Present address: South College, Departments of Materials Science and Engineering and Physics and Astronomy, University of Tennessee, Knoxville, TN 37996-1508 and Oak Ridge National Laboratory, Oak Ridge, TN 37831

Simon J.L. Billinge

Department of Physics and Astronomy, Michigan State University, East Lansing, MI 48825, USA

2003

PERGAMON
An Imprint of Elsevier
Amsterdam – Boston – Heidelberg – London – New York – Oxford – Paris
San Diego – San Francisco – Singapore – Sydney – Tokyo

ELSEVIER Ltd
The Boulevard, Langford Lane
Kidlington, Oxford OX5 1GB, UK

First edition 2003

Library of Congress Cataloging in Publication Data
Egami, Takeshi.
Underneath the Bragg Peaks: structural analysis of complex materials / by Takeshi Egami, Simon J. L. Billinge.
p. cm. – (Pergamon materials series; v. 7)
Includes bibliographical references and index.
ISBN 0-08-042698-0 (alk. paper)
1. Crystallography. 2. Solids – Analysis. I. Title. II. Series.

QD905.2.E34 2003
548–dc21 2002192953

British Library Cataloging in Publication Data
Egami, Takeshi
Underneath the Bragg peaks : structural analysis of complex materials. – (Pergamon materials series ; 7)
1. Composite materials – Analysis 2. Nanostructured materials – Analysis
I. Title II. Billinge, S. J. L.
620.1'18'99

ISBN: 0 08 042698 0

♾ The paper used in this publication meets the requirements of ANSI/NISO Z39.48-1992 (Permanence of Paper).
Printed in The Netherlands.

Series Preface

My editorial objective in this Series is to present to the scientific public a collection of texts that satisfies one of two criteria: the systematic presentation of a specialised but important topic within materials science or engineering that has not previously (or recently) been the subject of full-length treatment and is in rapid development: or the systematic account of a broad theme in materials science or engineering. The books are not, in general, designed as undergraduate texts, but rather are intended for use at graduate level and by established research workers. However, teaching methods are in such rapid evolution that some of the books may well find use at an earlier stage in university education.

I have long editorial experience both in covering the whole of a huge field–physical metallurgy or materials science and technology–and in arranging for specialised subsidiary topics to be presented in monographs. My intention is to apply the lessons learned in 40 years of editing to the objectives stated above. Authors have been invited for their up-to-date expertise and also for their ability to see their subject in a wider perspective.

I am grateful to Elsevier Ltd., who own the Pergamon imprint, and equally to my authors and editors, for their confidence, and to Mr. David Sleeman, Publishing Editor, Elsevier Ltd for his efforts on behalf of the Series.

Herewith, I am pleased to present to the public the seventh title in this Series, on a topic of great current concern.

ROBERT W. CAHN, FRS
(Cambridge University, UK)

This Page Intentionally Left Blank

Preface

This book focuses on the structural determination of crystalline solids with extensive disorder. Well-established methods exist for characterizing the structure of fully crystalline solids or fully disordered materials such as liquids and glasses, but there is a dearth of techniques for the cases in-between, crystalline solids with internal atomic and nanometer scale disorder. The purpose of this book is to discuss how to fill the gap using modern tools of structural characterization. While this subject might sound rather narrow, the fact is that today this problem is encountered in the structural characterization of a surprisingly wide range of complex materials of interest to modern technology and is becoming increasingly important.

General wisdom has always commanded that being pure and simple would not necessarily be good, and complexity could provide a better alternative. This is particularly true when it comes to materials. An airplane made of pure aluminum or a pure iron sword would invite a disaster, since pure metals are soft and easily deformed. Copper and other elements are added to aluminum to form a complex multi-phase alloy to build an airplane. Refined weapons in the Middle Ages such as Damascus swords and Japanese swords are made of intricately complex iron and iron carbide composites with delicate microstructures.

Today modern technology demands more and more sophisticated complex materials. While classic materials mentioned above are complex at the length-scale of micrometer, today engineering at the *atomic scale or nanometer scale* is becoming required for high-performance functional materials. For instance, artificial superlattices or multilayered thin films are atomic scale composites. Carbon nano-tubes and nano-crystals of various materials are other examples of a nanometer scale structures that can be engineered into highly complex nano-composites. These nano-engineered materials are closely related to *nanotechnology* that is rapidly becoming fashionable even among the public. Usually nanotechnology means technology to form objects of nano-meter size out of relatively simple materials, such as silicon and carbon. However, nano-scale engineering of the atomic structure of materials should also be considered as a very important and emerging ingredient of nanotechnology. For instance complex oxides, such as the copper oxide compounds that show high temperature superconductivity or manganese oxide compounds exhibiting giant magnetoresistivity, have complicated atomic and nanometer level structures, and engineering such complex structure is a major focus of materials research in these fields.

Why are today's technologically advanced materials complex at the atomic and nanometer level? A part of the answer is that we discovered the synergy of competing forces. Just as the British Empire maintained its preeminence by the principle of *divide and conquer*, a solid is more susceptible to external forces when two or more internal

forces are competing and balanced. Many high-sensitivity functional materials are made precisely that way. As will be discussed in detail later in this book such competing forces produce a complex atomic structure, even when the structure is crystalline in average. To understand and design materials with competing forces it is crucial that we have precise knowledge of the complex atomic structure. However, that is not so simple a task, since the tools widely available at present often do not work adequately for this purpose.

The standard tool to study the atomic structure is crystallography but conventional crystallography was not developed with such complex materials in mind. A periodic lattice is a prerequisite for a crystallographic study. However, small randomness and local deviations from perfect periodicity often characterize complex materials, and they usually are crucial to their properties. Thus determining these deviations is an essential part of structural characterization. In extending crystallography to the study of these imperfectly periodic materials serious compromises have to be made, rendering the results inaccurate. What we need is another tool, a local probe, to study the structure of such complex materials and understand how the structural features are related to the properties we desire.

A number of such local probes exist. Most, such as x-ray absorption fine structure (XAFS) and nuclear magnetic resonance (NMR), give only very short-range information. Imaging methods such as transmission electron microscopy (TEM) and scanning probe microscopies, such as scanning tunneling microscopy (STM) and atomic force microscopy (AFM), are highly complementary to the bulk local probes. They yield compelling two-dimensional real-space pictures of thin samples in the case of TEM, or surfaces in the case of scanning probes, but do not yield bulk average information or atomic positions with high accuracy. In this book we discuss an alternative method of analyzing diffraction data without the assumption of lattice periodicity. It is the method of atomic pair-distribution function (PDF) analysis imported from the research field of non-crystalline materials. While crystallographic analysis takes into account only the Bragg peaks, which are tall and clearly visible in the diffraction pattern, the PDF method utilizes information buried in-between the Bragg peaks in the form of diffuse scattering, in addition to the Bragg peaks. The title of this book describes our focus on recovering important information from the data scattered *underneath the Bragg peaks* that are usually discarded in conventional crystallographic analysis.

If the deviations in the atomic positions from perfect periodicity in nominally crystalline materials are sparse and far apart, they may be described as lattice defects. Various methods such as electron microscopy can accurately determine the nature of these defects in most cases. However, if the density of defects is high and they overlap each other, such a description is no longer useful. It may be better to consider the system to be locally non-crystalline, even though on the average there may be a long-range order. That is why the solution we offer to this problem is to import the concept and methodology of PDF analysis from the field of non-crystalline materials to that of crystalline materials. Non-crystalline materials such as liquids and glasses have no structural periodicity at all.

The atomic structure in such a system is usually described by the distribution of distances between two atoms, given as the PDF.

For a long time the field of structural analysis in the materials sciences has been partitioned into two, crystalline and non-crystalline. There has been little cross talk of any significance between the two fields. However, the complex advanced materials we mentioned above are crossover materials between the two, and cannot be correctly studied without breaking down the barrier. The purpose of this book is to widen the crack or create yet another hole in the wall between the two fields, and to establish a gate. It is our hope that the gate is wide open to everybody and easy to pass through. Important recent developments making this crossover possible are the advent of synchrotron radiation sources and pulsed spallation neutron sources, and the availability of cheap high-speed computing. These advanced tools provide sufficient accuracy of measurement, and the quantitative analysis, necessary for the PDF method to be applied successfully to crystalline materials. As the use of these facilities becomes more widespread, more researchers have opportunities to practice such crossover techniques.

A typical reaction to the PDF technique is that it is too complex for practical use. However, it is, conceptually, remarkably simple and with the advent of optimized beamlines and improved computer analysis programs it is becoming also straightforward to apply. This book is designed to introduce and explain the power and usefulness of the technique. A number of practical applications are presented in later chapters. It is also intended as a reference book. Some chapters (and many of the appendices) are correspondingly technical. A number of user-friendly and easy-to-use computer programs now exist for carrying out the analyses described here. This book should make these "black box" programs less black. The reader might want to skip the technical sections on a first reading.

Another, completely opposite, reaction is that the PDF is just a Fourier transformation of the diffraction data, and does not provide any new information. First of all, the same data presented in a different way can greatly facilitate extracting useful information. Moreover, the PDF analysis requires accurate determination of the diffuse and background intensities, and through this analysis actually new information is garnered. In addition, it is very difficult to determine the difference between the average structure and local structure using conventional methods, while the PDF clearly displays it.

In Chapter 1 we introduce the subject and describe the need for local probes in the structural studies of imperfect crystals, using some recent examples. Conventional crystallographic methods are briefly reviewed in Chapter 2, with emphasis on how disorder can be incorporated in crystallographic analysis and what the limitations are. The method of PDF analysis is introduced and discussed in depth in Chapter 3. Technical issues of data taking for accurate PDFs are summarized in Chapter 4, followed by the description of the method of data collection and analysis in Chapter 5. Modeling of the PDF by a three-dimensional structure is discussed in Chapter 6. Chapter 7 deals with lattice dynamics in the PDF, in particular the effect of localized lattice dynamics. We then discuss some of the

recent examples for which the PDF method has proven to be effective in the remaining chapters. Examples of the PDF of perfectly periodic crystals are given in Chapter 8, and those of nanocrystalline and highly defective crystals in Chapter 9. The local structure of solids with competing forces is discussed in Chapter 10, and new information that the PDF studies have revealed in the study of phase transition phenomena is discussed in Chapter 11. Lastly some final remarks are made in Chapter 12 to conclude the book.

As the primary reader of the book we have in mind advanced undergraduate students or beginning graduate students. We focused on getting the concepts across rather than describing full details of the technique, while we do go into some crucial details that may be difficult to garner from other professional journals and books. While the primary purpose of this book is to be a guide for the beginners in the PDF analysis of imperfect crystals, this book hopefully will be useful also to researchers who are already knowledgeable in PDF analysis, for instance with respect to the modern tools and advanced methods of analysis such as error analysis and modeling. In fact we hope this book will stimulate those who apply the PDF analysis only to liquids and glasses to consider its extension to disordered crystals.

This book would have been impossible to write without the efforts of past and present members of the Egami group at the University of Pennsylvania, including Wojtek Dmowski, Brian H. Toby, Xiao Yan, Yoshio Waseda, Shian Aur, Susumu Nanao, Yoshio Suzuki, Wendy Spronson (Frydrych), Daniel D. Kofalt, Ruizhong Hu, H. David Rosenfeld, Despina A. Louca, Srdjan Teslic, Rob J. McQueeney, and Eugene Mamontov, and the Michigan State University group of Billinge, another Egami graduate, including Emil Bozin, Il-Kyoung Jeong, Pete Peterson, Xiangyun Qiu, Jeroen Thompson, Thomas Proffen, Valeri Petkov and Matthias Gutmann and Farida Mohiuddin-Jacobs. Their contributions are gratefully acknowledged. SJLB would also like to thank Antonio Bianconi and Naurang Saini for their gracious hospitality as he finished the book during his sabbatical year in Rome. The authors are equally thankful to a number of collaborators who directly or indirectly contributed to the fruition of the technique including, but not limited to, David L. Price, David E. Cox, Masatoshi Arai, Mike Thorpe, Phil Duxbury, Mercouri Kanatzidis, Tom Pinnavaia and George Kwei, and to the editor of the series, Prof. Robert W. Cahn, for his encouragements, patience and editing. Last but not the least, they are extremely thankful to their spouses, Sayuri Egami and Debby Billinge, and children for their understanding and support over many years.

TAKESHI EGAMI
University of Pennsylvania

SIMON J. L. BILLINGE
Michigan State University

Summer 2002

Contents

CHAPTER 5
DATA COLLECTION AND ANALYSIS

Chapter 1

Structure of Complex Materials

This Page Intentionally Left Blank

Chapter 1
Structure of Complex Materials

1.1. CRYSTALLOGRAPHY AND BEYOND

1.1.1 Complexity at the atomic and molecular level

For a long time complexity has been a bad word for scientists. Simplicity has been the preferred choice, and pronouncing a problem complex was an artful way of giving up any attempt to find a solution. However, major changes are taking place today, placing complexity at the forefront of research in various fields including materials research. Historically, the first materials humankind used were complex materials made by nature, such as wood and animal bones. But after they discovered the art of extracting pure materials such as copper and iron, simple materials started to prevail. This tendency was greatly accelerated during the industrial revolution that enabled production of simple materials in abundance at a low cost.

However, complex materials are on the come-back, since in recent years technological progress made it possible to produce man-made complex materials with superior properties. Composites such as graphite–boron are used in all kinds of sporting equipment from golf shafts to tennis rackets. Multi-layered thin films are used in magnetic heads of disk-memories, and computer chips are very complex constructs of silicon, oxide films and metal interconnects. While many of these artificial structures are composed of relatively simple materials built into a complex structure, other materials are atomistically complex. Many of the modern electronic materials that exhibit remarkable properties such as high-temperature superconductivity, colossal magnetoresistivity, or high dielectric response, have intrinsically complex atomic and nano-scale structures that appear to be critically important to their performance. Polymers are structurally highly complex, with millions of atoms constituting chain molecules, which are assembled in a complex morphology, partly crystalline and partly amorphous. Humankind has started with complex natural materials, developed civilization with simple man-made materials, and is now moving forward to close the circle with man-made complex materials.

However, while polymers are in many ways similar to biological materials, they are still much simpler than proteins. Biological protein molecules are enormously complex; they self-organize with their unique ways of folding up. The functionality of a living organism comes from a multitude of folded proteins, each with a very precise and unique function. For example, the enzyme desaturase is found in plants. It has the job of desaturating fat molecules used in the plant's cell walls in order to maintain their flexibility when the weather gets cold. It does nothing else but its unique, directed, function is of critical importance to the survival of the plant. There is a clear universal trend; the more directed

the functionality of a material, the greater its structural complexity. To harness this law to our benefit in future man-made materials it is clearly necessary to have control over complex structures and to be able to characterize them in detail.

1.1.2 Local view of the structure

One of the major reasons why nano-scale structural complexity is important to advanced functional materials is that solids which contain competing internal forces are often highly sensitive, and these forces result in a complex structure. If two or more forces are competing against each other, the balance can be tipped by a small external force and the system responds with vigor. An example is the colossal magnetoresistive (CMR) oxides which have recently been studied extensively. The CMR materials are located in the phase diagram right at a metal-to-insulator (MI) transition, and an applied magnetic field greatly increases their conductivity by inducing a transition from an insulator to a metal. In these materials there are forces that are competing to localize and delocalize charge carriers, and they are balanced right at the MI transition. A magnetic field helps the delocalizing force and propels the system into the metallic state.

Such competition usually produces a complex structure. The competition can be manipulated by changing composition, temperature, as well as the nano-scale structure. For example to induce the MI transition at a particular temperature, the charge density in the material is adjusted chemically by randomly substituting one element for another. When there are competing forces at the atomic scale, the structure will reflect the conflict, for instance by introducing a slight distortion. If this occurs in a random alloy, the distortion will vary from one atomic site to the next, resulting in a highly aperiodic structure with nano-scale variations. As will be discussed later in this book as an example, the CMR oxides are made up of nano-scale regions of insulating and metallic domains, each having a slightly different local distortion in the structure. In addition these regions are not necessarily static, but could be moving dynamically. Therefore we have to consider not only various length-scales, but various time-scales as well. However, since these dynamics are usually not accessible by X-ray scattering, in this book we focus mainly on the static or instantaneous structure, and only one chapter will be devoted to the dynamic phenomena observed by neutron inelastic scattering.

As a result of such competition these complex materials have a structure that locally deviates from the perfect crystal structure, even when they may appear superficially crystalline. In real life as well a complex person is always more interesting than a simple one, since such a person is unpredictable. A perfectly periodic crystal may be beautiful in some sense, but is totally predictable and can be extremely boring; even the most beautiful theme of Mozart would become boring if it were repeated a million times! Modern complex materials, on the other hand, are far from boring.

In studying such complex crystals with local deviations we need to take two distinct points of view. One is a global view and the other is a local view. They are like national

statistics and personal reports in describing an event such as a war between nations. The death tolls are certainly needed to grasp the scale and economic impact of the war, but novels such as 'War and Peace', 'All Quiet on the Western Front', 'For Whom the Bell Tolls', or even 'Gone with the Wind' tell us more vividly what really happened at a human level and what the war meant to individual people. The average structure determined by crystallography presents a global view of the structure. However, since the real interactions are taking place at a local level, they are more directly related to the local structure, which can only be studied by local probes. In the case of well-ordered crystals the distinction is irrelevant. The global structure also reveals the local structure. However, as we describe in this book, this is no longer the case when local distortions are present in which case the local structure must be studied directly in conjunction with the global structure.

This distinction has a direct implication for the method of theoretical analysis as well. The global view in this case is the simple mean-field approximation (MFA), in which numerous competing forces are volume-averaged into two or more representative competing forces. The conflict is then assessed at a global scale. However, in a complex, nonlinear system the conflict often remains local. In order to describe such local conflicts the average structure is nearly powerless, and we have to know the precise local structure where the conflicts take place.

The problem of competing forces in complex systems has interesting political and sociological analogies. G.W.F. Hegel (1770–1831) was probably the first European philosopher who recognized the dynamic and creative effect of competition. Marxism has the Hegelian philosophy as its basis, but in its application the complex sociological competition was abstracted as the struggle between two social classes. This is the philosophical equivalent of taking the mean field approximation. An irony of this is that, in the implementation of Marxism in the communist societies of the 20th century, competition was essentially eliminated. In large part this was at the root of the demise of communism since competition is the vital force that drives development, as Hegel originally pointed out. In materials, the competition between comparable forces gives rise to dynamic and interesting effects. These effects are primarily local, varying sharply from atom to atom. As in the case of Marxism, taking the MFA and considering only the global effects may mask the important underlying local physics. In this case a study of complex competing forces in solids has to start at a local level. The condition of balance between competing forces should be evaluated locally rather than globally, just like voting to elect local representatives in a democracy. The macroscopic properties are determined as a consequence of interactive accumulation of local properties. That is why the study of local structure is ever more important in understanding complex structures containing competing interactions.

Depending on the length-scale of the complexity, different tools are required to investigate the state of such complex structures. Since we focus on complexity in

the structure at the atomic to nanometer (10^{-9}–10^{10} m) scale, the methods to use are X-ray and neutron diffraction techniques as well as computer modeling. However, the regular crystallographic methods of structural analysis are not going to be sufficient in studying these complex materials, since the crystallographic method *a priori* assumes perfect lattice periodicity. Actually, strictly speaking, even a perfect crystal is not truly periodic, because of quantum-mechanical and thermal vibrations. If one takes a snapshot of the structure, the crystal symmetry is gone, including the translational symmetry. As we will discuss later, in the case of harmonic lattice vibrations the Debye–Waller approximation does an excellent job of recovering the symmetry. However, in complex structures the Debye–Waller approximation usually fails, and we have to determine local structural details by using a different approach. Another philosophical point is that we have to accept a probabilistic description, rather than a deterministic description, to describe the structure. For a perfect crystal translational symmetry works the miracle of Bragg's law and reduces the number of parameters to describe the structure to a precious few. In complex materials the structure is often described in terms of probabilities and parameters to specify these probabilities.

Both of these points suggest that some fundamental departures from crystallography are required to know the true structure of complex materials. However, we are creatures of habit, and too often we rely upon crystallography to describe the structure of materials, no matter how complex they are. In this book we will first discuss how dangerous such a practice is, introduce the alternative local tools of structural study, and go over several examples to illustrate the purpose of the local structural study. Reflecting the two philosophical points mentioned above in our new approach we will not assume periodicity, and the structure will be described statistically.

1.1.3 Shadow of Bragg's law: Why knowing the crystal structure is not sufficient

Bragg's law is the foundation of crystallography, one of the first subjects that an undergraduate student in materials science or condensed matter physics learns in class. It is so basic and taken so completely for granted that we tend to forget how powerful this law really is. However, it is a truly mighty magic wand. One way of describing the atomic structure of a material is to specify the position of each atom. But if a piece of crystal has 10^{23} atoms, in order to specify the position of these atoms one would need 3×10^{23} numbers describing the x, y, and z coordinates of each atom. If one goes about determining these positions atom by atom, it will take forever to accomplish such a task. However, by using Bragg's law based upon the translational symmetry these 3×10^{23} numbers can be reduced to a small set of numbers specifying the lattice symmetry and atomic positions within the unit cell.

Also by applying Bragg's law, the lattice constant can be determined routinely with accuracy exceeding 10^{-5} Å. This is, however, an amazing feat, since usually to measure a length with such accuracy requires the use of a probe with a comparable wavelength

($\lambda = 10^{-5}$ Å). If we use a gamma-ray its energy must be over 1 GeV, and if we use an electron the energy necessary is over 40 GeV. In either case one has to use major particle accelerators costing billions of dollars to produce probes with such energy. But with the use of Bragg's law this is achieved with a small, inexpensive, 50 keV X-ray generator. It is indeed magic.

The secret to this magic can be uncovered by going back to basics. Since the success of Bragg's law has been so spectacular we tend to forget that the crucial presumption for Bragg's law is the periodicity of the crystal lattice. Because of the translational symmetry the description of the crystal structure is reduced to specifying the symmetry group and one or a few lattice parameters, a, b, c. However, by the diffraction measurement we actually measure not the lattice constant, but the lattice coherence length, $\xi = Na$. If the uncertainty in ξ is λ, the uncertainty in a is λ/N, which can easily be as small as 10^{-5} Å if $\lambda = 1$ Å and $N = 10^5$.

The lattice periodicity is crucial to the success of Bragg's law. If the structure of a crystal is not perfectly periodic we cannot reap the benefit of Bragg's law and we then have to face the unpleasant reality of describing the structure in other ways. Again, trying to determine all the atomic positions is out of the question. If the deviations from perfect crystallinity are small in number, the concept of lattice defects is often useful. Also if the deviations are smoothly varying in space they may be described by elasticity theory. Several methods have been developed in crystallography to deal with limited amounts of disorder, as we will discuss in Chapter 2. However, in some cases, the deviations are so pervasive that neither of these concepts and remedial methods is sufficient. A more pertinent approach is to leave the familiar protection of Bragg's law behind, and directly face the complex and unfamiliar reality. The precedent for this kind of study is found in the research field of non-crystalline materials.

1.1.4 The methods of local crystallography

Glasses and liquids have no structural periodicity, and yet their atomic structure is not altogether random as in gases. What does it mean, then, to know the structure? Specifying all the atomic positions is not only impractical, but also useless. Even if we were given a huge table of numbers containing 3×10^{23} atomic coordinates, we would be completely overwhelmed and would not be able to comprehend and use such information. The amount of information is simply too big. Intelligence, on the other hand, means the capability to select the essential pieces out of a vast sea of information, and to reorganize them into a new meaningful statement called understanding. As we go through our lives we experience a huge number of events. Experiences themselves, however, would not make us wise. Only after reflecting upon the experience and deducing the essential message from these experiences, do we learn something from life.

The purpose of structural analysis is to relate the structure to the properties so that we can understand the properties from the atomistic point of view. This understanding can

lead to improvement of the material or creation of new ones with better properties. Clearly the properties are not determined by the absolute position of each atom, but by the relative positions of the atoms which are close enough to have some interaction. In other words local atomic environment, the relative positions of the near neighbor atoms, is what we have to know in deliberating about the properties of the material. From this point of view, the crystal symmetry, so highly revered in the world of crystallography, may not be as important as is often portrayed. If the distortion that breaks the symmetry is extremely small, the effect on the properties may be very small, even if strictly speaking the symmetry is altered. On the other hand, large aperiodic local displacements of atoms usually have serious consequences on the properties, even when they do not change the average symmetry.

The relative atomic positions, or the interatomic positional correlations, can be described by a set of interatomic distances, $\{r_{\nu\mu}\}$ where ν and μ refer to the individual atoms. If the system is macroscopically isotropic, as in liquids, the distribution of the interatomic distances is given by

$$\rho(r) = \rho_0 g(r) = \frac{1}{4\pi N r^2} \sum_{\nu} \sum_{\mu} \delta(r - r_{\nu\mu}), \tag{1.1}$$

where ρ_0 is the number density of atoms in the system of N atoms. The δ is a Dirac delta function. The function $\rho(r)$ is called the *atomic pair density function* (PDF). The function $g(r)$ is called the *atomic pair distribution function*, also abbreviated as PDF. The PDF is a one-dimensional function which has peaks at distances, $r_{\nu\mu} = |\mathbf{r}_\nu - \mathbf{r}_\mu|$, separating the νth and μth atoms. The sums are taken over all the atoms in the sample. What results is a histogram of all the atom–atom distances in the solid. In practice, there are so many atoms in the material that $\rho(r)$ becomes a quasicontinous distribution function. An example of a PDF for an amorphous metallic alloy is shown in Figure 1.1. Note that $\rho(r) = \rho_0 g(r)$ is practically zero below a certain value of r, since two atoms cannot come too close to each other. There is a large peak at the average atomic separation, usually 2–3 Å, representing the nearest neighbors, and there are some oscillations beyond the first peak due to short-range order.

In this example of a material with no long-range order $\rho(r)$ asymptotes to the value of ρ_0 at high r (note that $g(r)$ asymptotes to 1). At low-r $\rho(r)$ oscillates up and down above and below the average density. These oscillations contain the useful local structural information. Because we are *measuring deviations from the average density*, these oscillations are referred to as 'correlations' and $\rho(r)$ and $g(r)$ are often called 'pair correlation functions'. They give information about correlations (deviations from average behavior) of pairs of atoms.

From these functions one can learn various pieces of information regarding the local environment of atoms, such as how many neighbors there are and how far away they are. While the PDF provides only one-dimensional information, it is possible to recreate

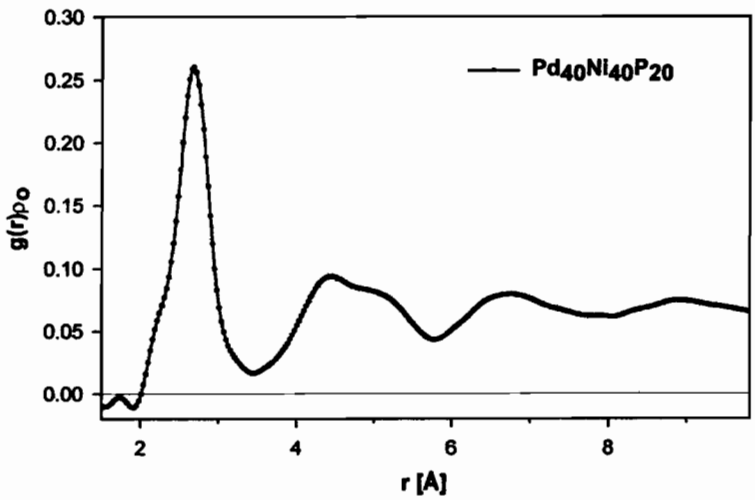

Figure 1.1. The atomic pair density function, $\rho(r) = \rho_0 g(r)$, from the amorphous metallic alloy $Pd_{40}Ni_{40}P_{20}$ showing the generic behavior of $g(r)$ for an amorphous material. The data asymptote to zero at low-r and to $\rho_0 = 0.07$ Å^{-3} at high-r equivalent to $g(r) = 1$. In between the PDF oscillates showing atomic correlations (deviations from the average density), for example a greater probability of finding an atom at the hard-sphere separation distance of 2.9 Å, followed by a less than average probability of finding a neighbor between the first and second neighbor shell at 3.5 Å, and so on (Egami *et al.*, 1998).

the three-dimensional structure with a relatively high degree of confidence by creating a three-dimensional model whose PDF agrees with the experimental PDF (Chapter 6). In principle, the approximation of an isotropic sample can be removed and the extension of the equations to define three-dimensional distribution functions is treated in Chapter 3.

The PDF can be experimentally determined by diffraction measurements using X-rays, neutrons, or electrons, as discussed in Chapter 4, or by the method of X-ray absorption fine structure (XAFS). The XAFS method is not the focus of this book; however, for completeness a discussion of this technique, and its relationship to diffraction techniques, is given in Appendix 3.4. These methods of structural study are applicable for any system, amorphous or crystalline, isotropic or anisotropic, powder or single crystal. In this book we mainly deal with the PDF determined by powder diffraction. Powder diffraction experiments are the simplest measurements, and in many cases provide enough relevant information to understand the phenomena of interest.

While the PDF method is an established technique in the field of structural study of glasses and liquids until recently it has hardly been used for the study of crystalline solids. There are two reasons for this lack of activity. The primary reason is that technology was not ready. If one uses X-rays from the regular sealed X-ray tube in the laboratory or thermal neutrons from a nuclear reactor as radiation, the wavelength of the radiation is too long for the PDF to be determined accurately, as we discuss later. The advent of

synchrotron based radiation sources, such as pulsed spallation neutron sources and X-ray synchrotron sources, that provide high-intensity short-wavelength particles has made the PDF method accurate and reliable. The secondary reason is that with these techniques data analysis and modeling is highly computationally intensive and has only become practical with the recent advent of high-speed computing. Finally, as we mentioned above the need for studying the detailed atomic structure of complex materials is relatively new, instigated by the discovery of such materials.

Many of the subjects discussed in this book are dealt with in a number of standard textbooks listed in the bibliography. However, due to advances in facilities, equipment, experimental techniques and modeling, it is worthwhile to cast a new light on the subjects. In particular the application of the PDF method for the structural study of crystalline solids is outside the scope of these classical books, while that is the main focus of the present book, with recent results being used as examples of application.

1.1.5 Real and reciprocal space

Diffraction methods measure diffracted intensity as a function of the momentum transfer of the scattering particle, $\mathbf{Q}$, which is defined as $\mathbf{Q} = \mathbf{k}_{\text{init}} - \mathbf{k}_{\text{final}}$, where $\mathbf{k}_{\text{init}}$ and $\mathbf{k}_{\text{final}}$ are the incident and scattered wavevectors, respectively. For this reason $\mathbf{Q}$ is also called the diffraction vector. The data naturally appear in the so-called reciprocal space as intensity as a function of wavevector. Clearly, from the definition of $\rho(r)$ this function is a direct representation of the real structure and exists in real space as a function of position. These two domains are linked by a Fourier transform, as we discuss in detail later. However, it becomes immediately apparent that the same information about the local structure can be equally well represented in either real- or reciprocal-space. The reciprocal space equivalent of $\rho(r)$ is $S(Q)$ the *total scattering structure function.*[1] The name 'total scattering' comes from the fact that included in the intensity is scattering coming from Bragg peaks (the global structure), elastic diffuse scattering (the static local structure) and also inelastic scattering from moving atoms that contains information about atom dynamics. Since these intensities are not resolved and differentiated, the resultant scattering intensity is referred to as total scattering. The study of local structure described in this book generically comes down to the study of the total scattering intensity, $S(Q)$. This can be studied directly in reciprocal space or by Fourier transforming to real space and studying the PDF. Both approaches are valid and tend to provide complementary information. Examples of both approaches are described in this book, though the emphasis is on the study of the PDF since this is the particular expertise of the authors.

[1] $S(Q)$ is widely referred to as the *structure factor* in the world of non-crystalline materials. This is an unfortunate misnomer and causes confusion when these ideas are introduced to crystallographers who have their own, quite distinct and appropriately named, crystallographic structure factor, F_{hkl}. We prefer to call $S(Q)$ the *total scattering structure function* since it is a continuous function of *intensity* vs. Q and not a factor that scales a Bragg peak *amplitude* as in the case of F_{hkl}.

1.2. THE POWER OF TOTAL SCATTERING AND PDF METHODS

Before we submerge ourselves into the details of the diffraction physics and the PDF method, let us quickly review some examples that illustrate the power of the PDF and total scattering methods. Details regarding each example will be expanded upon later in the book. However, these brief descriptions should help the reader to have some concrete images of what we are talking about, and also will hopefully motivate the reader to read further.

1.2.1 The difference between the local and average structures: alloys

What exactly is meant by the difference between the local structure and the average crystallographic structure? A simple example is found in the case of an alloy semiconductor. Semiconductors GaAs and InAs have the same structure but different band gaps; the band gap can be engineered by alloying them to form a pseudo-binary compound $(Ga_{1-x}In_x)As$. The lattice constant changes approximately linearly with x, following Vegard's law. Crystallographically then, the distance between the (Ga,In) site and the As site changes linearly with x. This, however, does not mean that *actual* bond length changes linearly with x. We know that a large energy is needed to change the bond length, and it is most likely that the Ga–As distances and the In–As distances endeavor to remain more or less constant even when x is changed. In this covalent solid the structural disorder due to the alloying is predominantly relaxed by bond bending that requires relatively less energy.

The crystallographic (Ga,In)–As distance represents only the average distance between the atoms at the (Ga,In) and As sites, and corresponds to neither the actual Ga–As nor In–As distances. When x is changed the number of Ga–As and In–As bonds changes linearly with x, resulting in the linear change in the average lattice constant. Crystallography gives you only the average bond distance and the lattice constant, and does not tell you the actual *local* bond length. In order to determine the local bond one requires *local* probes.

Indeed the PDF determined by high-energy X-ray diffraction clearly shows that the nearest neighbor (Ga,In)–As peak at $\sim$2.4 Å is split into two sub-peaks, as shown in Figure 1.2 (Petkov *et al.*, 1999). The dependence of the positions of the sub-peaks on composition x is shown in Figure 1.3. The sub-peak positions connect smoothly to the Ga–As and In–As distances in the pure compounds, revealing the chemical identity of these peaks.[2] A weak dependence of the peak position on x means that the size-mismatch leads to a small amount of local atomic-level strain (Eshelby, 1956; Egami and Aur, 1987).

1.2.2 Short- vs. long-range correlations: molecular solids

Another example that illustrates the notion of local vs. global structure is a molecular solid, for instance a crystal of C_{60}, or buckyballs (Figure 1.4(a)). Buckyballs form an f.c.c.

[2] This behavior was first seen in another local technique, XAFS (Mikkelson and Boyce, 1982); however, the PDF study reveals the intermediate range order and gives a more complete structural solution.

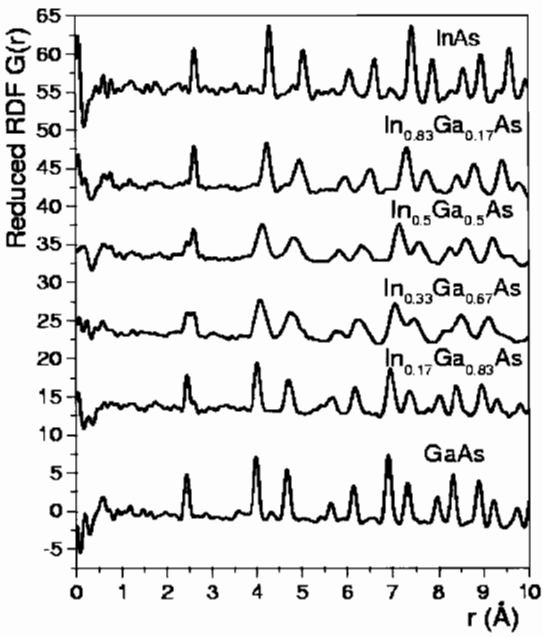

Figure 1.2. PDFs in the form $G(r) = 4\pi r(\rho(r) - \rho_0)$ from $In_{1-x}Ga_xAs$ alloys. Data were measured from high-energy X-ray diffraction data at Cornell High Energy Synchrotron Source (CHESS) at 10 K. Notice the first peak is split indicating the presence of short Ga–As and a long In–As bonds (Petkov *et al.*, 1999; Jeong *et al.*, 2001).

solid (Figure 1.4(b)). At and above room temperature each molecule is randomly rotating. Thus the time-averaged structure is just an f.c.c. structure of uniform hollow balls with the diameter of about 7 Å. However, within each buckyball the network of carbon atoms is rigid. Translated into the language of the PDF, this means that the carbon atoms within the same buckyball are highly correlated, but those on different buckyballs are not correlated. Thus, as shown in Figure 1.4(d), the PDF exhibits sharp features up to 7 Å which is the diameter of the buckyball, reflecting the discrete interatomic distances within the molecule, while it becomes a slowly varying function beyond, without atomic details.

The broad peaks in the PDF beyond 7 Å are real and come from the f.c.c. arrangement of isotropic spherical balls. The nearest-neighbor ball–ball separation, a, is ~ 10 Å corresponding to the first broad peak. The second and third neighbors are at $\sqrt{2}a$ and $\sqrt{3}a$, i.e. ~ 14 and ~ 17 Å, as observed.

This shows that, within the same PDF different information about the local structure (intra- and inter-domain correlations) is contained at different values of r. It also shows that even when rigid local objects are rotationally (and translationally) disordered the PDF still yields the intra-object structure, information that is lost in a crystallographic measurement in such a case.

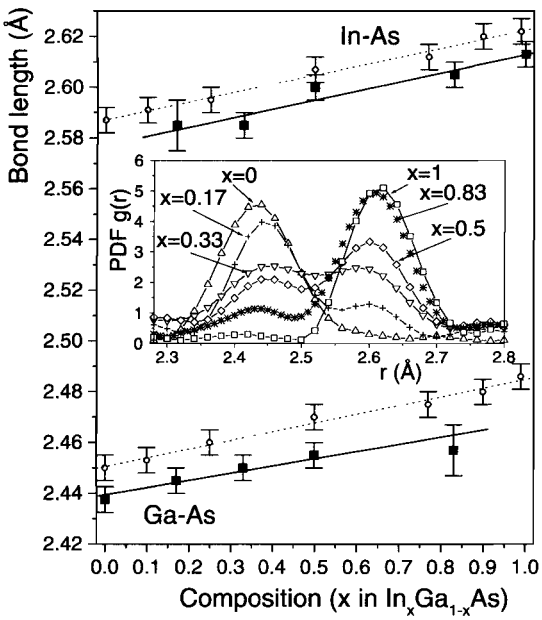

Figure 1.3. The dependence of the lengths of the short- and long-bonds in $In_{1-x}Ga_xAs$ alloys as a function of doping. The inset shows a close-up of the PDF of the near-neighbor In/Ga–As bonds for various compositions with model predictions superimposed (Petkov *et al.*, 1999).

1.2.3 Relevance to the properties I: high-temperature superconductors

High-temperature superconductivity in copper oxides is one of the most remarkable phenomena in condensed matter physics. Not only is the critical temperature surprisingly high, but the mechanism appears to be fundamentally different from that of the conventional 'low-temperature' superconductors, such as Hg or Nb. For the low-temperature superconductors the Bardeen–Cooper–Schrieffer (BCS) theory (Bardeen *et al.*, 1957) works beautifully, but the critical temperatures of cuprate superconductors are too high to be accounted for by the BCS theory. The mechanism of high-temperature superconductivity apparently is deeply rooted in quantum-mechanical many-body phenomena involving spins and local coulomb repulsion between electrons.

Since the BCS theory was set aside early on, phonons, which form the basis for the BCS mechanism, have been all but completely ignored by most theoreticians. However, the lattice shows very anomalous behavior near the superconductive transition temperature (Egami and Billinge, 1994, 1996). An example is shown in Figure 1.5. Here the temperature dependence of the height of the PDF peak at 3.4 Å, determined by pulsed neutron scattering, is plotted for $Tl_2Ba_2CaCu_2O_8$ (Toby *et al.*, 1990). This peak describes the oxygen–oxygen distance adjacent to Cu, and the peak height is expected to become

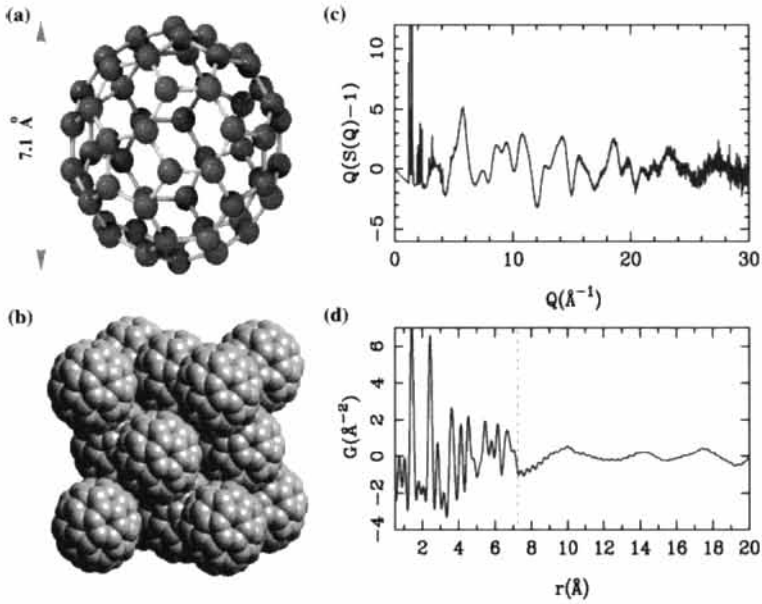

Figure 1.4. (a) The structure of a single C_{60} molecule. (b) The f.c.c arrangement of C_{60} balls in solid C_{60}. (c) Room temperature neutron powder diffraction data from a sample of solid C_{60} at room temperature. Note the pronounced diffuse scattering. The Bragg peaks from the f.c.c. arrangement of the balls are evident at very low Q. (d) Fourier transform of the data in (c) showing the PDF, $G(r)$, of solid C_{60}. The sharp features at low-r are the intra-ball C–C correlations. Above 7.1 Å only inter-ball correlations are present which are very weak because the balls are spinning.

reduced with increasing temperature because of lattice vibration, as shown by a solid line that was calculated from the phonon density of states measured by neutron inelastic scattering. The measured peak height deviates strongly from the prediction, and peaks around the superconductive transition temperature, T_c. Clearly the local structure does reflect the superconducting phase transition. It may even be intimately involved in the phenomenon of high-temperature superconductivity.

Another example is the PDF peak width of $La_{2-x}Sr_xCuO_4$. In this system as the value of x is increased holes are doped into the system, driving the system to superconduct in the range $0.06 < x < 0.22$. The width of the first peak of the PDF, coming from Cu–O nearest neighbor distances, first increases and then decreases as x is changed through the superconducting composition range, as shown in Figure 1.6 (Bozin *et al.*, 2000). The PDF in this range is a superposition of the PDF at $x = 0$ (insulating) and that at $x = 0.25$ (metallic), indicating that the system is microscopically phase-separated into regions rich and poor in doped charge. This is supported by the observation that the intermediate range of the PDF of the $x = 0.1$ sample is well described by a mixture of the $x = 0$ (undoped) and $x = 0.2$ (heavily doped) PDFs (Figure 1.7; Bozin *et al.*, 1999). Such microscopic phase separation

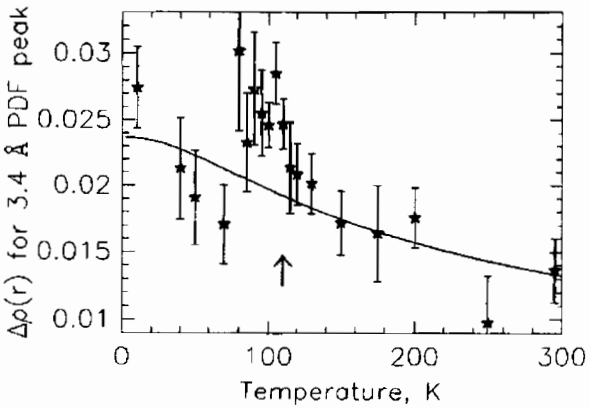

Figure 1.5. PDF peak height vs. temperature of the peak at 3.4 Å for the high-T_c superconductor $Tl_2Ba_2CaCu_2O_8$. An anomaly from the expected Debye-behavior is observed at around $T = 110$ K close to the superconducting transition temperature, T_c (Toby *et al.*, 1990).

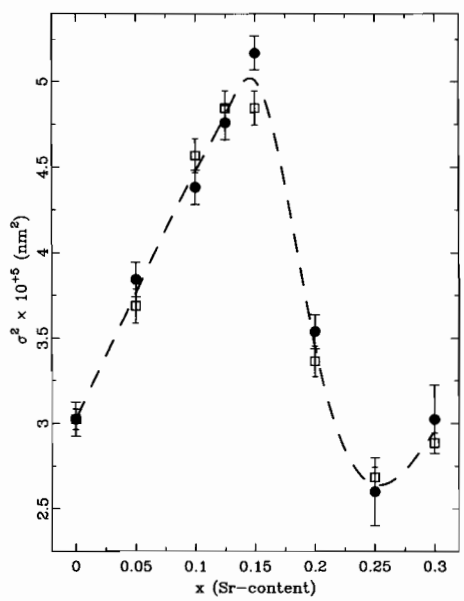

Figure 1.6. Width of the PDF peak at $r \sim 1.90$ Å vs. doping for the material $La_{2-x}Sr_xCuO_4$. The peak broadens with increasing doping until $x = 0.15$ whereupon it abruptly sharpens again. The broadening is thought to be due to electronic inhomogeneities in the materials in the form of dynamic charge stripes in the low-doped region. These inhomogeneities disappear at high doping (Bozin *et al.*, 2000).

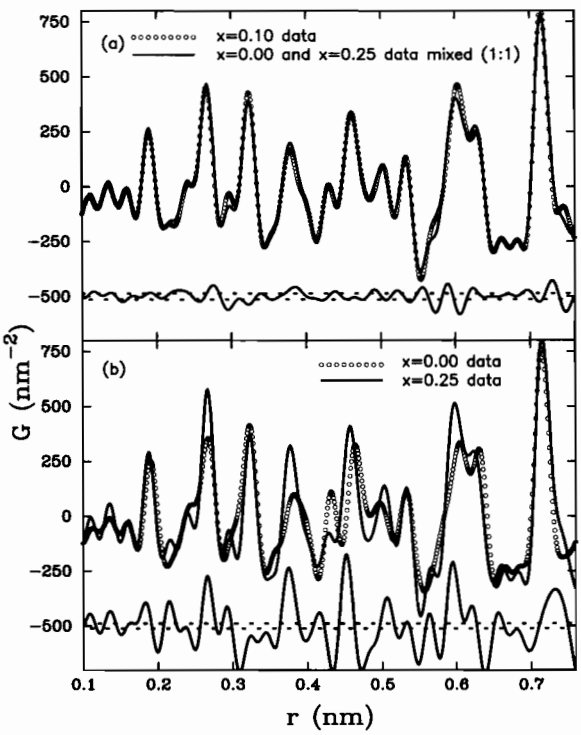

Figure 1.7. Direct evidence in the PDF for charge inhomogeneities in the $La_{2-x}Sr_xCuO_4$ system. The PDF of the $x = 0.1$ sample (open symbols in (a)) is well reproduced by a 1:1 mixture of the PDFs from undoped ($x = 0.0$) and heavily doped ($x = 0.25$) samples. The PDFs from each of these two samples are shown in (b) and the 1:1 linear combination is shown as a solid line in (a). Note the good agreement as evident by a weakly fluctuating difference curve as shown below the data in (a) (Bozin *et al.*, 1999).

was observed in the stripe phase in $(La_{1.475}Nd_{0.4})Sr_{0.125}CuO_4$, where the metallic stripes with the width of about a unit cell are formed in the insulating matrix, with the periodicity of four unit cells (Tranquada *et al.*, 1995). While $(La_{1.475}Nd_{0.4})Sr_{0.125}CuO_4$ is not superconducting, and the stripes are static, it is suspected that similar micro-phase separation, but a dynamic one, may exists even in the superconducting compositions. Since the Cu–O distance in the insulating phase is larger than that in the metallic phase, the first peak due to the Cu–O distance becomes wide in the mixed phase. The change in the peak width with x, and its relationship to the x-dependence of T_c, indicates that the phase separation may be required for superconductivity to take place.

1.2.4 Relevance to the properties II: CMR manganites

The CMR phenomenon is related to a magnetic field-induced insulator-to-metal transition. It turns out that hole localization due to polaron formation is an important component and

the PDF method played a major role in elucidating this mechanism. The key to the problem is the coupling of electrons to the lattice via a Jahn–Teller (JT) distortion (Goodenough *et al.*, 1961): locally, MnO_6 octahedra elongate to break an electronic degeneracy. In the $La_{1-x}Sr_xMnO_3$ system, the undoped, insulating compound, $LaMnO_3$, is JT distorted. This is clearly seen in the local structure (Figure 1.8) (Proffen *et al.*, 1999) as the first Mn–O

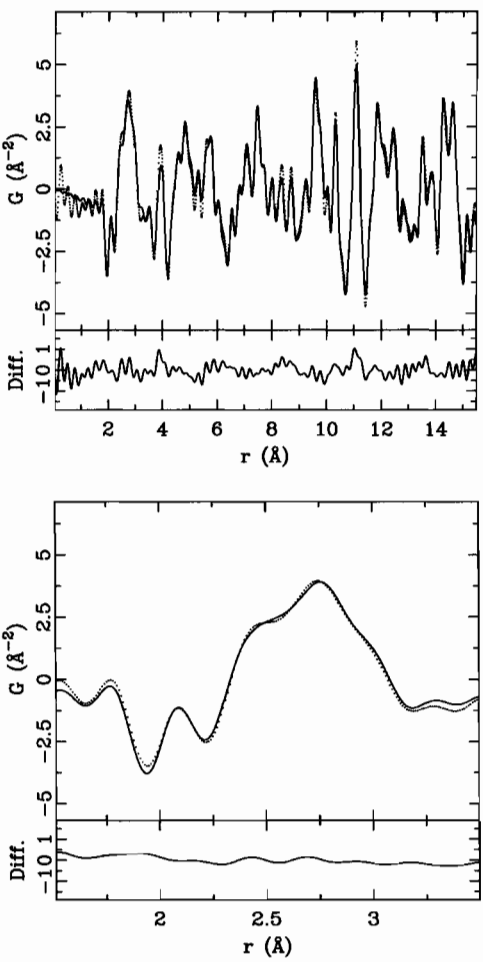

Figure 1.8. PDF of $LaMnO_3$ from neutron powder diffraction data collected at 10 K on the SEPD instrument at IPNS (dots). Note the first (negative) peak around $r = 2$ Å coming from Mn–O pairs is split into a well-resolved doublet showing the existence of short and long Mn–O bonds. This directly shows the Jahn–Teller distorted MnO_6 octahedra and is shown on an expanded scale in the lower panel. The solid line is the PDF calculated from a refined model of the structure using PDFFIT. The difference curve is shown below (Proffen *et al.*, 1999).

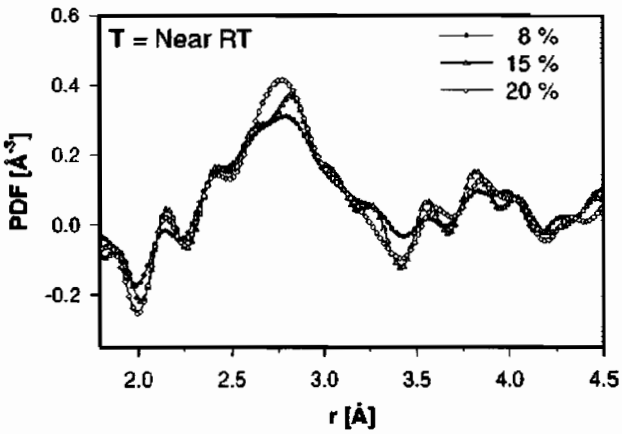

Figure 1.9. PDF from $La_{1-x}Sr_xMnO_3$ with different values of x showing the persistence of the Mn–O long-bond around 2.15 Å in the PDF despite the fact that the crystal structure indicates that the Jahn–Teller distortion has disappeared on average (Louca and Egami, 1997).

peak in the PDF at $r \sim 2.0$ Å being split into two components.[3] Because the JT distorted octahedra have long-range orientational order the 'distortions' are also seen in the average structure. The crystal structure indicates that the JT distortion is quickly reduced as the valence of Mn is increased from 3 + towards 4 + by replacing La^{3+} with Sr^{2+}. By the time the MI transition occurs at $x = 0.16$ the JT distortion in the global structure is completely gone. However, it is still evident in the local structure since long Mn–O bonds are evident in the PDF (Figure 1.9) (Louca and Egami, 1997). The distortion disappears in the average structure because the distorted octahedra become orientationally disordered with the long axes lying along x, y and z directions with equal probability. The importance of this electron lattice interaction to the CMR phenomenon itself was also demonstrated from a PDF measurement. An anomalous broadening at the MI transition of the PDF peaks associated with the $Mn–O_6$ octahedra was interpreted as electron localization and polaron formation (Figure 1.10) with the appearance locally of Jahn–Teller lattice distortions (Billinge *et al.*, 1996).

1.2.5 Dynamical disorder and symmetry lowering in silica

Silica (SiO_2) is the basis of window glass. It also comes in crystalline forms, the best known being quartz. The silicon atoms are tetrahedrally coordinated with oxygen. Since each oxygen has two silicon neighbors this forms into a continuous tetrahedral network. At low temperature silica forms the so-called α-quartz phase; on heating this transforms into

[3] It appears as a negative peak because of the negative neutron scattering length of Mn. The reason why will be clear after studying the detailed definition of the PDF in Chapter 3.

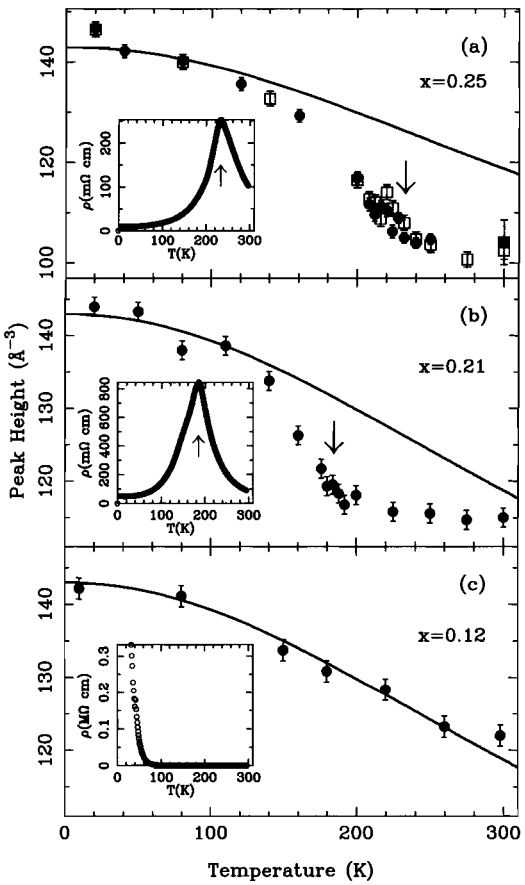

Figure 1.10. PDF peak height vs. temperature of the PDF peak at $r = 2.75$ Å in $La_{1-x}Ca_xMnO_3$. The solid lines show the expected decrease in peak height from increasing PDF peak-width due to enhanced thermal motion at higher temperature. In the two samples which have a MI transition (indicated by an arrow) there is an anomalous drop off in peak height indicating additional non-thermal disorder which is coming from polaron formation at high temperature. This PDF evidence was some of the most compelling supporting the view that polaron formation and electron–lattice interactions were important for understanding these CMR materials (Billinge *et al.*, 1996).

β-quartz, then HP-tridymite, then β-cristobalite before melting at 1727°C. These are all phases with slightly different crystal structures. If cooled quickly or under pressure yet more phases appear including, on fast cooling, the glass phase. These phase transitions have recently been studied using total scattering techniques which revealed unique information (Tucker *et al.*, 2000a,b; Keen and Dove, 1999; Keen, 1998). These studies show that that the old ideas of displacive vs. order–disorder transitions do not capture the whole truth of what is happening, at least in the transitions in these materials. This became

clear by studying the average structure *and* the local structure at the same time using total scattering methods. For example, in the phase transition in quartz at $T = 846$ K the Si–O bond length changes smoothly from 1.61 Å at low temperature to 1.586 Å above the transition. These bond lengths were obtained from the average structure using Rietveld refinement of neutron powder diffraction data. However, PDFs obtained from these same data showed that, over the same temperature range, the local Si–O bond evolved from 1.61 Å at low temperature to 1.62 Å at 1000 K. This modest increase in bond length was a result of the natural thermal expansion of the SiO_4 octahedra and in sharp contrast to the behavior of the average bond length. This is shown in Figure 1.11 that shows the Si–O bond length obtained from the PDF and from Rietveld on the same plot (Tucker *et al.*, 2000a,b). Both results were obtained from the same sample and, indeed, from the same sets

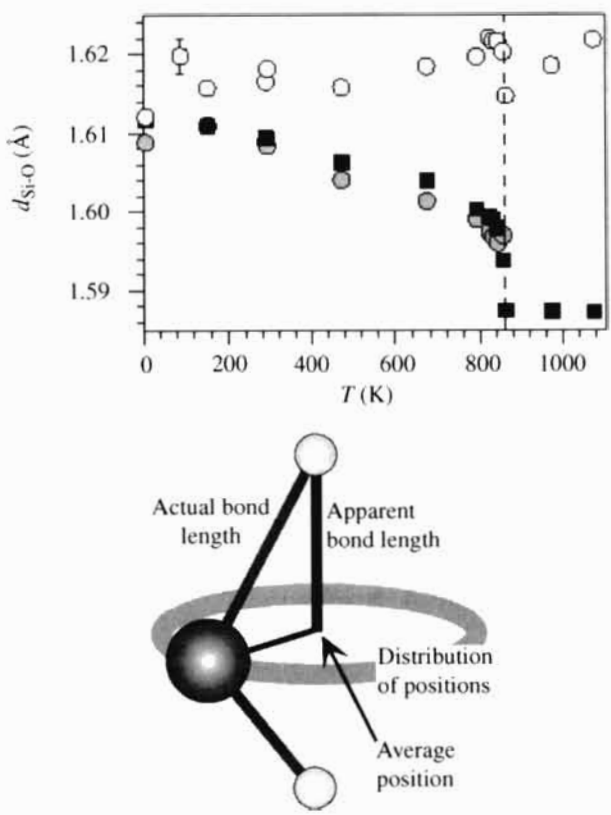

Figure 1.11. Si–O bond length in α-quartz vs. temperature determined from the average structure and from the PDF. The actual bond length increases modestly due to thermal expansion up to 1000 K as seen from the PDF measurement (○). The anomalous shortening of the Si–O bond evident in the average structure (■) comes about because of thermally induced rotations of the $Si–O_4$ tetrahedra about the Si–Si axis as shown in the lower part of the figure (Tucker *et al.*, 2000a, 2002).

of data. The reason for this observation is that, in the high temperature phase, the tetrahedra are dynamically rotating in such a way that the oxygen atom between the tetrahedra can rotate about the average bond axis. Consequently the Si–O–Si bond in the average structure is straight and the Si–O bond is therefore given by half the Si–Si distance. In reality the local bond angle for the Si–O–Si bond remains closer to 150° and the oxygen atom rotates around the average bond. This is illustrated in the bottom of Figure 1.11 (Tucker *et al.*, 2000a).

1.3. RESOURCES FOR LEARNING TOTAL SCATTERING AND PDF METHODS

A number of resources are available to help people get started using PDF and total scattering methods beyond reading references cited in this book. A web-page has been developed which contains useful programs, tutorials and links related to total scattering and PDF measurements as well as examples of scientific studies and recent papers that have been published. The web-page is at www.totalscattering.org. Useful programs can be downloaded from this website such as data analysis and modeling software described in this book. This software mostly comes with extensive documentation including tutorial examples to give new users experience in carrying out analyses. There are also online tutorials present on this web-page to help learn basic diffraction theory and to help understand the origin of diffuse scattering (Proffen *et al.*, 2001). Finally, from time-to-time PDF and total scattering workshops will be organized, for example, at major national meetings such as the annual meeting of the American Crystallographic Association. By registering your name and contact address at the www.totalscattering.org web-page you can be added to the total scattering mailing list where news about software developments, workshops and other relating to total scattering will be posted.

REFERENCES

Bardeen, J., Cooper, J.D. & Schrieffer, J.R. (1957) *Phys. Rev.*, **108**, 1175.

Billinge, S.J.L., DiFrancesco, R.G., Kwei, G.H., Neumeier, J.J. & Thompson, J.D. (1996) *Phys. Rev. Lett.*, **77**, 715.

Bozin, E.S., Billinge, S.J.L., Kwei, G.H. & Takagi, H. (1999) *Phys. Rev. B*, **59**, 4445.

Bozin, E.S., Billinge, S.J.L., Takagi, H. & Kwei, G.H. (2000) *Phys. Rev. Lett.*, **84**, 5856.

Egami, T. & Aur, S. (1987) *J. Non-Cryst. Solids*, **89**, 60.

Egami, T. & Billinge, S.J.L. (1994) *Prog. Mater. Sci.*, **38**, 359.

Egami, T. & Billinge, S.J.L. (1996) in *Physical Properties of High-Temperature Superconductors V*, Ed. Ginsberg, D.M., World Scientific, Tokyo, p. 265.

Egami, T., Dmowaski, W., He, Yi & Schwarz, R. (1998) *Met. Mater. Trans.*, **29A**, 1805.

Eshelby, J.D. (1956) Solid State Physics, Eds. Seitz, F. & Turnbull, D., Academic Press, New York, vol. **3**, p. 79.

Goodenough, J.B., Wold, A., Arnott, R.J. & Menyuk, N. (1961) *Phys. Rev.*, **124**, 373.

Jeong, I.-K., Mohiuddin-jacobs, F., Petkov, V. & Billinge, S.J.L. (2001) *Phys. Rev. B*, **63**, 205202.

Keen, D.A. (1998), in *Local Structure from Diffraction*, Eds. Billinge, S.J.L. & Thorpe M.F., Plenum Press, New York, p. 101.
Keen, D.A. & Dove, M.T. (1999) *J. Phys.: Condens. Matter*, **11**, 9263.
Louca, D. & Egami, T. (1997) *Phys. Rev. B*, **56**, R8475.
Mikkelson, J.C. & Boyce, J.B. (1982) *Phys. Rev. Lett.*, **49**, 1412.
Petkov, V., Jeong, I.-K., Chung, J.S., Thorpe, M.F., Kycia, S. & Billinge, S.J.L. (1999) *Phys. Rev. Lett.*, **83**, 4089.
Proffen, Th., DiFrancesco, R.G., Billinge, S.J.L., Brosha, E.L. & Kwei, G.H. (1999) *Phys. Rev. B*, **60**, 9973.
Proffen, Th., Neder, R.B. & Billinge, S.J.L. (2001) *J. Appl. Crystallogr.*, **34**, 767.
Toby, B.H., Egami, T., Jorgensen, J.D. & Subramanian, M.A. (1990) *Phys. Rev. Lett.*, **64**, 2414.
Tranquada, J.M., Sternlieb, B.J., Axe, J.D., Nakamura, Y. & Uchida, S. (1995) *Nature*, **375**, 561.
Tucker, M.G., Dove, M.T. & Keen, D.A. (2000a) *J. Phys. Condens. Matter*, **12**, L425.
Tucker, M.G., Dove, M.T. & Keen, D.A. (2000b) *J. Phys. Condens. Matter*, **12**, L723.
Tucker, M.G., Dove, M.T. & Keen, D.A. (2002), in *From Semiconductors to Proteins: Beyond the Average Structure*, Eds. Billinge, S.J.L. & Thope, M.F., Kluwer/Plenum, New York, p. 85.

SELECTED BIBLIOGRAPHY

The following books and review articles give traditional introductions to the PDF technique as applied to non-crystalline materials using conventional sources. They are useful resources since the mathematics and definitions do not change between amorphous and crystalline materials. For completeness, all the important relations are reproduced in later chapters of this book. Apart from Billinge and Thorpe (1998) which contains an overview of a number of different techniques for studying local structure, these books are quite out of date regarding X-ray sources, experiments and data modeling.

Billinge, S.J.L. & Thorpe, M.F., Eds. (1998) *Local Structure from Diffraction*, Plenum Press, New York.
Klug, H.P. & Alexander, L.E. (1974) *X-ray Diffraction Procedures*, 2nd Edition, Wiley, New York.
Wagner, C.N.J. (1978) Direct Methods for the Determination of Atomic-Scale Structure of Amorphous Solids (X-ray, Electron and Neutron Scattering), *J. Non-Cryst. Solids*, **31**, 1.
Warren, B.E. (1990) *X-ray Diffraction*, Dover, New York.
Waseda, Y. (1980) *The Structure of Non-crystalline Materials*, McGraw-Hill, New York.

Chapter 2

Crystallographic Analysis of Complex Materials

This Page Intentionally Left Blank

Chapter 2
Crystallographic Analysis of Complex Materials

2.1. THEORETICAL BACKGROUND

2.1.1 Scattering intensity

In diffraction experiments, one directs a beam or ray of particles at the sample (Figure 2.1), and measures the intensity of the scattered beam as a function of scattering angle, 2θ, and the wavelength of the probe. The procedures to carry out such measurements are discussed in Chapter 4. The task of the researcher is to analyze the intensity data and relate them to the structure or dynamics of the sample. The analysis is usually made in two stages. The first stage is to correct the observed intensity for secondary effects such as absorption and background, etc., to obtain a normalized intensity that can be theoretically analyzed. The second is to explain and numerically reproduce the normalized intensity using a structural model. These steps are discussed in Chapters 5 and 6. Before these subjects are introduced we will first present the theoretical basis in this chapter, and introduce the PDF method in the next chapter. From this chapter to Chapter 7 pages are crowded with equations that are sometimes long, but the meaning of each equation is relatively simple. They are all included in the software used in the analysis that can be downloaded to your computer.

X-rays and neutrons interact relatively weakly with atoms, which makes the measurement hard, since the scattered intensity is weak, but at the same time makes the data analysis easy. This should be contrasted to the case of electrons that interact with atoms more strongly, which makes the measurement easier but analysis harder. For this reason we focus on X-rays and neutrons in this book. Extension to electron scattering is

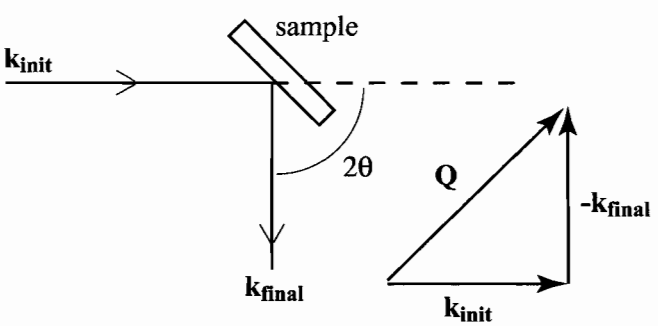

Figure 2.1. Geometry of the powder diffraction measurement and definition of the scattering vector, **Q**.

straightforward in most respects, but needs additional considerations at times. The readers should consult other books (e.g. see the bibliography at the end of this chapter) for this purpose.

The actual total intensity of the scattered X-ray or neutron beam, I_T, is composed of several parts,

$$I_T = I_C + I_{IC} + I_{MC} + I_{BG} \tag{2.1}$$

where I_C is the coherent scattering intensity, I_{IC} the incoherent scattering intensity, I_{MC} the multiple-scattering intensity, and I_{BG} the background intensity. The scattering intensity I_T is measured as a function of the scattering angle, 2θ, and the wavelength of the probe, λ. For *elastic* scattering the diffraction vector, **Q**, defined in Section 1.1.5 and Figure 2.1, has a magnitude

$$|\mathbf{Q}| = \frac{4\pi \sin\theta}{\lambda} \tag{2.2}$$

where λ is the wavelength of the scattered particle and $\theta = 2\theta/2$ where 2θ is the angle between the incident and diffracted beams. In the case of powder measurements the only relevant quantity is the *magnitude* of the diffraction vector, $Q = |\mathbf{Q}|$. We note that since $\sin\theta \leq 1$, the experimentally accessible range for Q is limited to less than $4\pi/\lambda$. For instance Cu K_α radiation, which is most widely used in laboratory X-ray facilities, has a wavelength of 1.54 Å. This means the range of Q is limited to about 8 $Å^{-1}$, while for most of the applications discussed in this book the Q range of ~ 30 $Å^{-1}$ is required. This is an important point that will be discussed in Chapter 3.

Incoherent scattering arises from Compton scattering in the case of X-rays and nuclear spin scattering in the case of neutrons. Multiple-scattering occurs mainly within the sample, but double scattering involving the sample and the environment can be significant. The background intensity here includes scattering without the sample, due to the sample holder, air, optical systems, etc. This is different from the so-called 'background' in crystallographic analysis, the intensity in-between the Bragg peaks, which includes diffuse scattering from the sample. In crystallographic analysis the 'background' is curve-fitted and discarded. But as we will see the diffuse scattering intensity contains a wealth of information about local structure, and in this context discarding the diffuse scattering amounts to throwing the baby out with the bathwater. The title of this book, *Underneath the Bragg Peaks*, implies the importance of the diffuse scattering intensity, which is usually overlooked in standard crystallographic analysis. Note that in the PDF method the true background intensity has to be independently measured, by carrying out a scattering measurement without a sample.

The information on structure and lattice dynamics is contained in the coherent scattering cross-section, $d\sigma_C/d\Omega$. Here $d\Omega$ is the solid angle that the detector subtends with the origin where the sample is located. The formalism of 'scattering cross-sections' is

introduced and defined more formally in Appendices 2.1 and 5.1.[1] The experimentally measured intensity of coherent scatting, I_C, is related to $d\sigma_C/d\Omega$, but is modified by absorption and polarization factors;

$$I_C = APC\frac{d\sigma_C}{d\Omega} \tag{2.3}$$

The absorption factor, A, depends on the geometry of the sample and the nature of the scattering particle. More detailed discussions on this factor are given in Chapter 5. The electric polarization factor for X-rays and spin polarization factor for neutrons are well known, and will not be repeated here (e.g. see Warren (1990) and Bacon (1975), respectively). C is the normalization factor needed to express $d\sigma_C/d\Omega$ in the appropriate units of intensity per atom. In the following we focus on $d\sigma_C/d\Omega$, and discuss how to obtain the structural information from this quantity.

2.1.2 Sample scattering amplitude

For the most part of this book, we need a surprisingly small amount of basic theoretical background. The only equation that truly needs to be understood is that for the *sample scattering amplitude*,

$$\Psi(\mathbf{Q}) = \frac{1}{\langle b\rangle}\sum_{\nu} b_\nu \, e^{i\mathbf{Q}\mathbf{R}_\nu} \tag{2.4}$$

where $\mathbf{Q}$ is the diffraction vector or the momentum transfer, and is defined by[2]

$$\mathbf{Q} = \mathbf{k}_{\text{init}} - \mathbf{k}_{\text{final}} \tag{2.5}$$

where $\mathbf{k}_{\text{init}}(|\mathbf{k}_{\text{init}}| = 2\pi/\lambda_{\text{init}})$ is the wavevector of the incoming beam and $\mathbf{k}_{\text{final}}(|\mathbf{k}_{\text{final}}| = 2\pi/\lambda_{\text{final}})$ is the wavevector of the scattered beam (Figure 2.1). For elastic scattering $\lambda_{\text{init}} = \lambda_{\text{final}}$, thus the magnitude of $\mathbf{Q}$ is given by Eq. 2.2,

$$Q = |\mathbf{Q}| = 2k\sin\theta = \frac{4\pi\sin\theta}{\lambda} \tag{2.6}$$

where $k = |\mathbf{k}_{\text{init}}| = |\mathbf{k}_{\text{final}}|$.

In Eq. 2.4, $\mathbf{R}_\nu$ defines the position of the νth atom, b_ν is the scattering amplitude of the atom ν, i.e. a measure of how strongly it scatters, and $\langle\cdots\rangle$ represents a compositional

[1] The concept of the scattering cross-section is a very useful one which relates a sample dependent property (the probability of a particular scattering event occurring) to a real experimental value (the number of detected counts in a detector). For those readers unfamiliar with it, we recommend spending a short time to understand and get comfortable with the basic ideas (see Section A5.1.1 in Appendix 5.1 as well as standard textbooks). Do not be put off by the mathematical looking nature of the expressions, an unfortunate legacy of its origin in theoretical physics. The ideas behind the scattering cross-section are highly intuitive and physical.

[2] Note that in some textbooks $\mathbf{Q}$ is defined as $\mathbf{Q} = \mathbf{k}_{\text{final}} - \mathbf{k}_{\text{init}}$, i.e. with the opposite sign as used here. This is fine, though in that case Eq. 2.4 becomes $\Psi(\mathbf{Q}) = (1/\langle b\rangle)\sum_\nu b_\nu \, e^{-i\mathbf{Q}\mathbf{R}_\nu}$ and Eq. 2.12 becomes $\mathbf{Q} = -\mathbf{K}$.

average,

$$\langle b \rangle = \frac{1}{N} \sum_{\nu} b_{\nu} = \sum_{\alpha} c_{\alpha} b_{\alpha} \tag{2.7}$$

Here the sum over ν is over every atom in the sample. In practice, this is more conveniently expressed as a sum, α, over atomic species where c_{α} is the atomic fraction and b_{α} is the scattering amplitude of the element α, as indicated in Eq. 2.7.

For X-rays, b_{ν} depends fairly strongly on Q and is usually denoted as $f(Q)$, but for neutrons b_{ν} is independent of Q. This difference reflects the quite different spatial spread of the scatterer, electron density for X-rays and nucleus for neutrons. In solids atoms are not static, but are vibrating due to atomic vibration. Consequently $\mathbf{R}_{\nu}$ changes with time, and $\Psi(\mathbf{Q})$ really is a function of time,

$$\Psi(\mathbf{Q}, t) = \frac{1}{\langle b \rangle} \sum_{\nu} b_{\nu} \, \mathrm{e}^{\mathrm{i}\mathbf{Q}\mathbf{R}_{\nu}(t)} \tag{2.8}$$

However, in the following we suppress the variable t, unless noted, for the sake of simplicity. The time-dependent structure factor will be discussed in the next section when we introduce the *Debye–Waller approximation*, and in Chapter 7 in relation to *inelastic scattering*.

The derivation of Eq. 2.4 is given in Appendix 2.2 in two different ways, one intuitive and the other more formal. In deriving this result, only single scattering of the incident beam with the atoms was considered and coherent multiple-scattering was neglected. This simplification is known as the *kinematic* approximation, and is accurate only when the scattering is weak and the structural coherence is not too large as in powders. In highly perfect large crystals, coherent multiple-scattering often is as important as single scattering, and they together can create dramatic effects such as anomalous transmission. In such a case the diffraction phenomena can be described accurately only by the *dynamical* scattering theory. In this book we do not enter this subject, since we are concerned with imperfect crystals that do not require dynamical theories.

In general, the Fourier transform of a function $f(\mathbf{x})$ is given by $F(\mathbf{Q}) = \sum_{j=-\infty}^{\infty} f(\mathbf{x}_j) \, \mathrm{e}^{\mathrm{i}\mathbf{k}\mathbf{x}_j}$. Upon inspection of Eq. 2.4 it is evident that $\Psi(\mathbf{Q})$ is just the Fourier transform of the atomic position, $\mathbf{R}_{\nu}$. The structural information is contained in the phase of the exponential factor. Thus, if we know this scattering amplitude we can determine the atomic structure exactly, merely by taking the inverse Fourier transformation of $\Psi(\mathbf{Q})$. Crystallography would be a trivial task if that were possible. However, as is well known we cannot directly measure the scattered *amplitude* $\Psi(\mathbf{Q})$ but only the *intensity* of the diffracted beam, which is directly related to the square of the magnitude of $\Psi(\mathbf{Q})$,

i.e. $|\Psi(\mathbf{Q})|^2$. In detail,

$$\frac{d\sigma_C(\mathbf{Q})}{d\Omega} = \frac{\langle b\rangle^2}{N}|\Psi(\mathbf{Q})|^2 = \frac{1}{N}\sum_{\nu,\mu} b_\nu b_\mu \, e^{i\mathbf{Q}(\mathbf{R}_\nu - \mathbf{R}_\mu)}$$

$$I(\mathbf{Q}) = \frac{d\sigma_C(\mathbf{Q})}{d\Omega} + \langle b\rangle^2 - \langle b^2\rangle \tag{2.9}$$

$$S(\mathbf{Q}) = \frac{I(\mathbf{Q})}{\langle b\rangle^2}$$

where $S(\mathbf{Q})$ is called the *total scattering structure function*, or often just *structure function*, which converges to unity at large $\mathbf{Q}$. In the liquid and glass community $S(\mathbf{Q})$, an *intensity*, is usually, and confusingly, called the *structure factor*, while in the crystallographic community the term structure factor scales the *amplitude*, $\Psi(\mathbf{Q})$, (Eq. 2.4). The crystallographic structure factor is defined in Eq. 2.15. Also, in the inelastic scattering community $S(\mathbf{Q}, \omega)$, discussed in Chapter 7, is called the *dynamic structure factor*. The conflicting naming in different communities has been a source of much confusion. In order to avoid such confusion in this book we use the term *sample scattering amplitude* to define $\Psi(\mathbf{Q})$ and call $S(\mathbf{Q})$ the *structure function*. The term $\langle b\rangle^2 - \langle b^2\rangle$ in the expression for $S(\mathbf{Q})$ is called the Laue monotonic scattering, and is needed for convenience simply because $d\sigma_C/d\Omega$ approaches $\langle b^2\rangle$ at large Q, while we want to make $S(\mathbf{Q})$ approach unity at large Q. Actually it is possible to define $S(\mathbf{Q})$ differently by normalizing with respect to $\langle b^2\rangle$ rather than $\langle b\rangle^2$. In this case the Laue term is no longer necessary.

Since the measured intensity is proportional to the *square* of the scattering amplitude, $\Psi(\mathbf{Q})$, the phase information of $\Psi(\mathbf{Q})$ is lost. All that survives is the phase difference between scattering events from different atoms. Specialized indirect methods of recovering the lost phase information exist that make use of dynamical diffraction from perfect single crystals, substitution of heavy atoms at known locations in molecules, and using anomalous diffraction, for example. These are extraordinarily powerful techniques that have revolutionized the structure determination of solids and small and large molecular structures. However, they are time consuming and difficult, and unwarranted or impossible in the structure determination of most inorganic materials. These techniques will not be discussed here (see, for example, Giacovazzo *et al.* (1992) or Woolfson (1997)). In the absence of this phase information, the structure must be reconstructed by creating a model structure and comparing the calculated scattering intensity from this structure with the measured structure function. That is why the structure determination is not a trivial task, and sometimes involves extensive analysis and modeling.

For a perfectly periodic lattice (a crystal) the scattering amplitude becomes extremely simple because of the lattice sum formula. For a monotonic crystal in one-dimension,

$R_\nu = \nu a$, where a is the lattice repeat distance, and we get

$$\lim_{N\to\infty}\left(\frac{1}{N}\sum_{\nu=1}^{N} e^{iQ\nu a}\right) = \delta(Q - na^*) \tag{2.10}$$

where $\delta(z)$ denotes the Dirac delta-function, n is an integer and $a^* = 2\pi/a$. Derivation of this equation is also given in the standard textbooks. Thus in three-dimensions the scattering occurs only at a discrete set of wavevectors, **K**, forming the reciprocal lattice,

$$\mathbf{K} = h\mathbf{a}^* + k\mathbf{b}^* + l\mathbf{c}^* \tag{2.11}$$

where $\mathbf{a}^*$, $\mathbf{b}^*$, $\mathbf{c}^*$ are the reciprocal lattice vectors. The Bragg condition for allowed scattering now restricts **Q** to being equal to **K**:

$$\mathbf{Q} = \mathbf{K} \tag{2.12}$$

For more than one atom in the unit cell we can denote

$$\langle \mathbf{R}_\nu \rangle - \langle \mathbf{R}_\mu \rangle = \mathbf{R}_k + \mathbf{r}_n - \mathbf{r}_m \tag{2.13}$$

where $\mathbf{R}_k$ specifies the separation between the unit cells, and $\mathbf{r}_n$ and $\mathbf{r}_m$ are the position vectors of the nth and mth atoms within the unit cell. Then, from Eqs. 2.9 and 2.13 we get

$$\frac{d\sigma_C(\mathbf{Q})}{d\Omega} = \frac{\delta(\mathbf{Q}-\mathbf{K})}{n_c}\sum_{n,m} b_n b_m e^{i\mathbf{Q}(\mathbf{r}_n-\mathbf{r}_m)} = \frac{\delta(\mathbf{Q}-\mathbf{K})}{n_c}\sum_{n,m} b_n b_m e^{i\mathbf{K}_{hkl}(\mathbf{r}_n-\mathbf{r}_m)}$$

$$= \frac{\delta(\mathbf{Q}-\mathbf{K})}{n_c}\left|\sum_n b_n e^{i\mathbf{K}_{hkl}(\mathbf{r}_n)}\right|^2 \tag{2.14}$$

where the sum over n is now taken only over all the atoms in the unit cell, n_c. The term

$$F_{hkl} = \sum_n b_n e^{i\mathbf{K}_{hkl}(\mathbf{r}_n)} \tag{2.15}$$

is the well-known *crystallographic structure factor* that gives the intensity of the Bragg peak located at $\mathbf{Q} = \mathbf{K}_{hkl}$ where h, k and l are the integers defining the particular reciprocal lattice vector in Eq. 2.11. Thus by determining **K**, or the *position of the Bragg peak* in the reciprocal space, the *lattice constants and symmetry* are directly known. The *intensity of the Bragg peak*, Eq. 2.14, translates to the *atomic positions within the unit cell.* An example of the structure function $S(Q)$ for a crystalline powder sample ($LaMnO_3$) is shown in Figure 3.1(a).

The enormous simplification in the problem that comes about when the sample is crystalline is evident by comparing Eqs. 2.9 and 2.14. In the former, general, case the sums run over all the atoms in the sample; in the latter, crystalline case, the double sum runs only over the atoms in the unit cell. It is this more complicated situation, when the structure is not perfectly periodic and Eq. 2.14 no longer strictly applies, that is the main subject of this book. Furthermore, in the actual measurement the intensity is modified by absorption,

polarization and other factors. The total intensity of the scattered beam includes contributions from the multiple-scattering, inelastic scattering, and background due to sample holders and containers. These effects will be discussed in stages throughout this book.

2.1.3 Debye–Waller approximation

As has been repeated numerous times, the assumption of perfect periodicity is the centerpiece for crystallography. However, a crystal structure is never perfectly periodic even when the crystal is perfect, because atoms are vibrating due either to thermal or zero-point quantum vibrations. The Debye–Waller (DW) approximation was developed to incorporate the effect of lattice vibrations, and is an integral part of the crystallographic analysis.

We will start with the time-dependent scattering amplitude, Eq. 2.8. Since the position of the atom, **R**, changes with time, it is convenient to describe it in terms of the deviation from the average position, $\mathbf{R}(t) = \mathbf{u}(t) + \langle\langle R \rangle\rangle$, where **u** is the deviation and $\langle\langle \mathbf{R} \rangle\rangle$ is the time-averaged position of the atom. The subscript ν is suppressed for simplicity. Eq. 2.8 will now be, after averaging over time (denoted by $\langle\langle \cdots \rangle\rangle$),

$$\begin{aligned} \langle\langle e^{i\mathbf{QR}} \rangle\rangle &= \langle\langle e^{i\mathbf{Q}(\langle\langle \mathbf{R} \rangle\rangle + \mathbf{u})} \rangle\rangle = e^{i\mathbf{Q}\langle\langle \mathbf{R} \rangle\rangle} \langle\langle e^{i\mathbf{Qu}} \rangle\rangle \\ &= e^{i\mathbf{Q}\langle\langle \mathbf{R} \rangle\rangle} \left[1 + i\langle\langle \mathbf{Qu} \rangle\rangle - \frac{1}{2}\langle\langle (\mathbf{Qu})^2 \rangle\rangle + \cdots \right] \end{aligned} \tag{2.16}$$

Since $\langle\langle \mathbf{Qu} \rangle\rangle = \mathbf{Q}\langle\langle \mathbf{u} \rangle\rangle = 0$ by definition, if **u** is small enough this approximates rather nicely to the expression for a Gaussian function, and we get,

$$\langle\langle e^{i\mathbf{QR}} \rangle\rangle \approx e^{i\mathbf{Q}\langle\langle \mathbf{R} \rangle\rangle} e^{-W} = e^{i\mathbf{Q}\langle\langle \mathbf{R} \rangle\rangle} e^{-\frac{1}{2}Q^2\langle\langle u^2 \rangle\rangle} \tag{2.17}$$

where e^{-W} is called the Debye–Waller factor. It can also be shown (Warren, 1990) that if the probability distribution of **u** is Gaussian then this Debye–Waller approximation is also exact even if **u** is not small. It is clear from this that the effect of lattice vibrations is not to broaden out the Bragg peaks. *The Bragg peaks remain perfectly sharp but their intensity is diminished* by the factor $\exp(-\frac{1}{2}Q^2\langle u^2 \rangle)$. Thus if the vibrational amplitude of each atom is equal, the structure function becomes

$$\begin{aligned} S(\mathbf{Q}) &= e^{-\langle\langle u^2 \rangle\rangle Q^2} S_0(\mathbf{Q}) + 1 - e^{-\langle\langle u^2 \rangle\rangle Q^2} \\ S_0(\mathbf{Q}) &= \frac{\delta(\mathbf{Q} - \mathbf{K})}{\langle b \rangle^2} \left[\sum_{\nu,\mu} b_\nu b_\mu \, e^{i\mathbf{Q}(\langle\langle \mathbf{R}_\nu \rangle\rangle - \langle\langle \mathbf{R}_\mu \rangle\rangle)} - \langle b^2 \rangle + \langle b \rangle^2 \right] \end{aligned} \tag{2.18}$$

We will discuss in Chapter 7 why the term $[1 - \exp(-\langle\langle u^2 \rangle\rangle Q^2)]$ was added in Eq. 2.18 (see Eq. 7.24). This term approximately describes the diffuse inelastic scattering intensity due to phonons.

It should be noted that the assumption in the approximation in Eq. 2.17 is that the distribution of u is described as a Gaussian distribution. Whenever this assumption is violated the DW approximation cannot be accurate. The structure function of the average lattice sites, $S_0(Q)$, is composed of delta-functions that spreads over the entire Q-space. However, because of the Debye–Waller factor the intensity decreases with increasing Q, and the Bragg peaks practically disappear beyond certain values of Q.

2.1.4 Diffuse scattering

The Debye–Waller factor reduces the intensities of the Bragg scattering (Eq. 2.18) but where does the lost intensity go? It appears in between the Bragg peaks and becomes what is called *diffuse scattering*. The diffuse intensity is often hard to see and measure. It is widely spread over Q-space, compared to the Bragg peaks that are strongly confined at reciprocal lattice points in Q-space. However, a significant proportion of the total integrated intensity can reside in the diffuse scattering. Indeed, in the high-Q region where the Bragg peaks are small due to the Debye–Waller factor, the scattering is predominantly diffuse.

In powder measurements, the diffuse scattering only weakly depends upon $\mathbf{Q}$ and forms a continuous background which is usually discarded in crystallographic analyses. However, the diffuse scattering provides important information regarding the local deviations from the average structure. The subtitle of this book, *Underneath the Bragg Peaks*, is meant to emphasize the importance of this diffuse scattering intensity which is usually not given the attention it deserves.

In this section, we will explain how the diffuse scattering arises and what information it carries. This is a conventional treatment and a full understanding of it is not needed to understand the PDF. It is included for those readers who are comfortable with scattering equations and want an intuitive idea of how defects in crystals affect the measured scattering. One of the beneficial features of PDF analysis is that the *structural information* in the diffuse scattering appears in a direct and intuitive way, circumventing the need to grapple with the mathematics of diffuse scattering presented here. First time readers can skip directly to Section 2.2 without loss of continuity. Ultimately, it is very helpful to develop an understanding of the relationship between defects and diffuse scattering, from the equations presented here. It is also possible to develop an intuitive understanding of this relationship using the online diffraction tutorials at http://www.totalscattering.org. These allow the user to calculate the diffuse scattering patterns interactively from different arrangements of atoms and defects within simulated crystals.

Here we consider the diffuse scattering in a crystalline material. The starting point is again the scattering amplitude, Eq. 2.4. We assume that the position of the νth atom, $\mathbf{R}_\nu$, deviates from the ideal crystallographic site, $\mathbf{R}^0_\nu$, by $\mathbf{u}_\nu$;

$$\mathbf{R}_\nu = \mathbf{R}^0_\nu + \mathbf{u}_\nu \tag{2.19}$$

Thus the scattering amplitude is

$$\Psi(\mathbf{Q}) = \frac{1}{\langle b \rangle} \sum_{\nu} \mathrm{b}_{\nu} \, \mathrm{e}^{\mathrm{i}\mathbf{Q}\mathbf{R}_{\nu}} = \frac{1}{\langle b \rangle} \sum_{\nu} \mathrm{b}_{\nu} \, \mathrm{e}^{\mathrm{i}\mathbf{Q}\mathbf{R}_{\nu}^{0}} [1 + \mathrm{i}\mathbf{Q}\mathbf{u}_{\nu} + \cdots] \tag{2.20}$$

where we have made the same expansion as we did in Eq. 2.16. We can then consider the intensity contributions to $\Psi(\mathbf{Q})$ term by term:

$$\Psi(\mathbf{Q}) = \Psi_1(\mathbf{Q}) + \Psi_2(\mathbf{Q}) + \cdots \tag{2.21}$$

where

$$\Psi_1(\mathbf{Q}) = \frac{1}{\langle b \rangle} \sum_{\nu} b_{\nu} \, \mathrm{e}^{\mathrm{i}\mathbf{Q}\mathbf{R}_{\nu}^{0}}, \qquad \Psi_2(\mathbf{Q}) = \frac{1}{\langle b \rangle} \sum_{\nu} \mathrm{i}\mathbf{Q}\mathbf{u}_{\nu} b_{\nu} \, \mathrm{e}^{\mathrm{i}\mathbf{Q}\mathbf{R}_{\nu}^{0}} \tag{2.22}$$

and so on. The first term describes the Bragg scattering. If we apply volume averaging to the second term in the bracket of Eq. 2.20, just as in Eq. 2.16, it disappears because, by definition, $\langle\langle u \rangle\rangle = 0$. However, this kind of mean-field approximation as we discussed in Chapter 1 is a case of throwing the baby out with the bathwater. Actually if we examine Eq. 2.22, we see that $\Psi_2(\mathbf{Q})$ is not zero when these deviations are locally correlated. This can be understood by applying the Fourier expansion to $\mathbf{u}_{\nu}$,

$$\mathbf{u}_{\nu}(\mathbf{R}_{\nu}^{0}) = \frac{1}{\sqrt{N}} \sum_{\mathbf{q}} \mathbf{u}_{\mathbf{q}} \, \mathrm{e}^{\mathrm{i}\mathbf{q}\mathbf{R}_{\nu}^{0}} \tag{2.23}$$

Then the second term in Eq. 2.22 becomes

$$\Psi_2(\mathbf{Q}) = \frac{\mathrm{i}}{\langle b \rangle} \sum_{\nu} b_{\nu} \, \mathrm{e}^{\mathrm{i}\mathbf{Q}\mathbf{R}_{\nu}^{0}} \mathbf{Q}\mathbf{u}_{\nu} = \frac{\mathrm{i}}{\sqrt{N}\langle b \rangle} \sum_{\nu,q} b_{\nu} \mathbf{Q}\mathbf{u}_{q} \, \mathrm{e}^{\mathrm{i}(\mathbf{Q}-\mathbf{q})\mathbf{R}_{\nu}^{0}} \tag{2.24}$$

Again the lattice sum (Eq. 2.10) results in

$$\Psi_2(\mathbf{Q}) = \frac{i\sqrt{N}}{\langle b \rangle} \sum_{q} g(\mathbf{K})(\mathbf{Q}\mathbf{u}_{q}) \delta(\mathbf{Q} - \mathbf{q} - \mathbf{K}) \tag{2.25}$$

where $g(\mathbf{K}) = (1/N) \sum_n b_n \, \mathrm{e}^{\mathrm{i}\mathbf{K}\mathbf{R}_{n}^{0}}$, with n running over atoms in the unit cell. As before, $\mathbf{K}$ is the reciprocal lattice vector, Eq. 2.11. The intensity will be

$$I(\mathbf{Q}) = I_{\mathrm{BG}}(\mathbf{Q}) + I_{\mathrm{D}}(\mathbf{Q}) + \cdots \tag{2.26}$$

$$I_{\mathrm{D}}(\mathbf{Q}) = \frac{\langle b \rangle^2}{N} |\Psi_2(\mathbf{Q})|^2 = |g(\mathbf{K})|^2 |\mathbf{Q}\mathbf{u}_{\mathbf{Q}-\mathbf{K}}|^2$$

where $I_{\mathrm{BG}}(\mathbf{Q})$ represents the Bragg diffraction intensity and $I_{\mathrm{D}}(\mathbf{Q})$ the diffuse scattering intensity. The cross-terms between Ψ_1 and Ψ_2 vanish because of the two different δ-functions involved. While the Bragg peak appears at the reciprocal lattice point where $\mathbf{Q} = \mathbf{K}$, diffuse scattering appears at $\mathbf{Q} = \mathbf{K} + \mathbf{q}$, at a point separated by $\mathbf{q}$ from the Bragg peak. If there is only one $\mathbf{q}$ value for which $\mathbf{u}_{\mathbf{q}}$ is non-zero, we have a modulated structure with the wave vector $\mathbf{q}$. If the deviations are local, a range of $\mathbf{q}$ vectors are needed to

describe the structure. For instance, if the deviation occurs only at one atomic site, or delta-function in real space, then its Fourier transform covers the entire Q-space. That is why the scattering from a local object results in broadly spread diffuse scattering.

An example of diffuse scattering from a single crystal is shown in Figure 2.2. The most common diffuse scattering is due to thermal vibration of atoms, and is called *thermal diffuse scattering* (TDS). For a *simple monatomic solid* the amplitude of thermal vibration is given in terms of the phonon density,

$$\langle |\mathbf{Q}\mathbf{u}_\mathbf{q}|^2 \rangle = \frac{\hbar}{2M} \sum_j \frac{|\mathbf{Q}\boldsymbol{\epsilon}_j(\mathbf{q})|^2}{\omega_j(\mathbf{q})} \left\{ n_j(\mathbf{q}) + \frac{1}{2} \right\} \tag{2.27}$$

where M is the atomic mass, $j = 1, 2, 3$ indexes the three modes with polarization vector $\boldsymbol{\epsilon}_j(\mathbf{q})$, $\omega_j(\mathbf{q})$ is the frequency of the phonon and $n_j(\mathbf{q})$ is the phonon density,

$$n_j(\mathbf{q}) = \frac{1}{e^{\hbar\omega_j(\mathbf{q})/kT} - 1} \tag{2.28}$$

This result is described in greater detail in the books on lattice vibrations (see bibliography). This result is reintroduced in Chapter 7 that deals with inelastic scattering.

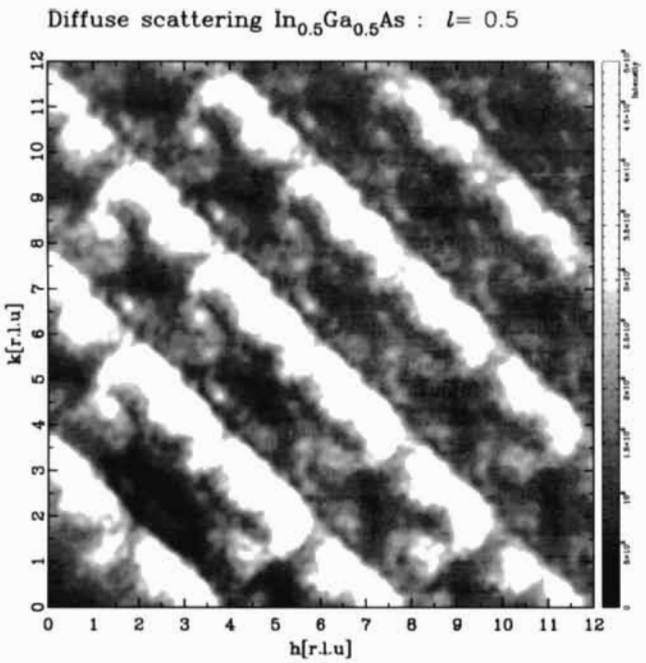

Figure 2.2. Example of diffuse scattering calculated for the (hk0.5) plane of reciprocal space is shown for the case of an $In_{0.5}Ga_{0.5}As$ alloy. Bright indicates strong intensity, dark weak intensity. Units are reciprocal lattice units (Jeong et al. 2001).

If the spectrometer has enough energy resolution to resolve phonon energy the equations developed in Chapter 7 describe the inelastic scattering intensity. On the other hand, in the usual powder diffraction experiment the diffractometer has no energy discrimination, so that Eqs. 2.27 and 2.28 are sufficient to describe the TDS.

Let us examine the case when q is sufficiently small and T is large so that $\hbar\omega_j(q) \ll kT$. In this limit we are considering the long wavelength sound waves propagating in the solid:

$$\omega_j(\mathbf{q}) = c_j|\mathbf{q}| \tag{2.29}$$

In this case,

$$\langle|\mathbf{Q}\mathbf{u}_\mathbf{q}|^2\rangle \approx \frac{1}{2M}\sum_j \frac{|\mathbf{Q}\boldsymbol{\epsilon}_j(\mathbf{q})|^2}{Q^2}\frac{Q^2}{q^2}\frac{kT}{c_j^2} \tag{2.30}$$

Thus the TDS intensity is proportional to T. From Eq. 2.27 it is clear that when $\mathbf{q}$ is parallel to $\mathbf{Q}$ only the longitudinal mode ($\boldsymbol{\epsilon}\|\mathbf{q}$) is observed, while when $\mathbf{q}$ is perpendicular to $\mathbf{Q}$ only the transverse mode ($\boldsymbol{\epsilon} \perp \mathbf{q}$) is observed. The TDS intensity in each case depends only on the sound velocity of each mode. Since the TDS intensity is proportional to q^{-2} and diverges toward $q = 0$, it is strong only around the Bragg peak. The TDS pattern around each Bragg peak is similar, but its intensity increases with Q as Q^2. This is a common characteristic of *displacive* deviations. The local deviation may not take the form of local displacement, but atomic substitution, as in the case of alloying. In this case the diffuse intensity does not increase with increasing Q and is similar for all the Bragg peaks, if it is corrected for the atomic scattering factor and the Debye–Waller factor. For a multi-component solid the expression of the phonon intensity becomes more complex. This is discussed in Chapter 7.

Another important class of diffuse scattering is called *Huang scattering* (Huang, 1947; Borie, 1957, 1959, 1961), and originates from extended structural defects such as the strain fields around vacancies and dislocations. The strain field in a solid can also be Fourier transformed as in Eq. 2.23, and results in the diffuse scattering (Eq. 2.26). The screened strain field from a point source,

$$u_\mathrm{p}(r) = u_0\frac{\mathrm{e}^{-r/\lambda}}{r^2} \tag{2.31}$$

yields the Fourier transform,

$$u_\mathrm{p}(q) = \frac{u_0}{\mathrm{i}q - (1/\lambda)} \approx \frac{u_0}{\mathrm{i}q} \tag{2.32}$$

resulting in a q^{-2} power law for the intensity when substituted in Eq. 2.26, i.e. the diffuse intensity falls off as $1/q^2$ from each Bragg position as with the TDS. Note that the strain field (Eq. 2.31) is not accurate when r is comparable to the atomic distance, at the core of the defect. Indeed it diverges at $r = 0$, while such divergence is unphysical. However,

the volume of the defect core is small, and its contribution to the Fourier transform is negligibly small.

For general defects, most of the defect can be described as a distribution of point defects and the strain field due to the defect can be expanded in terms of Eq. 2.31 as

$$u(\mathbf{r}) = \int v(\mathbf{r} - \mathbf{r}')u_p(\mathbf{r}')d\mathbf{r}' \tag{2.33}$$

Its Fourier transform is the product of Eq. 2.32 and the form factor, which is the Fourier transform of $v(\mathbf{r})$.

$$u(\mathbf{q}) = v(\mathbf{q})u_p(\mathbf{q}) \tag{2.34}$$

If the defect is localized, the form factor $v(\mathbf{q})$ does not depend too strongly on q, so that the total diffuse scattering follows the q^{-2} law. Thus the Huang scattering has a similar q dependence as the TDS. They can be differentiated only by studying their temperature dependence, since the Huang scattering is usually independent of temperature. On the other hand, if the defect is spatially extended, the form factor itself may be described by a power law, $v(q) \sim q^{-s}$. Then the total intensity will follow a $q^{-(2+s)}$ power law. In general, the diffuse scattering intensity follows some power law for small q, $q^{-\alpha}$, and the power index α may be related to the effective dimensionality (fractal dimension) of the object (Sinha *et al.*, 1991).

2.2. CRYSTALLOGRAPHIC ANALYSIS

2.2.1 Rietveld refinement method

In the classical method of crystallographic data analysis each Bragg peak is isolated, a table of the position and integrated intensity for each peak is produced, and the fitting to the calculated position and intensity attempted. This is still the approach used in single crystal structure determinations, though the process is fully automated by computer. However, this approach severely limits the application of powder diffraction to solving crystal structures because as structures get more complicated, and as Q (or 2θ) increase, the Bragg peaks get closer together and begin to overlap each other. Structure determination (of unknown structures) from powder diffraction is growing in importance though is not preferred if single crystals are available. However, powder diffraction is very important in refining structural parameters from known structures. A prior guess at the structural model is made. Then the positions and relative intensities of the Bragg peaks are known. In the *Rietveld method* (Rietveld, 1969) the whole pattern of diffracted intensity, the diffraction profile, as a function of the diffraction angle 2θ is calculated for the model. This includes modifications to the profile due to experimental effects such as the peak shape, absorption, polarization correction, the Debye–Waller factor, sample geometry, and the background. The calculated intensity profile, $I_{calc}(\mathbf{Q})$, is compared to the data, and each parameter of

the model is refined to obtain the best-fit structural model. For this purpose the R-factor (R-factor derives from its name, the *residuals function*) defined as the difference between the model and experiment,

$$R = \frac{\int [I_{\text{meas}}(Q) - I_{\text{calc}}(Q)]^2 \mathrm{d}Q}{\int [I_{\text{meas}}(Q)]^2 \mathrm{d}Q} \tag{2.35}$$

is minimized in a procedure of least square fitting. Ideally R should become zero, but because of various errors it remains non-zero. The residual value of R indicates the quality of the fit. Usually a R-value of a few % is considered to represent excellent fitting, while a value such as 10% represents rather poor fitting. Other R-factors can also be defined and are used. A common one is the weighted profile R-factor (R_{wp}) in which the statistical significance of each data-point is taken into account by weighting its contribution to the residuals function. It is defined as

$$R_{\text{wp}} = \frac{\int \left(\frac{1}{\sigma(Q)}\right)^2 [I_{\text{meas}}(Q) - I_{\text{calc}}(Q)]^2 \mathrm{d}Q}{\int \frac{I_{\text{meas}}(Q)^2}{\sigma(Q)^2} \mathrm{d}Q} \tag{2.36}$$

where $\sigma(Q)$ is the estimated random error on each data-point at the level of one standard deviation.

In all current standard Rietveld codes any diffuse scattering is dealt with somewhat arbitrarily. If it is widely spread in Q-space, it will be removed with the arbitrary background subtraction. If it is sharply peaked at Bragg peaks (for example TDS) it may be included in part as contributing to the Bragg intensity, or it may not be fitted and give rise to a larger R-value. In the high-Q region of the pattern, strongly overlapping Bragg peaks generally mean that even the diffuse scattering peaked at Bragg peaks may be removed by the background function. Recently, attempts have been made to extract explicit lattice dynamical information from the 'background' function by treating it as thermal diffuse scattering (Lawson *et al.*, 2000). More of these kinds of developments can be expected in the future.

When the Rietveld method was proposed it met with strong skepticism. However, it is more amenable to modern computers, and with the progress of computer technology it gained popularity. Its power was proven in many instances, including the early days of research on high-temperature superconductors. Whenever a new superconducting compound was discovered the Rietveld method was used to determine its structure. Today it is the standard method of data analysis in powder diffraction. It may be interesting to compare this history with the short history of the use of the PDF method for crystalline materials. It takes a long time for a new method to become developed enough, and widely enough used, to be trusted and accepted. For the method to be widely used the availability

of standard software is crucial. There are a wide variety of Rietveld programs available (for example, see the programs section of the International Union of Crystallographers (IUCr); web-page: http://www.iucr.org), some of the most commonly used are GSAS (Larson and Von Dreele, 2000), DBWS (Wiles and Young, 1981) and FULLPROF.

2.2.2 Single crystal Fourier (Patterson) analysis

In single crystal scattering studies, the Bragg peak intensities are sometimes Fourier transformed. This results in a periodic real-space pair-correlation function known as the crystallographic Patterson function, or just *Patterson function* (Patterson, 1934). Of more interest to us is to generalize this to the case where the atomic density is continuous, or not periodic.

First we consider the relationship between the real-space atomic density and the scattering amplitude. Consider the case where the atomic density of the material under study is not described by a periodic distribution of delta functions but by the continuous density, $\rho(\mathbf{r})$. In this case, Eq. 2.4 becomes

$$\Psi(\mathbf{Q}) = \frac{1}{\rho_0 V} \int \rho(\mathbf{r}) e^{i\mathbf{Q}\mathbf{r}} d\mathbf{r} \tag{2.37}$$

where ρ_0 is the average number density of the scatterers. The Fourier back-transform of $\Psi(\mathbf{Q})$ will give $\rho(\mathbf{r})$, the microscopic electron (X-ray or electron scattering) or nuclear (neutron scattering) density; a map of the structure. However, as we have described, we measure only the intensity and not the scattering amplitude directly. The scattering amplitude is proportional to the square root of the intensity, but the phase factor is unknown;

$$\Psi(Q) \propto e^{i\theta} \sqrt{I(Q)} \tag{2.38}$$

What happens if we Fourier transform the measured intensity instead of $\Psi(\mathbf{Q})$? When properly normalized, the intensity yields the total scattering structure function, $S(\mathbf{Q})$, which is the square of $\Psi(\mathbf{Q})$. Thus,

$$S(\mathbf{Q}) = |\Psi(\mathbf{Q})|^2 = \frac{1}{(\rho_0 V)^2} \int\int \rho(\mathbf{r})\rho(\mathbf{r}') e^{i\mathbf{Q}(\mathbf{r}-\mathbf{r}')} d\mathbf{r}\, d\mathbf{r}' \tag{2.39}$$

The Fourier transform of $S(\mathbf{Q})$ is the density–density correlation function called the *generalized Patterson function*. Atomic distances are directly determined by this method, even before determining the whole structure.

As we mentioned above, Patterson maps are often generated in crystallographic studies by Fourier transforming just the Bragg intensities. This results in a discrete sum rather than the continuous integral as shown here. Also the commonly encountered ones are Fourier difference maps where the difference between the measured and the calculated (from a model) Bragg peak intensities are Fourier transformed to search in real-space for

inadequacies in the model. The generalized Patterson function described above, where the scattered intensity is a continuous function of **Q**, is rarely encountered in practice, but is the basis for the PDF as we describe in more detail in Chapter 3.

2.2.3 Reverse Monte-Carlo method

Another method, which is gaining popularity as computer power is increased, is the *reverse Monte-Carlo method* (McGreevy and Pusztai, 1988; see Keen (1998), for a brief history of this method). The Monte-Carlo method is a general method of modeling which uses statistical principles. The name Monte-Carlo comes from this stochastic nature of the process (gambling!), and is widely used in various modeling applications. The idea is to start with some density function $\rho(\mathbf{r})$ and improve it numerically until it can reproduce the observed diffraction intensity. The goal is to minimize the difference of Eq. 2.35 or 2.36 using the Metropolis method (Metropolis *et al.*, 1953). Let us assume that $\rho(\mathbf{r})$ is described by a set of atomic positions, $\{\mathbf{r}_\nu\}$. We then move one of the atoms by a certain amount, $\Delta\mathbf{r}_\nu$. This produces a change in the R-factor by ΔR. This move is randomly accepted or rejected with a probability, which is a certain function of ΔR. As the probability function, for instance, the Fermi–Dirac function could be used,

$$P = \frac{1}{1 + e^{\Delta R/T}} \tag{2.40}$$

where T is a fictitious temperature utilized to control the process of convergence. This process is repeated a very large number of times for each atom. The process is stopped when it can no longer improve the value of R. This process of minimizing the difference by numerical modeling is also called simulated annealing, for an obvious reason. The reverse Monte-Carlo method is frequently used in modeling the diffuse scattering intensity both from single crystals (Nield, 1998) and powders (Keen, 1998). This subject will be revisited in Chapter 6 in context of the PDF modeling.

2.3. CRYSTALLOGRAPHIC METHODS AND DISORDER: LIMITATIONS OF CRYSTALLOGRAPHIC METHODS

While crystallography assumes perfect periodicity, it is possible to include some deviations from periodicity into the analysis. Structural disorder is generally introduced through two parameters:

(a) Enlarged Debye–Waller factors.
(b) Partial occupation of lattice sites.

These two crystallographic 'band aids' can correctly characterize the extent of local disorder only in limited cases, and they can provide misleading information on the nature

of local disorder. It is worth considering how much disorder in a crystal can be usefully accounted for using these approximations and asking, 'What are the limits of crystallographic methods in dealing with disorder'? In this section we explore some of these limitations and show that the remedial methods for incorporating disorder, such as allowing for enlarged thermal factors, can underestimate and mischaracterize the disorder. This presents a motivation for applying total scattering and PDF methods more widely in the future in situations where it has not traditionally been done. Examples where 'solved' structures in the literature were shown to be wrong by applying PDF techniques are discussed in Chapters 9 and 10.

2.3.1 Debye–Waller factor

Atomic displacements due to phonons are well described by the Debye–Waller factor that was derived for this purpose (Debye, 1913; Waller, 1923). This method is usually extended to describe other kinds of local disorder than lattice vibrations as well. We will first discuss how to evaluate the DW factor and find whether or not the factor is anomalously large. The DW factor is usually expressed as Eq. 2.18,

$$e^{-Q^2\langle\langle u^2\rangle\rangle} = e^{-2Bs^2} \qquad B = 8\pi^2\langle\langle u^2\rangle\rangle \tag{2.41}$$

where $s = \sin\theta/\lambda$. Thus the DW factor is directly related to the r.m.s. amplitude of lattice vibration, $\langle\langle u^2\rangle\rangle$. Within the Debye model it can be expressed in terms of the Debye temperature, Θ_D, as,

$$\langle\langle u^2\rangle\rangle = \frac{\hbar}{m\omega}\left(\langle\langle n\rangle\rangle + \frac{1}{2}\right) \qquad \langle\langle n\rangle\rangle = \frac{1}{N}\int_0^{\Theta_D} \frac{\Theta^2\, d\Theta}{e^{\Theta/T} - 1} \tag{2.42}$$

where m is the atomic mass. If the phonon density of states, $g(w)$, is known explicitly then $\langle\langle n\rangle\rangle$ can be evaluated explicitly as

$$\langle\langle n\rangle\rangle = \int_0^{\infty} \frac{g(\omega)}{e^{\hbar\omega/kT} - 1} d\omega \tag{2.43}$$

The value of $\langle\langle u^2\rangle\rangle^{1/2}$ is usually less than 0.1 Å at and below room temperature for all the elements. Any Debye–Waller factor corresponding to a thermal amplitude greater than this is most likely due to the effect of disorder.

It should be noted, however, that extending the DW approximation to describe disorder has serious limitations which are too often not sufficiently recognized. The DW approximation is inaccurate in the following cases:

(i) *Strong anharmonicity*: If the local potential for an atom is a double-well the atomic distribution will be bimodal. However in the DW approximation this appears simply as a widely distributed atom density in a soft potential (Appendix 2.3).

(ii) *Uneven distribution of mean-square displacement amplitudes on crystallographically equivalent sites*: If a relatively small number of atoms have larger amplitudes of displacement while others remain normal, fitting one DW factor results in a significant underestimate of the displacements. The atoms with very large displacements are practically ignored.

(iii) *Correlated atomic displacements*: If two atoms move in the same direction the change in the interatomic distance is smaller than the displacements of each, and the DW factor overestimates the relative displacements of atoms. On the other hand if the motions are anti-correlated, the DW factor underestimates the relative displacements.

As an example let us consider a system in which 60% of the atoms have a root-mean-square displacement amplitude of $u_1 = 0.05$ Å, while the rest of the atoms have an amplitude of $u_2 = 0.2$ Å. The r.m.s. of displacement is then,

$$\langle\langle u^2 \rangle\rangle^{1/2} = [0.6 \times (0.05)^2 + 0.4 \times (0.2)^2]^{1/2} = 0.132 \tag{2.44}$$

Now the total Debye–Waller factor will be the weighted sum of the two DW envelopes,

$$0.6 \exp(-\langle\langle u_1^2 \rangle\rangle Q^2) + 0.4 \exp(-\langle\langle u_2^2 \rangle\rangle Q^2) \tag{2.45}$$

If this is approximated by a single Debye–Waller factor, as shown in Figure 2.3, the fitted value is

$$\langle\langle u^2 \rangle\rangle_{\text{fit}}^{1/2} = 0.062 \tag{2.46}$$

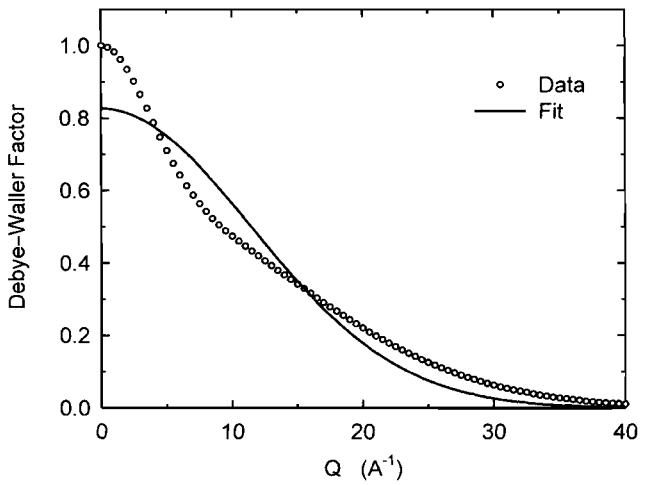

Figure 2.3. Debye–Waller factor as a sum of two components (dots) fit with a single component (solid line).

which is barely $\frac{1}{2}$ of the true value. If we try to estimate the value of $\langle\langle u_2 \rangle\rangle$ by knowing the value of $\langle\langle u_1 \rangle\rangle$,

$$\langle\langle u_2^2 \rangle\rangle_{\text{fit}} = \{[\langle\langle u^2 \rangle\rangle_{\text{fit}} - 0.6 \times (0.05)^2]/0.4\}^{1/2} = 0.076 \tag{2.47}$$

which is only about 1/3 of the correct value.

This severe underestimate occurred because the Debye–Waller factor due to $\langle\langle u_2 \rangle\rangle$ decreases quickly with Q, as shown in Figure 2.3, and contributes relatively little to the fitting. For that reason the DW factor depends upon the range of fitting, as shown in Figure 2.4. While the case above is a rather extreme case, this example demonstrates the grave danger in estimating the amplitude of displacement for minority atoms by the Debye–Waller approximation. It is often blindly assumed that even though the Debye–Waller approximation neglects atomic correlation at least the value of $\langle\langle u^2 \rangle\rangle$ determined by the Debye–Waller factor is correct. This example shows even this assumption should be treated with some caution.

2.3.2 Values of refined parameters I: imperfect models

As we discussed, because of the crystallographic phase problem structures can only be inferred, and not deduced, from experimental intensity data. This implies that the expected scattering from models must be compared to the observed intensities through a process of 'fitting'. In any fitting procedure, the results are limited by the accuracy of the underlying model. Inadequacies in the model (for example, imperfect profile functions, imperfect

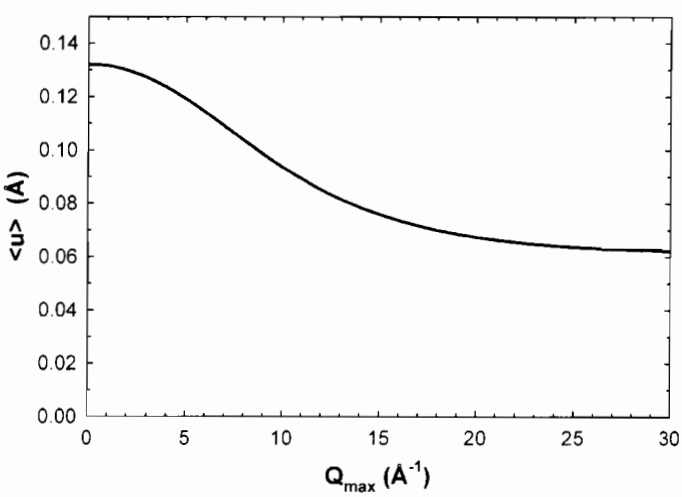

Figure 2.4. Value of DW factor as a function of fitting range obtained from fitting a single Gaussian to the two-component Gaussian shown in Figure 2.3. The 'refined' value depends strongly on the range of fitting.

background subtraction, etc.) have to be accommodated in the fitting process by other degrees of freedom in the model. When this occurs, the refined values of these degrees of freedom are compromised, or biased in the language of regression. To make this concrete, let us consider an example. Let us assume that the sample has a finite absorption (as all samples do) but that this is not included (or is not correctly incorporated) in the structural refinement. If it is a symmetric flat-plate transmission measurement the sample absorption increases with increasing diffraction angle as the path length of the rays through the sample increases. Thus, the measured intensity decreases with increasing angle. This appears similar to the effect of the Debye–Waller factor. The fitting program can (and will) partially correct for this 'mistake' by decreasing the overall intensity scale factor and increasing the DW factor somewhat. Because the functional form of the intensity fall off is different from the DW form the correction is not perfect and there is a concomitant increase in the residuals function. Nonetheless, this illustrates how imperfections in the underlying model bias the refinement leading to unphysical values of certain parameters.

2.3.3 Values of refined parameters II: correlated parameters

The same example can also be used to illustrate how different parameters in the fit can become correlated. Correlated parameters are also prone to conspire with each other to yield biased, unphysical values. In the example used in the previous paragraph both the absorption correction and the DW factors give rise to rather slowly varying decreases in the Bragg peak intensities with increasing angle. The difference is in the exact functional form. For instance for a flat plate in the transmission mode the absorption correction to the intensity falls off as $\exp(-\mu t/\cos\theta)$ where μt is the absorption length of the sample (measure of how absorbing it is) and $\theta = 2\theta/2$ where 2θ is the diffraction angle. The DW factor falls off as $\exp(-A\sin^2\theta)$ where A is a positive constant (see Eq. 2.41). If we expand the trigonometric terms in the exponents we find that, to leading order, they both yield corrections of the form $A'\exp(-\theta^2)$. They become different only in the terms of higher order. What this means practically is that the Bragg peak intensities need to be fit over a wide range of angle or Q to reliably differentiate these effects. If the range of fitting is not wide enough the program does not know whether it should vary the absorption correction or the DW factor, for example. These parameters can then take on arbitrary values provided that, together, they account for the intensity variation adequately. This effect is known as parameter correlation. It can happen to a greater or lesser degree. It is often more dangerous when it happens to a lesser degree because slightly, but not grossly, unphysical parameters will be refined.

The problem of parameter correlation is also exacerbated by the other problem we discussed of an inadequate underlying model. Two partially correlated parameters (such as absorption and the DW factor) may be able to vary in some creative way to account for a fall off in intensity, due to some effect not accounted for in the model, that has a different

functional form to either of them. For example, as discussed in Appendix 2.3, static atomic displacements in the form of a bimodal anharmonic potential whose wells are occupied randomly give rise to an intensity fall-off which has a $\cos^2 Q\delta$ functional form, where δ is the magnitude of the displacements. An enthusiastic collaboration between site occupancy factors, scale factor, absorption factor and DW factor (and possibly other parameters) will be used to accommodate this effect. Exactly how this occurs will also depend on the range over which data are fit. We note that relatively small displacements affect the intensity most strongly at high values of Q. Displacement of atoms by δ will most strongly modify the diffraction intensity around $Q_d = \pi/\delta$. If $\delta = 0.1$ Å, $Q_d = 31$ Å^{-1} which corresponds to a d-spacing of ~ 0.2 Å, well beyond the range of most crystallographic refinements.

2.3.4 Values of Rietveld refined DW factors: Caveat emptor

In general, the wider the range over which data are fit the less acute are the problems of parameter correlations. However, in relation to this we issue one final *caveat emptor*. In Rietveld refinement the range over which data are fitted is usually limited by the problem of Bragg peak overlap at high angles. The acuteness of this problem depends on the symmetry of the material and the resolution of the measurement. Higher symmetry and higher resolution mean that higher values of Q can be fit. For many real-world applications (for example, high-temperature superconductors measured on standard neutron powder diffractometers) the minimum d-spacing fit is ~ 0.4–0.5 Å corresponding to a Q_{max} of ~ 12–15 Å^{-1}. However, with respect to DW factors, higher is not necessarily better. An arbitrary background is subtracted before peak intensities are calculated. This background subtraction is reliable in regions where Bragg peaks do not overlap since the baseline can be seen. An arbitrary functional form is fit to remove residual intensity in these regions. However, in the high-Q region the Bragg peaks overlap and the baseline is never accessed. The background function is basically extrapolated into this region from its fit in the low-Q region. In this high-Q region the Bragg peak intensities are small because of the DW factor. A small error in this extrapolated background could wipe out (or increase) a significant proportion of the real intensity in the Bragg peaks. Also, overlapped Bragg peaks yield craggy peaks sitting on top of a plateau of intensity coming, not only from the background and diffuse scattering, but also from the overlapping tails of the Bragg peaks themselves. Again, this will result in inaccurate DW factors being refined. Given these problems it is a miracle that DW factors refined from Rietveld are as good as they are. *Caveat emptor*: these problems should be borne in mind by the careful reader when assigning significance to Rietveld DW factors.

In the future, for greatest accuracy, it is likely that Rietveld refinements will be carried out on fully corrected $S(Q)$ functions instead of on the raw intensities. In this way factors such as absorption and backgrounds will not be parameterized in the fit but will be explicitly corrected. This has the disadvantage that significant data processing

must be carried out before the fitting is attempted. However, as we describe later, data reduction programs to obtain $S(Q)$ are becoming faster, easier to use, will propagate errors reliably, and maintain data processing histories. All four of these requirements will be necessary to persuade Rietveld aficionados to change from their current approach of fitting raw data.

APPENDIX 2.1. SCATTERING CROSS-SECTION

Let us consider a beam of particles (photons, neutrons, electrons, etc.) with the wave function,

$$\phi_0 = e^{i\mathbf{kr}} \tag{A2.1.1}$$

When this wave is scattered by a collection of atoms at $\mathbf{R}_i$, as discussed in Appendix 2.2, the scattered wave is given by ϕ_1 in the first order Born approximation Eq. A2.2.24,

$$\phi_1 = \frac{e^{ikr}}{r}\langle V\rangle \Psi(\mathbf{Q}), \qquad \Psi(\mathbf{Q}) = \frac{1}{\langle V\rangle}\sum_i V_i\, e^{i\mathbf{QR}_i} \tag{A2.1.2}$$

If the flux density of the incoming wave is I_0, the intensity of the scattered beam per area dr^2, $I_s\, dr^2$, is given by,

$$I_s\, dr^2 = I_s r^2\, d\Omega = I_0 |\phi_1|^2 r^2\, d\Omega = I_0\, d\sigma \tag{A2.1.3}$$

where σ is the cross-section. Now from Eq. A2.1.3

$$\frac{d\sigma}{d\Omega} = |\phi_1|^2 r^2 = \langle V\rangle^2 |\Psi(\mathbf{Q})|^2 \tag{A2.1.4}$$

APPENDIX 2.2. SAMPLE SCATTERING AMPLITUDE

A2.2.1 Simple derivation

In the main text of this chapter, we introduced the sample scattering amplitude,

$$\Psi(\mathbf{Q}) = \frac{1}{\langle b\rangle}\sum_\nu b_\nu\, e^{i\mathbf{QR}_\nu} \tag{A2.2.1}$$

which forms the basis for the theory of scattering. This equation can be easily deduced as in the following. Let us assume that the incident wave (X-rays or neutrons) is described by a wave equation,

$$\phi_{\mathbf{k}_{init}}(\mathbf{r}) = e^{i\mathbf{k}_{init}\mathbf{r}} \tag{A2.2.2}$$

where $\mathbf{k}_{\text{init}}$ is the wavevector (momentum) of the incident wave. In the case of elastic scattering the scattered wave has the wavevector with the same magnitude but a different direction,

$$\chi_{\mathbf{k}_{\text{final}}}(\mathbf{r}) = A\, e^{i\mathbf{k}_{\text{final}}\mathbf{r}} \tag{A2.2.3}$$

The basis for this expression is the so-called Born approximation, and is given below. However, the phase of this wave may not be same as the incident wave, and that is the point of our interest. When the incident wave reaches the atom ν, its amplitude is

$$\phi_{\mathbf{k}_{\text{init}}}(\mathbf{R}_\nu) = e^{i\mathbf{k}_{\text{init}}\mathbf{R}_\nu} \tag{A2.2.4}$$

where $\mathbf{R}_\nu$ describes the position of the νth atom. After scattering, the wave changes direction and becomes the scattered wave. The ratio between the amplitudes of the incident wave and the scattered wave is determined by the nature of the scatterer, and is independent of the position of the scatterer

$$\chi_{\mathbf{k}_{\text{final}}}(\mathbf{R}_\nu) = B\phi_{\mathbf{k}_{\text{init}}}(\mathbf{R}_\nu), \qquad A\, e^{i\mathbf{k}_{\text{final}}\mathbf{R}_\nu} = B\, e^{i\mathbf{k}_{\text{init}}\mathbf{R}_\nu} \tag{A2.2.5}$$

Therefore,

$$A = B\, e^{i(\mathbf{k}_{\text{init}} - \mathbf{k}_{\text{final}})\mathbf{R}_\nu} \tag{A2.2.6}$$

By expressing B by an absolute value B_0 and the phase, δ,

$$A = B_0\, e^{i[(\mathbf{k}_{\text{init}} - \mathbf{k}_{\text{final}})\mathbf{R}_\nu + \delta]} \tag{A2.2.7}$$

and the scattered wave is now expressed as

$$\chi_{\mathbf{k}_{\text{final}}}(\mathbf{r}) = B_0\, e^{i[(\mathbf{k}_{\text{init}} - \mathbf{k}_{\text{final}})\mathbf{R}_\nu + \delta + \mathbf{k}_{\text{final}}\mathbf{r}]} \tag{A2.2.8}$$

By defining the scattering vector as

$$\mathbf{Q} = \mathbf{k}_{\text{init}} - \mathbf{k}_{\text{final}} \tag{A2.2.9}$$

we obtain

$$\chi_{\mathbf{k}_{\text{final}}}(\mathbf{r}) = F(\mathbf{Q})\chi_0(\mathbf{r}), \qquad F(\mathbf{Q}) = e^{i\mathbf{Q}\mathbf{R}_\nu}, \qquad \chi_0(\mathbf{r}) = B_0\, e^{i\delta}\, e^{i\mathbf{k}_{\text{final}}\mathbf{r}} \tag{A2.2.10}$$

Finally, superposing the amplitudes of the waves scattered from each atom by summing over ν, we obtain the static structure factor for the total wave scattered by an assembly of N

scattering objects (atoms),

$$\chi_{\mathbf{k}_{\text{final}}}(\mathbf{r}) = F(\mathbf{Q})\chi_0(\mathbf{r}), \qquad F(\mathbf{Q}) = \frac{1}{\langle b \rangle} \sum_{\nu} b_\nu \, \mathrm{e}^{\mathrm{i}\mathbf{Q}\mathbf{R}_\nu} \tag{A2.2.11}$$

A2.2.2 Born approximation

A more rigorous derivation is the standard Born approximation (e.g. Wu and Ohmura, 1962). The total wavefunction, ϕ, is the sum of the incoming and outgoing waves and satisfies the Schrödinger equation,

$$\left(-\frac{\hbar^2}{2m}\nabla^2 + \lambda V\right)\phi = E\phi \tag{A2.2.12}$$

where $V(\mathbf{r})$ is the scattering potential located near the origin, and λ is a controlling variable which will be equated to unity after the analysis. At large values of $\mathbf{r}$, $V = 0$, so that

$$E = \frac{\hbar^2 \mathbf{k}_{\text{init}}^2}{2m}, \qquad \phi_{\text{init}}(\mathbf{r}) = \mathrm{e}^{\mathrm{i}\mathbf{k}_{\text{init}}\mathbf{r}} \tag{A2.2.13}$$

We now consider expanding ϕ by λ:

$$\phi = \phi_0 + \lambda\phi_1 + \lambda^2\phi_2 + \cdots \tag{A2.2.14}$$

Then Eq. A2.2.12 becomes, equating each order in λ,

$$\begin{aligned} -\frac{\hbar^2}{2m}\nabla^2\phi_0 &= E\phi_0 \\ \left(-\frac{\hbar^2}{2m}\nabla^2 - E\right)\phi_1 &= -V\phi_0 \\ \left(-\frac{\hbar^2}{2m}\nabla^2 - E\right)\phi_2 &= -V\phi_1 \\ &\vdots \end{aligned} \tag{A2.2.15}$$

Thus,

$$\phi_0 = \phi_{\text{init}} \tag{A2.2.16}$$

To solve for the first order scattered wave ϕ_1 we have to consider the Greens function,

$$\left(-\frac{\hbar^2}{2m}\nabla^2 - E\right)G(\mathbf{r} - \mathbf{r}') = \delta(\mathbf{r} - \mathbf{r}') \tag{A2.2.17}$$

$$G(\mathbf{r}-\mathbf{r}') = \frac{e^{i\mathbf{k}|\mathbf{r}-\mathbf{r}'|}}{4\pi|\mathbf{r}-\mathbf{r}'|} \tag{A2.2.18}$$

Thus,

$$\phi_1 = \frac{1}{4\pi}\int \frac{e^{i\mathbf{k}|\mathbf{r}-\mathbf{r}'|}}{|\mathbf{r}-\mathbf{r}'|} V(r')e^{ikr'}\,dr' \tag{A2.2.19}$$

At large distance ($r \gg r'$),

$$|\mathbf{r}-\mathbf{r}'| \approx r - r'\cos\theta \tag{A2.2.20}$$

where θ is the angle between $\mathbf{r}$ and $\mathbf{r}'$. Then,

$$k|\mathbf{r}-\mathbf{r}'| \approx kr - \mathbf{k}'\mathbf{r}' \tag{A2.2.21}$$

where $\mathbf{k}'$ is a wavevector parallel to $\mathbf{r}$ and $|\mathbf{k}'| = k$. Thus Eq. A2.2.19 becomes

$$\phi_1 \approx \frac{e^{ikr}}{4\pi r}\int V(\mathbf{r}')e^{i(\mathbf{k}-\mathbf{k}')\mathbf{r}'}\,d\mathbf{r}' \tag{A2.2.22}$$

Here the multiplier represents a spherical wave. If the scattering potential is a collection of nuclear potentials at the atoms in the solid,

$$V(\mathbf{r}) = \sum_i V_i\delta(\mathbf{r}-\mathbf{R}_i) \tag{A2.2.23}$$

Then the scattered wave is given by

$$\phi_1 = \frac{e^{ikr}}{r}\langle V\rangle\Psi(\mathbf{Q}), \qquad \Psi(\mathbf{Q}) = \frac{1}{\langle V\rangle}\sum_i V_i\, e^{i\mathbf{Q}\mathbf{R}_i} \tag{A2.2.24}$$

which leads to Eq. A2.2.1.

APPENDIX 2.3. DIFFRACTION SIGNATURE OF ATOMIC DISPLACEMENTS

To illustrate how the signature of a non-Gaussian distribution of atomic displacements shows up in the diffraction pattern, let us consider a one-dimensional chain of atoms separated by a, displaced by δx, in alternating directions on neighboring sites. This happens if the local potential of an atom is double-well, and there is an anti-ferroelectric correlation among the displacements. The atomic position is then given by,

$$R_\nu = \nu a + \delta x\, e^{i\nu\pi} \tag{A2.3.1}$$

Then the crystallographic structure factor is,

$$F(Q) = \sum_{\nu} e^{iQR_\nu} = \sum_{\mu} \left[e^{iQ\delta x} + e^{iQ(a-\delta x)} \right] e^{i2Q\mu a}$$

$$= 2N \sum_{n} \left[\delta\left(Q - \frac{2n\pi}{a}\right) \cos(Q\delta x) + i\delta\left(Q - \frac{(2n+1)\pi}{a}\right) \sin(Q\delta x) \right] \quad \text{(A2.3.2)}$$

Thus, if δx is small the superlattice diffraction peaks at $Q = (2n+1)\pi/a$ have the intensity proportional to $\sin^2(Q\delta x)$, with the maximum intensity appearing at $Q = \pi/(2\delta x)$. If δx is ~ 0.1 Å this corresponds to a Q of 15.7 $Å^{-1}$. This is why the signature of displacements appears at high values of Q. At low Q the intensity is proportional to $\delta x^2 Q^2$. This Q^2 dependence is recovered in the derivation for the diffuse scattering. The main Bragg peaks at $Q = 2n\pi/a$ are modulated by $\cos^2(Q\delta x)$. At small values of Q this is approximately,

$$\cos^2(\mathbf{Q}\delta x) = 1 - \frac{1}{2}(Q\delta x)^2 + \cdots \approx e^{-Q^2\delta x^2/2} \quad \text{(A2.3.3)}$$

Thus, the effect of these displacements merely adds to the Debye–Waller factor. If the directions of displacements are not ordered but random, Eq. A2.3.2, is

$$F(Q) = \sum_{\nu} e^{iQR_\nu} = \sum_{\nu} e^{i\ \mathrm{sign}(\nu)Q\delta x}\ e^{i2Q\nu a}$$

$$= 2N \sum_{\nu} [\cos(Q\delta x) + i\ \mathrm{sign}(\nu)\sin(Q\delta x)] e^{i2Q\nu a}$$

$$= 2N \cos(Q\delta x) \sum_{n} \delta\left(Q - \frac{2n\pi}{a}\right) \quad \text{(A2.3.4)}$$

where $\mathrm{sign}(\nu)$ is randomly $+1$ or -1. Thus the superlattice peaks would not be present but the intensity of the fundamental Bragg peaks is modulated by $\cos^2(Q\delta x)$. Thus, as in Eq. A2.3.3 it is not easy to differentiate this factor from the DW factor unless Q is larger than $\pi/\delta x$. This is why the DW approximation has undeserved successes, since crystallographic analysis is usually done in the low Q region below $\pi/\delta x$.

REFERENCES

Bacon, G.E. (1975) *Neutron Diffraction*, Clarendon Press, Oxford.
Borie, B. (1957) *Acta Crystallogr.*, **10**, 89.
Borie, B. (1959) *Acta Crystallogr.*, **12**, 280.
Borie, B. (1961) *Acta Crystallogr.*, **14**, 472.
Debye, P. (1913) *Verh. D. Deutsch. Phys. Ges.*, **15**, 678, 738, 857.

Giacovazzo, C., Monaco, H.L., Viterbo, D., Scordari, F., Gilli, G., Zanotti, G. & Catti, M. (1992) *Fundamentals of Crystallography*, International Union of Crystallography Monograph, Oxford Science Publications, Oxford.

Huang, K. (1947) *Proc. Roy. Soc. A*, **190**, 102.

Jeong, I.-K., Mohiuddin-Jacobs, F., Petkov, V., Billinge, S.J.L. & Kycia, S. (2001) *Phys. Rev. B*, **63**, 205202.

Keen, D. A. (1998), in *Local Structure from Diffraction*, ed. Billinge, S.J.L. & Thorpe M.K., Plenum Press, New York, p 101.

Larson, A.C., & Von Dreele, R.B. (2000) *General Structure Analysis System (GSAS)*, Los Alamos National Laboratory Report LAUR, 86–748.

Lawson, A.C., Martinez, B., Von Dreele, R.B., Roberts, J.A., Sheldon, R.I., Brun, T.O. & Richardson, J. W. (2000) *Phil. Mag. B*, **80**, 1869.

McGreevy, R.L. & Pusztai, L. (1988) *Mol. Sim.*, **1**, 359.

Metropolis, N., Rosenbluth, A.W., Rosenbluth, M.N., Teller, A.H. & Teller, E. (1953) *J. Chem. Phys.*, **21**, 1087.

Nield, V.M. (1998), in *Local Structure from Diffraction*, Eds. Billinge, S.J.L. & Thorpe, M.K., Plenum, New York, p 121.

Patterson, A.L. (1934) *Phys. Rev.*, **46**, 372.

Rietveld, H.M. (1969) *J. Appl. Crystallogr.*, **2**, 65.

Sinha, S.K. (1991) *Physica B*, **173**, 25.

Waller, I. (1923) *Zeit F. Phys.*, **17**, 398.

Warren, B.E. (1990) *X-ray Diffraction*, Dover, New York.

Wiles, D.B. & Young, R.A. (1981) *J. Appl. Crystallogr.*, **14**, 149.

Woolfson, M.M. (1997) *An introduction to X-ray Crystallography*, 2nd Edition, Cambridge University Press, Cambridge.

Wu, T.-Y. & Ohmura, T. (1962) *Quantum Theory of Scattering*, Prentice-Hall, Englewood Cliffs.

SELECTED BIBLIOGRAPHY

General texts on electron diffraction:

Cowley, J.M. (1995) *Diffraction Physics*, 3rd Edition, North-Holland Personal Library, Elsevier, Amsterdam.

Fultz, B. & Howe, J.M. (2001) *Transmission Electron Microscopy and Diffractometry of Materials*, Springer, Berlin.

Williams, D.B. & Carter, C.B. (1996) *Transmission Electron Microscopy: A Textbook for Materials Science*, vols., **1–4** Plenum, New York.

Diffuse scattering:

Billinge, S.J.L. & Thorpe M.F., editors (1998) *Local Structure from Diffraction* Plenum Press, New York.

Krivoglaz, M.A. (1969) *Theory of X-Ray and Thermal-Neutron Scattering by Real Crystals*, Plenum Press, New York.

Krivoglaz, M.A. (1996) *Diffuse Scattering of X-rays and Neutrons by Fluctuations*, Springer, Berlin.

Nield, V.M., Keen, D.A (2001) *Diffuse Neutron Scattering from Crystalline Materials*, Oxford Series on Neutron Scattering in Condensed Matter.

Schweika, W. (1998) *Disordered Alloys: Diffuse Scattering and Monte Carlo Simulations, Tracts in Modern Physics*, Springer, Berlin.

Lattice vibrations:

Born, M. & Huang, K. (1954) *Dynamical Theory of Crystal Lattices*, Oxford University Press, Oxford.

Willis, B.T.M. & Pryor, A. W. (1975) *Thermal Vibrations in Crystallography*, Cambridge University Press, Cambridge.

This Page Intentionally Left Blank

Chapter 3

The Method of Total Scattering and Atomic Pair Distribution Function Analysis

Chapter 3
The Method of Total Scattering and Atomic Pair Distribution Function Analysis

3.1. TOTAL SCATTERING AND THE PDF

3.1.1 Introduction

As we discussed in Chapter 2, in standard crystallographic analysis the Bragg peaks and diffuse scattering intensities were treated separately. The structure is determined solely based upon the information provided by the position and intensity of the Bragg peaks, while additional information regarding deviations from the perfect lattice is obtained through the study of diffuse scattering. This approach makes sense when the deviations are small, but when the structure is extensively disordered it fails in practice.

In this chapter, we present an alternative approach which treats both the Bragg and diffuse scattering on an equal basis, the so-called *total scattering* technique. Data from throughout reciprocal space, over a wide range of Q-values, are utilized. The technique is both straightforward and intuitively easy to comprehend. A convenient tool here is the *Fourier transformation*. In analyzing a complex function, Fourier analysis quite often provides distinct and useful information that is easier to interpret. For instance, a computer distinguishes human voices more readily in their Fourier transforms and holographic radar also uses Fourier analysis as the principle of the method. In the case of diffraction it is even more compelling to consider the Fourier transformation since it has a very well defined physical meaning. Fourier analysis of the total scattering data is known as *atomic pair distribution function* (PDF) analysis.

We first introduce the basic ideas and equations of total scattering and PDF analysis and give a brief and incomplete history of the subject. From Section 3.2 onwards we explore in more detail the application of the technique to different specialized situations such as obtaining *compositionally resolved information*, *magnetic short-range order* and studying samples in *special geometries*. These sections can be omitted on a first reading without affecting the reader's ability to understand later chapters. Finally, we discuss *errors of the PDF*, with respect to their origin and methods to minimize them. This is an important section, as the accuracy of the PDF method is often underestimated, and given as an excuse to avoid this powerful technique. This subject is discussed also in Appendix 5.3 in further detail.

3.1.2 *The PDF as the Fourier transform of the scattered intensity*

The basis of the total scattering method is the normalized, measured, scattering intensity from a sample, the total scattering structure function, $S(\mathbf{Q})$. This intensity distribution is a continuous function of the wavevector, $\mathbf{Q}$, and in general contains both Bragg and diffuse intensity. It was discussed in detail in Section 2.1 and was derived in Eq. 2.9.

The wavevector, $\mathbf{Q}$, is a vector quantity and in general the intensity variation, $S(\mathbf{Q})$, will depend on which direction one looks in Q-space. However, in many situations the scattering is isotropic; it depends on the magnitude of the wavevector, Q, but not its direction. This is true of scattering from microscopically isotropic samples such as gases, liquids, and glasses. It is also true from samples of finely powdered crystallites. Each crystallite is not isotropic, but scattering from the ensemble is isotropic. Later in the Chapter we will discuss extensions to cases where the scattering is not isotropic. However, the greatest utility of the technique to date has been to study the isotropic scattering from powdered, liquid or glassy samples. We therefore consider the subject in this straightforward limit first. Examples of some $S(Q)$ functions (expressed as the reduced structure function, $F(Q) = Q[S(Q) - 1]$) from exemplar crystalline and amorphous materials are shown in Figure 3.1.

The equations shown in this section are derived in greater detail in Appendix 3.1. As we discussed in Section 2.1.2, it is a happy accident of the kinematical scattering equations that the microscopic real-space density of a material is simply given by a Fourier transform of the scattering *amplitude*, $\Psi(Q)$. Similarly, the Fourier transform of the scattered *intensity*, in the form of the structure function $S(Q)$, yields the *atomic pair distribution function*, $g(r)$, defined by Eq. 3.1. This is happy in the sense that $S(Q)$ is a directly measurable quantity and $g(r)$ is a quantity of profound physical importance; the crystal structure can be determined from it. Since $\rho_0 g(r)$ is a representation of the microscopic atomic pair density, this relationship allows us to directly *measure* the relative positions of atoms in a solid. A straightforward numerical Fourier transform of our measured scattering intensity, $S(Q)$, can be carried out in a computer according to

$$G(r) = 4\pi r\rho_0(g(r) - 1) = \frac{2}{\pi}\int_0^\infty Q[S(Q) - 1]\sin(Qr)\mathrm{d}Q \tag{3.1}$$

to yield $g(r)$, the pair-distribution function.

As described in Section 1.1.4, $g(r)$ is like a distance map of the inside of the solid. The function gives the probability of finding two atoms separated by the distance, r. An example of a PDF is shown in Figure 3.2 (Louca and Egami, 1999). The circles are the measured PDF of nickel obtained by Fourier transforming the measured total scattering structure function. The solid line is the PDF of the nickel crystal structure calculated using Eq. 1.1. The closest that two atoms can approach each other is the nearest neighbor distance, r_{nn}, which in nickel is 2.50 Å, and corresponds to the first peak. There is no peak in the PDF before this value; small peaks at shorter distances come from noise (both

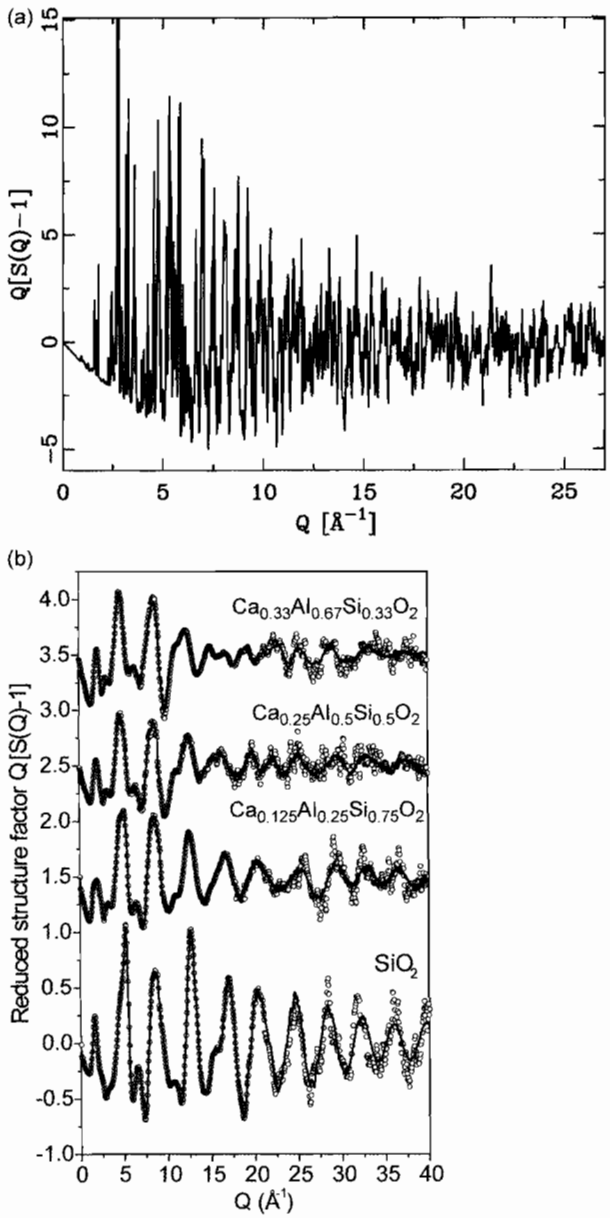

Figure 3.1. Exemplar total scattering structure functions, $S(Q)$, (plotted as $Q(S(Q) - 1)$, for representative crystalline and amorphous materials: (a) Crystalline $LaMnO_3$ powder at $T = 10$ K (Proffen *et al.*, 1999); (b) amorphous alumino-silicates (Petkov *et al.*, 2000b). Note the sharp features in the crystalline $S(Q)$ compared with the broad diffuse scattering from the amorphous materials.

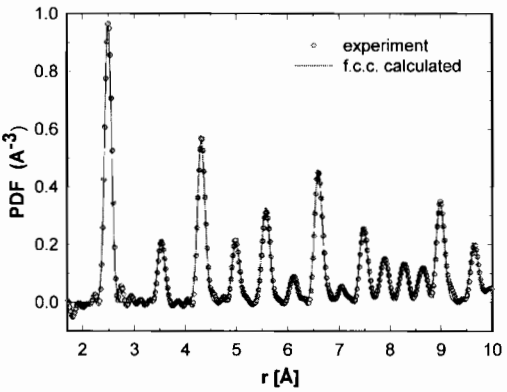

Figure 3.2. The PDF of crystalline Ni at $T = 10$ K (Louca and Egami, 1999).

systematic and random). Nickel has the f.c.c. structure with a lattice parameter of $a = 3.54$ Å. Therefore, the nearest neighbor peak is from the unit cell corner to the face center: $a/\sqrt{2} = 2.50$ Å which appears as expected in the figure. Each of the peaks in the PDF can be attributed to some such atom–atom relationship or *atomic-atom correlations*. If we have a model for the atomic structure, specified by atomic positions in space, it is trivial to calculate $g(r)$ and compare with experimentally measured correlation functions.

The PDF is related to the Patterson function introduced in Section 2.2.2. Usually, only the Bragg peaks are used in calculating the Patterson function which therefore has the periodicity of the lattice. Both the Bragg peaks *and* diffuse intensity are included in obtaining the PDF. Thus the PDF does not necessarily have the lattice periodicity, and will be able to describe the deviations from lattice periodicity. One may also say that the PDF defined by Eq. 3.1 is a spherically averaged generalized Patterson function.

The inverse transformation of Eq. 3.1 can be defined and it yields the structure function $S(Q)$ in terms of $G(r)$,

$$S(Q) = 1 + \frac{1}{Q}\int_0^\infty G(r)\sin(Qr)\mathrm{d}r \tag{3.2}$$

3.1.3 The PDF and all its friends and relations

3.1.3.1 The pair distribution function, g(r), and the pair density function, ρ(r). We have chosen to define the atomic pair distribution function in terms of $g(r)$ in Eq. 1.1. However, there are a host of rather similar correlation functions that the reader is likely to come across. They are mostly related simply by multiplicative and additive constants and contain the same structural information. Each has its own properties and advantages and disadvantages which we will try and highlight here. It is important to be able to distinguish

them in any given situation. Another complication lies in the fact that different authors use different letters for the same function, though it is common practice to define the function in most papers.

As discussed in Section 1.1.4, $g(r)$ is called *the pair distribution function*. It is normalized so that, as $r \rightarrow \infty$, $g(r) \rightarrow 1$. Also, as we discussed in Chapter 1, as $r \rightarrow 0$ (for r shorter than the distance of closest approach of pairs of atoms) $g(r)$ becomes zero. It is closely related to the *pair density function*, $\rho(r) = \rho_0 g(r)$. Clearly, $\rho(r)$ oscillates about, and then asymptotes to, the average number density of the material, ρ_0 at high-r and becomes zero as $r \rightarrow 0$. The main advantage of these functions is that they emphasize the low-r short-range order. In a sample with perfect structural coherence (for example a perfect crystal) the amplitude of the oscillations (containing the structural information) in these functions falls off like $1/r$. However, when these functions are determined experimentally the uncertainties in the data also fall off like $1/r$. In this respect the fact that the low-r structure is emphasized is cosmetic rather than real because the uncertainties in the data (the error bars) scale with the amplitude of the signal. This brings us to our next correlation function, $G(r)$.

3.1.3.2 The reduced pair distribution function, G(r). Another widely used correlation function is the *reduced pair distribution function*, $G(r)$. This is defined as $G(r) = 4\pi r\rho_0 (g(r) - 1)$. From the definition, and our previous discussion, it is clear that this function oscillates around zero in the limit of large r. It also becomes evident by considering the definition that, as $r \rightarrow 0$ this function behaves like $-4\pi\rho_0 r$. That is, at low-r this function is a straight line going through zero with a slope that is proportional to the average number density of the material.

Though less physically intuitive than $g(r)$ itself, this function has some distinct advantages and is very widely used. The main advantage is that this function is the one directly obtained from the Fourier transform of $S(Q)$. It is therefore the function which is most directly related to the data. For example, to obtain either $g(r)$ or $\rho(r)$ from the data it is necessary to assume a value for the average number density, ρ_0. This is not necessary in $G(r)$, on the contrary this information is already contained in $G(r)$ as the slope of the function at low-r. From a philosophical point of view, there is a cleaner separation of *data analysis* to obtain the correlation function and *data modeling* to obtain the structural information from that function since there is nothing about the underlying structure that is assumed in obtaining $G(r)$.

A second advantage of $G(r)$, related to the fact that it is the direct Fourier transform of the intensity data, is that the random uncertainties on the data are constant in r. This comes about as a direct result of the error propagation process described later. This has two advantages. The first is sociological. It is common to plot a correlation function calculated from a model on top of the measured one and to plot a difference curve underneath

which highlights the differences. Because the uncertainties are constant in r, fluctuations in the difference curve have the same significance at all values of r. Thus, for example, if the fluctuations in the difference curve decrease with increasing r this implies that the model is getting better at longer distances (perhaps it is a model of the average crystallographic structure). This inference cannot be made from a difference curve to $\rho(r)$ or $g(r)$ since we expect the fluctuations to fall off as $1/r$ simply due to the statistical fluctuations. In this case the reader's eye then has to judge whether the fluctuations are falling off faster or slower than $1/r$ (not an easy task) to judge whether the model is getting better or worse with increasing r.

A danger also lurks when fitting models to $\rho(r)$ or $g(r)$. Unless a statistically weighted residuals function (often called the A-factor in PDF work) is used, the refinement will be giving statistically unwarranted importance to the low-r data. If $G(r)$ is fit this problem is avoided regardless of whether a weighted or unweighted residuals function is used since the statistical uncertainties are constant in r anyway.

A further advantage of the $G(r)$ function is that the amplitude of the oscillations gives a direct measure of the structural coherence of the sample. In a crystal with perfect structural coherence, oscillations in $G(r)$ extend to infinity with a constant peak–peak amplitude. In the $G(r)$ from a real crystal the peak–peak amplitude of the signal gradually falls off due to the finite Q-resolution of the measurement, which is then the limitation on the spatial coherence of the measurement rather than the structural coherence itself. A higher Q-resolution results in data extending over a wider range of r. In samples with some degree of structural disorder, the signal amplitude in $G(r)$ falls off faster than dictated by the Q-resolution and this becomes a useful measure of the structural coherence of the sample. This is nicely illustrated in Figure 3.3 (Petkov *et al.*, 2000). The top panel, (a), shows $G(r)$ from a pristine sample of WS_2, a layered material with relatively good crystallinity. Figure 3.3(b) shows the data from a sample where the layers have been ripped apart in solution (so-called exfoliation) and then restacked again. In this case, the structure of the layers has changed as evident by the differences in $G(r)$ at low-r. However, it is also apparent that the signal is dropping off more rapidly with r in the restacked sample. This means that, even within the layers, the structure is more disordered and there is less structural coherence. These restacked samples are metastable and decay back to the highly ordered pristine structures over a period of time.

There is one final feature of $G(r)$, again related to its experimental importance. In a real experiment $S(Q)$ is measured only over a finite range of Q. The consequence in the Fourier transform is that termination ripples appear; ripples with a wavelength $\sim 2\pi/Q_{max}$. Mathematically this comes about because the theoretical $G(r)$ becomes convoluted with the Fourier transform of the termination function. This is discussed in more detail in Section 3.5. For completeness, we simply make the point that it is $G(r)$ that should be thus convoluted, not $\rho(r)$ or $g(r)$.

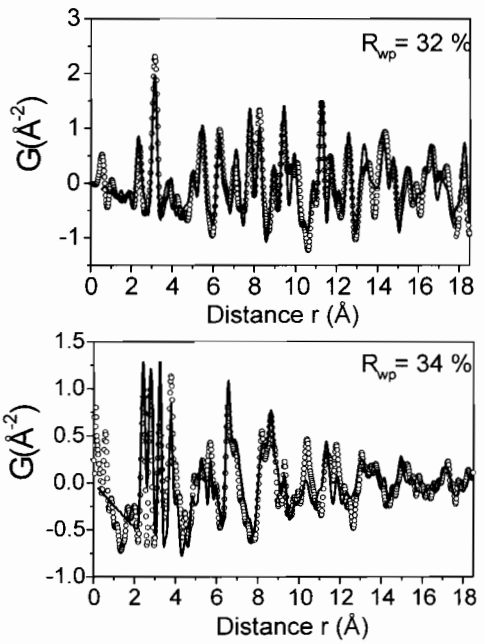

Figure 3.3. (top panel) X-ray $G(r)$ of pristine WS_2; (lower panel) $G(r)$ of reformed sample after exfoliation. Circles are the data, solid lines are PDFs calculated from structural models. Note that the amplitude of the ripples in $G(r)$ die out in the nanocrystalline reformed sample (Petkov *et al.*, 2000a,b,c).

3.1.3.3 The radial distribution function, R(r). The next correlation function we discuss is the most physically intuitive. The PDF, $g(r)$ is related to the *radial distribution function* (RDF), $R(r)$[1], by

$$R(r) = 4\pi r^2 \rho_0 g(r) \tag{3.3}$$

The radial distribution function has the useful property that the quantity $R(r)\mathrm{d}r$ gives the number of atoms in an annulus of thickness $\mathrm{d}r$ at distance r from another atom. For example, the coordination number, or the number of neighbors, N_C, is given by

$$N_C = \int_{r_1}^{r_2} R(r)\mathrm{d}r \tag{3.4}$$

where r_1 and r_2 define the RDF peak corresponding to the coordination shell in question. This suggests a scheme for calculating PDFs from atomic models. Consider a model consisting of a large number of atoms situated at positions $\mathbf{r}_\nu$ with respect to some origin. Expressed mathematically, this amounts to a series of delta functions, $\delta(\mathbf{r} - \mathbf{r}_\nu)$. The RDF

[1] The radial distribution function is often denoted by $T(r)$ in the literature.

is then given as

$$R(r) = \sum_{\nu} \sum_{\mu} \frac{b_\nu b_\mu}{\langle b \rangle^2} \delta(r - r_{\nu\mu}) \tag{3.5}$$

Here the b values are the atomic scattering lengths of the ions and the sums are over every atom in the sample. This is a restatement of Eq. 1.1 and, indeed, this property of $R(r)$ is the origin of that equation. In the case of X-rays the b values are replaced by $f_\nu(0)$, the value of the atomic scattering factor for the ν-th atom at $Q = 0$. Note that $f_\nu(0) \sim Z_\nu$, the atomic number of the species. The value $r_{\nu\mu} = |\mathbf{r}_\nu - \mathbf{r}_\mu|$ is the magnitude of the separation of the νth and μth ions. The angle brackets are an average over all atoms (and isotopes) in the model.

The RDF has the other useful property that peaks in the function coming from well-defined atom–atom pairs reflect the precise shape of the pair-probability distribution. In the harmonic approximation (which is rather well obeyed in most cases) these peaks will have a Gaussian shape in the RDF[2]. In the other distribution functions we describe they are close to, but not exactly, Gaussian. The disadvantage of $R(r)$ is that it diverges (like r^2) with increasing r making it less satisfactory to plot if the structure is being considered over an extended range of r.

A number of other correlation functions come about because of different definitions of partial structure functions in multi-component systems. A discussion of these will be left until later. A thorough comparison of different correlation function conventions has been made recently (Keen, 2001)

3.1.4 Brief history

As early as 1915, Debye (Debye, 1915) took a three dimensional average of the sample structure amplitude (Eq. 2.8) to obtain the scattering expected from an isotropic sample such as an amorphous material or a powder. The formalism of correlation functions was introduced later and Zernicke and Prins (1927) showed the famous relationship between the two-point atom pair correlation function and the isotropically averaged scattering function that we give in Eq. 3.1. At the time there were no high-speed computers. Nonetheless, the approach was applied as early as 1930 by Debye and Menke to study liquid mercury. Significant early work was done with the method by Warren and co-workers (Tarasov and Warren, 1936; Warren *et al.*, 1936) by inverting the data manually using Beevers–Lipson strips; a device as unfamiliar to modern science as the slide-rule. Pictures of Beevers–Lipson strips are shown in Figure 3.4 and a short

[2] Even in the case of Gaussian probability distributions, small modifications to the Gaussian lineshape come from the three-dimensional powder averaging process, especially in the case of anisotropic thermal motions, as pointed out by Dimitrov *et al.* (2000) and discussed by Thorpe *et al.* (2002). These corrections are small but need to be taken into account for the greatest accuracy.

Figure 3.4. Picture of Beevers–Lipson strips (American Crystallographic Association).

description of their use is presented in Appendix 3.2. Needless to say it was a tedious and time-consuming affair and the approach was not widely embraced. In the 1960s computers, often with charming names[3], began to be used in an increasing number of studies (e.g. Henshaw, 1960[3]; Clayton and LeRoy, 1961[3]; Kaplow *et al.*, 1964, 1968; Ocken and Wagner, 1966), including studies of polycrystalline materials (Ruppersberg and Seemann, 1965; Fessler *et al.*, 1966; Temkin *et al.*, 1973).

The technique may have played a part in one of the most famous and controversial of all Nobel prizes. James Watson and Francis Crick were awarded the 1962 Nobel prize for chemistry for solving the double-helix structure of DNA. The breakthrough came in 1953 at Cambridge University. Their main competitors, Maurice Wilkins and Rosalind Elsie Franklin, were at the University of London. Rosalind Franklin, had superb X-ray diffraction data from DNA (J. D. Bernal called her X-ray photographs of DNA, 'the most beautiful X-ray photographs of any substance ever taken'). While Franklin struggled to

[3] The computer used to transform the Henshaw data was named the 'Datatron' and located at Chalk River Laboratories in Canada. The Clayton and LeRoy data were transformed by 'George' at Argonne National Laboratory!

analyze the data using crystallographic analysis, including Fourier methods that Franklin was well familiar with from her studies of carbon (Section 9.3.2), Crick and Watson came up with their insightful, simple and elegant solution to the scattering data using model building and chemical intuition. It is interesting that Watson had his insight only after being shown one of Franklin's excellent diffractograms of DNA; they had no X-ray data of their own. Sadly, in 1958, at the age of 37 and 4 years before Crick and Watson won their Nobel prize, Franklin died of ovarian cancer. Rather differing accounts of the controversy surrounding Franklin's role in the discovery of the structure of DNA can be read in Watson's book (2001), 'The double Helix; a personal account of the discovery of the structure of DNA', 'Rosalind Franklin: the dark lady of DNA' by Brenda Maddox (2002), and 'Rosalind Franklin and DNA' by Ann Sayre (2000), respectively.

As computers got faster and more widely available in the 1960s and 1970s, the application of the technique in the areas of liquids and amorphous materials grew immensely (Warren, 1969; Klug and Alexander, 1968). However, the technique was not widely applied to crystalline materials. At the same time computers were also applied in the analysis of crystallographic data, for example, with the development of the Rietveld refinement of powder diffraction data. There seemed little point in Fourier transforming diffraction data to obtain $G(r)$ when you could learn everything directly from the diffraction pattern, including the space-group symmetry, unit cell size, and with the advent of quantitative Bragg peak analyses such as Rietveld analysis, atomic positions. PDFs were low resolution affairs blighted by spurious ripples which came from the Fourier transform (*termination errors*, discussed in Section 3.5.2 and Appendix 3.3) and which people went to elaborate lengths to reduce artificially (Kaplow *et al.*, 1964; Konnert and Karle, 1973). These large amplituded artificial ripples had a similar frequency to the data themselves and could be mistaken for real atomic correlations: the 'fools gold' of the PDF world. PDF analysis was the technique of last resort, used only in situations when crystallography was inapplicable.

The power of the PDF in the study of liquids and amorphous materials was recognized, but even here there were problems. A case in point was the study of amorphous selenium. The PDF of a-Se was first collected as early as 1942 by Hendus (1942). New datasets from a-Se appeared at a rate of about one per decade (Krebs and Schultze-Gebhardt, 1955; Grimminger *et al.*, 1955; Andrievskii *et al.*, 1960; Henninger *et al.*, 1967) until the late 1960s. Despite this, no consensus emerged even on basic facts such as whether the structure was made of rings or chains. In 1968 the MIT group of Kaplow and Averbach, pioneers of computer based PDF work, took over. They were forced to bemoan that 'there is no general agreement on the structure of amorphous selenium....the interpretation of the diffraction data is severely limited by the spurious detail in the experimental distribution functions....it frequently appears that the methods of amorphous structure determination are being developed along with the structure.' (Kaplow *et al.*, 1968) The MIT group attempt to resolve the situation involved an iterative computer based data analysis procedure to get high quality PDFs and, to our knowledge, the first example of a reverse

Monte Carlo modeling analysis. Research continued over the decades and as recently as 1999 a letter appeared in Physical Review Letters discussing the structure of a-Se, which turns out to be ideal as a photoreceptor material in photocopiers. Now the bottleneck appears to be the ability to create reliable *ab initio* computer models of a-Se rather than with the PDF data themselves. In this 1999 study, calculated PDFs were compared to data collected in 1982 (Bellissent, 1982), and to the venerable data of Kaplow *et al.*, from 1968!

Termination ripples, and other artifacts coming from improper data normalization (which is another problem associated with low Q_{max} values) are not a problem if data are measured to high enough Q_{max} values. The reason is that, as discussed in Chapter 2, the signal in the real $S(Q)$ dies off due to the Debye–Waller factor. Terminating the data at more than ~ 3 times the standard deviation of the Debye–Waller envelope results in small termination ripples and more reliable data normalization (Toby and Egami, 1992). This is dramatically demonstrated in Section 9.3.2 where PDFs of disordered carbon from data taken by Rosalind Franklin in 1950 are compared with PDFs from modern data. Since in Eq. 2.2 $\sin\theta$ takes a maximum value of 1, Q_{max} is $<4\pi/\lambda$. To obtain higher Q_{max}s it is necessary to use short wavelength particles. This means higher energy X-rays and epithermal neutrons. Widely available laboratory X-ray sources such as Cu K_α give $Q_{max} \sim 8$ Å^{-1} and Mo K_α gives $Q_{max} \sim 16$ Å^{-1} whereas data in excess of $Q = 30$ Å^{-1} are required in general. Similar limitations apply to reactor based thermal neutron sources. It has been the advent of synchrotron based X-ray sources and spallation neutron sources (as well as affordable high speed computing) that has revolutionized our ability to measure highly accurate PDFs. The PDF is no longer a technique of last resort and, as applied to crystals, yields important complementary information to a traditional crystallographic analysis (Egami, 1990).

3.1.5 Multi-component systems

The equations relating $S(Q)$ and $G(r)$ given above, and the definition of $g(r)$ in Eq. 1.1, are quite general. However, when the system under study is composed of more than one kind of atom, it is generally desirable to understand the distinct structure about a particular chemical species. If the local coordination environment of a particular chemical species is well defined, this may also allow us to simplify the double-sum in Eq. 1.1. In the original definition, Eq. 1.1, the double sum is taken over all the atoms in the solid. We can define a *partial pair distribution function*, $g_{\alpha\beta}(r)$, that gives the distribution of atom pairs in the material coming only from atoms of type β around atoms of type α (Faber and Ziman, 1965; Waseda, 1980; Suzuki, 1987). Starting from Eq. 1.1, we could define this as, $g'_{\alpha\beta}(r) = \frac{1}{4\pi N\rho_0 r^2} \sum_{\nu\in\{\alpha\}} \sum_{\mu\in\{\beta\}} \delta(r - r_{\nu\mu})$, in which case the total pair distribution

function derived in Eq. 1.1 would clearly be

$$g(r) = \sum_{\alpha} \sum_{\beta} g'_{\alpha\beta}(r) \tag{3.6}$$

The normalized total scattering from the entire ensemble will be given by the contributions from each partial,

$$S(Q) = \sum_{\alpha} \sum_{\beta} S'_{\alpha\beta}(Q) \tag{3.7}$$

This shows intuitively how a total distribution function can be built up from a superposition of different sub-distributions.

Although perfectly valid, these definitions for the partial distribution functions and partial structure functions are not unique, and indeed are not the widely used standards. The most usual form for these partials is due to Faber and Ziman (1965). As we have discussed, in the limit of large Q, $S(Q) \rightarrow 1$. From Eq. 3.7 it is clear that $\sum_{\alpha} \sum_{\beta} S'_{\alpha\beta}(Q) \rightarrow 1$ in the high-Q limit and the scattering from each partial, $S'_{\alpha\beta}(Q) \rightarrow \langle b_{\alpha\beta} \rangle^2 / \langle b \rangle^2$, the ratio of the scattering cross-section of the partial to that of the sample as a whole. It is convenient to take this weighting factor out of the definition for the partial structure functions giving us the Faber–Ziman definition

$$S_{\alpha\beta}(Q) = \frac{\left(\sum_{\alpha} c_{\alpha} b_{\alpha} \right)^2}{c_{\alpha} c_{\beta} b_{\alpha} b_{\beta}} S'_{\alpha\beta}(Q) \tag{3.8}$$

where it can be readily verified that $\langle b_{\alpha\beta} \rangle^2 = c_{\alpha} c_{\beta} b_{\alpha} b_{\beta}$. The Faber–Ziman partial structure functions have the property that, like the total structure function, they tend to unity as $Q \rightarrow \infty$ (i.e. they are the $S(Q)$ that you *would* measure if your entire sample was made of only that partial). The total structure function is then given by

$$S(Q) = \sum_{\alpha} \sum_{\beta} \frac{c_{\alpha} c_{\beta} b_{\alpha} b_{\beta}}{\left(\sum_{\alpha} c_{\alpha} b_{\alpha} \right)^2} S_{\alpha\beta}(Q) \tag{3.9}$$

As a result of this normalization, the partial reduced pair distribution function can be obtained as a Fourier transform of the partial structure function,

$$G_{\alpha\beta}(r) = \frac{2}{\pi} \int_0^{\infty} Q[S_{\alpha\beta}(Q) - 1] \sin(Qr) \mathrm{d}Q \tag{3.10}$$

and substituting Eq. 3.9 into Eq. 3.1 it is readily seen that

$$G(r) = \sum_{\alpha\beta} \frac{c_{\alpha} c_{\beta} b_{\alpha} b_{\beta}}{\langle b \rangle^2} G_{\alpha\beta}(r) \tag{3.11}$$

Similarly, in this formalism

$$g_{\alpha\beta}(r) = \frac{\left(\sum_{\alpha} c_\alpha b_\alpha\right)^2}{c_\alpha c_\beta b_\alpha b_\beta} g'_{\alpha\beta}(r) = \frac{1}{4\pi N \rho_0 r^2} \frac{\left(\sum_{\alpha} c_\alpha b_\alpha\right)^2}{c_\alpha c_\beta b_\alpha b_\beta} \sum_{\nu\in\{\alpha\}} \sum_{\mu\in\{\beta\}} \delta(r - r_{\nu\mu}) \tag{3.12}$$

and the total distribution function,

$$g(r) = \sum_{\alpha\beta} \frac{c_\alpha c_\beta b_\alpha b_\beta}{\langle b\rangle^2} g_{\alpha\beta}(r) \tag{3.13}$$

Note that the measured coordination number (Eq. 3.4) also is a weighted sum of the coordination number of each pair,

$$N_{\mathrm{C}} = \sum \frac{c_\alpha c_\beta b_\alpha b_\beta}{\langle b\rangle^2} N_{\mathrm{C}}^{\alpha\beta}(r) \tag{3.14}$$

where $N_{\mathrm{C}}^{\alpha\beta}$ denotes the number of β atoms around an α atom. In the case of X-rays an approximation has to be made, since the structure function is given by

$$S(\mathbf{Q}) = \sum_{\alpha\beta} \frac{c_\alpha c_\beta f_\alpha(Q) f_\beta(Q)}{\langle f(Q)\rangle^2} S_{\alpha\beta}(\mathbf{Q}) \tag{3.15}$$

and the weighting factor, $w_{\alpha\beta} = c_\alpha c_\beta f_\alpha(Q) f_\beta(Q)/\langle f(Q)\rangle^2$, is a function of Q. Thus the total PDF is not exactly the weighted sum of partial PDFs. It can be made to approximate this situation by separating the absolute value and the Q-dependence of $f(Q)$. This is the so-called *Morningstar–Warren approximation* (Warren *et al.*, 1936). First the Q-dependence of the average form factor is found,

$$\bar{f}(Q) = \frac{\sum_{\alpha} c_\alpha f_\alpha(Q)}{\sum_{\alpha} c_\alpha f_\alpha(0)} \tag{3.16}$$

where $f_\alpha(0) \cong Z_\alpha$ is the atomic number of the αth element. The approximation is then made that $f_\alpha(Q) = Z_\alpha \bar{f}(Q)$. The weighting factors $w_{\alpha\beta}$ are a slowly varying function of Q and, as poor as this approximation is, it does not pose a serious problem in practice. This is largely borne out by how successfully X-ray PDFs from multi-component systems can be fit by structural models.

For binary systems the method by Bhathia and Thornton (1970) provides very useful insight. In this method partial structure functions are rearranged so that $S(Q)$ is expressed as the sum of terms representing density correlation, $S_{\mathrm{NN}}(Q)$, compositional correlation,

$S_{CC}(Q)$, and density–composition correlation, $S_{NC}(Q)$;

$$S(Q) = S_{NN}(Q) + 2\frac{\Delta b}{\langle b\rangle}S_{NC}(Q) + \left(\frac{\Delta b}{\langle b\rangle}\right)^2 S_{CC}(Q) \tag{3.17}$$

where

$$\begin{aligned}
\langle b\rangle &= c_A b_A + c_B b_B,\ \Delta b = |b_A - b_B| \\
S_{NN}(Q) &= c_A^2 S_{AA}(Q) + 2c_A c_B S_{AB}(Q) + c_B^2 S_{BB}(Q) \\
S_{NN}(Q) &= c_A c_B[c_A S_{AA}(Q) - (c_A - c_B)S_{AB}(Q) - c_B S_{BB}(Q)] \\
S_{NN}(Q) &= c_A c_B[S_{AA}(Q) + S_{BB}(Q) - 2S_{AB}(Q) + 1]
\end{aligned} \tag{3.18}$$

The corresponding PDF and RDF are expressed as the Fourier transform of each term. By integrating the RDF over the first peak we obtain coordination numbers, $N_C(NN)$ and $N_C(CC)$. The ratio is the so-called Warren chemical or compositional short-range order parameter (Warren *et al.*, 1951),

$$\alpha = \frac{N_C(NN)}{N_C(CC)} \tag{3.19}$$

The value of α is zero for a completely random alloy, but positive for a system with segregation tendency, and negative for a system with AB association tendency. Chemical affinity between two elements results in a negative Warren order parameter.

3.2. COMPOSITIONALLY RESOLVED PARTIAL PDF

As we have discussed, it is often true that the three-dimensional structure of a material under study can be recovered from the total PDF by quantitative structural modeling. However, it is sometimes desirable to determine the structure explicitly around a particular chemical species. In this section we describe how compositionally resolved PDFs can be determined in practice.

3.2.1 Differential PDF

In Section 3.1.5 we showed that $G(r)$ can be defined as a sum of partial PDFs which are correlation functions between chemically distinct species. The partial PDFs, often referred to simply as partials, have a special physical significance since it is often the case that the relationship between particular chemical species and their neighbors is of interest.

In order to determine all the partial PDFs of a system composed of n elements one needs a set of at least $n(n-1)/2$ independent $S(Q)$ data determined by diffraction measurements. Moreover, the measured $S(Q)$ often are very similar to each other, and information is hidden in small differences among the data, thus tending to suffer strongly from noise.

Thus a dataset of extremely high quality is required in order to determine the partials, and even in such a case it is an extremely difficult task. Nonetheless, in liquids and amorphous materials this approach is necessary and successfully undertaken (Soper, 2000; Petri *et al.*, 2001). Closely related 'Differential PDFs (DDFs)' are experimentally much more accessible using differential techniques as we discuss below (Fuoss *et al.*, 1981). DDFs over narrow ranges of r can be obtained by the XAFS measurement. This is one of the great strengths of the XAFS technique, which yields chemical specific local structural information. The relative merits and complementarities of the XAFS and PDF approaches are discussed in Appendix 3.4. In general the XAFS measurement is much easier to carry out, while a diffraction measurement provides DDFs over a much wider range of distances than the XAFS method can. Data interpretation is also more direct in the diffraction method because of the kinematical scattering.

The differential PDF is the pair correlation function between all atoms and a particular chemical species that can be thought to be located at the origin;

$$G_\alpha(r) = \sum_\beta \frac{c_\beta b_\beta}{\langle b \rangle} G_{\alpha\beta}(r) \tag{3.20}$$

For example, an AB alloy will have A–A, B–B and A–B partials and it will have A and B differentials where the A-differential is the A–A + A–B partials and the B differential the B–B + B–A partials. In terms of DDFs the total PDF is given by,

$$G(r) = \sum_\alpha \frac{c_\alpha b_\alpha}{\langle b \rangle} G_\alpha(r) \tag{3.21}$$

The DDF is related to the differential structure function (DSF),

$$S_\alpha(\mathbf{Q}) = \sum_\beta \frac{c_\beta b_\beta}{\langle b \rangle} S_{\alpha\beta}(\mathbf{Q}) \tag{3.22}$$

through the Fourier transformation,

$$G_\alpha(r) = \frac{2}{\pi} \int_0^\infty Q[S_\alpha(Q) - 1]\sin(Qr)\mathrm{d}Q \tag{3.23}$$

The DSF is related to the total structure function by

$$S(\mathbf{Q}) = \sum_\alpha \frac{c_\alpha b_\alpha}{\langle b \rangle} S_\alpha(\mathbf{Q}) \tag{3.24}$$

3.2.2 Anomalous X-ray scattering

The scattering factor of an atom is nearly independent of the energy of X-rays except in the vicinity of the absorption edge of the atom where it depends rather strongly on the X-ray energy E,

$$f(Q, E) = f_0(Q) + f'(E) + if''(E) \tag{3.25}$$

An example of the energy dependence of f' is shown in Figure 3.5. This energy dependence is known as anomalous dispersion, and originates from the resonance of the X-ray with the excitation of electrons in the core of an atom. Thus, if one tunes the X-ray energy to the edge of an element the scattering power from that particular element varies strongly with energy while the scattering from other elements remain more or less constant. We can take advantage of this special nature of the interaction between an atom and X-ray to determine the differential and partial PDFs. By carrying out the measurement at two or more energies in the vicinity of the edge of the element α, the scattering power $f_\alpha(Q)$ of the α atoms change but those of the other constituent ions do not. By taking the derivative of $S(Q)$ with respect to $f_\alpha(Q)$,

$$\frac{\partial S(\mathbf{Q})}{\partial f_\alpha(Q)} = \frac{c_\alpha}{\langle f(Q)\rangle} \sum_\beta \frac{c_\beta f_\beta(Q)}{\langle f(Q)\rangle} S_{\alpha\beta}(\mathbf{Q}) = \frac{c_\alpha}{\langle f(Q)\rangle} S_\alpha(\mathbf{Q}) \tag{3.26}$$

we get an expression for the DSF with respect to element α. This is why $S_\alpha(Q)$ and $G_\alpha(r)$ are called 'differential' SF and PDF. Thus, the DSF can be determined by measuring $S(Q)$ from the sample at two photon energies. Even though f' changes most rapidly right at the edge, it is advisable to stay a little away from the edge. The reason is that the absorption

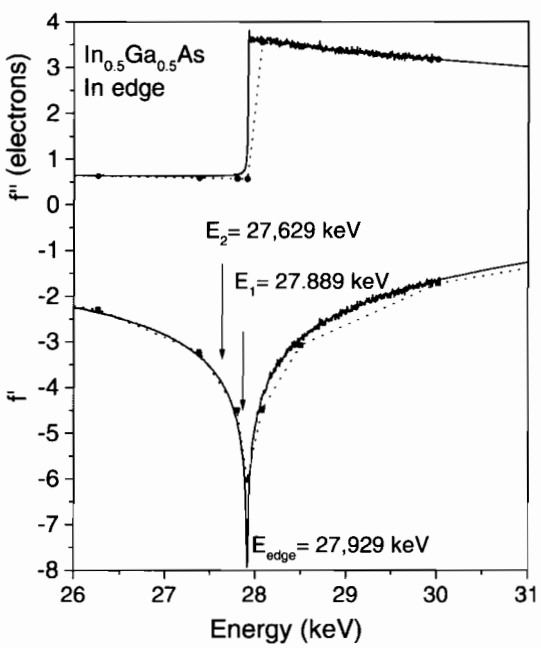

Figure 3.5. The anomalous dispersion of In scattering factors calculated near the K absorption edge. (top) Imaginary part, f''; (bottom) Real part, f' (Petkov *et al.*, 2000c).

factor changes so rapidly near the edge, and makes the absorption correction very difficult since the difference in the total scattering measured at two energies is usually rather small. For this reason and to minimize fluorescence from the sample it is strongly advised to stay *below the absorption edge* of the sample. Examples of a DSF and a DDF determined by anomalous scattering are shown in Figures 3.6 and 3.7 (Petkov *et al.*, 2000).

By determining the second derivative we obtain the partial structure function,

$$\frac{\partial^2 S(\mathbf{Q})}{\partial f_\alpha(Q)\partial f_\beta(Q)} = \frac{c_\alpha c_\beta}{\langle f(Q)\rangle^2} S_{\alpha\beta}(\mathbf{Q}) \tag{3.27}$$

However, the experimental accuracy of the second derivative is low, making the determination of the full partials extremely difficult. For this reason such a feat is rarely attempted, with some successes for relatively simple systems (Waseda, 1980, 1993). Actually, physical understanding of the atomic environment can be achieved pretty well by knowing the differential PDFs alone (Price and Saboungi, 1998). If the DDF (or even the total PDF) shows several distinct peaks it is often not difficult to assign the chemical identity to each peak knowing the atomic radii.

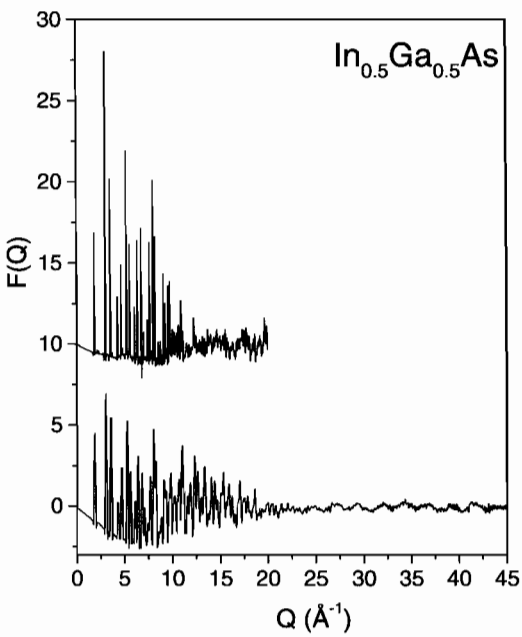

Figure 3.6. (top) The In-differential structure function of $In_{0.5}Ga_{0.5}As$ determined at the In K-edge and (bottom) the total scattering function, both plotted as $F(Q) = Q[S(Q) - 1]$ (Petkov *et al.*, 2000c).

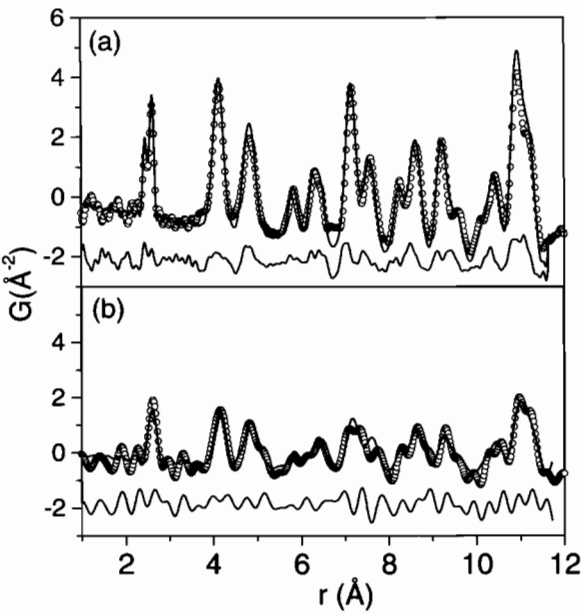

Figure 3.7. Total PDF of $In_{0.5}Ga_{0.5}As$ (top) and In-DDF (bottom) from the data in Figure 3.6. Open circles are the data, solid lines are calculated from a model (Petkov *et al.*, 2000c). This confirms that the higher-r peak in the nearest neighbor doublet at ~2.5 Å originates from In–As bonds. Here a high resolution total PDF and chemically resolved DPDF were both fit with the same structural model further constraining the structural solution.

3.2.3 Isotopic substitution

Elements found in nature are usually composed of various nuclear isotopes which differ from each other in the number of neutrons in the nucleus. While isotopes have almost identical chemical properties and result in virtually the same structure in the solid state, they can have different neutron scattering lengths. For instance, the value of b for ^{63}Cu is 6.43 fm, while that for ^{65}Cu is 10.61 fm. Thus by obtaining the total neutron PDF for two samples with identical chemical composition and structure but made of two different isotopes, one can determine the differential PDFs. Let us assume that one has a sample with the isotope 1 of an element α. The total structure function will be given by,

$$S_1(\mathbf{Q}) = \frac{1}{\langle b_1 \rangle^2}\left[(c_\alpha b_{\alpha 1})^2 S_{\alpha\alpha}(\mathbf{Q}) + 2c_\alpha b_{\alpha 1}\sum_{\beta\neq\alpha} c_\beta b_\beta S_{\alpha\beta}(\mathbf{Q}) + \sum_{\beta\gamma\neq\alpha} c_\beta c_\gamma b_\beta b_\gamma S_{\beta\gamma}(\mathbf{Q})\right] \tag{3.28}$$

where $b_{\alpha 1}$ is the scattering length of the α isotope 1, and

$$\langle b_1 \rangle = c_\alpha b_{\alpha 1} + \sum_{\beta\neq\alpha} c_\beta b_\beta \tag{3.29}$$

Thus by carrying out the measurement with α isotopes 1 and 2, the difference in the intensity is,

$$\begin{aligned}\Delta I(\mathbf{Q}) &= \langle b_1\rangle^2 S_1(\mathbf{Q}) - \langle b_2\rangle^2 S_2(\mathbf{Q}) \\ &= c_\alpha^2(b_{\alpha 1}^2 - b_{\alpha 2}^2)S_{\alpha\alpha}(\mathbf{Q}) + 2c_\alpha(b_{\alpha 1} - b_{\alpha 2})\sum_{\beta\neq\alpha} c_\beta b_\beta S_{\alpha\beta}(\mathbf{Q}) \\ &= 2c_\alpha(b_{\alpha 1} - b_{\alpha 2})c_\alpha b_\alpha S_{\alpha\alpha}(\mathbf{Q}) + 2c_\alpha(b_{\alpha 1} - b_{\alpha 2})\sum_{\beta\neq\alpha} c_\beta b_\beta S_{\alpha\beta}(\mathbf{Q}) \\ &= 2c_\alpha(b_{\alpha 1} - b_{\alpha 2})S_\alpha(\mathbf{Q}) \end{aligned} \tag{3.30}$$

where $b\alpha = (b\alpha_1 + b\alpha_2)/2$. Thus, the DSF, therefore DDF, can be determined by using two isotopes. In principle, by using isotopes of various elements and carrying out a required number of measurements all the partial PDFs can be determined. However, the accuracy deteriorates as the number of elements involved is increased. An example of the DDF determined for Cu in $YBa_2Cu_3O_{6.93}$ by using ^{63}Cu and ^{65}Cu is shown in Figure 3.8 (Louca *et al.*, 1999).

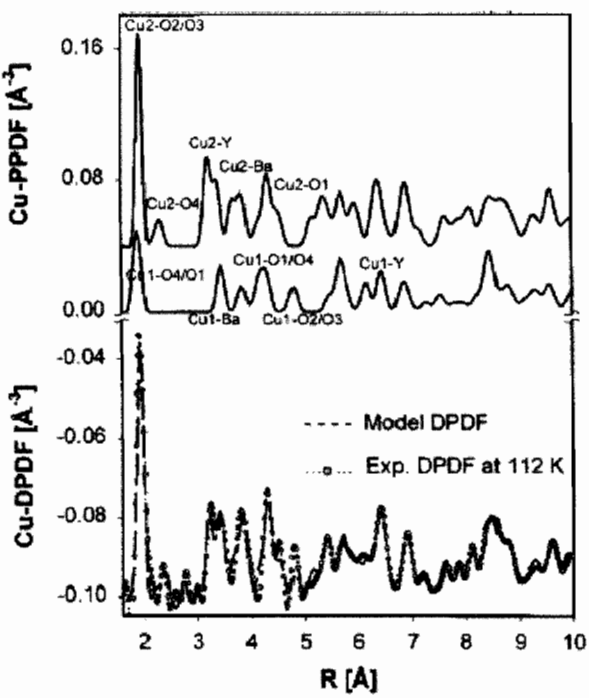

Figure 3.8. The DDF determined for Cu in $YBa_2Cu_3O_{6.93}$ by using ^{63}Cu and ^{65}Cu. Data are the dots, the solid lines are calculated from models (Louca *et al.*, 1999).

The greatest shortcoming of this technique is that the isotopically separated elements are expensive. Since neutron scattering experiments require samples weighing 10 g or more, the cost of isotopes to produce such samples can be very significant. Also sometimes isotopes do not show sufficient differences in scattering length, such as ^{16}O ($b = 5.803$ fm) and ^{18}O ($b = 5.84$ fm). Another problem is that two samples with different isotopes may not be identical in structure, especially if the sample preparation is difficult. In fact the vibrational frequency of the lattice depends on the atomic mass, so that the isotopically substituted samples do not have the same Debye–Waller factor. In spite of these shortcoming the method of isotopic substitution is a powerful technique in identifying the local chemistry. A poor man's version is the chemical substitution method in which an element is replaced by another element with very similar chemical nature and different scattering length. The DDF of quasicrystalline Al–Mn was determined by replacing Mn with Cr that has a positive b and similar chemistry (Nanao *et al.*, 1987).

3.2.4 Joint total and differential PDF studies

It is now possible to measure total PDFs with very high real-space resolution using high energy X-rays or spallation neutrons. By the techniques mentioned above it is also possible to measure differential PDFs. Differential PDFs measured using anomalous X-ray diffraction are often of low real-space resolution because the energy of X-rays used is limited to the absorption edge of the atomic species in question. For transition metal oxides this is generally below 10 keV; a severe limitation, though for a useful subset of elements in the fifth and sixth row of the periodic table it is high enough to give good real-space resolutions. Even when the real-space resolution is low, the chemically resolved PDF contains useful complementary information to the high resolution total PDF. It is also useful to combine two sets of PDF's determined by X-ray and neutron diffraction, since the partials are differently weighted. As we describe in Chapter 6, modeling programs exist which can simultaneously fit the same structural model to multiple datasets, including total and differential PDFs, There is likely to be a lot more of this kind of study in the future where the high real-space resolution measurement and the low resolution but chemically resolved PDFs put additional constraints on the modeling making the resulting structural solution more unique.

3.3. MAGNETIC CORRELATION FUNCTIONS

3.3.1 Magnetic scattering of neutrons

Neutrons are spin-1/2 particles. The spin of the neutron interacts with electron spins that give rise to magnetism in materials. Neutron scattering can be used to determine the spin configurations and magnetic structures of the material. In general the scattering intensity from magnetic scattering is complicated because of its vector nature; the intensity depends

on the dot product of the electron spin and the scattering vector **Q**. We will not get into the details of physics of magnetic scattering and delegate it to standard textbooks (e.g. Lovesey, 1984), but we should note that the intensity of scattering of spin polarized neutrons from a magnetic material has three parts, representing magnetic (spin–spin), spin–nucleus, and nuclear (nucleus–nucleus) interference functions;

$$I_{\text{total}} = I_{\text{M}} + I_{\text{S-N}} + I_{\text{N}}. \tag{3.31}$$

Spin-polarized neutron beams can be created, usually by using Bragg diffraction from a magnetic crystal such as a heusler alloy, or reflection from multilayered magnetic films, and most recently by sending the beam through spin polarized ^{3}He. If a similar magnetic crystal is used as an analyzer one can measure the intensity of scattered neutrons with the same spin as the incoming beam (spin non-flip) or opposite (spin flip). These two measurements can be done with the neutron spins either parallel or perpendicular to the scattering vector, **Q**, i.e., the polarization of the incoming beam lies either in the scattering plane or perpendicular to it. By combining these four sets of data the three terms in Eq. 3.31 can be sorted out.

A less unique but useful way of distinguishing nuclear scattering from magnetic scattering is to look at the Q-dependence of the scattering intensity. Magnetic scattering falls off quickly with increasing Q due to the magnetic form factor as we describe below. The magnetic scattering intensity, I_{M}, is related to the magnetic structure function, $S_{\text{M}}(Q)$,

$$I_{\text{M}}(Q) = f_{\text{M}}^2(Q) S_{\text{M}}(Q) \tag{3.32}$$

where $f_{\text{M}}(Q)$ is the magnetic form factor which is the Fourier transform of the spin density distribution function of an atom. For instance in transition metals such as Fe the radius of magnetic electrons (three-dimensional) is about 0.5 Å. This means at $Q = 3$ Å^{-1} the value of $f_{\text{M}}(Q)/f_{\text{M}}(0)$ is about 0.5, and if $S(Q) = 1$ as in the paramagnetic state $I_{\text{M}}(Q)/I_{\text{M}}(0)$ is about 0.25. In comparison thermal diffuse scattering due to phonons increases as Q^2, as shown in (Eq. 2.30). Thus magnetic and phononic contributions can be separated by examining the dependence on Q.

3.3.2 Magnetic PDF

A direct Fourier transformation of $I_{\text{M}}(Q)$ by

$$\rho_{\text{M}}(r) = \frac{1}{2\pi^2 r} \int I_{\text{M}}(Qr)\sin(Qr) Q \, \mathrm{d}Q \tag{3.33}$$

gives the spin–spin correlation function. This function has broad peaks as shown in Figure 3.9, since the width of the peak is equal to $\sqrt{2}$ times the radius of the spin distribution function around each atom. By dividing $I_{\text{M}}(Q)$ by the magnetic form factor to

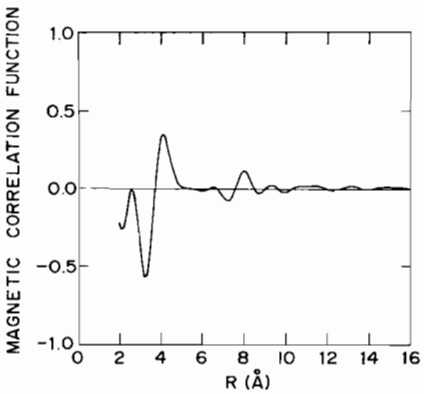

Figure 3.9. Magnetic PDF of amorphous Mn–Ni obtained by the direct Fourier transformation of magnetic intensity, $I_M(Q)$, determined by spin-polarized neutron diffraction (Wu *et al.*, 1987).

obtain $S_M(Q)$ by Eq. 3.32, we can determine the atom–atom spin correlation function,

$$\rho_A^M(r) = \frac{1}{2\pi^2 r}\int S_M(Q)\sin(Qr)Q\,dQ \tag{3.34}$$

which is more sharply defined, as shown in Figure 3.10. The relation between $\rho_M(r)$ and $\rho_A^M(r)$ is similar to that between the Fourier transform of $I(Q)$ for X-ray diffraction which gives an electron-electron distribution function and $\rho_0 g(r)$ which is an atomic correlation function.

As is well known nickel is magnetic. Why, then, is the magnetic contribution invisible in the PDF, shown in Figure 3.2? The answer is that the magnetic correlation peaks are wide

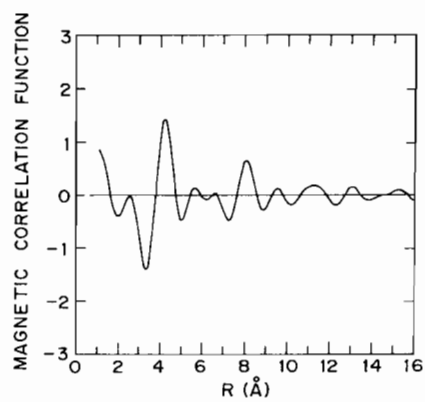

Figure 3.10. Atomically resolved magnetic PDF of amorphous Mn–Ni obtained by dividing $I_M(Q)$ by the magnetic form factor to obtain $S_M(Q)$ before Fourier transformation (Wu *et al.*, 1987).

and low, and completely buried under the nuclear peaks. For instance since the radius of the three-dimensional electron cloud in Ni is $\langle r \rangle = 0.5$ Å, the full width of the magnetic PDF is $2\sqrt{2}\langle r \rangle = 1.4$ Å, which is 10 times of the peak width for the nuclear PDF. The magnetic scattering length is 0.27 fm for 1 Bohr magnetron, thus for Ni it is about 0.16 fm, while the nuclear scattering length is $b_{\text{Nuclear}} = 1$ fm, so that $[b_{\text{Magnetic}}/b_{\text{Nucleus}}]^2 = 0.025$. So that the magnetic peak intensity will be only 0.25% of the nuclear peak intensity, completely negligible in Figure 3.2. While this is a rather extreme case since the magnetic moment of Ni is small and nuclear scattering length is large, in general magnetic correlation is not detectable from the PDF which is dominated by nuclear scattering. Spin polarized neutron scattering measurements are necessary to determine the magnetic PDF.

3.4. THE PDF IN HIGHER DIMENSIONS

When the PDF technique is mentioned it is usually assumed to apply to isotropic samples. In this case the data are averaged over all directions in three-dimensional space resulting in a one-dimensional function, $g(r)$. However, there can be a case where the averaging takes place only over two-dimensions rather than three-dimensions. In this case the scattering data are isotropically averaged in a single, well-defined, scattering plane in reciprocal space. These data can then be transformed to real-space coordinates resulting in a two-dimensional function $g(r, Q_n)$. In this case $\mathbf{Q}_n$ is a vector normal to this scattering plane and Q_n is the distance along $\mathbf{Q}_n$ from the origin to the scattering plane of interest. This is known as the two-dimensional PDF. It is appropriate for studying samples with particular two-dimensional geometries, for example, thin films and multilayers, though to date its only application has been in a cylindrical geometry quasicrystal (He *et al.*, 1993). This is destined to change with the advent of third generation synchrotron sources.

A related subject is that of surface scattering and surface correlation functions. In this case a two dimensional average of the scattering is taken; however, because the scattering is from a two-dimensional object there is no structure in the scattering along the direction in q-space perpendicular to the scattering plane: the scattering appears as structureless diffuse rods parallel to $\mathbf{Q}_n$. What results is a one-dimensional correlation function, the surface correlation function.

It is also possible to measure the entire reciprocal space of a single crystal, $S(\mathbf{Q})$, and transform the data to real-space using a vector transform. The resulting function is a three dimensional PDF, $g(\mathbf{r})$. Finally, we also note that lower dimensional correlation functions distinct from those mentioned above can be obtained by determining $S(\mathbf{Q})$ from a single crystal along specific directions in Q-space, $\mathbf{Q}_z$, and Fourier transforming this information. This results in a layer–layer correlation function, $g_{\text{layer}}(z)$, where the information in the real-space layer perpendicular to the $\mathbf{Q}_z$ vector has been averaged. All these correlation functions are defined below.

3.4.1 PDF defined in three-dimensions

Let us go back to the definition of the PDF in Section 3.1. Since we live in the three-dimensional world both the scattering vector $\mathbf{Q}$ and the real space vector $\mathbf{r}$ are three-dimensional. Only by taking the spherical average, representing the powder average, did we arrive at the standard expression for the powder PDF (Appendix 3.1). If we do not take such averaging, the PDF is a three-dimensional function, given by

$$\rho_0[g(\mathbf{r}) - 1] = \frac{1}{8\pi^3}\int[S(\mathbf{Q}) - 1]\exp(-i\mathbf{Q}\mathbf{r})d\mathbf{Q} \tag{3.35}$$

where $S(\mathbf{Q})$ is the structure function determined in the three-dimensional Q-space, and $g(\mathbf{r})$ is the three-dimensional density correlation function,

$$g(\mathbf{r}) = \frac{1}{\rho_0^2 V}\int \rho(\mathbf{r}')\rho(\mathbf{r}' + \mathbf{r})d\mathbf{r}' \tag{3.36}$$

Here V is the sample volume, and $\rho(\mathbf{r})$ is the single atom density function. The trouble is that in order to obtain this function the structure function $S(\mathbf{Q})$ has to be determined in continuous three-dimensional Q-space, and this is not an easy task. For instance if we use a relatively coarse resolution of $\Delta Q = 0.01$ Å^{-1}, in order to scan the entire three-dimensional Q-space of ± 40 Å^{-1}, scattering data have to be collected at as many as 5.12×10^{11} points. This is not impossible with the aid of a two-dimensional area detector, but it requires a long measurement time and a very large memory space (500 GB). To date, such a feat has never been accomplished, while an attempt on a smaller scale is under preparation. In addition there are many complications in this type of measurement as we discuss below. While theoretically measuring the three-dimensional PDF may be the best approach to solve the problem of complex crystal structure, in practice there are many alternatives that can be even better than the brute force three-dimensional measurement.

3.4.2 Anisotropic PDF

If the three-dimensionality of the PDF is weak and the PDF is nearly spherically symmetric (isotropic), an expansion by the spherical harmonics is the easiest way to describe the anisotropy. We use a polar coordinate and expand $S(Q)$ and the PDF in radial and angular functions,

$$S(\mathbf{Q}) = \sum_{\ell,m} S_\ell^m(Q)Y_\ell^m\left(\frac{\mathbf{Q}}{Q}\right) \qquad g(\mathbf{r}) = \sum_{\ell,m} g_\ell^m(r)Y_\ell^m\left(\frac{\mathbf{r}}{r}\right) \tag{3.37}$$

where $Y_\ell^m(\mathbf{a})$ are the spherical harmonics. $S(Q)$ and $G(r)$ are connected by

$$g_\ell^m(r) = \frac{i^\ell}{2\pi^2\rho_0}\int S_\ell^m(Q)J_\ell(Qr)Q^2dQ \tag{3.38}$$

$$S_\ell^m(r) = \frac{i^\ell}{2\pi^2\rho_0} \int g_\ell^m(Q) J_\ell(Qr) Q^2 \mathrm{d}Q \tag{3.39}$$

where $J_\ell(x)$ is the ℓth order spherical Bessel function. Note that $\ell = 0$ corresponds to the powder PDF, Eq. 3.1, since $J_0(x) = \sin x/x$.

This technique was applied to the analysis of anisotropic amorphous materials (Suzuki *et al.*, 1987). In particular, if metallic glasses were exposed to both stress and heat, anelastic deformation could occur and store memory of deformation. If the same sample is heated without stress, the stored anelastic deformation is released, and the sample changes its shape. The microscopic origin of this memory effect was found in the topological change of the metallic glass structure. By measuring $S(Q)$ after the anelastic deformation with the Q vector in two directions, parallel and perpendicular to the direction of the stress, $S(Q)$ was found to be anisotropic, as shown in Figure 3.11. By applying the spherical Bessel transformation with $\ell = 2$, the anisotropic PDF was obtained as shown in Figure 3.12 (Suzuki *et al.*, 1987). A later study showed that the higher order terms do exist, but are really small compared to the $\ell = 2$ term (Egami *et al.*, 1996). The result made it very clear that what changes as a result of anelastic deformation is the exchange of the atomic bonds as shown in Figure 3.13. In metallic glasses the most frequently found local topology is a triangle made of three atoms. The effect of stress is to cut some of the bonds that are

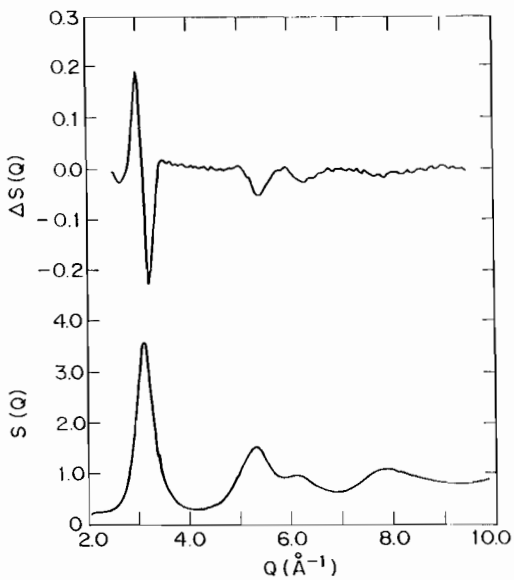

Figure 3.11. Anisotropic structure function of amorphous Fe annealed under stress to induce anelastic deformation. ΔS shows the difference of measurements with Q parallel and perpendicular to the direction of anelastic deformation (Suzuki *et al.*, 1987).

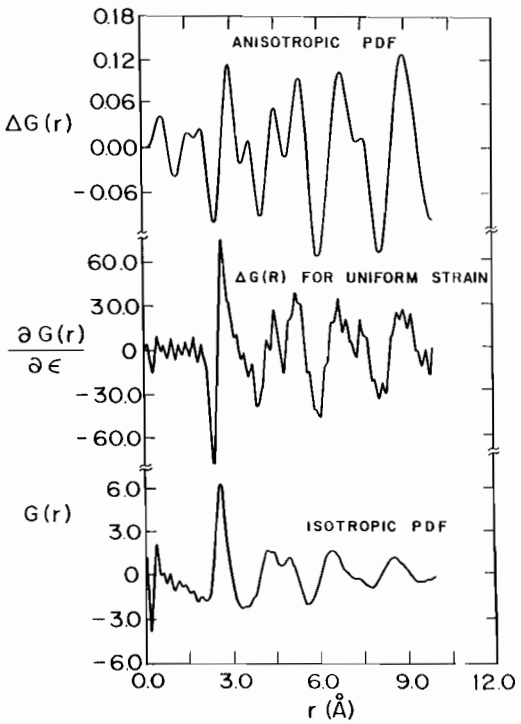

Figure 3.12. Anisotropic PDF of amorphous Fe annealed under stress to induce anelastic deformation obtained by spherical Bessel-transformation of $\Delta S(Q)$ shown in Figure 3.11 (Suzuki *et al.*, 1987).

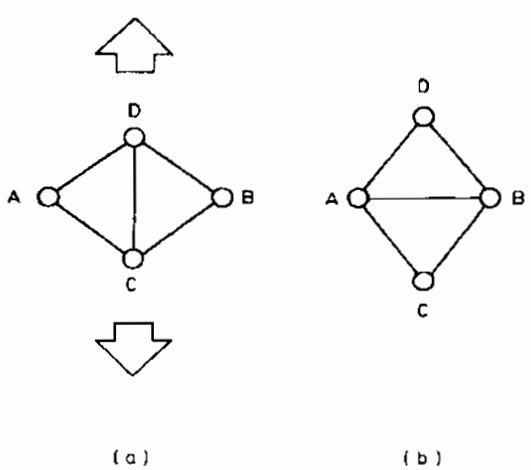

Figure 3.13. Bond exchange mechanism of anelasticity to produce the anisotropic PDF shown in Figure 3.12 (Suzuki *et al.*, 1987).

parallel to the direction of the stress, and form some that are perpendicular. In this way the sample becomes anelastically elongated.

This technique can also be applied to the study of crystalline materials. In such a case instead of the spherical harmonics one may use a set of linear combinations of the spherical harmonics that retain the crystal symmetry, such as the cubic harmonics. The advantage of this method is that we decouple the resolution of the radial function and that of the orientational function. Often if we have a high radial resolution we can understand the phenomenon well, without having a high orientational resolution. This way the amount of data we have to determine is very much reduced. This scheme can be implemented by using the pulsed neutron time of flight (tof) measurement with position-sensitive detectors (PSD). The resolution of the tof measurement, of the order of 10^{-3}, defines the radial resolution, while the resolution of the PSD determines the orientational resolution, usually of the order of 10^{-2}. If we collect 10^4 data points for a PDF at $10^2 \times 10^2$ two-dimensional mesh points the total data amounts only to 10^8, a much more reasonable size than in the full three-dimensional $g(\mathbf{r})$ is measured.

3.4.3 One-dimensional PDF and layer–layer correlations

Quite often it is mistakenly assumed that if a one-dimensional scan of the single crystal scattering data is Fourier transformed it produces the atomic PDF along that direction. The fact is that if one collects the scattering intensity from a single crystal along Q_z including the diffuse scattering and applies the Fourier transform, what is produced by such a procedure is not the atomic PDF but the atomic layer-layer correlation function,

$$g_{\text{layer}}(z) = \frac{1}{L}\int \rho_2(z')\rho_2(z'+z)\mathrm{d}z' \tag{3.40}$$

where z is parallel to $\mathbf{Q}$, L is the length of the sample in the z-direction, and $\rho_2(z)$ is the layer-averaged single atom density function,

$$\rho_2(z) = \frac{1}{A}\int \rho(r)\mathrm{d}x\mathrm{d}y \tag{3.41}$$

where A is the area of the sample in x–y plane. The layer–layer correlation function 3.40 is often confused with the one-dimensional correlation function averaged over the entire sample,

$$g_{1\text{-d}}(z) = \frac{1}{\rho_0^2 V}\int \rho(\mathbf{r}')\rho(\mathbf{r}'+\mathbf{z})\mathrm{d}\mathbf{r}' \tag{3.42}$$

Note that in this case the correlation function is volume averaged, while in Eqs. 3.40 and 3.41 the density function is averaged first, before evaluating the correlation function. In order to obtain the one-dimensional correlation function (3.42), one has to carry out an integration of $S(\mathbf{Q})$ over Q_x–Q_y space,

$$S_z(Q_z) = \frac{1}{A_Q}\int\int S(\mathbf{Q})\mathrm{d}Q_x\mathrm{d}Q_y \tag{3.43}$$

where A_Q is the area in the $Q_x - Q_y$ space over which the integration is carried out, and then apply the Fourier transform,

$$g_{1\text{-d}}(z) = \frac{1}{8\pi^3 L} \int [S_z(Q_z) - 1] \exp(-iQ_z z) dQ_z \tag{3.44}$$

Thus $S(Q)$ has to be determined over the entire three-dimensional space before this analysis can be carried out. There is no easy short cut in producing a three-dimensional PDF.

The layer–layer correlation is useful in some cases. For instance, this procedure has been applied to multi-layered films to determine their interfacial roughness. By measuring the specular reflectivity of the film with the **Q**-vector along the normal of the surface, the roughness of the interface can be evaluated through Eq. 3.40. It should be noted, however, the concept of lengthscale of roughness is absent from this expression. Roughness can be of the atomistic level, originating from atomic diffusion, or of mesoscopic scale coming from the imperfect surfaces such as steps in the vicinal surface. These two can be separated if one measures the diffuse scattering in the off-specular directions, as shown in Figure 3.14. By integrating the intensity in the $Q_x - Q_y$ plane, one obtains the one-dimensional correlation function 3.42, instead of the inter-layer correlation function 3.40 (Yan and Egami, 1993). In the case of the Pt/Co multilayered films with the ⟨111⟩ orientation the total thickness of the interface determined from the specular reflectivity is

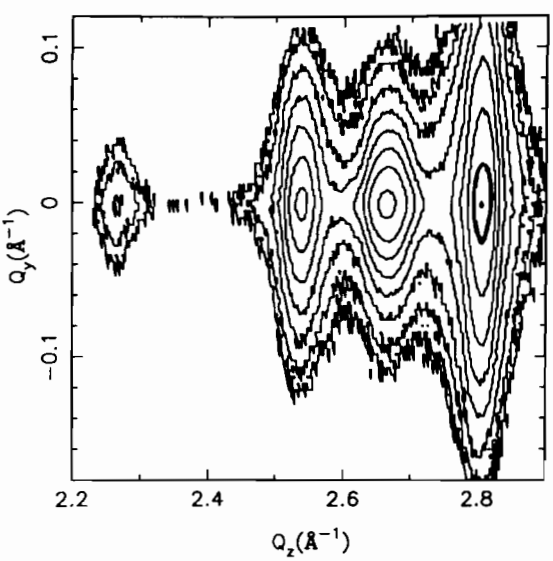

Figure 3.14. Scattering intensity from a Pt/Co multilayered film as a function of Q_z, normal to the surface and Q_y, parallel to the surface showing off-specular (i.e. $Q_y \neq 0$) diffuse scattering (Yan *et al.*, 1992).

8.7 Å, while the true local thickness due to diffusion is 6.9 Å. The difference is due to the mesoscopic correlated roughness.

3.4.4 Two-dimensional PDF and intra-layer correlation

If the data such as those in Figure 3.14 are averaged over the angle in the plane retaining the radial Q length $Q_r = \sqrt{Q_x^2 + Q_y^2}$,

$$S_2(Q_r, Q_z) = \frac{1}{2\pi Q_r} \int S(\mathbf{Q}) \mathrm{d}\varphi \tag{3.45}$$

where φ is the angle in the $Q_x - Q_y$ plane, the Fourier transform of this function is the in-plane two-dimensional PDF,

$$\rho_0 g(R, Q_z) = \frac{1}{2\pi} \int [S_2(Q_r, Q_z) - 1] J_0(Q_r r) Q_r \mathrm{d}Q_r \tag{3.46}$$

where $J_0(Q_r, Q_z)$ is the 0-th order spherical Bessel function. By Applying Eq. 3.46 on the off-specular diffuse scattering in Figure 3.14 one obtains the auto-correlation function for the film roughness as Figure 3.15 (Yan *et al.*, 1992). It gives the interfacial height–height correlation function similar to the surface height–height correlation function (Sinha *et al.*, 1988).

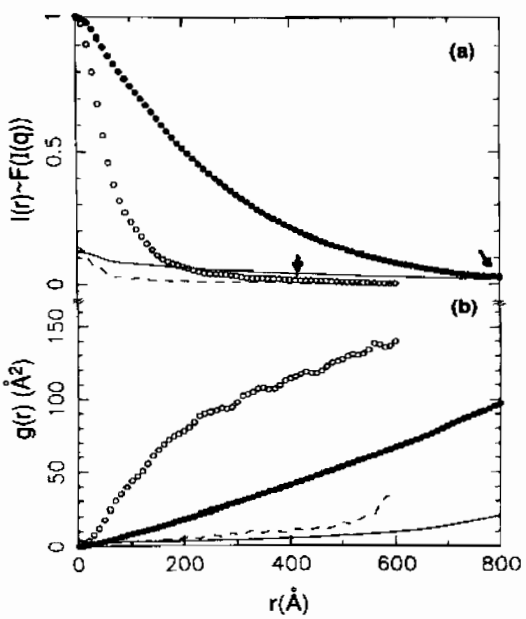

Figure 3.15. Roughness auto-correlation function obtained by Fourier transforming the diffuse scattering in Figure 3.14 (Yan and Egami, 1993).

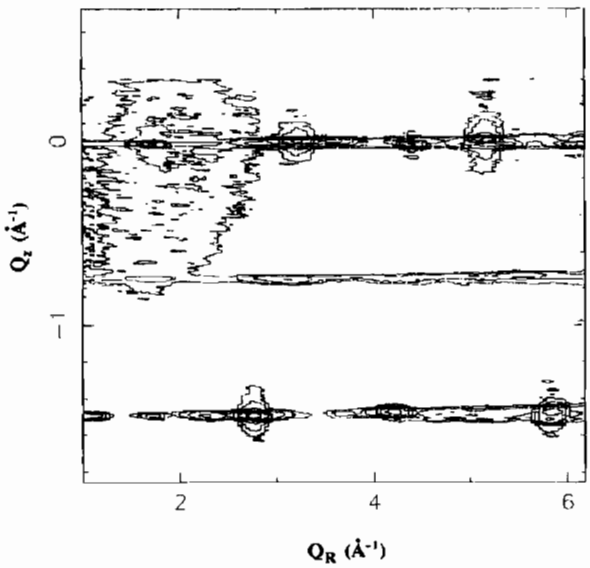

Figure 3.16. Two-dimensional intensity contour plot of scattering from a decagonal quasicrystal $Al_{65}Cu_{15}Co_{20}$. The sample was rotated about the z-axis during the experiment resulting in the intensity being averaged over h and k-directions. This intensity is plotted as Q_R at different values of Q_z (He *et al.*, 1993).

This method was also applied on a decagonal quasicrystal $Al_{65}Cu_{15}Co_{20}$ which is quasiperiodic in the $x-y$ directions, but is periodic in the z-direction (He *et al.*, 1993). The averaging over the planar angle can easily be done by rotating the sample around an axis (z-axis) during the measurement. By using the PDF resolved for l the in-plane atomic structure of this compound was analyzed. The results are shown in Figures 3.16 and 3.17. This technique can also be applied to the PDF of a surface.

3.4.5 Three-dimensional PDF and the powder PDF

As we discussed above theoretically the best way to determine the three-dimensional structure is to collect the diffraction data in three-dimensions and obtain the three-dimensional PDF. However, such a measurement is very time-consuming, and also a single crystal may not be always available, particularly when we are studying new materials. Furthermore, there are many technical complications associated with this method. First is the dynamic range of the measurement. The intensity of the Bragg peak is much stronger than the diffuse scattering by many orders of magnitude. The ratio depends upon the resolution, but a difference by 5–7 orders of magnitude is not rare. The detector has to be able to accommodate such a wide dynamic range, without saturation at high count rates and without background electrical noise at low count rates. Then, in order to measure the diffuse scattering accurately the background scattering has to be very low.

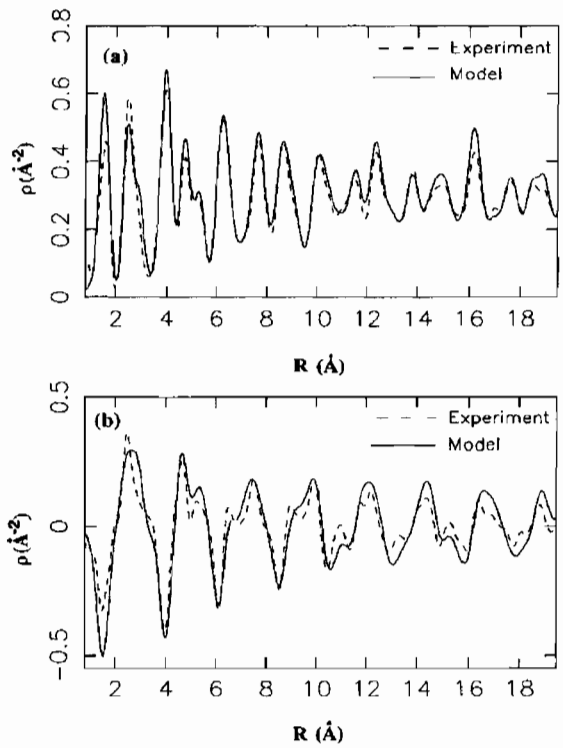

Figure 3.17. PDFs obtained from the data in Figure 3.16. The PDFs shown result from Fourier transforming data from $Q_z = 0$ (top) and $Q_z = 1.52$ Å $= 2\pi/c$ (bottom). The dashed lines are from models (He *et al.*, 1993).

The spectrometer has to be specially designed to reduce the background scattering. In addition for large crystals the extinction and multiple scattering of the Bragg peaks present a major problem. It is relatively easy to carry out a qualitative, or semi-quantitative, measurement of $S(\mathbf{Q})$ over three-dimensions. It is very difficult to determine $S(\mathbf{Q})$ with the precision required to obtain an accurate PDF.

Thus the PDF is usually reduced to one-dimension by making the measurement on a powder sample. By taking the orientational averaging, we lose the angular information. This might appear as a very severe compromise, and one might argue that an accurate three-dimensional single crystal study of the Bragg peaks coupled with a measurement of the diffuse scattering over a limited Q-space as is usually done is still better than the PDF study when some disorder is present. However, the argument is not so simple. Firstly the merit of collecting all the diffuse scattering in the powder scattering should not be underestimated. Unless one has a very good idea where the diffuse scattering occurs in the three-dimensional Q-space one may miss important information in the study of diffuse scattering from a single crystal. The merit of being able to collect all the diffuse

scattering by the powder measurement often overweighs the disadvantage of losing angular information.

3.5. ERROR ANALYSIS FOR THE PDF

3.5.1 Error diagnostics

Let us assume that you finally obtained a PDF, by the methods explained in the next two chapters. How do you know if the results are correct? For instance if a small, unexpected peak was found in your PDF, how do you know if that peak is real, or just some noise? Particularly if this peak fits to your theory or expectations, how do you know that you are not fooling yourself? A short answer is that you do not know. However, features of typical errors are well known, so that by elimination you can reduce the chance of making a mistake. The most conspicuous errors are ripples at short distances. It is physically impossible for atoms to come too close to each other, so that $g(r)$ has to be equal to zero below a certain distance. In reality, however, $G(r)$ oscillates around zero as shown in Figure 3.3, for example. In the following we discuss where these oscillations come from and how to reduce them.

3.5.2 Termination and normalization errors

As discussed in Section 3.1.4, terminating the integration in Eq. 3.1 results in spurious oscillation in the data, known as termination ripples or errors. In Appendix 3.3 this effect was shown to be given by,

$$G'(r) = \frac{1}{\pi}\int_0^\infty G(r')\left[\frac{\sin Q_{\max}(r-r')}{r-r'} - \frac{\sin Q_{\max}(r+r')}{r+r'}\right]dr' \qquad (3.47)$$

where $G(r)$ is the true reduced pair-density function. The convoluting function defined by Eq. 3.47 is shown in Figure 3.18. If the PDF has a peak given by a δ-function, the measurement yields a peak with many satellites given by Eq. 3.47. Fortunately the PDF is not composed of δ-function peaks, but of wider Gaussian-like peaks because of the atomic vibrations. Figure 3.19 shows how the original shape of the PDF peak is restored as the value of $Q_{\max}$ is increased. In general, if the value of $Q_{\max}$ is greater than $3/\langle\langle u^2\rangle\rangle^{1/2}$ the effect of termination is negligible (Toby and Egami, 1992). It is useful to consider this problem in Q-space. The non-zero width of the PDF peak gives rise to the Debye–Waller factor as discussed in Chapter 2. Because of this effect $S(Q)$ approaches unity. That means the value of $S(Q) - 1$ becomes smaller with increasing Q, and if it is small enough at $Q_{\max}$, the effect of termination is minimal. If $Q_{\max}$ is roughly equal to $3/\langle\langle u^2\rangle\rangle^{1/2}$ the Debye–Waller factor is about 0.03, which is usually small enough.

As we just mentioned, ideally $S(Q)$ converges to unity at large Q values. However, if the data are not normalized well enough, $S(Q) - 1$ will have a step at the termination at $Q_{\max}$, and produces strong ripples in $G(r)$, i.e., a normalization error produces termination errors

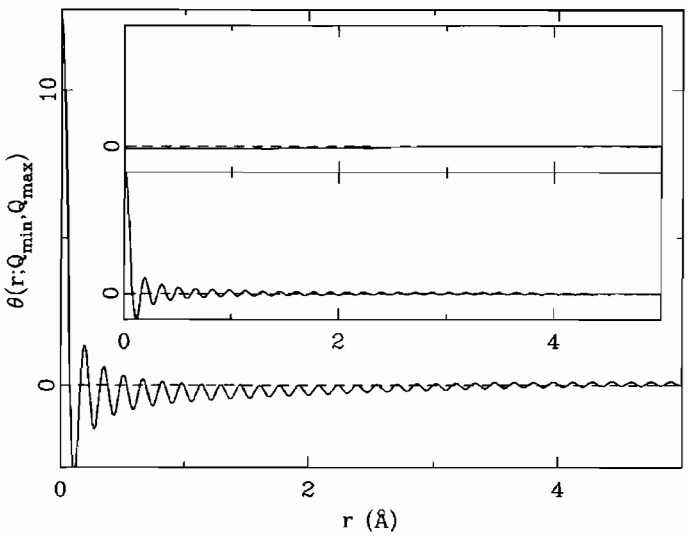

Figure 3.18. PDF termination function plotted for the case of $Q_{min} = 0.9$ Å^{-1} and $Q_{max} = 40$ Å (Peterson *et al.*, 2002).

even when the true structure function converges to unity before $Q_{\max}$. This is explored in more detail by Peterson *et al.* (2002).

3.5.3 Statistical errors

In order to eliminate the termination errors a high enough value of $Q_{\max}$ should be chosen. However, extending the range of Q increases the chances of including noise due to statistical errors. These are roughly proportional to $S(Q)/N$, where N is the detector count. Since in Eq. 3.1 the integral includes the multiplication by Q, the damage due to noise increases with Q. The error in $S(Q)$, $\Delta S(Q)$, affects the PDF through (Toby and Egami, 1992),

$$\rho_0^2 \Delta g(r)^2 = \frac{1}{4\pi^4 r^2} \sum_{\nu} [\Delta S(Q_\nu) Q_\nu \mathrm{d}Q_\nu \sin(Q_\nu r)]^2 \tag{3.48}$$

where ν enumerates data points, and $\mathrm{d}Q_\nu$ is the Q-spacing between the data points. The derivation of Eq. 3.48 is discussed in Appendix 5.3 in more detail. If the noise is purely due to statistics, this can be approximated as

$$\rho_0 \Delta g(r) = \frac{1}{2\sqrt{2}\pi^2 r} \left[\int \frac{Q^2 \mathrm{d}Q}{I(Q)} \right]^{1/2} \tag{3.49}$$

where $I(Q) = N(Q)/\mathrm{d}Q$, $N(Q)$ being the detector count. These results tell us a couple of points regarding the statistical noise:

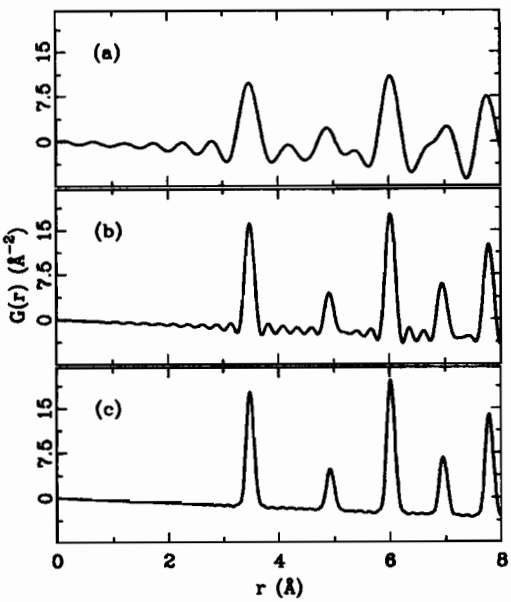

Figure 3.19. Calculated PDF of Lead assuming $\langle u^2 \rangle = 0.0025$ Å^{-2} comparable to that expected at low temperature. The calculated PDF has then been convoluted with the termination function (Eq. 3.47) assuming a Q_{max} of (a) 12 Å^{-1}, (b) 24 Å^{-1} and (c) 36 Å^{-1}. Because of the DW effects giving finite width Gaussian PDF peaks, the ripples have almost gone by $Q_{max} = 36$ Å^{-1}. This highlights the fact that accurate PDFs can be obtained if data are collected to sufficiently high Q_{max} without resorting to artificially damping the data.

1. The noise in $g(r)$, decreases with r as $1/r$ and is constant with r in $G(r)$.
2. The noise is cumulative; extending the Q range always increases noise.

Thus it is important to determine where to terminate $S(Q)$, by balancing termination error and noise.

3.5.4 Effect of Q-resolution

The effect of Q-resolution is different for the diffraction measurement with a monochromatic beam, such as high-energy X-ray scattering, and for the pulsed neutron tof measurement. In the case of the monochromatic beam the Q-resolution, ΔQ, is nearly constant in Q, while for the tof measurement it is approximately proportional to Q. Interestingly the mathematics involved in the analysis of the effect of Q-resolution is an exact inverse of the effect of atomic vibration discussed in Section 2.1.3. If the resolution is independent of Q, the effect of Q-resolution can be expressed as a convolution of the true scattering intensity, $I_t(Q)$, by the resolution function, $\Phi(Q)$;

$$I(Q) = \int I_t(Q - Q')\Phi(Q')\mathrm{d}Q' \tag{3.50}$$

Thus the Fourier transform is the product of the Fourier transform of each, according to the convolution theorem;

$$g(r) = g_t(r)\Gamma(r) \tag{3.51}$$

where $\Gamma(r)$ is the Fourier transform of the resolution function. Thus if the resolution function is Gaussian, the Fourier transform is a Gaussian function as well, with the standard deviation given by $1/\sigma_Q$, where σ_Q is the standard deviation of the resolution function, in analogy of the Debye–Waller factor. Thus the effect is not felt until r is large enough ($>2\pi/\Delta Q$).

However, in the case of the tof measurement the resolution is approximately proportional to Q. Thus the convolution theorem cannot be used in this case. Since the details of the PDF is determined by the high-Q portion of the data, the worsening resolution at high-Q is problematic. In Figure 3.20 the effect of Q-resolution in this case is illustrated. For $\sigma_Q =$ 0.006 the PDF becomes less defined even at 10 Å, and in the medium-range distance of 10–20 Å the effect is quite visible. Thus in order to determine the PDF over a large distance range it is important to use a high Q-resolution, even at the expense of intensity.

3.5.5 Effect of other systematic errors

As we will discuss later inaccuracies in various data processing procedures, such as absorption correction, contribute to systematic errors. They typically affect the data in the form of (Peterson *et al.*, 2002)

$$S_{obs}(Q) = A(Q)S_{true}(Q) + B(Q) \tag{3.52}$$

As we will discuss below inaccuracies in absorption correction are represented by $A(Q)$, while inaccuracies in the multiple-scattering correction and inadequate background correction are included in $B(Q)$. The effect of $A(Q)$ can be described by a convolution Usually $A(Q)$ is a slowly varying function of Q, and consequently its Fourier transform resembles the termination function 3.47. Thus if the characteristic Q values that represent the periodicity of $A(Q)$ is Q_E, ripples appear at $7.8/Q_E$. As for the effect of $B(Q)$, clearly its Fourier transform adds to the PDF. Again $B(Q)$ usually varies slowly with Q, and the effect in the PDF decreases quickly with r. In the distance range of interest the effect is usually small. That is why the PDF is remarkably reliable, even though it is impossible to eliminate all the errors in $S(Q)$ (Peterson *et al.*, 2002).

3.5.6 Remedies of errors

Various methods have been proposed to reduce the effects of termination error and other errors. Historically the most commonly used method to combat the termination error is to use a damping function for the window function in A3.3.1, so that $S(Q) - 1$ converges

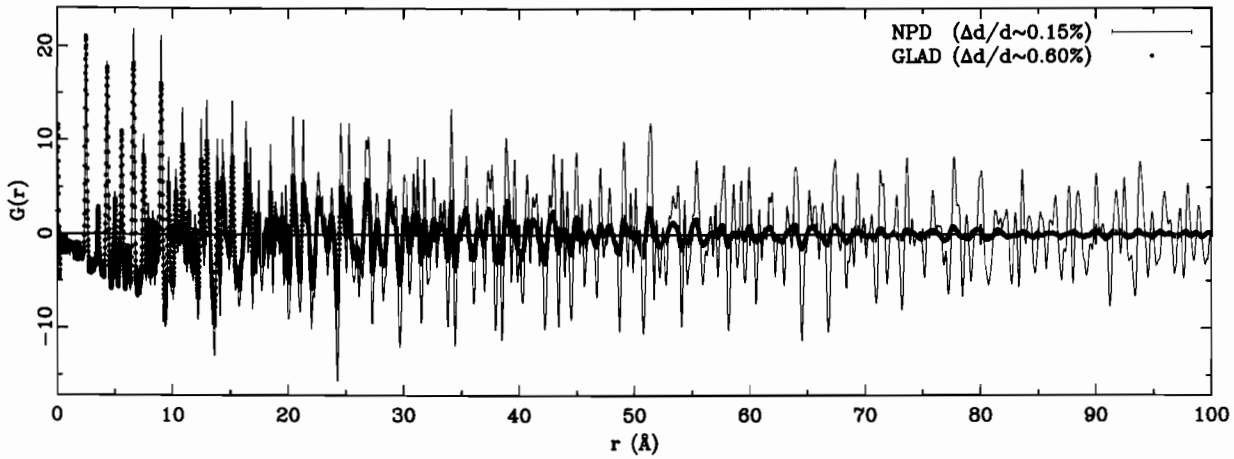

Figure 3.20. Effect of Q-resolution on the PDF. (a) Data are Nickel powder measured at GLAD at IPNS (low-resolution diffractometer, $\Delta d/d \sim 0.6\%$) and NPD at the Lujan Center (high resolution diffractometer, $\Delta d/d \sim 0.15\%$). The resulting PDFs are shown plotted on top of each other all the way to 100 Å. The loss of information in the nanometer range in the low resolution measurement is clearly apparent.

smoothly to zero. For instance a Gaussian function,

$$W(Q) = e^{-BQ^2} \tag{3.53}$$

is frequently used. Its effect is to add to the Debye–Waller factor and make the PDF peak wider than it really is.

Another approach is to extend $S(Q)$ artificially beyond the range over which it is actually experimentally determined, so that obvious errors are reduced. One possibility is to force $g(r) = 0$ below a certain cut-off distance, and extend $S(Q)$ either using an iterative method, or using the maximum entropy method. The use of the maximum entropy method is an attractive, but potentially dangerous, approach. While beautiful PDFs without oscillations can be obtained by this method, the uniqueness of the result is lost, since the result is strongly dependent upon the details of the constraint. For instance, depending upon the range in r over which $g(r) = 0$ is enforced, the PDF peak height changes by a large amount. This is discussed further in Chapter 6. Generally, *nothing is better than actually collecting the data accurately up to high values of* Q. Other corrections are largely cosmetic, and would not help recovering useful information. One of the reasons why they are cosmetic is that the PDF is obtained by the Fourier transformation, which already is an excellent noise screening method.

APPENDIX 3.1. DERIVATION OF THE PDF

Starting from the definition of the structure factor, we derive the PDF as a convolution of the atomic density function. In Section 2.1 we introduced the sample scattering amplitude (2.4),

$$\Psi(\mathbf{Q}) = \frac{1}{\langle b \rangle} \sum_{\nu} b_\nu e^{i\mathbf{Q}\mathbf{R}_\nu} \tag{A3.1.1}$$

For simplicity, here we assume that the atomic scattering factor is the same for all atoms, $b_\nu = \langle b \rangle / N$. Eq. A3.1.1 can be written in terms of the atomic density function, $\rho(\mathbf{r})$, as

$$\Psi(\mathbf{Q}) = \int \rho(\mathbf{r}) e^{i\mathbf{Q}\mathbf{r}} \, d\mathbf{r} \tag{A3.1.2}$$

The structure function is

$$S(\mathbf{Q}) = \frac{1}{N} |\Psi(\mathbf{Q})|^2 = \frac{1}{N} \int \int \rho(\mathbf{r}) \rho(\mathbf{r}') e^{i\mathbf{Q}(\mathbf{r}-\mathbf{r}')} d\mathbf{r} \, d\mathbf{r}' \tag{A3.1.3}$$

The PDF is the Fourier transform of the structure function, since,

$$\begin{aligned} P(\mathbf{R}) &= \frac{1}{(2\pi)^3}\int S(\mathbf{Q})e^{i\mathbf{QR}}\,d\mathbf{Q} \\ &= \frac{1}{8\pi^3 N}\int\int\int \rho(\mathbf{r})\rho(\mathbf{r}')e^{i\mathbf{Q}(\mathbf{r}-\mathbf{r}'+\mathbf{R})}d\mathbf{r}\,d\mathbf{r}'\,d\mathbf{Q} \\ &= \frac{1}{N}\int\int \rho(\mathbf{r})\rho(\mathbf{r}')\delta(\mathbf{r}-\mathbf{r}'+\mathbf{R})d\mathbf{r}\,d\mathbf{r}' \\ &= \frac{1}{N}\int \rho(\mathbf{r})\rho(\mathbf{r}+\mathbf{R})d\mathbf{r} = \rho_0 g(\mathbf{R}) \end{aligned} \tag{A3.1.4}$$

Note that

$$\int_V \rho(\mathbf{r})d\mathbf{r} = N \tag{A3.1.5}$$

For powders or isotropic amorphous materials both $S(\mathbf{Q})$ and $g(\mathbf{R})$ are isotropic, and angular variables can be integrated out;

$$\begin{aligned} \rho_0 g(R) &= \frac{1}{8\pi^3}\int\int\int S(Q)e^{iQR\cos\theta}\,d\cos\theta\,d\phi Q^2\,dQ \\ &= \frac{1}{4\pi^2}\int_0^\infty\int_{-1}^1 S(Q)e^{iQR\cos\theta}\,d\cos\theta Q^2\,dQ \\ &= \frac{1}{2\pi^2}\int_0^\infty S(Q)\frac{\sin(QR)}{QR}Q^2\,dQ \end{aligned} \tag{A3.1.6}$$

In practice the integral has to be terminated at a finite value of Q. The trouble is that $S(Q)$ approaches unity at large values of Q, so that the integration,

$$H(R) = \int_0^{Q_{\max}} S(Q)\frac{\sin(QR)}{QR}Q^2\,dQ \tag{A3.1.7}$$

oscillates wildly as a function of $Q_{\max}$. To avoid this problem it is customary to subtract unity from $S(Q)$. In this procedure what is really being done is to subtract the contribution from the average continuum, which corresponds to subtracting unity from $S(Q)$ and $g(R)$, since when the density is uniform there is no diffraction and the structure function has to be unity. Thus we obtain the standard expression,

$$\rho_0[g(R)-1] = \frac{1}{2\pi^2 R}\int[S(Q)-1]\sin(QR)Q\,dQ \tag{A3.1.8}$$

which is Eq. 3.1. The value of ρ_0 has to be supplied either by calculating theoretically from the structure, or by actually measuring the physical density.

APPENDIX 3.2. BEEVERS–LIPSON STRIPS

This account relies heavily on the excellent article 'The Mechanism of Beevers–Lipson Strips' Gould (1998) and the account of Warren (1990) since the authors have never had the pleasure of actually using Beevers–Lipson strips ourselves!

To Fourier transform a quasicontinous function like $S(Q)$ involves a sum over every point in $S(Q)$ for each point in $G(r)$. With modern computers we routinely utilize 1500 points in $S(Q)$ and compute 1000 points in $G(r)$ which requires the computer to make 10^6 calculations. This would clearly be a highly arduous task for the most ardent of graduate students, slide-rule in hand. It became significantly easier in 1936 with the development of Beevers–Lipson strips.

The Beevers–Lipson strips were strips of cardboard which contained pre-computed values of

$$A \sin\frac{2\pi hi}{120} \tag{A3.2.1}$$

(there were also cosine strips containing $A\cos(2\pi hi/120)$). There was one strip for each value of A and h (4000 strips in all) and on the strip wa
s printed 30 numbers which were the values of Eq. A3.2.1 for $1 < i < 30$. Strips for integer values of h from 1 to 30 were available for each value of A. The values of A that were available were $-100 < A < 100$ in integer steps, then $-900 < A < 900$ in steps of 100.

Now, let us assume that we want to Fourier transform a measured $F(Q) = Q[S(Q) - 1]$ according to Eq. 3.1, reproduced here,

$$G(r) = \frac{2}{\pi}\int_0^\infty Q[S(Q) - 1]\sin(Qr)\mathrm{d}Q \tag{A3.2.2}$$

This can be rewritten as a sum

$$G(r_i) = \frac{2}{\pi}\sum_{h=1}^{N} Q_h[S_h - 1]\sin(Q_h r_i)\Delta Q \tag{A3.2.3}$$

The argument of Eq. A3.2.1 can be written as $(4\pi h/60)(n/4)$. Thus, if we make the assignment $Q_h = (4\pi h/60)$ and $r_i = (i/4)$ we see that we can transform 30 Q-points in steps of ~ 0.2 Å^{-1} up to $Q_{\max} \sim 6.2$ Å^{-1}. Furthermore, using the identity

$$A \sin\frac{2\pi hi}{120} = -(-1)^n A \sin\frac{2\pi(60 - h)i}{120} \tag{A3.2.4}$$

allows Q-points in the range 30–60 to be evaluated (extending $Q_{\max}$ to ~ 13 Å^{-1}) using the available strips. Then, we make the assignment $A_h = (2/\pi)Q_h[S_h - 1]\Delta Q$. To increase accuracy it is necessary to work with A in the region -100 to 100 and so in practice it would be scaled to bring the values into this range, the final PDF then being divided in turn by this same factor.

The evaluation would then go as follows. For each Q-point the Beevers–Lipson strip corresponding to the right h and A value was selected from the box (Figure 3.4) and placed on a large table. Each subsequent strip was placed below the previous one such that the columns of i-values lined up. The Fourier transform could then be evaluated at each i-point by summing the numbers on the strips in each i-column. The summation was either done using a mechanical calculator, or more commonly, using mental arithmetic. The assignment above allowed the PDF to be calculated up to 7.5 Å in steps of 0.25 Å. By using the identity A3.2.4 suitably modified so that h and i are interchanged it is possible to extend the i-points in the range 30–60 and r_{max} to 15 Å.

As Warren (1990) points out 'The whole procedure is very simple and it is readily performed in 3 or 4 h". Nonetheless, the use of an electronic computer is definitely to be preferred: as Gould (1998) mentions 'Today,...Fourier transforms on several thousand data items...require less time than it takes to gulp down a cup of coffee'. The Beevers–Lipson strips approach may be healthier, but certainly more arduous and prone to error! Other historical gems from the Gould (1998) article include the fact that 500 boxes of Beevers–Lipson strips were sold between 1948 and 1970 and the big stir caused by the publication, in a crystallography newsletter of the British Crystallography Association, of a picture of Arnold Beevers and Henry Lipson in swimming costumes entitled 'Beevers and Lipson stripped'.

APPENDIX 3.3. TERMINATION ERROR

When the Fourier transformation in Eq. 3.1 is terminated at Q_{max}, the result can be rewritten as

$$G'(r) = 4\pi r\rho_0[g'(r) - 1] = \frac{2}{\pi}\int_0^{Q_{max}} [S(Q) - 1]\sin(Qr)Q\,dQ$$

$$= \frac{2}{\pi}\int_0^{\infty} W(Q)[S(Q) - 1]\sin(Qr)Q\,dQ \qquad \text{(A3.3.1)}$$

where $W(Q)$ is the window function,

$$W(Q) = 1\ (Q \leq Q_{max}) = 0\ (Q > Q_{max}) \qquad \text{(A3.3.2)}$$

In mathematics it is well known that the Fourier transform of a product A and B, $F\{AB\}$, is a convolution of the transform of each, $F\{A\}$ and $F\{B\}$;

$$F\{AB\}(r) = \int F\{A\}(r')F\{B\}(r - r')\,dr' \qquad \text{(A3.3.3)}$$

since

$$\begin{aligned}\int F\{A\}(r')F\{B\}(r-r')\mathrm{d}r' &= \frac{1}{(2\pi)^2}\int\int\int A(Q')\mathrm{e}^{\mathrm{i}Q'r'}\mathrm{d}Q'B(Q)\mathrm{e}^{\mathrm{i}Q(r-r')}\mathrm{d}Q\,\mathrm{d}r' \\ &= \frac{1}{(2\pi)^2}\int\int\int A(Q')B(Q)\mathrm{e}^{\mathrm{i}Qr}\mathrm{e}^{\mathrm{i}(Q'-Q)r'}\mathrm{d}r'\mathrm{d}Q'\,\mathrm{d}Q \\ &= \frac{1}{2\pi}\int\int A(Q')B(Q)\mathrm{e}^{\mathrm{i}Qr}\delta(Q'-Q)\mathrm{d}Q'\,\mathrm{d}Q \\ &= \frac{1}{2\pi}\int A(Q)B(Q)\mathrm{e}^{\mathrm{i}Qr}\,\mathrm{d}Q = F\{AB\}(r) \qquad \text{(A3.3.4)}\end{aligned}$$

Now,

$$G'(r) = \frac{1}{\mathrm{i}\pi}\int_0^\infty W(Q)[S(Q)-1](\mathrm{e}^{\mathrm{i}Qr}-\mathrm{e}^{-\mathrm{i}Qr})Q\,\mathrm{d}Q \qquad \text{(A3.3.5)}$$

then

$$\begin{aligned}G'(r) = \frac{1}{\mathrm{i}\pi}\Bigg[&\int_0^\infty W(Q)[S(Q)-1]\mathrm{e}^{\mathrm{i}Qr}Q\,\mathrm{d}Q \\ &+\int_{-\infty}^0 W(-Q)[S(-Q)-1]\mathrm{e}^{\mathrm{i}Qr}Q\,\mathrm{d}Q\Bigg]. \qquad \text{(A3.3.6)}\end{aligned}$$

Since $S(-Q) = S(Q)$, if we define $W(Q)$ as,

$$W(Q) = 1\ (-Q_{\max} < Q < Q_{\max}) = 0\ \text{(otherwise)} \qquad \text{(A3.3.7)}$$

we obtain

$$G'(r) = \frac{1}{\mathrm{i}\pi}\int_{-\infty}^\infty w(Q)[S(Q)-1]\mathrm{e}^{\mathrm{i}Qr}Q\,\mathrm{d}Q = \int_{-\infty}^\infty wt(r-r')G(r')\mathrm{d}r' \qquad \text{(A3.3.8)}$$

where $G(r)$ is the ideal PDF,

$$\begin{aligned}G(r) &= \frac{1}{\mathrm{i}\pi}\int_{-\infty}^\infty [S(Q)-1]\mathrm{e}^{\mathrm{i}Qr}Q\,\mathrm{d}Q \\ &= \frac{1}{\mathrm{i}\pi}\Bigg[\int_0^\infty [S(Q)-1]\mathrm{e}^{\mathrm{i}Qr}Q\,\mathrm{d}Q + \int_{-\infty}^0 [S(Q)-1]\mathrm{e}^{\mathrm{i}Qr}Q\,\mathrm{d}Q\Bigg] \\ &= \frac{1}{\mathrm{i}\pi}\Big[\int_0^\infty [S(Q)-1]\mathrm{e}^{\mathrm{i}Qr}Q\,\mathrm{d}Q - \int_0^\infty [S(Q)-1]\mathrm{e}^{-\mathrm{i}Qr}Q\,\mathrm{d}Q\Big] \\ &= \frac{2}{\pi}\int_0^\infty [S(Q)-1]\sin(Qr)Q\,\mathrm{d}Q \qquad \text{(A3.3.9)}\end{aligned}$$

and $wt(r)$ is the Fourier transform of the window function,

$$wt(r) = \frac{1}{2}\int_{-Q_{max}}^{Q_{max}} e^{iQr}\,dQ = \frac{\sin(Q_{max}r)}{r} \tag{A3.3.10}$$

This function, shown in Figure 3.18, has a large central peak, and becomes a δ-function at the limit of infinite Q_{max}. However, for finite values of Q_{max} it has side ripples that decay with distance. These ripples produce the termination errors. The first side peak is located at $r \sim 7.8/Q_{max}$. Eq. A3.3.8 may be expressed as,

$$\begin{aligned} G'(r) &= \int_0^\infty wt(r - r')G(r')dr' + \int_{-\infty}^0 wt(r - r')G(r')dr' \\ &= \int_0^\infty [wt(r - r') - wt(r + r')]G(r')dr' \end{aligned} \tag{A3.3.11}$$

or,

$$G'(r) = \frac{1}{\pi}\int_0^\infty G(r')\left[\frac{\sin Q_{max}(r - r')}{r - r'} - \frac{\sin Q_{max}(r + r')}{r + r'}\right]dr' \tag{A3.3.12}$$

APPENDIX 3.4. THE X-RAY ABSORPTION FINE STRUCTURE (XAFS) METHOD AND THE PDF METHOD

The X-ray absorption coefficient of a solid has many oscillations as a function of energy just above the absorption edge, which is called the X-ray absorption fine structure (XAFS). This phenomenon has been known for a long time, but was interpreted only in the 1970s in terms of the interference between the wavefunction of outgoing photoelectrons with that of photoelectrons backscattered by the near neighbors (Stern *et al.*, 1975; Lytle *et al.*, 1975). By analyzing these oscillations the distance to the neighboring atoms can be determined. Since photoelectrons come out primarily from the element, of which absorption edge is just below the energy of the incident X-ray, the XAFS provides the information about the environment of a particular element. Details about the technique can be found in a recent general text (Koningsberger and Prins, 1988).

The X-ray absorption coefficient, $\mu(E)$, where E is the energy of X-ray, may be expressed in terms of the momentum of the outgoing photoelectron,

$$k = \frac{\sqrt{m(E - E_{edge})}}{\hbar} \tag{A3.4.1}$$

where m is the mass of an electron, and E_{edge} is the absorption edge energy, as $\mu(k)$. By normalizing it against that of an isolated atom, $\mu_0(k)$, one obtains $X(k)$,

$$X(k) = \frac{\mu(k)}{\mu_0(k)} - 1 \tag{A3.4.2}$$

Its Fourier transform

$$G(r) = \int e^{2ikr} X(k) k^n \, dk \tag{A3.4.3}$$

where $n = 2$ or 3, is called the PDF. Indeed the position and intensity of the peaks of $|G(r)|$ roughly correspond to interatomic distances and coordination number. Also from the phase of $G(r)$ it is often possible to determine the chemical identity of the neighboring atoms.

However, because of many factors involved in scattering of electrons, $X(k)$ is modified in various ways. For instance the PDF peak appears usually at a distance significantly shorter than the real distance due to the phase shifts. Also $X(k)$ can be strongly affected by multiple scattering, in particular if atoms are nearly linearly lined up. Furthermore, $X(k)$ is given as the sum of contributions from various neighbors,

$$X(k) = \sum_j \chi_j(k) e^{-2ikr_j} \tag{A3.4.4}$$

where r_j is the distance to the neighbor j, while the form factor, $\chi_j(k)$, depends strongly on j. This form factor describes the atomic potential that scatters electrons and the life-time of photoelectrons, and its amplitude decreases rapidly with r_j. Thus the Fourier transform of $X(k)$ is not exactly the pair-density function (PDF). As shown in Figure A3.4.1 as an example $G(r)$ is significantly different from the PDF both in the peak shape and intensity. Thus the experimental data themselves do not directly provide the structural information, and the structure is determined only through calculating $X(k)$ and its Fourier transform for

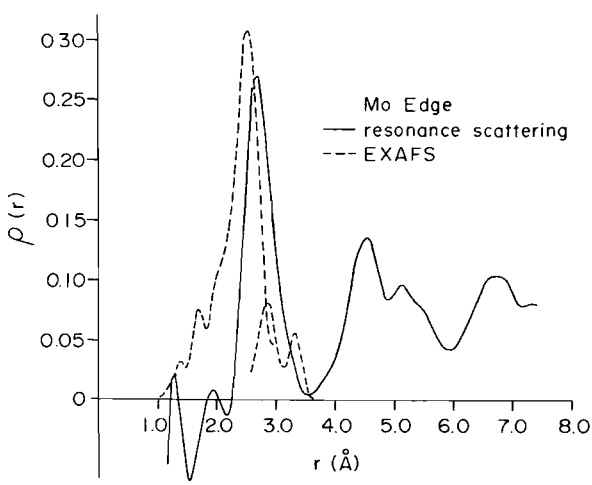

Figure A3.4.1. Comparison of the differential PDF of amorphous $Mo_{50}Ni_{50}$ determined using EXAFS and anomalous X-ray scattering at Mo and Ni edges (Aur *et al.*, 1983).

a particular model. The problem is that the theoretical $X(k)$ depends upon the method of calculation, and there is no unique way of calculating it. This lack of uniqueness is the greatest weakness of the XAFS method. Even though the XAFS method is easy to implement it is dangerous to rely upon the results of the XAFS analysis alone.

REFERENCES

Andrievskii, A.I., Nabitovitch, I.D. & Voloshchuk, Ya.V. (1960) *Kristallografiya*, **5**, 369 [English transl.: *Sov. Phys. Crystallogr.* **5**, 349 (1960)].

Aur, S., Kofalt, D., Waseda, Y., Egami, T., Wang, R., Chen, H.S. & Teo, B.-K. (1983) *Solid St. Commun.*, **48**, 111.

Bellissent, R. (1982) *Nucl. Instrum. Methods*, **199**, 289.

Bhathia, A.B. & Thornton, D.E. (1970) *Phys. Rev. B*, **2**, 3004.

Clayton, G.T. & LeRoy, H. (1961) *Phys. Rev.*, **121**, 649.

Debye, P. (1915) *Ann. Phys.*, **46**, 809.

Egami, T. (1990) *Mater. Trans.*, **31**, 163.

Egami, T., Dmowski, W., Kosmetatos, P., Boord, M., Tomida, T., Oikawa, E. & Inoue, A. (1995) *J. Non-Cryst. Solids*, **193**, 591.

Faber, T.E. & Ziman, J.M. (1965) *Philos. Mag.*, **11**, 153.

Fessler, R.R., Kaplow, R. & Averbach, B.L. (1966) *Phys. Rev.*, **150**, 34.

Fuoss, P.H., Eisenberger, P., Warburton, W.K. & Bienenstock, A. (1981) *Phys. Rev. Lett.*, **46**, 1537.

Gould, R (1998) *Crystallography News*, the newsletter of the British Crystallographic Association, No. **67**, December 1998. Available online at http://gordon.cryst.bbk.ac.uk/BCA/CNews/Dec98/strips.html. Also, reproduced in the ACA newsletter, spring 1999 edition, available online at the home-page of the American Crystallographic Association (http://www.hwi.buffalo.edu/ACA/).

Grimminger, H., Gruninger, H. & Richter, H. (1955) *Naturwissenschaften*, **42**, 256.

He, Y., Hu, R., Egami, T., Poon, S.J. & Shiflet, G.J. (1993) *Phys. Rev. Lett.*, **70**, 2411.

Hendus, H. (1942) *Z. Phys.*, **119**, 265.

Henninger, E.H., Buschert, R.C. & Heaton, L. (1967) *J. Chem. Phys.*, **46**, 586.

Henshaw, D.G. (1960) *Phys. Rev.*, **119**, 9.

Kaplow, R., Averbach, B.L. & Strong, S.L. (1964) *J. Phys. Chem. Solids*, **25**, 1195.

Kaplow, R., Rowe, T.A. & Averbach, B.L. (1968) *Phys. Rev.*, **168**, 1068.

Keen, D.A. (2001) *J. Appl. Crystallogr.*, **34**, 172.

Klug, H.P. & Alexander, L.E. (1968) *X-ray Diffraction Procedures for Polycrystal-line and Amorphous Materials*, Wiley, New York.

Koningsberger, D.C. & Prins R., Editors (1988) *X-Ray Absorption: Principles, Applications, Techniques of Exafs, Sexafs and Xanes*, Wiley-Interscience, New York.

Konnert, J.H. & Karle, J. (1973) *Acta Crystallogr. A*, **29**, 702.

Krebs, H. & Schultze-Gebhardt, F. (1955) *Acta. Crystallogr.*, **8**, 412.

Louca, D. & Egami, T. (1999) *Phys. Rev. B*, **59**, 6193.

Louca, D., Kwei, G.H., Dabrowski, B. & Bukowski, Z. (1999) *Phys. Rev. B*, **60**, 7558.

Lovesey, S.W. (1984) *Theory of Neutron Scattering from Condensed Matter*, Oxford Science Publications, Oxford.

Lytle, F.W., Sayers, D.E. & Stern, E.A. (1975) *Phys. Rev. B*, **11**, 4825.

Maddox, B. (2002) *Rosalind Franklin: The Dark Lady of DNA*, Harper-Collins, New York.

Nanao, S., Dmowski, W., Egami, T., Richardson, J.W. & Jorgensen, J.D. (1987) *Phys. Rev. B*, **35**, 435.
Ocken, H. & Wagner, C.N.J. (1966) *Phys. Rev.*, **149**, 122.
Peterson, P.F., Bozin, E.S., Proffen Th. & Billinge, S.J.L. (2002) *J. Appl. Crystallogr.*, unpublished.
Petkov, V., Billinge, S.J.L., Heising, J. & Kanatzidis, M.G. (2000a) *J. Am. Chem. Soc.*, **122**, 11571.
Petkov, V., Billinge, S.J.L., Shastri, S.D. & Himmel, B. (2000b) *Phys. Rev. Lett.*, **85**, 3436.
Petkov, V., Jeong, I-K., Mohiuddin-Jacobs, F., Proffen, Th. & Billinge, S.J.L. (2000c) *J. Appl. Phys.*, **88**, 665.
Petri, I., Salmon, P.S. & Fischer, H.E. (2001) *Phys. Rev. Lett.*, **84**, 2413.
Price, D.L. & Saboungi, M.-L. (1998) in *Local Structure from Diffraction*, Eds. Billinge, S.J.L. & Thorpe, M.F., Plenum, New York, p. 23.
Proffen, Th., DiFrancesco, R.G., Billinge, S.J.L., Brosha, E.L. & Kwei, G.H. (1999) *Phys. Rev. B*, **60**, 9973.
Ruppersberg, H. & Seemann, H.J. (1965) *Z. Naturforsch. Tell A*, **20**, 104.
Sayre, A. (2000) *Rosalind Franklin and DNA*, W.W. Norton & Company.
Sinha, S.K., Sirota, E.B., Garoff, S. & Stanley, H.B. (1988) *Phys. Rev. B*, **38**, 2297.
Soper, A.K. (2000) *Chem. Phys.*, **258**, 121.
Stern, E.A., Sayers, D.E. & Lytle, F.W. (1975) *Phys. Rev. B*, **11**, 4836.
Suzuki, K. (1987) in *Methods of Experimental Physics,* vol. **23**, Neutron Scattering, Part B. Eds. Price, D.L. & Sköld, K., Academic Press, New York, p. 243.
Suzuki, Y., Haimovich, J. & Egami, T. (1987) *Phys. Rev. B*, **35**, 2162.
Tarasov, L.P. & Warren, B.E. (1936) *J. Chem. Phys.*, **4**, 236.
Temkin, *et al.* (1973) *Adv. Phys.*, **22**, 581.
Toby, B.H. & Egami, T. (1992) *Acta Crystallogr. A*, **48**, 336.
Warren, B.E., Krutter, H. & Morningstar, O. (1936) *J. Am. Ceram. Soc.*, **19**, 202.
Warren, B.E., Averbach, B.L. & Roberts, B.W. (1951) *J. Appl. Phys.*, **22**, 1493.
Warren, B.E. (1969, 1990) *X-ray Diffraction*, Addison-Wesley, Reading; Dover, New York.
Warren, B.E. (1990) *X-ray Diffraction*, Dover, New York, p. 131.
Waseda, Y. (1980) *The Structure of Non-crystalline Solids*, McGraw-Hill, New York.
Waseda, Y. (1993) in *Methods in the Determination of Partial Structure Factors of Disordered Matter by Neutron and Anomalous X-ray Diffraction*, Eds. Suck, J., Watson, B., Chieux, P., Raoux, D. & Riekel, C., World Scientific, Singapore.
Watson, J.D. (2001) The double helix: a personal account of the discovery of the structure of DNA, Touchstone Books.
Wu, Y., Dmowski, W., Egami, T. & Chen, M.E. (1987) *J. Appl. Phys.*, **61**, 3219.
Yan, X. & Egami, T. (1993) *Phys. Rev. B*, **47**, 2362.
Yan, X., Egami, T., Marinero, E.E., Farrow, R.F.C. & Lee, C.H. (1992) *J. Mater. Res.*, **7**, 1309.
Zernicke, F. & Prins, J.A. (1927) *Z. Phys.*, **41**, 184.

This Page Intentionally Left Blank

Chapter 4

Total Scattering Experiments

This Page Intentionally Left Blank

Chapter 4
Total Scattering Experiments

4.1. GENERAL CONSIDERATIONS

4.1.1 Monochromatic and polychromatic (energy-dispersive) diffraction methods

A powder diffraction experiment consists of measuring the scattered intensity as a function of momentum transfer, Q. As is clear from Eq. 2.6 the value of Q can be varied by changing either θ, or $k(\lambda)$. The former corresponds to the monochromatic beam angle-dispersive diffraction and the latter the polychromatic (white) beam energy-dispersive method. In the energy-dispersive method, the diffraction pattern is determined by the spectroscopy of the diffracted beam.

In the case of X-ray scattering the spectroscopy is most conveniently and quickly done by using an energy sensitive solid state detector, such as a Li-drifted Si detector or an intrinsic Ge detector. These detectors have an energy resolution of about 1% that limits the Q resolution. The spectrum from a diffracted white (non-monochromatic) beam includes not only the diffracted peaks, but also other peaks such as the fluorescent peaks, escape peaks, and two-photon peaks, in addition to the inelastic Compton modified scattering intensity. The analysis of the spectrum is complex, but totally feasible (Egami, 1978). The greatest advantage of the energy-dispersive method is the speed of data acquisition. It is therefore most often used where intensity is an issue or when the geometry prevents wide diffraction angles being accessed, for example, in the study of amorphous materials under high pressure in diamond cells and studies of surfaces. However, the data analysis is troublesome and angle resolved diffraction is preferred when intensity is not an issue. In the case of neutron scattering, on the other hand, spectroscopy can be done by the time-of-flight (tof) method. Pulsed neutrons generated by a spallation source are used for such measurements. By knowing the time of pulse generation the tof can be determined by the time of arrival of the scattered neutron. The Q resolution is determined by the ratio of the size of the moderator to the length of the flight path, which can be 1:1000, achieving the Q resolution of 0.1%. As we discuss below, this is the preferred method for neutron powder diffraction in total scattering studies.

4.1.2 Single crystal and powder diffraction methods

The key to single crystal diffraction measurements is to align the reciprocal lattice vector of the material, **K**, to **Q**, so that the Bragg condition is achieved (Eqs. 2.11 and 2.12). For this purpose the sample orientation as well as the diffractometer setting have to be changed to achieve the maximum agreement of **K** and **Q**. In the modern diffractometer the

orientation of the crystal is changed by a motorized goniometer that is run by a computer. Once the crystal orientation is recorded in the computer, the crystal and detector can be oriented to scatter from any desired Miller indices simply by specifying them.

Powder experiments are simpler since the sample is isotropic and there is no need to worry about the sample orientation. In this case only the magnitude of Q is of importance. Varying Q is achieved by varying 2θ. It is important, however, that the powder is truly isotropic. Often because of gravity, stress or surface the powder is textured, that is the crystalline grains are preferentially oriented. The diffraction data from a textured sample can be very misleading unless the texture is well characterized.

4.1.3 Accuracy of the measurement

We will now consider the general principles that govern the accuracy of the measurement. In discussing accuracy it is important to separate accuracy in determining the Q values and accuracy in measuring the intensity. The accuracy of the Q values defining the positions of the Bragg peaks determines the accuracy of the derived lattice parameters. It is relatively easy to obtain high accuracy in the Q values by using a high quality monochromator, good collimation and good alignment. The intrinsic resolution of a monochromator is determined by its Darwin width, or mosaic spread if it is a mosaic crystal. The Darwin width can be calculated by using dynamical diffraction theory, but it can be rationalized by recognizing the fact that when the Bragg condition is met the X-ray can penetrate the crystal only by a certain amount even without absorption, since it is diffracted. This penetration depth, or the extinction length, λ_{ext}, defines the uncertainty in the momentum transfer by $\Delta q = 2\pi/\lambda_{ext}$. In practice, monochromator line-widths are determined experimentally by measuring a rocking curve. This is accomplished by initially fixing θ and 2θ to fulfill the desired Bragg condition. The crystal is then 'rocked' by varying θ at fixed 2θ.

The best way to obtain high collimation is to use a synchrotron radiation source that has a natural collimation due to the small source size and the large source-monochromator distance. The source size is defined by the size of the electron or positron bunch in the storage ring. Source-monochromator distances are generally more than 10 m and can be considerably longer than that, especially at third generation synchrotron sources. The beam intensity remains high despite these long source-mono distances because of the relativistic squeezing of the radiation emitted by the electrons into a narrow cone around their direction of motion, i.e. tangential to the ring. In high-resolution X-ray measurements using a synchrotron source the resolution can approach the Darwin width of the monochromator, which is of the order of 10^{-5}. Thus, a lattice constant can be determined down to four decimal points. The resolution of neutron spectrometers is lower since neutron beams cannot be as highly collimated because of the lower source intensities. Presently the best resolution achieved by neutron diffractometers

is of the order of 10^{-3}. By curve fitting, however, the lattice constant can still be determined with the accuracy of 10^{-4}.

Of great importance in a PDF measurement is the accurate determination of the *intensity* of diffraction. This gives information about the position of atoms within the unit cell through Eq. 2.14. The intrinsic accuracy of the intensity measurement, $\Delta I/I$, is determined by the statistical accuracy of the particle count,

$$\frac{\Delta I}{I} = \frac{1}{\sqrt{N}} \tag{4.1}$$

where N is the number of phonons or neutrons counted by the detector. However, the measured intensity is affected by other factors such as absorption, sample geometry, polarization and the Debye–Waller factor, and it is not necessarily easy to correct for these effects with high accuracy. Thus one has to use good judgment before accepting the atomic position determined down to many digits as is often published in the literature. Errors in measured intensities are discussed in more detail in Appendix 5.3.

4.2. THE NEUTRON SCATTERING EXPERIMENT

4.2.1 Sources

Pulsed neutrons can be produced either by an accelerator based spallation method, or by using a mechanical chopper at a reactor source. In the spallation method protons are accelerated to high energies (~ 1 GeV) and hit a target made of a heavy metal such as tungsten or uranium. Through violent collision protons shake down some neutrons from the nuclei of the target element by spallation, producing fast neutrons with the energy of several MeV. These fast neutrons are slowed down by a moderator, usually made of water or organic solid or liquid methane. See the Selected Bibliography for more information about spallation sources.

At a spallation neutron source data are best collected using the time-of-flight method. This makes the best use of the natural time-structure of the source that results in large fluxes of neutrons at the peaks of the pulses despite rather modest time-averaged fluxes. Spallation neutron sources are particularly valuable for PDF measurements. This is because of the large flux of *epithermal neutrons* that are under-moderated: they exit the neutron moderator before reaching thermal equilibrium. The epithermal neutrons are the short-wavelength neutrons that yield the important high-Q information (Section 3.1). With such sources, $Q_{\max}$'s in excess of 100 Å^{-1} can be possible. Table 4.1 gives the existing (and proposed) sources, and the instruments suitable for high resolution, wide angle, total scattering and PDF measurements at the time of writing. For convenience, web-site addresses are also included where more information can be obtained about these facilities

Table 4.1. Present and future spallation neutron sources and instruments suitable for PDF measurements.

Source	Location	URL	Instruments
Intense pulsed neutron source (IPNS)	Argonne National Laboratory, Argonne, IL, USA	www.pns.anl.gov	SEPD, GLAD, GPPD
ISIS	Rutherford Appleton Laboratory, Chilton, Oxon, UK	www.isis.rl.ac.uk	POLARIS, GEM
KENS	Tsukuba, Japan	neutronwww.kek.jp	HITT-II
MLNSC (Lujan Center)	Los Alamos National Lab, New Mexico, USA	www.lansce.lanl.gov/lansce12/index_12.htm	HIPD, HIPPO, NPDF
Spallation neutron source (SNS)	Oak Ridge National Lab, Tennessee, USA	www.ornl.gov/sns/	
European spallation source (ESS)		www.ess-europe.de	

and the procedures for obtaining beamtime. For up-to-date web information check the total scattering web page, http://www.totalscattering.org.

4.2.2 Diffractometer

Neutron powder diffractometers can be split into two main categories: angle-dispersive diffractometers at reactor sources and time-of-flight diffractometers at spallation neutron sources.[1] PDFs can be obtained from either kind, though as discussed in Section 4.1.1 the tof method is more useful for high resolution total scattering. Angle dispersive neutron diffractometers resemble two-circle X-ray powder diffractometers that are described in more detail in Section 4.3; in fact, similar diffractometer hardware can often be seen at neutron and X-ray sources. Because they are more useful for PDF measurements we describe in more detail tof diffractometers.

The diffractometer itself consists of a sample holder surrounded by fixed detectors. A collimated beam of neutrons emerges from the moderator close to the neutron source and travels down a beam-pipe to the sample position. This is shown schematically in Figure 4.1.

In total scattering measurements from crystals a balance must be struck between Q-space resolution and intensity. Conventional wisdom was that PDF experiments are flux limited and the primary beam-path should be as short as possible. What has become apparent more recently is that because of details of the strange Q-dependent asymmetric instrument resolution function (a legacy of the non-Gaussian source spectrum), the Q-space resolution does affect the real-space resolution and at least moderately good

[1] A number of other more exotic possibilities are also possible such as time-of-flight diffractometers at reactor sources, Fourier diffractometers such as HRPD at JINR at Dubna in Russia, and so on, though are not considered here.

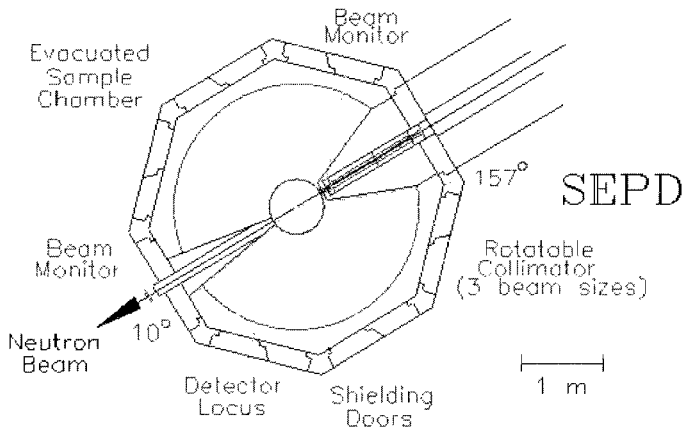

Figure 4.1. Schematic of a neutron time-of-flight powder diffractometer. The SEPD at IPNS, a first generation TOF diffractometer is shown. This diffractometer has ~160 detectors arranged in banks in the scattering plane along the locus of the large circle.

Q-space resolution is desirable for high-quality total scattering and PDF work. Additionally, there is a trend emerging for studying samples using both conventional crystallographic methods (e.g. Rietveld refinement) and PDF, in which case Q-space resolution is clearly beneficial. The best compromise is an instrument on a relatively short flight-path which still has a $\Delta d/d$ resolution of ~0.2% or better. The instruments of the greatest utility are situated on primary flight paths in the range of 10–25 m. Diffractometers can be moved farther from the source without completely compromising the intensity with the use of neutron guides in the primary flight path. Unfortunately, these guides are very inefficient at propagating epithermal neutrons that give the important high-Q information in $S(Q)$ and do not result in performance gains for total scattering measurements. Diffractometers without guides on longer flight paths are viable for PDF measurements at brighter sources such as the SNS. The higher resolution is always desirable if flux is not compromised too greatly.

The neutron beam is collimated, usually using boron containing rectangular shaped inserts placed before the sample, into a beam of dimensions ~1 cm × 4 cm. To optimize the scattering from the sample, it is therefore desirable to make the sample of similar dimensions. Samples generally are held in cylindrical containers made of natural abundance vanadium which is a metal that can be extruded and machined but which happens to scatter neutrons almost totally incoherently. It therefore contributes an almost smooth (tiny residual Bragg peaks remain) flat background that can be subtracted. The sample cans can be designed with seals allowing a heat-exchange gas (e.g. He for low temperature measurements) to be incorporated which helps to keep the large sample in a state of thermal equilibrium with the sample environment without having to rely on

inefficient heat conduction through the loosely packed powder. This results in rather small temperature gradients across the sample despite its large size.

The secondary flight path is usually in the vicinity of 1–2 m. Low angle detectors can be located further from the sample to compensate somewhat for their inferior resolution. Indeed, by placing detectors continuously along a carefully designed locus of sample-detector distances almost complete resolution compensation can be achieved meaning the resolution in each detector is approximately constant. Indeed, this will be the basis of a next generation tof powder diffractometer at SNS. The vicinity of the sample is usually evacuated to cut down air scattering and to facilitate the use of sample environments that require vacuum such as cryostats and furnaces. Because of the large dimensions of these instruments the full secondary flight-path is not generally evacuated since this would require very strong steel vacuum cans to support the atmospheric forces. Beam absorption by dry gas (air, nitrogen or another inert gas) is small so there is no particular gain in intensity by evacuating the flight paths.

In contrast to most angle-dispersive measurements, the detectors sit at fixed angle and do not move. Instead, the intensity vs. *Q diffractogram* appears as an intensity vs. neutron energy *spectrogram* in each detector. The data consist of the histogram of neutrons that arrived at various time intervals after the generation of the incident pulse, as shown in Figure 4.2. The time-of-flight, t, over the path L, translates into the neutron velocity, $v = L/t$. This gives the momentum $\hbar k = mv$, and the diffraction vector Q for elastic scattering by Eq. 2.6,

$$Q = \frac{2mL}{\hbar t} \sin \theta. \tag{4.2}$$

Thus tof is inversely related to Q (Figure 4.2).

In principle the experiment could be carried out with a single, energy resolving, detector at a fixed position. In practice, enormous gains in efficiency are possible by filling more solid angle with detectors. Early tof diffractometers had 10s or 100s of detectors which were grouped into 'banks' centered at certain diffraction angles. The modern trend is to fill as much solid angle as possible with detectors. This is immediately apparent by comparing the schematic of SEPD in Figure 4.1 with those of GEM at ISIS (Figure 4.3) and NPDF (Figure 4.4) at the Lujan Center at Los Alamos, both second generation diffractometers. NPDF has been upgraded from a conventional first generation tof powder diffractometer to be optimized for total scattering and PDF measurements and its layout before and after the upgrade are shown in Figure 4.4 for comparison. GEM was designed and built from the ground up as a second generation diffractometer and has 6500 detectors filling 3.5 steradians (sr) (out of 12.6) with detectors. Another excellent example of a second generation diffractometer is HIPPO at the Lujan Center.

The diffractograms in each detector are shifted in energy, or time-of-flight, due to the different diffraction angles (Eq. 2.2). In older diffractometers detectors were grouped

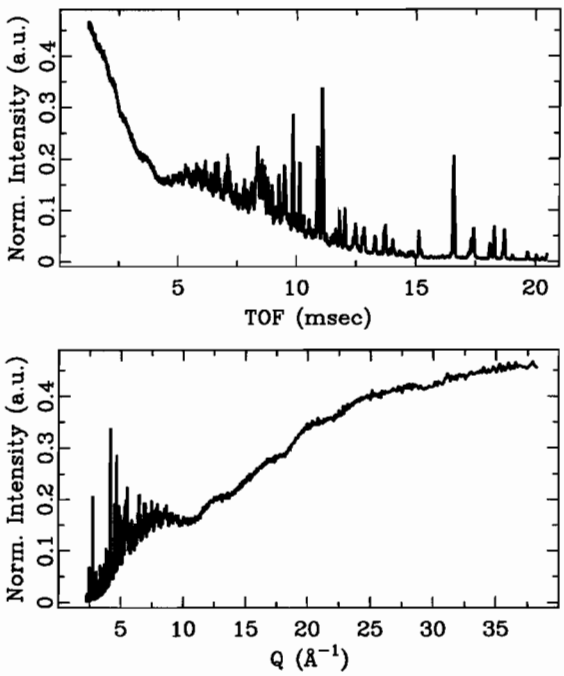

Figure 4.2. Data from SEPD showing intensity vs. time-of-flight from a crystalline sample of $Rb_3D(SeO_4)_2$. In (b) the same data are shown with the time-of-flight variable converted to Q using Eq. 4.2.

together in banks that had comparable resolution. The data from the detectors in a bank are combined by shifting the spectrum to account for the different position of the detector, a process known as 'time-focussing'. This was done electronically in early diffractometers to avoid the creation of large data-sets from spectra of thousands of points from hundreds of detectors. With the increase in computer speed, and reduction in cost of data storage, this is no longer necessary, even with the thousands of detectors on modern instruments: spectra from individual detector elements are now typically stored. The data corrections and reduction are then carried out using software allowing greater flexibility for choosing to include or exclude particular detector elements or to reprocess data a posteriori.

An important consideration with tof diffractometers for quantitative measurements is to have a stable, constant temperature, moderator resulting in a time-stable incident spectrum. An example of the incident source spectrum from a spallation source is shown in Figure 4.5. At lower power sources the moderator material of choice has been solid or liquid methane that has good spectral characteristics for diffraction. Water moderators seem to have better stability making them attractive for PDF work and the advantages of methane for conventional diffraction (more intensity at longer wavelengths, or lower Qs)

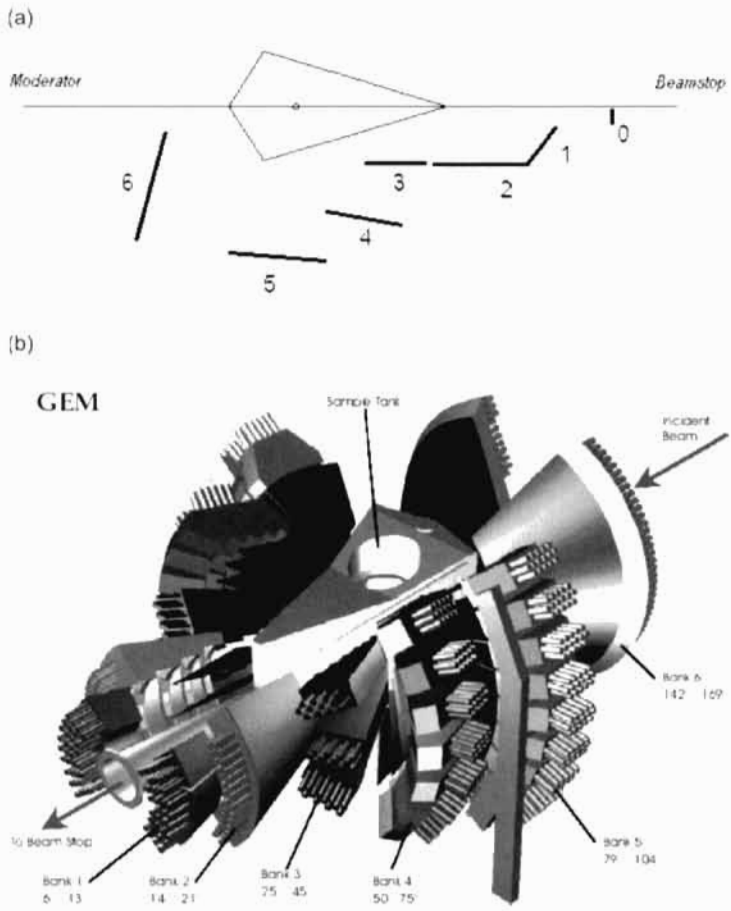

Figure 4.3. (a) Plan view of the second generation TOF powder diffractometer, GEM at ISIS showing the Gem-shaped sample tank and the positions of the six detector banks. Note that symmetrically arranged banks are present on the other side (not shown) (b) 3D computer generated design drawing of GEM showing the ~3.5 sr of detector coverage.

are less apparent in total scattering measurements. Moderators at the SNS are likely to be liquid-H_2 which are expected to be well suited to PDF measurements.

Finally, data corrections are made for instrument specific effects such as backgrounds and moderator instabilities (Chapter 5). These effects must be kept to a minimum for accurate PDFs to be determined. Fundamental additional requirements for the diffractometer therefore are low backgrounds, stable detectors and detector electronics, stable beam monitors and a stable moderator. The low backgrounds are achieved primarily by excellent collimation and shielding, including a well shielded primary beam dump, or 'get lost tube'(Figure 4.1). Tight secondary collimation between the sample and the

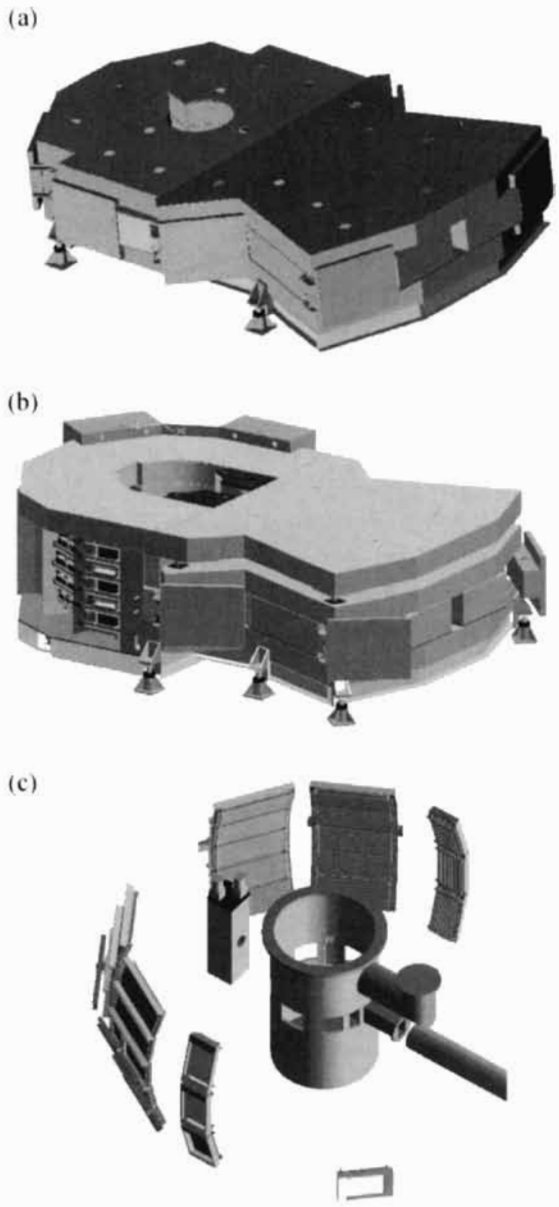

Figure 4.4. Schematic of the NPDF tof diffractometer at the Lujan Center at LANSCE before, (a), and after, (b) and (c), being upgraded from a conventional first generation diffractometer to one optimized for total scattering studies. The exploded view in (c) shows the enormously enhanced detector coverage. The detectors are position sensitive ^{3}He tubes. As a result of the upgrade the number of detector pixels is increased from 62 to 6544 and detector area coverage is increasing from 4960 to 27 800 cm^2. The increase in detector coverage is concentrated in the important backscattering region.

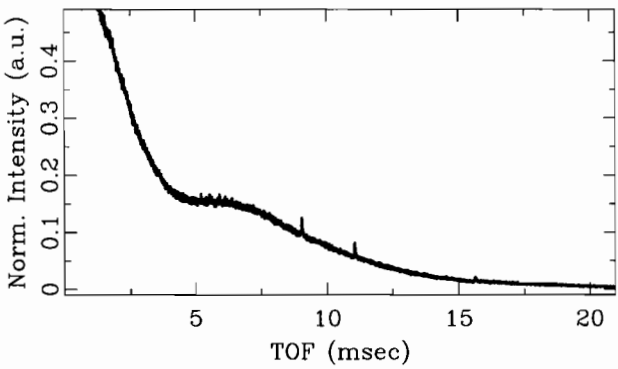

Figure 4.5. Example of a source spectrum from a spallation neutron source. The one shown is from SEPD at IPNS. It is measured using an incoherently scattering vanadium rod and some residual Bragg-peaks are evident. Note the Maxwellian peaked around 7 ms crossing over into a quickly rising epithermal tail at short times (high energies).

detectors is useful to lower backgrounds from special environments such as the heat shields from cryostats and furnaces, as well as lining the sample can and secondary flight path with borated[2] absorbing material. For the lowest backgrounds, oscillating radial collimators can be used. These solve the competing problems of wanting absorbing collimators in the secondary flight path (so only neutrons scattered at the sample position enter the detector) and wanting to fill solid angle with detectors. Radial collimators will tend to shadow the detectors, but by oscillating the collimators, no detector is shadowed all the time. The radial collimator for GEM is shown in Figure 4.6. There is, of course, some loss in intensity so their use will depend on whether more intensity, or lower backgrounds, are the primary consideration in a particular measurement.

4.2.3 Neutron detection

Neutrons are weakly interacting neutral particles and are difficult to detect. The usual method is to incorporate a special isotope into a gas or a solid that captures neutrons and then decays quickly with the production of a some strongly ionizing radiation such as high energy protons. The problem then becomes to detect the ionizing radiation which is done using similar technologies to those used for detecting X-rays as discussed in Section 4.3.3.

The most common detectors use pressurized ^{3}He gas in a tube (Figure 4.7). The relevant nuclear reaction in this case is $^3\mathrm{He} + \mathrm{n} \rightarrow \mathrm{p} + \tau + \gamma$ where n is the neutron, p is a proton, γ is a gamma ray and τ is a triton, the nucleus of a tritium atom. The tube is constructed as

[2] Cadmium, sometimes used as a neutron absorber, is not suitable in total scattering diffractometers that make use of the epithermal neutrons because of its strongly energy dependent absorption in this energy range due to a ^{113}Cd absorption resonance.

Figure 4.6. Photograph of the radial collimator that is now installed on GEM at ISIS. The vertical vanes are thin and borated.

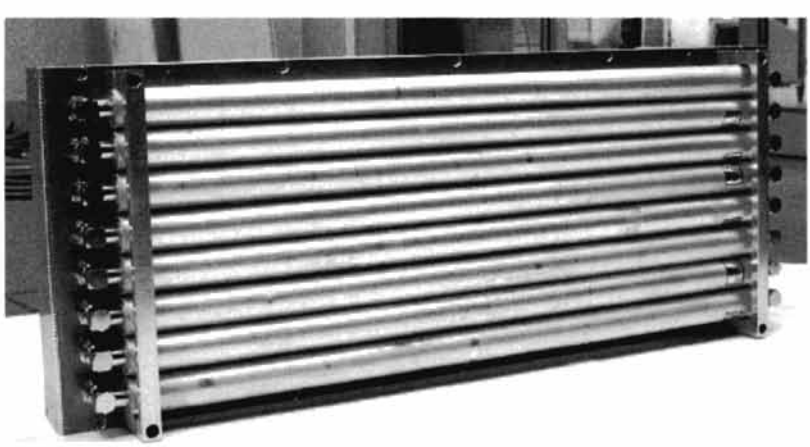

Figure 4.7. Photograph of a bank of ^{3}He tube position sensitive detectors that are now installed on NPDF at the Lujan Center.

a proportional counter with a wire down the middle that is maintained at a high voltage. The gas in the tube in the vicinity of the nuclear reaction is ionized by the high energy proton and triton and the ionized gas results in a charge pulse in the wire of the proportional counter. The charge pulse is swept out of the detector due to the applied voltage, amplified, converted to a digital pulse and recorded in a computer. In tof diffractometers, the time of arrival of the neutron must also be determined accurately which is accomplished electronically. These ^{3}He tubes can also have a position sensitivity such that the position *along* the wire where the neutron arrived is also recorded. This is done by determining the relative time it takes the positive and negative charge pulses to reach the ends of the detector, the ratio giving the distance of arrival along the detector. These tubes are typically 1–2.5 cm in diameter and 0.5–1 m in length. The gas inside is typically a mixture of ^{3}He with small amounts of other gases (for example, propane) for absorbing the proton and the triton more effectively and quenching the charge avalanche. To improve neutron detection efficiency the gas is maintained over pressurized to a few atmospheres. To reduce background counts it is desirable to lower the sensitivity of the detector to gamma rays by an appropriate choice of gas mixture. ^{3}He tubes are known for their high detection efficiency, low sensitivity to gammas and adequate position sensitivity and count-rate capability. Another factor is the many years of experience with this kind of technology.

Other useful nuclei for neutron detection are ^{6}Li, ^{10}B, ^{155}Gd and ^{157}Gd. The Li, B and Gd isotopes tend to be used in scintillator detectors or as thin solid foils, though BF_3 is gaseous and can be used in a proportional counter similar to a ^{3}He tube. A scintillator material is either doped with the absorbing nuclei or manufactured out of it (e.g. LiF or LiI). The nuclear reaction results in ionizing radiation that is absorbed by the scintillator that then gives off visible light. This light is shone onto an anode that emits electrons through the photoelectric effect. These are accelerated and amplified in a photomultiplier tube to produce a charge pulse that is converted to a neutron count. Position sensitivity is produced in these detectors by pixelating the detector and extracting light from each pixel using shielded optical fibers. An advantage of this technology is that the detector can be manufactured in any shape allowing solid angle to be filled very effectively with small amounts of dead area (see Figure 4.8). Also, with improved commercial manufacturing processes used the cost per steradian of these detectors is becoming rather low. Earlier problems with gamma sensitivity and low efficiency, especially for higher energy neutrons, are also now being successfully resolved. There is some probability that this technology will replace ^{3}He tubes in a number of applications.

4.2.4 Beam monitor

Quantitative experiments such as total scattering measurements need to be normalized by the total neutron flux on the sample. This is accomplished by measuring the incident

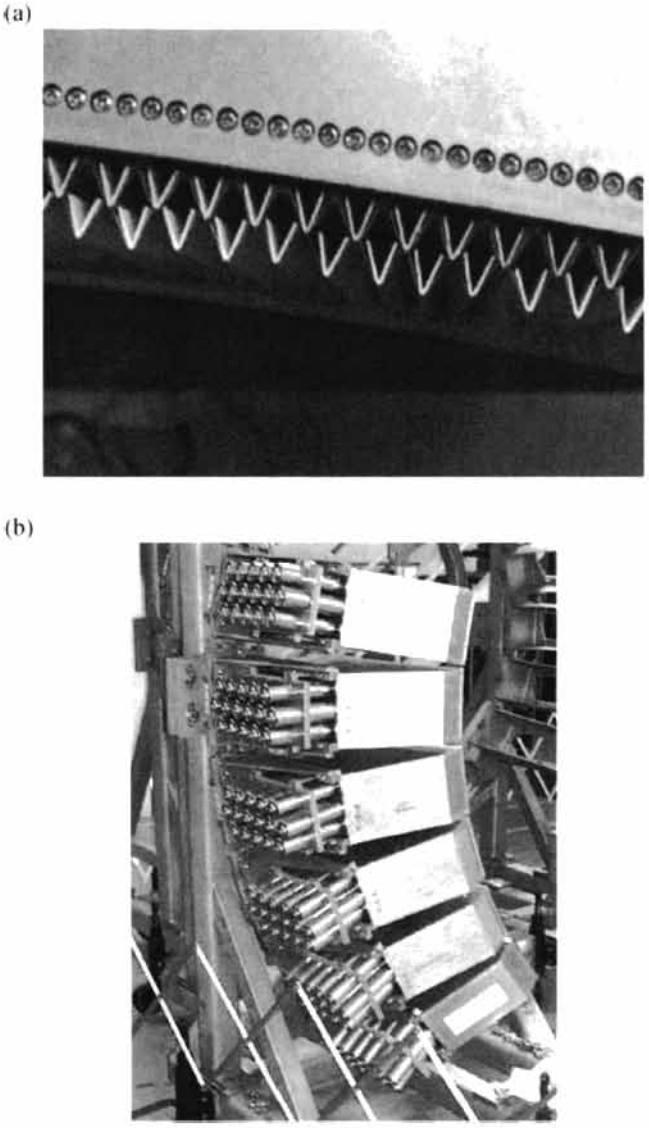

Figure 4.8. Photographs of scintillator detectors now installed on GEM at ISIS. (a) shows a close-up of V-shaped scintillator elements. (b) shows the elements built into space-filling modules with shielded photomultiplier tubes sticking out of the back of the modules. The light from the scintillator reaches the photomultiplier tubes via optical cables which cannot be seen inside the modules.

beam intensity using a beam monitor. Beam monitors are placed upstream of the sample (Figure 4.1). They usually consist of an incoherently scattering vanadium foil placed in the beam with one or more neutron detectors located off the axis of the beam. In order not to

compromise the counting statistics of the measurements it is desirable to have as many counts as possible in the monitor which is why multiple detectors around the vanadium foil are now considered desirable, as for example, on GEM. If the incident spectrum from the moderator is very time-stable, the spectrum in the beam monitor can be integrated over all energy and just used to scale the intensities in the main detectors. However, it is sometimes preferred to normalize the detector spectrographs point-by-point by the monitor spectrograph to account for spectral instabilities. In this case, the spectrum from the beam-monitor is often smoothed (it contains no sharp features anyway) so counting statistics becomes less of an issue, although, there is the possibility that this smoothing introduces systematic errors. These days moderator stability and adequate beam monitoring are probably the accuracy limiting factors in most tof neutron PDF measurements and they are receiving renewed attention in current and next generation diffractometers.

One of the key parameters required in the data analysis (Chapter 5) is the total scattering cross-section of the sample. This depends on energy, but to a good approximation is inversely related to the neutron energy. It is often, therefore, calculated theoretically knowing the neutron scattering cross-sections of the constituents (measured traditionally at 1.3 Å neutron wavelength), the sample density and size (therefore the number of scatterers) and using the approximate energy dependence mentioned above. A more precise determination of the total attenuation cross-section can be made if a second beam-monitor is placed after the sample (Figure 4.1). The ratio of the two monitors then gives a measure of the sample attenuation cross-section as a function of energy. This is not done on most utilitarian tof powder diffractometers due to engineering difficulties and lack of enthusiasm. One notable exception is the liquids diffractometer, SANDALS at ISIS.

4.2.5 Measurement geometry

Because of the fixed detector geometry, wide solid angle coverage and rectangular beam-shape, the normal geometry of the measurement is to have cylindrical samples. This is particularly appropriate in previous generation diffractometers where all of the detectors were arranged in the (horizontal) scattering plane at the same height as the sample. This geometry is the most natural when multiple detectors at different angles are used. Current and next generation diffractometers have detectors that sit above and below the scattering plane. In this case a square or circular beam and spherical samples would be the most natural geometry though to date the cylindrical sample shape has been retained for practical reasons: ease of making and filling sample cans. If the strongly off-axis detectors have spectra that cannot be corrected the beam dimensions can be changed to be more square, or these detectors can be left out of the analysis. So far, this seems not to be a significant problem.

4.3. THE X-RAY SCATTERING EXPERIMENT

4.3.1 Sources

The most commonly used X-ray generator is a system having a sealed tube with a copper (Cu) target (see Klug and Alexander, 1974, for detailed descriptions of conventional sources and measurement geometries). The characteristic K_α X-rays generated by such a tube have the wavelength of 1.544 Å and a wavevector magnitude of $k_0 = 4.069$ Å^{-1}. This, however, limits the range of Q to be below 8 Å^{-1} since $\sin\theta < 1$ so $Q_{max} < 2k_0$ (Eq. 2.2). Consequently only a few diffraction peaks can be detected by using such a system. Let us suppose that N diffraction peaks were recorded by the powder diffractometer. This translates to $2N - 1$ pieces of information since the position and the intensity of each peak provide $2N$ numbers as a data set, while the normalization of the intensity usually is not in the absolute scale, thus unknown. If the structure is fully crystalline and the number of parameters is less than $2N - 1$, this set of numbers can fully determine the structure. However, aperiodic deviations from the periodicity cannot be described by such a small set of parameters, and require a larger range of Q-space over which the data must be measured.

For the highest resolution and accuracy measurements the use of an X-ray synchrotron source is preferred as we describe below. However, perfectly acceptable low-resolution PDFs can be obtained in the laboratory. The range of Q-space accessible with the readily available sealed tubes is limited as shown in Table 4.2. Molybdenum tubes give relatively good flux and will yield $S(Q)$ up to Q_{max} of around 14–15 Å^{-1}. This kind of source is often used for laboratory liquid and amorphous measurements and provides a good work-horse for low-resolution basic sample characterization type measurements. Silver tubes give Q_{max} of around 20–21 Å^{-1} which can be satisfactory (though not optimal) for PDF measurements even in crystalline materials at room temperature. However, the big tradeoff is a significant reduction in intensity, even from the low intensities of Mo tubes. This results in very long measurement times. Measurement times of a number of days duration are not unusual and adequate statistics at higher Q-values may mean measurements running into the range of weeks. The drop in intensity on going from Mo to Ag has two

Table 4.2. X-ray energies, wavelengths and approximate Q_{max} values for common laboratory X-ray sources.

Source	E_0 (keV)	λ (Å)	Q_{max} (Å^{-1})
Cu	8.05	1.538	8.0
Mo	17.48	0.708	17.5
Ag	22.16	0.559	22.0
W	59.32	0.209	59.0

Energies shown are the $k_{\alpha 1}$ emission energies. The Q_{max} values are calculated assuming a maximum accessible scattering angle of 160°. Note the convenient property that the Q_{max} value in Å^{-1} is almost the same as the X-ray energy in keV. A useful resource for finding X-ray properties of elements is the 'X-ray data book' published by Lawrence Berkeley National Laboratory and available online at http://xdb.lbl.gov/.

origins. First, Ag has a lower melting point and so less power in the form of accelerated-electron current can be used. Second, an empirical relation gives the X-ray flux in a characteristic emission line according to $I \propto (E - E_c)^{1.63}$ where E is the accelerating voltage and E_c is the energy of the characteristic emission line. Thus, for a typical source operating at 45 keV the ratio of intensity,

$$I_{Mo}/I_{Ag} \approx \left(\frac{45 - 16}{45 - 22}\right)^{1.63} = 1.46 \tag{4.3}$$

The power, and therefore the flux, from a laboratory source can be increased by the use of a rotating anode source. This gives an increase in flux of approximately 5 times over an equivalent sealed tube source.

A rarely used but notable exception is the tungsten (W) tube that provides the K_α radiation that can cover Q-space up to 60 Å^{-1}. However, to operate such a tube an applied voltage of nearly 100 keV is needed. This requires a special power system since the conventional power system is capable of applying the voltage only up to 50 keV. Furthermore dealing with 100 keV X-rays is not trivial because of the high penetrability. Shielding requires heavy metal (lead) lining.

Synchrotron radiation is an intense, white X-ray beam, that can be used either 'as is' as a white beam or, more commonly, monochromatic beam using a single-crystal monochromator. There are now a large number of synchrotron x-radiation sources operating in the world. At the time of writing the extensive list of X-ray storage rings on the Stanford Synchrotron Radiation Facility web-site (http://www-ssrl.slac.stanford.edu/sr_sources.html) listed 75 sources either operating or under construction in 23 countries ranging from Armenia to the USA. A number of these are soft X-ray or ultra-violet beamlines that are unsuitable for PDF measurements. The sources with an electron energy of 2.5 GeV or greater are required for PDF work on crystals. The new 'third generation' sources such as the European Synchrotron Radiation Facility (ESRF) (Grenoble, France http//www.esrf.fr/), the Advanced Photon Source (APS) (Argonne National Laboratory, Illinois, USA, http//www.aps.anl.gov/) and SPRING-8 (Harima, Japan, http/www.spring8.or.jp/) feature high luminosity in addition to high intensity at high X-ray energies. Many scattering experiments which have been impossible or impractical so far are now feasible.

Synchrotrons produce high fluxes of X-rays with tunable wavelengths. The flux of X-rays at different energies depends on the characteristic energy of operation of the synchrotron ring itself, and on details of the beamline source and optics, such as whether it has an insertion device such as a wiggler or undulator. A number of books and resources are available describing the characteristics of X-ray synchrotron sources. A brief introduction can be found in Woolfson (1997) as well as on the web-pages of the synchrotron sources themselves. A multimedia introduction has been put together by the ESRF called 'Synchrotron Light' that is published by Springer-Verlag (2001). Much more

detail is available in complete books on the subject such as Duke (2000), Mills (2001) and Ciocci *et al.* (2000), for example, in the Bibliography.

Relatively low real-space resolution measurements with $Q_{max} \sim 28$ Å^{-1} are possible using a bending magnet line at a second generation source such as NSLS. Higher Q_{max} are possible using an undulator line at the same source. However, best results are obtained by using a higher energy synchrotron such as the Cornell High Energy Synchrotron Source (CHESS) or one of the three new third-generation sources: ESRF, APS and Spring8. With these sources large fluxes of X-rays with energies of 100 keV and higher are available allowing Q_{max} of >50 Å^{-1} to be accessed.

4.3.2 Diffractometer

A two-circle diffractometer is all that is required for these measurements, though typically beamlines are equipped with 4- or 6-circle diffractometers. The two circles are denoted θ and 2θ. This is shown schematically in Figure 4.9. They are coaxial but the θ circle rotates the sample and the 2θ circle the detector. As the naming scheme suggests the circles are linked in such a way that the detector moves at twice the rate of the sample. This is discussed in more detail in Section 4.3.5. A similar, though less common arrangement is the so-called $\theta-\theta$ geometry. This is useful for the measurement of samples that must remain horizontal and cannot be tilted, in particular, liquids. In this geometry the sample remains stationary and the source and the detector each rotate about the sample in such a way as to maintain a symmetric source-sample-detector arrangement. This geometry is less well suited to a synchrotron source!

Diffractometers with these geometries are commercially available. Important considerations are that they are carefully engineered to be precise and accurate as well as easy to use. They should also be strong and properly counter-balanced to allow for trouble free operation when special pieces of equipment are used such as detectors with

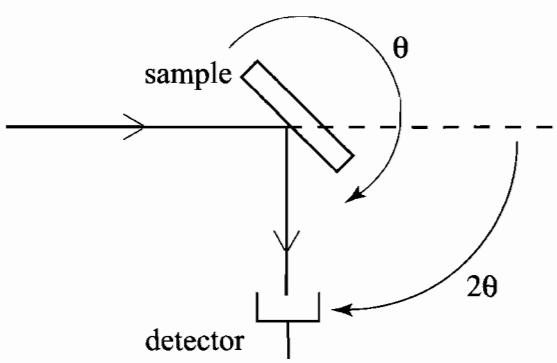

Fig. 4.9. Schematic of the $\theta-2\theta$ geometry angle dispersive experiment commonly used in X-ray studies.

liquid nitrogen dewars and sample cryostats. This is especially true at synchrotron sources where the scattering plane (the plane defined by the incident and scattered wavevectors) is vertical. heavy detectors then have to be moved in the vertical plane.

An alternative approach to collecting data for PDF studies is to use a Debye–Scherrer camera. In this case the powder is placed in a capillary tube on the axis of a cylindrical container. Holes are cut in the container so a collimated X-ray beam can enter and exit. An X-ray sensitive film is then placed around the inside surface of the cylinder. They are described in much more detail in Klug and Alexander (1974). Historically, Debye–Scherrer cameras were extensively used for high-resolution measurements of d-spacings and lattice parameters of powders. However, X-ray film has a limited use when quantitative intensities of Bragg peaks are required. Intensities can be measured with the use of a densitometer; however, neither the dynamic range of the film nor its linearity with intensity is very good and diffractometer experiments were preferred. This situation is changed somewhat with the development of image-plate technology as we describe in the next section and Debye–Scherrer geometry measurements may become popular for quantitative measurements in due course, e.g. see Stachs *et al.* (2000) (Figure 4.10).

4.3.3 X-ray detection

The most commonly used detector is a scintillation detector. However, this type of detector is less ideal for the most accurate PDF measurements, especially when higher energy X-rays are used. The reason is that the energy resolution of a scintillation detector is very poor, only about 20–30%, and it cannot efficiently discriminate artifacts such as fluorescence and Compton scattered intensities. The advantage is the ease of use and low cost as well as the good characteristics of high count-rates and good linearity. In this kind of detector absorbed X-ray photons cause a scintillator material such as Pt doped NaI to radiate visible light. In the early days of X-ray detection the light flashes were observed by eye in a dark room. These days photomultiplier tubes are used to convert the light pulse to a charge pulse and to amplify it and have completely replaced graduate students as X-ray detectors. Check the resources listed in the section seclected bibliography for more information.

A preferred detector is a single-element or multi-element solid state detector (SSD) (Figure 4.11). The main component of an SSD is a highly pure intrinsic semiconductor (Si or Ge) single crystal. A bias voltage (1000–1500 keV) is applied to the crystal. The crystals are cooled (Ge crystals must be cooled to cryogenic temperatures) to minimize dark current. Ge crystals are preferred for higher energy X-rays because of higher detection efficiency due to the more absorbing, higher atomic number, of Ge.

An X-ray photon impinging on the detector will produce a number of hole-electron pairs (formation energy ~ 3 eV), which produce a pulse of current because of the bias voltage. The charge pulse is electronically amplified and shaped to produce a clean

(a)

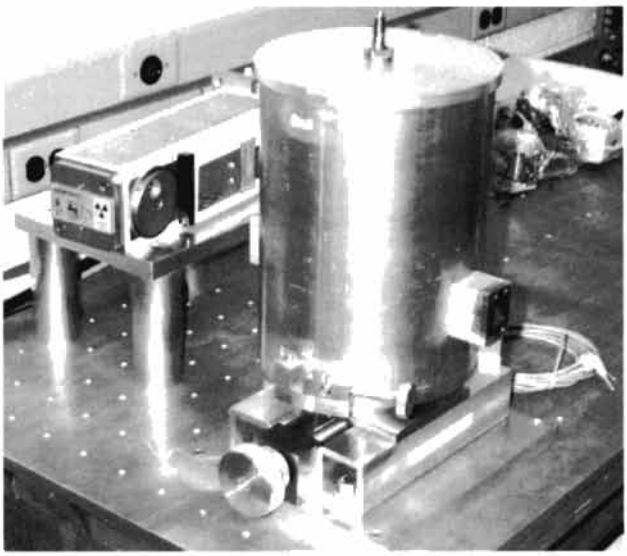

(b)

Figure 4.10. (a) Image-Plate Debye–Scherrer camera suitable for PDF studies. (b) Example of data collected from powdered nickel in 15 s at beamline ID1 at the APS using the camera.

Gaussian (or some other choice of) line-shape. This can be converted into a computer-readable count in two ways. The pulse height can be gated so that only pulses whose peak voltage fall within a predetermined range are accepted. The successful pulses are then fed into an analogue-digital converter to produce an electronic (e.g. TTL) signal which is counted in a scaler. The analog signal from the amplifier can be daisy chained to a series of single-channel analyzers (SCAs) with different gate voltage settings to measure different phenomena such as the elastic signal, fluorescences and so on. The alternative approach is to use a multi-channel analyzer (MCA) which samples the peak and assigns a count to a particular channel (or bin) depending on the peak height. Modern MCAs are just computer

Figure 4.11. Photograph of a multi-element solid-state Germanium detector. This image shows a 13-element detector. A 100 element Ge detector is in use at the Photon Factory synchrotron source in Japan.

cards that plug into the bus of the experiment control computer. After a period of counting, the MCA spectrum can be output and plotted. Typically 1024 channels are used. This gives a histogram of peak heights resulting in a quasicontinous spectrum of intensity vs. channel number. The number of e–h pairs created in the semiconductor crystal, and therefore the integrated charge in the pulse, is proportional to the energy of the X-ray. Thus, the peak height, and therefore the channel number, gives the energy of the detected X-ray. The spectrum in the MCA is therefore a plot of intensity vs. X-ray energy. An example of an MCA spectrum is shown in Figure 4.12. The main advantage of the SSD is the low noise, relatively good energy resolution ($\propto E$, $\sim$230 eV at 20 keV), and high efficiency. Disadvantages are the relatively high cost and long pulse shaping time and thus a substantial dead time ($\sim$ 14 μs) which limits the counting rate. Fully digital electronics that are more efficient are now becoming available that make the dead time shorter and allow higher counting rates.

A linear detector (position-sensitive detector, PSD) is also useful in increasing the total count rate by parallel detection. Various forms of metal wire gas detectors (proportional counters) and semiconductor Si-diode array detectors are already available. Both have a relatively low energy resolution (20–30%), and high background noise. Also the normalization of the sensitivity of the wire detector is a non-trivial problem for quantitative measurements. The detection efficiency of a Si-diode detector drops quickly at high energies, and above 20 keV X-ray energies they are practically transparent. Thus they are rather unsuited for the high-Q measurements discussed here.

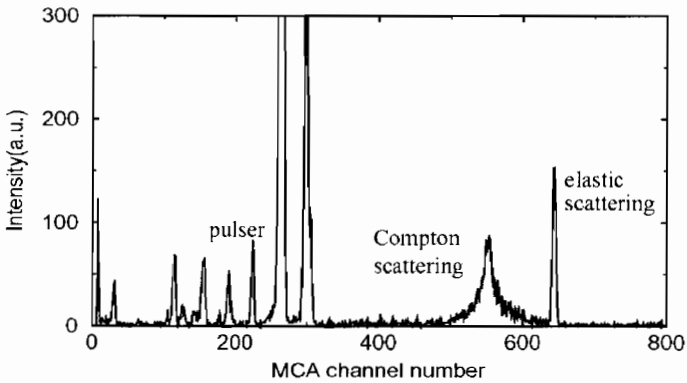

Fig. 4.12. MCA spectrum from a Ge detector. The data are diffraction data from a sample of $In_{1-x}Ga_x$ As collected at an X-ray energy of 60 keV. The sharp line centered at channel number ~640 comes from the elastically scattered X-rays. The broader line next to it is the inelastic Compton modified scattering. Peaks at lower channel numbers are fluorescence and escape peaks.

Two-dimensional detection can also be used to increase detector solid angle coverage and speed up measurements. One approach is to line up PSD wires in a grid. These detectors have the same problems as the 1-D proportional counters discussed above. Two-dimensional charge-coupled-device (CCD) X-ray detectors are also beginning to be used in diffraction measurements. At present these are flat, relatively small in area and expensive making it a less desirable technology for wide angle measurements. Since they are charge integrating devices they have no energy resolution and simply record the number of events in a pixel. An alternative is to use image-plate (IP) technology. These devices are the modern equivalent of X-ray film. As with CCDs (and X-ray film) they integrate the incident intensity. Unlike X-ray film they can be read out digitally using a rastered laser and then photobleached with bright light 'resetting' them for reuse. The IP material is mounted on flexible bases allowing it to be cut and bent into different shapes. It is available in fairly large sheets, the size ultimately being limited by the size that can be handled by the laser readout device. An inconvenience is that the IP has to be removed to be read making it difficult to automate when multiple data-sets are to be collected. IP cameras are becoming available which have the readout laser and bleaching lamp mounted on the camera allowing the IP to be read-out in situ, though at the time of writing none suitable for PDF work is available. IP's have the advantage that they are very linear over a wide dynamic range making them suitable for PDFs from crystalline materials where both highly intense Bragg peaks and the weak diffuse scattering underneath the Bragg peaks must both be measured quantitatively. An example of an IP camera suitable for PDF work is shown in Figure 4.10 (Stachs *et al.*, 2000).

For a large array of digital detectors, reading out a massive amount of data is a major problem. Advances in computer and communication technologies are making such fast

read-out possible. Another issue common to 2-D detection devices is to calibrate the point-to-point sensitivity. Also, since these technologies are currently under development there is no established software to calibrate position, correct for pixel solid angle and integrate the intensities around the Debye–Scherrer rings. Because of the obvious advantages of area detectors in flux limited wide angle experiments such as PDF experiments these problems will undoubtedly be addressed in the future.

The whole experiment is controlled by a computer which moves the diffractometer arms, starts and stops data collection and resets the MCA at each data-point. A commonly used diffractometer software at synchrotron sources is SPEC that was developed originally at Harvard University but is now developed, distributed and supported commercially by Certified Scientific.

4.3.4 Beam monitor

In addition to the measurement detector, it is necessary to have an accurate and stable beam monitor. Ion chambers placed in the direct beam can be used. Scintillation detectors placed perpendicular to the beam in front of the sample are also often used. These are often placed so that the detector aperture sees scattering at 90° from an angled kapton tape (but in the same scattering plane as defined by the incident beam-sample-detector relationship). The scattering from the tape is fairly incoherent at 90° and this scattered intensity is a good measure of the average beam intensity. In high flux, high energy, experiments at CHESS the scattering from air has been used with no kapton tape in place. Scintillator detectors have the advantage that they have some, albeit poor, energy resolution. This means that higher harmonics can be excluded. On the downside, the count-rates possible, in the region where these devices are linear and do not have excessive deadtime, are limited to a few times 10^4 per second. This limits the statistics of the measurement since random fluctuations from the monitor contribute to the total errors. In contrast ion chambers can count reliably at rates $\sim 10^6$ per second with little deadtime. The monitor must be stable. Ion chambers are stable if the gas flow through them is slow and constant. If the pressure in the ion chamber fluctuates too much, this can affect stability. Scintillators are relatively stable, but can suffer from effects such as variations in density or thickness of the Kapton tape. This can be a problem if the X-ray beam position shifts, a phenomenon which is not uncommon with synchrotron sources. This effect is not a problem if the scintillator is looking at air scattering alone. Ion chambers have no energy resolution and so may be susceptible to harmonic contamination. This is a problem if the harmonic component of the beam changes with time that can sometimes be the case. The harmonic component of the beam is reduced if the monochromator is detuned so that the primary and secondary monochromator crystals are not perfectly parallel. This loses intensity from the fundamental, but the intensity of the harmonics fall off more quickly with detuning so, as a percentage of the total flux, the harmonic component is reduced. If this approach is

used it is necessary to maintain stability, usually using a piezo feedback system which maintains the detuning at a specific value. Harmonic contamination can also be removed by using an X-ray mirror in the beam optics. However, this tends also to remove the high energy portion of the incident beam which is not reflected by the mirror. Mirrors are therefore not used in high energy measurements. Harmonics are discriminated away in the detected beam, but their possible presence in the monitor means that a time-dependent harmonic content will lead to Q-dependent normalization errors. When the incident intensity is high, harmonics also increase the deadtime in the detector and the electronics. They deposit so much charge into the Ge detector. They can also lead to space charging problems and an inability to sweep all of the charge out of the Ge crystal quickly enough. If another photon arrives, it will not have the correct charge in its pulse and will be binned incorrectly in the MCA. Thus space-charging effects appear as background noise in the MCA spectrum and can be quite bothersome. Thus, in practice, taking steps to limit the harmonic component of the beam is generally advised.

4.3.5 Measurement geometry

Different powder diffractometer geometries are discussed in more detail in Klug and Alexander (1974). Here we compare and contrast different geometries in the context of PDF measurements at different sources.

Sealed tube and rotating anode laboratory sources are highly divergent. Large increases in scattering intensity can be gained by using a parafocussing Bragg-Brentano geometry (Figure 4.13), although the gains are greatest at the lower diffraction angles which yield

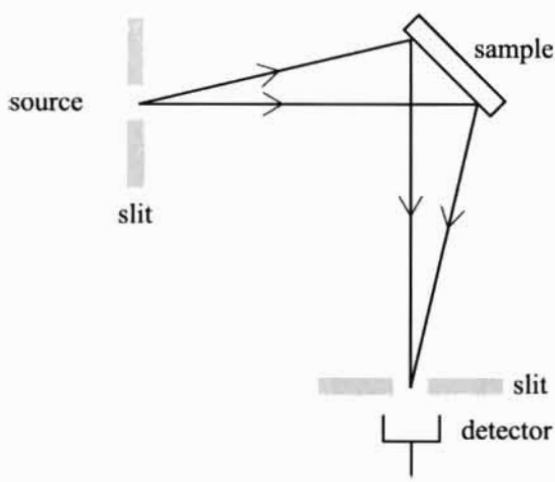

Figure 4.13. Schematic of the Bragg-Brentano flat plate symmetric reflection geometry that is widely used on divergent sources (i.e. laboratory sources) and for opaque samples.

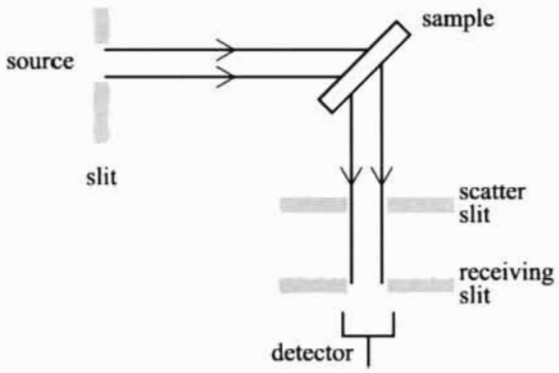

Figure 4.14. Schematic of the flat plate symmetric transmission geometry that is most useful for high energy synchrotron total scattering studies.

low-Q information that is less critical for PDF studies. This is a flat-plate symmetric (θ–2θ) *reflection* geometry. Except when parallel detection schemes (wire or blade PSDs or IP cameras for example) are used, in which case a cylindrically symmetric geometry is more natural, Bragg-Brentano geometry is widely used with laboratory sources. Flat plate symmetric *transmission* geometry may also be used for accurate quantitative intensity measurements (Figure 4.14). Flat plate geometries have the advantage that a fairly large quantity of sample is in the beam compared with a capillary geometry (Figure 4.15). It is also easier to support the sample without a large amount of parasitic scattering from the sample holder. Finally, absorption corrections are easy with straightforward analytic expressions describing the sample absorption at all angles (Appendix 5.2). The choice between reflection and transmission geometry depends on the transparency of the sample.

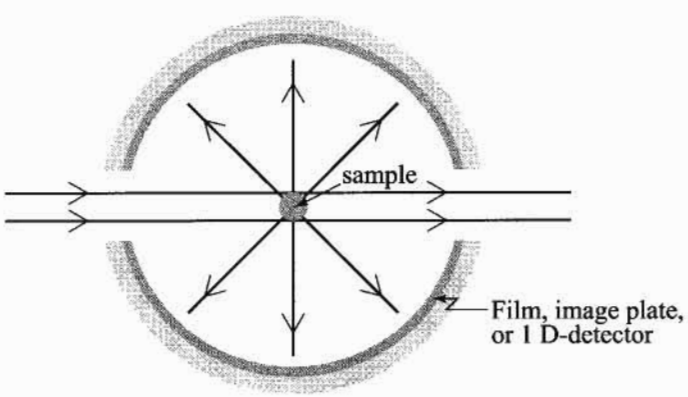

Figure 4.15. Schematic of capillary (Debye–Scherrer) geometry.

As well as the parafocussing property, reflection geometry has the benefit that the absorption and sample active volume corrections are somewhat self correcting (they are fully self correcting if the sample is infinitely thick, or completely absorbing). These latter advantages mean that it is sometimes also used at synchrotron sources even though the parallel incident beam renders parafocussing of no value.

If the sample is significantly transparent, which is often the case when high-energy X-rays are used, then transmission geometry generally gives stronger scattering, especially at high angles where the beam footprint is largest in transmission geometry. Since good intensity at high angles is the most important consideration this geometry is most often used for high energy scattering at synchrotrons. This geometry is also more robust than reflection geometry against alignment errors, especially at low angles.

When samples are made they should have very uniform thickness and no holes. The thickness can be varied but it is optimal in transmission geometry if it has an absorption coefficient, μt, of ~ 0.5 at the X-ray energy of the experiment. Low atomic number samples would have to be centimeters thick to fulfill this criterion at 60 keV X-ray energy, in which case the sample thickness should be limited by other considerations such as the resolution and physical geometry of the experiment. In general, sample thicknesses greater than 5 mm or so are avoided in transmission measurements.

Care must be taken that the beam footprint does not extend over the edge of the sample surface area at the extremes of angle (Figures 4.13 and 4.14). The problem is particularly acute at low angles in reflection mode. This will result in an angle dependent drop off in the intensity of the sample which is difficult to correct. One approach is to use transmission geometry at low angles and reflection geometry at high angles. This means that the data have to be properly matched where they overlap, which can be successfully done if proper absorption and active volume (sometimes called gauge volume) corrections are carried out, respectively, on each set of data. Another approach is simply to ignore the problem at low angle. The data are then corrupted, but only in the very low-Q region which does not contribute significantly to the Fourier transform. Of course, in the most accurate measurements this is to be avoided. This problem does not exist when data are collected entirely in symmetric transmission geometry, again making this a preferred geometry for synchrotron work.

When making the flat plate samples the most important consideration is that they be of uniform thickness and density with no macroscopic holes or cracks. The surface should also be as flat and smooth as possible (both surfaces if it is a transmission sample). As with any powder samples the particle size should be small (<40 μm) and uniform. This is usually accomplished by sieving the sample through a 400 mesh sieve. It is particularly important to avoid texture, preferential powder orientation, in the sample. This is generally easier when the particle size is smaller, but can still be a problem if the powder grains have a particularly oblate or prolate morphology. Powders are often supported with thin kapton tape over the surface (Figure 4.16).

Figure 4.16. Photograph of a flat-plate transmission sample supported between kapton foils.

This is particularly important if the sample is to be cooled in a vacuum. Uncovered powders rarely survive the pump down as air trapped between the grains forces its way out. Differential thermal contraction between the sample holder and the powder itself can also loosen a tightly packed powder. The kapton gives rise to parasitic scattering which can be significant at low angle, but is relatively easy to remove by measuring the background scattered intensity from an empty holder supporting a kapton tape. The background scattering should be corrected for relevant sample absorption effects before being subtracted from the data as discussed in Chapter 5. A small amount of grease, or DUCO cement mixed with acetone, can also be mixed with a loose powder to stabilize it if the sample does not have to be recovered in its pristine state after the experiment. The scattering from the stabilizing agent is relatively weak. Traditional techniques of supporting a thin film of powder on a glass slide, widely used, for example, in sample characterization and d-spacing measurements, are unlikely to result in thick or uniform enough samples for the short wavelength X-rays needed for PDF measurements.

A number of factors affect the slit openings of the exit slits before the sample and the receiving slits before the detector. The X-ray measurements are generally higher resolution than neutron measurements. In PDF measurements it is therefore possible to compromise the resolution to obtain higher intensities by working with a relatively large beam height (defined by the exit slit opening) and receiving slit opening. Values of 1–2 mm are typical for in-house setups and 0.5–1 mm at synchrotron sources. In the latter case larger beam

sizes would be preferred but are limited by the natural beam height. In this case slits are still used to physically define the beam and to try and select a more uniform beam profile and polarization from the center of the beam. For ease of data analysis it is often the case that data are collected in steps of constant ΔQ, though steps of constant $\Delta 2\theta$ can also be used. The step size depends on the resolution of the measurement. It is important to collect enough points that the step size is always smaller than the instrument resolution so all of Q-space is probed. The resolution varies with Q. It is set by a variety of factors such as sample size and beam divergence, but in a synchrotron experiment the beam-height is an important factor. The uncertainty in the scattering angle, $\Delta 2\theta \sim h/L_2$ where h is the height of the beam and L_2 is the length of the secondary flight path from the sample to the receiving slit. Since $Q = 4\pi \sin \theta/\lambda$, the resolution in Q due to the finite beam size is given by

$$\Delta Q = \left(\frac{2\pi}{\lambda}\right)\cos\left(\frac{2\theta}{2}\right)\Delta 2\theta = \left(\frac{2\pi h}{\lambda L_2}\right)\cos\,\theta \tag{4.4}$$

This equation reflects the fact that the resolution gets better at high angle, a widely known result.[3] In principle, to maintain a constant resolution, the receiving slit width should be increased with angle. This has the added benefit of increasing statistics in the important high-Q region. However, this is seldom done in practice because of the difficulty of normalizing data correctly when the receiving slit width is changed in the middle of a measurement, as well as the obvious additional complexity of the measurement.

One thing to make sure of is that none of reciprocal space is missed in the measurement. Obviously this means that the angular step-size, $\delta 2\theta$, must be less than $\Delta 2\theta$ or h/L_2. If the measurement is carried out in steps of constant 2θ this is easily accomplished. However, if the measurement is carried out in steps of constant δQ then some care must be exercised because the step size, $\delta 2\theta$, will change with angle. From Eq. 4.4, we get

$$\delta Q < \Delta Q_{\min} = \left(\frac{2\pi h}{\lambda L_2}\right)\cos\,\theta_{\max} \tag{4.5}$$

Higher resolution measurements with smaller receiving slits and smaller step-sizes are rarely warranted in the case of X-rays since the Fourier transform controls the frequency at which the data are sampled. Higher Q-space resolution results in PDFs extending to higher-r which is almost never the limiting factor in a measurement.

Good collimation after the sample is desirable to minimize background from air scattering and sample environments such as heat shields and windows in vacuum shrouds. This is often accomplished with a set of slits positioned fairly close to the sample (sometimes known as scattering slits, see Figures 4.13 and 4.14). However, care must be taken to ensure that the sample is well aligned in the center of the diffractometer circle so that at no time in the measurement is the sample shadowed by the scattering slits. This is

[3] This is also true in time-of-flight neutron measurements where the backscattering detectors have much higher resolution than the low angle detectors.

particularly relevant in a PDF measurement where data are collected over such a wide range of scattering angles (typically $0.5° < 2\theta < 135°$). This shadowing is disastrous since it introduces an unknown Q-dependent modulation in the measured intensity which makes the data virtually impossible to correct. The primary role of this collimation is to eliminate parasitic scattering rather than to increase resolution by limiting divergence so there is no particular advantage in using Soller slits.

In a high energy measurement there can be a great deal of penetrating stray scattering in the experiment hutch during the measurement. It is important to minimize the effect of this on the measurement itself. This is done by limiting the amount of stray scattering by shielding the beam and covering beam-line components which cause scattered radiation (slits for example) with lead. Finally, the detectors must be well shielded with lead to avoid X-rays entering the detector from another direction than the sample position. The usual construction of commercial semiconductor detectors is to mount the crystal in an aluminum housing that is woefully inadequate for keeping at bay 60 keV X-rays.

4.3.6 Instrument alignment

By way of example for those unfamiliar with instrument alignment, we give below, a typical set of steps taken to align the diffractometer before beginning measurements. We are assuming a flat plate transmission measurement at a synchrotron source. However, many of the principles are common to other geometries and sources.

1. *Ensure the sample is at the mechanical center of the diffractometer.* This is usually done by centering a pin at the sample position. The pin is viewed through a cross-hair telescope whilst being rotated. The sample mount is then translated in two directions perpendicular to the beam direction until no parallax is observed. If a low-temperature stage is being used this must be done with the cold-stage in place.
2. *Select beam energy and optimize the intensity at this energy.* Monochromators at modern synchrotron sources tend to be two-crystal double bounce geometry. A number of alignments are necessary including vertical and horizontal offset, as well as a lateral and longitudinal rotations. These all affect beam position, uniformity and intensity. Upstream slits are generally set at this point, for example, the slits before and after the monochromator. These slits do not define the beam and so should not be set too tightly. Make sure the hottest part of the beam is not being cut and that the beam intensity profile is approximately symmetric. Other upstream beam conditioning optics should also be set and aligned such as monochromator focusing and harmonic rejection mirrors, although these are rarely used at the energies of interest for PDF measurements. These alignments are often carried out by beamline staff.
3. *Center the beam on the pin at the center of the diffractometer.* At a synchrotron the diffractometer table has to be translated up and down to do this. The pin from step 1 is used and checked to see that it shadows the beam.

4. *Set the exit slits* (last slits before the sample) to the desired opening and center them on the beam and the pin. These slits should be independent of the diffractometer. These slits define the beam height and the beam position. After alignment they should not be moved (or bumped!).
5. *If it is not known, measure the detector dead times,* τ. This is best done with a series of calibrated foils of known material and (uniform) thickness. These are systematically placed in front of the detector and the count rate (normalized by the monitor) recorded for each successive foil added. The data are fitted to the equation for detector deadtime $I = I_0/(1 + I_{\text{tot}}\tau)$. Detector dead time can also be estimated dynamically during the experiment with the use of an electronic pulser, or using the MCA 'live time/real-time' ratio, as we describe later.
6. *Set the receiving slits.* These slits sit right in front of the detector. They should be set to the desired opening (see the discussion in Section 4.3.5) and centered on the detector, as close as possible to the axis of the 2θ diffractometer arm.
7. *Find the* $2\theta = 0$ *position.* Avoid destroying the detector by putting direct beam into it when doing this alignment! The object is to find the nominal angle when the direct beam is in the center of the detector receiving slit. This is done by measuring the direct beam profile by scanning the receiving slit, with an ion chamber detector behind it, or the solid state detector with a lot of attenuation in the beam, through the direct beam. Another useful setup is a silicon photodiode mounted on a strongly absorbing plate, such as hevimet, that can tolerate the intense direct beam and can be placed in front of the detector. The beam profile should be symmetric (if the beam is well aligned) and the center of the peak is the $2\theta = 0$ position. It is worthwhile after finding the $2\theta = 0$ position and setting the diffractometer software to zero 2θ at this position, to record the physical angles from the diffractometer circles and motors. In this way the integrity of the 2θ-zero can be easily checked at various times during or after the measurement without having to remeasure it. This is sometimes useful to reassure oneself that none of the circle motors has slipped or missed steps at any time.
8. *Remove the aligning pin and install the sample on the diffractometer.* The sample position must be reliable and reproducibly close to the position of the pin. This is usually done by carefully machining the sample mount to ensure the center of diffraction of the sample is at the same position as the pin. In a transmission sample this will be the center of the sample. In a reflection sample it will depend on the thickness and penetrability of the sample (and on the scattering angle) but is likely to be somewhere between the center of the sample and the front face. This complication means that it is unwise to make a reflection sample more than a few mm thick at most, even if this means that the sample has a finite transparency.
9. *Measure* μt *of the sample.* The easiest way is with the sample perpendicular to the beam measure the direct beam intensity (normalized by the monitor) with and without the sample in place. Another approach is to rotate the flat plate sample through $\pm 60°$

while recording the intensity (remember, do not put direct beam into a sensitive detector). The resulting intensity will have the form $\ln(I/I_0) = -\mu t/\cos\theta$, thus plotting $\ln(I/I_0)$ vs. sec θ will give you a straight line of slope $-\mu t$.

10. *Set the scatter slits.* These are the slits that sit immediately after the sample. Find a strong Bragg peak from the sample. Bring in each blade of the slits separately until the intensity falls to zero. Record these positions which define the edges of the scattered beam. Set the scatter slits as close as you dare (but not too close) to the beam edges. Check the slits by studying a few Bragg peaks (or other features which give significant scattering) at widely separated scattering angles. If the sample is well aligned the beam edges should be in the same positions independent of angle. Make sure the scatter slits are set so that the scattered beam is never cut by a slit. A wise experimenter errs on the safe side here.
11. *Check the sample powder averaging.* Measure a rocking curve at one or two Bragg-peak positions. With the detector fixed at the 2θ of a Bragg peak, rock the sample (θ angle) back and forth through a few degrees recording the intensity. In general, the sample will have to be rocked to ensure good powder averaging. The intensity should be more or less constant (after normalizing for incident flux) and not fluctuate too greatly. This problem is especially acute at synchrotron sources where beam footprints can be very small.
12. *Set the $\theta = 0$ position.* In this position the sample is parallel (perpendicular) to the beam in reflection (transmission). The $\theta = 0$ is set with the sample parallel to the beam and the detector at the $2\theta = 0$ position (again, care must be taken not to destroy the detector with the direct beam). In this position the sample will shadow approximately half the beam. If the sample is rotated in either direction by a small angle the sample will completely shadow the beam. By scanning the θ angle through zero with the detector held at $2\theta = 0$, a symmetric minimum should be apparent in the intensity. This alignment is not crucial in a powder measurement and is often done by eye or with the help of a spirit level.

4.3.7 Dedicated and optimized synchrotron beamlines

At the time of writing no dedicated or optimized beamlines for high energy total scattering powder diffraction measurements exist at synchrotron sources. In contrast to neutron sources the general philosophy, especially in the US, seems to be to build relatively flexible, unspecialized diffraction instruments. This makes setup and alignment relatively arduous for these somewhat unconventional measurements. This is changing with time as the utility of total scattering measurements becomes more widely recognized, and a number of high energy powder/total scattering beamlines are being planned (e.g. BM6 at the APS). It is expected that instrument setup and alignment will be significantly facilitated at these beamlines making these measurements much more routine.

REFERENCES

Bacon, G.E. (1975) *Neutron Diffraction*, Clarendon Press, Oxford.
Egami, T. (1978) *J. Mat. Sci.*, **13**, 2587.
Klug, H.P. & Alexander, L.E. (1974) *X-ray Diffraction Procedures*, 2nd Edition, Wiley, New York.
Stachs, O., Gerber, T. & Petkov, V. (2000) *Rev. Sci. Instrum.*, **71**, 4007.
Woolfson, M.M. (1997) *An Introduction to X-ray Crystallography*, 2nd Edition, Cambridge University Press, Cambridge.

SELECTED BIBLIOGRAPHY

Spallation neutrons and sources:

Windsor, C.G. (1981) *Pulsed Neutron Scattering*, Taylor & Francis, London.
Newport, R.J., Rainford, B.D. & Cywinski, R. (Eds.) (1988) *Neutron Scattering at a Pulsed Source*, Hilger, Bristol. Somewhat out of date but useful background information. Lectures given at the Summer School on Neutron Scattering at a Pulsed Source held at the Rutherford Appleton Laboratory (ISIS) and in Mansfield College, Oxford, for the period 16–24 Sept. 1986.
The ISIS website has a nice introduction to spallation and pulsed neutron scattering: http://www.isis.rl.ac.uk.

Synchrotron X-rays and sources:

Ciocci, F., Torre, A. & Dattoli, G. (2000) *Insertion Devices for Synchrotron Radiation and Free Electron Laser*, World-Scientific, Singapore.
Duke, P.J. (2000) *Synchrotron Radiation: Production and Properties*, Oxford University Press, Oxford.
Mills, D. (2001) *Third Generation Hard X-ray Synchrotron Radiation Sources Properties, Optics, and Experimental Techniques*, Wiley, New York.
Synchrotron Light (2001) Springer, Berlin.

X-ray and neutron detection:

Brief introductions are available in many introductory books on X-ray and neutron scattering, for example, Klug and Alexander (1974) for X-rays and Bacon (1975) for neutrons. One of the best ways to learn about details of X-ray detection is to read the tutorial sections of the product catalogs of the main detector manufacturers such as Ortep and Canberra, or to consult their websites. Otherwise books tend to be rather specialized and/or out of date such as: Allen, W.D (1960) *Neutron Detection*, Philosophical library, New York; or Combes, C. (1999) *Scintillation Properties of ^{6}Li-based Materials for Thermal-neutron Detection*, Coronet Books.

Powder diffraction and diffractometry:

Jenkins, R. & Snyder, R.L. (1996) *Introduction to X-ray Powder Diffractometry*, Wiley, New York.
Klug, H.P. & Alexander, L.E. (1974) *X-ray Diffraction Procedures*, 2nd Edition, Wiley, New York.
Young, R.A. (1995) *The Rietveld Method*, Oxford University Press, Oxford.

This Page Intentionally Left Blank

Chapter 5

Data Collection and Analysis

Chapter 5
Data Collection and Analysis

5.1. INTRODUCTION

The raw data collected in a diffraction experiment take the form of photon or neutron counts vs. some variable, such as diffraction angle, energy, time of flight (tof) and so on, which will be converted to a Q value. The purpose of the diffraction experiment, however, is to determine the normalized total scattering structure function $S(Q)$ as we have discussed. The data have to be collected and processed so that they yield the structure function with high accuracy. Also the experimental setup has to be designed to make the data analysis easier and more accurate. Here we spend some time on the strategy of data collection and analysis.

The measured intensity of scattered neutrons or X-rays contain, in addition to scattering from the sample, scattering from the addenda such as the sample holder and experimental apparatus. The first order job is to remove all the photon or neutron counts due to scattering from the addenda. Thus, we have to perform scattering measurements without the sample in place to account for instrumental backgrounds. Note, however, when the sample is present a part of the scattering from the addenda is modified due to sample absorption. This complicates the process. In addition some photons or neutrons are scattered twice or more times in the sample and elsewhere in the apparatus before reaching the detector. This multiple-scattering intensity has to be evaluated. The scattered intensity has to be normalized with respect to the intensity or spectrum of the incoming beam. Then the scattered beam intensity has to be corrected for polarization effects, sample absorption, and normalized with respect to the number of atoms in the sample. The properly normalized structure function is obtained only after these laborious steps. Any imperfection in the corrections procedure will affect the outcome.

There are two pieces of good news in this regard. First, most of the corrections are pretty well understood and can be reliably estimated. The second piece of good news is that the structural information in the PDF is fairly robust with respect to analysis errors. The reason is that most data-corrections give rise to data-modulations that are much more slowly varying with Q than the experimental signal itself. The net result of this is that imperfections in the data correction procedure have a large effect on the very low-r region of the PDF since long wavelength features in $S(Q)$ give rise to sharp features in $G(r)$ at low-r. This is the region below the nearest-neighbor distance where there is no physical information about the structure. Whilst accurate data-corrections are clearly important, the physical information in the PDF is somewhat robust to imperfect corrections. Having said this, spurious information from this low-r portion of the PDF can propagate into

the physical region of the data and one should be guarded against over-interpreting small, individual, features, especially in the low-r region of the PDF. In contrast to other local structural techniques such as XAFS, the quality of the data does not diminish with increasing r. By fitting models over a range of r to get the structural information it is unlikely that experimental artifacts will be wrongly interpreted.

In this chapter we discuss in detail the equations and procedures used to correct the data to obtain $S(Q)$ and subsequently $G(r)$. We develop the equations for the data analysis using the language of differential cross-sections. This formalism will be much more familiar to neutron scatterers than X-ray scatterers; however, as defined it is completely universal. It is also a very intuitive way to describe the real physical measurement and, for those unfamiliar with the slightly mathematical looking formalism, a few moments spent understanding the definition (Section A5.1.1 of Appendix 5.1) in detail will pay back handsomely. The desired structure function, $S(Q)$, depends on the coherent single scattering sample cross-section, $(\mathrm{d}\sigma^{\mathrm{s}}/\mathrm{d}\Omega)$, from Eq. 2.9:

$$S(Q) = \frac{1}{\langle b \rangle^2}\left(\frac{\mathrm{d}\sigma^{\mathrm{s}}}{\mathrm{d}\Omega}\right) + \left(\frac{\langle b \rangle^2 - \langle b^2 \rangle}{\langle b \rangle^2}\right). \tag{5.1}$$

In Section 5.2 we give general equations for $(\mathrm{d}\sigma^{\mathrm{s}}/\mathrm{d}\Omega)$ in terms of the measured intensities from sample and background data-sets. These equations are derived in an intuitive step-by-step fashion in Appendix 5.1. In Section 5.3 we discuss specific corrections for X-ray and time-of-flight neutron data and present the equations that are relevant for these specific cases. In Section 5.4 some aspects of real-world data-analysis, including where to get data analysis programs, are laid out.

5.2. DATA ANALYSIS OVERVIEW

In this section, we give the most general equations that are necessary to reduce raw data to the total scattering structure function $S(Q)$. As per Eq. 5.1, this requires determining $(\mathrm{d}\sigma^{\mathrm{s}}/\mathrm{d}\Omega)$ from the experimentally measured intensities. The equations given here are systematically defined in Appendix 5.1. The derivation is involved and can be skipped on a first reading. However, we believe that glancing over the derivation steps reveals considerable insight into the philosophy of the data corrections and is well worth the effort.

The problem is set up initially in the most general terms possible by dividing the sample into microscopic volume elements and considering the scattering from each element in turn. There is more than one approach that can be taken to obtain $S(Q)$ from the raw data. Also, exactly which equations are used to make specific corrections depends on the geometry of the particular measurement. By developing the problem in general terms

first we hope that it becomes clear to the reader exactly what the problems are facing the data analyst. For convenience the resulting equations are reproduced below from Appendix 5.1.

In general, to obtain a reliable $S(Q)$ three measurements need to be made: sample in a can in its sample environment, empty can in the sample environment, empty environment (sometimes called background). The letters s, c and a are used to denote the presence of sample, container and sample environment (or apparatus), respectively, in the measurement. In these three experiments the integrated counts in the detector, N, normalized by the monitor counts, M, are given by Eqs. A5.1.23–A5.1.25

$$\left(\frac{N}{M}\right)^{\mathrm{sca}} = \mathrm{d}\Omega\,\mathrm{d}E_{\mathrm{s}}\,K\varepsilon_{\mathrm{d}}\{p^{\mathrm{s;sca}} + p^{\mathrm{c;sca}} + p^{\mathrm{a;sca}} + m^{\mathrm{sca}}\} \tag{5.2}$$

$$\left(\frac{N}{M}\right)^{\mathrm{ca}} = \mathrm{d}\Omega\,\mathrm{d}E_{\mathrm{s}}\,K\varepsilon_{\mathrm{d}}\{p^{\mathrm{c;ca}} + p^{\mathrm{a;ca}} + m^{\mathrm{ca}}\} \tag{5.3}$$

$$\left(\frac{N}{M}\right)^{\mathrm{a}} = \mathrm{d}\Omega\,\mathrm{d}E_{\mathrm{s}}\,K\varepsilon_{\mathrm{d}}\{p^{\mathrm{a;a}} + m^{\mathrm{a}}\} \tag{5.4}$$

where all the symbols are defined in Appendix 5.1. Here the single scattering contributions are given by Eq. A5.1.18,

$$p^{y;\{w\}} = \left(\frac{\mathrm{d}^2\sigma^y}{\mathrm{d}\Omega\,\mathrm{d}E_{\mathrm{s}}}\right)\rho^y D\int_y h\left(\prod_{x\in\{w\}} A_x\right)\mathrm{d}\vec{r} \tag{5.5}$$

and m^{xyz} are the multiple scattering terms defined in Appendix 5.1. Making certain approximations these equations can be combined and rearranged to yield Eq. A5.1.36

$$\left(\frac{\mathrm{d}^2\sigma^{\mathrm{s}}}{\mathrm{d}\Omega\,\mathrm{d}E_{\mathrm{s}}}\right) = \left[\left(\frac{N}{M}\right)^{\mathrm{sc}} - \left(\frac{V'_{\mathrm{c;sca}}}{V'_{\mathrm{c;ca}}}\right)\left(\frac{N}{M}\right)^{\mathrm{c}}\right]\left(\frac{1}{\rho^{\mathrm{s}}V'_{\mathrm{s;sca}}D\mathrm{d}\Omega\,\mathrm{d}E_{\mathrm{s}}\,K\varepsilon_{\mathrm{d}}}\right) - m' \tag{5.6}$$

for the sample double differential cross-section (Appendix 5.1) where

$$\left(\frac{N}{M}\right)^{\mathrm{sc}} = \left(\frac{N}{M}\right)^{\mathrm{sca}} - \left(\frac{N}{M}\right)^{\mathrm{a}}$$

and

$$\left(\frac{N}{M}\right)^{\mathrm{c}} = \left(\frac{N}{M}\right)^{\mathrm{ca}} - \left(\frac{N}{M}\right)^{\mathrm{a}}$$

From here it is a straightforward integration over the energy window of the measurement, $W(E)$, to obtain an expression for the desired single scattering cross-section in terms of the measured counts (Eq. A5.1.37),

$$\left(\frac{\mathrm{d}\sigma^{\mathrm{s}}}{\mathrm{d}\Omega}\right) = \int\left(\frac{\mathrm{d}^2\sigma^{\mathrm{s}}}{\mathrm{d}\Omega\,\mathrm{d}E_{\mathrm{s}}}\right)W(E_{\mathrm{s}})\mathrm{d}E_{\mathrm{s}} \tag{5.7}$$

$$= \left[\left(\frac{N}{M} \right)^{sc} - \left(\frac{V'_{c;sca}}{V'_{c;ca}} \right) \left(\frac{N}{M} \right)^{c} \right] \left(\frac{1}{\rho^{s} V'_{s;sca} D \, d\Omega \, K \varepsilon_{d}} \right) - m' \qquad (5.8)$$

In this equation the $V'_{y;\{w\}}$ terms give the absorption weighted 'effective scattering volume' of the sample. They are discussed further in Section 5.3.6 and defined in detail in Appendix 5.1. They can be evaluated numerically knowing the linear absorption coefficients, $\mu(E)$, of the sample, container and apparatus. For some simple geometries such as flat-plate transmission and reflection, there are analytic expressions which are derived in Appendix 5.2.

Within the assumptions we have made, this equation for $(d\sigma^{s}/d\Omega)$ is quite general. We have not assumed any particular origin for the double differential cross-section. We have not presumed that the scattering is elastic or inelastic or coherent or incoherent, nor have we stipulated that the measurement be made at constant wavelength, or in a particular geometry. We have not even specified that the scatterers be X-rays or neutrons. Eq. 5.8 is valid provided the scattering is weak, that the experimental apparatus other than the sample container is sufficiently far from the sample, that each component of the experimental apparatus, and the sample, are homogeneous and that we can evaluate the multiple scattering contributions adequately. Clearly, an accurate determination of the sample cross-section also implies that we can evaluate the integrals, $V'_{y;\{w\}}$, accurately and that we know, or can measure, our sample density, detector solid angle and detector efficiencies. These issues will be dealt with below.

Finally, as we discussed at the beginning of the chapter, $S(Q)$ is obtained from $(d\sigma^{s}/d\Omega)$ according to Eq. 5.1.

5.3. OBTAINING $S(Q)$ IN PRACTICE

We will now discuss how to obtain the total scattering structure function, $S(Q)$, in practice in two specific cases: angle dispersive X-ray diffraction and time-of-flight neutron diffraction. It is possible to obtain good PDFs from reactor neutron sources using a constant wavelength angular dispersive mode as well, although except when using a very hot moderator the Q range is very limited. In this case the data corrections are much closer to those used for X-ray analysis than the time of flight data collections, the main difference being that the form-factor is Q-independent and there are no polarization corrections to be carried out. These corrections are not explicitly discussed here.

Up to now we have defined the sample cross-section in a very general way. We did not say that it was only coherent scattering nor did we even specify the scattering mechanism. The cross-section was simply the probability that a particle is scattered by a given volume

element in a given direction, by any process. In this Section we will explore this in more detail taking the case of X-ray and neutron scattering separately. Before we do this we will summarize some of the terminology.

5.3.1 Elastic, inelastic, coherent and incoherent scattering

All scattering can be characterized using two important concepts into four distinct categories. The two concepts are whether the scattering was elastic or inelastic and whether it was coherent or incoherent. These terms are often used imprecisely leading to confusion. This is particularly apparent when a person with a neutron scattering background talks to a person with an X-ray scattering background where the concept of inelastic scattering generally has a very different meaning. We discuss this further here. First we define the terms; the easier to define first. In an *elastic scattering* event there is no exchange of energy between the scattering particle and the system it is scattering off (the sample). Conversely, in an *inelastic scattering* event there is an exchange of energy. The coherence of the scattering refers to whether there is a definite phase relationship between scattered waves allowing them to interfere constructively and destructively. In the case of coherent scattering, the waves interfere and the resulting intensity is given by the square of the sum of the wave amplitudes. For example, if there are two scattered waves of amplitude ψ_1 and ψ_2, then $I = |\psi_1 + \psi_2|^2$. In the case of incoherent scattering there is no definite phase relationship between the waves, they do not interfere, and the resulting intensity is simply the sum of the intensities of the individual waves themselves, i.e. $I = |\psi_1|^2 + |\psi_2|^2$. Since structural information in the scattering comes from the interference effects of scattered waves it is clear that only coherent scattering contains any structural information.

There are many different scattering processes that occur in materials, but all scattering processes can be categorized as being coherent or incoherent and elastic or inelastic. To illustrate this, we mention some types of scattering and categorize them. We will discuss this more below in the Sections 5.3.7 and 5.3.8. Bragg scattering is elastic and coherent. Laue monotonic diffuse scattering (coming from the mixture or different chemical species in a sample) is elastic and incoherent. The incoherent cross-section of the nuclear scattering, coming from the different isotopes and spin-states of nuclei in a sample, is elastic and incoherent (in some sense it is the same as Laue monotonic scattering). Thermal diffuse scattering is inelastic and coherent. Compton scattering is inelastic and incoherent. Neutron (and X-ray) scattering from phonons and magnons is inelastic and coherent (actually the same origin as thermal diffuse scattering). All the coherent scattering, elastic (e.g. Bragg) and inelastic (e.g. TDS), becomes incoherent at high enough values of Q due to Debye–Waller effects. We will use these concepts more below.

In Section 5.3.2 we discuss methods for obtaining 'quick and dirty' $S(Q)$ values for real-time data processing and characterization. In subsequent subsections we discuss in more detail the various corrections that are carried out for X-ray and neutron tof measurements.

The discussion is laid out more-or-less in the order in which the corrections are applied in practice. Finally, equations for $(d\sigma^s/d\Omega)$ specific to the particular cases of X-ray and tof neutron are given in Eqs. 5.19 and 5.27, respectively.

5.3.2 Quick S(Q)

Whilst modern computers and data analysis programs allow data to be processed very quickly the time pressures of working at a 24 h a day X-ray or neutron facility often are not compatible with making a careful analysis in real-time during data collection. In this case it is convenient to be able to calculate quickly a rough, but representative, $S(Q)$. This is straightforward in the case of X-rays, especially when Compton scattering is being discriminated in the measurement. Data must be corrected for detector deadtime and divided by the beam monitor. At this point the data can be aggressively smoothed (for example, a box-car smooth with a box-car of a few hundred points in length). This heavily smoothed data will then be used as $\langle f^2(Q)\rangle$ and divided into the unsmoothed data. This results in a function that resembles $S(Q)$, though is not quantitatively accurate because the low-Q portion of the data are not properly scaled (the smoothing process works better at high-Q where the features in the scattering are less pronounced). It is especially good for assessing whether significant diffuse scattering is present at high-Q and checking the statistics of the data in this region. This is shown in Figure 5.1 where data from CHESS are shown as measured intensities and as $Q(S(Q) - 1)$ evaluated in the above way. For now what is apparent is oscillating diffuse scattering at high-Q that is easily seen in $Q(S(Q) - 1)$ but is not clearly visible in the as-measured data even when plotted on an expanded scale (inset to Figure 5.1).

In the case of neutrons there is no Q-dependent form-factor but the incident source spectrum must be accounted for. The quantity actually measured in the experiment is the number of counts in a particular time-of-flight channel in a detector or detector pixel. For simplicity we can simply neglect the contribution of unwanted parasitic scattering (background, multiple scattering, etc.) and other distortions such as sample absorption and inelasticity effects. Thus, by dividing the total flux normalized measured, N/M, by those from the vanadium, N_v/M_v, we get an approximate form of $S(Q)$ to within an arbitrary constant scale factor. Ensuring that $S(Q)$ asymptotes to one at high-Q gives us the desired quick $S(Q)$.

5.3.3 Detector dark counts and deadtime corrections

Counts are detected even when the X-ray beam is switched off. These are known as dark counts and come from thermally excited events in the detector and noise in the electronics. Detectors are designed to minimize the dark counts, for example, by cooling. Nonetheless, the dark count-rate of the experimental detector and electronics setup should be measured by determining the detected counts with the electronics live but the X-rays switched off.

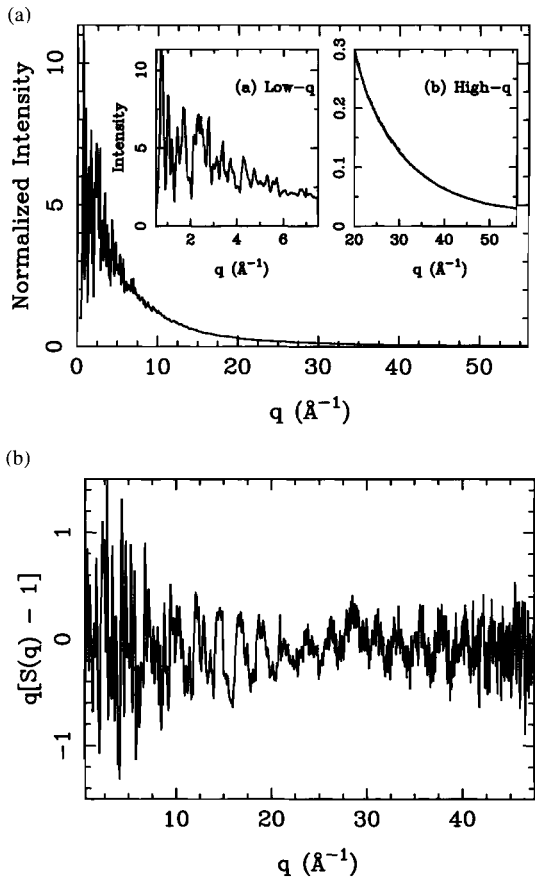

Figure 5.1. (a) Deadtime corrected raw data and (b) quick $S(Q)$, from Pt-I ethylene diamene, a charge density wave polymer. Very little structure is evident in the raw data at high-Q (e.g. see the right hand inset of (a)). However, after dividing by $\langle f^2(Q)\rangle$ and plotting as the reduced total scattering structure function (bottom) the features in the scattering become evident.

To ensure long-time stability in the detector/electronics setup it is good practice to repeat the dark count measurement periodically throughout the experiment. The measured dark count-rate should be subtracted from the data first, before proceeding further with data analysis.

Every time an X-ray or a neutron is detected the detector, and its associated electronic circuits, have to reset before another event can be detected. This takes some time called the deadtime. As the count-rate increases, the probability that a second neutron will arrive during this dead period, and therefore not be counted, increases. There is, therefore, a

count-rate dependent correction to be made to the observed total counts. This effect is distinct from the quantum efficiency of the detectors, ε_d and ε_m, because it is an additive correction to the detected counts that depends on the total count-rate into the detector. The quantum efficiency is simply a multiplicative correction: it says that if a particle impinges on the live detector, it will be detected with the probability $1/\varepsilon_d(E_s)$ to get the total number of particles incident on the detector you take the measured counts and divide by ε_d. The detector deadtime was not specifically taken into account in the discussion of general data corrections. This correction should be applied before proceeding with any other corrections.

Provided the deadtime is of the order of a few percent it can be effectively be corrected using the standard formula for deadtime correction,

$$N' = \frac{N}{1 - R_d \tau_d} \tag{5.9}$$

where N are the measured counts and τ_d is the time the detector takes to reset: the detector deadtime. R_d is the count-rate (counts per second) in the entire detector. This includes all the particles incident on the detector and not just those that are saved after discrimination. This equation has to be modified in certain circumstances. For example, in time of flight measurements the count-rate in one time-channel can affect the deadtime in a neighboring time-channel if the detector deadtime is comparable to the channel width. This complication was discussed by Soper *et al.* (1989) and is presented briefly in Section 5.3.8.4. The detector deadtime, τ_d, can be measured, for example, by attenuating the beam systematically with foils of known attenuation coefficient. The resulting curve can be fit by Eq. 5.9 to obtain τ_d.

There are alternative methods for assessing detector deadtimes. For example, the charge pulses output from an electronic pulser may be fed into the pre-amp of the detector. This pulser produces charge pulses at a known rate, either at random or regular time intervals. The charge pulses propagate through the detector electronics and are recorded on a scaler or in the MCA. The integrated charge in the charge pulses can be adjusted so that the pulser counts appear at a quiet part of the X-ray energy spectrum and do not interfere with real data. The ratio of detected pulses to the known total number of pulses (pulse-rate × count-time) therefore yields an instantaneous estimate of the deadtime. Clearly, this will be accurate only if the deadtime is dominated by the detection and acquisition electronics and not the time it takes to extract the charge from the detector itself. This method of estimating deadtime also introduces noise into the data unless the signal from the pulser is smoothed. Another method is to compare the elapsed time and the live time of the multi-channel analyzer electronics, should one be used; a piece of information which is sometimes available depending on the MCA. This only gives an accurate estimate of the deadtime due to the MCA conversion.

An example of the importance of accurately correcting for deadtime is shown in Figure 5.2. These are synchrotron X-ray data shown before and after a deadtime correction.

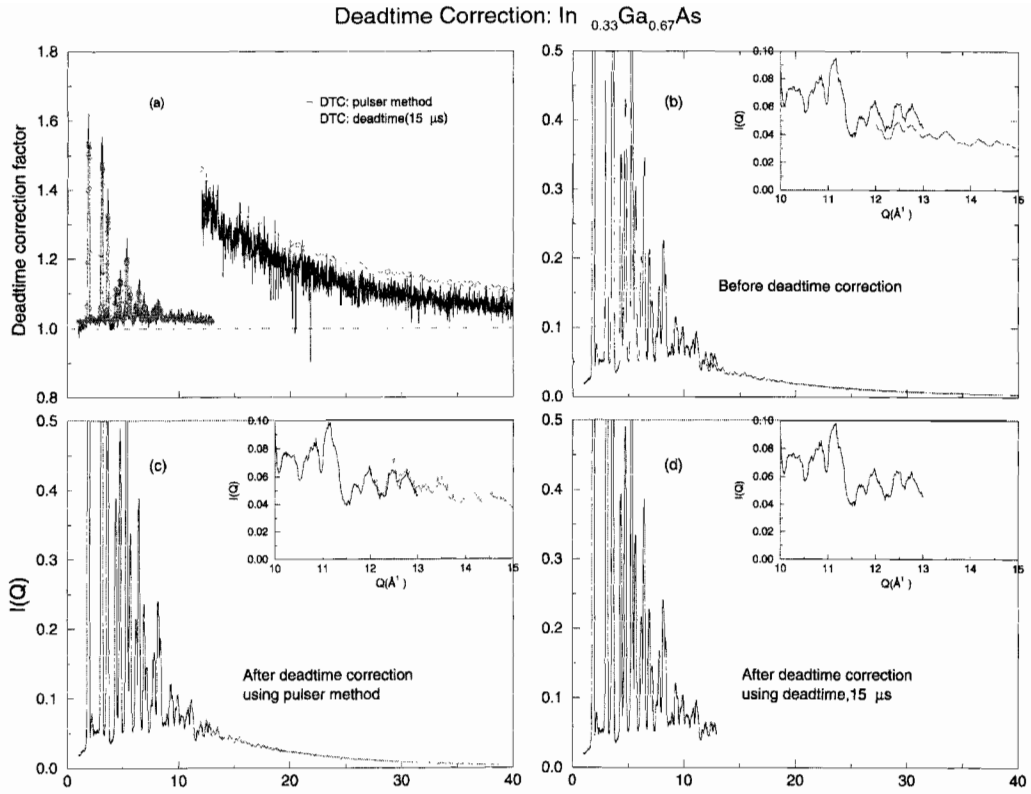

Figure 5.2. Comparison of raw and deadtime corrected data from the CHESS high energy synchrotron source. The data are from the high-Q region from a sample of GaAs. The data have been normalized for incident flux. The sharp discontinuities coincide with points in time when the synchrotron ring was refilled or attenuators were removed from the beam and the source intensity discontinuously increased. After carrying out the deadtime correction the discontinuities are not apparent (PDFgetX manual).

Discontinuities in non-deadtime-corrected intensities occur at synchrotron beam fills when the incident intensity, and therefore count-rate into the detector suddenly takes a significant jump. In the case of the Figure, an incident beam attenuator was removed in the middle of the experiment accounting for the change in intensity and the discontinuity. Note the poor overlap, but also the amplitude of features in the overlap region are only preserved after the deadtime correction (inset to Figure 5.2(b), (c), and (d)). The factor by which the data had to be scaled to account for the detector deadtime is shown in Figure 5.2(a) determined both using the analytic method (Eq. 5.9 and $\tau_d = 15$ μs) and using the pulser method. The pulser method results in a slightly better correction but introduces unwanted noise into the data. The region of overlap is collected to ensure that this correction works well, as is evident. Clearly, the effects of deadtime are less (but not necessarily negligible) in low intensity situations such as laboratory X-ray sources and many neutron experiments.

5.3.4 Propagating random errors

A scattering experiment involves estimating an underlying scattering cross-section by sending well characterized scattering particles into the sample and detecting the scattering pattern. As with all such stochastic measurements, the resulting intensity distribution is just an estimate of the underlying scattering probability. Since the scattering process is completely random this process obeys Poisson statistics (e.g. see Prince, 1982). An estimate of the uncertainty of this measurement is therefore obtained by taking the square root of the number of counts. Thus, if N' particles are detected, the uncertainty in this measurement is $\sqrt{N'}$. As we have seen above, many data corrections are carried out before $S(Q)$ is deduced. Note that the standard deviation of the counts is given by the square root of the *dark current and deadtime corrected* counts not the raw counts. The detector deadtime makes the scattering/detecting process non-random by introducing correlations between events. As a result the detector deadtime corrected counts rather than the raw counts are Poissonian.

We would like to propagate the known uncertainties due to the random counting statistics through to the final $S(Q)$. This can be done with a high degree of certainty using standard error propagation procedures (Prince, 1982). This was discussed briefly in Section 3.5.3. The mechanics of error propagation, and some aspects pertinent to the PDF, are discussed in detail in Appendix 5.3. For now it is sufficient to note that error arrays that will be propagated through the data analysis with the data arrays, should be created at this point, after the detector deadtime correction has been applied but before the data are normalized by the monitor counts and any subsequent corrections are applied. At each step, when the data-arrays get modified by sample corrections, the error arrays are correspondingly modified according to the principles laid out in Appendix 5.3.

5.3.4.1 Data collection strategy for optimizing the statistics on G(r). Note that because the coherent scattering signal diminishes with increasing Q the signal to noise ratio is poorest at high-Q. Thus, this is the region of the diffraction pattern where the most time should be spent in collecting the data. The effect can be dramatic in the case of X-rays as we describe below. We are interested in optimizing the statistical errors on $G(r)$. This has been discussed by Thijsse (1984) for the case of a constant source intensity where he minimizes the expression for var($G(r)$) (Eq. A5.3.9) using calculus of variations with the constraint of a fixed total counting time, T. The result indicates, given a fixed amount of time for the experiment, how much time should be spent on each point. The result is not exactly equal to, though similar (Thijsse, 1984), to the case of giving equal statistical significance to every point in $S(Q)$ in the Fourier transform. Starting with Eq. A5.3.9 we see that this amounts to ensuring that $Q_i^2 \Delta Q_i^2$ var($S(Q_i)$) is approximately constant in Q. For the case of X-ray scattering, where we have some control over this, we can assume that ΔQ_i^2 is constant and

$$\text{var}(S(Q_i)) = \left(\frac{1}{\langle f(Q) \rangle^4} \right) \text{var}(I^{coh}) \approx \left(\frac{1}{\langle f(Q) \rangle^4} \right) \text{var}\left(\frac{N}{M} \right)$$

where we neglect all the absorption and multiple scattering corrections, etc. to N/M. The approximation is much better in high-Q experiments if the Compton scattering is discriminated away and the N/M only in the elastic channel is considered. The variance of N/M is

$$\text{var}\left(\frac{N}{M} \right) = \frac{N}{M^2} \left(1 + \frac{N}{M} \right)$$

or, in a well-designed experiment where the monitor counts are much higher than the signal counts,

$$\text{var}\left(\frac{N}{M} \right) \approx \frac{N}{M^2} \approx \frac{\langle f^2(Q) \rangle}{M}$$

Thus, for every measured point to contribute equally to the Fourier transform we need to approximately satisfy the condition $M(Q_i) \propto Q_i^2 / \langle f^2(Q_i) \rangle$. For very high-$Q$ experiments this is a demanding criterion. $\langle f^2(Q) \rangle$ falls smoothly from a value of Z^2 at $Q = 0$ to a value of order unity at very high-Q. For a Q of 40 Å^{-1} the counting time at high-Q could be as much as 5 orders of magnitude higher than at low-Q!

The calculus of variations method (Thijsse, 1984) results in the less demanding criterion of $M(Q_i) \propto Q_i / \langle f(Q_i) \rangle$, but still the monitor counts at $Q \sim 40$ Å^{-1} should be 2–3 orders of magnitude higher than at $Q \sim 1$ Å^{-1}. If these criteria are not adhered to a perfectly valid $G(r)$ is still obtained but not with optimal statistics. Also, information in $S(Q)$ about small atomic displacements is strongest at high-Q (its intensity scales approximately like $Q^2 \delta r^2$) so it is important to collect the high-Q data with good statistics.

5.3.5 Flux normalization

For very stable sources such as sealed tube sources, the measurement time can be used to scale data points, provided the primary and secondary beam slits remain unchanged. However, in general, as described in Chapter 4, the incident flux is measured using an incident beam monitor. In this case the data points are simply divided by the monitor as indicated in Eqs. 5.17–5.19 and the flux normalization is a simple division of the (deadtime corrected) detector counts, N', by the (deadtime corrected) monitor counts, M'. In the case of an angle dispersive monochromatic synchrotron measurement the incident flux decays with time as the synchrotron beam current decays, with periodic refills where the flux recovers.

In the case of a time-of-flight neutron measurement the flux is strongly energy dependent and the data must be divided by the *source spectrum*. This consists of a Maxwellian peaked at the temperature of the moderator with an exponential tail on the low-λ, high-E, side due to undermoderated epithermal neutrons. This is shown in Figure 4.5. An empirical expression has been proposed to explain the spectral shape (Howells, 1984)

$$\phi(\lambda) = \phi_{\max} \frac{\lambda_T^4}{\lambda^5} \exp\left\{-\left(\frac{\lambda_T}{\lambda}\right)^2\right\} + \frac{\phi_{\text{epi}}}{\lambda^{1+2a}} \frac{1}{1+\exp\{(\lambda-\lambda_1)/\lambda_2\}} \tag{5.10}$$

where $\phi_{\max}$, ϕ_{epi}, λ_T, λ_1, λ_2, and a are fitting parameters. The spectrum is measured with high accuracy by using an almost incoherent scatterer such as vanadium, or a completely incoherent (null-scattering) alloy such as V–Nb. The scattering from this simply reflects the source spectrum and dividing the data point-by-point by the vanadium data results in a proper flux normalization. This has the additional advantage that detector efficiencies, solid angles and the detector profile, D, are automatically corrected since the same detectors are used to collect the sample and vanadium data. In fact, this division is carried out after absorption and multiple scattering corrections have been carried out on the sample and vanadium data, Eq. 5.27. Since the shape of the spectrum is accounted for in the measurement of the incoherent scatterer (vanadium) the *total* monitor counts (integrated over all times of flight) can simply be used to scale a particular data-set. However, to help correct for temporal instabilities in the experimental setup the sample and vanadium data are often both divided point-by-point on the time-axis by the counts from the vanadium monitor that also reflects the source spectrum. This results in a fairly accurate normalization for the source spectrum that, nonetheless, becomes fully corrected for detector geometry, efficiency, solid angle and profile by the subsequent division by the vanadium data as described above, though introduces more noise in the data unless the monitor data are smoothed. Note that, because the monitor is upstream of the sample and the detectors downstream, the same λ value occurs at different times of flight, τ, in the monitor and detectors and the monitor spectrum has to be interpolated and the ratio made for neutrons of the same wavelength, not the same τ.

5.3.6 Absorption and multiple scattering corrections

The absorption corrections were described in some detail in Appendix 5.1 and are practically the same for X-rays and neutrons. The objective is to evaluate the effective volume integrals $V'_{y;\{w\}}$ laid out in Eq. A5.1.30. These are integrals of the attenuation factors, A_x, defined in Eq. A5.1.3, over all trajectories that beams take through the sample, weighted by the incident beam profile function $h(\vec{r})$ (Eq. A5.1.13). To evaluate them correctly $h(\vec{r})$ needs to be known as well as the linear absorption coefficients of the sample. In the single scattering case the integrals are over volume elements in the sample, for double scattering they are double integrals over all volume elements, and so on.

The beam profile function, $h(\vec{r})$, must be evaluated experimentally. For example, this can be done by stretching an incoherently scattering fiber, such as piece of nylon, across the sample position and measuring the intensity. In general the fiber should be first stretched vertically and systematically translated horizontally, then stretched horizontally and translated vertically. If the experiment has cylindrical symmetry the horizontal translation is all that is needed. In practice, both making this measurement and correlating the resulting beam profile with the integral over volume elements are non-trivial and it is common practice to neglect $h(\vec{r})$ and assume that the beam is homogeneous without serious detrimental effect on the corrections. In this case an 'effective' beam cross-section $A' < A$ is sometimes used in the corrections (Sections A5.1.6) (Soper *et al.*, 1989).

For specific flat-plate geometries there are analytic expressions for the effective volume integrals as a function of scattering angle. These are derived in Appendix 5.2. Examples of absorption corrections for symmetric flat-plate geometries are shown in Figure 5.3. For cylindrical, and other more general, sample geometries the integrals can be evaluated at each scattering angle numerically by dividing the sample into volume elements and evaluating the attenuations due to trajectories to and from each volume element. In this case it is computationally efficient to take advantage of any symmetries that are present (Paalman and Pings, 1962; Poncett, 1977; Soper and Egelstaff, 1980).

It is important to know the attenuation coefficients, $\mu_x(E)$, fairly accurately for sample and sample holder at the energy of interest. These are tabulated for the various elements for X-rays (Wilson, 1995) and neutrons (Bodek *et al.*, 2000) and are now available on the web (for example, at the US National Institute of Standards and Technology (NIST) website). For flat-plate geometries it is most accurate to *measure* the absorption (attenuation) length, $\mu_x(E)t$, of the sample where here t refers to the sample thickness, as described in Chapter 4. If an energy resolving detector, such as a solid-state detector, is used with an MCA then $\mu(E)t$, for each MCA channel is directly determined, though do not destroy the detector with unattenuated direct beam! Because powders are used the beam spends part of its trajectory traversing the space between grains where it is not attenuated. In this case, the lower powder density, rather than the fully-dense material density, should be used when calculating the sample linear absorption coefficient. In time-of-flight neutron experiments the energy dependence of the neutron absorption has to be approximated. A linear

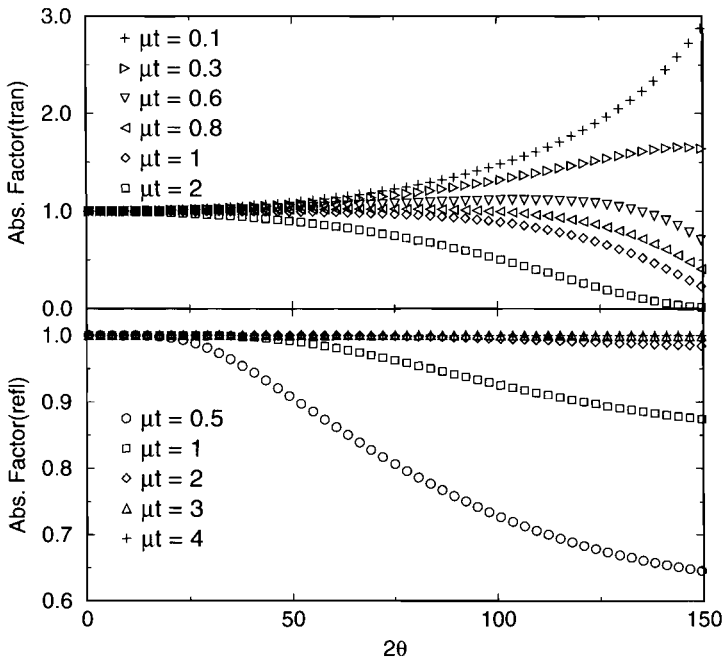

Figure 5.3. Calculated absorption factor (defined as the sample effective volume divided by the real volume, V'/V) as a function of scattering angle for symmetric flat-plate geometry. (top) transmission (bottom) reflection. The curves show the factors calculated for different sample absorption, μt, where a large μt means a highly absorbing sample. The sample effective volume can be greater than the actual sample volume in transmission in the back scattering region. This is because of the long path-length the beam takes through the sample. Note the useful property that for an infinitely thick sample (large μt) in reflection geometry the absorption correction is independent of angle and is simply a constant (PDFgetX manual).

dependence of the absorption cross-section with wavelength is assumed: $\sigma^{abs}(\lambda) = \lambda\sigma^{abs}(1)$ where $\sigma^{abs}(1)$ denotes the neutron absorption resonance at $\lambda = 1$ Å (Nield and Keen, 2001). Conventionally neutron absorption cross-sections are reported for neutrons with velocities of 2200 ms^{-1} which is equivalent to $\lambda = 1.798$ Å. This assumption works fairly well except close to neutron absorption resonances. There corrections become more complicated (e.g. see Hannon *et al.*, 1990) with the scattering cross-sections, as well as the absorption cross-section, having anomalous scattering corrections in exact analogy with the case for X-rays. In general, data in the vicinity of absorption resonances are not used.

These days the X-ray mass absorption coefficients and neutron absorption cross-sections of the elements are often tabulated within data analysis software programs and it suffices to tell the programs the composition of the sample and container and their respective (powder) mass densities.

Multiple scattering corrections are less straightforward to calculate. They depend on sample thickness and sample transparency and therefore also depend on the sample

absorption. As can be seen from Eqs. A.5.1.6 and A.5.1.10 the exact calculation of double and higher order multiple scattering is difficult and requires evaluation of nested integrals. Furthermore, these integrals contain the sample double-differential cross-section, precisely the quantity that we are trying to measure. When $S(Q)$ is not highly directional an approximation can be made that this cross-section is isotropic. Another approximation can also be made that higher orders of scattering are just multiples of lower order scattering. This results in a series that converges quickly since each higher order of scattering is significantly weaker than the previous one. Furthermore, it means that only the second order scattering need be evaluated explicitly. In this way the multiple scattering can be straightforwardly, though arduously, calculated (Warren, 1990; Blech and Averbach, 1965; Dwiggins, 1972; Dwiggins and Park, 1971; Sears, 1975; Serimaa *et al.*, 1990). Examples of X-ray double scattering ratios, I_2/I_1, are shown in Figure 5.4 for symmetric flat-plate geometries and samples of varying degrees of transparency. Multiple scattering is moderate in low energy X-ray experiments because of the relatively large sample absorption/scattering ratio. It is a much more significant problem in most neutron measurements where the sample absorption cross-section is much less than the scattering cross-section.

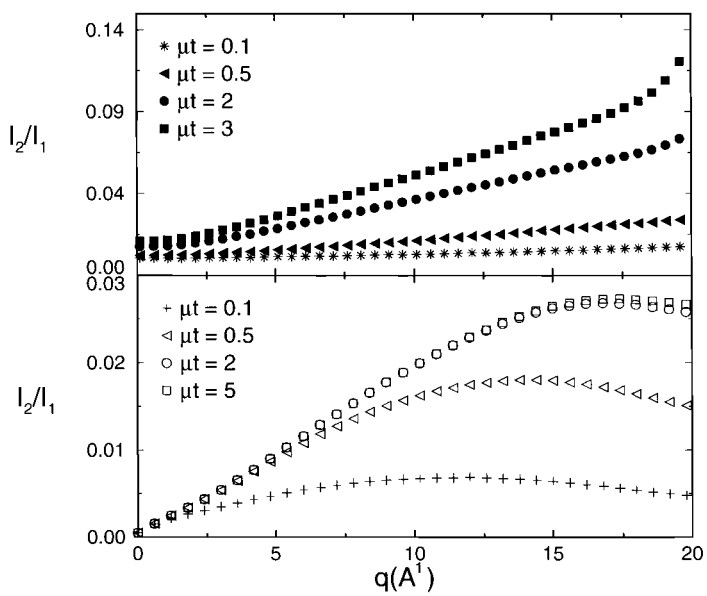

Figure 5.4. Calculated double scattering ratios, I_2/I_1, for symmetric flat-plate geometries and samples of varying degrees of transparency. (top) transmission (bottom) reflection. The double scattering includes elastic and inelastically scattered contributions and was calculated for nickel using X-rays of wavelength $\lambda = 0.7107$ Å (PDFgetX manual).

As can be seen in Figure 5.4, in the case of X-rays the multiple scattering contribution to the intensity is very small in reflection but can be significant in transmission geometry, especially at high scattering angles. Calculation of the X-ray multiple scattering intensity is considerably simplified when only purely 'elastic' scattering is collected (the Compton scattering is discriminated away) since only completely elastic multiple scattering events need to be considered.

For crystalline samples the isotropic approximation is disastrously wrong (the scattering cross-section is strongly peaked in the directions of Bragg-peaks!). Nonetheless, the extensive averaging, both due to the powder and of the nested integrals, means that the isotropic approximation is thought still to work rather well and no more sophisticated corrections are generally applied. As we mentioned before, a more accurate approach is to simulate the real experiment using Monte Carlo (e.g. see Howells, 1986) though this is rarely needed in practice. The standard approximate corrections appear only begin to break down when more than $\sim 20\%$ of the incident beam is getting scattered. For very thin samples it is often adequate to carry out no multiple scattering corrections at all without problem. Again, multiple scattering corrections are present in most modern software data analysis programs.

5.3.7 X-ray specific corrections

5.3.7.1 Overview. Typical X-ray energies used in diffraction experiments are in the range 7–120 keV. Most excitations in materials, such as phonons and magnons, have energies on the scale of meV to eV. In order to resolve these inelastic processes explicitly it is necessary to have an energy resolution of your measurement of $\Delta E/E \approx 10^{-6}$ or 0.0001% which is an extremely demanding task. Standard experimental practices in powder diffraction do not give nearly this resolution; for example, the use of an energy resolving detector such as an intrinsic semiconductor detector gives an energy resolution of $\approx 200/20000 = 10^{-3}$ or 0.1%. As a result, the coherent inelastic scattering from the sample, such as phonon scattering, is not resolved and these counts are integrated into the total measured counts: the measured 'elastic' X-ray scattering includes all the unresolved low energy inelastic scattering. The integral over energy of Eq. 5.7 is already carried out in the detector. Furthermore, on the energy scale of the measurement, this coherent inelastic scattering component lies very close to the elastic line and to a very good approximation the integration is carried out at a constant value of Q. This is described in detail in Chapter 7. The 'elastic' scattering in an X-ray experiment is, to a high degree of precision, the total (or energy integrated) scattering that was defined in Eq. 5.7, plus any elastic incoherent contributions. A consequence of this fact is that the X-ray measurement is very fast on the timescale of lattice vibrations. As far as the X-ray measurement is concerned

the atoms appear stationary and the resulting structure that is measured is the time, and sample, average of instantaneous snap-shots of the lattice vibrations (sometimes called the static approximation resulting in the 'same-time' correlation function).

A second scattering process occurs for X-rays as well as the scattering that gives rise to the coherent elastic scattering. This is Compton scattering. Unbound, or weakly bound electrons recoil during the scattering process. The scattering event must conserve momentum and energy. Consider an electron that is initially at rest. After an X-ray scatters off it the momentum of the X-ray has changed and therefore the momentum of the electron must also change. Since the electron was initially at rest it is clear that this collision with the photon starts it moving and therefore some energy was imparted to the electron from the X-ray: it is an inelastic process. It is also an incoherent process. This incoherent, inelastic, Compton scattering is often referred to by X-ray scatterers simply as 'inelastic scattering'. This is correct but imprecise and can lead to the confusion we referred to in conversations between X-ray and neutron scatterers. The latter group generally thinks of phonon scattering and other inelastic coherent types of scattering on hearing the expression 'inelastic scattering'. In general, the electron that is scattering the X-ray is not at rest; it can be moving towards or away from the incoming X-ray. There is therefore a range of energies where Compton scattering occurs, symmetric about the energy shift of the stationary electron. Compton scattering contains information about the momentum distribution of electrons in the atoms and is sometimes used to probe this. An example of Compton and elastic scattering, measured at various Q-values in an MCA using a germanium solid-state detector, is shown in Figure 5.5. For our purposes it is an annoying incoherent background that must be removed. The best way to do this is to eliminate it by carrying out an experiment with good enough energy resolution. Failing this, the Compton scattered intensity can be calculated theoretically and subtracted as we describe below.

Another elastic incoherent contribution to the scattering is the self-scattering which occurs in the forward scattering direction. In general, this scattering is confined to very small angles and is inaccessible experimentally because of the incident beam. When large length-scale (nanometer) inhomogeneities exist in the sample, this forward scattering is spread out and becomes visible as small angle scattering. Strictly speaking this should be removed from the data before obtaining $S(Q)$. In practice the contribution from small angle scattering is generally very small at angles accessible in a normal powder diffraction measurement and this contribution is rarely considered explicitly. However, if it is significant it should be removed.

Another feature of the X-ray experiment is that the Thompson scattering process polarizes the scattered beam. The scattered beam is polarized such that the electric vector lies in a direction perpendicular to the scattering plane (the plane defined by the incoming and outgoing beams). Most X-ray detection schemes are not sensitive to beam polarization so, on first thought, this fact should not matter. However, on further thought it becomes

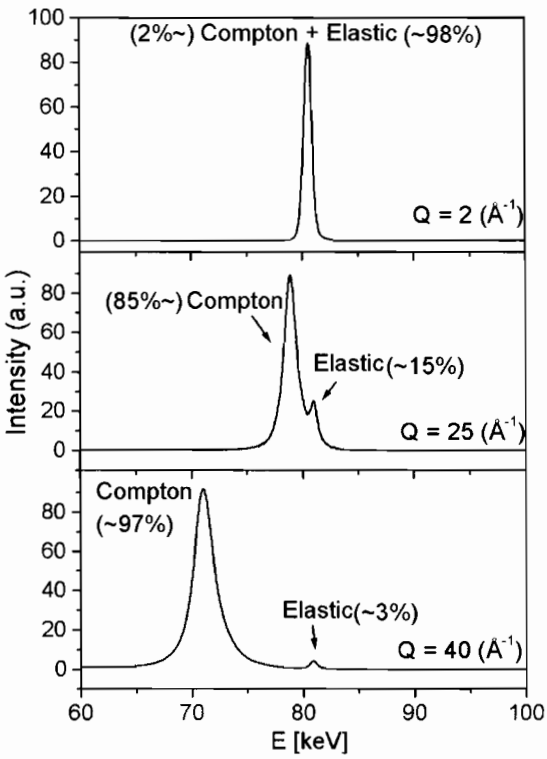

Figure 5.5. Comparison between measured Compton and elastic scattering intensities measured in silica glass using 80 keV X-rays. Note the Compton scattering is much stronger than the elastic signal at high-Q (Petkov *et al.*, 2000).

obvious that the sample is acting as a polarizer and so the measured *intensity* will depend on the degree and nature of the polarization of the incident beam. If the incident beam is also polarized with the electric vector perpendicular to the scattering plane then the full intensity will be transmitted at all angles. However, if the incident beam is polarized in the scattering plane, the scattered intensity will depend on the scattering angle: it is modulated by a polarization correction that is given by the projection of the incident beam electric vector on a plane perpendicular to the scattered beam. For example, at a 90° scattering angle and the electric vector lying in the scattering plane, the scattered beam lies along the direction of the electric vector and the projection gives zero intensity. Clearly, even an unpolarized incident beam results in a polarization correction because an unpolarized beam can be decomposed into components that are parallel and perpendicular to the scattering plane. In this case the scattered intensity will be a minimum, but will not fall to zero, at $2\theta = 90°$. We note two interesting side effects of this polarization dependence of the scattering. First, it explains why most synchrotron X-ray experiments are carried out

with a vertical scattering plane despite this configuration being more difficult from an engineering standpoint; it is because the X-ray beam from the synchrotron is polarized in the plane of the synchrotron ring. It is easier to stand the experiment on its side than to stand the synchrotron beam on its side! The second point to bear in mind is that a crystal monochromator that monochromatizes a beam by Bragg scattering, also polarizes the beam. This should be accounted for in all quantitative X-ray data corrections protocols.

5.3.7.2 Polarization correction. As discussed above, X-rays become polarized by the scattering process and this affects the measured intensity as a function of scattering angle. The correction factor to account for this angle dependence of the scattering is

$$P_i = \frac{(1 + A\cos^2 2\theta)}{(1 + A)} \tag{5.11}$$

where 2θ is the scattering angle and A depends on the degree of polarization of the incident beam. The term A is given by $A = (1 - f)/(1 + f)$. Here f is the polarization rate of the incident radiation in the direction perpendicular to the scattering plane. If the radiation is unpolarized, $f = 0$ and $A = 1$; if it is fully plane polarized perpendicular to the scattering plane (the situation for synchrotron radiation exactly in the plane of the synchrotron ring) $f = 1$ and $A = 0$. In this case there is no angle dependence to the scattered intensity due to polarization effects and therefore no polarization correction. In a real synchrotron experiment the beam is not 100% plane polarized and A will take a small value in the vicinity of 5%.

A number of special cases are worthy of note. When the source is unpolarized but a crystal monochromator is used in the incident beam the beam becomes partially polarized by the monochromator. In this case $A = \cos^2 2\alpha$, where 2α is the scattering angle of the monochromator. Another common geometry is to have an unpolarized source incident on the sample but a monochromator in the scattered beam. In this case the polarization correction becomes $P_i = ((1 - \cos^2 2\alpha \cos^2 2\theta)/2)$. Where it is not known, the degree of polarization of the beam can be determined experimentally (Egami, 1978).

Note that the commonly quoted Lorentz polarization factor, given by $\mathrm{LP} = ((1 - \cos^2 \theta)/2 \sin 2\theta)$ that includes the Lorentz factor, $1/\sin 2\theta$, should not be used. This contains two corrections; the first is the normal correction for beam polarization described above, P_i. The second is a phase-space correction that should be applied to single crystal data when peak integrated intensities are measured. It effectively normalizes the integrated intensity by the volume of reciprocal space that it is measured over. This correction happens automatically in a powder diffractometer measurement.

5.3.7.3 Compton scattering correction. The idea of Compton scattering was introduced in Section 5.3.1. Traditional low energy resolution, low X-ray energy measurements were

carried out by collecting the elastic and Compton scattering together and then subtracting the theoretical Compton contribution, $n^{\text{inc}}(Q)$ which is expressed as an intensity per atom in the sample. The Compton cross-section (per atom) is given by

$$n^{\text{inc}}(Q) = \left(\frac{E_c}{E_0}\right)^{\alpha}\left[\sum_{a=1}^{n} c_a Z_a - \sum_{a=1}^{n} c_a f_a^2(Q)\right] \tag{5.12}$$

(Warren, 1990). It is simply (neglecting small cross-terms between non-orthogonal electrons in neighboring atoms) the classical Thompson scattering intensity minus the coherent scattering power, expressed as $f_a^2(Q)$ for a particular atom, summed over all the atoms. The factor $(E_c/E_0)^{\alpha}$ is known as the Breit–Dirac recoil factor and is a small correction that takes into account the effects of radiation pressure. The exponent, α can take values 2 (Ergun, 1968) or 3 (Warren, 1990) depending on the nature of the measurement. When photon flux is measured in a counter the value 2 is used (Ergun, 1968). Compton intensities for all the atoms are tabulated in the International Tables of Crystallography C (Wilson, 1995). These curves have been fit using an empirical expression and parameterized for all the elements, see, for example, Thijsse (1984). Note that the calculated intensities from the International tables should be scaled by the Breit–Dirac recoil factor, before being subtracted from the data. Here E_0 is the energy of the elastic scattering, and the average energy of the Compton scattering, E_c is given by

$$\frac{E_0 - E_c}{E_c} = \frac{E_0}{m_e c^2}(1 - \cos\theta) \tag{5.13}$$

where m_e is the rest-mass of the electron, c, the speed of light and θ half the scattering angle.

The parameters for determining $n^{\text{inc}}(Q)$ are now contained in a number of X-ray data analysis programs. The calculated Compton scattering should also be corrected for absorption before being subtracted, where account should be taken for the fact the Compton scattering has a different energy than the elastic scattering when evaluating the absorption correction (e.g. see Appendix 5.2).

When higher X-ray energies are used, and at higher scattering angles, the elastic scattering cross-section decreases and the Compton cross-section increases. The ratio of modified (Compton):unmodified scattering also increases as the elements in the sample get lighter. For modern high resolution PDF measurements at high-Q the Compton scattering can be considerably stronger than the elastic signal. This is shown in Figure 5.5 where the measured elastic and Compton scattering from silica glass measured with 80 keV X-rays is plotted. In this case serious signal to noise problems are encountered if the old mode of data collection is utilized and now it is common practice to discriminate away the Compton scattering directly. However, at low-Q the elastic and Compton shifted intensities often cannot be resolved. In this case a method is used where the theoretical

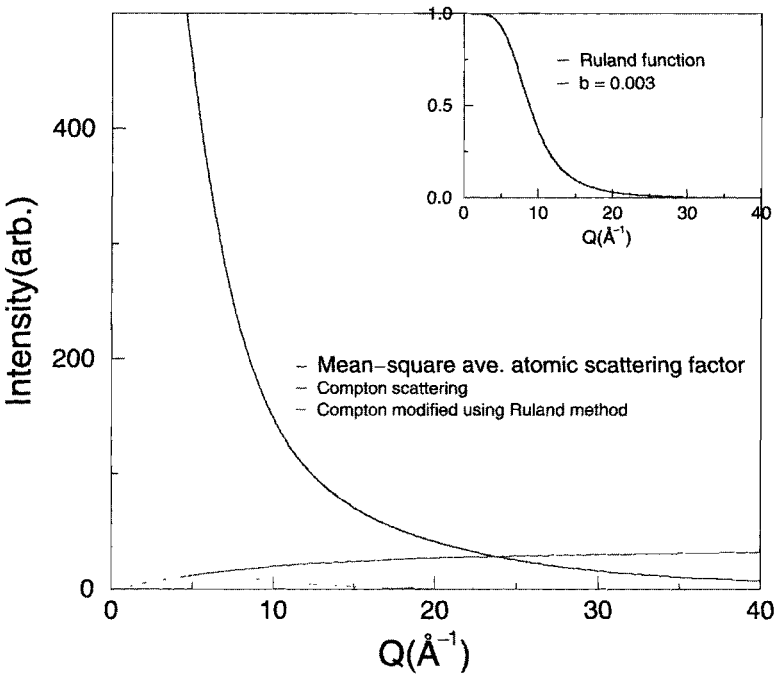

Figure 5.6. Comparison between mean-square average atomic scattering factor, $\langle f^2(Q)\rangle$, Compton, and modified Compton contributions to the intensity as a function of Q. The modified Compton curve was multiplied by the Ruland function shown in the inset calculated for an integral width of $b = 0.003$ (PDFgetX manual).

Compton is subtracted from the low-Q data and the Compton scattering is discriminated away at high-Q. In the crossover region the subtracted theoretical Compton component is gradually reduced using a smooth interpolation function. A road-map for doing this that takes into account the finite width of the Compton scattering (generally ignored in the simple Compton subtractions described above) was suggested by Ruland (1964). The proportion of Compton modified scattering that appears in the measured elastic scattering is then given by $R(Q) = \int W(E)n^{\text{inc}}(Q,E)\text{d}E / \int n^{\text{inc}}(Q,E)\text{d}E$ where $W(E)$ is the band-pass function of the detection device and $n^{\text{inc}}(Q,E)$ is the Compton profile. The Compton profile $n^{\text{inc}}(Q = 40\ \text{Å}, E)$ for silica glass can be seen in Figure 5.5 as the broad, Lorentzian-like, peak just below the elastic scattering intensity at channel number 640. Then $R(Q)n^{\text{inc}}(Q)$ is subtracted from the data rather than $n^{\text{inc}}(Q,E)$ directly. In practice, neither $W(E)$ nor the exact energy dependence of the Compton profile are known accurately and an empirically determined $R(Q)$ is used. The form

$$R(Q) = \left\{\left(1 + \frac{Y}{b}\right)\left[1 + \frac{Q^2 d}{(Y+b)^2}\right]\right\}^{-1}$$

has been suggested by Ruland (1964). Here λ and λ' are the wavelengths of the elastic, and Compton modified, scattering, respectively. Y is a Q-dependent function given by $Y = cQ^3/(a^2 + Q^2)$. In these equations, a, b, c and d are constants. The Ruland function given above is not entirely satisfactory (e.g. see Thijsse, 1984) and is not strictly applicable to the modern experimental setup with energy discrimination by MCA and a purely empirical function is often used (Petkov, private communication) as illustrated in Figure 5.6.

A more accurate method for removing Compton scattering is to calculate the full profile, $n^{\text{inc}}(Q, E)$, within some approximation for the momentum distribution in the atom, at every Q value. Then the X-ray spectrum contained in the MCA can be fit with two peaks originating from the Compton and elastic scattering, respectively. The fit can be constrained. For example, the energy shift of the center of the Compton peak is known (Eq. 5.13). The desired elastically scattered intensities are then obtained from the integrated area under the fit elastic peak, or better, by subtracting the calculated Compton peak and integrating numerically the residual counts. This approach has been demonstrated by Laaziri *et al.* (1999). It is computationally very intensive and is easier on simple systems with low-Z elements, as in the case of amorphous silicon (Laaziri *et al.*, 1999). In general, the empirical Ruland method is more often used except where the highest accuracy is required.

5.3.7.4 Atomic form-factor. The final step in determining $S(Q)$ is to divide the data by $\langle f(Q)\rangle^2$ (Eq. 5.1) where this is defined as

$$\langle f(Q)\rangle^2 = \left[\sum_a c_a (f_0^a(Q) + f_a' + \mathrm{i}f_a'')\right]^2 = \left[\sum_a c_a (f_0^a(Q) + f_a')\right]^2 + \left[\sum_a c_a f_a''\right]^2 \quad (5.14)$$

Here the sum is over atomic species of concentration c_a, $f_0^a(Q)$ is the atomic form-factor for species a, and f_a' and f_a'' are the anomalous scattering corrections to the form-factor. The i indicates an imaginary number. The anomalous scattering corrections can be neglected unless the incident X-ray energy is close (within ~ 100 eV) to an absorption edge of one of the elements.

The factor $f_0^a(Q)$ is strongly Q-dependent. It has been calculated for all the elements using relativistic or non-relativistic Hartree–Foch or Dirac–Slater atomic wavefunctions and the results tabulated (Wilson, 1995; Doyle and Turner, 1968; Fox *et al.*, 1989). They are tabulated in one place for all the elements in the International Tables for Crystallography C (Wilson, 1995). These data have been fit and parameterized. Originally, they were expressed as a sum of Gaussians in the low-Q region up to $Q \sim 20\text{Å}^{-1}$ and in the high-Q region $\ln(f(Q))$ was expressed as a polynomial series (Wilson, 1995). The parameters for each element are in the International Tables of Crystallography C, Tables 6.1.1.4 and 6.1.1.5 (Wilson, 1995). Clearly, having to join the low and high-Q ranges is something of a pain. More recently, Waasmaier and Kirfel (1995) have presented new parameterizations for all the elements where the $f(Q)$ functions have been successfully fit

over the full range of Q to 75 Å^{-1} using a fit to a sum of 5 Gaussians plus a constant:

$$f(s) = \sum_{i=1}^{5} a_i \, \mathrm{e}^{-b_i s^2} + c, \tag{5.15}$$

where $s = Q/4\pi$.

Anomalous scattering factors for the elements have also been calculated (Cromer and Liberman, 1970, also see the discussion in Kissel *et al.*, 1995). When these need to be known accurately, for example in an anomalous scattering experiment, it is generally better to evaluate them experimentally by measuring the absorption edge of the element in question and carrying out a Kramers–Kronig transformation on the experimental data (e.g. see Price and Saboungi, 1998; Petkov *et al.*, 2000b and references therein).

Because of their importance over a wide spectrum of the sciences and the fact that they are difficult to determine accurately, calculations of atomic scattering factors are constantly being reexamined and improved. See for example, Kissel *et al.* (1995) for a thorough reexamination of the situation as of 1995. With improvements in computing it is also possible to start trying to take into account solid-state effects that change the electron distribution, and therefore modify the scattering factor (in general free-atom scattering factors are used) (Ankudinov and Rehr, 2000).

The other important average form-factor average needed is $\langle f^2(Q)\rangle$. This is proportional to the total sample scattering cross-section, including coherent and Laue incoherent scattering, and is defined as

$$\langle f^2(Q)\rangle = \sum_a c_a \left[(f_0^a(Q) + f_a')^2 + (f_a'')^2 \right] \tag{5.16}$$

where the symbols have the same meaning as in Eq. 5.14.

An example of corrected, normalized data with $\langle f^2(Q)\rangle$ superimposed on top is shown in Figure 5.7. When the data are divided by $\langle f^2(Q)\rangle$ and plotted with the Q weighting as $Q(S(Q) - 1)$ significant diffuse scattering is evident at high-Q that is not apparent in the corrected but undivided data, as shown in Figure 5.8.

5.3.7.5 Putting it all together. Putting together the general expression for the sample single scattering cross-section, Eq. 5.8, and the specific X-ray corrections, we get

$$\left(\frac{\mathrm{d}\sigma^{\mathrm{s}}}{\mathrm{d}\Omega}\right) = \left[\left(\frac{N'}{M'}\right)^{\mathrm{sc}} - \left(\frac{V'_{\mathrm{c;sca}}}{V'_{\mathrm{c:ca}}}\right)\left(\frac{N'}{M'}\right)^{\mathrm{c}} \right] \left(\frac{1}{P_i V'_{\mathrm{s;sca}} \rho^s D \, \mathrm{d}\Omega \, K \varepsilon_{\mathrm{d}}} \right) - m' - R[n^{\mathrm{inc}} + m^{\mathrm{inel}}] \tag{5.17}$$

where the terms not defined above are defined in Appendix 5.1. The primes on the N and M denote that the data are deadtime corrected. Here, m' is the multiple scattering calculated assuming only elastic scattering and m^{inel} is the additional multiple scattering where at

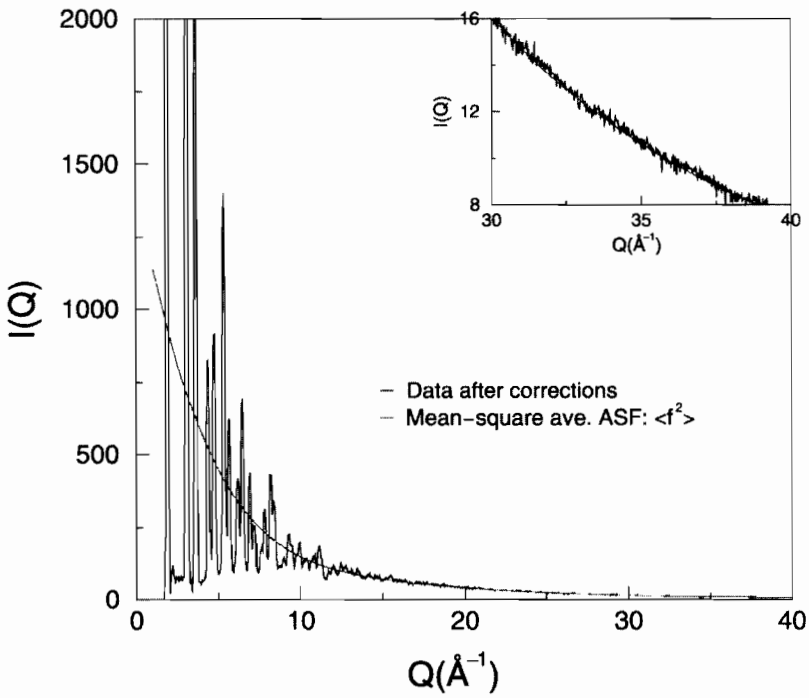

Figure 5.7. Comparison between normalized data after corrections and the calculated mean-square average atomic scattering factor, $\langle f^2(Q)\rangle$ (PDFgetX manual).

least one of the scattering events was an inelastic (Compton) event. Since in the high-Q region where the multiple scattering becomes important the Ruland window function $R(Q)$ is almost zero, m^{inel} is often neglected. m^{inel} can be significant, and should be calculated, when the Compton is not experimentally discriminated away.

In Eq. 5.17 everything is known well except the product $\rho^s D\, d\Omega\, K\varepsilon_d$. In general none of these factors depends on Q (only $d\Omega$, the detector solid angle, may change with Q if the detector slits or the detector–sample distance vary during the experiment) and so the product is simply an unknown constant, β. This scale factor can be estimated by observing that in the high-Q region the scattering from the sample is mostly incoherent and approximately equal to $\langle f^2(Q)\rangle$. Thus, substituting $\langle f^2(Q)\rangle$ for $(d\sigma^s/d\Omega)$ in Eq. 5.17 and rearranging we get

$$\beta = \frac{\lim\limits_{Q\to Q_{\max}} \left[\left(\frac{N'}{M'}\right)^{sc} - \left(\frac{V'_{c;sca}}{V'_{c;ca}}\right)\left(\frac{N'}{M'}\right)^{c} \right]}{P_i V'_{s;sca}(\langle f^2(Q)\rangle + m' + R(n^{inc} + m^{inc}))} \tag{5.18}$$

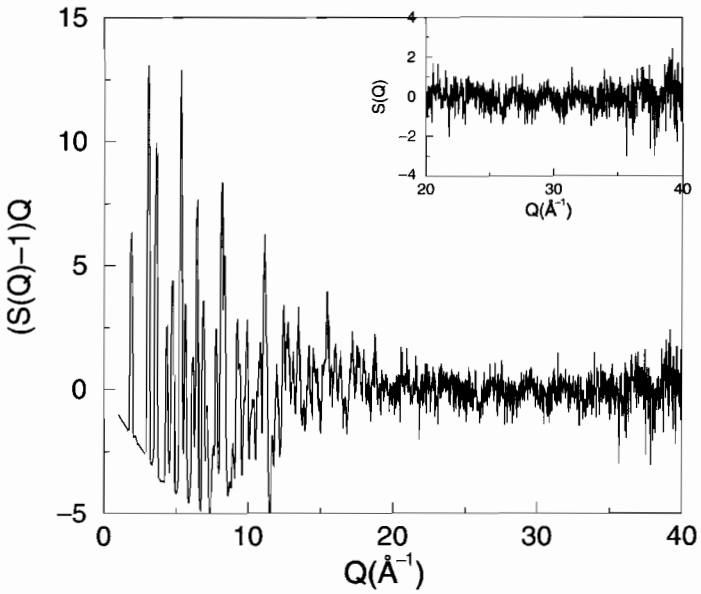

Fig. 5.8. Same data as shown in Figure 5.9 but the data are now plotted in the form of $Q(S(Q) - 1)$ after being divided by $\langle f(Q)\rangle^2$ to obtain $S(Q)$. Significant diffuse scattering is evident at high-Q that is not immediately apparent in Figure 5.7 (PDFgetX manual).

Note that if the Compton scattering has been completely discriminated at high-Q then R is zero here and the theoretically calculated Compton scattering, n^{inc}, and inelastic multiple scattering, m^{inc}, should not be included. More elaborate approaches for data normalization making use of a wider range of data have also been proposed (Thijsse 1984; Kaszkur, 1990; Cumbrera and Sanchez-Bao, 1995).

Finally,

$$\left(\frac{d\sigma^s}{d\Omega}\right) = \left[\left(\frac{N'}{M'}\right)^{sc} - \left(\frac{V'_{c;sca}}{V'_{c;ca}}\right)\left(\frac{N'}{M'}\right)^{c}\right]\left(\frac{1}{P_i V'_{s;sca}\beta}\right) - m' - R(n^{\text{inc}} + m^{\text{inc}}) \quad (5.19)$$

5.3.8 Time-of-flight neutron specific corrections

5.3.8.1 Overview. Neutrons that have appropriate wavelengths for structural studies have thermal energies: ≈ 100 meV. This is comparable to the energy of solid-state excitations such as phonons and magnons. Many typical diffraction geometries will have sufficient energy resolution to choose whether these effects are included or excluded in the measured scattering intensity. Thus, it is possible to obtain two distinct differential scattering cross-sections: the elastic differential cross-section $d\sigma/d\Omega(\Delta E = 0)$ and the total

scattering differential cross-section, $d\sigma/d\Omega$, as we discuss in Chapter 7. A perfectly legitimate PDF can be obtained from either cross-section; the former giving the time-averaged structure (time-dependent atomic correlations are lost) and the latter giving the average of the instantaneous structure (time-dependent correlations are preserved). By varying the range of energy over which the data are integrated, the time-scale of the experiment can be continuously varied. For example, if the range of integration, ΔE, is larger than the energy range of the phonons (≈ 100 meV) then the measurement is quicker than the lattice vibrations and the correlated atom displacements (the phonons) will be seen explicitly in the resulting PDF. This is (approximately) the situation in the most common neutron PDF experiments; the time of flight powder diffraction experiment at a spallation neutron source. In this case, as with the X-rays, the measured intensity is automatically integrated over all energy transfers.

As with X-rays, there are additional scattering processes for neutrons that do not yield structural information. In the case of neutrons it is the magnetic scattering. To obtain a purely structural PDF it is necessary to remove magnetic scattering from the measured intensity. In practice this is often neglected. The reason that this is possible is that the magnetic scattering contributes rather weakly to the PDF. Because of the magnetic form-factor, coherent magnetic scattering is confined to rather low Q-values whereas the nuclear scattering extends to high-Q. All data at all Q-values are used in the PDF, but high-Q scattering is relatively more important because of the Q-weighting in the kernel of the Fourier transform. If the magnetic scattering is not explicitly removed from the data it distorts the resulting structural PDF. However, experience suggests that the distortion to the PDF is small enough (it is a weak long-wavelength oscillation) to be neglected in most cases. On the other hand, as was discussed in Section 3.3.2, it is possible to remove the nuclear scattering component and Fourier transform the magnetic scattering to learn about magnetic correlations in the solid or model it directly in Q-space. As with X-rays, significant small angle scattering should be removed, though similar arguments that apply to the magnetic scattering also apply to the small angle intensity. Finally, we note that the scattering of neutrons by nuclei is isotropic (s-wave) and does not introduce any polarization so there is no polarization correction for nuclear scattering.

Thus, to obtain $S(Q)$ from the corrected intensity from an energy integrated experiment (time-of-flight neutron powder diffraction experiment, or a two-circle reactor experiment with no energy analysis), first, if desired, the magnetic scattering should be removed. Then the elastic incoherent scattering, small angle and $\langle b \rangle^2 - \langle b^2 \rangle$, is removed and the resulting coherent single scattering intensity divided by the mean scattering length squared, $\langle b \rangle^2$ according to Eq. 5.1. $\langle b \rangle^2$ and $\langle b^2 \rangle$ are defined in the same way as the average form-factors (Eqs. 5.14 and 5.16) except the sums run over all isotopes and spin-states of the nuclei as well as over chemical species. In practice, the information about the sum over isotopes and nuclear spin-states are contained in tabulated values of the coherent and incoherent nuclear cross-sections for elements in their natural abundances.

The energy dependence of the neutron scattering cross-sections is assumed to be linear with wavelength. A better approximation is to measure the energy dependence of the ratio of the transmitted beam to the incident beam. This is done by placing a vanadium monitor downstream of the sample in addition to the upstream monitor. This ratio yields the total attenuation cross-section of the sample from which can be extracted the average scattering cross-section (Howe *et al.*, 1989; Soper *et al.*, 1989).

In an energy analyzed experiment (triple-axis measurement at a reactor or a measurement at a chopper spectrometer at a spallation source), the data should be integrated over the desired range of energy transfer to obtain $d\sigma/d\Omega$ (Chapter 3). This should then be treated in the same way as the energy integrated measurements to obtain $S(Q)$.

5.3.8.2 Data-sets. It is normal to collect a number of data-sets as well as the sample data in order to make the necessary data corrections.

1. *Sample data.* Sample is usually in a container, or can, and mounted in some sample environment (cold-stage, furnace, cryostat, magnet, pressure cell, etc.)
2. *Empty sample can.* The sample container is mounted in the same environment as the sample was measured but empty. This data-set is typically collected with less integrated incident flux than the sample data-sets received. However, better statistics are required in the container data if the scattering from the container is significant. The rule of thumb is that the measurement time should be in proportion with the strength of the scattering. Provided there is good reproducibility between sample containers it is not necessary to measure exactly the same container as held the sample.
3. *Empty environment.* An additional background is measured from the diffractometer without anything at the sample position but all the rest of the sample environment in place. This is the instrument background. Collection time depends on how large the background is. The data can be collected for considerably less time (1/4 the collection time for example) if there is a negligibly small background as is generally the case for measurements in ambient temperatures and pressures. However, if an environment is used with significant background such as a furnace or pressure cell so that the background scattering is a significant proportion of the total measured scattering then data should be collected for longer.
4. *Vanadium rod.* Vanadium is an almost perfectly incoherent scatterer of neutrons. It is customary to measure a sample of vanadium to determine the source spectrum. This data-set should be measured with good accuracy as it will be used to normalize all the other data-sets. This need not be measured in a sample environment (indeed it is better to make this measurement with a low background for increased accuracy). However, it should be made close in time to the main measurements to ensure that slowly varying changes in the source spectrum are accounted for as well as possible. Careful

experimenters often measure a series of vanadium data-sets periodically throughout an experiment. These are combined together for increased statistics and to average out long time-scale fluctuations in the spectrum.

5. *Crystalline standard.* A sample with known lattice parameters is also run periodically. This is used to convert accurately the neutron time-of-flight information into momentum-transfer, Q. This must be done individually for each detector for the greatest accuracy and resolution to be obtained when detectors are combined. The standard sample is often silicon or quartz.
6. *Intensity standard.* As discussed in Section 5.4.2, a crystalline standard with similar total scattering cross-section to the sample may also be measured to help achieve an absolute intensity normalization.

Data-sets 5 and 6 are optional. The Q-calibration is often carried out by the instrument scientist of the diffractometer and standard calibrations are available on file. The intensity calibration is only required if the absolute intensity of a PDF is required with high accuracy. Additional vanadium container and vanadium background runs may also be required if, for some reason, the vanadium is supported in a container.

5.3.8.3 Converting time-of-flight to Q. For a given value of 2θ, the value of Q depends on the wavelength which is obtained from the time of flight of the neutron. A polychromatic pulse of neutrons of width ~ 1 μs emerges from the moderator at time $t = 0$. The neutrons fly down the primary flight path, L_1, which is typically of order 10 m or more to the sample. After scattering the neutrons fly along the secondary flight path ($L_2 \sim 1$ m) to the detectors. The time-of-flight, τ, is the time it takes for the neutron to get from the moderator to the detector. If an elastic scattering event is assumed in the sample, this directly gives the velocity of the neutron, v, its momentum and therefore its wavelength using the de Broglie relationship, i.e.

$$v = \frac{L_2 + L_1}{\tau} = \frac{L}{\tau}, \qquad p = m_n v = \hbar k, \qquad \lambda = \frac{2\pi}{k} = \frac{2\pi\hbar\tau}{m(L_1 + L_2)} \tag{5.20}$$

Some useful empirical relationships that hold for neutrons are given below:

$$k(\text{Å}^{-1}) = \frac{1588.2\,L(\text{m})}{\tau(\mu\text{s})}, \qquad \lambda(\text{Å}) = \frac{0.0039562\,\tau(\mu\text{s})}{L(\text{m})} \tag{5.21}$$

$$E(\text{meV}) = \frac{81.807}{\lambda^2(\text{Å})} \tag{5.22}$$

In practice, the $t = 0$ point is not perfectly known and the exact trajectory through the instrument can depend on the sample position for example. To obtain accurate Q-values it is therefore necessary to make corrections to the above expressions using a calibration

standard. A standard crystalline sample is run and a number of diffractometer constants are determined for each detector or detector bank. The same practice is used when powder diffractometers are used for Rietveld refinement studies. However, we note here that the diffractometer constants used in Rietveld refinements are not, in general, suitable for PDF measurements. The reason is that pulsed neutron peaks are highly asymmetric. Rietveld refinements determine the peak position according to some arbitrary consideration, for example, the peak maximum. This is fine if the same Rietveld code is used to analyze the calibration sample and the data themselves since the Q-assignment is done in a self-consistent way. However, in a PDF analysis the data are Fourier transformed and the continuous distribution of intensity as a function of Q is required; the absolute value of Q of each data point is therefore needed. Ideally, the data should be deconvoluted from the instrument resolution function. In practice empirical diffractometer constants are determined with different Q-dependences to account for these effects.

5.3.8.4 Detector deadtime corrections. Corrections have to be made to the simple detector deadtime equations (Eq. 5.9) if the deadtime is greater than the time-of-flight channel width (Soper *et al.*, 1989). Then the deadtime correction in a particular time-channel depends on the count-rate in nearby earlier time-channels. In this case

$$R = \frac{\Delta R_m}{(\Delta - \tau_d \sum_j \Delta_j R_j)} \tag{5.23}$$

where the sum goes over all the time-channels which affect the channel in question. Other complications can arise if detectors are multiplexed so that more than one detector feeds through some part of the data-acquisition electronics. In this case an additional deadtime can be introduced because of a high count-rate in a different detector and the sum in Eq. 5.23 should be a double sum over all the time-channels and detectors which affect the time-channel in the detector in question.

Detector deadtime corrections are generally sorted out by the staff at the neutron facility and are not generally the concern of the user other than to ensure that they are properly accounted for.

5.3.8.5 Inelasticity (Placzek) corrections. Unlike with X-rays, the energy of the thermal neutron is comparable to the energies of low energy excitations (phonons and magnons) in the solid. Thus, when the neutrons are scattered inelastically their energy changes significantly. This is made extensive use of in the field of inelastic neutron scattering. Lattice dynamics and inelastic scattering in the context of total scattering studies is discussed in detail in Chapter 7. Here we discuss simply corrections that have to be applied to the data to account for inelastically scattered neutrons that become incorrectly binned in Q. This occurs because of the geometry of the experiment. It amounts to making

the integration of the double differential cross-section over energy not along a path of constant-Q as assumed in the definition. It occurs for reactor based angle dispersive measurements as well as tof neutron measurements though the corrections are different. It is described in detail in Section 7.5.2. To carry out a precise correction the sample dynamic structure factor, $S(Q, \omega)$, must be known as well as the loci through (Q, ω) space along which inelastic neutrons are integrated due to the specific geometry of the measurement. For example, loci of integration for various detectors on the, now retired, LAD diffractometer at ISIS are shown in Figure 5.9. The deviations from ideal (constant-Q) loci are clearly largest at small diffraction angle and small-Q. A complete correction is impossible because in general we are trying to measure $S(Q)$, so if we already knew $S(Q, \omega)$ as required to make the correction, we would not have to measure $S(Q)$! An approximate approach is to expand $S(Q, \omega)$ in moments. The first few moments do not involve details of the potential and phonon band-structure and so the approximation is

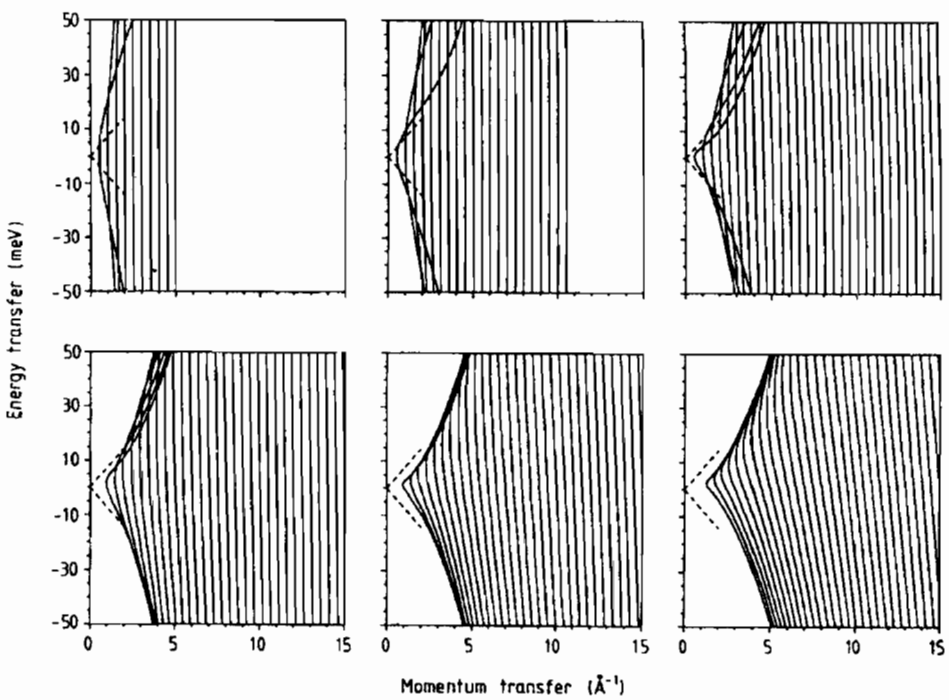

Figure 5.9. Loci of integration from time of flight neutron powder diffractometer LAD. The vertical axis shows energy transfer, $\hbar\omega$, and the horizontal axis shows Q. Neutrons that are scattered inelastically (i.e. at finite ω) will be assigned an incorrect Q-value because of the geometry of the tof experiment. The Q-value that will be assigned to an inelastically scattered neutron can be deduced by following the line from the (Q, ω) value of the scattering event to the $\omega = 0$ line. The six panels correspond to the six detector banks on LAD at (top left to bottom right) $2\theta = 5°$ 10°, 20°, 35°, 58° and 90° (Howe *et al.*, 1989).

made that the correction involving only these first few terms is sufficient (Section 7.5.2). This approach was first laid out by Placzek (1952) and developed by Yarnell *et al.* (1973) and Powles (1973) for reactor experiments and further refined and extended to tof neutron experiments by Howe *et al.* (1989). By way of example the corrections for a model system of free atoms is shown in Figure 5.10 (Howe *et al.*, 1989) with mass of 84.2 g/mol (the average of Cs and Cl) and assuming the LAD detectors (Howe *et al.*, 1989).

The result of this kind of analysis is an additive correction, $P^{\text{inc}}(Q, 2\theta)$, to the measured intensities. The corrections are small since the scale in these plots is 10^{-3} b sr^{-1} that compares with typical scattering cross-sections of the order 1 b sr^{-1}. The corrections become more significant as the mass of the scatterer gets less. From Figure 5.10 we see that the corrections become significant at low-Q. In this model system $S(Q, \omega)$ is known and the exact correction can be calculated and is shown as a dotted line. It is apparent from this test

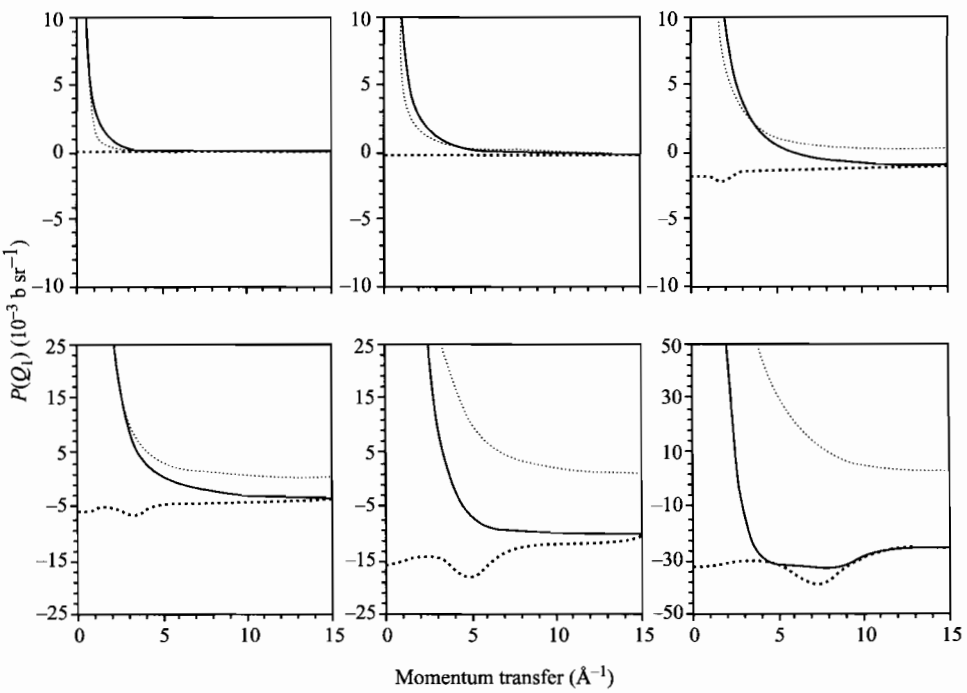

Figure 5.10. Inelasticity corrections to the scattered intensity as a function of Q for the six detector banks of LAD shown in Figure 5.9 (from top left to bottom right $2\theta = 5°$ 10°, 20°, 35°, 58°). The dotted curves are the exact result from model calculations on CsCl. The dashed curves are given by the approximate Placzek correction taken to first order. The solid curves are the approximate Placzek correction taken to second order. Notice that the corrections are most significant at low-Q and that the approximate corrections to second order work best at low detector angles (Howe *et al.*, 1989).

that the approximate Placzek corrections to second order work well for the low-angle detectors but not very well at higher scattering angle. Therefore, for studying liquids of low atomic mass (water and organic liquids for example) low angle detectors should be utilized. This insight led to the building of the SANDALS diffractometer at ISIS. Bound atoms do not recoil so much and there is much less inelastic scattering as a proportion of the total scattering so this becomes less of an issue (though does not go away) in solids.

5.3.8.6 Putting it all together. As in the case of X-ray scattering we can put together the specific corrections discussed here with the general corrections Eq. 5.8. In this case the flux, detector efficiencies and detector profiles are Q-dependent; however, by measuring an incoherently scattering vanadium sample we have a dynamic measurement of all these quantities. Thus we have

$$\left(\frac{\mathrm{d}\sigma^{\mathrm{s}}}{\mathrm{d}\Omega}\right)=\left[\left(\frac{N'}{M'}\right)^{\mathrm{sc}}-\left(\frac{V'_{\mathrm{c;sca}}}{V'_{\mathrm{c;ca}}}\right)\left(\frac{N'}{M'}\right)^{\mathrm{c}}\right]\left(\frac{1}{V'_{\mathrm{s;sca}}\rho^{\mathrm{s}}D\,\mathrm{d}\Omega\,K\varepsilon_{\mathrm{d}}}\right)-m'-P^{\mathrm{inel}} \tag{5.24}$$

and

$$\left(\frac{\mathrm{d}\sigma^{\mathrm{v}}}{\mathrm{d}\Omega}\right)=\left[\left(\frac{N'}{M'}\right)^{\mathrm{vc}}-\left(\frac{V'_{\mathrm{c(v);vca}}}{V'_{\mathrm{c(v);ca}}}\right)\left(\frac{N'}{M'}\right)^{\mathrm{c(v)}}\right]\left(\frac{1}{V'_{\mathrm{v;vca}}\rho^{\mathrm{v}}D\,\mathrm{d}\Omega\,K\varepsilon_{\mathrm{d}}}\right)-m'_{\mathrm{v}}-P^{\mathrm{inel}}_{\mathrm{v}} \tag{5.25}$$

from the sample and vanadium experiments, respectively. Note that $c(v)$ refers to scattering from the vanadium container, if one was used. The primes on the N and M denote that the data are deadtime corrected. In general there is no sample can (or experimental apparatus) to subtract from the vanadium data because a self supporting solid V rod is used; however, these terms are retained in Eq. 5.25 for completeness. Here $P^{\mathrm{inel}}(Q)$ is the Placzek correction for inelastically scattered neutrons as discussed in Section 5.3.8.5. Since vanadium is an incoherent scatterer its differential cross-section is just equal to $(\mathrm{d}\sigma^{\mathrm{v}}/\mathrm{d}\Omega)\mathrm{d}\Omega=\langle b_{\mathrm{v}}^2\rangle$. Therefore, we get

$$DK\varepsilon_{\mathrm{d}}=\left[\left(\frac{N'}{M'}\right)^{\mathrm{vc}}-\left(\frac{V'_{\mathrm{c;vca}}}{V'_{\mathrm{c;ca}}}\right)\left(\frac{N'}{M'}\right)^{\mathrm{c(v)}}\right]\left(\frac{1}{V'_{\mathrm{v;vca}}\rho^{\mathrm{v}}(\langle b_{\mathrm{v}}^2\rangle+m'_{\mathrm{v}}+P^{\mathrm{inel}}_{\mathrm{v}})}\right) \tag{5.26}$$

and the desired

$$\left(\frac{\mathrm{d}\sigma^{\mathrm{s}}}{\mathrm{d}\Omega}\right)=\frac{\left[\left(\frac{N'}{M'}\right)^{\mathrm{sc}}-\left(\frac{V'_{\mathrm{c;sca}}}{V'_{\mathrm{c;ca}}}\right)\left(\frac{N'}{M'}\right)^{\mathrm{c}}\right]}{\left[\left(\frac{N'}{M'}\right)^{\mathrm{vc}}-\left(\frac{V'_{\mathrm{c(v);vca}}}{V'_{\mathrm{c(v);ca}}}\right)\left(\frac{N'}{M'}\right)^{\mathrm{c(v)}}\right]}\left(\frac{(\langle b_{\mathrm{v}}^2\rangle+m'_{\mathrm{v}}+P^{\mathrm{inel}}_{\mathrm{v}})V'_{\mathrm{v;vca}}\rho^{\mathrm{v}}}{V'_{\mathrm{s;sca}}\rho^{\mathrm{s}}\mathrm{d}\Omega}\right)-m'-P^{\mathrm{inel}} \tag{5.27}$$

As in the case of X-rays, $\rho^s d\Omega$ is independent of Q and can be treated as a constant scaling factor that can be varied to give the right asymptotic behavior for $(d\sigma^s/d\Omega)$ and $S(Q)$. However, it should be noted that the common practice of using ρ^s as a parameter in the data analysis for obtaining the correct normalization affects not only the scale of the data but the V' integrals too. It is not a purely multiplicative scale factor and it should retain a value close to the real powder density. This is discussed further in Section 5.4.2.

5.3.9 Combining data-sets

The data to be processed often is not contained in a single continuous data-set. It may have originated from more than one detector, or from multiple repeated data-runs to improve statistics. If the detector position and solid angle is the same between two measurements, by far the easiest approach is to combine data at the beginning of the analysis by summing together the deadtime corrected data at each Q point. The monitor counts from each run should also be summed. This underscores the importance of having a stable monitoring system.

An approach similar to this has been utilized in time-of-flight neutron experiments where the detector angles were not identical, but close. In this case the data from a series of detectors close to the nominal average angle are summed together and the small differences in angle between the detectors is ignored in the subsequent corrections which are computed assuming all the intensity originated from a detector at the average position. Care must be taken to bin together data on the same λ- or Q-grid. Because the tof to Q conversion depends on detector angle the same Q point will occur at a different tof in each detector. Correcting for this sometimes takes the grand title of 'time focusing'. It can be done electronically before the data are stored, or using software after data collection.

In general, when the detector solid angle or position is different the data corrections and normalization are different. In this case the most precise approach is to propagate the data all the way through to a properly corrected and normalized $S(Q)$ and to combine the $S(Q)$ values to improve the statistics of the compound $S(Q)$. The resolutions of the different detectors also depends on angle and is not included in the corrections described above so the different $S(Q)$ values will have different resolutions and will cover different regions of Q-space. In this case, it is prudent to make a patchwork so that as wide a range of Q-space is covered but the lower resolution detectors are not contaminating data from higher resolution detectors. These arguments particularly apply to tof neutron experiments where, also, data from the most intense part of the source spectrum should be used (a rule of thumb is to take the wavelengths $0.2 < \lambda < 2$ Å). At the same time it is of great importance to obtain sufficient statistics, especially at high-Q, and it is common practice to combine data from as many detectors as possible in this region, keeping in mind the comments above about resolution. When combining the data from normalized $S(Q)$ values it is important to weight them according to their statistical significance. This is easy if the random errors have been propagated through with the data.

Problems arise if the corrected $S(Q)$ functions do not overlap due to imperfect corrections. Small deviations are often ignored and large deviations are handled by not including data-banks that are too deviant. In the former case blending should be done carefully or it introduces noise into the blended $S(Q)$. These issues have not really been adequately addressed up to now (though see Howe *et al.*, 1989). This may change in the future as the next generation of powder diffractometers are expected to yield data in 'frames' that are highly fragmented. Correcting and overlapping this kind of data to obtain an undistorted $S(Q)$ will require careful attention to this point. One of the challenges in this regard is to match both the baseline and the integrated intensity of features using additive and multiplicative corrections.

5.3.10 Terminating data

The Fourier transform to get $G(r)$ from $S(Q)$, Eq. 3.1, involves an integral over Q from zero to infinity. However, the data are only measured over finite range, $Q_{\min} < Q < Q_{\max}$. Errors in $G(r)$ due to the finite range of data, so called termination errors, have been discussed in Section 3.5.2.

The low-Q cutoff rarely presents a problem. Data can usually be measured down to rather low values in Q so little information is lost, other than the small angle scattering that, according to the definition of $S(Q)$, should not be included anyway. When low-Q Bragg-peaks or coherent diffuse intensity is lost (or mistakenly included as in the case of magnetic scattering) it gives rise to weak long-wavelength oscillations in $G(r)$ (for example, see Peterson *et al.*, 2002) which add to the residuals in modeling but rarely present a significant problem. As always, the only remedy for this problem is somehow to extend the measurement range to include the missing low-Q information. For example, in tof neutron experiments missing Bragg peaks can often be found in the data from very low-angle detectors that otherwise would not be of much interest. When all the low-Q Bragg peaks are recovered, or methods to extend the measurement are exhausted, it is common practice to take the data at $Q_{\min}$ and extrapolate it to zero. This is better than setting the data to zero because, in general, $S(Q)$ asymptotes to the value of $(\langle f^2(0)\rangle - \langle f(0)\rangle^2)/\langle f(0)\rangle^2$ at $Q = 0$. Thijsse (1984) suggests fitting the first 40 or so data points of $Q[S(Q) - 1]$ with a form $c_1Q + c_2Q^3$ and extrapolating to zero. This is equivalent to a quadratic dependence of $S(Q)$ at low-Q. Note that this extrapolation scheme (or any other for that matter) relies on the fact that there is *no measured coherent scattering at* $Q_{\min}$ and should not be attempted if $Q_{\min}$ lies on top of a low-Q Bragg peak!

As discussed in Section 3.5.2, the high-Q termination results in short-wavelength ripples in $G(r)$. There are a number of ways of artificially reducing these spurious ripples as has been discussed at length. These typically use a method of damping the $S(Q)$ with increasing Q so that the Fourier ringing dies out more quickly in real-space (Warren, 1990; Lorch, 1969; Waser and Schomaker, 1953). This always has the effect of reducing the

resolution of the resulting $G(r)$ as discussed by Leadbetter and Wright (1972). An alternative is to use an inverse method for carrying out the Fourier transform as we discuss below, though these approaches also have their drawbacks. Fourier transform ripples are not a problem if $S(Q)$ is measured over a sufficiently wide range that the real signal in the data has died out due to Debye–Waller effects and there is really no substitute for taking this approach where possible. The Fourier ripples can also be included when modeling the data.

The term 'termination ripples' is often used generally to describe spurious ripples in the Fourier transform. These often result from systematic errors in the processing giving rise to sharp unphysical features at low-r in $G(r)$ that become convoluted with the termination function, Eq. 3.47. This should be distinguished from the narrower but more precise definition above. Clearly the best way to remove these is to improve the processing to remove the systematic errors. Iterative filtering methods have been proposed to deal with these and they are successful at removing ripples below the first peak (Kaplow *et al.*, 1965; Narayan and Ramaseshan, 1979); however, it is not clear how successful they are at removing features in the region of real physical interest. Along the same lines approaches where data measured over finite ranges and including systematic errors are 'sampled' so that $G(r)$ is only plotted at the nodes of the largest ripples (Lovell *et al.*, 1979). Again, there is no substitute for measuring data over a wide range with good statistics and making good data corrections.

The choice of where to terminate data is made such that $Q_{\max}$ is chosen where the signal-noise ratio becomes unfavorable. Accepting data to higher Q values introduces unnecessary statistical noise into the data (which becomes convoluted by the termination function and has the appearance of termination ripples) and terminating lower lowers the resolution of the measurement and results in unnecessarily large termination ripples (i.e. the data themselves are convoluted with the termination function). Note that the termination ripples from the data can be modeled accurately but the ripples from the correlated statistical errors cannot.

5.3.11 Fourier transforming the data

The most common method of Fourier transforming the data is a straightforward direct numerical transform. The fast Fourier transform (FFT) often used in spectroscopy is rarely used as it results in an r-grid that is too sparse. This is particularly true when considering data from crystalline materials, or other cases such as network glasses, which contain sharp features in $G(r)$. The grid of points used in the FFT is limited by the density of independent points in $G(r)$ that depends on the measured Q range. The point spacing is $\Delta r = \pi/Q_{\max}$. This results in too few points defining the sharp features and resulting inaccuracies in extracting peak integrated intensities and model fitting. Despite the fact that it introduces no new information and is, from that point of view, redundant, it is common practice to

evaluate $G(r)$ on a much finer grid resulting in smooth and functionally well-defined peaks in $G(r)$. As we discussed in Section 4.3.5 when measuring the data the Q-space grid spacing should be less than the measurement resolution. This should also be taken into account when setting the grid (sometimes called quadrature) for the Fourier transform. It results in the criterion $\Delta Q \leq \pi/r_{max}$ (Ino, 1957; Leadbetter and Wright, 1972) where r_{max} is a measure of the range in r-space where structural features are evident in $G(r)$. For reasonably high resolution measurements and crystalline materials this can be $r_{max} > 300$ Å requiring a grid spacing of $\Delta Q < 0.01$ Å^{-1}.

An interesting alternative approach to the direct Fourier transform is to use an 'inverse' method where a $G(r)$ is constructed directly in real-space that is consistent with the measured $S(Q)$ but not determined by a direct transform. This can be accomplished using Monte Carlo methods (Soper, 1990; Pusztai and McGreevy, 1997) or using a Maximum Entropy approach (Soper, 1990; Terwilliger, 1994; Petkov and Danev, 1998). The main drawback to these approaches is philosophical that there is no unique relationship between the measured $S(Q)$ and the resulting $G(r)$.

From a practical point of view the Monte Carlo methods work best if the real-space $G(r)$ is calculated to a point where it becomes flat which can be impractically far out in r in the case of crystalline materials. If this criterion is not satisfied the measured $S(Q)$ has to be convoluted with the Fourier transform of the real-space box being used to determine $G(r)$, thus artificially reducing the resolution of the measurement. This is a somewhat small problem since in practice $G(r)$ is often only modeled over a rather narrow r-range anyway. On the plus side, the resulting PDFs are very clean and free of termination errors.

The maximum entropy method has most utility in cases where the data-range is limited, data are unacceptably noisy, or other troublesome systematic errors are present (Petkov and Danev, 1998). Where possible, in such cases where the data are 'bad' the best solution is to repeat the measurement taking care of the problems. There is really no substitute for good data.

To summarize, the choice of using a direct or inverse method for determining $G(r)$ from $S(Q)$ remains largely a matter of personal choice. Directly transformed data contain spurious ripples from termination effects that one must guard against misinterpreting. As we discuss in the next chapter, this is less likely when data are modeled over a wider range using physically reasonable models. In addition, it is the actual transformed data that are presented, including all the deficiencies of the measurement such as statistical and systematic errors. This allows a critical assessment to be made by the reader about the quality of the data that gave rise to this $G(r)$. With an inverse transform the effects of experimental uncertainties, such as termination ripples, instrument resolution function, and inadequacies in the corrections, are removed. On the other hand the resulting $G(r)$ is not unique and depends on the assumptions and method used to make the inverse transform. In some respect the uncertainties inherent in making a non-ideal measurement (with finite range, statistics and resolution) that appear as distortions to $G(r)$ in the direct transform,

have not been removed in the inverse transform but are manifest in the uncertainty about the uniqueness of the resulting $G(r)$. A drawback to the inverse approach is that the resulting $G(r)$ does not reflect the quality and uncertainties of the measurement and it is therefore harder to gauge the quality of a fit with respect to the extent of the errors in the data. In some respect, making an inverse transform amounts to fitting the data in Q-space. Modeling total scattering data directly in real-space using the RMC method has been applied with considerable success as we discuss in the next chapter, in which case there is no need to Fourier transform the data at all.

5.3.12 Instrument resolution function

The resolution of a measurement depends on a number of factors such as detector pixel solid angle, incident beam divergence, sample size, diffractometer misalignment, and so on (e.g. see Klug and Alexander, 1968). This has the effect of broadening features in $S(Q)$ as was discussed in Section 3.5.4. The effects on $G(r)$ are rather mild and the instrument resolution function is often not deconvoluted as part of the data corrections, rather the effects are incorporated into calculated models of the PDF. This is discussed in Chapter 6. Attempts have been made to deconvolute data directly (e.g. see Howells, 1984, 1985; Ida and Toraya, 2002). Also, when fitting Q-space, or carrying out an inverse Fourier transform, the calculated $S(Q)$ can be convoluted with the instrument resolution function before being compared with the data (Howe *et al.*, 1989; Dimitrov *et al.*, 1999).

5.4. REAL-WORLD DATA ANALYSIS

5.4.1 Data analysis programs

A large number of programs exist for carrying out data analysis to obtain PDFs from X-ray sources, constant-wavelength neutron sources and time-of-flight neutron sources. An excellent resource for finding out about developments in data analysis is the Journal of Applied Crystallography, a journal of the International Union of Crystallography (IUCr, http://www.iucr.org), where many new programs are reported. A number of programs are also listed and some available for download, from the PDF home-page on the world-wide-web: http://www.totalscattering.org.

Because the number of spallation neutron facilities where time-of-flight neutron experiments are carried out is limited, the number of time-of-flight neutron codes is also limited. The most popular are the ATLAS suite of programs which are maintained at the ISIS facility, and a GUI based program, PDFgetN (Peterson *et al.*, 2000), that grew out of the IPNS GLASS package but has been considerably extended. It can now analyze data from virtually all of the major time-of-flight powder diffractometers in the world. PDFgetN is well documented and easy to use. An example of an analysis carried out using this package is shown in Appendix 5.4. It will run on linux, most unix, and windows platforms

and is available free from the authors or by visiting http://www.totalscattering.org. Two valuable features of this program for analyzing data from crystalline powders is the fact that statistical errors are propagated, allowing estimates to be made of refinement parameters (see the discussion in Section 5.4.2 below), and the fact that all of the data analysis parameters used in the data processing are stored as a header in the final PDF file. This is particularly important for a technique like the PDF where the 'data' that are used for modeling and extracting structural information are somewhat removed from the raw measured data by processing. Maintaining a quantitative data analysis history in the header of the PDF file facilitates *post-facto* checking and comparison of a particular PDF. Data analysis codes are perpetually updated. On the horizon is a reworking of the ATLAS routines within the ISAW project which is a JAVA based data analysis and visualization 'workbench'. These developments can be followed on the total scattering web-page.

There are almost as many X-ray analysis codes as there are groups doing X-ray PDF analysis. An example of a recent code that incorporates atomic scattering factors and Compton factors, is PDFgetX. As with the neutron codes it propagates errors and has the data analysis history feature. This program was written, and is supported, by the Billinge group and is available from the total scattering web-page as are a number of other X-ray data analysis programs including IFO which uses maximum entropy based algorithms (Petkov and Danev, 1998). Two codes for Monte-Carlo Fourier inversion are MCGOFR (Soper, 1990) and MCGR (Pusztai and McGreevy, 1997; Tucker *et al.*, 2001). Another useful and versatile X-ray data preprocessing package is Brian Toby's 'Swiss army knife' for diffraction, CMPR (e.g. see the NIST crystallography web-page http://www.ncnr.nist.gov/programs/crystallography/. This web-page also contains a number of useful applications for calculating sample absorption as a function of composition and X-ray energy and also neutron absorption and activation).

5.4.2 Optimizing data for direct Fourier transform

The sample $S(Q)$ is obtained after making all the corrections outlined in Section 5.3. This function has certain known properties, such as the high-Q and low-Q asymptotes, that allow the data analyst to check the efficacy of the sample corrections. When these functional properties are not obeyed the corrections procedure can be adjusted and $S(Q)$ recalculated. The most important asymptote that must be obeyed is $\lim_{Q\to\infty} S(Q) = 1$. This will automatically be obeyed in the case of X-ray data analysis where this criterion is used to find the normalization constant for the data (Eq. 5.17). In the case of tof neutron analysis, in principle, it is possible to get an absolute $S(Q)$ directly from the corrections.

In this case, the usual procedure taken when $S(Q)$ does not asymptote properly is to vary a parameter such as sample density until the proper asymptote is achieved. The problem

with this is that some corrections are multiplicative and some additive and in any given situation it is not clear which corrections went wrong resulting in the improper asymptote. Varying the sample density is a somewhat arbitrary response which produces a mostly, but not completely, multiplicative correction. This is not a problem if the data are to be modeled since a scale factor can be used in any model; however, it can present a problem when a model independent analysis is to be applied to the data (Chapter 6).

Another more recent data analysis problem is simply that of handling very large numbers of data points that are being generated at high throughput instruments such as GEM at ISIS and upcoming instruments at the SNS. Arduous manual iterative corrections are clearly not feasible in this situation. An approach has been proposed for automating this '$S(Q)$ optimization' process (Peterson *et al.*, 2003). Constant multiplicative and additive constants are used to modify $S(Q)$ according to

$$S'(Q) = \alpha S(Q) + \beta \tag{5.28}$$

The factors α and β are varied in such a way as to optimize quantitative PDF quality criteria that give a measure of the quality of the PDF. In particular, the most useful quality criterion is one that empirically measures the size of ripples coming from systematic errors in the data in the unphysical low-r region of $G(r)$. This empirical quality parameter is defined as,

$$G_{\text{low}} = \frac{\int_0^{r_{\text{low}}} r^2[G(r) + 4\pi r\rho_{\text{fit}}]^2 \mathrm{d}r}{\int_0^{r_{\text{low}}} [4\pi r\rho_{\text{fit}}]^2 \mathrm{d}r}. \tag{5.29}$$

First a straight line is fit through $G(r)$ from $G(0) = 0$ to a point r_{low} below the first peak in the PDF. It was found that best results were obtained when an r^2 weighting was used in the fit so it was not biased by large ripples at very low-r (Peterson *et al.*, 2002). This line has a slope of $-4\pi\rho_{\text{fit}}$ which serves to define ρ_{fit}. G_{low} is then evaluated according to Eq. 5.29. A least-squares regression is then applied where α and/or β are systematically varied to minimize G_{low}. In this way the fine-tuning of the data normalization can be automated. The regression can also be constrained so that α and β are varied in such a way that $\rho_{\text{fit}} = \rho_0$, the real sample number density. In this way a $G(r)$ is produced with a scale factor of approximately one, though because of the arbitrariness of the corrections the real scale factor should be determined from modeling.

If the probable source of the problem is known some more meaningful steps can be taken to correct the data; for example, multiple scattering that takes place first in the sample, then elsewhere in the apparatus. This kind of multiple scattering is not accounted for in the corrections. This becomes a problem for samples that have a significant amount of incoherent scattering. In this case the ratio of multiple scattering (that depends on the total

scattering cross-section) to signal (that depends on the coherent cross-section) is higher and it becomes more critical to correct for this source of multiple scattering to get a properly normalized $S(Q)$. This effect has been noticed, for example, in scattering from compounds of elements with a mixture of positive and negative neutron scattering lengths such as the manganites (Louca, 2003). In this case a nickel standard can be measured that has the same total scattering cross-section (and therefore approximately the same sample/apparatus multiple scattering) as the sample under study. The Nickel data are analyzed using the imperfect corrections. The nickel data are modeled and additive and multiplicative corrections made to the data until a scale factor of one and the correct high-Q asymptote are obtained. The additive correction is presumed to come from the uncorrected multiple scattering which is proportional to the total sample cross-section. The additive correction suitable for the real experiment is then obtained by rescaling the additive constant found for the Ni by the ratio of the sample and nickel total cross-sections,

$$\beta_s = \beta_{Ni}\left(\frac{\rho^s V_s' \langle b_s^2 \rangle}{\rho^{Ni} V_{Ni}' \langle b_{Ni}^2 \rangle}\right). \tag{5.30}$$

Here it is the actual sample (powder) densities that are used. The effective sample volumes (Appendix 5.1) can be replaced by the real sample volumes without loss of accuracy provided the absorption cross-sections of the sample and data are similar.

The approach of using a standard and modeling it to obtain a scale factor, or indeed if the structure of the material is known with some certainty modeling the sample PDF itself, is a useful way of obtaining properly normalized data. Since two independent variables need to be known, α and β, two pieces of information are needed to constrain them. The high-Q asymptote of $S(Q)$ is one piece of information. A convenient but imprecise additional piece of information is ρ_{fit}, defined above. Using the scale factor from modeled data as described here is another, more arduous but more reliable method, for fixing the second parameter. This is true regardless of whether the scale error results from multiple scattering or not. As we said before, if no scale-dependent model independent analyses (such as integrating PDF peak intensities) are to be carried out, accurate data normalization is less important provided sample scale factor is present as a parameter in any modeling (Peterson *et al.*, 2003).

APPENDIX 5.1. DATA ANALYSIS EQUATIONS DERIVED

In this appendix, the general equations are derived for the scattering from a sample of finite dimension. These are used in Section 5.3 to determine equations allowing $S(Q)$ to be obtained from a real powder diffraction experiment.

A5.1.1 Definitions and things

The definition of the double differential scattering cross-section, $d^2\sigma/(d\Omega dE)$, of a scattering sample is as follows (e.g. see Lovesey, 1984). Let $I_s(\theta, \phi, E_i, E_s, t)$ be the number of scattered particles per second with energy between E_s and $E_s + dE_s$ entering a detector that subtends a solid angle of $d\Omega$ and is positioned at an angle of (θ, ϕ) to the origin where the sample is located. This is illustrated in Figure A5.1.1. Here, and in the following, the parameters in parentheses, the 'argument' of the quantity, indicate what the quantity depends on. For example, in the present case $I_s(\theta, \phi, E_i, E_s, t)$ depends on the angular position of the detector, (θ, ϕ), on the energy of the incoming and scattered beams, E_i and E_s, respectively, and in general on time, t. Then

$$I_s(\theta, \phi, E_i, E_s, t) = J(\vec{r}, E_i, t)\left[\frac{d^2\sigma(\theta, \phi, E_i, E_s)}{d\Omega\, dE_s}\right] d\Omega\, dE_s \qquad \text{(A5.1.1)}$$

where J is the number of scattering particles (neutrons or X-rays) per unit area per second impinging on the sample: the incident flux.

From this definition it is clear that σ has the units of area, and this is the origin of its name: cross-section. The cross-section contains the structural information from the sample. It gives the probability of a particle (X-ray or neutron) of a particular energy (E_i) being scattered in a particular direction (θ, ϕ) with a particular energy transfer $\Delta E = E_s - E_i$. For example, Bragg scattering is elastic ($\Delta E = 0$ and $E_i = E_s$). Pure elastic scattering can be measured if you have a detector with good energy resolution, dE_s, that is set up in such a way as to measure scattered particles with the same energy as the incident particles. This amounts to integrating the double differential cross-section over the band-pass of the detector, $W(E)$, as

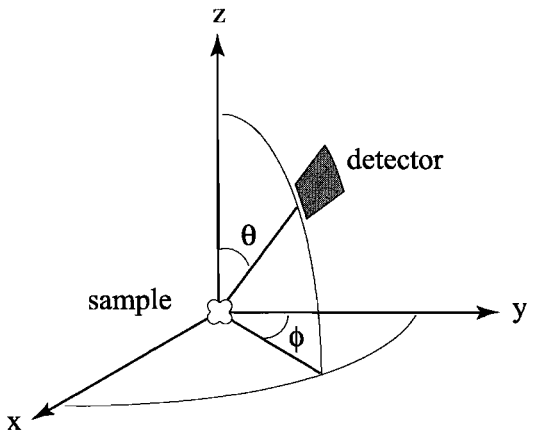

Figure A5.1.1. Schematic illustration of the angles used in the definition of the detector solid angle and the definition of the double differential cross-section.

discussed in Chapter 7, to yield the differential cross-section for our measurement,

$$\frac{d\sigma(\theta, \phi, E_i)}{d\Omega} = \int \frac{d^2\sigma(\theta, \phi, E_i, E_s)}{d\Omega\, dE_s} W(E_s) dE_s$$

In the case described here $W(E_s)$ is a sharply peaked function centered around $E_s = E_i$. The resulting differential cross-section contains the pattern of Bragg-peaks from the sample.

The measured intensities depend on this underlying cross-section, the structural information of interest. They also depend on experimental parameters such as the incident flux, detector energy resolution and the detector solid angle (or the angular width of the slits in front of the detector). This highlights the nice feature of this formalism. A real experimental intensity is described (i.e. the number of counts per second into a real detector) in terms of an underlying scattering probability (i.e. the cross-section which is the thing we are trying to measure), and some experimental factors $(J, d\Omega, E_s)$. The total scattering structure function, $S(Q)$, depends on the differential scattering cross-section according to Eq. 2.9. We will also develop the precise relationship in more detail below. For now, it is sufficient to realize that the objective of the data analysis steps is to recover the coherent single-scattering differential cross-section, $d\sigma_s/d\Omega$, from the measured intensity, I_s.

A5.1.2 Step 1: Single scattering intensity from a small volume element in the sample

In the definition of the double differential cross-section given above it was assumed that the sample is small compared to the dimension from the sample to the detector. We then placed the origin of our coordinate system at the sample position. We now want to consider the sample in finer detail. We will define the origin arbitrarily somewhere inside the sample; for example, it could be at the center of mass. We will then consider the scattering from tiny three-dimensional volume elements, $d\vec{r} = dx\, dy\, dz$, located at positions $\vec{r}$ away from the origin. This is illustrated in Figure A5.1.2. Initially, let us consider that our entire sample is just a single volume element. The scattered intensity entering the detector from this sample element will be

$$dI_s(\theta, \phi, E_i, E_s, t, \vec{r}) = J(\vec{r}, E_i, t)\left(\frac{d^2\sigma(\theta, \phi, E_i, E_s)}{d\Omega\, dE_s}\right) d\Omega\, dE_s \qquad \text{(A5.1.2)}$$

The incident flux is a function of the position of the scattering element, $\vec{r}$, because, in general, the incident beam will not be uniform. However, here we assume that the sample is uniform and the cross-section does not depend on position.

If this sample element is located at some position inside a macroscopic sample (Figure A5.1.2) then we have to consider two effects. First is the possibility that a particle being scattered in this volume element at $\vec{r}$ has already undergone a scattering event (or more than one) in another volume element(s) in the sample. This is called 'multiple scattering' and will be explicitly dealt with in the next section. In the rest of this section we consider

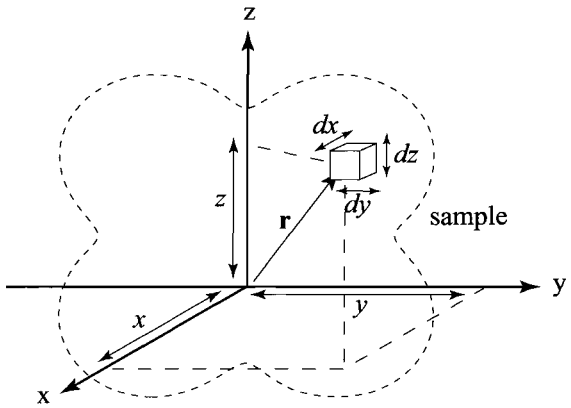

Figure A5.1.2. Schematic of the volume element dx dy dz at position x, y, z.

only the single-scattered intensity, dI_s^1, reaching the detector. The second effect is that the incident beam has first to reach the element and then to emerge from the sample to reach the detector. As the beam traverses the sample, it is attenuated according to $I = I_0\, e^{-\mu(E)l}$ where I and I_0 are the attenuated and unattenuated beam intensities, respectively, $\mu(E)$ is the linear attenuation coefficient (often, not strictly correctly, called the linear absorption coefficient) and l is the path length through the sample. In general the sample is held in a container. There may also be other pieces of experimental apparatus such as heat-shields and furnace elements in the beam. This is illustrated in Figure A5.1.3. We will refer to these different media as apparatus, container and sample. We can trace deterministic paths through the sample, container and apparatus and the absorption of an X-ray following this path is uniquely specified (see Figure A5.1.3).

Consider first the absorption of the incident beam before the sample element is reached. The ray travels through a length l_a^i of apparatus that has an absorption coefficient of $\mu_a(E_i)$, l_c^i of sample container with absorption coefficient $\mu_c(E_i)$ and l_s^i of the sample with absorption coefficient $\mu_s(E_i)$. The same set of parameters are generated for the scattered beam with the superscript i replaced with s and E_i replaced with E_s.The intensity of the ray following this path is therefore attenuated by the factor $\exp\{-(\mu_a(E_i)l_a^i + \mu_c(E_i)l_c^i + \mu_s(E_i)l_s^i + \mu_a(E_s)l_a^s + \mu_c(E_s)l_c^s + \mu_s(E_s)l_s^s)\}$. This is a product of attenuation factors, $A_sA_cA_a$, one for each medium; i.e.

$$A_x = \exp\{-(\mu_x(E_i)l_x^i + \mu_x(E_s)l_x^s)\} \qquad \text{(A5.1.3)}$$

where x takes the values a, c or s. If there are more items of apparatus then the set of values, $\{x\}$ can be extended as required and, in general, the intensity reaching the detector is attenuated by the product $\prod_x A_x(\vec{r}, \theta, \phi, E_i, E_s)$. The attenuation factors can be evaluated numerically (and sometimes analytically) if the $\mu_x(E)$ coefficients are known for the

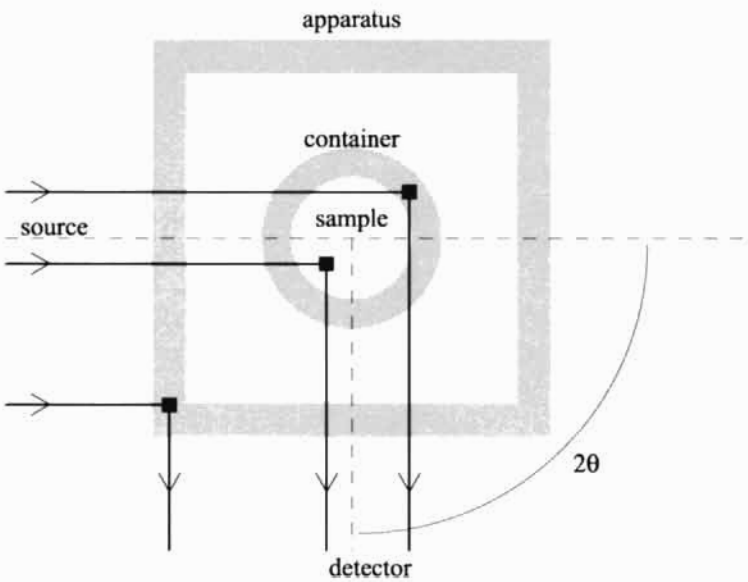

Fig. A5.1.3. Schematic cross-section of a sample surrounded by sample environments. Some particle tracks through the sample/can/apparatus are shown as the arrowed lines.

different media. The μ_x coefficients can be evaluated if the composition and density of the sample are known, or they can be measured directly by carrying out an absorption measurement on a sample of the material of known uniform thickness.

The number of particles per second reaching the detector that were singly scattered in volume element $d\vec{r}$ at position $\vec{r}$ is therefore given by

$$dI_s^1(\theta,\phi,E_i,E_s,t,\vec{r}) = J(\vec{r},E_i,t)\left(\frac{d^2\sigma(\theta,\phi,E_i,E_s)}{d\Omega dE_s}\right)\left(\prod_x A_x(\vec{r},\theta,\phi,E_i,E_s)\right)d\Omega\, dE_s \tag{A5.1.4}$$

Continuing our simulation of the scattering experiment, we have to take into account the efficiency of detection of the scattered particles. Two things affect this. The first, and most obvious, is the quantum efficiency of the detectors themselves, $\varepsilon_d(E_s)$. This is the probability that a scattered particle of energy E_s that is incident on the detector will be detected. The second factor that affects whether a scattered particle is detected comes from the scattered beam collimating optics of the diffractometer. Ideally, these are constructed so that every neutron/X-ray emerging from the sample position is detected and every neutron/X-ray whose scattered path originates away from the sample is not. However, it is clear that this can complicate corrections significantly since it becomes important to know whether a scattering event in part of the apparatus away from the sample position should be included in the corrections or not. This effect can be represented in our scattering

expression as a 'detector profile' (Soper and Egelstaff, 1980), $D(\vec{r}, \theta, \phi, E_s)$, which can take values between 0 and 1. If the detector element at position (θ, ϕ) has an unobstructed view of the scattering element at $\vec{r}$ then $D(\vec{r}, \theta, \phi, E_s) = 1$. If the view is completely obstructed it takes a value 0. In general it can take any intermediate value. The energy dependence comes about because the absorption of collimator materials is energy dependent. For simplicity later on, we will assume that the sample is small enough that D does not depend on $\vec{r}$, the position of the scattering element within the sample.

The expression for the number of particles per second counted in a detector at (θ, ϕ) due to single scattering events in the volume element $d\vec{r}$ at $\vec{r}$ is then

$$dI_s^1(\theta, \phi, E_i, E_s, t, \vec{r}) = J\left(\frac{d^2\sigma}{d\Omega\, dE_s}\right)\left(\prod_x A_x\right)\varepsilon_d D d\Omega\, dE_s \qquad \text{(A5.1.5)}$$

where the explicit position, angle and energy dependencies of the respective factors have been suppressed for conciseness.

This description of the measured single scattering intensity from a volume element is very general and it presents a road-map for how to correct measured intensities to obtain the differential scattering cross-section, and therefore obtain $S(Q)$. In the next section we develop a similar expression for multiple scattering intensity. We will then show how the required scattering cross-sections can be recovered from the measured raw intensities from the sample, container and backgrounds.

A5.1.3 Step 2: Double and multiple scattering from two volume elements in the sample

We now consider the intensity reaching the detector located at (θ, ϕ) from particles that were scattered twice in the sample/container/apparatus: the double scattering. This is shown schematically in Figure A5.1.4. The qualitative ideas behind this are very straightforward but the mathematical equations quickly become dense and complicated. On a first reading it is recommended that the qualitative ideas behind the multiple scattering phenomenon are understood by studying Figure A5.1.4. It is then sufficient to skip to the last paragraph in this section where the magnitude of multiple scattering effects is discussed. A qualitative understanding of multiple scattering is all that is required to understand the discussion of data corrections in general.

We derive an equation for the double scattering from two volume elements. We consider that the particle is first scattered in the volume element at $\vec{r}_1$ and then subsequently at $\vec{r}_2$. The scattered beam from the first event then becomes the incident beam for the second event. It becomes clear that the complexity of the situation increases dramatically because the *direction* of the incident beam for the secondary scattering event depends on the positions of $\vec{r}_1$ and $\vec{r}_2$. The angles (θ, ϕ) give the source-sample-detector angle, i.e. the *global* scattering angle. The angle dependence of the scattering cross-section

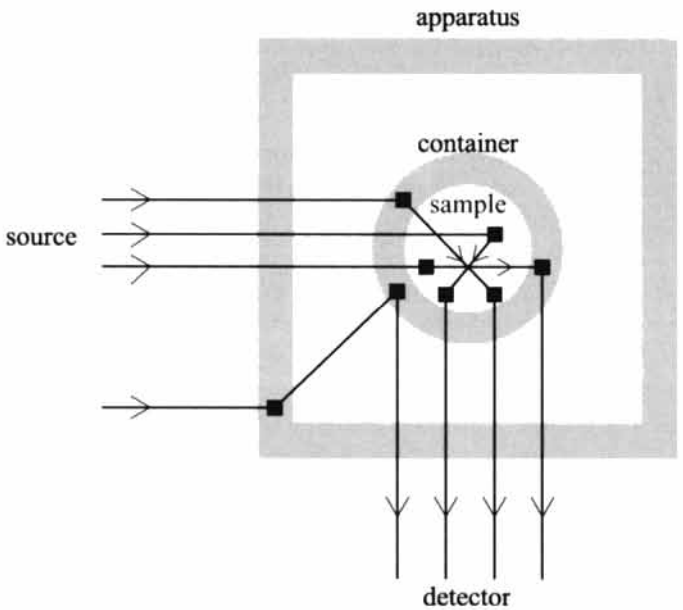

Figure A5.1.4. Reproduction of Figure A5.1.3 but with a number of different multiply scattered particle tracks illustrated.

refers to the *local* scattering angle; the angle between the incoming and outgoing beam locally. For single scattering events the global and local scattering angles are the same. For higher order scattering this is no longer the case.

The secondary scattering intensity reaching the detector at (θ, ϕ) can be written as follows:

$$\begin{aligned} \mathrm{d}I_{\mathrm{s}}^2 = J(E_{\mathrm{s}}^0, \vec{r}_1)\left(\prod_{\mathrm{x}} A_x^0(\vec{r}_1, E_{\mathrm{s}}^0)\right)\left[\int \mathrm{d}E_{\mathrm{s}}^1\left(\frac{\mathrm{d}^2\sigma(\vec{r}_1, E_{\mathrm{s}}^0, E_{\mathrm{s}}^1, P_{\mathrm{s}}^0, \theta', \phi')}{\mathrm{d}\Omega\,\mathrm{d}E_{\mathrm{s}}^1}\right)\right. \\ \left.\times\left(\prod_{\mathrm{x}} A_x^1(\vec{r}_1, \vec{r}_2, E_{\mathrm{s}}^1)\right)\left(\frac{\mathrm{d}^2\sigma(\vec{r}_2, E_{\mathrm{s}}^1, E_{\mathrm{s}}^2, P_{\mathrm{s}}^1, \theta'', \phi'')}{\mathrm{d}\Omega\,\mathrm{d}E_{\mathrm{s}}^2}\right)\right] \\ \times \mathrm{d}\Omega'(\vec{r}_2; \vec{r}_1)\left(\prod_{\mathrm{x}} A_x^2(\vec{r}_2, \theta, \phi, E_{\mathrm{s}}^2)\right)\varepsilon_{\mathrm{d}}(E_{\mathrm{s}}^2)D(\vec{r}_2)\mathrm{d}\Omega\,\mathrm{d}E_{\mathrm{s}}^2 \end{aligned} \tag{A5.1.6}$$

We now write E_{s}^n as the energy of the nth scattered radiation, where n takes values 0, 1 and 2. Thus, $E_{\mathrm{s}}^0 = E_{\mathrm{i}}$, and so on. Here, $A_x^n = \exp\{\mu_x(E_{\mathrm{s}}^n)l_x^n\}$ is the absorption factor for the nth scattered beam in medium x. The factor A_x^n depends on the trajectory of the beam and so depends on the relative source-$\vec{r}_1$, $\vec{r}_1 - \vec{r}_2$, and $\vec{r}_2$-detector positions for $n = 0$, 1 and 2, respectively, and $\mathrm{d}\Omega'(\vec{r}_2; \vec{r}_1)$ is the solid angle subtended at $\vec{r}_1$ by the volume element $\mathrm{d}\vec{r}_2$. There is an integral over all energies of the intermediate scattering event because only the initial and final energies of the radiation can be known, for example by having a

monochromatic beam and an energy sensitive detection scheme. Thus, all intermediate scattering events will be recorded at their final energy, regardless of the energy of the intermediate scattering. The equation for dI_s^2 has been written in a, more or less, chronological fashion to aid readability. The flux J is incident on the sample, this is attenuated by the A_x^0 factors before reaching the first scattering element at $\vec{r}_1$ where it is scattered through an angle (θ', ϕ') emerging in a direction towards the second element at $\vec{r}_2$ with the probability given by the double differential cross-section of the element at $\vec{r}_1$. On its way to $\vec{r}_2$ it is attenuated by the A_x^1 factors. These singly scattered particles reaching the second volume element will be scattered through an angle (θ'', ϕ'') with respect to the incoming direction, $\vec{r}_2 - \vec{r}_1$, emerging in a direction towards the detector with a probability given by the double differential cross-section of the second element. These secondary scattered particles are then attenuated by the A_x^2 factors before reaching the detector and being detected with probability $\varepsilon_d D$. Here we give the double differential cross-sections an $\vec{r}$ dependence since, in general, the multiple scattering could occur first in one medium then another.

This seems enormously complicated; and the complications diverge as we go to higher and higher orders of scattering. However, we are dealing with X-rays and neutrons which are weak scatterers. In the case of X-rays, the total multiple scattering corrections are generally less than 10% of the single scattering intensity (though we hope to do much better than this!), third and higher order scattering contributes less than 1%. In the case of neutrons the multiple scattering corrections are significant and must be carefully corrected. These corrections have been discussed in considerable detail by Sears (1975).

The multiple scattering intensity represents an annoying background signal in the data. It does not carry useful structural information and must be subtracted from the measured intensity before we can obtain $S(Q)$. The approach is to calculate the multiple scattering intensity in some reasonable way and then subtract it from the measured intensity. Since the multiple scattering contributions are small we can make certain approximations when we calculate them which, even if they give a 10% error on the calculated multiple scattering, result in a $\sim 1\%$ error on the data. Furthermore, the multiple scattering is quite featureless and changes the shape of $S(Q)$ somewhat but does not interfere with the structural information. In Section 5.3.6 we discussed approaches for calculating the multiple scattering intensity. Let us assume for now that the multiple scattering contribution can be evaluated in some reasonable way and proceed with the discussion of how to recover the differential scattering cross-section from the measured data.

A5.1.4 Step 3: The total single and multiple scattering intensities observed in the detector

The differential scattered intensity expressions, dI_s^n, we have derived up to now give the intensity appearing in a detector due to scattered particles being scattered in specific volume elements and taking a particular trajectory through the sample. The total intensity in the detector will clearly be the integral of the dI_s^n over all possible trajectories.

The total *single* scattered intensity in a detector at (θ, ϕ) will be $\int \mathrm{d}I_s^1$ where the integral is taken over all trajectories through the sample. For the single scattering case, this amounts to an integral over all *volume elements*. To do this it becomes useful to define a double differential cross-section *per scatterer*,

$$\frac{\mathrm{d}^2\sigma'(E_i, E_s, \theta, \phi)}{\mathrm{d}\Omega\,\mathrm{d}E_s} = \frac{1}{\rho(\vec{r})\mathrm{d}\vec{r}}\frac{\mathrm{d}^2\sigma(E_i, E_s, \theta, \phi)}{\mathrm{d}\Omega\,\mathrm{d}E_s} \tag{A5.1.7}$$

where $\rho(\vec{r})$ is the number density of scatterers in the volume element of volume $\mathrm{d}\vec{r} = \mathrm{d}x\,\mathrm{d}y\,\mathrm{d}z$ at position $\vec{r}$. This definition for $\mathrm{d}^2\sigma'(E_i, E_s, \theta, \phi)/\mathrm{d}\Omega\,\mathrm{d}E_s$ makes sense if we are considering volume elements that are much smaller than the macroscopic sample but larger than the coherence volume of the scattering. This will typically be a volume containing many thousands of atoms. The total single scattered intensity, I_s^1, detected in a detector of solid angle $\mathrm{d}\Omega$ at (θ, ϕ) will then be

$$I_s^1(\theta, \phi, E_i, E_s) = \int \mathrm{d}I_s^1 = \int J\left(\frac{\mathrm{d}^2\sigma'}{\mathrm{d}\Omega\,\mathrm{d}E_s}\right)\left(\prod_x A_x\right)\varepsilon_d D\,\mathrm{d}\Omega\,\mathrm{d}E_s\,\rho\,\mathrm{d}\vec{r} \tag{A5.1.8}$$

$$= \mathrm{d}\Omega\,\mathrm{d}E_s\varepsilon_d \int J\left(\frac{\mathrm{d}^2\sigma'}{\mathrm{d}\Omega\,\mathrm{d}E_s}\right)\left(\prod_x A_x\right)D\rho\,\mathrm{d}\vec{r} \tag{A5.1.9}$$

Similarly, the total double scattering in the detector is given by a double integral over all the volume elements in the sample:

$$\begin{aligned} I_s^2 &= \int_{\text{trajectories}} \mathrm{d}I_s^2 \\ &= \mathrm{d}\Omega\,\mathrm{d}E_s\,\varepsilon_d \int \mathrm{d}\vec{r}_1\left\{\rho(\vec{r}_1)J(\vec{r}_1)\int \mathrm{d}\vec{r}_2\left\{D(\vec{r}_2)\rho(\vec{r}_2)\int \mathrm{d}E_s^1\right.\right. \\ &\quad \left.\left.\left\{\left(\frac{\mathrm{d}^2\sigma_s(\vec{r}_1, \theta', \phi', E_s^0, E_s^1)}{\mathrm{d}\Omega\,\mathrm{d}E_s^1}\right)\left(\frac{\mathrm{d}^2\sigma_s(\vec{r}_2, \theta'', \phi'', E_s^1, E_s^2)}{\mathrm{d}\Omega\,\mathrm{d}E_s^2}\right)\left(\prod_{n=0}^{2}\prod_x A_x^n\right)\mathrm{d}\Omega'(\vec{r}_1; \vec{r}_2)\right\}\right\}\right\} \end{aligned} \tag{A5.1.10}$$

A5.1.5 Step 4: The total measured intensity in the detector

The total measured intensity in the detector at position (θ, ϕ) is given by the sum of all the orders of scattering, plus any other sources of counts in the detector other than scattering. These can include such things as fluorescence from the sample, ambient backgrounds not originating from close to the sample, noise in the electronics, and so on. We assume that these latter effects are kept to a minimum in regions of the energy spectrum of practical interest and can be neglected. Thus, the total measured intensity at time t in the detector,

I_s^m, is given by

$$I_s^m(\theta, \phi, E_i, E_s, t) = \sum_n I_s^n \tag{A5.1.11}$$

where the sum is over all orders of scattering.

A5.1.6 Step 5: normalizing for the incident flux

What is actually measured in the detector is the integrated counts:

$$N(\theta, \phi, E_i, E_s) = \int I_s^m(\theta, \phi, E_i, E_s, t)\mathrm{d}t \tag{A5.1.12}$$

where the integration is carried out over the elapsed time of the measurement. If desired, the average intensity can be obtained by dividing by the time of the measurement. To obtain the differential scattering cross-section it will be necessary to normalize the counts by the integrated flux. This is possible if we assume that the beam is stable in position and that the beam inhomogeneities are not time dependent. Thus,

$$J(\vec{r}, E_i, t) = \bar{J}(t, E_i)h(\vec{r}, E_i) \tag{A5.1.13}$$

where $\bar{J}(t, E_i) = I_i(t, E_i)/A$ is the flux averaged over the beam profile of area A. Here $I_i(t, E_i)$ is the integrated counts per second in the incident beam at time t as measured by the beam monitor. Thus, $h(\vec{r}, E_i)$ is a dimensionless factor that contains the information about the beam inhomogeneities or beam profile. In this case, $\int I_s^m(\theta, \phi, E_i, E_s, t)\mathrm{d}t = \{I_s^m\}' \int I_i(t, E_i)\mathrm{d}t$, where $\{I_s^m\}'$ is the same as I_s^m (Eqs. A5.1.8–A5.1.10) but with the Js replaced with hs. The integrated flux is generally measured using a beam monitor where the number of counts in the beam monitor, $M(E_i)$, is proportional to the number of particles in the incident beam, integrated over the length of the measurement: $\int I_i(t, E_i)\mathrm{d}t = K(E_i)M(E_i)$, where $K(E_i) = 1/\varepsilon_m(E_i)$ is the constant of proportionality and ε_m is the quantum efficiency of the monitoring system. A monitor with a fairly low quantum efficiency is desirable so as not to attenuate the incident beam significantly. Clearly, if the beam is inhomogeneous, it is important that the beam be smaller than the monitor. The measured, flux normalized, counts (really it is the probability of detecting a scattered particle) is then given by

$$n_s^m(\theta, \phi, E_i, E_s) = \frac{N(\theta, \phi, E_i, E_s)}{K(E_i)M(E_i)} = \{I_s^m\}' \tag{A5.1.14}$$

The number of counts in the detector, N, and the monitor, M, are known quantities and, therefore, so is $Kn_s^m(\theta, \phi, E_i, E_s)$. In a particular measurement n_s^m may only be known at a single value of E_i (monochromatic incident beam measurement) or at a single value of E_s (analyzer after the sample) or integrated over all values of E_s (detector with no energy resolution). However, in the most general case, $Kn_s^m(\theta, \phi, E_i, E_s)$ is known.

If we consider only the singly scattered counts, from Eq. A5.1.9 we see that

$$Kn_{\mathrm{s}}^{1} = K\{I_{\mathrm{s}}^{1}\}' = \mathrm{d}\Omega\,\mathrm{d}E_{\mathrm{s}}\,K\varepsilon_{\mathrm{d}}\int h\left(\frac{\mathrm{d}^2\sigma'}{\mathrm{d}\Omega\,\mathrm{d}E_{\mathrm{s}}}\right)\left(\prod_x A_x\right)D\rho\,\mathrm{d}\vec{r} \tag{A5.1.15}$$

where n_{s}^{1} denotes the singly-scattered normalized counts in the detector. Referring to Eq. A5.1.10 it is straightforward to get the respective expression for the double scattered contribution and, by generalizing this expression, the higher orders of scattering. The total normalized counts in the detector are then given by

$$\frac{N}{M} = K\sum_n n_{\mathrm{s}}^{n} = Kn_{\mathrm{s}}^{1} + K\sum_{n=2}^{\infty} n_{\mathrm{s}}^{n} \tag{A5.1.16}$$

A5.1.7 The inverse problem: obtaining the double differential cross-section from measured intensities

The measured normalized counts, $n_{\mathrm{s}}^{\mathrm{m}}$, contain contributions from backgrounds and containers. These contributions can be estimated by making measurements of empty sample containers and the empty apparatus. It is a reasonable approximation to make that the sample, can and apparatus, are each macroscopically homogeneous. In that case the double-differential scattering cross-section and the density from each volume element only depends on the medium in which it is located. The integral over volume elements in Eq. A5.1.15 can then be split into 3 (or more, as needed) integrals taken over volume elements in each medium. Thus, the single scattering is given by

$$Kn_{\mathrm{s}}^{1} = \mathrm{d}\Omega\,\mathrm{d}E_{\mathrm{s}}\,K\varepsilon_{\mathrm{d}}\{p^{\mathrm{s};\{w\}} + p^{\mathrm{c};\{w\}} + p^{\mathrm{a};\{w\}}\} \tag{A5.1.17}$$

where

$$\begin{aligned} p^{y;\{w\}} &= \int_y h\left(\frac{\mathrm{d}^2\sigma^y}{\mathrm{d}\Omega\,\mathrm{d}E_{\mathrm{s}}}\right)\left(\prod_{x\in\{w\}} A_x\right)D\rho^y\,\mathrm{d}\vec{r} \\ &= \left(\frac{\mathrm{d}^2\sigma^y}{\mathrm{d}\Omega\,\mathrm{d}E_{\mathrm{s}}}\right)\rho^y D\int_y h\left(\prod_{x\in\{w\}} A_x\right)\mathrm{d}\vec{r} \end{aligned} \tag{A5.1.18}$$

is the contribution to the normalized single scattering counts from scattering in medium y. Here, and hereafter, for notational simplicity the primes on the double differential cross-sections have been dropped but it is understood that the cross-sections are normalized per scatterer. The $\{w\}$ in the superscripts and subscripts refers to the set of media which are present in the experiment. In the sample experiment, $\{w\} = \{\mathrm{s},\mathrm{c},\mathrm{a}\}$, in the container experiment $\{w\} = \{\mathrm{c},\mathrm{a}\}$ (no sample present) and so on where, as usual, s, c and a refer to sample, container and apparatus, respectively. The integral is carried over all volume elements in medium y.

For the case of double scattering we get

$$p^{xy;\{w\}} = \int_y \mathrm{d}\vec{r}_2 \left\{ D\rho^y \int_x \mathrm{d}\vec{r}_1 \left\{ \rho^x \int \mathrm{d}E_\mathrm{s}^\mathrm{I} \left\{ h \left(\frac{\mathrm{d}^2\sigma^x}{\mathrm{d}\Omega\, \mathrm{d}E_\mathrm{s}^\mathrm{I}} \right) \right.\right.\right.$$
$$\left.\left.\left. \times \left(\frac{\mathrm{d}^2\sigma_\mathrm{s}^y}{\mathrm{d}\Omega\, \mathrm{d}E_\mathrm{s}^2} \right) \left(\prod_{n=0}^{2} \prod_{x=\{w\}} A_x^n \right) \right\} \mathrm{d}\Omega' \right\} \right\} \tag{A5.1.19}$$

which is the contribution from scattering first in medium x followed by scattering in medium y. This expression can be generalized to get the higher-order scattering terms, $p^{xyz;abc}$, and so on.

It is readily verified that the total normalized counts in the detectors from the three experiments are then given by

$$\left(\frac{N}{M} \right)^{\mathrm{sca}} = \mathrm{d}\Omega\, \mathrm{d}E_\mathrm{s}$$
$$\times K\varepsilon_\mathrm{d} \left[p^{\mathrm{s;sca}} + p^{\mathrm{c;sca}} + p^{\mathrm{a;sca}} + \left\{ \sum_x \sum_y p^{xy;\mathrm{sca}} \right\} + \left\{ \sum_{xyz} p^{xyz;\mathrm{sca}} \right\} + \cdots \right] \tag{A5.1.20}$$

$$\left(\frac{N}{M} \right)^{\mathrm{ca}} = \mathrm{d}\Omega\, \mathrm{d}E_\mathrm{s}\, K\varepsilon_\mathrm{d} \left[p^{\mathrm{c;ca}} + p^{\mathrm{a;ca}} + \left\{ \sum_x \sum_y p^{xy;\mathrm{ca}} \right\} + \left\{ \sum_{xyz} p^{xyz;\mathrm{ca}} \right\} + \cdots \right] \tag{A5.1.21}$$

$$\left(\frac{N}{M} \right)^{\mathrm{a}} = \mathrm{d}\Omega\, \mathrm{d}E_\mathrm{s}\, K\varepsilon_\mathrm{d} [p^{\mathrm{a;a}} + p^{\mathrm{aa;a}} + p^{\mathrm{aaa;a}} + \cdots] \tag{A5.1.22}$$

In Eq. A5.1.20 x, y and z can take values of s, c and a and in Eq. 5.21 x, y and z take values of c and a. The terms in braces are the second and higher orders of scattering.

The three measured intensities give us a set of three simultaneous equations containing three unknowns: the double-differential scattering cross-sections $(\mathrm{d}^2\sigma^x/(\mathrm{d}\Omega\, \mathrm{d}E_\mathrm{s}))$ with x being s, c and a. In principle, the remaining parameters in the equations consist of known experimental variables. The equations are, however, implicit equations. There is no way of solving them explicitly to get expressions for $(\mathrm{d}^2\sigma^x/(\mathrm{d}\Omega\, \mathrm{d}E_\mathrm{s}))$.

There are really two ways to proceed. The first is to simulate the experiment in a computer using an iterative process. The second is to make some approximations that allow explicit single-scattering cross-sections to be calculated. In the first approach, an initial trial is used for the cross-sections and the measured intensity calculated. The trial can then be updated and the process repeated. This can then be iterated until the calculated and measured intensities agree. This is a regression method; a kind of refinement method where it is the 'experimental data' (the relevant differential cross-sections to be precise) being refined against the raw data

rather than a model being refined against raw data. The initial trial could be the cross-section calculated from a model structure, or it could be the raw data themselves after a rough correction process has been carried out. The advantage of this approach is that the multiple scattering is treated in a self-consistent and accurate way. In practice this approach is enormously computationally intensive, even with modern high-speed computers, and in most cases is unwarranted; for example, if the multiple scattering is not the largest source of uncertainty in the measurement. As we have discussed, multiple scattering contributions often contribute less than 10% (and often much less than 10%). In these cases a less accurate estimation of the multiple scattering (or even no multiple scattering correction at all!) can give acceptable results. We now continue to discuss in more detail the second approach: an approximate method for extracting the cross-section explicitly from the raw data.

A5.1.8 Approximate method for extracting the sample scattering cross-section

We now explore the possibility of making reasonable approximations allowing us to solve the set of Eqs. A5.1.20–A5.1.22 to obtain $(\mathrm{d}^2\sigma^{\mathrm{s}}/(\mathrm{d}\Omega\,\mathrm{d}E_{\mathrm{s}}))$, the double differential scattering cross-section of the sample. First, we note that in most experiments, all the multiple scattering combined is a minor part of the total measured intensity. If the multiple scattering can be calculated in some reasonable way, then it can be subtracted directly from the data. For now, assume that it can be calculated to acceptable accuracy.

Eqs. A5.1.20–A5.1.22 yield the following expressions for the normalized counts in our detectors from each of the three measurements:

$$\left(\frac{N}{M}\right)^{\mathrm{sca}} = \mathrm{d}\Omega\,\mathrm{d}E_{\mathrm{s}}\,K\varepsilon_{\mathrm{d}}\{p^{\mathrm{s;sca}} + p^{\mathrm{c;sca}} + p^{\mathrm{a;sca}} + m^{\mathrm{sca}}\} \tag{A5.1.23}$$

$$\left(\frac{N}{M}\right)^{\mathrm{ca}} = \mathrm{d}\Omega\,\mathrm{d}E_{\mathrm{s}}\,K\varepsilon_{\mathrm{d}}\{p^{\mathrm{c;ca}} + p^{\mathrm{a;ca}} + m^{\mathrm{ca}}\} \tag{A5.1.24}$$

$$\left(\frac{N}{M}\right)^{\mathrm{a}} = \mathrm{d}\Omega\,\mathrm{d}E_{\mathrm{s}}\,K\varepsilon_{\mathrm{d}}\{p^{\mathrm{a;a}} + m^{\mathrm{a}}\} \tag{A5.1.25}$$

where the $p^{x;\{w\}}$ are defined in Eq. A5.1.19. The $m^{\{w\}}$ indicate all of the multiple scattering contributions which we assume to be adequately calculable.

If we subtract Eq. A5.1.25 from Eqs. A5.1.24 and A5.1.23 we get

$$\left(\frac{N}{M}\right)^{\mathrm{sca}} - \left(\frac{N}{M}\right)^{\mathrm{a}} = \mathrm{d}\Omega\,\mathrm{d}E_{\mathrm{s}}\,K\varepsilon_{\mathrm{d}}\{p^{\mathrm{s;sca}} + p^{\mathrm{c;sca}} + (p^{\mathrm{a;sca}} - p^{\mathrm{a;a}}) + (m^{\mathrm{sca}} - m^{\mathrm{a}})\} \tag{A5.1.26}$$

$$\left(\frac{N}{M}\right)^{\mathrm{ca}} - \left(\frac{N}{M}\right)^{\mathrm{a}} = \mathrm{d}\Omega\,\mathrm{d}E_{\mathrm{s}}\,K\varepsilon_{\mathrm{d}}\{p^{\mathrm{c;ca}} + (p^{\mathrm{a;ca}} - p^{\mathrm{a;a}}) + (m^{\mathrm{ca}} - m^{\mathrm{a}})\} \tag{A5.1.27}$$

Referring to Eq. A5.1.18 we see that

$$(p^{a;ca} - p^{a;a}) = \left(\frac{d^2\sigma^a}{d\Omega\, dE_s}\right) D\rho^a \int_a hA_a A_c d\vec{r} - \left(\frac{d^2\sigma^a}{d\Omega\, dE_s}\right) D\rho^a \int_a hA_a d\vec{r}$$

$$= \left(\frac{d^2\sigma^a}{d\Omega\, dE_s}\right) D\rho^a \left(\int_a hA_a A_c d\vec{r} - \int_a hA_a d\vec{r}\right) \quad \text{(A5.1.28)}$$

$$= \left(\frac{d^2\sigma^a}{d\Omega\, dE_s}\right) D\rho^a (V'_{a;ac} - V'_{a;a}), \quad \text{(A5.1.29)}$$

where

$$V'_{y;\{w\}} = \int_y h \left(\prod_{x \in \{w\}} A_x\right) d\vec{r} \quad \text{(A5.1.30)}$$

has dimensions of volume and contains all the information about incident beam inhomogeneities and absorption effects. It is thus represents the *effective scattering volume* of the experiment. The absorption factor A_x is defined in Eq. A5.1.3 and h describes the incident beam inhomogeneities introduced in Eq. A5.1.13. Referring to Eq. A5.1.29 we see that the cancellation would be perfect but for the correction for absorption of intensity scattered in the apparatus but traversing the sample can, A_c. By design we try to place shields, furnace elements, and so on as far as possible from the sample position. The result of this is that most of the apparatus scattering does not originate from close to the sample position (Figure A5.1.3). The contribution to the integral $V'_{a;ac}$ of trajectories traversing the sample container should therefore be small, $V'_{a;ac} \approx V'_{a;a}$, and the single scattering from the apparatus cancels. By the same argument the single scattering from the apparatus will also cancel quite effectively from the sample experiment, Eq. A5.1.27. Assuming the assumptions are reasonable, Eqs. A5.1.26 and A5.1.27 thus become

$$\left(\frac{N}{M}\right)^{sc} = \left(\frac{N}{M}\right)^{sca} - \left(\frac{N}{M}\right)^{a} = d\Omega\, dE_s\, K\varepsilon_d \{p^{s;sca} + p^{c;sca} + (m^{sca} - m^a)\} \quad \text{(A5.1.31)}$$

$$\left(\frac{N}{M}\right)^{c} = \left(\frac{N}{M}\right)^{ca} - \left(\frac{N}{M}\right)^{a} = d\Omega\, dE_s\, K\varepsilon_d \{p^{c;ca} + (m^{ca} - m^a)\} \quad \text{(A5.1.32)}$$

Some cancellation will also occur in the multiple scattering. For example, using similar arguments as were used above to justify canceling the single scattering from the apparatus, we see that multiple scattering occurring exclusively in the apparatus will effectively cancel in Eqs. A5.1.31 and A5.1.32. This leaves multiple scattering which occurs in the can or which is scattered at least once each in the container and the apparatus. The contribution of these events to the total scattering is expected to be very small.

We now consider what happens when we take the difference between Eqs. A5.1.31 and A5.1.32. As before we will get an expression $(p^{c;sca} - p^{c;ca})$ that will have the form

$$(p^{c;sca} - p^{c;ca}) = \left(\frac{d^2\sigma^c}{d\Omega\, dE_s}\right) D\rho^c \left\{\int_c hA_a A_c A_s \, d\vec{r} - \int_a hA_a A_c \, d\vec{r}\right\}$$

$$= \left(\frac{d^2\sigma^c}{d\Omega\, dE_s}\right) D\rho^c (V'_{c;sca} - V'_{c;ca}). \qquad \text{(A5.1.33)}$$

It is now no longer true that these terms nearly cancel out because the absorption by the sample of intensity scattered in the container will be highly significant: $V'_{c;sca} \neq V'_{c;ca}$. However, if the effective volume integrals, $V'_{c;\{w\}}$, can be adequately evaluated, we can get cancellation of the single scattering intensity from the can by scaling $p^{c;ca}$ by $V'_{c;sca}/V'_{c;ca}$. Thus,

$$\left(\frac{N}{M}\right)^s = \left(\frac{N}{M}\right)^{sc} - \left(\frac{V'_{c;sca}}{V'_{c;ca}}\right)\left(\frac{N}{M}\right)^c = d\Omega\, dE_s\, K\varepsilon_d \{p^{s;sca} + m'\} \qquad \text{(A5.1.34)}$$

where

$$m' = \{(m^{sca} - m^a) - (V'_{c;sca}/V'_{c;ca})(m^{ca} - m^a)\} \qquad \text{(A5.1.35)}$$

is the multiple scattering correction which we, *a priori*, assumed that we could adequately calculate. After subtracting the multiple scattering we are left with the normalized single scattering intensity from the sample alone: $d\Omega\, dE_s\, K\varepsilon_d p^{s;sca}$. The double differential cross-section for the sample is then given by

$$\left(\frac{d^2\sigma^s}{d\Omega\, dE_s}\right) = \left[\left(\frac{N}{M}\right)^{sc} - \left(\frac{V'_{c;sca}}{V'_{c;ca}}\right)\left(\frac{N}{M}\right)^c\right]\left(\frac{1}{\rho^s V'_{s;sca} D\, d\Omega\, dE_s\, K\varepsilon_d}\right) - m' \qquad \text{(A5.1.36)}$$

The actual measurement is carried out with a detection system of finite energy resolution (or perhaps the double-differential cross-section is determined with high energy resolution but it is desired to integrate over a finite range of energy transfers). Thus, what is really obtained from the measurement is a differential cross-section,

$$\left(\frac{d\sigma^s}{d\Omega}\right) = \int \left(\frac{d^2\sigma^s}{d\Omega\, dE_s}\right) W(E_s) dE_s$$

$$= \left[\left(\frac{N}{M}\right)^{sc} - \left(\frac{V'_{c;sca}}{V'_{c;ca}}\right)\left(\frac{N}{M}\right)^c\right]\left(\frac{1}{\rho^s V'_{s;sca} D\, d\Omega\, K\varepsilon_d}\right) - m' \qquad \text{(A5.1.37)}$$

where $W(E)$ is the band-pass function of the detector.

APPENDIX 5.2. ABSORPTION CORRECTIONS IN SOME COMMON GEOMETRIES

A5.2.1 Summary of equations in this appendix

In this appendix, various analytic expressions for the effective sample volume, $V'_{c;\{w\}}$, introduced in Eq. A5.1.30 and used in the data analysis equations such as Eq. A5.1.37, are derived for some specific geometries. For convenience the derived equations are summarized below.

Reflection geometry:

No support:

$V'_{s;s}$: general equation: Eq. A5.2.3
infinitely thick sample: Eq. A5.2.4
symmetric reflection, transparent sample: Eq. A5.2.5
symmetric reflection, infinitely thick sample: Eq. A5.2.6

Support above and below the sample

$V'_{s;sc}$: general equation: Eq. A5.2.7
infinitely thick sample: Eq. A5.2.7
thin or thick sample, symmetric reflection: Eq. A5.2.8
thin or thick sample, symmetric and elastic scattering: Eq. A5.2.9

$V'_{c;sc}$: general equation: Eq. A5.2.10

$V'_{c;c}$: general equation: Eq. A5.2.11

$V'_{c;sc}/V'_{c;c}$: general equation: Eq. A5.2.12
symmetric reflection: Eq. A5.2.13
symmetric reflection, elastic scattering: Eq. A5.2.14
symmetric reflection, elastic, infinitely-thick sample: Eqs. A5.2.15 and A5.2.16

Transmission geometry:

No support:

$V'_{s;s}$: general equation: Eq. A5.2.17
symmetric transmission: Eq. A5.2.18
symmetric transmission, elastic scattering: Eq. A5.2.20

Support above and below the sample:

$V'_{s;sc}$: general equation: Eq. A5.2.21
symmetric transmission: Eq. A5.2.22
symmetric transmission, elastic scattering: Eq. A5.2.23

$V'_{c;sc}$: general equation: Eq. A5.2.24

$V'_{c;c}$: general equation: Eq. A5.2.25

$V'_{c;sc}/V'_{c;c}$: general equation: Eq. A5.2.26
symmetric transmission: Eq. A5.2.27
symmetric transmission, elastic scattering: Eq. A5.2.28

A5.2.2 Attenuation coefficients

All the equations given here require accurate knowledge of the *linear attenuation coefficients* $\mu(E)$ for the sample and container. If the sample (powder) density is known this can be calculated for the case of X-rays using tabulated values for $\mu(E)$ of the different elements. These are generally tabulated as *mass absorption coefficients*, $\mu_\rho(E)$, (e.g. see probably the most complete and up-to-date compilation at http://physics.nist.gov/xaamdi (Hubbell and Seltzer, 2002)). The mass-attenuation coefficient of a compound can be found from its constituents using simple additivity: $\mu_\rho^s(E) = \sum_\alpha w_\alpha \mu_\rho^\alpha(E)$ where $\mu_\rho^\alpha(E)$ is the mass attenuation coefficient of the αth atom and w_α is the fraction by weight of this element, $w_\alpha = c_\alpha M_\alpha / (\sum_\alpha c_\alpha M_\alpha)$, where c_α and M_α are the concentration and molar mass, respectively. The sample linear absorption coefficient, $\mu^s(E)$, is then obtained by multiplying by the sample (powder) density, $\mu^s(E) = \rho^s \mu_\rho^s(E)$. If possible, it is better to measure the sample attenuation directly by making a flat, uniform sample (in the flat-plate geometries described later the samples already have this geometry). As described in Section 4.3.6, $\mu(E)t$ for the sample can then be measured. The simplest way is to measure the intensity in a detector in the direct beam with the sample, respectively, in the beam and out of the beam. The flat face of the sample must be perpendicular to the beam. The log of the ratio of the attenuated to unattenuated intensities then gives μt: $\ln(I/I_0) = -\mu t$. Thus, μ for the sample can be obtained by dividing by the sample thickness, t. In the flat-plate geometry equations μt appears rather than μ so there is no need to measure the sample thickness, provided the μt measurement was done on the same sample used in the experiment. If the detector used in the absorption measurement is energy resolving, such as a solid-state detector connected to an MCA, then $\mu(E)t$ can be measured for each channel in the MCA by applying the equation $\ln(I(E)/(I_0(E)) = -\mu(E)t$ independently to each channel in the MCA. When you make the measurement, do not destroy the delicate detector with unattenuated direct beam!

A5.2.3 Absorption: cylindrical geometry

Cylindrically symmetric geometry, or so-called Debye–Scherrer geometry, is common in time-of-flight neutron measurements and also some X-ray measurements. In this geometry the sample is held in a cylindrical container (often called a 'can') that is placed at the center of the diffractometer perpendicular to the scattering plane defined by the incoming and outgoing beams. It is not generally the geometry of choice for X-ray PDF measurements from divergent sources such as laboratory X-ray sources because of the small sample area that can be illuminated compared to flat-plate geometries. The Debye–Scherrer geometry is popular in powder diffraction for very high Q-space resolution measurements, for example, accurate lattice parameter determinations, but is less popular when quantitative intensity measurements are required. However, with the advent of bright synchrotron sources producing small, highly parallel, beams these considerations become less of a factor. The convenience of the Debye–Scherrer geometry may make it more popular at

high-flux synchrotrons in the future. Like laboratory sources, neutron beams tend to be weak and divergent so why is this geometry preferred in time-of-flight measurements? The reason is that these instruments have a wide array of detectors filling much of the scattering plane. The cylindrical geometry means that all of the detectors have the same view of the sample; it is the most natural geometry when wide ranges of solid angle are being filled with detectors. For this reason, this geometry will also find use in X-ray cameras using film (the original Debye–Scherrer cameras for example) or image plate detectors, and diffractometers with wide angular range 1-d detectors.

There is no adequate analytic form for the absorption corrections in this geometry and the corrections must be assessed using numerical calculations. The basic approach is the same as was discussed in Appendix A5.1 whereby the sample is split up into volume elements and the absorption integrals, $V'_{y;\{w\}}$, are determined by summing over all the possible paths through the sample. This procedure is made easier by taking advantage of the symmetry of the situation and the efficiency of the calculation can be greatly improved. This was first discussed by Paalman and Pings (1962, 1963). As with the discussion of Appendix 5.1, the Paalman and Pings approach yields the effective volume for the singly scattered particles and so the data must be corrected for multiple scattering first. In the original Paalman and Pings papers, and in many subsequent papers on the subject, the absorption corrected effective volume of the sample (or container, etc.), $V'_{y;\{w\}}$, is replaced by the absorption factor $A_{y;\{w\}} = V'_{y;\{w\}} / \int\int h(W,H)\mathrm{d}W\,\mathrm{d}H$ where the integrations are taken over the width, W, (perpendicular to the scattering plane) and the height, H, (in the scattering plane) of the beam, respectively, incident on the sample and $h(W,H)$ is a measure of the beam inhomogeneities, defined in Eq. A5.1.13. For a homogeneous beam h is constant and unity and $\int\int h(W,H)\mathrm{d}W\,\mathrm{d}H = WH$.

The original Paalman and Pings corrections presumed that the sample was completely bathed in the beam. For beams smaller than the sample diameter the approach was generalized by Kendig and Pings (1962) and further for inhomogeneous beams by Soper and Egelstaff (1980). This latter paper also describes an approach to carrying out the numerical integration which leads greatly improved computational efficiency without loss of significant accuracy.

A5.2.4 Absorption: flat-plate reflection geometry

Absorption corrections for flat-plate reflection geometry can be derived fairly straightforwardly for the approximation of a parallel incident beam. Small corrections are required for a divergent incident beam, though this is rarely necessary given the moderate divergences of normal diffractometers and the small thickness of samples (especially at low X-ray energies). The geometry is shown in Figure A5.2.1. The incoming beam makes an angle of γ with the sample surface. In the most general case the scattering is not symmetric and the outgoing beam makes an angle β with the sample surface.

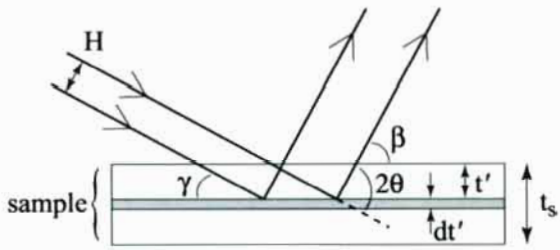

Fig. A5.2.1. Cross-section of a flat-plate geometry sample showing incoming and outgoing X-ray beams in reflection geometry. The incoming (outgoing) beam makes an angle $\gamma(\beta)$ with the sample. In Eq. A5.2.1 we consider the absorption of beams scattered at the planar volume element of thickness dt' at position t' below the sample surface. The total sample thickness is t_s.

The geometry suggests that volume elements should be selected that are parallel to the sample surface with thickness dt' (see Figure A5.2.1). We then consider scattering from a volume element at a distance t' below the sample surface. The attenuation of the beam in the sample above the element is $\exp\{-\mu_s(E_i)\ell_i\}$ where $\ell_i = t'/\sin\gamma$ is the path length through the sample before reaching the volume element and $\mu_s(E_i)$ is the linear absorption coefficient of the sample at the energy of the incoming beam. After being scattered the scattered beam is also attenuated, this time by $\exp\{-\mu_s(E_s)\ell_s\}$ where the absorption coefficient is now that of the sample at the energy, E_s, of the scattered beam that, again in the most general case of inelastic scattering, is different from the incoming beam. Because of the geometry, the integral along the length and the width of the sample simply yield L and W, the length and width of the beam footprint on the sample. The width, W is simply the beam dimension perpendicular to the scattering plane. The length of the beam footprint, L, depends on the height, H, of the beam (its dimension in the scattering plane) and the incident beam angle, $L = H/\sin\gamma$. Thus, for the case of a sample without any support we get for the effective sample volume

$$V'_{s;s} = \frac{WH}{\sin\gamma}\int_0^{t_s}\exp\left\{-t'\left(\frac{\mu(E_i)}{\sin\gamma}+\frac{\mu(E_s)}{\sin\beta}\right)\right\}dt' \qquad \text{(A5.2.1)}$$

The integration is carried out over the direction perpendicular to the sample surface from the top surface ($t' = 0$) to the bottom surface ($t' = t_s$) (Figure A5.2.1). The meaning of the subscripts on the effective volume, $V'_{y;\{w\}}$, are defined in Appendix 5.1 and indicate scattering taking place in medium y in the presence of media in the set $\{w\}$. In this case we are considering scattering in the sample in the presence of only the sample, $V'_{s;s}$. Eq. A.5.2.1 is straightforwardly generalized to the cases where sample supports need to be considered, as laid out below.

The above expression can easily be generalized to the case where the beam profile, $h(W,H)$, (Appendix 5.1), is inhomogeneous by replacing WH with an effective area

$$(WH)'(\gamma,\beta) = \int\int h(W,H)\mathrm{d}W\,\mathrm{d}H \tag{A5.2.2}$$

The integration in Eq. A5.2.1 can be straightforwardly evaluated as

$$V'_{s;s} = \frac{WH}{\sin\gamma}\left(\frac{1}{\left(\frac{\mu_s(E_i)}{\sin\gamma}+\frac{\mu_s(E_s)}{\sin\beta}\right)}\right)\left\{1-\exp\left\{-t_s\left(\frac{\mu_s(E_i)}{\sin\gamma}+\frac{\mu_s(E_s)}{\sin\beta}\right)\right\}\right\}$$

$$= \frac{WH\sin\beta}{(\mu_s(E_i)\sin\beta+\mu_s(E_s)\sin\gamma)}\left\{1-\exp\left\{-t_s\left(\frac{\mu_s(E_i)}{\sin\gamma}+\frac{\mu_s(E_s)}{\sin\beta}\right)\right\}\right\} \tag{A5.2.3}$$

where t_s is the thickness of the sample. If the sample is infinitely thick (in practice if $\mu t_s > 5$ or so) then

$$V'_{s;s} = \frac{WH\sin\beta}{(\mu_s(E_i)\sin\beta+\mu_s(E_s)\sin\gamma)} \tag{A5.2.4}$$

Furthermore, if symmetric reflection geometry is used (i.e. Bragg-Brentano geometry) then $\gamma = \beta = 2\theta/2 = \theta$, where 2θ is the scattering angle, and

$$V'_{s;s} = \frac{WH}{(\mu_s(E_i)+\mu_s(E_s))}\left\{1-\exp\left\{-\frac{t_s(\mu_s(E_i)+\mu_s(E_s))}{\sin\theta}\right\}\right\} \tag{A5.2.5}$$

A very convenient result is obtained in symmetric reflection if the sample is infinitely thick:

$$V'_{s;s} = \frac{WH}{(\mu_s(E_i)+\mu_s(E_s))} \tag{A5.2.6}$$

i.e. the absorption corrected effective sample volume is independent of scattering angle. This makes the absorption corrections in the case of angle resolved measurements in symmetric flat-plate geometry measurements rather straightforward.

A note of caution is warranted here. The derivation assumes above that the footprint of the incident beam on the sample is smaller than the sample area. In that case the length of sample illuminated is given by $H/\sin\gamma$. Especially at small scattering angles the beam footprint may get bigger than the sample. In this region of the diffraction pattern $H/\sin\gamma$ should be replaced by l_s, the length of the sample. This adds an additional angle dependence to V'_s. It is then quite important to control the alignment of the diffractometer so that you know precisely where the footprint exceeds the sample size. It may also be possible to measure the very low angle region of the diffraction pattern in transmission geometry, or asymmetric reflection, and join the low and high-angle portions of $S(Q)$ before Fourier transforming them. For low energy

laboratory measurements in reflection geometry, obtaining agreement between low angle reflection and transmission measurements has been advocated as a self-consistency check on the quality of the data and corrections (Thijsse, 1984). In practice, for samples and beam-heights of reasonable dimensions the region of $S(Q)$ that is affected is small and at very low Q and errors in the corrections will have a very small effect on the PDF. For example, for a 1 cm × 1 cm sample-face and a 1 mm beam height the footprint exceeds the sample length at $\gamma = 5.7°$ which is a Q-value of 1.8 Å^{-1} for Mo K_α in symmetric reflection. These low-Q data make a small contribution to $G(r)$ because of the $Q/\langle f\rangle^2$ weighting and is rarely missed, except in the most accurate measurements.

Often the sample is supported above and below with a thin tape such as a kapton foil to stabilize it. In this case, the various $V'_{s;\{w\}}$ can again be evaluated fairly straightforwardly. These corrections also apply to thick samples ($\mu t_s > 4$ or so) with a thin cover.

We now evaluate $V'_{s;sc}$ the effective volume of the *sample* in the presence of the foil. The integral is carried out as before in Eq. A5.2.1 except that the incident beam traverses the foil before reaching the sample. There is, therefore, an additional factor of

$$\exp\left\{-\frac{\mu_c(E_i)t_c}{\sin\gamma} - \frac{\mu_c(E_s)t_c}{\sin\beta}\right\},$$

where $t_c/\sin\gamma$ and $t_c/\sin\beta$ are the path-lengths through the foil as the beam enters and exits the sample, respectively. This is shown in Figure A5.2.2. Thus,

$$\begin{aligned} V'_{s;sc} &= \frac{WH}{\sin\gamma}\exp\left\{-\left(\frac{\mu_c(E_i)t_c}{\sin\gamma}+\frac{\mu_c(E_s)t_c}{\sin\beta}\right)\right\}\int_0^{t_s}\exp\left\{-t'\left(\frac{\mu_s(E_i)}{\sin\gamma}+\frac{\mu_s(E_s)}{\sin\beta}\right)\right\}dt' \\ &= \frac{WH\sin\beta}{(\mu_s(E_i)\sin\beta+\mu_s(E_s)\sin\gamma)}\exp\left\{-\left(\frac{\mu_c(E_i)t_c}{\sin\gamma}+\frac{\mu_c(E_s)t_c}{\sin\beta}\right)\right\} \\ &\quad\times\left[1-\exp\left\{-\left(\frac{\mu_s(E_i)t_s}{\sin\gamma}+\frac{\mu_s(E_s)t_s}{\sin\beta}\right)\right\}\right]. \end{aligned} \tag{A5.2.7}$$

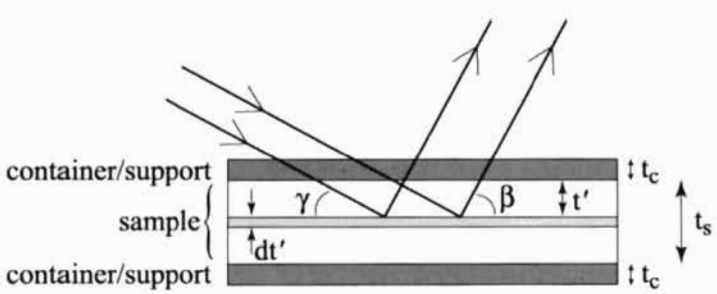

Figure A5.2.2. As Figure A5.2.1 but for the case of scattering in the sample when the sample is supported above and below by a support such as kapton foil.

In all these equations $\mu_c t_c$ is the absorption coefficient of the Kapton foil (or whatever the sample cover is) that can be readily measured. The result is exactly the same for the thick sample covered by a thin cover since in both cases the beam scattered from the sample never sees the back tape.

In the case of symmetric reflection, Eq. A5.2.7 reduces to

$$V'_{s;sc} = \frac{WH}{(\mu_s(E_i) + \mu_s(E_s))} \exp\left\{-\left(\frac{\mu_c(E_i)t_c + \mu_c(E_s)t_c}{\sin\theta}\right)\right\} \times\left\{1 - \exp\left\{-\frac{t_s(\mu_s(E_i) + \mu_s(E_s))}{\sin\theta}\right\}\right\} \quad \text{(A5.2.8)}$$

and for symmetric geometry and elastic scattering it reduces to

$$V'_{s;sc} = \frac{WH}{2\mu_s(E)} \exp\left\{-\left(\frac{2\mu_c(E)t_c}{\sin\theta}\right)\right\}\left\{1 - \exp\left\{-\frac{2\mu_s(E)t_s}{\sin\theta}\right\}\right\} \quad \text{(A5.2.9)}$$

Similarly, the effective volumes of the *scattering from the foils*, with and without the sample, can be obtained analytically. $V'_{c;sc}$ is straightforward but somewhat complicated. In this case we can consider two independent contributions to the intensity contributing to V' : scattering from the top foil and scattering from the bottom foil. The contribution from the top foil is the same as $V'_{s;s}$ with the t_s replaced by t_c. This is shown in Figure A5.2.3. The contribution from the bottom foil is like a reflection experiment on a transparent sample with a cover that is the top foil and the sample. The resulting expression gives

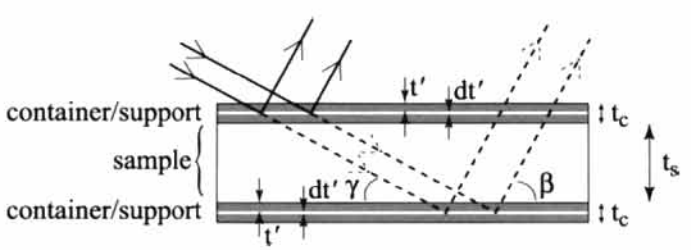

Figure A5.2.3. As Figure A5.2.2 for the case of a supported sample in reflection geometry, but showing the case of scattering occurring within the support.

$$
\begin{aligned}
V'_{\mathrm{c;sc}} = & \frac{WH}{\sin\gamma}\left\{\int_0^{t_\mathrm{c}} \exp\left\{-t'\left(\frac{\mu_\mathrm{c}(E_\mathrm{i})}{\sin\gamma} + \frac{\mu_\mathrm{c}(E_\mathrm{s})}{\sin\beta}\right)\right\}\mathrm{d}t' \right. \\
& + \exp\left\{-\left(\frac{\mu_\mathrm{c}(E_\mathrm{i})t_\mathrm{c} + \mu_\mathrm{s}(E_\mathrm{i})t_\mathrm{s}}{\sin\gamma} + \frac{\mu_\mathrm{s}(E_\mathrm{s})t_\mathrm{s} + \mu_\mathrm{c}(E_\mathrm{s})t_\mathrm{c}}{\sin\beta}\right)\right\} \\
& \left. \times \int_0^{t_\mathrm{c}} \exp\left\{-t'\left(\frac{\mu_\mathrm{c}(E_\mathrm{i})}{\sin\gamma} + \frac{\mu_\mathrm{c}(E_\mathrm{s})}{\sin\beta}\right)\right\}\mathrm{d}t'\right\} \qquad \text{(A5.2.10)} \\
= & \frac{WH\sin\beta}{(\mu_\mathrm{c}(E_\mathrm{i})\sin\beta + \mu_\mathrm{c}(E_\mathrm{s})\sin\gamma)}\left[1 - \exp\left\{-t_\mathrm{c}\left(\frac{\mu_\mathrm{c}(E_\mathrm{i})}{\sin\gamma} + \frac{\mu_\mathrm{c}(E_\mathrm{s})}{\sin\beta}\right)\right\}\right] \\
& \times\left[1 + \exp\left\{-\left(\frac{\mu_\mathrm{c}(E_\mathrm{i})t_\mathrm{c} + \mu_\mathrm{s}(E_\mathrm{i})t_\mathrm{s}}{\sin\gamma} + \frac{\mu_\mathrm{s}(E_\mathrm{s})t_\mathrm{s} + \mu_\mathrm{c}(E_\mathrm{s})t_\mathrm{c}}{\sin\beta}\right)\right\}\right]
\end{aligned}
$$

For the experiment with the top and bottom foils present in the absence of a sample between, the effective volume is the same as given in Eq. A5.2.10 but without the beam traversing the sample. Thus we get

$$
\begin{aligned}
V'_{\mathrm{c;c}} = & \frac{WH\sin\beta}{(\mu_\mathrm{c}(E_\mathrm{i})\sin\beta + \mu_\mathrm{c}(E_\mathrm{s})\sin\gamma)}\left[1 - \exp\left\{-t_\mathrm{c}\left(\frac{\mu_\mathrm{c}(E_\mathrm{i})}{\sin\gamma} + \frac{\mu_\mathrm{c}(E_\mathrm{s})}{\sin\beta}\right)\right\}\right] \\
& \times\left[1 + \exp\left\{-\left(\frac{\mu_\mathrm{c}(E_\mathrm{i})t_\mathrm{c}}{\sin\gamma} + \frac{\mu_\mathrm{c}(E_\mathrm{s})t_\mathrm{c}}{\sin\beta}\right)\right\}\right] \qquad \text{(A5.2.11)}
\end{aligned}
$$

Thus, the desired effective volume ratio is

$$
\frac{V'_{\mathrm{c;sc}}}{V'_{\mathrm{c;c}}} = \frac{\left[1 + \exp\left\{-\left(\dfrac{\mu_\mathrm{c}(E_\mathrm{i})t_\mathrm{c} + \mu_\mathrm{s}(E_\mathrm{i})t_\mathrm{s}}{\sin\gamma} + \dfrac{\mu_\mathrm{s}(E_\mathrm{s})t_\mathrm{s} + \mu_\mathrm{c}(E_\mathrm{s})t_\mathrm{c}}{\sin\beta}\right)\right\}\right]}{\left[1 + \exp\left\{-\left(\dfrac{\mu_\mathrm{c}(E_\mathrm{i})t_\mathrm{c}}{\sin\gamma} + \dfrac{\mu_\mathrm{c}(E_\mathrm{s})t_\mathrm{c}}{\sin\beta}\right)\right\}\right]} \qquad \text{(A5.2.12)}
$$

For symmetric reflection this reduces to

$$
\frac{V'_{\mathrm{c;sc}}}{V'_{\mathrm{c;c}}} = \frac{\left[1 + \exp\left\{-\left(\dfrac{\mu_\mathrm{c}(E_\mathrm{i})t_\mathrm{c} + \mu_\mathrm{s}(E_\mathrm{i})t_\mathrm{s} + \mu_\mathrm{s}(E_\mathrm{s})t_\mathrm{s} + \mu_\mathrm{c}(E_\mathrm{s})t_\mathrm{c}}{\sin\theta}\right)\right\}\right]}{\left[1 + \exp\left\{-\left(\dfrac{\mu_\mathrm{c}(E_\mathrm{i})t_\mathrm{c} + \mu_\mathrm{c}(E_\mathrm{s})t_\mathrm{c}}{\sin\theta}\right)\right\}\right]} \qquad \text{(A5.2.13)}
$$

and symmetric reflection and elastic scattering

$$
\frac{V'_{\mathrm{c;sc}}}{V'_{\mathrm{c;c}}} = \frac{\left[1 + \exp\left\{-\left(\dfrac{2\mu_\mathrm{c}(E)t_\mathrm{c} + 2\mu_\mathrm{s}(E)t_\mathrm{s}}{\sin\theta}\right)\right\}\right]}{\left[1 + \exp\left\{-\left(\dfrac{2\mu_\mathrm{c}(E)t_\mathrm{c}}{\sin\theta}\right)\right\}\right]} \qquad \text{(A5.2.14)}
$$

Note that, in the case where the sample is infinitely thick and there is no scattering from the

back support then Eq. A5.2.14 reduces to

$$\frac{V'_{c;sc}}{V'_{c;c}} = \frac{1}{\left[1 + \exp\left\{-\left(\frac{2\mu_c(E)t_c}{\sin\theta}\right)\right\}\right]}. \tag{A5.2.15}$$

In this situation, the ratio

$$\frac{V'_{c;sc}}{V'_{c;c}} = 1 \tag{A5.2.16}$$

should be used instead if, during the background run, only the scattering from the foil covering the sample is measured and any support under the sample is not measured.

A5.2.5 Absorption: flat-plate transmission geometry

In this case the geometry is similar to flat-plate reflection and so the construction of the integrals is also very similar. However, this time the beam exits out of the back of the sample and so the length of the scattered beam-path is $(t_s - t')/\sin\beta$ instead of $t'/\sin\beta$ for the case of reflection. This is shown in Figure A5.2.4. Also, in this geometry the scattering angle, $2\theta = \pi - (\gamma + \beta)$ instead of $2\theta = \gamma + \beta$ in the case of reflection. Making these substitutions we find that

$$\begin{aligned} V'_{s;s} &= \frac{WH}{\sin\gamma}\exp\left\{-\frac{t_s\mu_s(E_s)}{\sin\beta}\right\}\int_0^{t_s}\exp\left\{-t'\left(\frac{\mu_s(E_i)}{\sin\gamma} - \frac{\mu_s(E_s)}{\sin\beta}\right)\right\}dt' \\ &= \left(\frac{WH\sin\beta}{(\mu_s(E_i)\sin\beta - \mu_s(E_s)\sin\gamma)}\right)\left\{\exp\left\{-\frac{t_s\mu_s(E_s)}{\sin\beta}\right\} - \exp\left\{-\frac{t_s\mu_s(E_i)}{\sin\gamma}\right\}\right\} \end{aligned} \tag{A5.2.17}$$

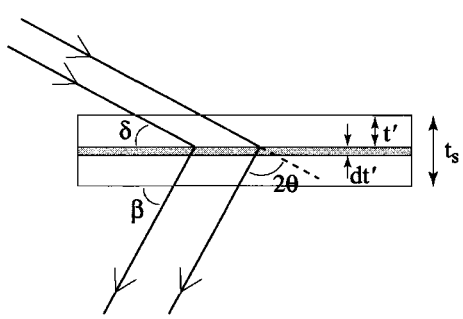

Figure A5.2.4. As Figure A5.2.1 for the case of scattering from an unsupported flat-plate sample in transmission geometry.

In symmetric transmission geometry we can take advantage of the fact that $\sin\gamma = \sin\beta = \cos\theta$ and we get

$$V'_{s;s} = \left(\frac{WH}{(\mu_s(E_i) - \mu_s(E_s))}\right)\left\{\exp\left\{-\frac{t_s\mu_s(E_s)}{\cos\theta}\right\} - \exp\left\{-\frac{t_s\mu_s(E_i)}{\cos\theta}\right\}\right\} \quad \text{(A5.2.18)}$$

In the case of elastic scattering this is singular. In this case we can define $\bar{\mu} = \mu(E_s) - \Delta\mu = \mu(E_i) + \Delta\mu$ and take the limit of $\Delta\mu \to 0$. We get

$$V'_{s;s} = \left(\frac{2WH}{\Delta\mu}\right)\exp\left\{-\frac{t_s\bar{\mu}_s}{\cos\theta}\right\}\sinh\left(\frac{t_s\,\Delta\mu_s}{2\cos\theta}\right) \quad \text{(A5.2.19)}$$

and expanding the sinh and taking the first term we arrive at

$$V'_{s;s} = \left(\frac{WHt_s}{\cos\theta}\right)\exp\left\{-\frac{t_s\mu(E)}{\cos\theta}\right\}. \quad \text{(A5.2.20)}$$

If the sample has a supporting structure above and below it (kapton tape, for example, see Figure A5.2.5) the equations are modified by the fact that the incoming and outgoing beams traverse the foils. Thus,

$$\begin{aligned} V'_{s;sc} &= \frac{WH}{\sin\gamma}\exp\left\{-\left(\frac{t_c\mu_c(E_i)}{\sin\gamma} + \frac{t_c\mu_c(E_s)}{\sin\beta}\right)\right\}\exp\left\{-\frac{t_s\mu_s(E_s)}{\sin\beta}\right\} \\ &\quad \int_0^{t_s}\exp\left\{-t'\left(\frac{\mu_s(E_i)}{\sin\gamma} - \frac{\mu_s(E_s)}{\sin\beta}\right)\right\}dt' \\ &= \left(\frac{WH\sin\beta}{(\mu_s(E_i)\sin\beta - \mu_s(E_s)\sin\gamma)}\right)\exp\left\{-\left(\frac{t_c\mu_c(E_i)}{\sin\gamma} + \frac{t_c\mu_c(E_s)}{\sin\beta}\right)\right\} \\ &\quad \left\{\exp\left\{-\frac{t_s\mu_s(E_s)}{\sin\beta}\right\} - \exp\left\{-\frac{t_s\mu_s(E_i)}{\sin\gamma}\right\}\right\}. \end{aligned} \quad \text{(A5.2.21)}$$

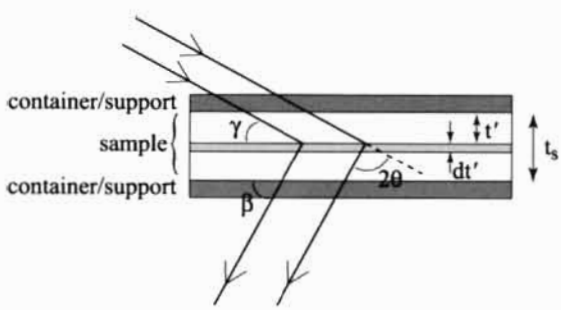

Fig. A5.2.5. As Figure A5.2.4 for the case of a sample supported by foils above and below.

For the case of symmetric scattering,

$$V'_{s;sc} = \left(\frac{WH}{\mu_s(E_i) - \mu_s(E_s)}\right)\exp\left\{-\left(\frac{t_c(\mu_c(E_i) + \mu_c(E_s))}{\cos\theta}\right)\right\} \times\left[\exp\left\{-\frac{t_s\mu_s(E_s)}{\cos\theta}\right\} - \exp\left\{-\frac{t_s\mu_s(E_i)}{\cos\theta}\right\}\right], \tag{A5.2.22}$$

and for symmetric and elastic scattering,

$$V'_{s;sc} = \left(\frac{WHt_s}{\cos\theta}\right)\exp\left\{-\left(\frac{2\mu_c(E_0)t_c + \mu_s(E_0)t_s}{\cos\theta}\right)\right\}. \tag{A5.2.23}$$

The effective volumes for the scattering from the *support* with and without the sample can also be evaluated. $V'_{c;sc}$ has two contributions; from the front and the back foil, both attenuated by the beam traversing the sample and the other foil:

$$\begin{aligned} V'_{c;sc} &= \frac{WH}{\sin\gamma}\exp\left\{-\left(\frac{\mu_c(E_i)t_c + \mu_s(E_i)t_s}{\sin\gamma}\right)\right\}\exp\left\{-\left(\frac{\mu_c(E_s)t_c}{\sin\beta}\right)\right\} \\ &\quad\times\int_0^{t_s}\exp\left\{-t'\left(\frac{\mu_c(E_i)}{\sin\gamma} - \frac{\mu_c(E_s)}{\sin\beta}\right)\right\}dt' + \frac{WH}{\sin\gamma}\exp\left\{-\left(\frac{\mu_c(E_s)t_c + \mu_s(E_s)t_s}{\sin\beta}\right)\right\} \\ &\quad\times\exp\left\{-\left(\frac{\mu_c(E_s)t_c}{\sin\beta}\right)\right\}\int_0^{t_s}\exp\left\{-t'\left(\frac{\mu_c(E_i)}{\sin\gamma} - \frac{\mu_c(E_s)}{\sin\beta}\right)\right\}dt' \\ &= \left(\frac{WH\sin\beta}{(\mu_s(Ei)\sin\beta - \mu_s(E_s)\sin\gamma)}\right)\left[\exp\left\{-\left(\frac{\mu_c(E_i)t_c + \mu_s(E_i)t_s}{\sin\gamma}\right)\right\}\right. \\ &\quad\left.+\exp\left\{-\left(\frac{\mu_c(E_s)t_c + \mu_s(E_s)t_s}{\sin\beta}\right)\right\}\right]\left\{\exp\left\{-\frac{t_c\mu_c(E_s)}{\sin\beta}\right\} - \exp\left\{-\frac{t_c\mu_c(E_i)}{\sin\gamma}\right\}\right\} \end{aligned} \tag{A5.2.24}$$

The result for scattering from the two foils without the sample give the same result but without the beam traversing the sample, thus,

$$\begin{aligned} V'_{c;c} &= \left(\frac{WH\sin\beta}{(\mu_s(E_i)\sin\beta - \mu_s(E_s)\sin\gamma)}\right) \\ &\quad\times\left[\exp\left\{-\left(\frac{\mu_c(E_i)t_c}{\sin\gamma}\right)\right\} + \exp\left\{-\left(\frac{\mu_c(E_s)t_c}{\sin\beta}\right)\right\}\right] \\ &\quad\times\left\{\exp\left\{-\frac{t_c\mu_c(E_s)}{\sin\beta}\right\} - \exp\left\{-\frac{t_c\mu_c(E_i)}{\sin\gamma}\right\}\right\} \end{aligned} \tag{A5.2.25}$$

The desired ratio, $V'_{c;sc}/V'_{c;c}$, is then

$$\frac{V'_{c;sc}}{V'_{c;c}} = \frac{\left[\exp\left\{-\left(\frac{\mu_c(E_i)t_c + \mu_s(E_i)t_s}{\sin\gamma}\right)\right\} + \exp\left\{-\left(\frac{\mu_c(E_s)t_c + \mu_s(E_s)t_s}{\sin\beta}\right)\right\}\right]}{\left[\exp\left\{-\left(\frac{\mu_c(E_i)t_c}{\sin\gamma}\right)\right\} + \exp\left\{-\left(\frac{\mu_c(E_s)t_c}{\sin\beta}\right)\right\}\right]}. \tag{A5.2.26}$$

For the case of symmetric scattering this becomes

$$\frac{V'_{c;sc}}{V'_{c;c}} = \frac{\left[\exp\left\{-\left(\frac{\mu_c(E_i)t_c + \mu_s(E_i)t_s}{\cos\theta}\right)\right\} + \exp\left\{-\left(\frac{\mu_c(E_s)t_c + \mu_s(E_s)t_s}{\cos\theta}\right)\right\}\right]}{\left[\exp\left\{-\left(\frac{\mu_c(E_i)t_c}{\cos\theta}\right)\right\} + \exp\left\{-\left(\frac{\mu_c(E_s)t_c}{\cos\theta}\right)\right\}\right]}, \tag{A5.2.27}$$

and for symmetric elastic scattering

$$\frac{V'_{c;sc}}{V'_{c;c}} = \exp\left\{-\left(\frac{\mu_s(E_0)t_s}{\cos\theta}\right)\right\}. \tag{A5.2.28}$$

APPENDIX 5.3. PROPAGATING RANDOM ERRORS IN THE DATA ANALYSIS

We briefly summarize some pertinent ideas of the error propagation here. More details and derivations of the general equations of error propagation presented here can be found in standard textbooks on the subject such as Prince (1982).

The variance of a stochastic variable, X, is defined as

$$\mathrm{var}(X) = \langle (X - \langle X \rangle)^2 \rangle \tag{A5.3.1}$$

where the angle brackets imply taking an average over multiple (unbiased) measurements of that variable. The Variance is therefore the mean-square deviation of a series of measurements from the average value. The standard deviation is the root-mean-square variation,

$$\sigma(X) = \sqrt{\mathrm{var}(X)}. \tag{A5.3.2}$$

In the case of our scattering experiment the statistics are Poissonian: the variance on the number of counts is simply the number of counts itself and $\sigma = \sqrt{N}$.

The covariance of two measurements, X and Y, is a measure of how much the uncertainty of one measurement depends on the result of the other and is defined as

$$\mathrm{cov}(X, Y) = \langle (X - \langle X \rangle)(Y - \langle Y \rangle) \rangle. \tag{A5.3.3}$$

Two measurements that are *statistically independent* will have a covariance of zero, otherwise the measurements are considered to be *statistically correlated*. A dimensionless

correlation coefficient can be defined as

$$\rho(X, Y) = \frac{\mathrm{cov}(X, Y)}{\sigma(X)\sigma(Y)}, \tag{A5.3.4}$$

which ranges from zero for statistical independence and values of ± 1 for complete correlation or anticorrelation.

Statistical dependence should be differentiated from functional dependence. Even when two observables are functionally dependent, measurements of these observables can still be made that are statistically independent (as is often done when the functional dependence is being measured or verified). The notion of covariance will become important later in the discussion of error propagation.

What is the variance on a quantity, F, that depends linearly on two stochastic variables X and Y, i.e. $F = aX + bY$? Then

$$\mathrm{var}(F) = a^2\,\mathrm{var}(X) + b^2\,\mathrm{var}(Y) + 2ab\,\mathrm{cov}(X, Y). \tag{A5.3.5}$$

This can easily be generalized to the case of more than two variables. This expression for finding the variance of a quantity that is a function of one or more stochastic observables can be extended to cases where the relationship is not linear in the case where the errors are small ($\sigma(F)/F \ll 1$). If F is some function of P observables $X_1 \ldots X_P$, then

$$\mathrm{var}(F) = \sum_{i=1}^{P} \left(\frac{\partial F}{\partial X_i}\right)^2 \mathrm{var}(X_i) + 2 \sum_{i,j=1(i<j)}^{P} \left(\frac{\partial F}{\partial X_i}\right)\left(\frac{\partial F}{\partial X_j}\right)\mathrm{cov}(X_i, X_j). \tag{A5.3.6}$$

If the measurements of the observables are statistically independent then only the first sum is required.

This equation results in the simple, well known, results that for $F = aX$,

$$\sigma(F) = a\sigma(X) \tag{A5.3.7}$$

and for $F = aXY$ that

$$\frac{\sigma(F)}{F} = \frac{\sigma(X)}{X} + \frac{\sigma(Y)}{Y}, \tag{A5.3.8}$$

if X and Y are statistically independent.

With this knowledge in hand it is straightforward to propagate errors in the data correction procedure. Let us say that the number of detected particles in a particular data-point is N_d. The detection process is random and so the uncertainty on the number of detected particles is $\sqrt{N_\mathrm{d}}$. We thus create two arrays, a data array which contains the set of counts, N_d, for each measured point, and an error array which contains $\sqrt{N_\mathrm{d}}$. These two arrays are then propagated side-by-side through the data analysis steps. Whenever the data-array is modified by a correction, the error array is also properly modified according to Eq. A5.3.6. Because we are using $\sqrt{N_\mathrm{d}}$ as the initial estimate for our errors, often

the detector dark current and deadtime corrections are made *before* the error array is created. The reason is that the detector deadtime introduces an inefficiency in detection which is not random (it is highly correlated: it depends on how closely spaced in time the photons arrive). On the other hand, *the deadtime corrected* counts will obey Poisson statistics because the underlying scattering and detection processes are random.

A reasonable starting assumption is that all the data-points are statistically independent. This is certainly true if a single detector is scanned through space and the data measured point-by-point. This means that all the covariance terms in Eq. A5.3.6 are zero. This remains true right up to the Fourier transformation step in the analysis, provided no smoothing or interpolation has been carried out on the data. However, the Fourier transform changes that.

There is often confusion regarding the way in which the Fourier transform introduces statistical correlations. It appears an obvious fact that *each* point in $G(r)$ contains information from *every* point in $S(Q)$ because each point in $G(r)$ comes from an integration over all of $S(Q)$. However, this does not introduce statistical correlations *per se*. To see this remember that the integration is just the limiting form of a sum. Each term in the sum contains a stochastic observation ($[S(Q) - 1]$) with a coefficient ($Q\sin(Qr)\Delta Q$) and so, according to Eq. A5.3.6, the variance on $G(r)$ is

$$\mathrm{var}(G(r_m)) = \frac{4}{\pi^2}\sum_i (Q_i \sin(Q_i r_m)\Delta Q_i)^2 \mathrm{var}(S(Q_i)). \qquad \text{(A5.3.9)}$$

This is a linear expression, and even though this point in $G(r)$ depends on the data in each and every point in $S(Q)$, there is no covariance term because the data-points themselves are statistically independent. Thus, $\sigma(G(r_m)) = \sqrt{Var(G(r_m))}$ gives a good estimate of the random errors on the mth point in $G(r)$ at r_m.

The problem arises when you want to consider the errors from a quantity which depends on a series of points in $G(r)$. For example, perhaps you want to ask the question, what is the error on the integrated peak intensity for a peak in $G(r)$? The problem here is that *neighboring points in G(r) are not statistically independent.* This is because there is a finite r-space resolution to the measurement of $G(r)$ that is dictated by the experiment: it comes from the finite range of Q over which the measurement was made. To a reasonable approximation we can estimate the resolution in $G(r)$ as being $\pi/Q_{\max}$. Based on this we can guess that points within a distance $\Delta r < \pi/Q_{\max}$ of each other in $G(r)$ will be statistically correlated. One approach to circumvent this problem is to evaluate $G(r)$ on a grid of points separated by $\Delta r < \pi/Q_{\max}$ and to a reasonable approximation the points in $G(r)$ will be statistically independent. This approach often presents difficulties when relatively sharp features are present in the PDF, such as is the case in crystalline materials, because there are then relatively few points defining each peak and therefore a poorly defined peak profile. This becomes hard to model quantitatively and this approach is not widely used. It is also approximate in any case since it is not true that points less widely

spaced than $\pi/Q_{\max}$ are completely correlated and those more widely spaced are completely uncorrelated.

The statistical correlations between points m and n in the PDF, $\text{cov}(G_m, G_n)$, can be determined. Assume that an experimentally measured $S(Q_i) = \bar{S}(Q_i) + \varepsilon(Q_i)$ where $\varepsilon(Q)$ is a small fluctuation due to random errors in the particular measurement and $\bar{S}(Q_i)$ is the average $S(Q)$ that you would get from making many measurements. Then, according to Eq. 3.1, the measured

$$\begin{aligned} G(r) &= \frac{2}{\pi} \sum_i Q_i[S(Q_i) - 1]\sin Q_i r\, \Delta Q_i \\ &= \frac{2}{\pi} \sum_i Q_i[\bar{S}(Q_i) - 1]\sin Q_i r\, \Delta Q_i + \frac{2}{\pi} \sum_i Q_i \varepsilon(Q_i)\sin Q_i r\, \Delta Q_i \\ &= \bar{G}(r) + \frac{2}{\pi} \sum_i Q_i \varepsilon(Q_i)\sin Q_i r\, \Delta Q_i. \end{aligned} \tag{A5.3.10}$$

From this we can get the variance on $G(r)$,

$$\begin{aligned} \text{var}(G) = \langle (G - \bar{G})^2 \rangle &= \left\langle \left(\frac{2}{\pi} \sum_i Q_i \varepsilon(Q_i)\sin Q_i r\, \Delta Q_i \right)^2 \right\rangle \\ &= \frac{4}{\pi^2} \sum_i Q_i^2 \langle \varepsilon^2(Q_i) \rangle \sin^2 Q_i\, r \Delta Q_i^2 \\ &\quad + \frac{4}{\pi^2} \sum_{i \neq j} Q_i Q_j \langle \varepsilon(Q_i)\varepsilon(Q_j) \rangle \sin Q_i r \sin Q_j r\, \Delta Q_i\, \Delta Q_j. \end{aligned} \tag{A5.3.11}$$

The second sum is zero since $\langle \varepsilon(Q_i)\varepsilon(Q_j) \rangle = 0$ because the errors on different points in Q are uncorrelated and averaging over many measurements will yield zero. Thus, since by definition, $\langle \varepsilon^2(Q_i) \rangle = \text{var}(S(Q))$ we recover Eq. A5.3.9 for $\text{var}(G)$.

From Eq. A5.3.6 we see that, similarly, $\text{cov}(G_m, G_n) = \langle (G_m - \bar{G}_m)(G_n - \bar{G}_n) \rangle$, where G_m is the value of $G(r)$ at the point $r = r_m$. Thus,

$$\begin{aligned} \text{cov}(G_m, G_n) &= \left\langle \left(\frac{2}{\pi} \sum_i Q_i \varepsilon(Q_i)\sin Q_i r_m\, \Delta Q_i \right) \left(\frac{2}{\pi} \sum_j Q_j \varepsilon(Q_j)\sin Q_j r_n\, \Delta Q_j \right) \right\rangle \\ &= \frac{4}{\pi^2} \sum_i Q_i^2 \langle \varepsilon^2(Q_i) \rangle \sin Q_i r_m \sin Q_i r_n\, \Delta Q_i^2 \\ &\quad + \frac{4}{\pi^2} \sum_{i \neq j} Q_i Q_j \langle \varepsilon(Q_i)\varepsilon(Q_j) \rangle \sin Q_i r_m \sin Q_j r_n\, \Delta Q_i\, \Delta Q_j. \end{aligned} \tag{A5.3.12}$$

As before the second sum is always zero. However, in this case terms in the first sum are not always positive as in the case of the variance, Eq. A5.3.11, because at a particular Q-point the

product ($\sin Q_i r_m \sin Q_i r_n$) can be positive or negative. In fact it will periodically oscillate from positive to negative and taking the sum to infinity will result in a complete cancellation of the terms in the sum. Thus, an ideal infinite Fourier transform results in $\mathrm{cov}(G_m, G_n) = 0$ and does not introduce statistical correlations between points in the PDF as we already discussed. However, summing over a finite range will yield a finite covariance given by

$$\mathrm{cov}(G_m, G_n) = \frac{4}{\pi^2} \sum_{i=1}^{N} Q_i^2 \sin Q_i r_m \sin Q_i r_n \, \Delta Q_i^2 \, \mathrm{var}(S(Q_i)). \tag{A5.3.13}$$

In particular, when the two points m and n are close together in r the two sine-waves will have nearly the same wavelength and be in phase, producing a positive product, over a significant range of the sum. When the points are further apart the two sine-waves go out of phase quickly and terms in the sum tend to cancel (though not completely).

Once the covariance matrix is calculated the true variance of functions of G can be determined using Eqs. A5.3.5 and A5.3.6. For example, the integral of a peak in $G(r)$ is simply $I_G = \sum_{m=l}^{h} G_m \, \Delta r_m$, where the sum runs from a point l below the peak to a point h above it, so

$$\mathrm{var}(I_G) = \sum_{m=l}^{h} \mathrm{var}(G_m)(\Delta r_m)^2 + 2 \sum_{m,n=l(m>n)}^{h} \mathrm{cov}(G_m, G_n) \Delta r_m \, \Delta r_n. \tag{A5.3.14}$$

To summarize, it is possible to estimate the random errors on each point individually in the PDF by propagating the random counting statistics of the raw data. This gives a variance on each point in the PDF that is accurate. However, because the number of points in the PDF is arbitrary, but the amount of information in the PDF is not, we find that the errors in neighboring points in the PDF are correlated. From a practical point of view, points in the PDF which are separated by more than $\approx \pi/Q_{\max}$ are statistically independent. Care must be taken when evaluating the errors on quantities that depend on more than one PDF point such as integrated peak intensities. The variance on this quantity is *not* given by the weighted sum of the variances on each of the PDF points in the sum because of the statistical correlations. However, in principle the covariance matrix between points in the PDF can be evaluated straightforwardly and using this information, statistically reliable variances can be determined even on functions involving more than one point in the PDF.

APPENDIX 5.4. DATA CORRECTIONS EXAMPLE: TIME OF FLIGHT NEUTRON: PDFGETN

To illustrate the process of obtaining the total scattering structure function, $S(Q)$, and thence a PDF from time-of-flight neutron data we show an example of a typical data analysis using the PDFgetN program (Peterson *et al.*, 2000). The analysis steps carried out

by the program are described in detail in Chapter 5 and Appendices 5.1–5.3. This program runs on windows, linux and most unix platforms. It is available from total scattering homepage (http://www.totalscattering.org/). The description reproduced here draws heavily from one of the tutorial examples in the program distribution.

The data analyzed in this illustration are from a sample of $La_{0.75}Ca_{0.25}MnO_3$ and belongs to the family of manganites exhibiting the so-called colossal magneto-resistance effect. The data were measured at 300 K on the Special Environment Powder Diffractometer (SEPD) at the Intense Pulsed Neutron Source (IPNS) at Argonne National Laboratory. This instrument has 160 detectors that are grouped into distinct banks centered at certain angles. Data from detectors away from the central angle are 'time-focussed' electronically so that the same '*Q*-value' is binned in the same 'time-channel' for all the detectors in the bank. The binning of data from various detectors into detector-banks is done electronically during the data collection. The assignment of detectors to detector banks is controlled by a user defined 'histogram' which is chosen at data-collection time. In the current histogram the beam monitor is designated as bank 5 and there are 8 banks in total. The sample was filled in an extruded vanadium container that had an inner radius and wall thickness of 0.5559 and 0.0127 cm, respectively. The experimental environment consisted of a closed-cycle helium refrigerator with an aluminum heat shield mounted. The data that were collected are summarized in Table A5.4.1

The PDFgetN program has an X-windows GUI interface for straightforward data input and analysis. It also has embedded data such as atomic weights and neutron scattering cross-sections to speed up the data analysis process. Finally, one of the philosophies behind the PDFgetN program is that all of the parameters used to obtain a particular PDF are stored within the PDF file itself. This is known as the data analysis HISTORY. This is important for the purposes of reproducibility and accountability: given the raw data and the analysis parameters it should always be possible for someone to reproduce a particular PDF; and to see exactly what input parameters were used to get it. However, it has one additional advantage. The PDFgetN program can read this history information from the PDF file and enter it into its various input fields. These can then be modified as desired to

Table A5.4.1. Data-sets that are used in the data analysis example presented here.

Data-set	Data run numbers
Sample	Sepd9085.asc
Empty container	Sepd9060.asc
Vanadium rod; no shields	Sepd9061.asc
Empty instrument	Sepd9062.asc

carry out the data analysis. This makes analyzing multiple similar data-sets (for example a temperature series) very straightforward because the great majority of the inputs do not change from one data-set to another.

The user first selects the correct template for the particular diffractometer that was used to collect the data; in this case SEPD. The experimental information is then typed into the various fields as shown in Figure A5.4.1. Note that no instrument background is subtracted from the vanadium rod. This is because SEPD has inherently a very low background that is negligible for the vanadium rod measurement which is carried out with no heat-shields in place. A background from the empty instrument is measured for the data collected with heat-shields in place. Data from the sample are not smoothed. By default the empty container, vanadium rod and sample background will be smoothed using a Savitzky-Golay filter of zeroth order. This is done to improve statistics on the assumption that all the backgrounds are slowly varying and smoothing them will not introduce significant distortions. Smoothing can be turned off if desired. The tiny residual Bragg peaks are also removed from the vanadium data by default. The severity of smoothing, and the smoothing protocol, are controlled by varying the 'smoothing parameters' fields.

Once the experimental information is filled in the sample information is entered, as shown in Figures A5.4.2 and A5.4.3. The chemical elements in the sample are selected from the pop-up periodic table window (Figure A5.4.2) and the chemical formula entered

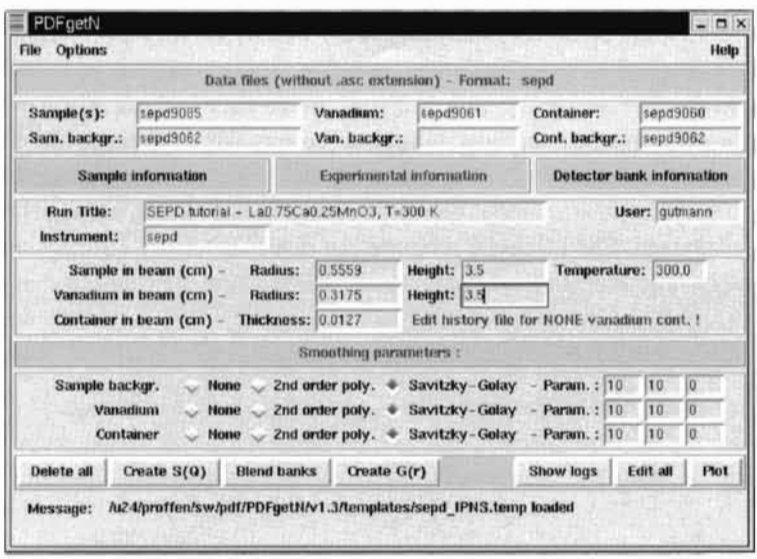

Figure A5.4.1. Experimental information window of PDFgetN. Note the 'Create $S(Q)$' and 'Plot' buttons. Once essential information, such as sample composition and dimensions, is entered, $S(Q)$, and $G(r)$ are just the click of a button away.

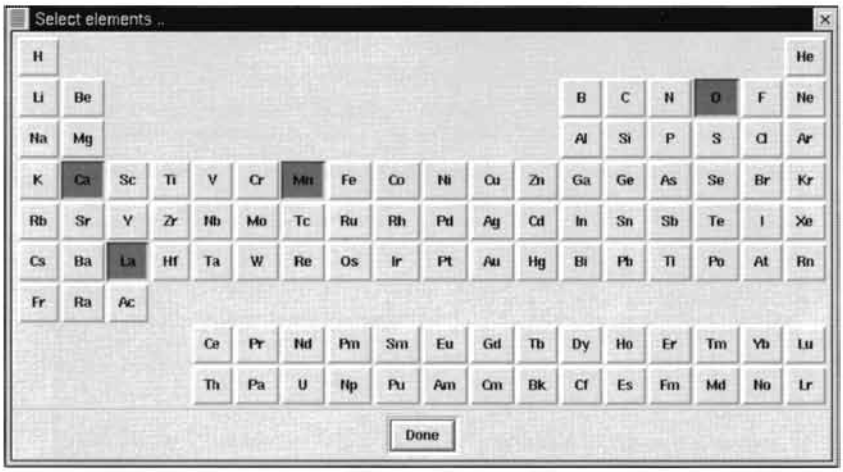

Figures A5.4.2. Window in PDFgetN for selecting chemical elements present in the sample.

from the keyboard. The neutron scattering cross-sections that will be used automatically appear as shown in Figure A5.4.3. All these values can be edited manually in the history file if necessary. The sample powder density is the weight of the sample divided by its volume (i.e. the density of the loose powder). This is not used explicitly anywhere in the analysis and may be left blank. Instead, the density is treated like a parameter that is used to normalize the data and takes the name 'effective density'. This field has to contain a value

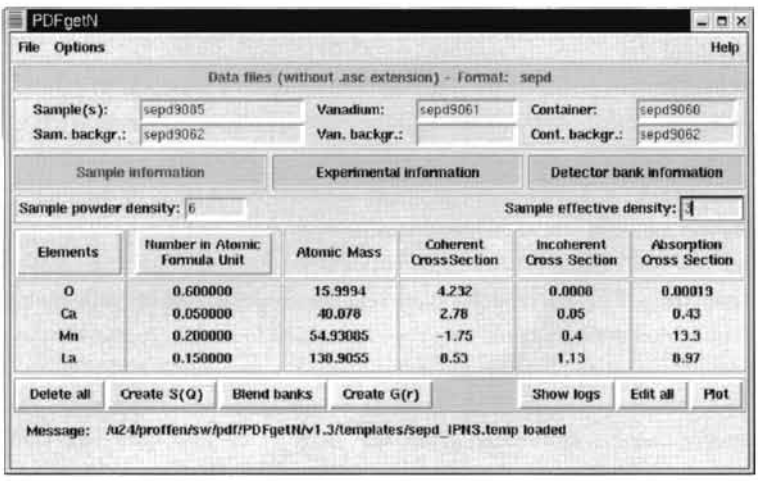

Figure A5.4.3. Sample information window of PDFgetN.

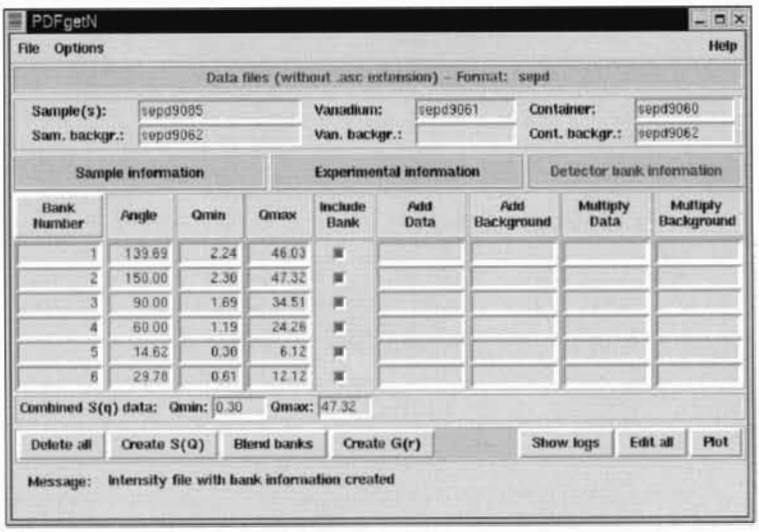

Figure A5.4.4. Detector-bank information in PDFgetN.

for the program to run and a good initial value is the true sample (powder) density, if it was measured, or alternatively 0.5 times the theoretical density of the sample.

Next, information about the detector histogram must be entered. This window is shown in Figure A5.4.4. This histogram information is contained in the header of the data runfile and can be automatically obtained by running a preliminary analysis (clicking the 'create $S(Q)$' button) which creates an intermediate file containing the detector bank information. PDFgetN will then ask the user if this information should be accepted and will automatically load it.

With the experimental information all entered, it is now possible to proceed with the analysis by clicking 'create $S(Q)$'. The resulting $S(Q)$ is calculated for each bank. When the program finishes, this information can be viewed using the interactive plotting capability, as shown in Figure A5.4.5. The user can zoom in on different parts of the PDF by defining regions using the mouse. If the data are not properly normalized; i.e. the $S(Q)$ values do not approach unity at high-Q, the effective density can be modified and the analysis rerun. If the $S(Q)$ values from different detector banks do not properly line up with each other, then the data can be scaled bank by bank, or a constant added to a bank, to line the data up. Bank by bank variations require corrections of less than 5% in general and a larger correction may indicate a problem with the data in one of the banks; for example a noisy detector. In this case, banks can be eliminated from the analysis or raw data can sometimes be reprocessed with particular detectors eliminated from the bank. Remember to reprocess the vanadium data, used for normalization, in the same way even if the detectors are all good in

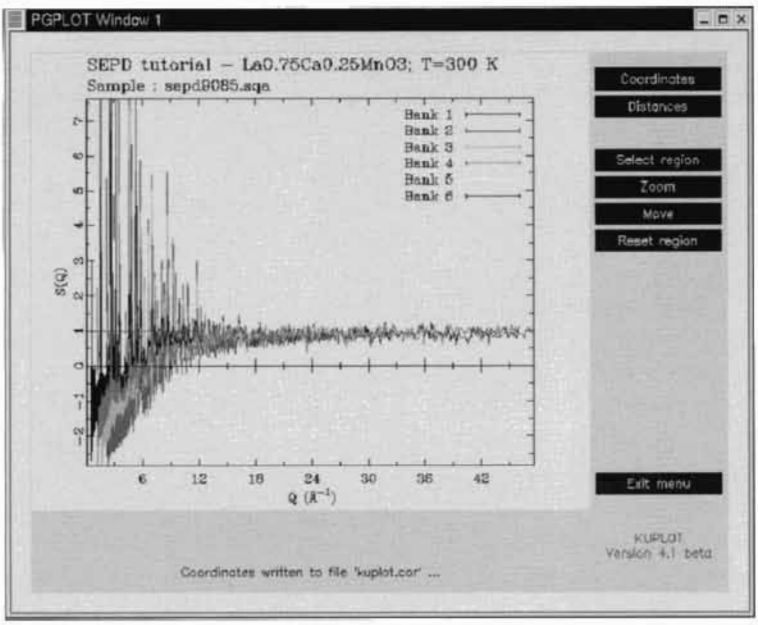

Figure A5.4.5. Plot window for PDFgetN here showing $S(Q)$ from six detector banks. The plot can be zoomed by selecting regions using the mouse. By positioning the cursor and clicking the mouse it is also possible to get coordinates.

the vanadium data-set! $S(Q)$ values that slope at high-Q often indicate problems with the background/empty can subtraction; it might be necessary to change some of the can parameters or scale the background.

Once satisfied with the result, the data can be blended. The range of data to be accepted from each bank is specified in the bank parameters. The bank by bank $S(Q)$ values are then combined into a single $S(Q)$ to improve the overall statistics. The result is shown in Figures A5.4.6 and A5.4.7 in the form of $S(Q)$ and the reduced structure function $Q[S(Q) - 1]$, respectively.

The reduced structure function, $Q[S(Q) - 1]$ oscillates around zero at high-Q. The signal-noise ratio is decreasing with increasing Q in $S(Q)$ because of the Debye–Waller factor. This effect is exacerbated in the reduced structure function, $Q[S(Q) - 1]$ because of the Q-weighting which multiplies the high-Q region by Q which can be as much as a factor of 50! The data are terminated at a value of Q_{max} that is chosen depending on the signal-noise ratio in the reduced structure function. This underscores the importance of getting good statistics in the high-Q region of the data. In this case a $Q_{\max}$ of 24 Å^{-1} was chosen. The data are then Fourier transformed by clicking the 'create $G(r)$' button resulting in the PDF shown in Figure A5.4.8.

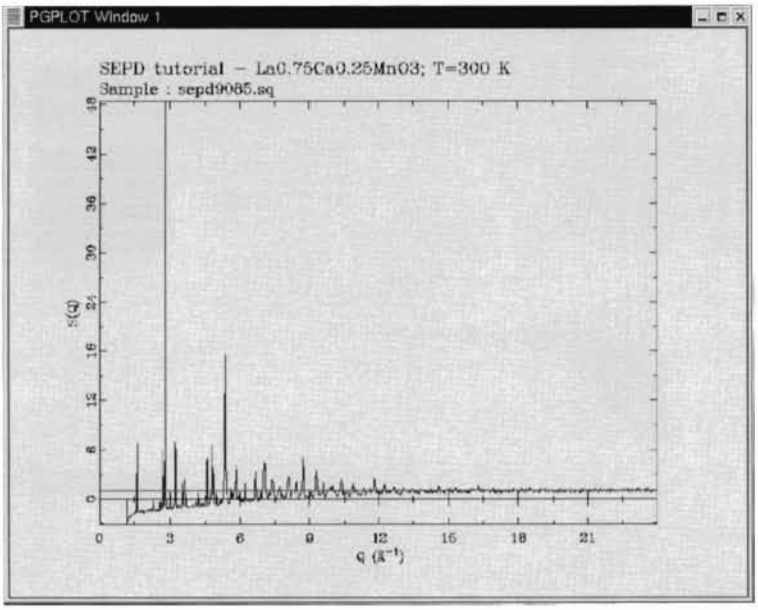

Figure A5.4.6. Blended $S(Q)$ in the PDFgetN plot window.

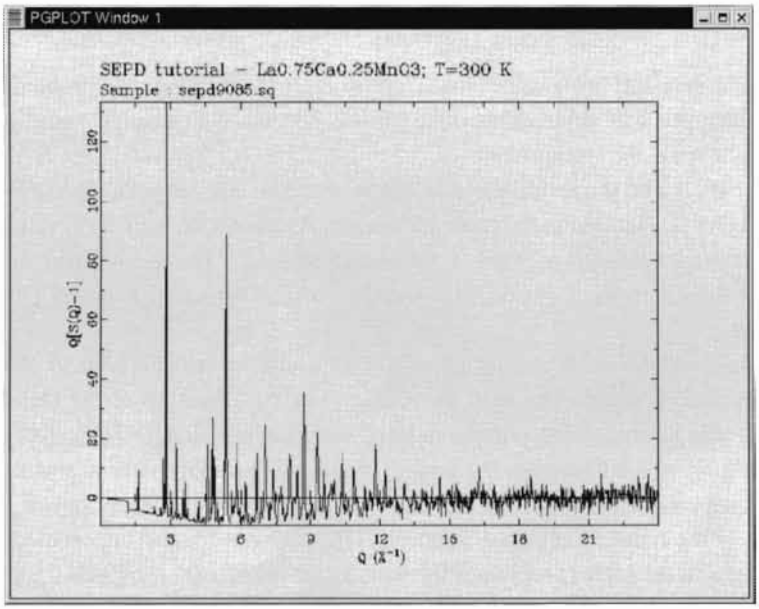

Figure A5.4.7. Same as Figure A5.4.6 but plotted as the reduced structure function, $Q[S(Q) - 1]$.

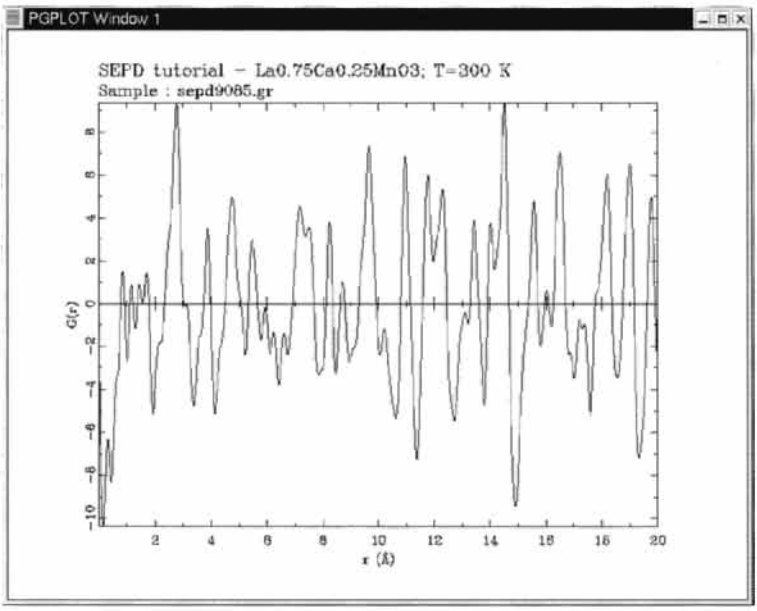

Figure A5.4.8. Reduced pair distribution function, $G(r)$, from the data shown in Figures A5.4.5–A5.4.7, shown in the PDFgetN plot window.

These data from a manganite sample are particularly challenging because of the relatively weak coherent, and strong incoherent, scattering of the sample due to the negative scattering length of manganese. This results in significant backgrounds relative to the coherent scattering intensity so that imperfections in the corrections have an exaggerated effect. The negative scattering length of manganese is evident by the observation of Mn–O and Mn– (La,Sr) peaks which are negative (for example, the peak at 1.9 Å). The imperfect corrections are apparent because the function $G(r)$ does not decrease linearly from the origin with the slope of $-4\pi\rho_0$ in the region below the first peak at 1.9 Å as expected theoretically. In fact, the deviations from this behavior are quite dramatic (and much worse than observed for typical data-sets on better behaved samples). Nonetheless, the data in the structural region are still of high quality. This is borne out by model fits to the data.

REFERENCES

Ankudinov, A.L. & Rehr, J.J. (2000) *Phys. Rev. B*, **62**, 2437.

Blech, I.A. & Averbach, B.L. (1965) *Phys. Rev. A*, **137**, 1113.

Bodek, P., Böni, C., Hilbes, J., Lang, M., Lasakov, M., Lüthy, S., Kistryn, M., Markiewicz, E., Medviediev, V., Pusenkov, A., Schebetov, A., Serebrov, J., Sromicki, & Vasiliev, A. (2000) *Neutron News*, **3**, 29.

Cromer, D.T. & Liberman, D.A. (1970) *J. Phys. Chem.*, **53**, 1891.
Cumbrera, F.L. & Sanchez-Bao, F. (1995) *J. Appl. Cryst.*, **28**, 408.
Dimitrov, D., Röder, H. & Louca, D. (1999) *Phys. Rev. B.*, **60**, 6204.
Doyle, P.A. & Turner, P.S. (1968) *Acta Cryst.*, **24**, 390.
Dwiggins, C.W., Jr. (1972) *Acta Crystallogr. A*, **28**, 155.
Dwiggins, C.W., Jr. & Park, D.A. (1971) *Acta Crystallogr. A*, **27**, 264.
Egami, T. (1978) *J. Mater. Sci.*, **13**, 2587.
Ergun, S. (1968), in *Chemistry and Physics of Carbon*, Ed. Walker, J.P.L., p. 211.
Fox, A.G., O'Keefe, M.A. & Tabbernor, M.A. (1989) *Acta Cryst. A*, **45**, 786.
Hannon, A.C., Howells, W.S. & Soper, A.K. (1990) in *Neutron Scattering Data Analysis, Institute of Physics Conference Series*, **107**, 193.
Howe, M.A., McGreevy, R.L. & Howells, W.S. (1989) *J. Phys: Condens. Matter*, **1**, 3433.
Howells, W.S. (1984) *Nucl. Instrum. Meth.*, **219**, 543.
Howells, W.S. (1985) *Nucl. Instrum. Meth.*, **235**, 553.
Howells, W.S. (1986) Rutherford Appleton Laboratory Report, RAL-86-042.
Hubbell, J.H. & Seltzer, S.M. (1997) Tables of X-ray Mass Attenuation Coefficients and Mass Energy-Absorption Coefficients (version 1.03), [Online]. Available: http://physics.nist.gov/xaamdi [2002, February 25]. National Institute of Standards and Technology, Gaithersburg, MD. Originally published as NISTIR 5632, National Institute of Standards and Technology, Gaithersburg, MD (1995).
Ida, T. & Toraya, H. (2002) *J. Appl. Cryst.*, **35**, 58.
Ino, T. (1957) *J. Phys. Soc. Jpn.*, **12**, 495.
Kaplow, R., Strong, S.L. & Averbach, B.L. (1965) *Phys. Rev. A*, **138**, 1336.
Kaszkur, Z. (1990) *J. Appl. Cryst.*, **23**, 180.
Kendig, A.P. & Pings, C.J. (1962) *J. Appl. Phys.*, **36**, 1692.
Kissel, L., Zhou, B., Roy, S.C., Sengupta, S.K. & Pratt, R.H. (1995) *Acta. Crystallogr. A*, **51**, 271.
Klug, H.P. & Alexander, L.E. (1968) *X-ray Diffraction Procedures for Polycrystalline and Amorphous Materials*, Wiley, New York.
Laaziri, K., Kycia, S., Roorda, S., Chicoine, M., Robertson, J.L., Wang, J. & Moss, S.C. (1999) *Phys. Rev. B*, **60**, 13520.
Leadbetter, A.J. & Wright, A.C. (1972) *J. Non-Crystal. Solids*, **7**, 141.
Lorch, E. (1969) *J. Phys. C*, **2**, 229.
Louca, D. (2003) *J. Phys. Chem. Solids*, **64**, 343.
Lovell, R., Mitchell, G.R. & Windle, A.H. (1979) *Acta Cryst. A*, **35**, 598.
Lovesey, S.W. (1984) *Theory of Neutron Scattering from Condensed Matter*, Oxford Science Publications.
Narayan, R. & Ramaseshan, S. (1979) *J. Appl. Cryst.*, **12**, 585.
Nield, V.M. & Keen, D.A. (2001) *Diffuse Neutron Scattering from Crystalline Materials*, Oxford Science Publications, Oxford.
Paalman, H.H. & Pings, C.J. (1962) *J. Appl. Phys.*, **33**, 2635.
Paalman, H.H. & Pings, C.J. (1963) *Rev. Mod. Phys.*, **35**, 389.
Peterson, P.F., Gutmann, M., Proffen, Th. & Billinge, S.J.L. (2000) *J. Appl. Crystallogr.*, **33**, 1192.
Peterson, P.F., Bozin, E.S., Proffen, Th. & Billinge, S.J.L. (2003) *J. Appl. Crystallogr.*, **36**, 53.
Petkov, V. & Danev, R. (1998) *J. Appl. Cryst.*, **31**, 609.
Petkov, V., Billinge, S.J.L., Shastri, S.D. &, Himmel, B. (2000a) *Phys. Rev. Lett.*, **85**, 3436.
Petkov, V., Jeong, I.-K., Mohiuddin-Jacobs, F., Proffen, Th. & Billinge, S.J.L. (2000b) *J. Appl. Phys.*, **88**, 665.

Placzek, G. (1952) *Phys. Rev.*, **86**, 377.
Poncett, P.F.J. (1977) *ILL Internal Report*, 77PO139S.
Powles, J.G. (1973) *Mol. Phys.*, **26**, 1325.
Price, D.L. & Saboungi, M.-L. (1998) in *Local Structure from Diffraction*, Eds. Billinge, S.J.L. & Thorpe M.F., Plenum, New York, p. 23.
Prince, E. (1982) *Mathematical Techniques in Crystallography and Materials Science*, Springer-Verlag, New York.
Pusztai, L. & McGreevy, R.L. (1997) *Physica B*, **234–236**, 357.
Ruland, W. (1964) *Br. J. Appl. Phys.*, **15**, 1301.
Sears, V.F. (1975) *Adv. Phys.*, **24**, 1.
Serimaa, R., Pitkanen, T., Vahvaselka, S. & Paakkari, T. (1990) *J. Appl. Crystallogr.*, **23**, 11.
Soper, A.K. & Egelstaff, P.A. (1980) *Nucl. Instrum. Meth.*, **178**, 415.
Soper, A.K., Howells, W.S. & Hannon, A.C. (1989) *Rutherford Appleton Laboratory Report*, RAL-89-046.
Soper, A.K. (1990) in *Neutron Scattering Data Analysis, Institute of Physics Conference Series*, **107**, 57.
Terwilliger, T.C. (1994) *Acta Crystallogr. D*, **50**, 11–16.
Thijsse, B.J. (1984) *J. Appl. Cryst.*, **17**, 61.
Tucker, M.G., Dove, M.T. & Keen, D.A. (2001) *J. Appl. Crystallogr.*, **34**, 780.
Waasmaier, D. & Kirfel, A. (1995) *Acta. Crystallogr. A*, **51**, 416.
Warren, B.E. (1990) *X-ray Diffraction*, Dover, New York.
Waser, J. & Schomaker, V. (1953) *Rev. Mod. Phys.*, **25**, 671.
Wilson, A.J.C., Ed. (1995) *International Tables for Crystallography*, Ed. Vol. C, Kluwer Academic Press, Dordecht.
Yarnell, J.L., Katz, M.J., Wenzel, R.G. & Koenig, S.H. (1973) *Phys. Rev. A*, **7**, 2130.

SELECTED BIBLIOGRAPHY

Overviews of data corrections:

Warren, B.E. (1990) *X-ray Diffraction*, Dover, New York.
Klug, H.P. & Alexander, L.E. (1968) *X-ray Diffraction Procedures for Polycrystalline and Amorphous Materials*, Wiley, New York.
Wagner, C.N.J. (1978) *J. Non-Crystal. Solids*, **31**, 1.
Waseda, Y. (1980) *The Structure of Non-Crystalline Materials*, McGraw-Hill, New York.
Pynn, R. (1990) *Neutron Scattering—a primer, Los Alamos Science* #19 (1990). Excellent background on neutron scattering in general.
Howe, M.A., McGreevy, R.L. & Howells, W.S. (1989) An excellent and highly readable summary of data corrections for time of flight neutron experiments. *J. Phys: Condens. Matter*, **1**, 3433.
Nield, V.M. & Keen, D.A. (2001) *Diffuse Neutron Scattering from Crystalline Materials*, Ch. 5, Oxford Science Publications, Oxford.
Wright, A.C., Vessal, B., Bachra, B., Hulme, R.A., Sinclair, R.N., Clare, A.G. & Grimley, D.I. (1995), in *Neutron Scattering for Materials Science II*, Eds. Neumann, D.A. & Russell T.P.

Program manuals:

Jeong, I.-K., Thompson, J., Proffen, Th. & Billinge, S.J.L. (2000) *PDFgetX Users Manual*. Available from the PDFgetX download page of http://www.totalscattering.org.

Soper, A.K., Howells, W.S. & Hannon, A.C. (1989) Rutherford Appleton Laboratory Report, RAL-89-046, *The excellent ATLAS program manual*.

Gutmann, M., Proffen, Th., Peterson, P.F. & Billinge, S.J.L. (2000) *PDFgetN Users Manual*. Available from the PDFgetN download page of http://www.totalscattering.org.

Chapter 6

Extracting Structural Information from the PDF

This Page Intentionally Left Blank

Chapter 6
Extracting Structural Information from the PDF

6.1. INTRODUCTION

The experimentally derived PDF is an absolute function: the data have been properly normalized and the absolute, rather than the relative, intensities of the peaks are meaningful. A great-deal of structural information can therefore be deduced directly from the data without resorting to models. Ultimately, the most information is obtained from the PDF by structural modeling: calculating the PDF from structural models and comparing them to the data. The structural origin of different features of the PDF function can be understood by careful consideration of the equations which define the PDF (Section 3.1). This is explicitly described in Section 6.2. Different approaches for modeling the data using regression techniques are described in Section 6.3. Finally, in Section 6.4, we describe some of the more subtle information that is present, and can be extracted from the PDF, by careful analysis.

6.2. DIRECT INFORMATION

6.2.1 The PDF from a structure

The relationship between an atomic structure (i.e. an arrangement of atoms in space) and the PDF was discussed in Chapter 3. We reiterate this argument here since it is highly pertinent to the discussion of obtaining structural information from the PDF. First, assume we have a model for our sample that consists of a set of N-atoms at positions $\mathbf{r}_n$ with respect to some origin. Intuitively, we obtain the PDF in the following way. We first choose an atom at random and place the origin of our space at the position of that atom. We then systematically find every other atom in the sample and measure the distance from the origin-atom to that atom. Each time we find an atom we place a unit of intensity at the position $r_m = |\mathbf{r}_m|$ on the axis of our function $R(r)$.We continue this until we have found every atom in the sample. We then move the origin of our space to another atom and repeat the process adding intensity to the same $R(r)$ function. This is systematically repeated until every atom in the sample has had its turn at the origin. To keep $R(r)$ as an intrinsic function (independent of sample size) it is divided by N to normalize it. If all the atoms in the sample are of the same chemical species, this is the end of the story. To take into account the different scattering powers of different chemical species, we multiply the unit of intensity for each atom-pair by $b_m b_n/\langle b\rangle^2$ where b_i is the scattering length of the ith atom.

Mathematically, this can be expressed as in Eq. 3.5:

$$R(r) = \frac{1}{N} \sum_{mn} \frac{b_m b_n}{\langle b \rangle^2} \delta(r - (r_n - r_m)). \tag{6.1}$$

To understand how this works in practice it is useful to consider a simple example. Let us consider a crystalline single-element material; for example, the neutron scatterers' favorite, nickel. A typical neutron sample is a fine powder which can be as much as 10 g. Such a sample contains $\sim 10^{23}$ atoms. To properly calculate $R(r)$ we would therefore need to carry out a double-sum over this many atoms; clearly impractical. Two things help us in practice. First, we are generally only interested in calculating $R(r)$ over a relatively narrow range or r, say 20 Å. Thus, we still need to put the origin on each of the 10^{23} atoms in turn, but the second sum need only be taken over atoms that lie within 20 Å of the origin-atom. Second, the material in question is crystalline. In this case the total sample is made up of many equivalent unit cells which are periodically repeated in space. In this favorable situation we need only place the origin on each atom in the unit cell since the equivalent atom in all the other unit cells has exactly the same atomic environment. This is now a computationally tractable problem: a double sum where the first sum is taken over the atoms in the unit cell (< 100 typically) and the second sum over all atoms within $r_{\max}$ of the origin atom where $r_{\max}$ is the maximum extent over which the PDF is to be calculated.

6.2.2 Direct information from the PDF

6.2.2.1 Atom-pair separation from peak positions. It is clear from this description that the PDF is a heavily averaged representation of the structure. First, directional information is lost since we consider only $r_n - r_m$ and not $\mathbf{r}_n - \mathbf{r}_m$. Second, it is a linear superposition of the local environments of many atoms; more than 10^{20} in fact! How can such a function contain any useful information at all? The reason is that, especially on very short length-scales, the possible environments of particular atoms are very limited. In Ni for example, all the atoms have the same nearest-neighbor distance, r_{nn}, if we neglect thermal vibration. There will be no intensity in $R(r)$ for $r < r_{nn}$ and a sharp peak at r_{nn}. This behavior is very general and true even in atomically disordered systems such as glasses, liquids and gasses. The second neighbor distance is generally less well defined, the PDF peak will be broader, but will still be apparent even in disordered materials. In crystals, because of the long-range order of the structure, all neighbors at all lengths are well defined and give rise to sharp PDF peaks. The position of these peaks gives the separations of pairs of atoms in the structure directly.

6.2.2.2 Coordination number from peak integrated intensity. It is clear from Eq. 3.5 that if a well-defined PDF peak can be observed, we can determine the coordination number of the origin atom by integrating the intensity under that peak. The correlation

function which yields the coordination number directly by integration is $R(r) = 4\pi r^2\rho(r)$. This is related to $G(r)$, the function obtained directly from the Fourier transform of the data, by $R(r) = r[G(r) + 4\pi r\rho_0]$. In the case of crystalline Ni there are four Ni atoms in the unit cell (fcc structure). Each nickel ion has 12 neighbors at 2.49 Å (Wyckoff, 1963). When we construct our PDF we will therefore place 48 units of intensity at position $r = 2.49$ Å (the weighting factor, $b_m b_n/\langle b\rangle^2$, is unity since there is only one kind of scatterer) and divide by $N = 4$ since we put four atoms, respectively, at the origin. Thus, integrating the first peak will yield 12 which is the coordination number of Ni. The same information can be obtained from multi-element samples if the chemical origin of the PDF peak, and therefore the weighting factor, is known. If, as is often the case, PDF peaks from different origins overlap this process is complicated. Information can be extracted by measuring the chemical specific differential or partial-PDFs directly (see Chapter 3) or with less certainty by fitting the peaks with a series of Gaussian functions. As we discuss later, full-scale structural modeling largely overcomes the problem of PDF peak overlap, at least in crystalline materials.

6.2.2.3 Atom-pair probability distribution from the peak-shape. The PDF is made up of a sum of well-defined delta-functions. In the real material (and therefore in the experimentally derived PDF) the sums are taken over the entire sample. Atomic disorder in the form of thermal and zero-point motion of atoms and any static displacements of atoms away from ideal lattice sites give rise to a distribution of atom–atom distances. The PDF peaks are therefore broadened resulting in Gaussian shaped peaks.[1] The width, and shape, of the PDF peaks therefore contains information about the real atomic probability distribution. In the case where a probability distribution is non-Gaussian, for example, if the atomic potential is multi-welled and atoms in the solid occupy each well in some disordered fashion, the PDF will reflect this and in principle this information can also be extracted from the PDF by an analysis of the PDF peak-shape.

To summarize, there are three independent pieces of information which are contained in a PDF peak: its position gives the average separation of the pair of atoms in question; its integrated intensity yields the coordination number of that pair of atoms; and the width and shape of the peak gives the underlying atomic probability distribution.

6.2.3 Examples

6.2.3.1 Peak position. The peak position yields bond-lengths directly. One clear example where this has proved to be useful is in understanding the local atomic structure of semiconductor alloys, as introduced in Section 1.2.1. In $In_{1-x}Ga_xAs$ the metal-ion

[1] The PDF peaks, even from Gaussian atomic probability distributions, are actually slightly non-Gaussian. However, the deviations from Gaussian are negligibly small as discussed in Section 6.4.

sublattice contains a random solid-solution of indium and gallium atoms which have very different covalent radii. The material on the whole forms a long-range-ordered crystal structure. However, the In/Ga bond-length obtained from the average crystal structure bears little resemblance to the real, local, bond lengths in the material: locally, In–As and Ga–As pairs have bonds that are close to their length in the endmember compounds. The two distinct bond-lengths (In–As and Ga–As) are different by $\sim$0.14 Å and can be resolved in a high-resolution PDF measurement. Then, by fitting two Gaussian functions (suitably convoluted with a Sinc function to account for termination effects in the Fourier transform), the evolution of the local bond lengths with alloy composition could be directly elucidated (Petkov *et al.*, 1999). This is shown in the so-called '*Z*-plot' in Figure 1.3. The inset shows the nearest-neighbor PDF peak which is clearly resolved into two features. The Gaussian fits are also shown. The main panel shows the evolution of the InAs and GaAs bond lengths with alloy composition obtained from these peak fits. Also shown are earlier results of XAFS (Mikkelson and Boyce, 1984) who were the first to observe this phenomenon experimentally. There is excellent agreement between the XAFS and the PDF data. Beyond the *Z*-plot, the PDF data have allowed different structural models for the local structure of the semiconductor alloy to be differentiated (Jeong *et al.*, 2001; Peterson *et al.*, 2001).

Another elegant example of the use of the PDF to measure local bond-lengths directly was demonstrated by Dove *et al.* (1997) in crystalline phases of silica and introduced in Section 1.2.5. The low temperature crystalline form of silica is α-quartz. It is made up of corner shared SiO_4 tetrahedra with a physically reasonable Si–O bond-length of 1.61 Å and a Si–O–Si bond angle of 144 degrees. As temperature increases, the Si–O–Si bond angle increases and the Si–O bond length decreases. The sample then transforms first into β-quartz, HP-tridymite and then β-cristobalite on further heating (Keen, 1998). The latter two phases both have Si–O–Si bond angles of 180°, known to be chemically unfavorable, and an unphysical Si–O bond length of 1.54 Å. Large thermal factors are also seen in the crystal structure refinements. An analysis of the PDF from these materials immediately shows (Figure 1.11) that the local Si–O and O–O bonds are significantly longer than those obtained from the average crystal structure. Furthermore, as a function of temperature the Si–O bond length determined from the PDF increases very slightly even though the average value obtained crystallographically is smoothly decreasing as the phase transition to β-cristobalite is approached (Tucker *et al.*, 2000). As in the semiconductor alloys, in silica the O ions do not lie on lattice sites of the crystallographic model but are displaced away from them in a disordered way. These examples illustrate convincingly, and in a model independent way, that the PDF contains *additional* information beyond the average structure in crystalline materials and that this information can be reliably recovered experimentally. Detailed modeling, as we describe later in the chapter, reveals a great-deal of additional information beyond this model independent analysis.

6.2.3.2 Integrated intensity in PDF peaks. The integrated intensity under a PDF peak yields the coordination number of that atom–atom correlation (the number of neighbors at a specific distance). This type of analysis is widely used in studies of glasses (Waseda, 1980); however, we will give two examples from partially crystalline samples. The first example is from disordered nanoporous carbon. Some of the earliest ever PDF studies were carried out on carbon blacks by Warren (1934). There is currently renewed interest in disordered carbons because of their potential uses for storing lithium in battery applications. A number of recent studies use the PDF method to study the local structure of disordered carbons (Claye and Fischer, 1999; Petkov *et al.*, 1999). In the latter study nanoporous disordered carbon is made by pyrolyzing poly furfuryl alcohol by heating it in an inert atmosphere. This produces a carbonaceous product which is more or less disordered depending on the temperature of pyrolysis. A PDF study showed that a 1200°C treatment produced almost perfect graphene sheets; an 800°C treatment introduced significant disorder into the sheets in the form of greater sheet fragmentation and non-6-membered rings. A 400°C treatment resulted in highly distorted carbon planes bearing little resemblance to graphitic material and more resembling the alcohol starting material. The data PDFs are shown in Figure 6.1. Two key pieces of evidence revealed the nature of the disorder in the 800°C sample. First, the integrated intensity of the first C–C peak fell from having 3.0 neighbors in the 1200°C sample to having 2.6 neighbors in the 800°C sample. Second, the third PDF peak, coming from the C–C bond diametrically across the six-member ring in graphite, became broader and lost intensity in the 800°C sample. This suggests the loss of, and an increased distribution of, third-neighbor correlations,

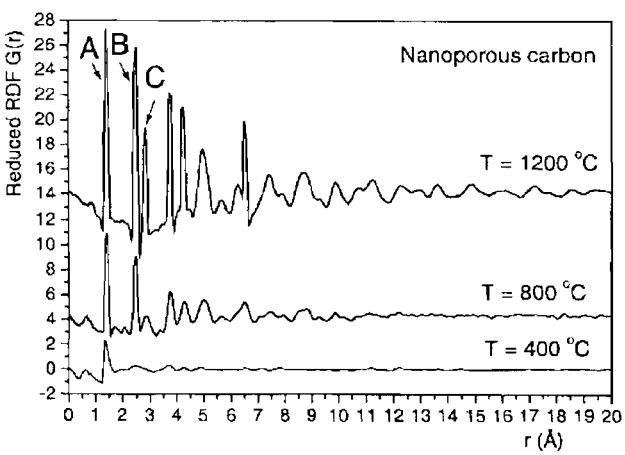

Figure 6.1. PDFs from disordered carbon made by pyrolyzing poly furfuryl alcohol at different temperatures (Petkov *et al.*, 1999). These PDFs were created by Fourier transforming the $S(Q)$ data shown in Figure 9.16(b).

at this position diagonally across the ring; a tell-tale indication for the presence of higher-membered rings in the structure (Figure 6.1). The graphene sheets are thus becoming fragmented and higher neighbor rings are being introduced. In a TEM image the sheets indeed appear more curved in this sample; a by-product of the presence of non-6-member rings. The near-neighbor C–C peak in the 400°C sample when integrated indicated 1.9 neighbors. This number is somewhat uncertain because this peak is not fully resolved in the structure; however, it is a clear indication that the graphene sheets are highly fragmented and even that the structure is closer to the polymeric starting material (2 carbon–carbon near neighbors) than the graphitic product. Again, additional information was elucidated from modeling, but significant knowledge of the structure could be deduced directly from the PDF.

Another example of the study of the integrated intensity of PDF peaks is the search for Jahn–Teller distorted MnO_6 octahedra in $La_{1-x}Sr_xMnO_3$ (Louca and Egami, 1999). Mn^{3+} is a Jahn–Teller ion: MnO_6 octahedra containing Mn^{3+} will spontaneously elongate (4 short Mn–O bonds and 2 long bonds) to lower the electronic energy of the system. On the other hand, Mn^{4+} is not a Jahn–Teller ion; MnO_6 octahedra containing Mn^{4+} will remain regular (six equal Mn–O bonds). As the strontium content of $La_{1-x}Sr_xMnO_3$ is increased, the number of Mn^{4+} species increases. Louca *et al.* (1997) showed that the integrated intensity in the low-r portion of the PDF double-peak coming from the Mn–O bonds increased linearly with doping (Figure 6.2). This is because, locally, Mn^{4+} and Mn^{3+} containing octahedra are coexisting and the number of *short* Mn–O bonds is smoothly increasing from four in the case of fully Mn^{3+}, to six in the case of fully Mn^{4+}, containing material. Interestingly the slope of the curve of number-of-short-bonds vs. strontium content is different at low and high temperature suggesting a change in the degree of carrier localization as a function of temperature.

6.2.3.3 PDF peak width. The width of PDF peaks reveals information about the static and dynamic disorder of atoms involved in the pair. Measuring the peak width as a function of temperature gives information about the Debye temperature of a bond; the width as a function of atomic separation yields information about correlated atom dynamics which, in turn, reveals information about the underlying atomic potential; the width as a function of doping gives information about doping induced disorder; and so on. In the manganite system $La_{1-x}Ca_xMnO_3$, sister to the manganite system described in the previous paragraph, a sharp deviation from canonical Debye behavior of the PDF peak width with temperature was observed (Figure 1.10) (Billinge *et al.*, 1996). This deviation correlated with the metal–insulator transition temperature in this material, which gave strong evidence for the appearance of lattice polarons and carrier localization at this phase transition. In the figure the peak width is not plotted directly but the PDF peak height is. The width can be extracted by fitting Gaussian functions or more commonly Gaussians convoluted with a Sinc function to account for termination effects. However, because the

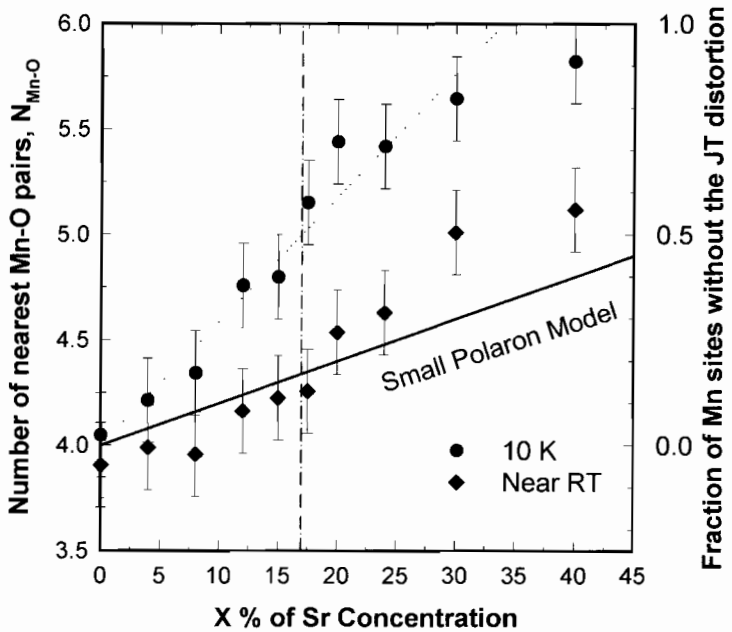

Figure 6.2. The number of short Mn–O bonds per Mn ion for $La_{1-x}Sr_xMnO_3$ determined by integrating the PDF, N_{Mn-O}, presented as the fraction of the Mn site without JT distortion, $\eta = (N_{Mn-O} - 4)/2$, as a function of x for $T = 10$ and 300 K (above T_C), except for $x = 0.3$ (320 K), 0.4 (350 K). The line named small polaron line connects $N_{Mn-O} = 4$, $\eta = 0$ for $x = 0$ and $N_{Mn-O} = 6$, $\eta = 1$ for $x = 1$ (Louca *et al.*, 1997, Egami and Louca, 2000).

number of neighbors is constant the integrated area under the peak is invariant and the peak height, extracted directly from the data, gives the inverse peak width. This can often give a more accurate determination of the peak width, especially when plotting trends such as temperature dependence, than carrying out Gaussian fitting.

The PDF peak width as a function of atomic separation, r, has been studied in a metallic and a semiconducting system (Jeong *et al.*, 1999). Peak widths were extracted by fitting Gaussians convoluted with Sinc functions. The peak width increases with r following a curve with a $(1 - 1/r^2)$ dependence (Figure 6.3). The sharpening of the low-r peaks arises because in a solid the neighboring atoms tend to move in a correlated fashion because they are directly bonded to each other. The strain field around a misfitting impurity in an elastic continuum is expected to fall off continuously as $1/r^2$ which explains why the correlations also die off somewhat continuously as they do. Interestingly, the peak widths deviate from the smooth curve and potential based modeling shows that these deviations are real. Certain directions in the solid (in the semiconductor alloys it is the $\langle 110 \rangle$ directions) are more stiffly bonded and displacement correlations extend further in these directions leading, for example, to the anomalously sharp fifth peak in the InAs PDF.

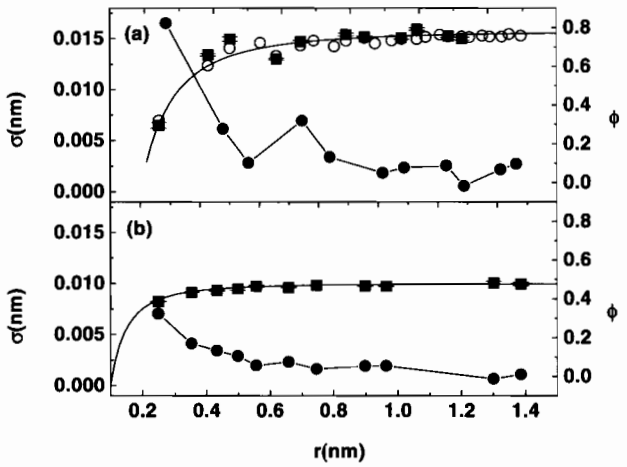

Figure 6.3. *r*-Dependence of the PDF peak width. Peaks at low-*r* become sharpened (σ becomes smaller) due to correlated atomic motion. (a) InAs and (b) Nickel were measured using high-energy X-rays at CHESS. Also shown is a correlation parameter (see Jeong *et al.*, 1999 for the definition) that is a measure of how correlated is the atomic motion. For near-neighbor atoms in InAs the motions are 80% correlated.

The width of the Cu–O bond as a function of doping in $La_{2-x}Sr_xCuO_4$ has also been used to probe the homogeneity of the electronic state in this high temperature superconducting material as described in Section 1.2.3 (Bozin *et al.*, 2000).

6.3 MODELING THE PDF

In the previous section, we described how structural information can be obtained in a model-independent way from the PDF. In practice, the most information, and the most quantitatively reliable information, is obtained by fitting structural models to the data. The method for calculating a PDF from a structural model was discussed in detail in Section 6.2. Once the model-PDF has been calculated it can be compared to a PDF derived from data to assess how good the structural model is. At this point it is typical to quantify the 'goodness-of-fit' with a suitably defined residuals-function. Two different models can then be compared with each other by comparing their goodness of fit. The model with the lower goodness-of-fit parameter is the better model; the difference between the models is significant if the difference in the goodness of fit exceeds the uncertainty in this parameter coming from the random errors in the data. This trial-and-error approach to finding a good model can then be automated using some regression technique where model parameters are allowed to vary, subject to certain user-defined constraints, and these variations continue until a minimum is found for the goodness-of-fit parameter.

There are two different philosophies used for calculating models and there are a wide range of different approaches used for the minimization procedure. The first approach for calculating the model is to specify the smallest possible unit cell that explains the structure and to calculate the PDF from this unit cell. Distributions in the atomic distances are accounted for by convoluting the resulting calculated PDF with Gaussian functions. The basic unit cell is periodically repeated in space as far as is necessary to calculate the PDF to the required r_{max}. The other basic approach is to model the sample as a large box of atoms which is much larger than the range over which the PDF is to be calculated. In this approach the atomic distributions are either explicitly included in the distribution of atom positions in the box, or if the box does not contain enough atoms to give smooth distributions the convolution approach can also be used. Often, both approaches of accounting for the atomic disorder are used together.

It should be pointed out that once a structural model has been defined, both the scattering in Q-space and the PDF can easily be calculated. Since the PDF is simply the Fourier transform of the total scattering structure factor, $S(Q)$, either approach should yield the same information and there is often debate about which approach is superior. Although, in principle, it is true that $S(Q)$ and the PDF contain the same information there are some pertinent differences between the two representations and it turns out that, from a practical point of view, the two representations lend themselves to being modeled in different ways. Depending on the question being asked, the answer is often more accurately determined in one representation or the other. Even though in principle you could, you would not attempt to change the oil on your car from under the hood, or change the spark plugs by lying under the car. In the same way, the total scattering yields its various pieces of information more readily either in real- or reciprocal-space depending on which piece of information is being sought. In the following sections we describe different modeling approaches in more detail and this discussion will be made more concrete at this point.

6.3.1 Real-space Rietveld analysis

The Rietveld full-profile fitting method (Rietveld, 1969) for extracting structural information from crystalline powder diffraction patterns has revolutionized the use of powder diffraction for structure studies (Young, 1993). Whilst powder diffraction is not the method of choice for determining new structures (although it can be, and is, used in certain circumstances), its simplicity and the ease of making samples, collecting and analyzing the data, make it by far the most widely used method for refining accurate structural parameters for a given sample under varying conditions. Furthermore, because the problem of extinction (a dynamical scattering effect) is much smaller in powder than single-crystal diffraction, once the gross-features of a structure have been determined from single-crystals, the quantitative fine details are often determined by crushing up the single-crystal and doing a powder measurement!

The Rietveld method (Rietveld, 1969) was motivated by the fact that in a powder measurement many of the Bragg-peaks are overlapped especially in the high-Q (small d-spacing) region of the pattern. Apart from the inherent loss of directional information in a powder measurement, this fact severely limited the set of data-points that could be obtained by integrating the intensity of separated Bragg-peaks to obtain the crystallographic structure factors needed for crystal structure solution. The Rietveld approach was to calculate the complete set of crystallographic structure factors, and therefore the Bragg-peak intensities and positions, for a trial structure. These were then convoluted with profile functions to account for the instrument resolution and sample-dependent peak broadening effects. The intensities were modulated with experimental effects such as absorption, extinction, incident flux, background intensities and so on and sample dependent effects such as Debye–Waller factors. In this way the entire experimental data-set was simulated and compared to the measured one. All of the above mentioned effects are parameterized and the parameters are allowed to vary until a best-fit is obtained, traditionally, using a least-squares approach. The sample dependent parameters thus derived include the unit cell parameters (unit cell lengths and angles), atomic positions in the unit cell expressed in fractional coordinates, anisotropic thermal ellipsoids for each atom and the average atomic occupancy of each site.

This approach has been applied, in exact analogy, to the PDF (Proffen and Billinge, 1999; Billinge, 1998) in the program PDFFIT. We highlight here the similarities and differences with conventional Rietveld. The main similarity is that the model is defined in a small unit cell with atom positions specified in terms of fractional coordinates. The refined structural parameters are exactly the same as those obtained from Rietveld. The main difference from conventional Rietveld is that the *local* structure is being fit which contains information about short-range atomic correlations. There is additional information in the data, which is not present in the average structure, about disordered and short-range ordered atomic displacements. To successfully model these displacements it is often necessary to utilize a 'unit cell' which is larger than the crystallographic one. It is also a common strategy to introduce disorder in an average sense without increasing the unit cell. For example, in the case where an atom is sitting in one of two displaced minima in the atomic potential, its probability of being in either well is random, can be modeled as a split atomic position with 50% occupancy in each well. This is not a perfect, but a very good, approximation of the real situation and is very useful as a first order attempt at modeling the data.

This 'Real-space Rietveld' approach is proving to be very useful and an important first step in analyzing PDFs from crystalline materials. This is because of two main reasons. First, its similarity with traditional Rietveld means that a traditional Rietveld derived structure can be compared *quantitatively* with the results of the PDF modeling. This is an important first step in determining whether there is significant evidence for local distortions beyond the average structure. The Rietveld model is refined to the PDF without

relaxing any of the symmetry constraints of the crystallographic model. The resulting fit can be assessed to look for significant deficiencies. In addition, the refined parameters can be compared directly with the results from Rietveld to make sure they are consistent. If evidence exists to suggest that local structural distortions beyond the average structure are present, these can then be incorporated in the PDF model. The second strength of the real-space Rietveld approach is the simplicity of the structural models making it quick and straightforward to construct the structural models and making physical interpretations from the models similarly quick and straightforward.

Why might one want to analyze a well-ordered crystalline material in real-space? In this case, there is no diffuse scattering in the diffraction pattern and there seems little advantage in going for the PDF. In fact, it can still be a worthwhile exercise for the reason illustrated with the oil-change analogy in Section 6.2. Below we describe three reasons for carrying out a real-space Rietveld refinement on a well-ordered material, beyond the obvious advantages that are apparent if disordered local atomic displacements are present.

Local structural parameters, such as thermal factors and anharmonicities in the crystal potential, may be more accurately determined in real-space than reciprocal space. On the other hand, average structure parameters, such as lattice parameters, are much more accurately obtained in Q-space. As a concrete example, let us consider thermal (or more precisely displacement) factors. The atomic thermal parameters are measured by considering the monotonic Gaussian fall-off in intensity of Bragg-peaks: the Debye–Waller factor. For a sample with a high Debye temperature, this fall-off can be quite slow. For example, a $U_{ii} = 0.0025$ Å^{-2} results in a Debye–Waller envelope with a standard deviation (half-width) of $\sigma = 14$ Å^{-1}. Many Rietveld refinements are not carried out over a range beyond 14 Å^{-1} ($d = 0.45$ Å) because of the problem of Bragg-peak overlap at high-Q. On the other hand, PDFs are routinely measured taking a range of data up to 30 Å^{-1} and beyond. Furthermore, the arbitrary background function used in most Rietveld refinements is extrapolated into the high-Q region where it cannot be separated explicitly from the data. A small error in the background at high-Q can have a significant effect on the refined thermal factor because of the low intensity in the Bragg-peaks themselves. In a PDF analysis the background is extracted explicitly. Similar arguments apply to other slowly Q-varying experimental effects such as absorption and multiple scattering. It is therefore to be expected that more reliable thermal factors can be obtained from a PDF analysis than from a Rietveld refinement; though it is clearly true that if Rietveld was carried out on a corrected $S(Q)$ function (as will increasingly happen in the future) over the same range of Q as the PDF analysis, the resulting thermal factors will have similar accuracy. To date, no quantitative comparison of the relative accuracy of Rietveld and PDF derived thermal parameters has been carried out. Where the values have been compared they are in rather good agreement with the PDF derived parameters showing less of a tendency to yield unphysical values (for example becoming negative) (Gutmann *et al.*, 2000; Proffen *et al.*, 1999). However, when a series of data-sets collected as a function of

temperature are compared more scatter is apparent in the PDF derived values than the Rietveld (Gutmann, Radaelli and Billinge, unpublished). The reason is not clear though it may result from inadequate (simple Gaussian!) profile functions being used in the PDF refinements and the situation may improve as the sophistication of the PDF modeling approaches that of Rietveld, the more mature technique.

Another possible reason to carry out a real-space Rietveld analysis on an well-ordered crystal is that the structural parameters are differently correlated in real- and reciprocal-space refinements because the equations to calculate the signal from the model are different. In any refinement, different refinement variables can become significantly correlated with each other and each one can take on an unphysical value which, nonetheless, when applied together reproduces the data well. This is true in real- and reciprocal-space refinements. However, since the various variables will be differently correlated with each other in the two cases, a joint refinement in real and reciprocal space can remove the correlations. At present there is no joint real- and reciprocal-space refinement code in existence though this will undoubtedly be remedied in the future.

Finally, more precise information about the atomic potential can be gleaned from a real-space analysis in a well-ordered material. This is exemplified by the measurement of atomic potential parameters from the correlated atomic motion in crystals using PDF measurements (Jeong *et al.*, 1998; Dimitrov *et al.*, 1999). Because they are directly bonded, nearest-neighbors tend to move in phase with each other and their motion is positively correlated. If the bond is very stiff the relative motion of these neighbors with respect to each other can be quite small (in covalent semiconductors the nearest neighbor motion is $>80\%$ correlated!). The motion of far neighbors is uncorrelated. The thermal factor measured in a conventional crystallographic refinement is the uncorrelated one. This often reflects the softest bonds in the material. For example, in the semiconductor alloys it reflects the weak bond-bending forces. The stiff bond-stretching force can be measured from the correlated motion of the near neighbors which is obtained from the width of near neighbor peaks in the PDF.

When local atomic displacements away from the average structure exist, and therefore significant diffuse scattering intensity is present in the scattering, a conventional Rietveld refinement becomes inadequate. At this point, a PDF analysis, or a quantitative assessment of the diffuse scattering in Q-space, is required. We note a couple of developments in traditional Rietveld approaches that are currently under way. First is a concerted effort to treat diffuse scattering intensity explicitly in a Q-space Rietveld refinement (Lawson *et al.*, 2000). Second is the desire to carry out Rietveld refinements, not on raw diffraction data, but on corrected data in the form of $S(Q)$ (Radaelli, private communication). The first development is especially useful in cases where it is difficult to obtain a high-quality PDF as was shown by Lawson *et al.* (2000) in a study of plutonium in which a nuclear absorption resonance limits the Q-range of the data and therefore the resolution of the PDF. The second development removes much of the uncertainty in conventional Rietveld

refinements coming from extrinsic effects such as absorption, multiple scattering and backgrounds from Compton scattering in X-rays. The goal is to extend the range of Q over which refinements can be reliably carried out. By explicitly correcting for these experimental effects, as is routinely done in a PDF analysis, the Rietveld refinement can be extended far into the region where Bragg-peaks are significantly overlapped with much greater confidence because no arbitrary background function is being extrapolated into that region.

There are a number of reasons why real-space-Rietveld is not more widely used to study the structure of materials. The main reason is that the technique is in its infancy: its accuracy and the stability and reliability of the results obtained from the codes are only recently being proved. The second reason is that the complimentarity of a PDF refinement and a conventional Rietveld refinement are only now becoming widely appreciated. Without this motivation there is no reason to explore real-space in the study of a well-ordered material. Finally, a Rietveld refinement is carried out on raw powder diffraction data. One has to have a very good reason to embark on a seemingly complicated and arcane data analysis procedure as is required for PDF analyses. To date, there are few user-friendly and straightforward to use data analysis packages. However, as we pointed out in the previous paragraph, there is a trend in Rietveld towards analyzing corrected data rather than raw data. GUI (graphical user interface)-based, easy to use data analysis programs for obtaining $S(Q)$ and the PDF, are also now becoming available, as are faster and faster computers. It has never been easier to obtain a PDF than now and so, on this third point, the real- and reciprocal-space communities are beginning to converge. We envisage increasing use of joint real- and reciprocal-space analyses in the future to solve challenging structural problems or to extract more complete structural information from well-ordered materials. As, increasingly, newly discovered materials are tending to be significantly disordered, the use of real-space analyses is expected to increase.

6.3.1.1 Example of real-space Rietveld: PDFfit. The most sophisticated and robust real-space Rietveld code available at the time of writing is the PDFfit code (Proffen and Billinge, 1999). This code allows multiple data-sets to be refined and can handle multiple phases. It has a command-line driven interface allowing great flexibility and user control. Arbitrary constraints can be introduced between the parameters as required, for example, to reproduce the average symmetry of the sample or to allow rigid rotations or translations of sets of atoms. The program also incorporates a FORTRAN style interpreter allowing mathematical formulas to be evaluated dynamically as the program executes. It can be controlled using macros allowing the refinement to be easily automated. The program uses a least-squares minimization procedure and yields parameters with estimated standard deviations associated with them. As with all Rietveld refinements, these tend to be underestimates of the real absolute errors because they do not account for systematic errors

in the data. However, they provide a good baseline for estimating the significance of structural parameters and should be a good estimate of the relative changes of parameters between similar data-sets (e.g. temperature dependence of parameters). We mention one caveat. The e.s.d. on refined parameters are only as good as the estimated random errors on the data themselves. A number of PDF analysis programs propagate random errors from the counting statistics of the measurement and these are a good estimate of the uncertainty on a particular point of the PDF. However, the errors from point to point in the PDF are correlated due to the finite range of the Fourier transform. To properly determine the estimated errors on the data these error correlations should be calculated. In principle this is straightforward, but in practice it is not generally carried out. It is expected that this will be addressed in future codes as the subject of quantitative real-space analysis matures. Interested readers are referred to the downloads section of the total scattering home-page (http://www.totalscattering.org).

The residuals functions used in PDFfit are equivalent to the Rietveld *R*-values. The weighted agreement factor, R_w is defined as

$$R_w = \sqrt{\frac{\sum_{i=1}^{N} w(r_i)[G_{\text{obs}}(r_i) - G_{\text{calc}}(r_i)]^2}{\sum_{i=1}^{N} w(r_i)G_{\text{obs}}^2(r_i)}}, \tag{6.2}$$

where G_{obs} and G_{calc} are the observed and calculated PDFs (in the form of $G(r)$) and w is the weighting factor, $w(r_i) = 1/\sigma^2(r_i)$, where σ is the estimated standard deviation on the ith data-point at position r_i. Note that PDF residuals functions are not strictly statistically significant quantities since neighboring points in the PDF are not statistically independent. This is discussed in more detail in Appendix 5.3. For example, a reliable χ^2 cannot be determined from R_{wp}^{PDF} as it can from a Rietveld refinement by dividing R_{wp} by $(N - P)$ where N are the numbers of points and P the numbers of parameters in the fit. Nonetheless R_{wp}^{PDF} is a quantitative measure of goodness of fit and can be used to compare models and minimized to optimize a model. Points in the PDF separated by $\Delta r \sim \pi/Q_{\text{max}}$ are approximately statistically independent and so a reasonable estimate of χ^2 is possible by taking (Billinge, 1992):

$$\frac{R_{wp}^{\text{PDF}}}{\left(\frac{(r_{\text{max}} - r_{\text{min}})Q_{\text{max}}}{\pi}\right) - P}.$$

6.3.1.2 Real-space Rietveld example: $YBa_2Cu_3O_{6+\delta}$. A long-standing controversy has existed between the diffraction and XAFS communities concerning the existence, or not, of a split atomic site for the apical oxygen ion in the structure of $YBa_2Cu_3O_{6+\delta}$: the oxygen

that lies immediately above the copper ion in the electronically active CuO_2 planes. Such a split site was observed in polarized XAFS measurements (Mustre de Leon *et al.*, 1990), but there was apparently no evidence for it in any Rietveld (Francois *et al.*, 1988; Kwei *et al.*, 1991), or single-crystal, refinements (Sullivan *et al.*, 1993; Schweiss *et al.*, 1994). A number of groups have reproduced the early XAFS result (Booth *et al.*, 1996; Stern *et al.*, 1993), although it is not seen in all samples, making it even more of a puzzle. Of course, XAFS and crystallography measure different things: XAFS local pair correlations and crystallography the average periodic structure. It is clear that the PDF method should be able to speak to this problem since it is a diffraction technique which, nonetheless, measures local atomic pair correlations. Data were collected on a series of $YBa_2Cu_3O_{6+\delta}$ samples with different oxygen contents, δ (Gutmann *et al.*, 2000). First, it was important to establish that the data agreed with earlier crystallographic studies. Conventional Rietveld and Real-space Rietveld were carried out on the same data-set in Q- and r-space, respectively. When the r-space refinement was constrained to have the space-group symmetry of the average structure, excellent quantitative agreement was obtained between the Q- and r-space results; and these agreed quantitatively with earlier crystallographic measurements. The real-space fit is shown in Figure 6.4. This showed that, even in the

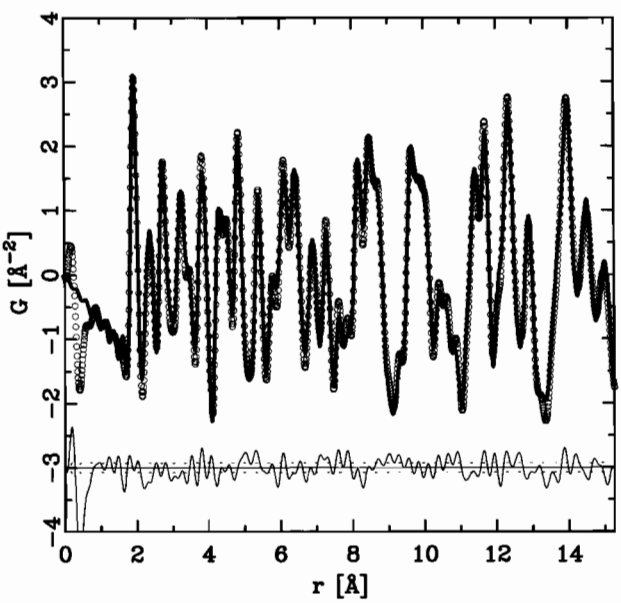

Figure 6.4. Experimental PDF from $YBa_2Cu_3O_{6+x}$ measured with neutrons on SEPD (circles). Fit to the data using the crystallographic structural model and the program PDFFIT (solid line). Below is plotted a difference curve. The dotted lines on the difference curve indicate the estimated errors at a level of $\pm\sigma$ (Gutmann *et al.*, 2000).

local structure, a diffraction measurement does not see evidence for a split position for the apical oxygen. An attempt was made to fit split atomic positions in the real-space refinement. The refinement was unstable to the presence of a split site for the apical oxygen; however, a split of the planar copper site along the z direction did converge with marginally improved agreement. The tentative conclusion from this was that there is disorder on the in-plane copper site rather than the apical oxygen. The strength of the Real-space Rietveld approach here was, first, to establish *quantitative* agreement between the local and average structure results by refining exactly the same model including similarly constrained anisotropic thermal factors. This established that the discrepancy between the XAFS and crystallographic results was not simply that they measure structure on a different length-scale. The second contribution of the real-space-Rietveld study was its ability to test for the presence of split sites. The splitting of displaced sites is small ($\sim 0.1-0.2$ Å) and the limited spatial resolution of the Q-space analysis obscures it except as an enlarged thermal factor: $d_{\min} = 0.4$ Å for the Rietveld refinement compared to $d_{\min} = 0.25$ for the real-space refinement. Since XAFS measures pair-correlations, it is hoped that the discrepancy between the diffraction and XAFS results can be resolved by the observation of the split copper site which will serve to split the in-plane copper to out-of-plane oxygen pair-correlation and might possibly explain the XAFS results. At the time of writing this issue is still not fully resolved.

6.3.2 Monte-Carlo simulated annealing based regression schemes

Rietveld refinement traditionally uses least-squares algorithms to minimize the residuals function. An alternative approach is to use a Monte-Carlo simulated annealing algorithm (Metropolis *et al.*, 1953). Conventional simulated annealing is used to find the global minimum in a complicated potential energy landscape. Parameters of the system, such as atom positions, are allowed to vary in some random way. After each change the energy of the system is calculated using the specified potential energy function. If a change reduces the energy of the system it is accepted. If it raises the energy of the system then it can be accepted or rejected. This decision is made randomly according to an underlying probability. It is this 'gambling' aspect of the technique that got its name: Monte-Carlo is the famous gambling center for the rich and famous on the French Riviera in the sovereign principality of Monaco. In simulated annealing the underlying probability is given by

$$P = \mathrm{e}^{-\Delta E/kT} \tag{6.3}$$

where ΔE is the change in energy, k is the Boltzmann constant and T is the 'temperature' of the system which is initially set by the experimenter. When T is higher, more 'bad' moves are accepted and more of the energy landscape is probed by the simulation (it is easier to get out of local minima). The temperature can then be systematically lowered to

guide the simulation into the global energy minimum. This is a widely used and powerful method in statistical physics and the computational technology is well developed (Binder and Heerman, 1992).

Clearly, Monte-Carlo simulated annealing is a powerful approach to minimization of any parameterized function and is particularly applicable if there are a large number of parameters and a complicated parameter-space. From this perspective it lends itself to being applied to solving complicated structural problems, where the function to be minimized is not an energy but a residual function: i.e. the agreement between structural data and a calculated scattering pattern from a model. In this case there is no obvious reason why the underlying probability should be a Boltzmann distribution as in simulated annealing. However, in the absence of rigorous arguments justifying the adoption of another form for the probability distribution, and the extensive understanding that exists of the behavior of simulated annealing with the Boltzmann distribution (Binder and Heerman, 1992), this was the natural place to start. The use of simulated annealing to minimize a residual function constitutes solving the famous 'inverse problem'. The direct problem is that given a potential energy function, the structure can be determined. The inverse problem is that, given a structure, can the potential energy be determined? The structural data are the input to the inverse problem; the structural model is then fit to the data by minimizing the residuals function to obtain a structure without specifying any potential energy. The approach was first used as long ago as the 1960s by the MIT group (Kaplow *et al.*, 1968; Renninger and Averbach, 1973). Limited computing power really hindered progress at that time and the widespread use of this approach has really occurred since the late 1980s. At this time, two approaches were taken by different groups. McGreevy and Puszati (1988) initially applied the technique to study the structure of liquid argon and coined the name Reverse Monte-Carlo (RMC) to differentiate the technique from conventional simulated annealing. Shortly afterwards, Toby *et al.* (1990) also used simulated annealing to study correlated local structural distortions in crystalline materials. The implementations of the technique were quite different and both have been applied with some success.

The strength of the McGreevy and Puszati (1988) implementation is also a potential weakness. In this case a large box of atoms is used as the structural model. These are allowed to arrange themselves, with the minimum of constraints, in such a way as to give good agreement with the diffraction data. In the most unconstrained case the hard-sphere repulsions, which prevent atoms overlapping, are the only constraints. Originally the data to be fit were in the form of a PDF (Keen *et al.*, 1990), but more recently total scattering data (Montfrooij *et al.*, 1996) and even single-crystal data (Nield *et al.*, 1995) have been used. Clearly the strength of this approach is that it is unbiased. The resulting structural model gives a solution that is unprejudiced but consistent with the data. Any structural motifs that emerge in the model, such as local tetrahedral atomic arrangements in network glasses, are probably real. The reason is that the simulated annealing, by its very nature,

will find the most probable, and therefore most disordered, structural solution that is consistent with the data. Any atomic correlations (ordered atomic arrangements) that emerge in the model must be more or less uniquely specified in the data themselves. The problem with the technique is that the diffraction data do not give a unique structural solution; far from it. Especially in disordered systems, where the structural information is limited, there is an enormous degeneracy in possible structural solutions consistent with the same data-set. If one does not constrain the structural model in physically reasonable ways your structural solution is quite likely to be wrong and often unphysical (in fact this is usually the way that one knows that the structural solution is wrong) (Keen, 1998). This does not detract from the method since it is a natural consequence of weakly constrained RMC modeling. However, clearly care must be taken when interpreting the results of this kind of modeling. At this point, the ways forward are to get additional data and to constrain the model. Additional data includes differential and partial PDFs, X-ray and neutron data, data from other techniques such as XAFS, and so on. Adding constraints to the model, such as limiting bond angle distortions to within physical ranges and ensuring connectivity of a network for example (Keen, 1998), ensure that only physically reasonable structural solutions are accessible to the simulation and dramatically reduces the phase-space of structural solutions. The danger, of course, is that the solution is biased towards the answer that is expected. In general, a balance has to be struck between constraining and not constraining.

When faced with crystalline data, a great deal is known about the structure from a conventional crystallographic analysis. It is clearly inefficient, and most probably disastrous, to specify the starting model by placing atoms randomly in the box and hoping that the correct crystal structure is found by random mutations of the model. In this case, a more conventional refinement is preferred where a well-defined starting model is specified and this is allowed to distort randomly to fit the data. When a Monte-Carlo algorithm is used for the regression the term RMC *refinement* has been coined (Keen, 1998), distinguishing the approach from RMC *modeling* as described in the previous paragraph. As RMC modeling becomes more constrained the distinction becomes somewhat cloudy; however, it is useful to distinguish the two approaches since in many people's eyes RMC equates to unconstrained RMC-modeling with all its shortcomings. The Toby *et al.*, 1990 approach to modeling constitutes RMC refinement. In this implementation a small unit cell is specified and periodic boundary conditions are applied analogous to real-space refinement. A unit cell larger than the crystallographic one is usually specified since one is generally interested in atomic displacements away from the average structure. A useful feature of this program is that fixed and varying interpenetrating cells can be specified allowing parts of the structure to be left invariant but distortions introduced on a sublattice of interest. A limitation of this implementation is that a single thermal factor is specified for the entire sample. Variations in thermal factor from site to site can only be incorporated by introducing static atom displacements in the model. This places this approach half way

between RMC modeling and real-space refinement. In the former approach all disorder, be it static or thermal, is modeled by the distribution of positions of the many atoms in the large box. In the latter approach, harmonic (Gaussian) distortions are specified by anisotropic thermal factors. Anharmonic components such as double-wells can be incorporated with static atom displacements. The danger of the intermediate approach is that static displacement amplitudes can be exaggerated if they are on a site with a larger thermal factor than the average and this should be borne in mind in the interpretation of the modeling results.

The notion of RMC refinement has been extended to modeling network glasses with some success (Wicks, 1993; Keen, 1998). In this case a large box of atoms is used, similar to RMC modeling, but the initial network is specified. This large box refinement approach has the advantage that the atomic probability distributions are represented by the ensemble average of atom positions in the box rather than by a global thermal factor. The problem with this is the lack of statistics and sometimes a global thermal factor is also introduced in these models. The large box also gives these refinements more of a flavor of the RMC modeling in that correlated atom displacements which emerge from the refinement do so in an unbiased way and are likely to have significance. On the other hand, disordered displacements will tend to be found if they are consistent with the data and correlated displacements might be masked. In these cases there is no substitute for more, and better, data.

A number of RMC modeling and refinement codes are freely available. The list of RMC programs supported by the McGreevy group can be found at the http://www.studsvik.uu.se web-site. A versatile and straightforward to use program for data simulation and structure refinement from single-crystal and powder/amorphous data, with built in RMC routines based on the McGreevy algorithms, is DISCUS (Proffen and Neder, 1997) that is available at http://www.pa.msu.edu/cmp/billinge-group/programs/discus/discus.html. A number of examples of data analyses using each of these programs will be presented in later chapters.

6.3.3 Empirical potential based modeling schemes

Both the real-space Rietveld and reverse Monte-Carlo techniques are essentially regression techniques: structural models are systematically altered in such a way as to improve the fit of the calculated and measured PDFs. These approaches do not contain any (or very little) of the underlying physics or chemistry of the material. This information is contained in the atomic interactions that, as we emphasize in later chapters, give rise to the interesting material properties. Once empirical potential parameters are known for a material it is possible to calculate many properties of the material from phonon dispersion curves to complex dynamical processes such as fracture. Generally, these potential parameters are determined by considering elastic constants, phonon frequencies, and in the best circumstances, fitting to complete sets of phonon dispersion curves determined from

single-crystal inelastic neutron diffraction data. In the absence of INS data, the limited number of elastic constants present in high-symmetry materials, and the limited number of phonon frequencies that can be measured using straightforward optical techniques such as Raman and IR spectroscopy, mean that empirical potentials determined in this way are quite under constrained and additional information is highly valuable. Total scattering data contains significant information about atomic dynamics and this can be utilized to get potential parameters.

In the case where the only important interactions are pair-wise, i.e. all of the properties can be explained with a set of potentials between pairs of atoms, there is a direct (and unique) relationship between the atomic potential and the resulting pair correlation function (when more than one atom-type is present all of the partial pair distribution functions are needed). When higher than pair-wise interactions are needed to explain the structure (e.g. 3-body interactions) there is not a unique relationship between the measured PDF (which only contains 2-body information, at least in the kinematical scattering limit of interest for X-ray and neutron diffraction) and the underlying potential. Nonetheless, progress can be made by introducing effective pair interactions. For example, a bond-bending force can be approximated by a spring between specific second neighbor atoms.[2]

One of the first attempts to extract pair potential information directly from measured PDF data was by Kaplow and co-workers (Kaplow *et al.*, 1964; Lagneborg and Kaplow, 1967). In simple metals such as solid lead and cobalt, they extracted the mean force potential, $U(r)$, (that is a weighted sum of all the pair potentials of atoms surrounding the atom at the origin, e.g. see Hansen and McDonald, 1986) from the expression

$$\rho(r) = \rho_0 \exp\left(\frac{-U(r)}{k_B T}\right) \tag{6.4}$$

where k_B is Boltzmann's constant (Kaplow *et al.*, 1964). The derivative of $U(r)$ with respect to distance gives the net force on the atom at the origin (due to all the neighbors at various distances). Since $\rho(r)$ was explicitly measured (it is the experimental PDF!) $U(r)$ can be obtained directly by inverting Eq. 6.4.

More recently, correlated and uncorrelated thermal motion have both been extracted from the PDF (Jeong *et al.*, 1999, 2002) by looking at the peak broadening as a function of pair separation, r. Information about dynamics in different directions in the crystal is also present in the PDF if the structural origin of particular peaks in the PDF is known. As we have discussed earlier, this is especially evident in the semiconductor alloys where ⟨110⟩ vibrations are stiffer than in other directions in the lattice (Jeong *et al.*, 1999). It is also seen in cubic systems in general and is prominent in cerium where longer-range potential parameters are important (Jeong *et al.*, 2002). In these cases the data were compared with

[2] Though see the very interesting toy model calculations of special 2-D structures that have significantly different atomic orderings, easily visible by eye, due to 3-body interactions but have identical pair–pair interactions and therefore identical scattering patterns (Welberry and Withers, 1991; Welberry and Butler, 1994).

PDFs calculated from large scale models with thousands of atoms which were relaxed using empirical potentials. The empirical potential parameters could be altered to improve the agreement between the calculated and measured PDFs. Thus, empirical potential parameters can be estimated by modeling PDF data. The approach is to start with an empirical potential and a trial structure and relax the structure to minimize the total energy. The dynamical matrix of the relaxed structure is then calculated and the phonon dispersion curves determined. At a given temperature the lattice dynamics can be determined by projecting the phonons into real-space, as discussed in more detail in Chapter 7, and convoluting the calculated PDF of the average structure appropriately. This approach yielded excellent agreement between calculated and measured PDFs for a series of semiconductor alloys (Jeong *et al.*, 2001; Peterson *et al.*, 2001). This was taken a step further by Dimitrov *et al.* (1999) who applied regression to the process, allowing the potential parameters to be updated and the process iterated until the fit to the data converged. Their claims that using this approach it is possible to obtain phonon dispersion curves with similar accuracy as from single-crystal inelastic neutron scattering studies have proved to be unfounded (Reichardt and Pintschovius, 2001; Thorpe *et al.*, 2002; Jeong *et al.*, 2002). Nonetheless, useful information about the underlying potential is available in the total scattering data from powders, especially about $q \neq 0$ phonons, that cannot be obtained from Raman, IR or elastic measurements. In the absence of large single-crystals, and ample beam-time on a neutron inelastic spectrometer, this approach certainly has merit. Furthermore, with increases in computing power, this approach may become a viable one for regular data modeling, replacing the pure regression schemes described in Sections 6.3.1 and 6.3.2. One of the evident advantages is that the refined parameters, the potential parameters, can then be used in lattice dynamical calculations and reveal other information such as specific heat, phonon frequencies, and so on.

A number of alternative approaches are also of interest. Soper (1996) has introduced a method for refining empirical potentials from liquids using a Monte-Carlo algorithm.[3] A model is set up with initial values for the pair potential parameters and the mean force potential, $U(r)$, calculated for each pair of atoms. This is the same $U(r)$ that was introduced above in Eq. 6.4. Inverting Eq. 6.4 we get

$$U(r) = -k_B T \ln\left(\frac{\rho(r)}{\rho_0}\right) = -k_B T \ln(g(r)) \tag{6.5}$$

where $g(r)$ is the pair distribution function defined in Section 3.1.3.1. We therefore have a reference $U^{\mathrm{m}}(r)$ from the model and a measured $U^{\mathrm{D}}(r)$. We would like to think of a way to

[3] This is an example of, so-called, 'inverse Monte-Carlo' (Gerold and Kern, 1987; Livet, 1987) which should be distinguished from 'reverse Monte-Carlo' discussed in Section 6.3.2. The principle difference is that in an inverse Monte-Carlo refinement potential parameters are modified and an energy is minimized using a Monte-Carlo algorithm whereas in reverse Monte-Carlo the χ^2 of the fit is used directly as an effective energy that is minimized using Monte-Carlo simulated annealing.

modify $U^{m}(r)$ to bring it closer to $U^{D}(r)$. To do this we add a perturbation to the original reference potential, $U_0^{m}(r)$ that is the difference between $U^{m}(r)$ and $U^{D}(r)$. i.e. the new potential,

$$U_1^{m}(r) = U_0^{m}(r) + kT \ln\left(\frac{g^{m}(r)}{g^{D}(r)}\right).$$

Using Monte-Carlo, the model is then relaxed using the new potential, resulting in a new calculated $g(r)$. The process is then iterated until it reaches convergence. This approach has proved to be very powerful in the study of complex liquids (Soper, 1996, 2000; Landron *et al.*, 2001).

Inverse Monte-Carlo approaches have also been used to extract information from single-crystal diffuse scattering data. For example, effective pair interactions were extracted from Vanadium hydride, an important potential hydrogen storage system, using this approach (Pionke *et al.*, 1995) which is described in detail and compared to other methods in Schweika (1997) and Schweika and Pionke (1998). The use of highly simplified 'toy model' potentials (e.g. Ising model Hamiltonian and springs between molecular units) combined with Monte-Carlo energy minimization has also proved very effective to understand diffuse scattering in crystalline materials (Welberry, 1998, 2002 and references therein).

6.4 ADDITIONAL INFORMATION AND ADVANCED MODELING

6.4.1 Joint real- and reciprocal-space refinements

The potential advantages of carrying out refinements in real vs. reciprocal space have been discussed in detail in Section 6.3.1. We simply reiterate here that both approaches are highly complementary. We envisage in the future that joint real and reciprocal space refinements will be required to solve the structures of complex materials with significant disorder. Often this disorder, or small and difficult to detect atomic displacements, can be very important for the properties. This paradigm is exemplified by ferroelectrics. Ferroelectrics have a switchable spontaneous electric polarization coming from small, symmetry breaking, atomic displacements. This property makes them very powerful dielectrics and potential gate materials on field-effect transistors for example. The atomic displacements can be quite subtle leading to long-standing debates about the nature of the atomic structure (see for example the debate on the venerable ferroelectric $BaTiO_3$ from Wul and Goldman (1946), through Comes *et al.* (1968), to Kwei *et al.* (1993) and beyond). Another long-standing debate existed about the detailed structure of the antiferroelectric material $PbZrO_3$. A full solution of the structure required a careful analysis in both real and reciprocal space (Teslic and Egami, 1998). The Rietveld and real-space refinements (this study used small-box RMC rather than real-space Rietveld) are reproduced in Figure 6.5. Another nice example where joint real-reciprocal space analysis let to new insight is in the

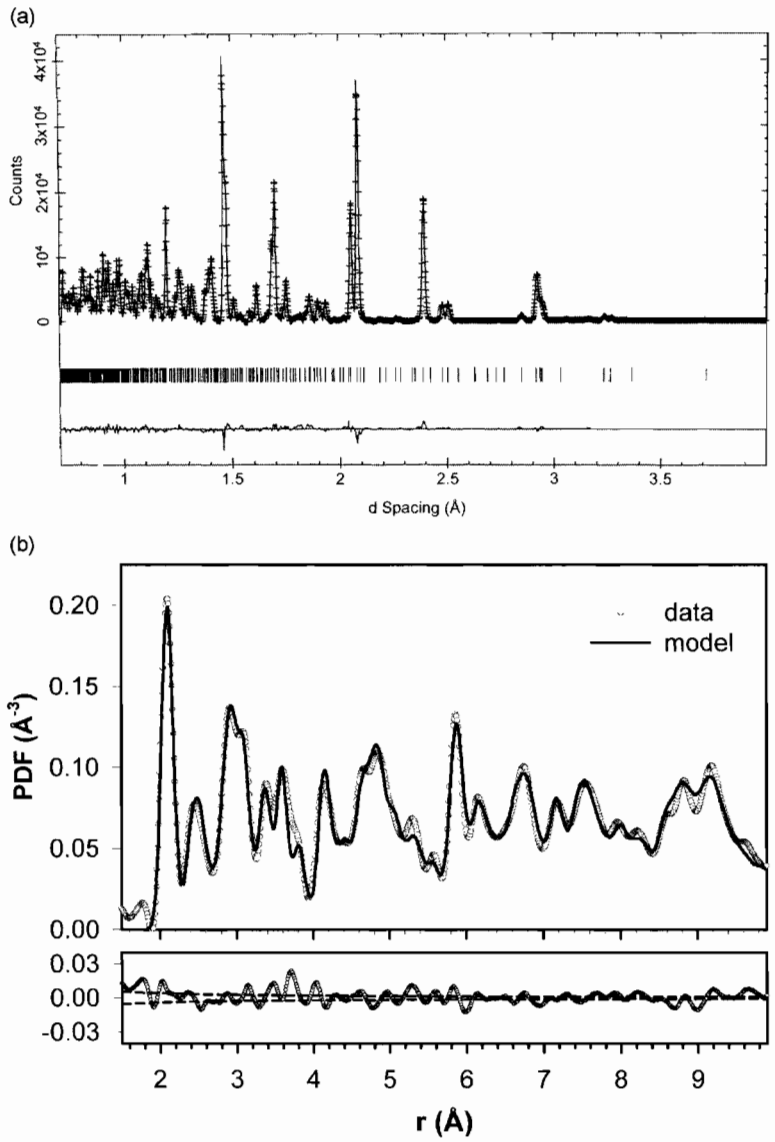

Figure 6.5. Fits of structural models of $PbZrO_3$ to neutron powder diffraction data taken at SEPD at $T = 10$ K model. (a) Rietveld refinement carried out in Q-space. (b) Real-space fit to the PDF from the same data (Teslic and Egami, 1998).

molybdenum oxide materials that have been extensively studied by Hibble and Hannon (2002). In the future it is expected that it will be possible to carry out *joint refinements* at the same time in real- and reciprocal-space, though at the time of writing no such code has been implemented.

6.4.2 *Difference modeling*

It is often the case that one is interested in understanding a structural *change* occurring at a phase transition or as a function of sample composition or processing. A useful approach to probing subtle changes in structure is difference modeling. With this approach, the actual PDF itself is not fit, but the difference curve between two PDFs is fit. For example, consider the case where higher symmetry structure (call it the reference structure) is transforming to a lower symmetry phase. The difference curve can be obtained by subtracting the PDF of the reference phase from that of the low symmetry phase. The difference curve is then fit with a difference between the model of the reference and symmetry broken phase.

Why would one want to do this rather than just fit each PDF separately? In general, it is useful if the structural changes are small. Taking the difference has the effect of canceling two contributions to the PDF that can potentially hide the structural changes. The first is the existence of systematic errors in the data. These are inevitably present because the data correction steps, though generally satisfactory, are not perfect, as discussed in Chapter 5. However, when two data-sets, measured on similar samples (or the same sample) under similar conditions, are compared the systematic errors are largely reproduced and can be cancelled by taking the difference. The second contribution that is cancelled in the difference is if there are subtle features of the reference structure, which are not properly modeled in the model of the reference structure, but which do not change at the phase transition. An example might be some dopant induced disorder in the structure of a doped material such as a transition metal oxide which is undergoing a displacive transition. In these cases, the change in structure at the phase transition can be smaller than the effects of these systematic effects. However, after canceling the systematic effects by taking a difference, the structural changes are significant.

An excellent example of this is the observation of lattice polaron formation at the metal–insulator transition in $La_{1-x}Ca_xMnO_3$. In the doping range $0.17 < x < 0.5$ this material is metallic at low temperature but has a metal–insulator transition at $\sim$200–300 K. A number of techniques (e.g. see Ramirez, 1997) indicate that the metal–insulator transition occurs because of carrier localization due to lattice polaron formation: the charge carriers localize and the lattice distorts around the localized carrier. One of the key pieces of evidence came from the PDF where peak broadening indicated polaron formation as described in Section 6.2.3.3. The nature of the polaronic distortion was studied by difference modeling. The results are shown in Figure 6.6. The difference is taken between a data-set just above and just below the MI transition. The main features of the difference curve could be fit well over a wide range of r by a model for the polaron where doped charges localize on Mn sites and contract the local octahedron isotropically. Neighboring octahedra (without a localized charge) becoming elongated along one direction consistent with the formation of a Jahn–Teller distortion. From the modeling it was found that the magnitude of the distortion is $\sim$0.12 Å.

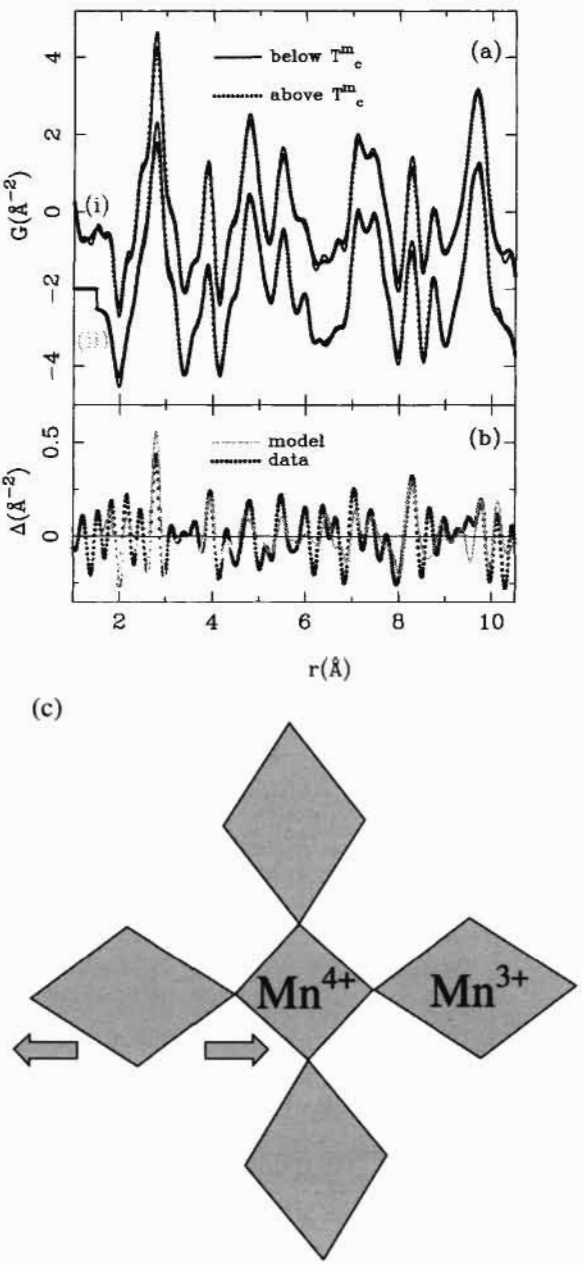

Figure 6.6. (a) PDFs of $La_{0.75}Sr_{0.25}MnO_3$ from above and below the metal–insulator transition (i) data (ii) models. (b) Difference curves between the data above and below the transition (i.e. solid line minus dotted line in (a)). The simple polaron model shown in (c) picks up the main structural changes with only a single parameter. Note that the distortions are exaggerated in the picture of the polaron to make them easier to visualize (Billinge *et al.*, 1996).

REFERENCES

Billinge, S.J.L. (1992) PhD thesis, University of Pennsylvania.

Billinge, S.J.L. (1998) in *Local Structure from Diffraction*, Eds. Billinge, S.J.L. & Thorpe M.F., Plenum Press, New York, p. 137.

Billinge, S.J.L., DiFrancesco, R.G., Kwei, G.H., Neumeier, J.J. & Thompson, J.D. (1996) *Phys. Rev. Lett.*, **77**, 715.

Binder, K. & Heerman, D.W. (1992) *Monte Carlo Simulation in Statistical Physics*, 2nd Edition, Springer, Berlin.

Booth, C.H., Bridges, F., Snyder, G.J. & Geballe, T.H. (1996) *Phys. Rev. B*, **54**, R15606.

Bozin, E.S., Billinge, S.J.L., Takagi, H. & Kwei, G.H. (2000) *Phys. Rev. Lett.*, **84**, 5856.

Claye, A. & Fischer, J.E. (1999) *Electrochim. Acta*, **45**, 107.

Comes, R., Lambert, M. & Guinier, A. (1968) *Solid State Commun.*, **6**, 715.

Dimitrov, D., Louca, D. & Röder, H. (1999) *Phys. Rev. B*, **60**, 6204.

Dove, M.T., Keen, D.A., Hannon, A.C. & Swainson, I.P. (1997) *Phys. Chem. Miner.*, **24**, 311.

Egami, T. & Louca, D. (2000) *J. of Superconductivity: Inc. Novel Magnetism*, **13**, 247.

Francois, M., Junod, A., Yvon, K., Hewat, A.W., Capponi, J.J., Strobel, P., Marezio, M. & Fischer, P. (1988) *Solid State Commun.*, **66**, 1117.

Gerold, V. & Kern, J. (1987) *Acta Metallurg.*, **35**, 393.

Gutmann, M.S., Billinge, S.J.L., Brosha, E.L. & Kwei, G.H. (2000) *Phys. Rev. B*, **61**, 11762.

Hansen, J.P. & McDonald, I.R. (1986) *Theory of Simple Liquids*, Academic Press, London.

Hibble, S.J. & Hannon, A.C. (2002), in *From Semiconductors to Proteins: Beyond the Average Structure*, Eds. Billinge, S.J.L. & Thorpe M.F., Kluwer/Plenum, New York, p 129.

Jeong, I.-K., Proffen, Th., Mohiuddin-Jacobs, F. & Billinge, S.J.L. (1999) *J. Phys. Chem. A*, **103**, 921.

Jeong, I.-K., Mohiuddin-Jacobs, F., Petkov, V., Billinge, S.J.L. & Kycia, S. (2001) *Phys. Rev. B*, **63**, 205202.

Jeong, I.-K., Graf, M., Heffner, R.H. & Billinge, S.J.L. (2002) *Phys. Rev. B.* submitted.

Kaplow, R., Averbach, B.L. & Strong, S.L. (1964) *J. Phys. Chem. Solids*, **25**, 1195.

Kaplow, R., Rowe, T.A. & Averbach, B.L. (1968) *Phys. Rev.*, **168**, 1068.

Keen, D.A. (1998) in *Local Structure From Diffraction*, Eds. Billinge, S.J.L. & Thorpe M.F., Plenum Press, New York, p 101.

Keen, D.A., Hayes, W. & McGreevy, R.L. (1990) *J. Phys. Condens. Matter*, **2**, 2773.

Kwei, G.H., Lawson, A.C., Hults, W.L. & Smith, J.L. (1991) *Physica C*, **175**, 615.

Kwei, G.H., Lawson, A.C., Billinge, S.J.L. & Cheong, S.-W. (1993) *J. Phys. Chem.*, **97**, 2368.

Lagneborg, R. & Kaplow, R. (1967) *Acta Metall.*, **15**, 13.

Landron, C., Hennet, L., Jenkins, T.E., Greaves, G.N., Coutures, J.P. & Soper, A.K. (2001) *Phys. Rev. Lett.*, **86**, 4839.

Lawson, A.C., Martinez, B., Von Dreele, R.B., Roberts, J.A., Sheldon, R.I., Brun, T.O. & Richardson, J.W. (2000) *Phil. Mag.*, **80**, 1869.

Livet, F. (1987) *Acta Metall.*, **35**, 2915.

Louca, D. & Egami, T. (1999) *Phys. Rev. B*, **59**, 6193.

Louca, D., Egami, T., Brosha, E.L., Röder, H. & Bishop, A.R. (1997) *Phys. Rev. B*, **56**, R8475.

McGreevy, R.L. & Puszati, L. (1988) *Mol. Sim.*, **1**, 359.

Metropolis, N., Rosenbluth, A.W., Rosenbluth, M.N., Teller, A.H. & Teller, E. (1953) *J. Chem. Phys.*, **21**, 1087.

Mikkelson, J.C. & Boyce, J.B. (1982) *Phys. Rev. Lett.*, **49**, 1412.

Montfrooij, W., McGreevy, R.L., Hadfield, R.A. & Andersen, N.-H. (1996) *J. Appl. Cryst.*, **29**, 285.

Mustre de Leon, J., Conradson, S.D., Batistic, I. & Bishop, A.R. (1990) *Phys. Rev. Lett.*, **65**, 1678.
Nield, V.M., Keen, D.A. & McGreevy, R.L. (1995) *Acta Crystallogr. A*, **51**, 763.
Peterson, P.F., Proffen, Th., Jeong, I.-K., Billinge, S.J.L., Choi, K.-S., Kanatzidis, M.G. & Radaelli, P.G. (2001) *Phys. Rev. B*, **63**, 165211.
Petkov, V., DiFrancesco, R.G., Billinge, S.J.L., Acharya, & Foley, H.C. (1999) *Phil. Mag. B*, **79**, 1519.
Pionke, M., Schweika, W., Springer, T., Sonntag, R. & Hohlwein, D. (1995) *Phys. Scripta*, **T57**, 107.
Proffen, Th. & Billinge, S.J.L. (1999) *J. Appl. Crystallogr.*, **32**, 572.
Proffen, Th. & Neder, R.B. (1997) *J. Appl. Crystallogr.*, **30**, 171.
Proffen, Th., DiFrancesco, R.G., Billinge, S.J.L., Brosha, E.L. & Kwei, G.H. (1999) *Phys. Rev. B*, **60**, 9973.
Ramirez, A.P. (1997) *J Phys: Condens. Matter*, **9**, 8171.
Reichardt, W. & Pintschovius, L. (2001) *Phys. Rev. B*, **63**, 174302.
Renninger, A.L. & Averbach, B.L. (1973) *Acta Crystallogr. B*, **29**, 1583.
Rietveld, H.M. (1969) *J. Appl. Crystallogr.*, **2**, 65.
Schweika, A. (1997) Disordered Alloys—Diffuse Scattering and Monte Carlo simulation Springer Tracts in Modern Physics, vol. **141**, Springer, Heidelberg.
Schweika, A. & Pionke, M. (1998) in *Local Structure from Diffraction*, Eds. Billinge, S.J.L. & Thorpe M.F., Plenum Press, New York, p. 85.
Schweiss, P., Reichardt, W., Braden, M., Collin, G., Heger, G., Claus, H. & Erb, A. (1994) *Phys. Rev. B*, **49**, 1387.
Soper, A.K. (1996) *Chem. Phys.*, **202**, 295.
Soper, A.K. (2000) *Chem. Phys.*, **258**, 121.
Stern, E.A., Qian, M., Yacoby, Y., Heald, S.M. & Meada, H. (1993) *Physica C*, **209**, 331.
Sullivan, J.D., Bordet, P., Marezio, M., Takenaka, K. & Uchida, S. (1993) *Phys. Rev. B*, **48**, 10638.
Teslic, S. & Egami, T. (1998) *Acta Crystallogr. B*, **54**, 750.
Thorpe, M.F., Levashov, V., Lei, M. & Billinge, S.J.L. (2002) in *From Semiconductors to Proteins: Beyond the Average Structure*, Eds. Billinge, S.J.L. & Thorpe M.F., Plenum/Kluwer, New York, p. 105.
Toby, B.H., Egami, T., Jorgensen, J.D. & Subramanian, M.A. (1990) *Phys. Rev. Lett.*, **64**, 2414.
Tucker, M.G., Dove, M.T. & Keen, D.A. (2000) *J. Phys. Condens. Matter*, **12**, L425.
Warren, B.E. (1934) *J. Chem. Phys.*, **2**, 551.
Waseda, Y. (1980) *The Structure of Non-Crystalline Materials*, McGraw-Hill, New York.
Welberry, T.R. & Withers, R.L. (1991) *J. Appl. Crystallogr.*, **24**, 18–29.
Welberry, T.R. & Butler, B.D. (1994) *J. Appl. Crystallogr.*, **27**, 205.
Welberry, T.R. (1998) in *Local Structure from Diffraction*, Eds. Billinge, S.J.L. & Thorpe M.F., Plenum Press, New York, p. 35.
Welberry, T.R. (2002) in *From Semiconductors to Proteins: Beyond the Average Structure*, Eds. Billinge, S.J.L. & Thorpe M.F., Plenum/Kluwer, New York, p. 1.
Wicks, J.D (1993) D.Phil. thesis, University of Oxford.
Wul, W. & Goldman, I.M.C.R. (1946) *Acad. Sci. Russ.*, **46**, 139.
Wyckoff, R.M.G. (1963) *Crystal Structures*, 2nd Edition, Interscience, New York.
Young, R. A., Ed. (1993) *The Rietveld Method*, International Union of Crystallography Monograph, Oxford Science Publications, Oxford.

This Page Intentionally Left Blank

Chapter 7

Dynamics of the Local Structure

This Page Intentionally Left Blank

Chapter 7
Dynamics of the Local Structure

7.1. MEASUREMENT OF INELASTIC SCATTERING

In the discussion so far, we assumed that the instrument of measurement has poor energy resolution, and measures the intensity integrated over all the energy transfers. It is possible, however, to set up equipment in a way that the energy lost or gained during the scattering can be measured. Such an experiment, an inelastic scattering measurement, is particularly straightforward for neutron scattering, since the energy of neutrons used in the measurement (10 meV – 1 eV) is comparable to the energy of excitations in the solids, such as lattice dynamics. An inelastic X-ray scattering (IXS) measurement is more difficult, since the incident X-ray energy is of the order of 10 – 100 keV, much larger than the energy scale of interest. It became feasible only recently with the advent of third-generation synchrotron sources and advances in monochromator technology. However, it is a very promising method to determine the dynamics of electrons and atoms.

In this chapter we describe how to carry out an inelastic scattering measurement and how the motion of atoms will affect the scattered intensity of neutrons and X-rays, introduce the concept of the dynamic PDF, and finally discuss how the lattice dynamics affect the neutron PDF. Magnetic excitations are outside the scope of this chapter, but the discussions on phonons can be readily extended into the treatments of magnons and crystal-field excitations. The pulsed neutron scattering measurements to determine the PDF, described in Chapters 4 and 5, are in-between pure elastic and inelastic measurements and this introduces complications as well as opportunities. The PDF determined by a regular powder neutron scattering measurement includes both elastic and inelastic scattering intensities; however, the special geometry of the measurement means that it captures part of the dynamics while ignoring the rest. Local lattice dynamics of a certain range of energy transfers result in irregular distortions of the PDF that depend upon the detector angle.

7.1.1 Neutron triple-axis-spectrometer

For a steady state neutron or X-ray source a triple-axis spectrometer offers the capacity of measuring the inelastic scattering intensity (for details see Tranquada *et al.*, 2002). A triple-axis spectrometer (Figure 7.1) consists of a monochromator, sample, and analyzer, each placed on a separate goniometer to allow the orientation of each to be independently controlled by a motor. Thus one can specify the energy and direction of the incident beam, the sample orientation, and the energy and direction of the detected scattered beam.

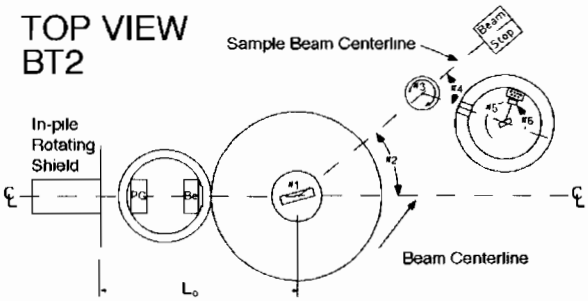

Figure 7.1. Schematic of a triple-axis spectrometer (actually BT2 at the national center for Neutron Research at NIST in Maryland, USA) used in inelastic neutron scattering measurement with a reactor source. The three axes are the monochromator (#1), the sample (#3), and the analyzer crystal. (#5). This spectrometer also has pyrolitic graphite (PG) and beryllium filters upstream of the monochromator. The monochromator and analyzers are either PG or Heusler alloy for unpolarized and polarized neutron experiments, respectively.

The scattering process is then determined by the energy and momentum transfers,

$$\hbar\omega = \hbar\omega_{\text{init}} - \hbar\omega_{\text{final}} \tag{7.1}$$

and

$$\mathbf{Q} = \mathbf{k}_{\text{init}} - \mathbf{k}_{\text{final}} \tag{7.2}$$

where an incoming neutron or X-ray photon has the energy $\hbar\omega_{\text{init}}$ and the momentum $\mathbf{k}_{\text{init}}$, and is scattered into the state with the energy $\hbar\omega_{\text{final}}$ and the momentum $\mathbf{k}_{\text{final}}$. Thus for neutrons,

$$\hbar\omega = \frac{\hbar^2}{2m}(k_{\text{init}}^2 - k_{\text{final}}^2) \tag{7.3}$$

where m is the neutron mass, $k_{\text{final}} = |\mathbf{k}_{\text{final}}|$, $k_{\text{init}} = |\mathbf{k}_{\text{init}}|$, and for X-rays,

$$\hbar\omega = \hbar c(k_{\text{init}} - k_{\text{final}}) \tag{7.4}$$

where c is the speed of light. For both cases,

$$Q^2 = k_{\text{final}}^2 + k_{\text{init}}^2 - 2k_{\text{final}}k_{\text{init}} \cos 2\theta \tag{7.5}$$

where 2θ is the angle between $\mathbf{k}_{\text{init}}$ and $\mathbf{k}_{\text{final}}$. For an elastic scattering ($\omega = 0$, $k = k_{\text{init}} = k_{\text{final}}$) process,

$$Q_0 = 2k \sin\theta = \frac{4\pi \sin\theta}{\lambda}. \tag{7.6}$$

However, for an inelastic process Q is different from Q_0. The energy and momentum lost by the probe particle are transferred to the solid. Thus the energy gained by the solid is $\hbar\omega$. This transferred energy and momentum can create or annihilate (with negative energy transfer) excitations such as lattice vibrations (phonons) or spin waves (magnons).

7.1.2 Inelastic X-ray scattering measurement

The measurement of phonons with X-rays is much more difficult since the energy transfer is smaller than the X-ray energy by many orders of magnitude. For instance, if one uses an X-ray of 10 keV and tries to measure a phonon with the energy of 10 meV an energy resolution of at least 10^{-7} is required. Only recently such a measurement became feasible because of advances in synchrotron sources and crystal monochromators. This is why, so far, most of the inelastic scattering measurements of phonons have been carried out with neutrons. On the other hand measurements of *electronic* excitations, such as the Compton scattering and interband transitions, do not require such high resolution. While these measurements are not easy because of low scattering intensity, inelastic X-ray scattering measurements of electronic process are becoming an important research technique. Unlike X-ray absorption spectroscopy it provides momentum resolved information, making it easier to make connection with the calculated band structure.

An example of the schematic plan of an IXS station is given in Figure 7.2. In order to achieve such a high-energy resolution backscattering geometry is used for the monochromator and analyzer. In addition, the monochromator and analyzer have to be thermally and mechanically well isolated so that they are extremely stable with respect to temperature and vibration. At the ESRF the energy scan is accomplished by changing the temperature, and therefore the d-spacing due to thermal expansion, of the analyzer crystal!

While neutrons track the dynamics of nuclei, X-rays bring out information on electron dynamics. While the dynamics of electrons tightly bound to the nuclei, the core electrons, simply follow the lattice dynamics, the dynamics of valence electrons provide direct information on the electronic band structure of the solid. For the determination of the phonon dispersion neutron scattering is a better choice most of the time. But since it is much easier to focus an X-ray beam than a neutron beam, IXS can be used in determining the phonon dispersion of very small crystals or even thin films and surfaces. For determining the dynamics of valence electrons in the bulk IXS is a unique method. The method of angle-resolved photoemission spectroscopy, though powerful, suffers from

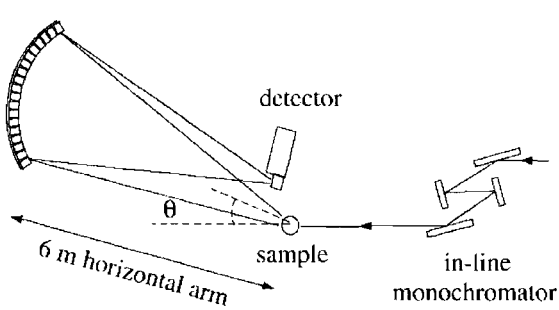

Figure 7.2. Schematic of the inelastic X-ray scattering spectrometer system, 3ID-C of the APS, Argonne National Laboratory (Sinn *et al.*, 2001).

electron life-time and surface effects (because the escape depth of photoelectrons is only a few nanometers) making the results difficult to interpret. IXS, on the other hand, is a cleaner method to probe the bulk, without the complication of the final-state interaction. It should become a powerful method to determine directly, not only the single particle electron dispersion, but also the electron–phonon coupling.

7.1.3 Chopper spectrometer

For a pulsed neutron source a chopper is used instead of a crystal monochromator to produce a monochromatic beam. A chopper is a cylinder with a narrow path that rotates at high speed. It allows neutrons within a certain energy range to pass through, and plays the role of a low resolution monochromator. The incident energy is chosen by adjusting the timing of the opening of the chopper with respect to the generation of the pulse of neutrons. The energy band-pass is set by changing the speed of rotation. The energy of the scattered neutron is determined by the time-of-flight method using a large array of detectors placed around the sample (Figure 7.3). The reverse of this method is to fix the energy of the scattered neutrons by using an array of filters or analyzer crystals placed between the sample and the detectors in the backscattering geometry, as used on the IRIS spectrometer at ISIS. Much higher resolution, though a narrower range of energy transfers, is attained by this method. This type of spectrometer is illustrated in Figure 7.4.

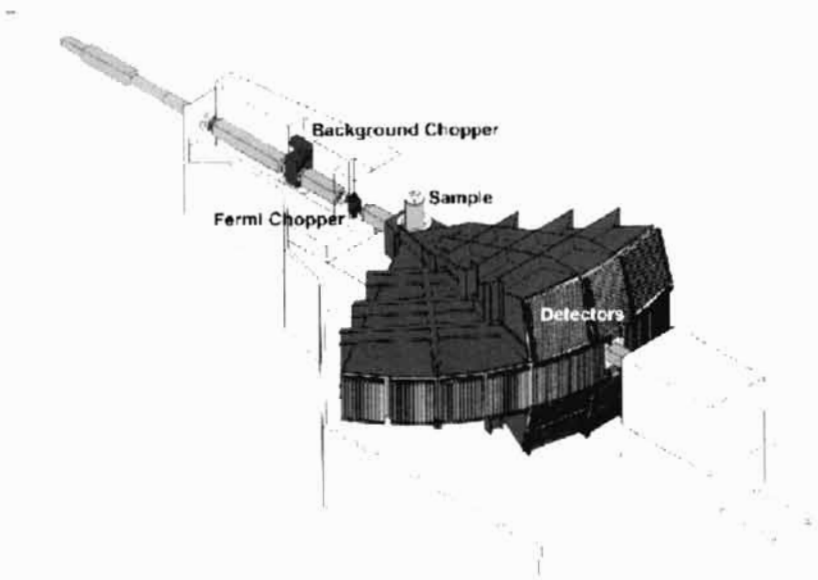

Figure 7.3. Chopper spectrometer (MAPS) used in inelastic neutron scattering measurement with a pulsed neutron source.

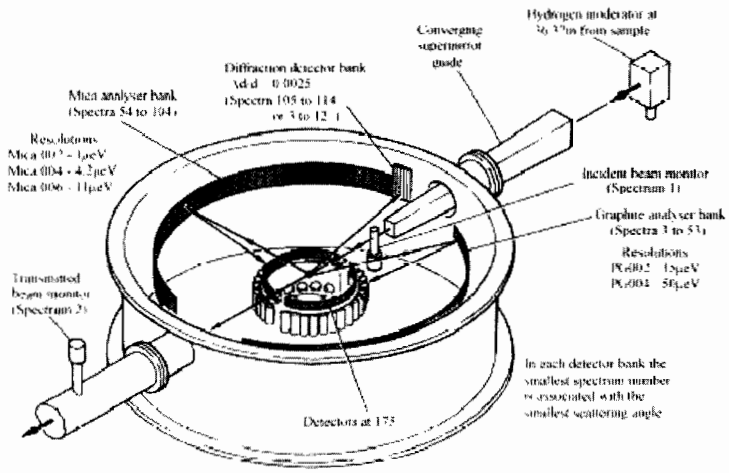

Figure 7.4. Backscattering spectrometer IRIS at ISIS. This configuration provides higher resolution but a narrower range of energy transfers can be accessed compared with chopper spectrometers such as MAPS.

For a fixed incident energy Eqs. 7.3 and 7.5 yield,

$$Q^2 = 2k_{\text{init}}^2\left[1 - \frac{m\omega}{\hbar k_{\text{init}}^2} - \cos(2\theta)\left(1 - \frac{2m\omega}{\hbar k_{\text{init}}^2}\right)^{1/2}\right]. \tag{7.7}$$

For each detector placed at an angle 2θ the *tof* spectrum produces the values of the dynamic structure factor, $S(Q, \omega)$ along the $Q-\omega$ curve determined by Eq. 7.7. $S(Q, \omega)$ is related to the double-differential scattering cross-section introduced in Chapter 5 according to

$$\frac{\mathrm{d}^2\sigma}{\mathrm{d}\Omega\,\mathrm{d}E_{\text{s}}} = \left(\frac{k_{\text{final}}}{k_{\text{init}}}\right)[\sigma_{\text{coh}}S_{\text{coh}}(Q, \omega) + \sigma_{\text{inc}}S_{\text{inc}}(Q, \omega)], \tag{7.8}$$

where σ is the scattering cross-section and 'coh' and 'inc' refer to the coherent and incoherent scattering, respectively. By assembling the data from various detectors placed all around the sample the entire $S(Q, \omega)$ map can be obtained. For example, $S(Q, \omega)$ from the MAPS spectrometer of ISIS as shown in Figure 7.5. Note that for a given Q the maximum in ω is obtained for $2\theta = \pi$ (backscattering). For this case the $Q-\omega$ relation is a simple parabola:

$$\omega = \frac{\hbar}{2m}Q(2k_{\text{init}} - Q) \tag{7.9}$$

$S(Q, \omega)$ can be determined only within this parabola. In particular, for small Q,

$$\omega \leq \frac{\hbar k_{\text{init}}}{m}Q = v_{\text{init}}Q \tag{7.10}$$

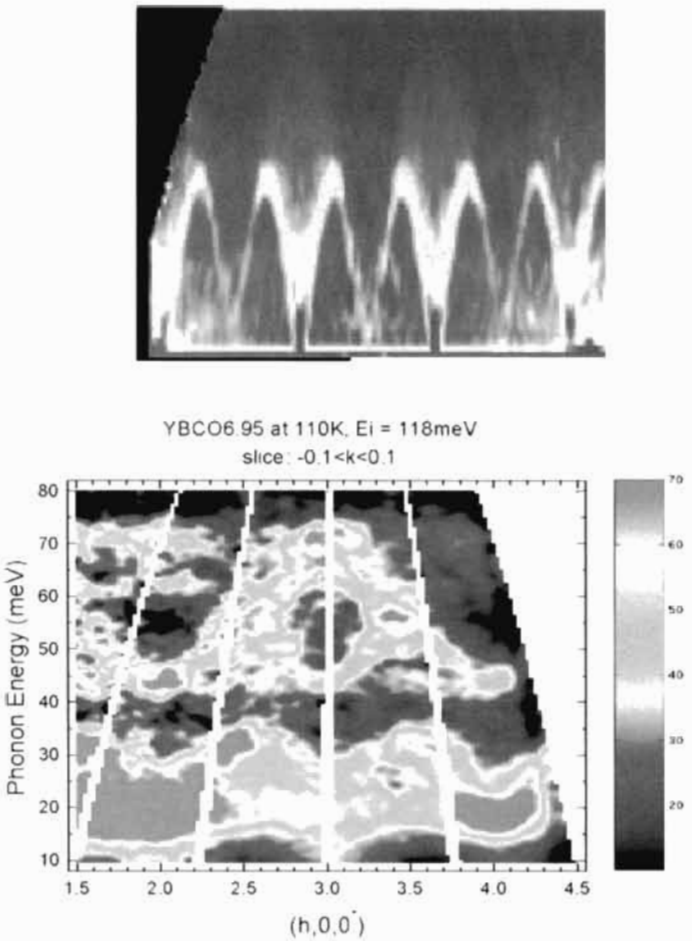

Figure 7.5. $S(Q, \omega)$ functions determined using the MAPS chopper spectrometers at ISIS. (a) Spin wave dispersion curves (magnetic excitations) from a quasi-1D quantum magnetic system, $KCuF_3$ (Lake *et al.*, 2000). (b) Phonon dispersion map of $YBa_2Cu_3O_{6.95}$. In both cases the vertical axis is energy transfer, ω, and the horizontal axis is momentum transfer, Q. The color scale indicates intensity, red being high and blue/black low. The dispersion curves of the excitations are directly evident in the raw data as regions of high intensity at well-defined positions of energy and momentum (Egami *et al.*, 2002).

where v_{init} is the velocity of the incident neutron beam. Thus, in order to measure excitations with small Q and large ω the use of neutrons with high initial velocity, thus high incident energy, is required. While it is impossible to set $2\theta = \pi$ because the detection system shadows the incoming beam, if 2θ is close to π, $cos(2\theta)$ is practically unity, justifying the use of Eq. 7.9.

7.2. DYNAMIC STRUCTURE FACTOR

7.2.1 Single-phonon scattering

The intensity of particles inelastically scattered by phonons is described by the phonon dynamic structure factor,

$$S(\mathbf{Q},\omega) = \frac{1}{N\langle b\rangle^2}\sum_{\nu,\mu} b_\nu b_\mu \int \langle\!\langle e^{i\mathbf{Q}(\mathbf{R}_\nu(0)-\mathbf{R}_\mu(t))}\rangle\!\rangle e^{-i\omega t}\,dt \tag{7.11}$$

where $\langle\!\langle \cdots \rangle\!\rangle$ represents an ensemble average. This expression is similar to Eq. 2.9, but is time-dependent. More detailed treatments are given, for instance, in Lovesey (1984). To derive this equation, we go back to Chapter 2 and derive the phase factor again (Appendix 2.1), but including the time dependence explicitly. Such a derivation is given in Appendix7.1.

To derive equations for the dynamics of particles it is useful to be able to switch between the time and frequency domains. This is done by a Fourier transform where we define the scattering function in the time-domain (called the intermediate scattering function) $S(Q,t)$ as

$$S(\mathbf{Q},\omega) = \int S(\mathbf{Q},t)e^{-i\omega t}\,dt \tag{7.12}$$

where by reference to Eq. 7.11, it is clear that for phonon scattering

$$S(\mathbf{Q},t) = \frac{1}{N\langle b\rangle^2}\sum_{\nu,\mu} b_\nu b_\mu \langle\!\langle e^{i\mathbf{Q}(\mathbf{R}_\nu(0)-\mathbf{R}_\mu(t))}\rangle\!\rangle. \tag{7.13}$$

We now express the atomic position $\mathbf{R}_\nu$ in terms of the time-average and time-dependent deviation;

$$\mathbf{R}_\nu(t) = \langle\!\langle \mathbf{R}_\nu\rangle\!\rangle + \mathbf{u}_\nu(t) \tag{7.14}$$

The intermediate scattering function (Eq. 7.13) can then be expressed as,

$$S(\mathbf{Q},t) = \frac{1}{N\langle b\rangle^2}\sum_{\nu,\mu} b_\nu b_\mu e^{i\mathbf{Q}\cdot(\langle\!\langle \mathbf{R}_\nu\rangle\!\rangle - \langle\!\langle \mathbf{R}_\mu\rangle\!\rangle)}\langle\!\langle e^{i\mathbf{Q}\cdot(\mathbf{u}_\nu(0)-\mathbf{u}_\mu(t))}\rangle\!\rangle \tag{7.15}$$

and expanding the exponential in the time-average we get,

$$S(\mathbf{Q},t) = \frac{1}{N\langle b\rangle^2}\sum_{\nu,\mu} b_\nu b_\mu\, e^{i\mathbf{Q}\cdot(\langle\!\langle \mathbf{R}_\nu\rangle\!\rangle - \langle\!\langle \mathbf{R}_\mu\rangle\!\rangle)}\Big\{1 + i\mathbf{Q}\cdot\langle\!\langle \mathbf{u}_\nu(0) - \mathbf{u}_\mu(t)\rangle\!\rangle - \frac{1}{2}\langle\!\langle(\mathbf{Q}\cdot[\mathbf{u}_\nu(0) - \mathbf{u}_\mu(t)])^2\rangle\!\rangle + \cdots\Big\}. \tag{7.16}$$

The linear term (the second term within the curly bracket) disappears by thermal averaging. If we denote the remaining first term by $S_0(\mathbf{Q},t)$ and third term by $S_1(\mathbf{Q},t)$ we

can write Eq. 7.16 as $S(\mathbf{Q},t) = S_0(\mathbf{Q},t) + S_1(\mathbf{Q},t) + \cdots$. Substituting back into Eq. 7.12 we get

$$S(\mathbf{Q},\omega) = S_0(\mathbf{Q},\omega) + S_1(\mathbf{Q},\omega) + \cdots \tag{7.17}$$

with

$$\begin{aligned} S_0(\mathbf{Q},\omega) &= \frac{1}{N\langle b\rangle^2}\sum_{\nu,\mu} b_\nu b_\mu \, \mathrm{e}^{\mathrm{i}\mathbf{Q}\cdot(\langle\langle\mathbf{R}_\nu\rangle\rangle - \langle\langle\mathbf{R}_\mu\rangle\rangle)} \int \mathrm{e}^{-\mathrm{i}\omega t}\,\mathrm{d}t \\ &= \frac{1}{N\langle b\rangle^2}\sum_{\nu,\mu} b_\nu b_\mu \, \mathrm{e}^{\mathrm{i}\mathbf{Q}\cdot(\langle\langle\mathbf{R}_\nu\rangle\rangle - \langle\langle\mathbf{R}_\mu\rangle\rangle)}\delta(\omega) \end{aligned} \tag{7.18}$$

where $\delta(\omega)$ is the usual Dirac delta-function. Thus S_0 is everywhere zero except when $\omega = 0$, $S_0(\mathbf{Q},\omega) = S_0(\mathbf{Q},0)$, and this first term in the expansion contains only elastic scattering.

Now we consider $S_1(\mathbf{Q},\omega)$ which after factoring the square can be written as

$$\begin{aligned} S_1(\mathbf{Q},\omega) = &-\frac{1}{2N\langle b\rangle^2}\sum_{\nu,\mu} b_\nu b_\mu \, \mathrm{e}^{\mathrm{i}\mathbf{Q}\cdot(\langle\langle\mathbf{R}_\nu\rangle\rangle - \langle\langle\mathbf{R}_\mu\rangle\rangle)} \\ &\times \int [\langle\langle(\mathbf{Q}\cdot\mathbf{u}_\nu(0))^2\rangle\rangle + \langle\langle(\mathbf{Q}\cdot\mathbf{u}_\mu(t))^2\rangle\rangle - 2\langle\langle(\mathbf{Q}\cdot\mathbf{u}_\nu(0))(\mathbf{Q}\cdot\mathbf{u}_\mu(t))\rangle\rangle]\mathrm{e}^{-\mathrm{i}\omega t}\,\mathrm{d}t. \end{aligned} \tag{7.19}$$

The first term in the integral is independent of time and can come out of the integral. The second term is also independent of t after thermal averaging (it is equal to the first term) and can also come out of the integral. Thus, as for the case of $S_0(\mathbf{Q},\omega)$, these terms contribute intensity only to the elastic scattering. In fact they form part of the Debye–Waller factor (Eq. 2.18). Thus only the third term represents the inelastic intensity. Let us now use the phonon coordinates,

$$\mathbf{u}_\nu(t) = \frac{1}{\sqrt{N}}\sum_{\mathbf{q}} \mathrm{e}^{\mathrm{i}(\mathbf{q}\cdot\langle\langle\mathbf{R}_\nu\rangle\rangle - \omega_\mathbf{q} t)}\mathbf{u}_\mathbf{q}^\nu(\omega) \tag{7.20}$$

where $\mathbf{q}$ is the phonon wavevector, $\omega_\mathbf{q}$ is the frequency of the $\mathbf{q}$ phonon, and $\mathbf{u}_\mathbf{q}\nu(\omega)$ is its amplitude at the νth atom. If there is more than one atom in the unit cell $\mathbf{u}_\mathbf{q}\nu(\omega)$ depends upon ν. If we define $G_{\nu\mu}(\omega) = 2\int \langle\langle(\mathbf{Q}\cdot\mathbf{u}_\nu(0))(\mathbf{Q}\cdot\mathbf{u}_\mu(t))\rangle\rangle \mathrm{e}^{-\mathrm{i}\omega t}\,\mathrm{d}t$ and substitute Eq. 7.20 we see that,

$$\begin{aligned} G_{\nu\mu}(\omega) &= \frac{2}{N}\sum_{\mathbf{q},\mathbf{q}'}\int \mathrm{e}^{\mathrm{i}[\mathbf{q}\cdot\langle\langle\mathbf{R}_\nu\rangle\rangle - \mathbf{q}'\cdot\langle\langle\mathbf{R}_\mu\rangle\rangle]}\langle\langle(\mathbf{Q}\cdot\mathbf{u}_\mathbf{q}^\nu)(\mathbf{Q}\cdot\mathbf{u}_{\mathbf{q}'}^\mu)\mathrm{e}^{-\mathrm{i}(\omega_{\mathbf{q}'}-\omega_\mathbf{q})t}\rangle\rangle \mathrm{e}^{-\mathrm{i}\omega t}\,\mathrm{d}t \\ &= \frac{2}{N}\sum_{\mathbf{q}}\delta(\omega-\omega_\mathbf{q})\mathrm{e}^{\mathrm{i}\mathbf{q}\cdot[\langle\langle\mathbf{R}_\nu\rangle\rangle - \langle\langle\mathbf{R}_\mu\rangle\rangle]}\langle\langle(\mathbf{Q}\cdot\mathbf{u}_\mathbf{q}^\nu)(\mathbf{Q}\cdot\mathbf{u}_\mathbf{q}^\mu)\rangle\rangle. \end{aligned} \tag{7.21}$$

By the lattice sum as in Eq. 2.10,

$$S_1(\mathbf{Q},\omega) = \frac{e^{-W}}{\langle b\rangle^2 N}\sum_{\mathbf{q}} \delta(\omega-\omega_{\mathbf{q}})\delta(\mathbf{Q}+\mathbf{q}-\mathbf{K})H(\mathbf{Q},\mathbf{q}) \tag{7.22}$$

where

$$H(\mathbf{Q},\mathbf{q}) = \sum_{n,m} b_n b_m\, e^{i(\mathbf{Q}+\mathbf{q})\cdot(\langle\langle \mathbf{R}_n\rangle\rangle - \langle\langle \mathbf{R}_m\rangle\rangle)} \langle\langle (\mathbf{Q}\cdot\mathbf{u}_{\mathbf{q}}^n)(\mathbf{Q}\cdot\mathbf{u}_{\mathbf{q}}^m)\rangle\rangle. \tag{7.23}$$

Here e^{-W} is the Debye–Waller factor that comes from the higher order terms and the sum over n and m is now over atoms in the unit cell and not all atoms in the sample. With the phonon operators,

$$\mathbf{u}_{\mathbf{q},\alpha}^n = \mathbf{e}_{\mathbf{q},\alpha}^n \frac{\hbar}{\sqrt{M\omega_{\mathbf{q},\alpha}}}(a_{\mathbf{q},\alpha} + a_{\mathbf{q},\alpha}^+) \tag{7.24}$$

where α denotes the phonon branch, $\mathbf{e}_{\mathbf{q},\alpha}^n$ is the polarization unit vector, M is the atomic mass, and $a_{\mathbf{q}}$ and $a_{\mathbf{q}}^+$ are phonon annihilation and creation operators, Eq. 7.23 becomes,

$$H(\mathbf{Q},\mathbf{q}) = \frac{\hbar^2 Q^2}{2\omega_{\mathbf{q}}} \sum_{n,m,\alpha} \frac{b_n b_m}{\sqrt{M_n M_m}} e^{i(\mathbf{Q}+\mathbf{q})(\langle\langle \mathbf{R}_n\rangle\rangle - \langle\langle \mathbf{R}_m\rangle\rangle)} (\hat{\mathbf{Q}}\cdot\mathbf{e}_{\mathbf{q},\alpha}^n)(\hat{\mathbf{Q}}\cdot\mathbf{e}_{\mathbf{q},\alpha}^m)(n_{\mathbf{q},\alpha}+1) \tag{7.25}$$

where $Q = |\mathbf{Q}|$ and $\hat{\mathbf{Q}} = \mathbf{Q}/Q$. The phonon density is given by the Bose–Einstein factor,

$$n_{\mathbf{q},\alpha} = \frac{1}{e^{\hbar\omega_{\mathbf{q},\alpha}/k_B T} - 1} \tag{7.26}$$

where k_B is the Boltzmann constant. Eqs. 7.25 and 7.26 describe the intensity of neutrons or X-rays inelastically scattered by creating single phonons on the energy loss side. The delta function $\delta(\omega-\omega_{\mathbf{q}})$ results in intensity from a given phonon mode appearing only at the energy transfer of the phonon mode frequency (times $\hbar$). The delta function $\delta(\mathbf{Q}+\mathbf{q}-\mathbf{K})$ results in intensity from that mode appearing at a momentum transfer of $\mathbf{K}-\mathbf{q}$, i.e. a distance $\mathbf{q}$ away from a reciprocal lattice (or Bragg) point. A contour plot of $S(\mathbf{Q},\omega)$ will thus exactly reproduce the phonon dispersion curves with the scattered intensity in each mode given by $e^{-W}/(\langle b\rangle^2 N)H(\mathbf{Q},\mathbf{q})$. An example of an energy scan of the inelastic scattering intensity is shown in Figure 7.5. Features resembling the phonon dispersion curves (indeed they are the phonon dispersion curves!) are clearly apparent. Actually, what is plotted in Figure 7.5(b) is $S(\mathbf{Q},\omega)$ and not $S_1(\mathbf{Q},\omega)$. The single-phonon dispersion curves are evident because of the happy consequence that the multi-phonon terms in the expansion of Eqs. 7.16(b) and 7.17 just contribute a rather featureless background intensity that $S_1(\mathbf{Q},\omega)$ sits on top of, as we discuss below.

If the dynamic structure factor is measured with a powder sample, at large Q the spherical averaging over Q is essentially equivalent to sampling every point in the Brillouin zone. Thus Eq. 7.25 yields the neutron weighted density of states. To ensure the accuracy

and improve statistics the data are usually integrated over a range of Q values. An example of the phonon density of states thus determined is shown in Figure 7.6.

7.2.2 Multi-phonon process

We will now go back to Eq. 7.16, and consider the effect of the higher order terms. When Q is small we only need to consider the leading term in the Q expansion, $S_1(\mathbf{Q}, \omega)$, which is the single phonon term as seen in Eqs. 7.22 and 7.25. In the PDF analysis we cover a wide range of Q values. Thus it is important to have some idea of the higher order terms describing the multi-phonon processes. This has been discussed in some detail by Thorpe *et al.* (2002) where the second and third order terms have been calculated explicitly for the case of *fcc* nickel, and powder averaged. These are shown in Figure 7.7 where it is evident that only the first order phonon terms have significant structure. However, note that higher order terms in the phonon spectrum contribute enough information to make them significant if PDF data are used to study lattice dynamics (Reichardt and Pintschovius, 2001; Thorpe *et al.*, 2002).

While it is difficult in general to account fully for the multiple-phonon process, we can safely use an approximate expression, since the multiple-sum makes the Q dependence weak and featureless. For this purpose we note the similarity of the expansions Eq. 7.16

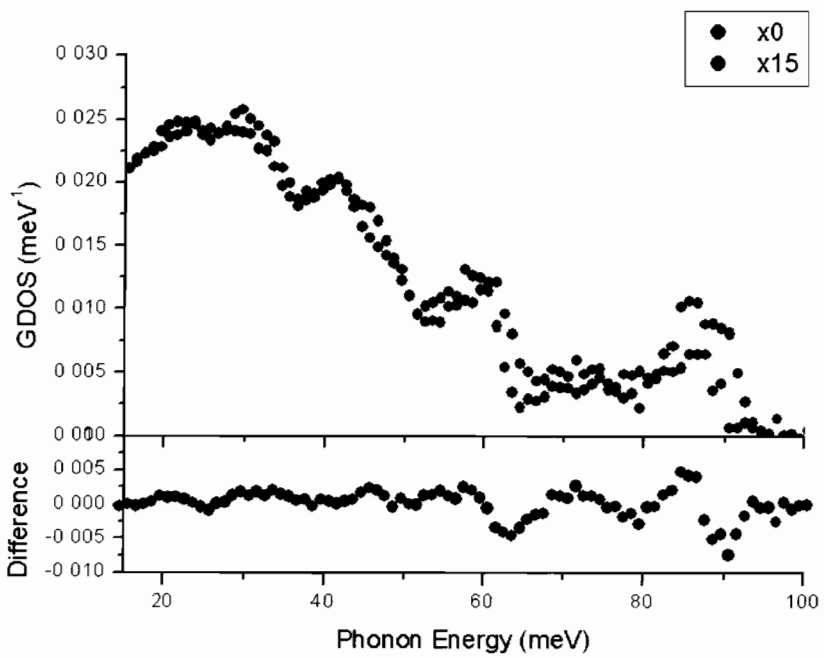

Figure 7.6. Phonon density of states of $La_{2-x}Sr_xCuO_4$ ($x = 0$, 0.15) determined by inelastic neutron scattering from LRMECS of the IPNS (McQueeney, 2002).

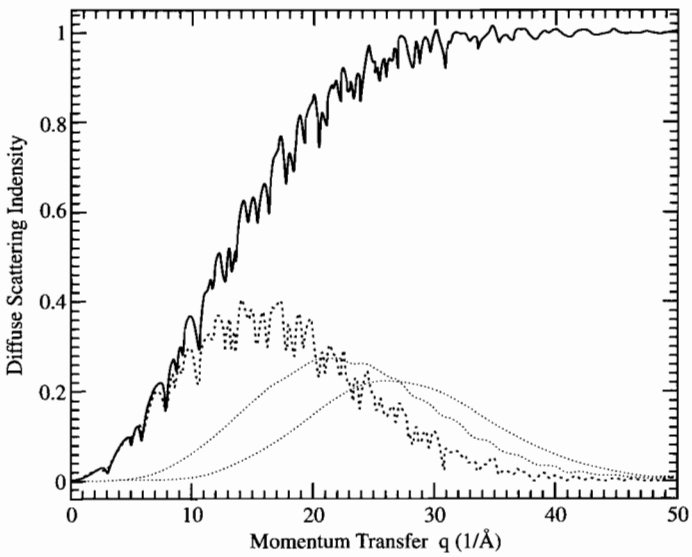

Figure 7.7. First (dotted), second (dot-dashed) and third (dot-dot-dashed) order phonon terms calculated explicitly for *fcc* nickel as it would appear in an ideal total scattering powder diffraction measurement. The solid line is the total phonon scattering (Thorpe *et al.*, 2002).

and 2.16. They are essentially the same expansion, except that Eq. 7.16 is time-dependent, while Eq. 2.16 is time-averaged. The next term in Eq. 7.16 is proportional to Q^4, and involves two-phonon scattering process. Thus if we integrate each term over energy, the expansion Eq. 7.16 strongly resembles Eq. 2.16. For large values of Q the prefactor in Eq. 7.16, which is the structure factor, approaches unity. Thus the total energy-integrated inelastic scattering intensity is approximated by,

$$S_{\text{inel}}(Q) = \langle\langle (Q \cdot u)^2 \rangle\rangle - \frac{1}{2}\langle\langle (Q \cdot u)^4 \rangle\rangle + \cdots \approx 1 - \mathrm{e}^{-\langle\langle (Q \cdot u)^2 \rangle\rangle} \tag{7.27}$$

where the Q^2 terms describes the single-phonon process, Q^4 the two-phonon process, etc. The contribution of each term is shown in Figure 7.7. The one phonon part is highly structured but the higher order terms have very little structure. This result justifies the expression 2.18.

Now at high enough values of Q the dynamic correlation among atoms is lost, and the scattering of a high-energy probe is described by a ballistic process in which the energy and momentum of the probe is transferred to a single atom. For neutrons this means the energy loss of

$$\hbar\omega = \frac{\hbar^2 Q^2}{2M} \tag{7.28}$$

where M is the mass of the atom.

7.3. CORRELATED DYNAMICS AND THE PDF

The phonons in materials give rise to correlations in the dynamics of atoms in real-space. This can be intuitively understood in the following way. The simplest model of a solid where the atoms are *not interacting* is the Einstein model. In this case every atom oscillates independently around its lattice site with a frequency ω_E. The atomic distribution functions are all Gaussians of the same width and the *pair* distribution functions (of pairs of atoms) will just be given by broad Gaussians of width two times the width of the *atomic* probability distributions. The PDF will consist of a series of peaks at different values of r of equal width, as shown in Figure 7.8(b). The simplest solid where the atoms are *strongly interacting* is a rigid-body solid where the atoms are rigidly joined (think of a solid metal rod joining them). In this case motions of the atoms are completely correlated and pairs of atoms are always separated by a fixed distance (the length of the metal rod). In this case, peaks in the PDF will all be delta-functions (Figure 7.8(a)). A more realistic situation is introduced when the atoms are joined to each other by stiff springs. In this case the usual treatment is to transform the problem into normal coordinates (the phonons modes), which are orthogonal and non-interacting, then project the phonon modes back into real-space to see what happens there, as we did in Section 7.2, above. This is mathematically more tractable but is not very intuitive. To understand intuitively what this does to the PDF consider our rigid body solid again, but this time cut the metal bar between each pair of atoms and insert a short piece of pliable rubber, the intuitive equivalent of placing a stiff spring there. Now we see that near neighbor pairs will tend to move in-phase as they did in the rigid body solid. The pair distribution will be sharp but not a delta-function because of

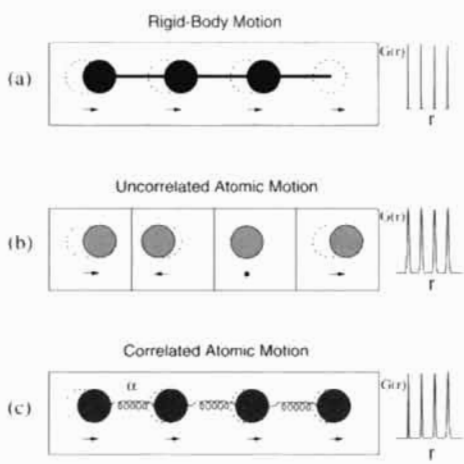

Figure 7.8. Schematic of correlated atomic motions showing the resulting PDF peaks on the right. (a) Perfectly correlated motion results in delta-function PDF peaks (a), uncorrelated motion in broad Gaussians (b), and partially correlated motion in sharp peaks at low-r that broaden with increasing r (Jeong *et al.*, 2003).

the presence of the soft rubber. The second neighbor pair distribution will also be fairly sharp but less so than the near-neighbor distribution because now we have the compliance of two pieces of rubber. The third neighbor motions will be less correlated still because of the third piece of rubber, and so on. Thus, we see that the presence of atomic interactions resulting in phonons introduces an r-dependence to the PDF peak width. At high pair separations the motions of the atom pairs asymptotes to the value appropriate for uncorrelated motion. This is shown in Figure 7.9 (Jeong *et al.*, 1999) with the r-dependence of the peak-widths of the PDF peaks from nickel and InAs shown in Figure 6.3. The peaks broaden with increasing r and saturate at the uncorrelated motion value. The amplitude of *uncorrelated* atomic motions is the information contained in the Debye–Waller factor. The additional information in the 1-phonon scattering gives rise to the r-dependent PDF peak-widths. In principle, by fitting this r-dependence we can extract information from the PDF about the atomic potential and the phonons. This is actually no different (other than practical considerations discussed below) than fitting the thermal diffuse scattering from powder diffraction data directly in Q-space, which was first attempted by Warren (1990) as early as 1952, albeit over a much wider range of Q-space.

7.4. THE DYNAMIC PAIR CORRELATION FUNCTION (DPCF)

Now we consider the correlated dynamics in more quantitative detail. Let us now go back to Eq. 7.11, and consider how to represent the lattice dynamics in real space, following McQueeney (1998). We will assume that the dynamic structure factor Eq. 7.11 was measured for a powder, and show how the dynamic correlation functions can be derived from them. Let us begin with the elastic intensity. In Eq. 7.11, since $\omega = 0, t$ can be anything.

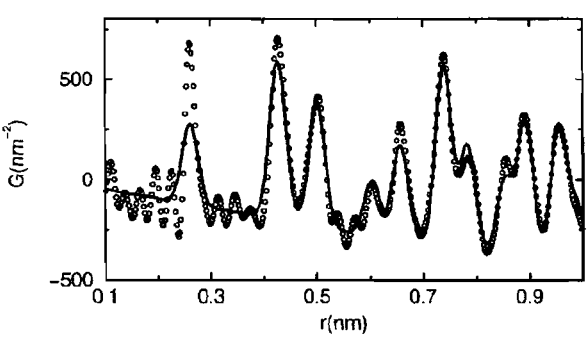

Figure 7.9. Calculated PDF of InAs neglecting motional correlations (solid line). Measured PDF of InAs at room temperature from X-ray data collected at CHESS (dots). Notice the low-r peaks are sharpened in the measurement with respect to the calculation (Jeong *et al.*, 1999).

That means the dynamic correlation between the atoms ν and μ is ignored;

$$S(\mathbf{Q},0) = \frac{1}{N\langle b\rangle^2}\sum_{\nu,\mu} b_\nu b_\mu \langle\!\langle e^{i\mathbf{Q}\cdot\mathbf{R}_\nu}\rangle\!\rangle\langle\!\langle e^{-i\mathbf{Q}\cdot\mathbf{R}_\mu}\rangle\!\rangle. \tag{7.29}$$

Using the Debye–Waller approximation from Chapter 2 we get,

$$S(\mathbf{Q},0) = \frac{1}{N\langle b\rangle^2}\sum_{\nu,\mu} b_\nu b_\mu \, e^{-(1/2)(W_\nu+W_\mu)} e^{i\mathbf{Q}\cdot(\langle\!\langle\mathbf{R}_\nu\rangle\!\rangle - \langle\!\langle\mathbf{R}_\mu\rangle\!\rangle)}. \tag{7.30}$$

Thus, the Fourier-transform of $S(Q,0)$ gives the atomic correlations among the time-averaged atomic density function, or the spatial auto-correlation of the time-averaged atomic density, just as the Patterson function does. This is different from the 'snap-shot' picture that is obtained when the phonon inelastic scattering is included; for example, in the usual PDF obtained in an X-ray diffraction measurement. In the simple one-dimensional, one atomic species, solid shown in Figure 7.8(b) it results in PDF peaks that are constant in width with increasing-r.

We will now discuss the inelastic term. Firstly a powder (orientational) averaging is performed on $S(\mathbf{Q},\omega)$. This gives,

$$S_1(Q,\omega) = \frac{e^{-W}}{N^2\langle b\rangle^2}\frac{\hbar^2Q^2}{2\omega}(n(\omega)+1)\sum_{\nu,\mu}\sum_{\mathbf{q},\alpha}\frac{b_\nu b_\mu}{\sqrt{M_\nu M_\mu}} e^{i\mathbf{q}\cdot(\langle\!\langle\mathbf{R}_\nu\rangle\!\rangle - \langle\!\langle\mathbf{R}_\mu\rangle\!\rangle)}\delta(\omega-\omega_{\mathbf{q},\alpha})$$
$$\times\left[\frac{1}{3}[\mathbf{e}^{\nu*}_{\mathbf{q},\alpha}\cdot\mathbf{e}^{\mu}_{\mathbf{q},\alpha}][j_0(QR_{\nu\mu})+j_2(QR_{\nu\mu})] - [\hat{\mathbf{R}}_{\nu\mu}\cdot\epsilon^{\nu}_{q,\alpha}]^*[\hat{\mathbf{R}}_{\nu\mu}\cdot\epsilon^{\mu}_{q,\alpha}]j_2(QR_{\nu\mu})\right] \tag{7.31}$$

where $j_n(x)$ is the spherical Bessel function of nth order, $R_{\nu\mu} = |\langle\!\langle\mathbf{R}_\nu\rangle\!\rangle - \langle\!\langle\mathbf{R}_\mu\rangle\!\rangle|$, and $\hat{\mathbf{R}}_{\nu\mu} = \mathbf{R}_{\nu\mu}/R_{\nu\mu}$. The Fourier transform of Eq. 7.31 gives the dynamic pair correlation function (DPCF),

$$g_1(r,\omega) = \frac{1}{\langle b\rangle^2}\sum_{\nu,\mu} b_\nu b_\mu\{F_{\nu\mu}(\omega)[K_0(r-R_{\nu\mu})+K_2(r-R_{\nu\mu})] - F^L_{\nu\mu}(\omega)K_2(r-R_{\nu\mu})\} \tag{7.32}$$

where

$$K_n(r-R_{\nu\mu}) = \frac{2r}{\pi}\int_0^\infty j_n(QR_{\nu\mu})e^{-W_{\nu\mu}}\sin(Qr)Q^3\,dQ \tag{7.33}$$

$$F_{\nu\mu}(\omega) = \frac{1}{3N}\frac{\hbar^2}{2\omega\sqrt{M_\nu M_\mu}}(n(\omega)+1)\sum_{q,\alpha}[\mathbf{e}^{\nu*}_{\mathbf{q},\alpha}\cdot\mathbf{e}^{\mu}_{\mathbf{q},\alpha}]e^{i\mathbf{q}\mathbf{R}_{\nu\mu}}\delta(\omega-\omega_{\mathbf{q},\alpha}) \tag{7.34}$$

and

$$F^{L}_{\nu\mu}(\omega) = \frac{1}{N}\frac{\hbar^2}{2\omega\sqrt{M_\nu M_\mu}}(n(\omega)+1)[\hat{\mathbf{R}}_{\nu\mu}\cdot\epsilon^{\nu}_{q,\alpha}]^{*}[\hat{\mathbf{R}}_{\nu\mu}\cdot\epsilon^{\mu}_{q,\alpha}]e^{i\mathbf{q}\mathbf{R}_{\nu\mu}}\delta(\omega-\omega_{\mathbf{q},\alpha}). \quad (7.35)$$

Examples of the DPCF are given in Figures 7.10 and 7.11 for a simple diatomic molecule. For instance if two atoms move in-phase, the distance between them does not change. Thus the DPCF should be a δ-function, not broadened by the Debye–Waller factor. On the other hand if they move out-of-phase, the DPCF peak becomes broader than estimated from the Debye–Waller factor. As we discussed in Section 7.2, near neighbors tend to move in-phase, because of the low energy long wave phonons. As shown in Figures 6.3 and 7.6, the PDF peak widths of neighboring atoms are narrower than average.

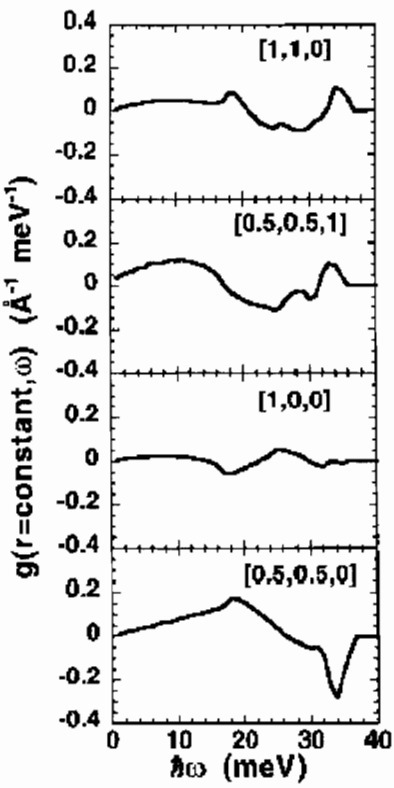

Figure 7.10. The dynamical radial distribution function $g(r = \text{const}, \omega)$, evaluated at the first four pair distances in nickel at $T = 0$ K. The atomic pairs are labeled in the cubic *fcc* lattice as [0.5, 0.5, 0], [1, 0, 0], [0.5, 0.5, 1], and [1, 1, 0]. For each neighbor, the frequency dependence is dominated by the longitudinal displacement–displacement correlations. More separated neighbors tend to have more oscillations in the frequency dependence (McQueeney, 1998).

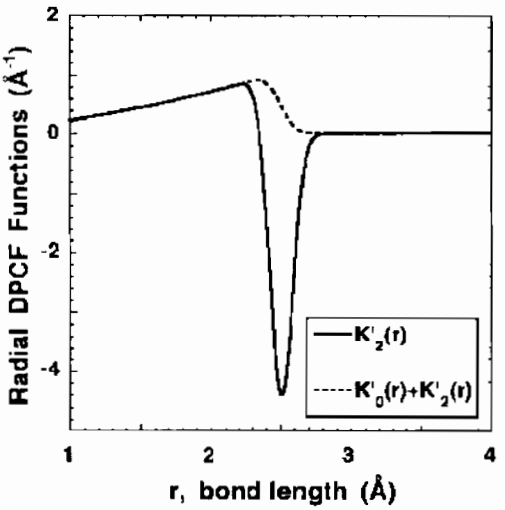

Figure 7.11. The dynamic pair correlation function (DPCF) inelastic radial functions, $K'_2(r)$ and $K'_0(r) + K'_2(r)$. $K'_2(r)$ has a single peak at the pair distances, unlike the dynamic RDF radial function, $K'_2(r)$, which has a W shape. Consequently, the DPCF formalism is more useful for identifying inelastic features. However, the DPCF peak has a long tail on the low-r side, making it difficult to determine the strength of atomic correlation (McQueeney, 1998).

7.5. EFFECT OF INELASTIC SCATTERING ON THE PDF

7.5.1 Phonon dispersion and the PDF

As early as 1952 attempts were made to extract phonon dispersions from X-ray powder diffraction data (Warren, 1990). It was quickly realized that the extensive powder averaging made this difficult and attention was switched to fitting thermal diffuse scattering from single crystals (Warren, 1990), and ultimately, with the advent of inelastic neutron scattering, to measure them directly. However, there is still great interest in the possibility of extracting atomic potential parameters and phonon information from powder data in cases where single crystals are not available or where data need to be measured in special environments such as high pressure cells. Powder diffraction has also traditionally had an advantage in phase diagram studies because of the relative ease of measuring and analyzing multiple data sets collected as a function of temperature and composition. In these cases, extracting phonon information from powder data would facilitate studies of, for example, phonon softening. One of the problems of the early studies was that the powder data were studied over a relatively narrow range of Q-space. Since the phonon intensity, $S_1(\mathbf{Q}, \omega)$, contributes relatively little to the total measured intensity it is necessary to measure $S(Q)$ over a wide range of Q with very good statistics to make progress. This happens as a fairly natural consequence of taking data to obtain the PDF as we discussed in detail in Chapter 5. Interest has therefore recently been reawaken in the

possibility of extracting phonon information from PDF-quality data measured at modern sources using modern techniques. Initial claims that force-constant variables could be measured with the same accuracy as possible from INS (Dimitrov *et al.*, 1999) are controversial (Jeong *et al.*, 1999; Reichardt and Pintschovius, 2001; Thorpe *et al.*, 2002; Graf *et al.*, 2002). Nonetheless, significant information about the atomic potential is present in the PDF (Jeong *et al.*, 2003; Graf *et al.*, 2002), the only question is how many variables can reasonably be extracted and with what accuracy. Work needs to be done to improve the accuracy of determining $S(Q)$ and at present it is not clear how much impact this kind of study will have in the future. We also note that with the use of high-energy X-ray diffraction it is becoming much quicker and easier to measure the thermal diffuse scattering from single crystals directly (Holt *et al.*, 1999).

7.5.2 Placzek correction

We now discuss another consequence of the presence of phonon inelastic scattering in regular powder diffraction measurements where the inelastic scattering is not explicitly resolved. As we discussed in Chapter 5, this results in distortions to the measured PDF from neutron diffraction. An empirical correction, often referred to as the Placzek correction (Placzek, 1952), is generally applied to correct the data for these distortions, and this is discussed below.

Let us first look at the case of X-ray scattering. It is often claimed that 'since the X-rays are so fast that X-ray diffraction is a snap-shot of the structure' (e.g. Warren, 1990). While this statement is not altogether wrong, it is extremely misleading. As we mentioned earlier X-ray inelastic scattering measurements are now becoming a reality, and even the lattice dynamics can be studied by X-ray scattering. We will show at first that the 'speed' of the measurement is not determined by the *velocity* of the probe, but by the *energy resolution* of the spectrometer. The velocity of the probe is relevant only in setting up the effective energy resolution when an energy analyzer is not used in the diffractometer.

In the derivation leading to Eq. 7.32 we assumed that both Q and ω are well defined. However, in any real measurement the energy resolution is finite, thus what is measured is the dynamic structure factor integrated over a certain energy range,

$$S_{\omega_0}(Q,\omega) = \int W(\omega,\omega')S(Q,\omega')\mathrm{d}\omega' \tag{7.36}$$

where $W(\omega,\omega')$ is a resolution (window) function centered around ω. As long as the resolution function is much narrower than the excitation energy the dynamic structure factor can be experimentally determined. However, in the conventional X-ray powder scattering experiment the energy resolution is in the range 10–1000 eV (depending on the measurement), far larger than the phonon energies. Using an analyzer crystal in a standard geometry the $\sim$10 eV resolution is sufficient to discriminate much of the electronic inelastic (Compton) scattering, but not the phonon scattering. Therefore the nominally

'elastic' X-ray scattering intensity includes the inelastic scattering contribution due to phonons. Now the velocity of light becomes important only here; since the velocity of light is high, the momentum transfer associated with the energy transfer of 10 eV is very small ($\sim 10^{-3}$ Å^{-1}) compared to the reciprocal lattice vector (~ 1 Å^{-1}). Thus the magnitudes of $\mathbf{k}_{\text{init}}$ and $\mathbf{k}_{\text{final}}$ are very close to each other, and Q is practically independent of ω. Since $W(\omega)$ is constant over the relevant range of ω (the window function is much wider than the phonon band width) from Eq. 7.11 we get,

$$\begin{aligned} S(\mathbf{Q}) &= \frac{1}{N\langle b\rangle^2} \sum_{\nu,\mu} b_\nu b_\mu \int\int \langle\!\langle e^{i\mathbf{Q}\cdot(\mathbf{R}_\nu(0)-\mathbf{R}_\mu(t))}\rangle\!\rangle e^{-i\omega t}\, dt\, d\omega \\ &= \frac{1}{N\langle b\rangle^2} \sum_{\nu,\mu} b_\nu b_\mu \langle\!\langle e^{i\mathbf{Q}\cdot(\mathbf{R}_\nu(0)-\mathbf{R}_\mu(0))}\rangle\!\rangle. \end{aligned} \tag{7.37}$$

Thus $S(\mathbf{Q})$ measures the instantaneous (same time) correlation. This is the other extreme than Eq. 7.30, and justifies the common declaration that the X-ray diffraction takes the 'snap-shot' of the atomic configuration. The snap-shots, however, are continuously taken, and time averaged. In that sense the 'snap-shot' is not really an appropriate expression, and students are often confused on this point. It is, therefore, more accurate to call $S(Q)$ the same-time correlation function. As we discussed above, this results in the correlated dynamics appearing in the PDF and yields r-dependent peak-widths.

Neutrons, on the other hand, have velocities that are much slower than the speed of light, and are even comparable to the velocity of atoms. Thus for neutron scattering the magnitudes of $\mathbf{k}_{\text{init}}$ and $\mathbf{k}_{\text{final}}$ can be significantly different, and for a fixed scattering angle Q is dependant upon ω as in Eq. 7.7. This causes a problem for a neutron powder diffraction measurement in which the actual energy and momentum transfers are not measured. In the powder diffraction measurement using a reactor only the initial energy is defined by a monochromator, while the final energy is not measured. In the *tof* measurement only the total time of flight is recorded, and neither the initial nor final energies are actually measured. To circumvent this problem what is usually done is to assume the momentum transfer of Q_0 for every scattering process, elastic or inelastic, and make appropriate corrections later. This correction is known as the Placzek correction (Placzek, 1952).

In the Placzek correction the neutron is assumed to have a high-energy and to be scattered by an atom ballistically, that means that the energy lost by a neutron is transferred entirely to the kinetic energy of the atom,

$$\begin{aligned} \hbar\omega &= \frac{\hbar^2}{2M}(|\mathbf{q}_{\text{final}}|^2 - |\mathbf{q}_{\text{init}}|^2) \\ \mathbf{Q} &= \mathbf{q}_{\text{init}} - \mathbf{q}_{\text{final}} \end{aligned} \tag{7.38}$$

where $\mathbf{q}_{\text{init}}$ and $\mathbf{q}_{\text{final}}$ are the momenta of the atom before and after scattering. In this case the energy transfer depends only on the atomic mass M, and not on the restoring force

represented by the Debye temperature (and therefore is independent of the underlying potential). In spite of such a simplification the Placzek correction works well most of the time.

The Placzek correction was developed for a triple-axis-spectrometer in which the energy of incident neutrons is fixed. By assuming that the energy of the incident neutron is much larger than the energy transfer, from Eq. 7.7 we obtain,

$$\begin{aligned} Q^2 &= 2k_i^2 - \frac{2m\omega}{\hbar} - 2k_i^2 \cos 2\theta \left(1 - \frac{2m\omega}{\hbar k_i^2}\right)^{1/2} \\ &= 2k_i^2 - \frac{2m\omega}{\hbar} - 2k_i^2 \cos 2\theta \left(1 - \frac{m\omega}{\hbar k_i^2} + \cdots\right) \\ &= 4k_i^2 \sin^2 \theta \left(1 - \frac{m\omega}{\hbar k_i^2} + \cdots\right) \end{aligned} \tag{7.39}$$

and

$$Q = 2k_i \sin \theta \left(1 - \frac{m\omega}{2\hbar k_i^2} + \cdots\right). \tag{7.40}$$

If we neglect the initial velocity of the atom the kinetic energy gain of the atom due to the momentum transfer of Q is,

$$\hbar\omega = \frac{\hbar^2}{2M} Q^2 \tag{7.41}$$

where M is the atomic mass. Thus we obtain the first order shift in Q,

$$\frac{\Delta Q}{Q_0} = \frac{-m\omega}{2\hbar k_i^2} = \frac{-m}{M} \sin^2 \theta + \cdots \tag{7.42}$$

From this we see that the Placzek shift becomes important at high scattering angles.

In the case of the *tof* measurement it is more complex because the result depends upon the neutron flight path length from the target to the sample, L_1, and that from the sample to the detector, L_2. The time-of-flight, τ, is the sum of the flight times over L_1 and L_2 with the velocities v_1 and v_2, respectively,

$$\tau = \frac{L_1}{v_1} + \frac{L_2}{v_2} = \frac{mL_1}{\hbar k_{\text{init}}} + \frac{mL_2}{\hbar k_{\text{final}}}. \tag{7.43}$$

Thus the nominal momentum, k_0, is given by,

$$k_0 = \frac{m}{\hbar} \frac{L}{\tau} = \frac{1}{\dfrac{L_1}{Lk_{\text{init}}} + \dfrac{L_2}{Lk_{\text{final}}}} \tag{7.44}$$

where $L = L_1 + L_2$. The nominal momentum transfer, Q_0, calculated assuming elastic scattering, is given by

$$Q_0 = 2k_0 \sin\theta = \frac{2\sin\theta}{\frac{L_1}{Lk_{\text{init}}} + \frac{L_2}{Lk_{\text{final}}}}. \tag{7.45}$$

Combining Eq. 7.44 with Eqs. 7.4 and 7.5 the relationship between the nominal momentum transfer and the real momentum transfer is obtained. Since usually $L_1 \gg L_2$ for most spectrometers, Eq. 7.44 can be expanded into,

$$Q_0 = \frac{2k_{\text{init}} \sin\theta}{1 + \frac{L_2}{L}\left(\frac{k_{\text{init}}}{k_{\text{final}}} - 1\right)}. \tag{7.46}$$

If we further assume $\hbar\omega \ll \hbar^2k^2/2m$, then,

$$Q_0 = \frac{2k_{\text{init}} \sin\theta}{1 + \frac{L_2}{L}\frac{m\omega}{\hbar k_{\text{init}}^2}} = 2k_{\text{init}} \sin\theta\left(1 - \frac{L_2}{L}\frac{m\omega}{\hbar k_{\text{init}}^2} + \cdots\right). \tag{7.47}$$

From Eq. 7.40,

$$Q = Q_0\left(1 - \left(1 - \frac{2L_2}{L}\right)\delta + \cdots\right) \tag{7.48}$$

where

$$\delta = \frac{m\omega}{2\hbar k_{\text{init}}^2}. \tag{7.49}$$

The main effect of the Placzek correction for the *tof* measurement is to correct the spectrum of the incident energies, since the normalization is usually done assuming elastic scattering alone. Incidentally, from Eq. 7.48 it is obvious that the first order Placzek correction vanishes if $L_2 = L/2$, or $L_1 = L_2$. However, the price to pay is the large size of the detector housing and the large angle the spectrometer takes up around the source. In terms of financial cost and real estate it is an expensive proposition.

7.5.3 Local lattice dynamics and the PDF

For regular phonons the Placzek shift has relatively little effect. The Placzek shift is important for strongly dispersing phonons, but they are usually low energy phonons so that the shift is small, whereas the high-energy phonons for which the shift is large usually have small dispersion. Since it is difficult to evaluate the effect analytically, the expected intensity was calculated numerically for a simple case of a diatomic molecule vibrating with the frequency ω (McQueeney, 1996). The result is summarized as follows:

1. If the frequency of the local vibration, ω, is less than ω_{min} the vibration appears static and the same-time correlation function is recovered approximately undistorted.

2. For $\omega_{min} < \omega < \omega_{max}$, distortions to the PDF are observed that are dependent on the detector angle θ.
3. For $\omega > \omega_{max}$ there is no angle dependence to the PDF but the time-averaged correlation function is recovered.

The values of ω_{min} and ω_{max} depend upon the interatomic distance and the design of the spectrometer, but for the interatomic distance of 3 Å and using the geometry of the GLAD diffractometer at IPNS, they are estimated to be about $\hbar\omega_{min} \sim 5$ meV and $\hbar\omega_{max} \sim 30$ meV. Thus the excitations in the range of 10–20 meV produce anomalous effects. The effects on the PDF from the calculated diatomic molecule are shown in Figure 7.12

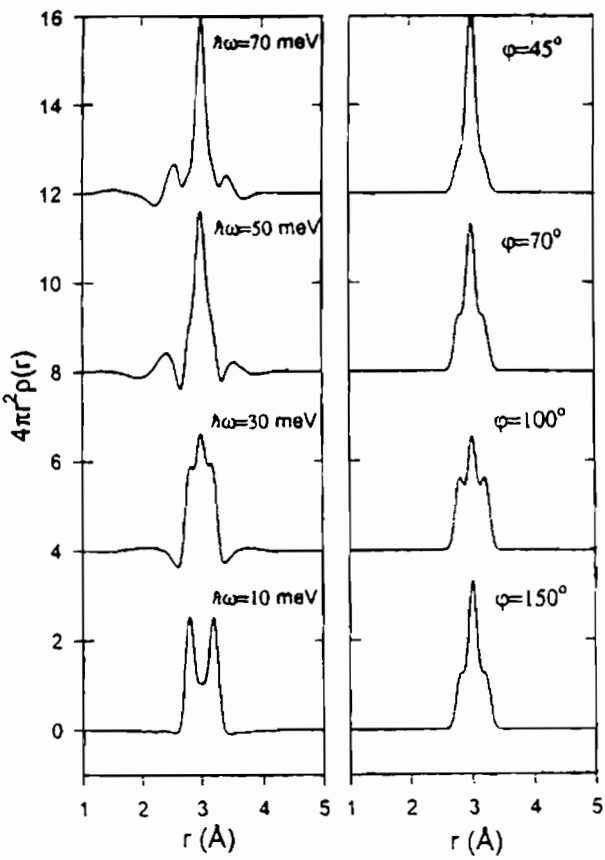

Figure 7.12. Time-of-flight PDF's calculated for several frequencies ($\hbar\omega = 10, 30, 50, 70$ meV) of the hopping diatomic molecule with the atomic separation, $d = 3$ Å, and displacement, $\Delta = 0.02$ Å. The diffractometer configuration is $L_1/L_2 = 10$ and $2\theta = 90°$ (left). Instantaneous PDF's for a hopping diatomic molecule whose atoms oscillate out-of-phase by φ (right) (McQueeney, 1996).

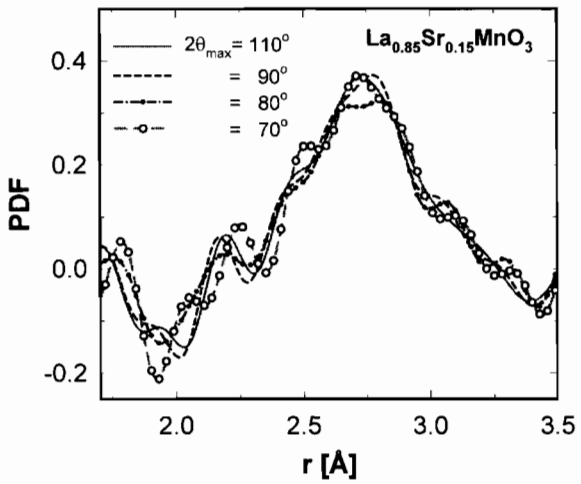

Figure 7.13. The dependence of the PDF on the detector angle in the case of local dynamics (see text) (Louca and Egami, 1999).

(McQueeney, 1996). An example of detector angle dependence of the PDF is shown in Figure 7.13, for $La_{0.8}Sr_{0.2}MnO_3$ (Louca and Egami, 1999).

7.5.4 Hybrid techniques

The measurement of $S(Q, \omega)$ with a monochromatic incident beam is inefficient since only a small portion of the incident spectrum is utilized in the incident beam. On the other hand regular *tof* neutron powder diffraction to determine $S(Q)$ is subject to the distortions described above. It is useful to consider a possible hybrid technique somewhere between the two. For a powder sample the dynamic structure factor depends only on the magnitude of Q, not on the direction, thus $S(Q, \omega)$ is the same for all the detectors. For truly elastic scattering every detector measures the same $S(Q, 0)$. Thus, assuming all angle dependent corrections are adequately carried out, any deviation in the measured $S(Q)$ among the detectors originates from the dynamic scattering. In principle, $S(Q, \omega)$ can then be reconstructed from the measured $S(Q)$ in each of the detectors. The reconstruction approach is called computed tomography and has been discussed by Johnson (1986). However, it requires a massive computational effort and the accuracy of the outcome is difficult to estimate. Another drawback is that in established diffractometers the distortions to $S(Q)$ are not really extensive enough (good news for measuring regular PDFs!). The method relies on the inelastic scattering from different detectors being integrated along distinct loci in (Q, ω)-space. Reference to Figure 5.9 shows that, except for very low angle detectors, the loci for detectors at different angles are rather similar to each other limiting the information available for the reconstruction.

A simpler compromise is to use a nearly monochromatic incident beam, but with a relatively wide momentum spectrum, $P(\Delta k_i, k_{i0})$, where k_{i0} is the average momentum and $\Delta k_i = k_i - k_{i0}$. Such a beam can be produced by a chopper with a wide aperture: a sloppy chopper. The use of a wide aperture increases the measured intensity. Then the detected intensity is given by

$$I(t, \theta) = \int P(\Delta k_i, k_{i0}) S(k_i, k_f) \mathrm{d}\Delta k_i \tag{7.50}$$

where $S(Q, \omega)$ is expressed in terms of k_i and k_f. From Eq. 7.41, $k_f = k_{f0} + \Delta k_f$, where

$$\frac{1}{k_{f0}} = \frac{\hbar t}{m L_2} - \frac{L_1}{L_2 k_{i0}} \tag{7.51}$$

and

$$\Delta k_f = -\frac{L_1 k_{f0}^2}{L_2 k_{i0}^2} \Delta k_i. \tag{7.52}$$

Now from Eqs. 7.3 and 7.5,

$$\hbar\omega = \hbar\omega_0 + \frac{\hbar^2}{m}(k_{f0}\,\Delta k_f - k_{i0}\Delta k_i) \tag{7.53}$$

$$Q^2 = Q_0^2 + 2(k_{i0} - k_{f0}\cos 2\theta)\Delta k_i + 2(k_{f0} - k_{i0}\cos 2\theta)\Delta k_f \tag{7.54}$$

where

$$\hbar\omega_0 = \frac{\hbar^2}{2m}(k_{f0}^2 - k_{i0}^2) \tag{7.55}$$

and

$$Q_0^2 = k_{f0}^2 + k_{i0}^2 - 2k_{f0}k_{i0}\cos 2\theta \tag{7.56}$$

Thus $S(Q, \omega)$ can be expanded in terms of $\Delta Q = Q - Q_0$ and $\Delta\omega = \omega - \omega_0$,

$$S(Q, \omega) = S(Q_0, \omega_0) + \frac{\partial S}{\partial Q}\Delta Q + \frac{\partial S}{\partial \omega}\Delta\omega + \frac{1}{2}\left[\frac{\partial^2 S}{\partial Q^2}(\Delta Q)^2 + \frac{\partial^2 S}{\partial \omega^2}(\Delta\omega)^2\right] + \frac{\partial S}{\partial Q}\frac{\partial S}{\partial \omega}\Delta Q\,\Delta\omega + \cdots \tag{7.57}$$

where

$$\Delta\omega = \frac{\hbar}{m}(k_{f0}\,\Delta k_f - k_{i0}\,\Delta k_i) \tag{7.58}$$

$$\Delta Q = \frac{1}{Q_0}[(k_{i0} - k_{f0}\cos 2\theta)\Delta k_i + (k_{f0} - k_{i0}\cos 2\theta)\Delta k_f] \tag{7.59}$$

Now we define the moments of $P(\Delta k_i, k_{i0})$,

$$K_0 = \int P(\Delta k_i, k_{i0}) \mathrm{d}\Delta k_i = 1, \qquad K_1 = \int P(\Delta k_i, k_{i0}) \Delta k_i \, \mathrm{d}\Delta k_i = 0$$
$$K_2 = \int P(\Delta k_i, k_{i0}) (\Delta k_i)^2 \mathrm{d}\Delta k_i \tag{7.60}$$

where we assumed that $P(\Delta k_i, k_{i0})$ is a symmetric function. Then Eq. 7.50 is given by,

$$I(t, \theta) = S(Q_0, \omega_0) + K_2(A_0 + A_1 \cos 2\theta + A_2 \cos^2 2\theta) \tag{7.61}$$

where A_0, A_1 and A_2 can be determined from Eqs. 7.52–7.59. Thus the dependence of $I(t, \theta)$ on $\cos 2\theta$ and the continuity condition for $S(Q, \omega)$ yield the coefficients $\mathrm{d}S/\mathrm{d}Q$, etc. These can be used in refining $S(Q, \omega)$ with the accuracy higher than the initial resolution warranted. In this method, using a forgiving energy resolution increases the count rate and reduces statistical noise, and $S(Q, \omega)$ can be determined with higher accuracy.

APPENDIX 7.1. DYNAMIC STRUCTURE FACTOR

A7.1.1 Simple derivation

In Chapter 7 we introduced the dynamical structure factor Eq. 7.11,

$$S(\mathbf{Q}, \omega) = \frac{1}{N\langle b \rangle^2} \sum_{\nu,\mu} b_\nu b_\mu \int \langle\langle \mathrm{e}^{\mathrm{i}\mathbf{Q}(\mathbf{R}_\nu(0) - \mathbf{R}_\mu(t))} \rangle\rangle \mathrm{e}^{-\mathrm{i}\omega t} \, \mathrm{d}t. \tag{A7.1.1}$$

As in the case of static structure function (sample scattering amplitude), this equation can be derived by comparing the phases of the incoming and outgoing waves, by explicitly including time dependence. The incoming wave is expressed by,

$$\phi_{\mathbf{k}_{\mathrm{init}}}(\mathbf{r}, t) = \mathrm{e}^{\mathrm{i}(\mathbf{k}_{\mathrm{init}}\mathbf{r} - \omega_{\mathrm{init}} t)}. \tag{A7.1.2}$$

The scattered wave is

$$\chi_{\mathbf{k}_{\mathrm{final}}}(\mathbf{r}, t) = A \, \mathrm{e}^{\mathrm{i}(\mathbf{k}_{\mathrm{final}}\mathbf{r} - \omega_{\mathrm{final}} t)} \tag{A7.1.3}$$

Here the amplitude A is independent of time. Otherwise the scattered wave (Eq. A7.1.3) would not have the energy of $\hbar\omega_{\mathrm{final}}$. Thus, at the point of scattering by the atom ν at time t', taking into account that the position of the atom, $\mathbf{R}_\nu$, changes with time, the continuity condition is

$$\chi_{\mathbf{k}_{\mathrm{final}}}(\mathbf{R}_\nu(t'), t') = B\phi_{\mathbf{k}_{\mathrm{init}}}(\mathbf{R}_\nu(t'), t')$$
$$A \, \mathrm{e}^{\mathrm{i}(\mathbf{k}_{\mathrm{final}}\mathbf{R}_\nu(t') - \omega_{\mathrm{final}} t')} = B \, \mathrm{e}^{\mathrm{i}(\mathbf{k}_{\mathrm{init}}\mathbf{R}_\nu(t') - \omega_{\mathrm{init}} t')} \tag{A7.1.4}$$

Thus,

$$A = B\,\mathrm{e}^{\mathrm{i}[(\mathbf{k}_{\mathrm{init}}-\mathbf{k}_{\mathrm{final}})\mathbf{R}_\nu(t')-(\omega_{\mathrm{init}}-\omega_{\mathrm{final}})t']} = B\,\mathrm{e}^{\mathrm{i}(\mathbf{Q}\mathbf{R}_\nu(t')-\omega t')} \tag{A7.1.5}$$

Therefore the scattering amplitude for inelastic scattering at time t' is given by,

$$\Psi(\mathbf{Q}, t') = \frac{1}{\langle b\rangle}\sum_\nu b_\nu\,\mathrm{e}^{\mathrm{i}(\mathbf{Q}\mathbf{R}_\nu(t')-\omega t')} \tag{A7.1.6}$$

At the time of observation, t, all the scattering incidents in the past have to be integrated over time t',

$$\Psi(\mathbf{Q}, \omega) = \int \Psi(\mathbf{Q}, t')\mathrm{d}t' = \frac{1}{\langle b\rangle}\sum_\nu b_\nu \int \mathrm{e}^{\mathrm{i}(\mathbf{Q}\mathbf{R}_\nu(t')-\omega t')}\mathrm{d}t'. \tag{A7.1.7}$$

The dynamical structure factor is defined by

$$S(\mathbf{Q}, \omega) = \frac{1}{N}|\Psi(\mathbf{Q}, \omega)|^2. \tag{A7.1.8}$$

Thus,

$$\begin{aligned}
S(\mathbf{Q}, \omega) &= \frac{1}{N}\int\int \Psi(\mathbf{Q}, t')\Psi^*(\mathbf{Q}, t'')\mathrm{d}t'\,\mathrm{d}t'' \\
&= \frac{1}{N\langle b\rangle^2}\sum_{\nu,\mu} b_\nu b_\mu \int\int \mathrm{e}^{\mathrm{i}(\mathbf{Q}\mathbf{R}_\nu(t')-\omega t')}\mathrm{d}t' \int \mathrm{e}^{-\mathrm{i}(\mathbf{Q}\mathbf{R}_\nu(t'')-\omega t'')}\mathrm{d}t'' \\
&= \frac{1}{N\langle b\rangle^2}\sum_{\nu,\mu} b_\nu b_\mu \int\int \mathrm{e}^{\mathrm{i}\mathbf{Q}[\mathbf{R}_\nu(t')-\mathbf{R}_\nu(t'')]}\mathrm{e}^{-\mathrm{i}\omega(t'-t'')}\mathrm{d}t'\,\mathrm{d}t'' \\
&= \frac{1}{N\langle b\rangle^2}\sum_{\nu,\mu} b_\nu b_\mu \int\int \mathrm{e}^{\mathrm{i}\mathbf{Q}[\mathbf{R}_\nu(t')-\mathbf{R}_\nu(t-t')]}\mathrm{e}^{\mathrm{i}\omega t}\,\mathrm{d}t'\,\mathrm{d}t \\
&= \frac{1}{N\langle b\rangle^2}\sum_{\nu,\mu} b_\nu b_\mu \int \langle\!\langle \mathrm{e}^{\mathrm{i}\mathbf{Q}[\mathbf{R}_\nu(0)-\mathbf{R}_\mu(t)]}\rangle\!\rangle \mathrm{e}^{\mathrm{i}\omega t}\mathrm{d}t.
\end{aligned} \tag{A7.1.9}$$

The last step uses the fact that the time average (over t') is equal to the ensemble (thermal) average.

REFERENCES

Dimitrov, D.A., Louca, D. & Röder, H. (1999) *Phys. Rev. B*, **60**, 6204.

Egami, T., Chung, J.-H., McQueeney, R.J., Yethiraj, M., Mook, H.A., Frost, C., Petrov, Y., Dogan, F., Inamura, Y., Arai, M., Tajima, S. & Endoh, Y. (2002) *Physica B*, **62**, 316.

Graf, M., Jeong, I.K., Heffner, R.H. (2002) unpublished.

Holt, M., Wu, Z., Hong, H., Zschack, P., Jemian, P., Tischler, J., Chen, H. & Chiang, T.-C. (1999) *Phys. Rev. Lett.*, **83**, 3317.

Jeong, I.-K., Proffen, Th., Mohiuddin-Jacobs, F. & Billinge, S.J.L. (1999) *J. Phys. Chem. A*, **103**, 921.

Jeong, I.-K., Heffner, R.H., Graf, M.J. & Billinge, S.J.L. (2003) *Phys. Rev. B*, **67**, 104301.
Lovesey, S.W. (1984) *Theory of Neutron Scattering from Condensed Matter*, Oxford Science Publications, Oxford.
Johnson, M.W. (1986) Rutherford Appleton Laboratory document RAL-86-041.
Lake, B., Tennant, D.A. & Nagler, S.E. (2000) *Phys. Rev. Lett.*, **85**, 832.
Louca, D. & Egami, T. (1999) *Phys. Rev. B*, **59**, 6193.
McQueeney, R.J. (1996) Thesis, University of Pennsylvania, unpublished.
McQueeney, R.J. (1998) *Phys. Rev. B.*, **57**, 10560.
McQueeney, R.J. (2002) Private communication. See McQueeney, R.J., Sarrao, J.L., Pagliuso, P.G., Stephens, P.W., Osborn, R (2001) *Phys. Rev. Lett.* **87**, 077001.
Placzek, G. (1952) *Phys. Rev.*, **86**, 377.
Reichardt, W. & Pintschovius, L. (2001) *Phys. Rev. B*, **63**, 174302.
Sinn, H., Alp, E.E., Alatas, A., Barraza, J., Bortel, G., Burkel, E., Shu, D., Sturhahn, W., Sutter, J.P., Toellner, T.S. & Zhao, J. (2001) *Nucl. Instr. Meth. Phys. Res. A*, **467**, 1545.
Thorpe, M.F., Levashov, V.A., Lei, M. & Billinge, S.J.L. (2002) in *From Semiconductors to Proteins: Beyond the Average Structure*, Kluwer/Plenum, New York, p. 105.
Tranquada, J.M., Shirane, G. & Shapiro, S.M. (2002) *Neutron Scattering with a Triple-Axis Spectrometer*, Cambridge University Press, Cambridge.
Warren, B.E. (1990) *X-ray Diffraction*, Dover, New York.

Chapter 8

Structure of Well-Ordered Crystals

This Page Intentionally Left Blank

Chapter 8
Structure of Well-Ordered Crystals

8.1. PDF OF IDEAL AND DISTORTED PEROVSKITES

In earlier chapters, we have already shown some simple examples of the application of the PDF technique for elementary metals such as fcc, Ni or Al, and the pseudo-binary compounds (Ga,In)As, as well as some highlights from recent PDF studies. In this chapter, we focus on oxides based upon the perovskite structure. Perovskite, ABO_3, is one of the most common oxide structures. In the ideal state it has a cubic unit cell, with an A-site at the center of the cube, B-sites at the corners, and oxygen ions at the edge centers. Equivalently, we can place a B-site ion at the center of the cube, A-site ions at corners, and oxygen ions at the face-centers (Figure 8.1). The B-site ion is characterized as having six oxygen nearest neighbors and residing in a BO_6 octahedron (Figure 8.2(a)). The A-site ion has 12 oxygen neighbors (Figure 8.2(b)). A very large number of oxide compounds have a structure that is a derivative of perovskite. In the ideal cubic structure the A–O and O–O bonds have to be equal in length, and have to be $\sqrt{2}$ times longer than the B–O bond that is

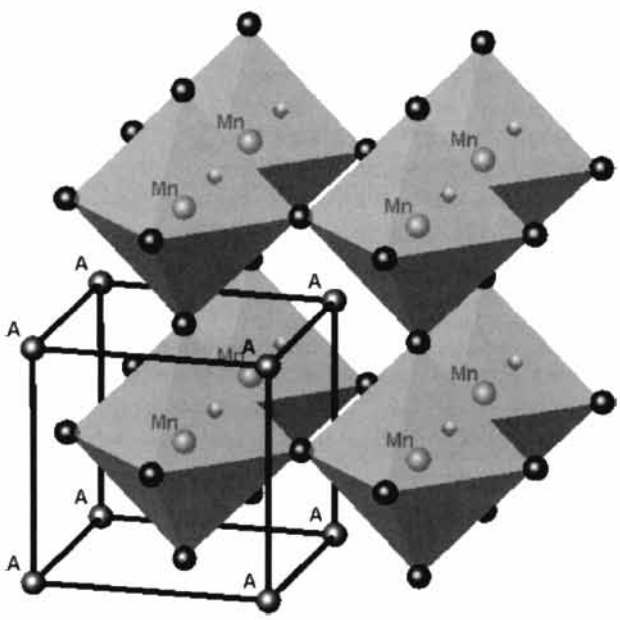

Figure 8.1. Picture of the perovskite structure. B-site ions (in this case Mn indicated in red) sit at the center of oxygen (blue) octahedra. The A-site (green) resides in the cavities made by the network of octahedra.

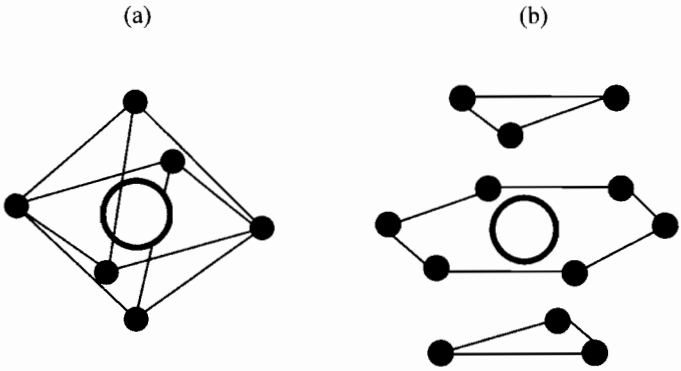

Figure 8.2. Coordination of the A and B site ions shown more explicitly. (a) BO_6 octahedron, (b) AO_{12} cluster.

the shortest bond. However, only in exceptional cases do the bond-lengths have such a ratio. If the ratio between the A–O and B–O bond lengths is not equal to $\sqrt{2}$, an ideal perovskite cannot be formed, and the structure becomes distorted. It is customary to express this balance in terms of the tolerance factor,

$$t = \frac{R_{A-O}}{\sqrt{2}R_{B-O}}. \tag{8.1}$$

The bond-length between two ions is, to a good approximation, the sum of their 'ionic radii', which is empirically specified for given valence and coordination (Shannon, 1976; Shannon and Prewitt, 1969). Thus in order to satisfy the condition for the ideal perovskite structure the ionic radius of the A ion has to be equal to that of oxygen ($R_O = 1.40$ Å), and the radius of the B ion has to be $(\sqrt{2} - 1)R_O = 0.58$ Å. This condition strongly limits the choice of ions, so that almost all perovskite compounds have a distorted structure. When t is less than unity most commonly the BO_6 octahedra become tilted, often around the [111] axis, and the structure becomes rhombohedral.

As we see below the BO_6 octahedron tends to behave as a unit, and its rotation or tilting is often a key to define the structure. A detailed analysis of the different classes and space-groups of octahedrally tilted perovskite structures has been given by Woodward (1997a,b). For instance, tilting of a BO_6 octahedron induces tilting of the adjacent BO_6 octahedron in the opposite sense resulting in a doubling of the unit cell. This often results in anti-ferroelectric or ferroelastic behavior. On the other hand, if t is greater than unity the BO_6 octahedron will be distorted, becoming usually elongated. Some of the B-site ions, such as Ti^{4+} or W^{6+}, have a tendency to become off-centered, resulting in ferroelectricity. In addition some A-site ions, such as Pb^{2+} or Li^{+}, prefer directional bonding with oxygen ions, and an asymmetric A-site environment, enhancing the ferroelectric polarization (e.g. see Cohen, 1992). In this way the ionic size has a direct consequence on the properties

of the compounds. A major goal of solid-state chemistry is to understand these structure–property relationships in the quest to design new compounds.

8.1.1 Structure of $SrTiO_3$

$SrTiO_3$ (STO) is a prototypical perovskite with the ideal perovskite structure at room temperature. Indeed the tolerance factor of STO is very close to unity ($t = 1.02$). Below 110 K, however, the structure deviates very slightly from cubic and becomes rhombohedral. The PDF of STO determined by pulsed neutron scattering at $T = 10$ K is shown in Figure 8.3 (Louca and Egami, 1999). The Glass-Liquid-Amorphous-Diffractometer (GLAD) of the IPNS was used for this measurement. A powder of STO weighing 15 g was sealed in a vanadium can with He exchange gas. The measurement took 5 h with a beam current of 14 μA. The PDF shown in Figure 8.3 has a negative first peak. This is because the neutron scattering length, b, is negative for Ti and positive for O so, as a result of Eq. 3.5, the Ti–O peak appears negative. The PDF compares very well with the calculated PDF with the thermal amplitude of 0.07 Å. The magnitude of the thermal factor is consistent with the Debye temperature of this solid. The distances and the coordination numbers obtained by integrating the RDF over the peak are shown in Table 8.1, and agree well with the values expected for the structure. Since the peaks start to overlap beyond the second peak, and positive and negative peaks cancel each other, the coordination number of high order peaks cannot be determined by direct integration. However, agreement of the PDF with the model PDF indicates that the PDF is accurate over the range shown.

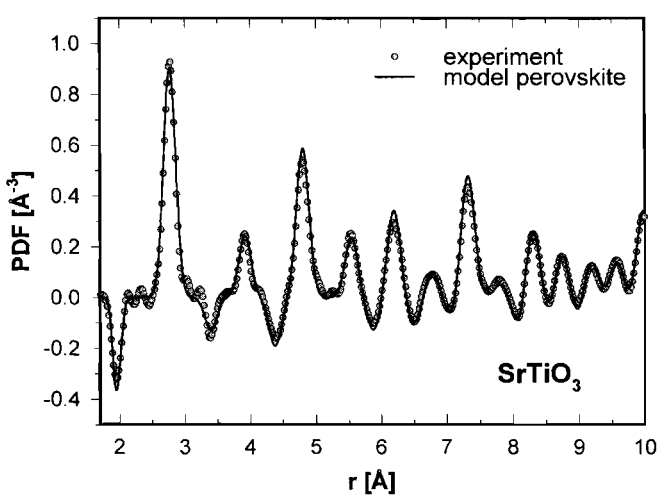

Figure 8.3. Pulsed neutron PDF of $SrTiO_3$ at $T = 10$ K (Louca and Egami, 1999).

Table 8.1. Peak positions and number of first and second neighbors in $SrTiO_3$ expected from the crystal structure and measured directly (in a model independent way) from the PDF.

		Peak position (Å)		Number of neighbors	
Compound	Coordination shell	Expected	Measured	Expected	Measured
$SrTiO_3$	First (Ti–O)	1.95	1.95	6	5.97
	Second (O–O, Sr–O)	2.77	2.77	36	36.87

8.1.2 Structure of $BaTiO_3$

$BaTiO_3$ is another prototypical ferroelectric perovskite and is one of the most heavily studied materials (Kwei *et al.*, 1993, and references therein). At high temperature it has a centrosymmetric cubic structure but on cooling it undergoes a series of distortive phase transitions into ferroelectric phases with the ferroelectric polarization vector along [001] (below 393 K, tetragonal) [011] (below 278 K, orthorhombic) and [111] (below 183 K, rhombohedral). These distortions are shown schematically in Figure 8.4. A long-standing controversy existed about the structure of this material that is highly pertinent to the discussions of this book. In each of the distorted phases crystallography revealed small atomic displacements of Ti and O along the directions of the polarization vectors (Kwei *et al.*, 1993). On the other hand, X-ray diffuse scattering (total scattering) measurements indicated that the atomic displacements of Ti were always along [111] directions

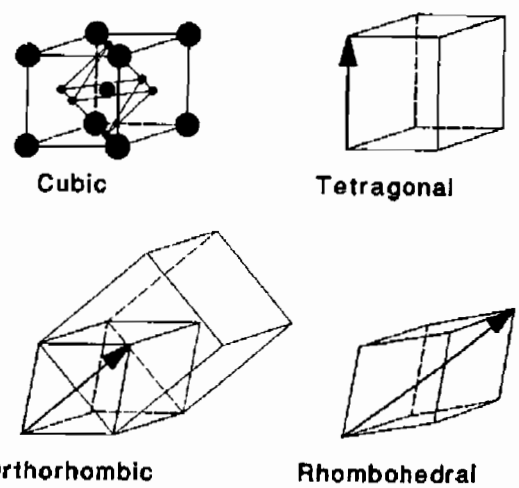

Figure 8.4. Schematic diagrams of the distortive phase transitions in $BaTiO_3$ on lowering temperature. The arrow indicates the direction along which the cubic unit cell is distorted, and also the direction of the ferroelectric polarization. The larger unit-cell superimposed in the orthorhombic case shows the relationship of the crystallographic orthorhombic unit cell to the distorted pseudo-cubic cell (Kwei *et al.*, 1993).

corresponding to the eight faces of the TiO_6 octahedra (Comes *et al.*, 1968, 1970). As the sample changed temperature the relative occupancies of the different displaced sites changed. Thus, in the low-temperature rhombohedral phase only one of the eight displaced sites was preferred, in the orthorhombic variant two out of the eight, in the tetragonal variant, four of the eight and in the high-temperature cubic all eight are equally populated (presumably dynamically). This result was somewhat controversial because $BaTiO_3$ was considered to be an archetypal phonon soft-mode material where the distortive phase transitions happened by the condensation of an unstable phonon mode (Jona and Shirane, 1962). This is discussed much more fully in Chapter 11. The local structural measurements that indicated a significant order–disorder component to the phase transition tended to muddy this elegant and simple soft-mode picture. As is discussed in Chapter 11, length-scales and time-scales need to be handled carefully, and models that explain the evolution of average properties at phase transitions do not necessarily explain well the actual local structure, and this is clearly the case here. PDF measurements of these materials tend to support the Comes *et al.* (1968, 1970) picture at the local level since changes in the local structure at these phase transitions are very small (Kwei *et al.*, 1995) as shown in Figure 8.5. This result can be understood if atomic displacements (to which the PDF is rather sensitive) are not changing significantly but ordering between the displaced sites (to which the PDF is rather insensitive) is changing.

8.1.3 Structure of $PbTiO_3$

$PbTiO_3$ (PT) is cubic at high temperatures, but it becomes ferroelectric below T_c and the structure distorts to tetragonal. The ionic radius of Pb^{2+} is 1.49 Å and that of Ti^{4+} is 0.605 Å. Thus the tolerance factor is equal to 1.019. However, in this case the tolerance factor is less important in determining the crystal structure. What is most important is the asymmetry of the atomic bonds for both Pb and Ti. Pb^{2+} has the electron configuration of $(Xe)(4f)^{14}(6d)^{10}(6s)^2$, and the two s electrons tend to form directional bonds by hybridizing with the oxygen p-orbitals. Consequently Pb^{2+} becomes off-centered in the oxygen cage of PbO_{12} resulting in shorter and longer Pb–O bonds of 2.54, 2.8 and 3.2 Å. Ti^{4+}, on the other hand, is ferroelectrically active, and tends also to become off-centered in the TiO_6 octahedra with bonds of 1.78, 1.97 and 2.37 Å. As a result of these off-centering tendencies PT becomes strongly ferroelectric, with a tetragonal distortion. The bond distances determined from the PDF and those from the crystallographic structure show good agreement (Dmowski *et al.*, 2002). The PDF method is an excellent technique to study ferroelectricity. Local polarization produces different metal–oxygen bond distances that induce the splitting of the metal–oxygen PDF peak. As shown in Figure 8.6 (Kwei *et al.*, 1995), at low temperatures the three kinds of Ti–O bonds are clearly evident, while in an ideal perovskite structure (Figure 8.1) there is only one distance between a B-site metal and its closest oxygen. The splitting of the Ti–O distance in Figure 8.6 indicates a strong

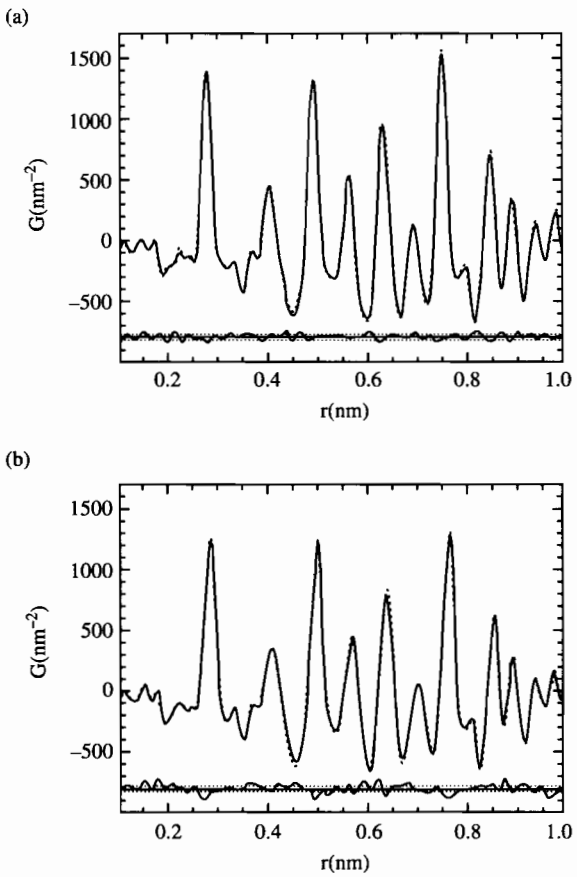

Figure 8.5. PDFs of $BaTiO_3$ on passing through the (a) rhombohedral to orthorhombic and (b) orthorhombic to tetragonal phase transitions shown in Figure 8.4. Data above (below) the transition are solid (dashed) lines. A difference curve is shown below the data. Changes in the *local* structure are very small at these transitions (Kwei *et al.*, 1995).

ferroelectric polarization of Ti in the TiO_6 octahedron. If we take Ti as the origin, at low temperatures Pb is displaced from the ideal position by 0.2 Å along the *c*-axis and oxygen by 0.3 Å in the opposite direction. Thus both Ti and Pb are strongly off-centered within the oxygen cage, and contribute to the ferroelectric dipolar moment.

8.1.4 Structure of $LaMnO_3$

Another example of a distorted perovskite is the Jahn–Teller distorted compound $LaMnO_3$. The tolerance factor of this compound is 0.986, and as a consequence MnO_6

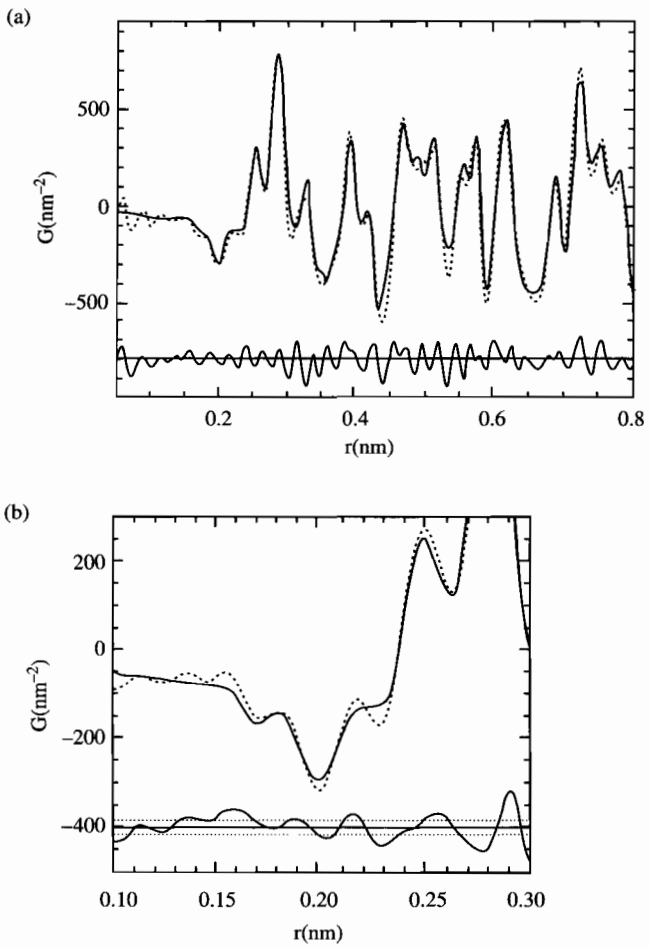

Figure 8.6. Pulsed neutron PDFs of $PbTiO_3$ at $T = 10$ K. Solid line is a model calculation using the tetragonal structure, dashed line indicates the data. A difference curve is shown below the data. (b) shows the PDF on an expanded scale to emphasize the near-neighbor Ti–O atom pairs. The vertical lines indicate the lengths of the six Ti–O bonds in a 1-4-1 configuration (Kwei *et al.*, 1995).

octahedra are rotated around the [111] axis. However, what makes this compound interesting is a further distortion due to *the Jahn–Teller effect*. In $LaMnO_3$ Mn is trivalent and has four d-electrons. The nearly cubic crystal-field splits the d-level into t_{2g} (triplet) and e_g (doublet) levels. The exchange coupling among the d-electrons (Hund coupling) is stronger than the crystal-field splitting, so that these d-electrons are fully spin polarized (the high-spin state). Thus the majority spin t_{2g} level is filled and the e_g orbital is singly occupied. The e_g level is further split into two by a Jahn–Teller (JT) distortion that

elongates the MnO_6 octahedra (Figure 1.8, Proffen *et al.*, 1999). As a result of the JT distortion the Mn–O bond distances are grouped into four short (1.92 and 1.97 Å) and two long (2.16 Å) bonds (Proffen *et al.*, 1999). $LaMnO_3$ has the orthorhombic (*Pnma*) structure (Mitchell *et al.*, 1996; Rodríguez-Carvajal *et al.*, 1998; Lebedev *et al.*, 1998; Proffen *et al.*, 1999; Louca *et al.*, 2000). In this structure the JT distortion is oriented in the a–b plane with alternating directions (antiferromagnetic orbital ordering). With an excess of oxygen that creates vacancies at the cation sites the structure changes to rhombohedral ($R3C$) symmetry in which all six Mn–O bonds are equal in length.

As we discussed in Chapter 1, conventional crystallographic methods are capable of obtaining the lattice constants with impressive accuracy since they are determined directly by the *position* of the Bragg peaks in Q space that can be located very precisely. However, for a complex crystal that has a number of atoms within the unit cell, the determination of the atomic positions is a much less precise operation since they are determined by the *intensities*, not the positions, of the Bragg peaks. The PDF method has several advantages over the crystallographic methods in determining the atomic positions in such a case. Firstly, by incorporating the scattering information from high Q values the real-space positional accuracy is improved. Secondly, by including the diffuse scattering, various dynamic effects such as vibrational anharmonicity are explicitly taken into account.

$LaMnO_3$ provided a nice example from a well-ordered crystal where structural parameters determined from the PDF and using Rietveld refinement of the same powder diffraction data could be compared (Proffen *et al.*, 1999). (Another excellent example is

Table 8.2. Structural data of LaMnO3 (*Pbnm*) from the Rietveld refinement and two PDF refinements, A and B, which vary in the range of r fit (see Proffen *et al.*, 1999 for details).

	Rietveld	Refinement A	Refinement B
a	5.542(1)	5.5422(7)	5.557(1)
b	5.732(1)	5.7437(8)	5.774(1)
c	7.6832(2)	7.690(1)	7.712(2)
x(La)	−0.0068(3)	−0.0073(2)	−0.0068(2)
y(La)	0.0501(3)	0.0488(2)	0.0504(1)
$\langle u^2 \rangle$(La)	0.0022(4)	0.00199(4)	0.00177(4)
$\langle u^2 \rangle$(Mn)	0.0011(6)	0.00067(7)	0.00071(7)
x(O1)	0.0746(4)	0.0729(3)	0.0734(2)
y(O1)	0.4873(4)	0.4857(3)	0.4800(2)
$\langle u^2 \rangle$(O1)	0.0031(5)	0.00233(7)	0.00178(5)
x(O2)	0.7243(3)	0.7247(3)	0.7232(2)
y(O2)	0.3040(3)	0.3068(3)	0.3060(1)
z(O2)	0.0390(2)	0.0388(3)	0.0369(2)
$\langle u^2 \rangle$(O2)	0.0030(4)	0.00378(5)	0.00439(4)
R_{wp}	12.1	16.2	9.1

La and O1 are on $(x, y, 0.25)$, Mn is on (0,0.5,0), and O2 is on (x, y, z). The units for the lattice parameters are Å, and for values of $\langle u^2 \rangle$, Å^2. The numbers in parentheses are the estimated standard deviation on the last digit. Note the overall good agreement.

found in Teslic and Egami (1998) on the structure of $PbZrO_3$, described in Section 8.2.) The measured PDF and the best-fit model are shown in Figure 1.8 with a difference curve underneath. The refined structural parameters are reproduced in Table 8.2. Clearly the agreement between Rietveld and PDF refined atomic positional parameters is excellent indicating that the PDF yields quantitatively accurate atomic positions when fit with an adequate model.[1] PDF refined thermal factors are also in good agreement and, in general, are smaller in the PDF refinements. Because the data used in the PDF-fits extend over a wider range of Q, refined thermal factors from PDF-fits are often more stable and give more physical values (e.g. see Gutmann *et al.*, 2000, and the discussion in Section 8.2.1, Teslic and Egami, 1998).

8.2. COMPLEX PERIODIC STRUCTURE: ANTIFERROELECTRIC LEAD ZIRCONATE

8.2.1 Low temperature phase

Lead zirconate ($PbZrO_3$, PZ) is an end member of the family of a well-known ferroelectric oxide solid solution, $PbZr_{1-x}Ti_xO_3$ (PZT). PZT is used as a ferroelectric or piezoelectric material in a wide variety of technological applications. Nevertheless, there have been raging controversies regarding the dielectric properties and atomic structure of PZ. The tolerance factor is equal to 0.973, so that ZrO_6 octahedra are expected to be tilted or rotated. In addition the polarizability of Pb, as discussed above, is expected to contribute to the distortion. Indeed, its structure is based upon the distorted and tilted perovskite but is rather complex with eight perovskite units forming the unit cell structure containing 40 atoms. Two different symmetries have been proposed; non-centrosymmetric (ferroelectric, FE) *Pba*2 (Jona *et al.*, 1951), and centrosymmetric (antiferroelectric, AFE) *Pbam* (Fujishita *et al.*, 1982). A recent total electron energy calculation using the local density approximation (LDA) demonstrated the coexistence of both FE and AFE instabilities in PZ, with a very delicate balance between them (Singh, 1995). In addition there is a possibility of a second high temperature phase with an unknown structure and ordering over a narrow temperature range near 510 K.

A powder pulsed neutron diffraction measurement was carried out at various temperatures, and the results were analyzed using both the Rietveld refinement method and the PDF analysis (Teslic and Egami, 1998). The neutron diffraction data were obtained using the Special Environment Powder Diffractometer (SEPD) at the IPNS. The sample, weighing 14.5 g, was sealed in a vanadium sample holder with He-exchange gas and cooled

[1] Note that he estimated standard deviations (e.s.d.) on the refined quantities are likely to be underestimates. This is a known problem with e.s.d. from Rietveld (D.E. Cox, private communication). In addition to these known problems of estimating reliable e.s.d. from non-linear least-squares refinements, the e.s.d. determined from the PDF data have not been corrected for statistical correlations in the data, as discussed in Appendix 5.3. These problems do not affect the accuracy of determining the values themselves, but only of determining their e.s.d.

using a closed-loop He refrigerator for the low temperature measurements. For the high temperature measurements the sample was sealed in a vanadium holder and heated using a vanadium furnace, and data were collected up to 523 K. The duration of each run was approximately 4 h per temperature point. Diffraction intensities were first analyzed by the Rietveld method using the IPNS Rietveld package over the d range of 0.5–4.0 Å with the resolution of $\Delta d/d = 0.006$. The overall scale factor, parameters defining peak shapes, counter-zero error, atomic position parameters, isotropic thermal (atomic displacement) factors, and unit-cell parameters were refined. The PDF was calculated using the data of $S(Q)$ up to 35 $Å^{-1}$, with small damping for $S(Q) - 1$ between 30 and 35 $Å^{-1}$.

The Rietveld analysis suggested that the symmetry of PZ at $T = 20$ K is not the non-centrosymmetric *Pba*2, but the centrosymmetric *Pbam*. The PDF calculated from the Rietveld-refined model showed excellent agreement with the PDF data as shown in Figure 6.5. Real-space refinement over the range of $1.8 \leq r \leq 9.5$ Å produced an almost identical result. Thus the Rietveld method and the PDF method are in full agreement with the structure of PZ at 20 K. Note that in the PDF analysis just 28 parameters were refined including position and thermal parameters and the $S(Q)$ normalization factor, while in the crystallographic refinement 27 structural parameters were refined in *Pbam* symmetry in addition to 9 parameters which include the scale factor, background parameters as well as extinction and absorption parameters. The maximum allowed number of independent parameters in this real space range is 80 (Billinge, 1992), more than twice as many as were refined. The best-fit model in the real-space refinement gave an A-factor of 7.87% with e.s.d.(A) = 0.12% over the range $1.8 \leq r \leq 9.5$ Å. Over this range, $A_{\min}$ was 2.15% and, therefore, the goodness of fit (GoF) value is 3.66. This value is comparable to the GoF value of 3.20 attained in the Rietveld refinement of the same data. The only significant difference between the Rietveld refined model and the real-space refined model was found in the value of the thermal (DW) factor of the equatorial oxygen O2. The Rietveld-refined thermal factor ($B = 0.42$ $Å^2$) corresponds to an unreasonably high mean-square displacement, $\langle u^2 \rangle$, of 5×10^{-3} $Å^2$, while the RDF-refined value is 1.5×10^{-3} $Å^2$. The value of $\langle u^2 \rangle$ calculated by the Einstein model is 2.07×10^{-3} $Å^2$ for O, much closer to the value obtained by the PDF analysis.

In order to compare the refined variables in the Rietveld and PDF analyses it is important to estimate their accuracy. This is possible by considering the uncertainties in the A and R_w- factors and their best-fit curves as functions of a refined parameter. Then the uncertainty in the refined parameter is given by the range of values for this parameter for which the A or R_w factors change by less than their e.s.d. The e.s.d. for the A-factor calculated by the propagation of e.s.d. of the data is ±0.12%, which when calculated in this way results in uncertainties in O2(c), O3(c) and O4(c) parameters in the PDF analysis of ±0.01, ±0.02 and ±0.02 Å. Similarly, the e.s.d. of the R_w-factor is ±0.08% and the uncertainties for O2(c), O3(c) and O4(c) were found to be ±0.07, ±0.02 and ±0.04 Å,

respectively, in the Rietveld analysis. Thus the uncertainties in these position parameters in the PDF analysis are significantly smaller than those in the Rietveld analysis. Consequently, the atomic positions refined by the PDF analysis are most likely to be more accurate.

8.2.2 High temperature phases

8.2.2.1 Temperature dependence. The crystal structure determined by the Rietveld analysis evolved smoothly and slowly with temperature. On the contrary, the PDF shows appreciable temperature dependence as shown in Figure 8.7. In particular, the changes in the peak heights with temperature are not uniform across r, some peaks becoming much more smeared at 300 K than at 20 K. An increase in the thermal vibrational amplitude can account for only a small part of this change. For instance, the dramatic decrease in the height of the PDF peak at 5.9 Å cannot be explained by thermal phonons. This implies the existence of displacive disorder developing with temperature. It was found that disordered oxygen displacements at the equatorial sites lead to an improved fit. Introducing disorder in the pattern of alternative O3, O4 displacements improved the fit, lowering the A-factor nearly 1%.

8.2.2.2 Anharmonic displacements. The Rietveld-refined value for the thermal (DW) factor on the Pb site was anomalously large even at $T = 20$ K. The reason is probably

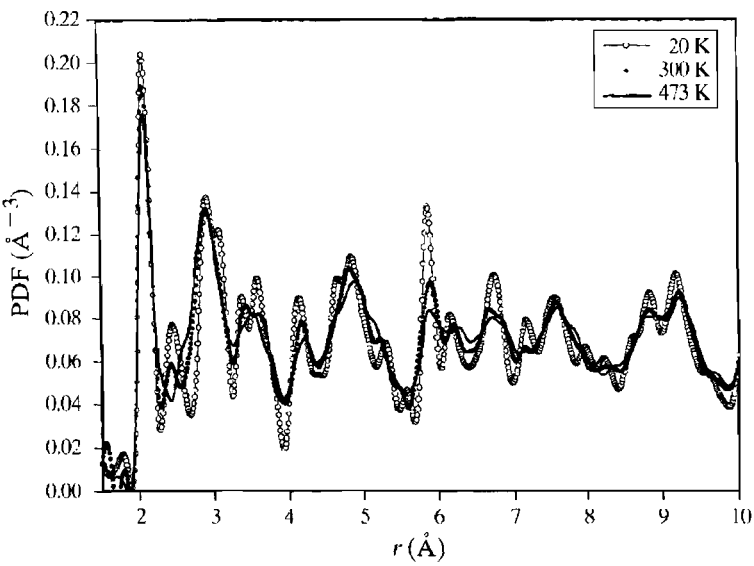

Figure 8.7. Variation of the neutron PDF of $PbZrO_3$ with temperature (Teslic and Egami, 1998).

the presence of some disordered static or quasistatic displacive disorder on the Pb site along the c-axis leading to a large uncertainty in the atom position. In order to characterize such Pb displacements the weighted Rietveld reliability factor R_w was evaluated as a function of the Pb displacement. To allow for such displacements the refinement was carried out in the non-centrosymmetric *Pba*2 space-group keeping the oxygen positions unchanged. The best-fit R_w-factor as a function of a static displacement of Pb in the c-direction, FE Pb_c, is shown in Figure 8.8.

A similar analysis with the PDF real-space method yielded a set of curves for the A-factor that shows minima more clearly than the Rietveld derived results. Thus, we can conclude that a small static or quasistatic local FE Pb displacement in the c-direction develops. Using the PDF analysis we can also detect the existence of correlation among Pb_c displacements and its range. Keeping fixed the magnitude of the Pb_c displacement that produced the best-fit model in the range 1.8–9.5 Å, the PDFs with FE and random Pb_c displacements for interatomic distances up to 40 Å were compared. It was found that the FE correlation length at low temperatures was estimated to be about 10 Å. For this reason we conjecture that the Pb_c displacements must be quasistatic rather than static.

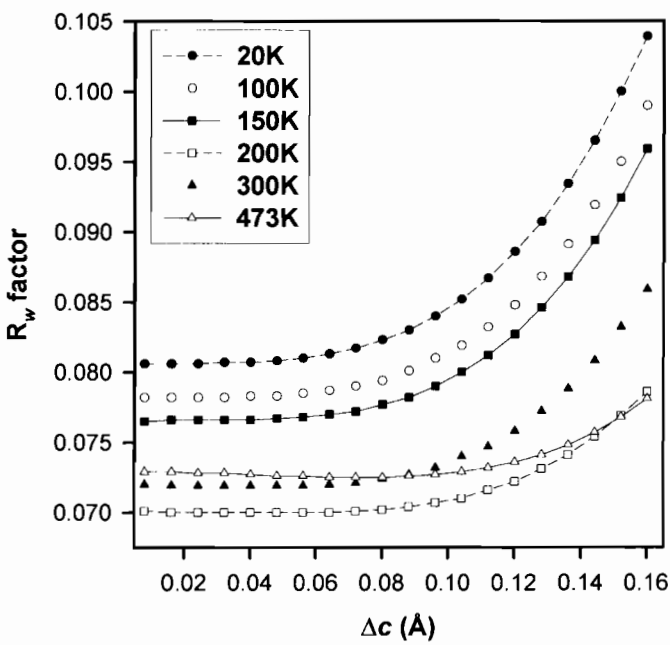

Figure 8.8. The best-fit Rietveld R_{wp} factor as a function of Pb displacement along the c-axis in $PbZrO_3$. (Teslic and Egami, 1998).

At 473 K both the reciprocal- and real-space refinements indicated a FE displacement of Pb in the *c*-direction. The best-fit curve for the R_w-factor shows shallow minima at ± 0.08 Å. In the PDF refinement, the *A*-factor curve has somewhat deeper minima at ± 0.14 Å before finally diverging at a larger value of $\Delta = 0.20$ Å, as shown in Figure 8.9. It was found that the Pb_c correlation length to be about 20 Å at this temperature.

8.2.2.3 Intermediate phase. The Rietveld analysis for the intermediate phase turned out to be extremely difficult, yielding large R_w factors and thermal factors. The structure apparently is not correctly described by either the *Pbam* or *Pba*2 symmetry phases. The PDF analysis also encountered great difficulties. However, a different, simpler AFE pattern with alternating Pb displacements within the *ab* plane (AFE-II, Figure 8.10(b)), as opposed to the double row AFE pattern at low temperatures (AFE-I, Figure 8.10(a)), was found to provide good agreement. This phase also has a large FE Pb displacement in the *c*-direction, and the correlation extends up to 30 Å, while it is inconclusive whether the FE long range order is established.

8.2.2.4 Paraelectric phase. Although PZ at high temperatures (above 508 K) was crystallographically refined as cubic, very small differences were observed in the PDF between 508 and 523 K (Teslic and Egami, 1998). This implies that the PE phase is locally

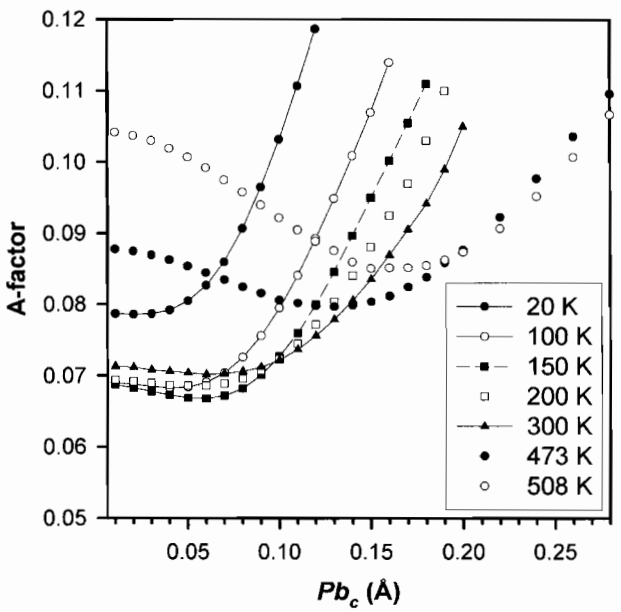

Figure 8.9. The best-fit PDF *A*-factor as a function of Pb displacement along the *c*-axis in $PbZrO_3$ (Teslic and Egami, 1998).

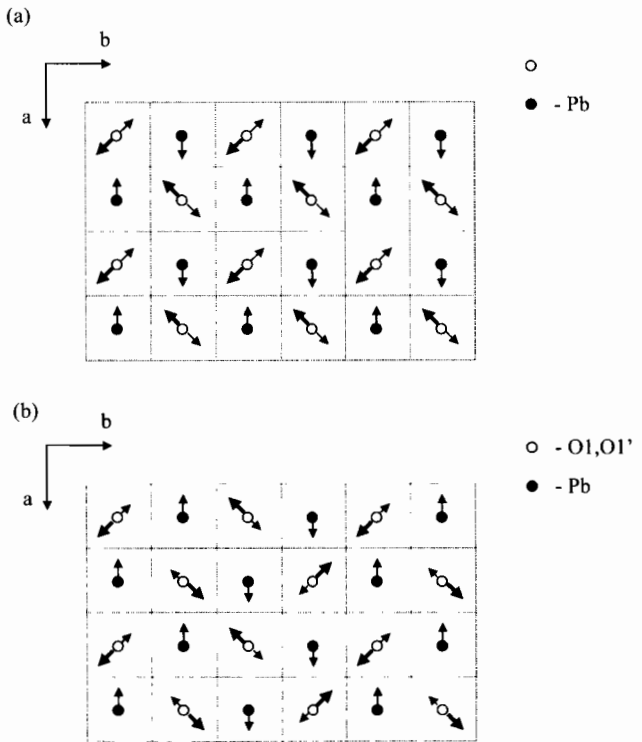

Figure 8.10. (a) AFE pattern of atom displacements for the intermediate phase (AFE-II), (b) AFE pattern for the low temperature phase (AFE-I). View is down the crystallographic *c*-axis. Solid circles indicate Pb and the open circles oxygen. The arrows indicate the directions of atomic displacement (Teslic and Egami, 1998).

polarized, and that the FE phase transition has the order/disorder character (Stern and Yacoby, 1996). This point, however, requires further discussion developed in Chapter 11. The PDF refinement of the data at 523 K showed that Pb atoms were displaced along the [111] direction. The displacements are spatially correlated only over short range, therefore, they are not directly observable in the reciprocal-space analysis.

8.2.3 Pb polarization

As we discussed above, Pb^{2+} has two 6s electrons that are high in energy, and readily hybridize with the oxygen p-orbitals, forming covalent bonds with 2–4 oxygen ions. Consequently the PbO_{12} dodecahedral cluster becomes strongly off-centered as shown in Figure 8.11. The center of gravity of the O_{12} cage is separated from the position of the Pb ion by as much as 0.5 Å. This produces a strong local ionic polarization of the PbO_{12} cluster. The structure and structural transition in PZ can be understood in terms of interaction among these local PbO_{12} polarizations and their reorientation as we will discuss

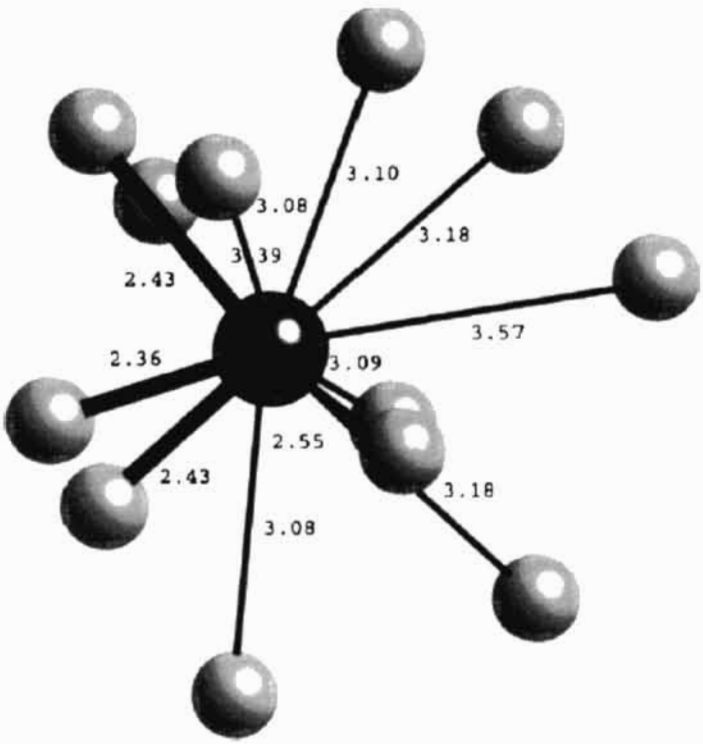

Figure 8.11. Oxygen neighbors of Pb in $PbZrO_3$ in the ferrelectric phase. Numbers indicate distances in Å (Teslic and Egami, 1998).

in Chapter 10. In PT Pb^{2+} is displaced in the [100] direction, forming covalent bonds with four oxygen ions. In PZ the direction of the Pb^{2+} displacement is [110], in the coordinates of the pseudo-cubic perovskite lattice, again with four close oxygen ions. In the average structure of rhombohedral PZT Pb^{2+} is displaced in the [111] direction, but locally the direction is closer to [110] as discussed later. Thus Pb^{2+} apparently prefers to be off-center either in [100] or [110] directions, but not in the [111] direction. This could be due to the partial involvement of the p-orbital in the covalent bond. This is very similar to the behavior seen in the covalent alloy $In_{1-x}Ga_xAs$ (Sections 1.2.1 and 9.2.1)

REFERENCES

Billinge, S.J.L. (1992) PhD thesis, University of Pennsylvania.
Cohen, W.E. (1992) *Nature*, **358**, 136.
Comes, R., Lambert, M. & Guinier, A. (1968) *Solid State Commun.*, **6**, 715.
Comes, R., Lambert, M. & Guinier, A. (1970) *Acta Crystallogr. A*, **26**, 244.

Dmowski, W., Akbas, M.K., Egami, T. & Davies, P.K. (2002) *J. Phys. Chem. Solids*, **63**, 15.
Fujishita, H., Shiozaki, Y., Achiwa, N. & Sawaguchi, E. (1982) *Phys. Soc. Jpn*, **51**, 3583–3591.
Gutmann, M.G., Billinge, S.J.L., Brosha, E.L. & Kwei, G.H. (2000) *Phys. Rev. B*, **61**, 11762.
Jona, F. & Shirane, G. (1962) *Ferroelectric Crystals*.
Jona, F., Shirane, G., Mazzi, F. & Pepinsky, R. (1951) *Phys. Rev.*, **105**, 849–850.
Kwei, G.H., Lawson, A.C., Billinge, S.J.L. & Cheong, S.-W. (1993) *J. Phys. Chem.*, **97**, 2368.
Kwei, G.H., Billinge, S.J.L., Cheong, S.-W. & Saxton, J.G. (1995) *Ferroelectrics*, **164**, 57.
Lebedev, O.I., Van Tendeloo, G., Amelinckx, S., Leibold, B. & Habermeier, H.-U. (1998) *Phys. Rev. B*, **58**, 8065.
Louca, D. & Egami, T. (1999) *Phys. Rev. B*, **59**, 6193.
Louca, D., Brosha, E.L. & Egami, T. (2000) *Phys. Rev. B*, **61**, 1351.
Mitchell, J.F., Argyriou, D.N., Potter, C.D., Hinks, D.G., Jorgensen, J.D. & Bader, S.D. (1996) *Phys. Rev. B*, **54**, 6172.
Proffen, Th., DiFrancesco, R.G., Billinge, S.J.L., Brosha, E.L. & Kwei, G.H. (1999) *Phys. Rev. B*, **60**, 9973.
Rodríguez-Carvajal, J., Hennion, M., Moussa, F. & Moudden, A.H. (1998) *Phys. Rev. B*, **57**, R3189.
Shannon, R.D. (1976) *Acta Crystallogr. A*, **32**, 751.
Shannon, R.D. & Prewitt, C. (1969) *Acta Crystalallogr. A*, **25**, 925.
Singh, D. (1995) *Phys. Rev. B*, **52**, 12559–12563.
Stern, E.A. & Yacoby, Y. (1996) *J. Phys. Chem. Solids*, **57**, 1449–1455.
Teslic, S. & Egami, T. (1998) *Acta Crystalallogr. B*, **54**, 750.
Woodward, P.M. (1997a) *Acta Crystalallogr. B*, **53**, 32.
Woodward, P.M. (1997b) *Acta Crystalallogr. B*, **53**, 44.

Chapter 9

Defects, Nanocrystalline and Crystallographically Challenged Materials

This Page Intentionally Left Blank

Chapter 9
Defects, Nanocrystalline and Crystallographically Challenged Materials

9.1. LATTICE DEFECTS AND THE PDF METHOD

Since the principal power of the PDF method resides in its capacity to describe deviations from perfect periodicity, it is a good method to consider in studying the nature and density of the lattice defects in crystals. In many materials of scientific and technological interest it is actually the defects that give them their interesting properties. It is thus very important to be able to study the defects as well as the average structure. A variety of techniques exist for characterizing defects including electron microscopy, scanning microscopies and spectroscopies, nuclear spectroscopic methods such as μSR and NMR, and so on. Each method has advantages and disadvantages and it is important to choose the method commensurate with the purpose of the study. The PDF is a volume averaged quantity, so that in order for the lattice defects to become detectable in the PDF their density has to be sizable. For instance there is little chance of detecting thermal vacancies or lattice dislocations in metals by the PDF method since their densities are usually far smaller than 10^{-4}. However, when the defect densities are sizeable the PDF yields quantitative atomic scale information about them. Materials where defect densities are large we refer to here as crystallographically challenged materials. This signifies that they are, indeed, periodic crystals; however, a significant aperiodic component exists that may be important in determining their properties.

The minimum detectable density of defects varies case by case. The best way to detect them in the PDF is by comparing two samples with and without defects. The difference can be characterized by computing the agreement-factor (Chapter 6) between the two PDFs. Experience tells us that if the density of defects is 10% they are easy to detect, while if the density is below 1% it is difficult to become convinced from the PDF that the defects really exist. Why do we bother thinking about the PDF method when there are many other methods to detect defects? In fact, if the nature of the defects is well understood and the only issue is determining their density, the PDF method is not the method of choice. However, if the detailed nature of the defect, such as the local structure within the defect and the lattice relaxation around the defect, is not well known, the PDF method can be an excellent tool. Also when the density of defects is very high they start to interact with each other and their structure will become modified compared to the isolated state. The PDF method can determine such subtle changes in the local structure with high accuracy.

Another class of materials we identify is that of nanocrystalline materials, defined in more detail below. These materials have limited structural coherence and are not really long-range crystals at all. As such they do not diffract with delta-function Bragg-peaks making them difficult to analyze crystallographically, yet the structural order is extensive enough (typically a number of nanometers) to make them distinct from traditional amorphous materials where the short-range order is very short-range. The PDF method has proved useful in solving the structure of a number of these materials as we describe below.

9.2. DEFECTS IN WELL-ORDERED CRYSTALS

9.2.1 Semiconductor alloys: the development of high-resolution X-ray PDF measurements

The semiconductor alloys, $In_{1-x}Ga_xAs$, were introduced in Chapter 1. Interest here was to study the local atomic displacements, beyond the average structure, due to the alloying. High real-space resolution was needed to resolve the short and long Ga–As and In–As bonds, respectively. However, the Q-range, and therefore real-space resolution, was limited in neutron measurements due to the presence of a neutron absorption resonance in indium. The solution lay in X-ray PDF measurements. The success of these high real-space-resolution X-ray PDF measurements has opened a new chapter in PDF analysis of crystals.

Increasing the real-space resolution of X-ray measurements, as opposed to spallation neutron measurements, presents a special challenge: the X-ray form-factor, $f(Q)$. The square of this is a measure of the structural-information containing coherent scattering from the material under study. The structure factor falls off sharply with increasing Q resulting in a weak signal at high momentum transfer (Chapter 5). This is illustrated in Figure 9.1(a) that shows the raw intensity from nanocrystalline WS_2 (described below). The overall drop-off in intensity follows $|f(Q)|^2$ with very little apparent structure in the scattering in the high-Q region above 15 Å. However, when the data are divided by $|f(Q)|^2$, as per Eq. 2.9, diffuse structure becomes apparent in this region (Figure 9.1(b)). It is therefore important to measure to these high-Q values with good statistics. This does not present a problem when new high-flux, high-energy, synchrotrons are used such as Cornell High Energy Synchrotron Source (CHESS) and the Advanced Photon Source (APS) at Argonne National Laboratory. The incident flux at high energies is so great that, despite the inefficient coherent scattering, sufficient statistics can be obtained to yield accurate data up to 45 $Å^{-1}$ (Petkov *et al.*, 1999a; Jeong *et al.*, 2001).

The high quality data from the $In_{1-x}Ga_xAs$ series, measured at CHESS at 10 K, are shown in Figure 9.2(a) with the high-Q region magnified. Noise is apparent, but the signal, a sine-wave feature with a period ~ 0.2 Å, is clearly evident especially in the alloys where Bragg-peaks at high-Q are suppressed by the alloy-induced structural disorder. When these

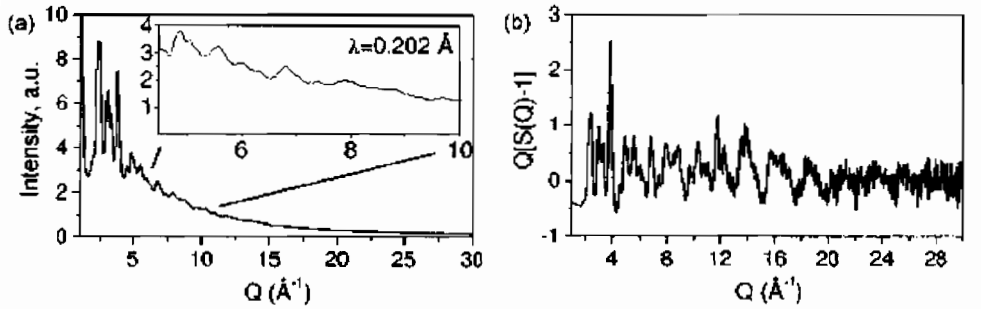

Figure 9.1. (a) Raw intensity data from a sample of exfoliated-restacked WS_2 measured using X-rays of $\lambda = 0.202$ Å ($E \sim 60$ keV) from CHESS. This Figure illustrates the effect of the atomic form-factor in suppressing intensity at high-Q. (b) The same data after making corrections and dividing by $|f(Q)|^2$ showing significant diffuse intensity in the high-Q region (Petkov *et al.*, 2000c).

data are Fourier transformed they result in the PDFs in Figure 9.2(b). What is clearly apparent is that the nearest neighbor In–As peak is split into two, partially resolved, peaks in the alloys. The short Ga–As and long In–As bonds survive almost unstrained in the alloy. Extensive modeling of the data, including comparison with chemically specific but

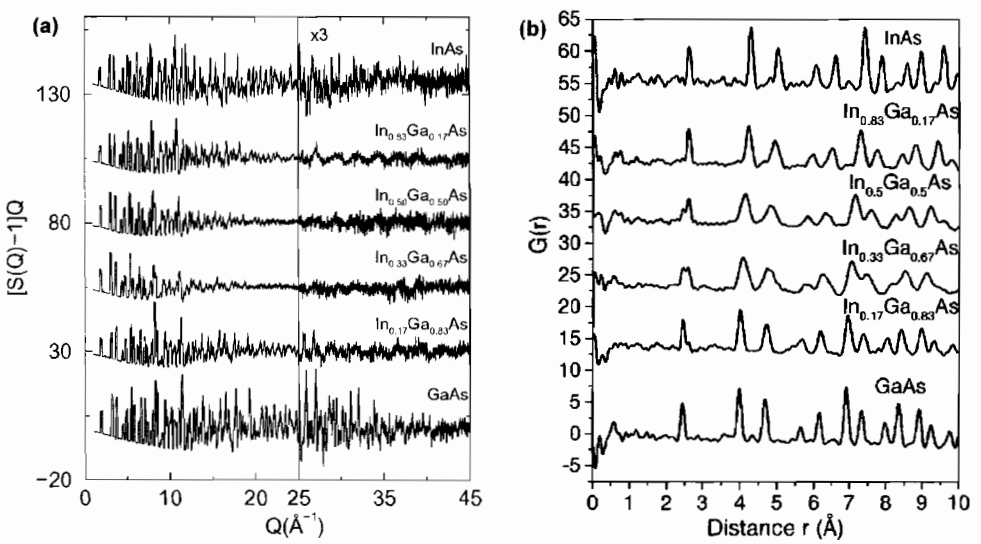

Figure 9.2. (a) The reduced total scattering structure functions $[S(Q) - 1]Q$ for $In_xGa_{1-x}As$ measured at 10 K. The data-sets from the different members of the alloy series are offset for clarity. The high-Q region is shown on an expanded scale (× 3) to highlight the presence of the diffuse scattering. (b) The PDFs, $G(r)$, obtained from the data in (a) by Fourier transformation. Note the nearest neighbor peak is split into two components in the alloys (Petkov *et al.*, 1999; Jeong *et al.*, 2001).

low spatial resolution differential PDFs obtained using anomalous diffraction methods (see below, Petkov *et al.*, 2000a), resulted in a fairly complete understanding of the local structure of these technologically important alloys and confirmed, but significantly extended, the information available from earlier XAFS studies (Mikkelson and Boyce, 1982). Equally high real-space resolution is also available in the best neutron measurements as evidenced by a study on the closely related $ZnSe_{1-x}Te_x$ semiconductor alloy material (Peterson *et al.*, 2001).

These technique developments, motivated by the desire to study crystals, have now been fed back into the traditional study of glasses. Of interest here was the ability to study covalently bonded network glasses such as silicates and alumino-silicates. In this case the structural coherence is limited to less than 10 Å due to the random orientations of connected tetrahedra and peaks in the PDF beyond first and second neighbors are broad (Figure 9.3(b)). However, PDF peaks below 2 Å originating from the SiO_4 tetrahedra themselves are extremely sharp because of the well-defined covalent bonding as is evident in Figure 9.3(b). The ability to resolve the short and long bonds in the semiconductor alloys that differed

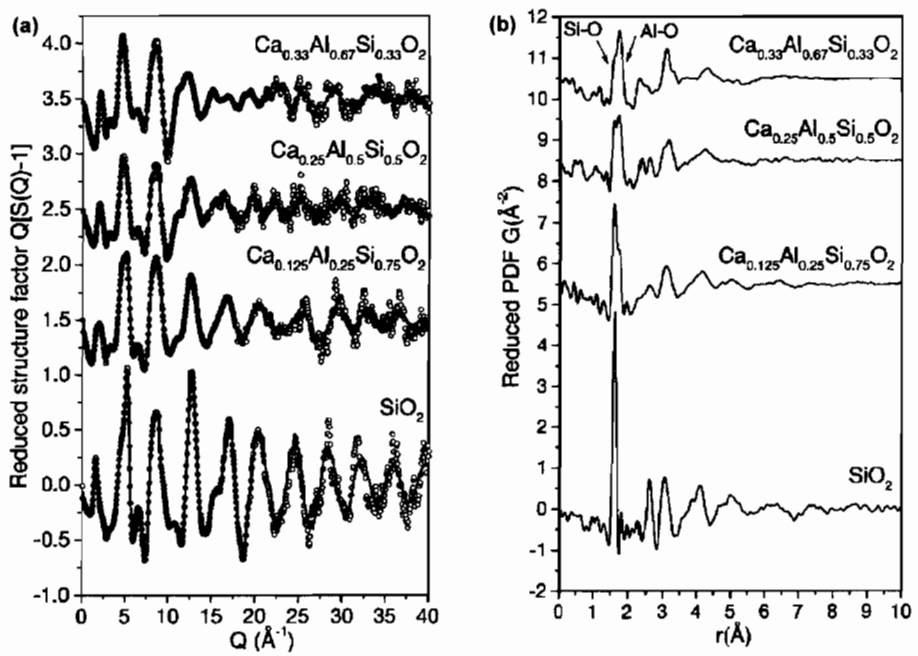

Figure 9.3. (a) Structure functions from alumino-silicate glasses measured at the Advanced Photon Source to high-Q values. (b) Resulting PDFs, $G(r)$. Note that the characteristic glassy structure, with features disappearing by 10 Å, indicating the presence of only short-range order in the structure. However, what is also apparent is that the local structure is well defined, especially in the pure silica glass (bottom curve) with very sharp PDF peaks (Petkov *et al.*, 2000b).

by only 0.14 Å motivated a study of alumino-silicate glasses (Petkov *et al.*, 2000b). These materials consist of continuous covalently bonded random networks of corner shared tetrahedra; however, some of the tetrahedra contain silicon and others aluminum. Despite their importance these materials present special challenges in their structural characterization. In general, the Al and Si ions are arrayed randomly. They are close in the periodic table making it hard to differentiate them by scattering power in an X-ray experiment, and by quirk of fate, they have very similar neutron scattering lengths too. They are low atomic number materials making XAFS measurements difficult, and NMR signals get broad when the Al and Si coexist. However, when they form their tetrahedra with oxygen the Si–O bond is shorter than the Al – O bond by around 0.14 Å. In a high real-space resolution PDF measurement it was possible to *spatially* resolve the Si–O and Al–O peaks and watch how the peak intensities, widths and positions shifted with changes in the composition (Petkov *et al.*, 2000b). The Q-space structure functions and the PDFs are shown in Figure 9.3. In Figure 9.4 $g(r)$ functions are shown on an expanded r-scale with fits to the Si–O and Al–O sub-components of the peaks. The data were collected at ID-1 of the Advanced Photon Source. This is a particularly nice example where chemical specific analysis is a special

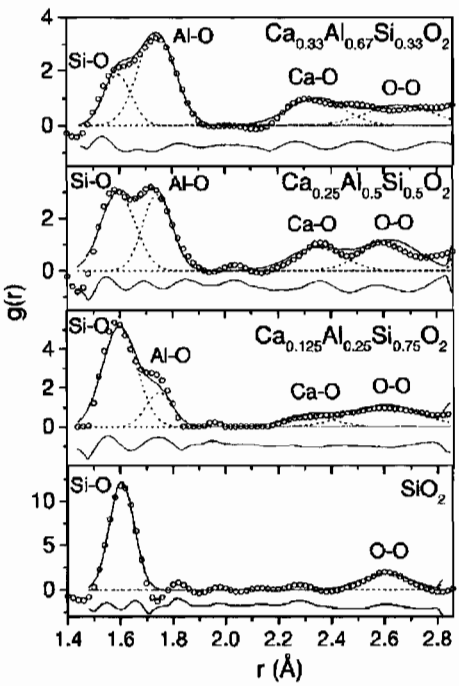

Figure 9.4. PDFs, $g(r)$, shown in Figure 9.3, now on an expanded scale, with fits shown to the Si–O and Al–O sub-components of the peaks (Petkov *et al.*, 2000b).

challenge because of randomly arranged low-Z (and chemically similar) constituents, but where the chemistry of the different species could be studied independently by *spatially resolving* them due to the high real-space resolution attained.

9.2.2 Defects in catalytic support oxide, CeO_2

Fine particle ceria, CeO_2, is an important material for the automotive industry. Automotive engine exhaust contains various toxic gases such as CO and NO_x that have to be cleaned by catalytic converters. Thus, the converters have to perform conflicting tasks of *reducing* NO_x while at the same time *oxidizing* CO and hydrocarbons. By a miracle of modern chemical engineering, small particles of precious metal catalysts such as Pd and Rh can produce simultaneous chemical reactions, such as, $NO_x \rightarrow (1/2)N_2 + (x/2)O_2$, $CO + (1/2)O_2 \rightarrow CO_2$, and $CH_x + O_2 + (x/4)O_2 \rightarrow CO_2 + (x/2)H_2O$, on the surface of these particles. However, this is possible only within a narrow specific range of oxygen partial pressure, since O_2 is necessary for oxidation while it makes reduction difficult. The prime role of ceria, CeO_2, as a catalyst support, is to maintain the local oxygen pressure within this window by releasing or absorbing oxygen through the reaction, $CeO_2 \leftrightarrow CeO_{2-x} + (x/2)O_2$.

One of the major problems with ceria as the catalyst support is an irreversible deterioration of its oxygen storage capacity (OSC) during operation of a catalytic converter. While the old idea was that the loss of surface area due to crystal growth causes this deterioration, it is now well established that the surface area is not the only important parameter. Various chemical studies suggest that there exist two kinds of oxygen ions, active and inactive. After long use, the active oxygen ions in the ceria are replaced by inactive ones, and ceria loses its capability to store oxygen. However, no microscopic information was available so far as to what differentiates these two kinds of oxygen ions.

Neutron PDF analysis carried out using the SEPD of IPNS gave the answer to this question (Mamontov and Egami, 2000). The sample was a 99% pure fine powder of CeO_2, with grain size of about 70 Å. The data were analyzed both by the Rietveld method and the PDF method. The PDF of ceria powder shown in Figure 9.5 agrees with the model PDF calculated for the perfect ceria (fluorite) structure reasonably well, but there are significant systematic differences. After extensive Monte-Carlo modeling it was found that the PDF is best explained by introducing interstitial oxygen defects and a balancing amount of oxygen vacancies (Frenkel type defects) as shown in Figure 9.6. The agreement-factor was reduced from 14.7% (GoF value 2.22) to 9.05% (GoF value 1.37), by introducing 12% of Frenkel defects (Figure 9.7). This reduction represents a major improvement in fitting. This result was confirmed by Rietveld analysis of the same data as well, after introducing various constraints suggested by the PDF model. Without these constraints the Rietveld analysis did not converge with the interstitial model. Thus it is highly doubtful if it were possible to discover these defects by the Rietveld method alone. The concentration of the defects refined by the Rietveld method is comparable, about 8%.

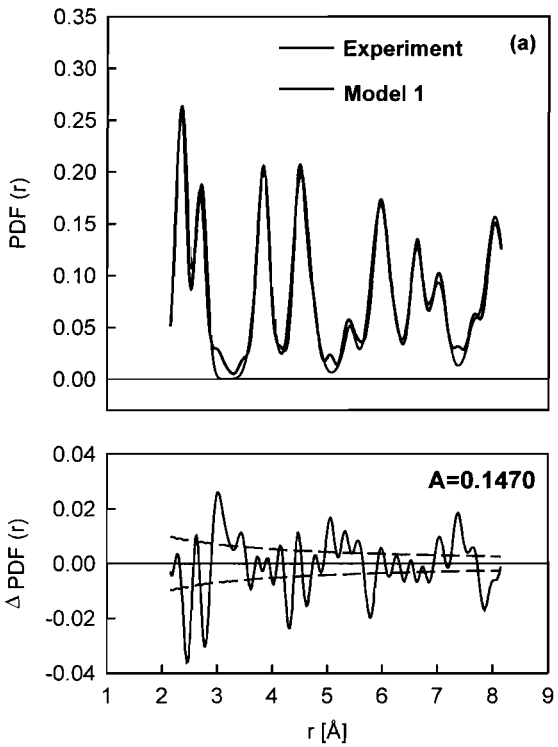

Figure 9.5. PDF of nano-particle ceria, CeO_2, determined by pulsed neutron scattering (thick line) compared with the PDF calculated for perfect ceria (thin line) and the difference between them (below) (Mamontov and Egami, 2000).

The difference between the measured PDF and the model PDF for the perfect structure is plotted also in Figure 9.5. High-frequency oscillations in the difference PDF are most probably noise, mostly due to the termination error introduced in the Fourier-transformation (Section 3.5.2). The wavelength of the high-frequency noise is close to that of the termination error, $7.8/Q_{max} \sim 0.33$ Å for $Q_{max} \sim 24$ Å^{-1}. Other errors quickly decrease with r as discussed before, and are less likely to affect the PDF beyond the range of 2–3 Å. However, the difference PDF has in addition slowly varying components that are not readily caused by the error in $S(Q)$, and therefore are likely to be true. Furthermore the differences in the PDF occur only at peaks involving oxygen, and Ce–Ce peaks are well explained by the model PDF. These observations are consistent with the presence of oxygen defects.

An inspection of Figure 9.5 might lead one to think that the observed PDF may be brought to better agreement with the calculated PDF by subtracting a constant from $g(r)$; one may argue that something went wrong with the normalization of $S(Q)$, so that $g(r) - 1$

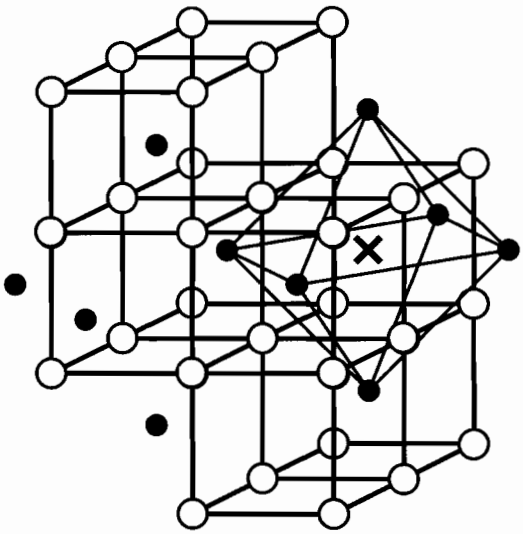

Figure 9.6. Interstitial oxygen defects in ceria. (Mamontov and Egami, 2000).

is not correctly normalized. As reasonable as it may sound, this argument has a major flaw, which is interesting by itself. First of all, the normalization of $g(r) - 1$ affects tall peaks more than the $g(r) = 0$ line. Since the peaks are in agreement normalization cannot be much off. Secondly it is impossible that some error ends up in adding a constant to the PDF. As discussed in Section 3.1.3.2, $G(r)$ is defined to become zero at large r, and the average density is supplied by hand. So if there is an error it has to come from the value of ρ_0. If the value of ρ_0 is reduced the heights of the PDF peaks also have to be reduced, again resulting in disagreement.

In CeO_2 crystal Ce ions form an fcc lattice, and O-ions occupy the tetrahedral interstitial site of the fcc structure (Figure 9.6). Remarkably the octahedral interstitial site is unoccupied in the crystal structure, even though it is more spacious than the tetrahedral site. Since the interstitial oxygens in these octahedral cavities are less strongly bound they are more likely to come out, and facilitate the oxygen storage capacity. Thus, the interstitial oxygen ions are most likely to be the 'active' oxygen ions for the oxygen storage capacity.

A direct proof of the annealing effect was obtained by studying the effect of thermal treatment on the ceria sample (Mamontov *et al.*, 2000). As shown in Figure 9.8 the density of the defects determined by the Rietveld analysis decreased rapidly above 600°C. At this temperature also the oxygen storage capacity (OSC), determined by the temperature-programmed reduction (TPR) method, also appreciably decreased providing the direct connection between the structural defects and the ability of ceria as a catalyst support. While thermal treatment results in the coarsening of crystal grains as well, its temperature

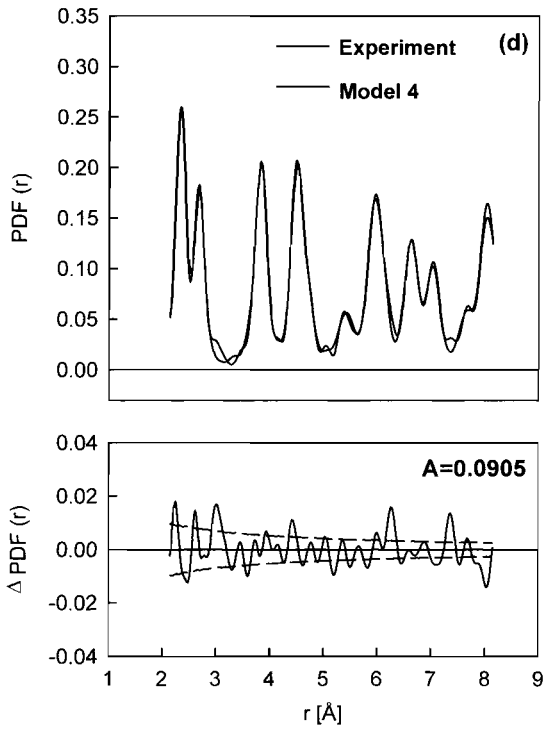

Figure 9.7. PDF of nano-particle ceria, CeO_2, determined by pulsed neutron scattering (solid line) compared with the PDF calculated for ceria with oxygen defects of Frenkel-type (Mamontov and Egami, 2000).

dependence does not agree with the change in the defect density and OSC. Thus it is clear that the reduction in the surface area of powder and thermal diffusion are not the reason for the decrease in the density of defects. The PDFs before and after the heat treatment are compared in Figure 9.9. The PDF after the treatment is much closer to the model PDF for a perfect structure.

When oxygen ions are reintroduced after reduction, they are likely to occupy the octahedral site first, before they move into the more stable tetrahedral site. Only when the sample is annealed at high temperature the defects will return to the proper site. This explains why long annealing can deactivate ceria. The nano powder sample used in this study was prepared by the low temperature (300°C) calcination of cerium nitrate. Thus the sample was never exposed to high temperature that would deactivate ceria.

The figure also shows the concentration of the defects in $(Ce_{0.8}Zr_{0.2})O_2$ as a function of temperature. It is clear that mixing zirconia greatly stabilizes the ceria defects. A possible mechanism of this effect is that alloying zirconia reduces the lattice constant, thus makes the tetrahedral site even tighter. This will destabilize oxygen in the tetrahedral site,

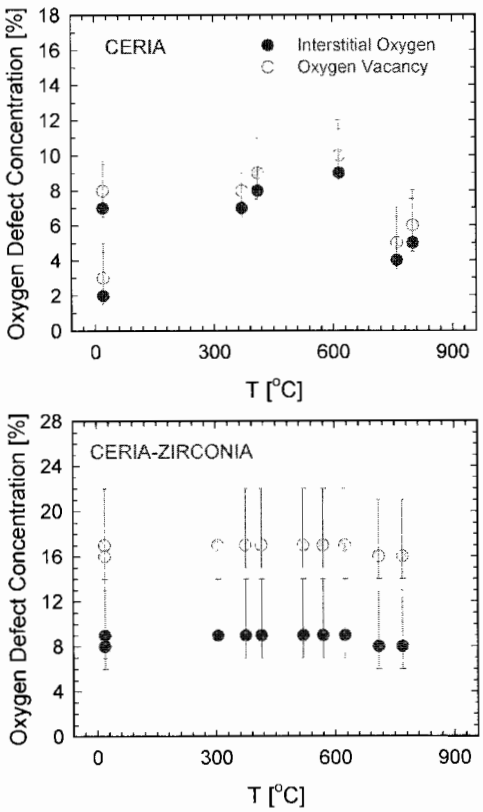

Figure 9.8. The density of defects (vacancies and interstitials) as a function of annealing temperature (Mamontov *et al.*, 2000).

and make it more difficult for the interstitial oxygen in the octahedral site to return to the tetrahedral site.

The interstitial defects, similar to those found in ceria, were observed for the first time in $Ca(Y)F_{2+\delta}$ (Cheetham *et al.*, 1971). They have been observed since then in a number of compounds with the fluorite structure. Usually such defects are found in doped systems where the interstitial anions are charged-compensated by cation excess charges. Thermally induced defects of similar type were also observed in pure tetravalent systems (Hutchings *et al.*, 1984). In the latter case the interstitial anions are charge-compensated by vacancies in the regular anion sublattice.

These results strongly indicate that the oxygen Frenkel type defects constitute the 'active', weakly bound oxygen observed in the series of recent experiments, and define the oxygen storage capacity of ceria in automotive three-way catalytic converters. Thus

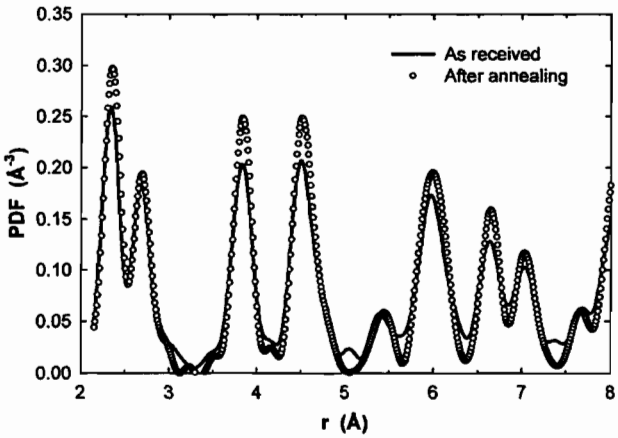

Figure 9.9. PDF of ceria before and after thermal treatment (Mamontov *et al.*, 2000).

the PDF study has identified a very important aspect of the catalyst support oxide. When the density of defects is high enough, greater than a few percent, then the PDF study can be used in identifying and quantifying these defects.

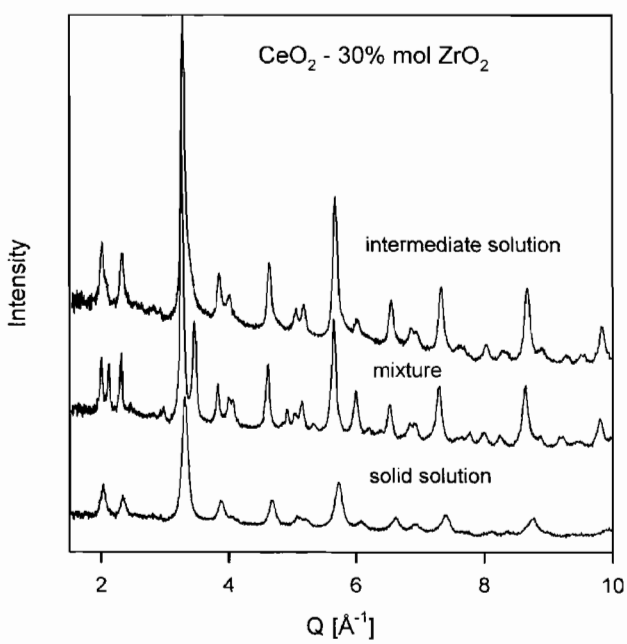

Figure 9.10. Diffraction pattern of ceria/zirconia system, in physical mixture, solid solution, and optimal mixture (Egami *et al.*, 1997).

9.2.3 Nanosegregation in ceria–zirconia mixture

As shown above, mixing zirconia with ceria stabilizes the lattice defects and extends the life of ceria as catalyst support. However, zirconia has additional effects of reinforcing the oxygen storage capacity of ceria. It has been known in the field of catalytic support that a true solid solution of ceria–zirconia is not necessarily the best, but some special processing was needed to produce the best performing ceria–zirconia mixture. The PDF study revealed that the best performing mixture has nano scale ceria–zirconia segregation within the crystalline grain (Egami *et al.*, 1997). While the crystalline size is of the order of 100 Å the nano segregation of about 20 Å exists within the grain. As shown in Figures 9.10 and 9.11, while the diffraction pattern appears to resemble that of a solid solution, the real local structure is closer to the two phase physical mixture. This was later confirmed by the X-ray small angle scattering. It is conjectured that the nano segregation

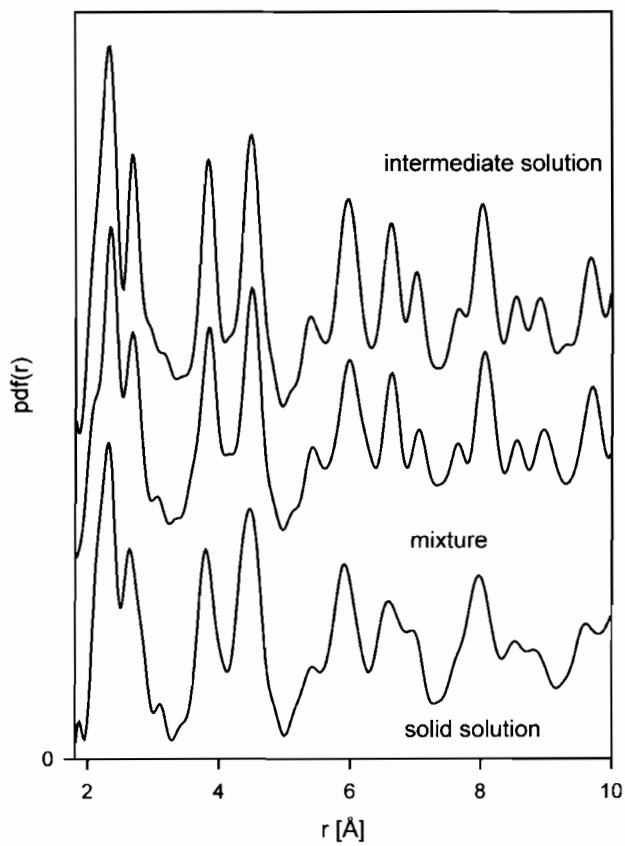

Figure 9.11. Pulsed neutron PDF of ceria/zirconia system, in physical mixture, solid solution, and optimal mixture (Egami *et al.*, 1997).

helps to create pathways for oxygen. It appears that engineering such nano scale structure is one of the keys of producing an effective catalyst support.

9.3. NANOCRYSTALS AND CRYSTALLOGRAPHICALLY CHALLENGED MATERIALS

9.3.1 Introduction

Crystals have long-range order. Their structure can be defined by a small number of parameters that define the unit cell (its shape and size) and its contents (atomic coordinates and thermal factors). The complete structure is then obtained by periodically repeating this unit cell *ad-infinitum*. Towards the opposite end of the structural order–disorder spectrum are glasses and liquids that have only short-range order and no long-range order. The local environment of a particular atom type may be well ordered, but the correlations die out over the range of a few angstroms, as discussed above in relation to Figure 9.3(b). In this case, the complete structure is never completely 'solved', but is described statistically in terms of atomic distributions or atom-pair distributions.

Increasingly, new materials are being discovered that lie between these two extremes. They have a well-defined structure over local and *intermediate range* that can be described rather well by a small unit cell and a small number of parameters. However, they are not long-range ordered and the structural coherence dies out on a nanometer length-scale. We call these materials 'nanocrystals'. In these materials the scattering pattern does not contain Bragg-peaks making it impossible to study using conventional crystallographic techniques. However, the PDF is a tractable and intuitive approach to solving the structures of these materials resulting in robust and quantitative structural solutions.

Note that this definition of nanocrystals goes beyond perfect crystals that are simply very small (nanometer in size) such as passivated gold and semiconductor nanoclusters (Whetten *et al.*, 1996; Alivisatos, 1996) and includes materials where the particle size can be larger but the *structural coherence* is nanometer length-scale. As we discuss below, this includes a large number of interesting materials. The important point is that the materials are ordered over a sufficiently long range to allow a concise description of the structure in terms of a small number of parameters, but are not ordered over sufficiently long range to allow a structural solution using conventional crystallographic techniques. Examples that have been studied using the PDF technique include MoS_2 and related compounds (Petkov *et al.*, 2000c, 2002a; Petkov and Billinge, 2002), $V_2O_5{\cdot}n(H_2O)$ xerogel (Petkov *et al.*, 2002b), pyrolitic carbon (Kane *et al.*, 1996; Petkov *et al.*, 1999b) and hydrous RuO_2 (Dmowski *et al.*, 2002).

Another class of interesting materials are those where long-range order exists but where significant structural distortions are also present that are not reflected in the average structure. These can be considered as defects to the average structure, for example, the cases of the semiconductor alloys and ceria described above. However, sometimes

the distortions are rather extensive, or it is the aperiodic component of the structure that is of particular interest, in which case it makes less sense to consider the disorder as a defect away from the ideal structure. This class of material is rather widespread if molecular systems are included, for example, plastic crystals that have periodically arranged but orientationally disordered molecules, would fall into this class.

All of these materials, where deviations from perfect crystallinity are rather severe but a remnant of the crystallinity is apparent, we term 'crystallographically challenged materials' to distinguish them, on the one hand, from well-ordered crystals and, on the other, glasses.

9.3.2 Carbon nanostructures

Carbon nanostructures, in particular nanotubes (Bethune *et al.*, 1993; Iijima and Ichihashi, 1993) have been a very fertile source of new science in the past few years across several fields including, for example, electron transport and nanoscale electronics (Dresselhaus *et al.*, 1996; Saito *et al.*, 1998). Structures range from simple and intuitive, such as the C_{60} molecule, to complex and highly disordered. The complex disordered structures have nanoporous properties but details of the structure are hard to characterize.

Even relatively simple solid C_{60} contains disorder since the C_{60} balls sit on high-symmetry special positions in the lattice. The point symmetry of the balls themselves is lower than the point symmetry of the crystallographic site they sit on. This means *a-priori* that the internal structure of the balls themselves cannot be solved from the Bragg-scattering alone. In fact, in solid C_{60} considerable diffuse scattering exists that can be straightforwardly analyzed to extract information about the ball-structure (Figure 9.12). At room-temperature the balls are spinning at a fairly high rate. To a good approximation the structure can be modeled as being made up of isotropic balls making a close-packed

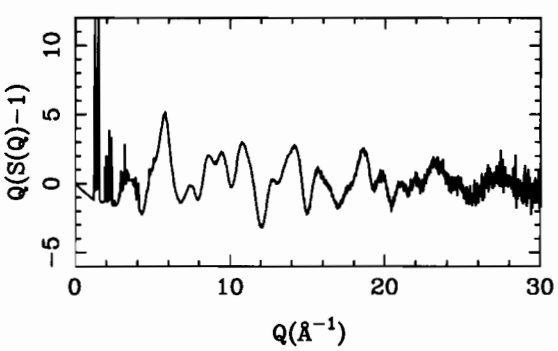

Figure 9.12. Reduced structure function from C_{60} from neutron data collected at room-temperature. The Bragg-peaks from which the *fcc* structure of C_{60} solid was solved are evident at low-Q. The significant diffuse scattering comes from the internal structure of the C_{60} molecule itself.

fcc lattice (Heiney *et al.*, 1991; David *et al.*, 1991) and below 260 K the balls freeze into a partially ordered arrangement where there is a tendency for the C–C double bonds on one molecule to align with the centers of pentagonal faces on the neighboring ball (David *et al.*, 1991; Hu *et al.*, 1992).

As we described in Chapter 1, C_{60} provides an excellent example of the importance of studying total scattering (Bragg and diffuse scattering) when analyzing complex solids. The large amounts of diffuse scattering are evident in Figure 9.12. The resulting PDF is shown in Figure 9.13 with sharp correlations at low-r coming from the balls themselves and broad correlations at higher-r from the ball–ball correlations. The total scattering data can be studied in real-space (Li *et al.*, 1991; Hu *et al.*, 1992; Soper *et al.*, 1992; Thorpe *et al.*, 2002) or directly in reciprocal-space (David *et al.*, 1991; Copley *et al.*, 1992; Leclercq *et al.*, 1993; Damay and Leclercq, 1994), but in either case both the Bragg and diffuse scattering must be analyzed. Both neutron and X-ray single crystal diffuse scattering has also been measured from C_{60} and summarized in Pintschovius (1998) and Neild and Keen (2001).

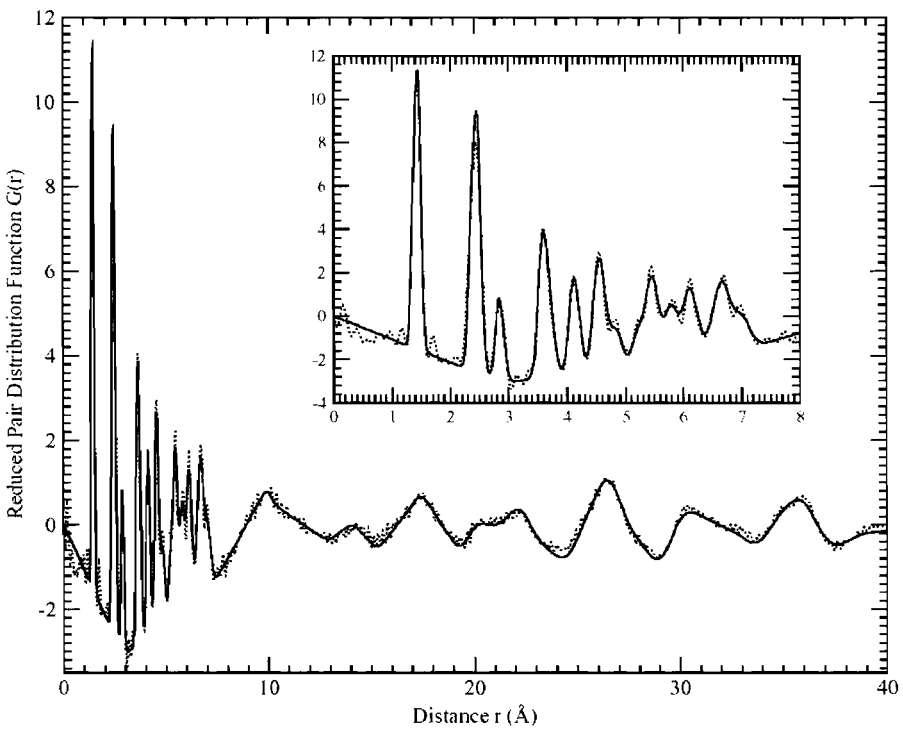

Figure 9.13. PDF, $G(r)$, from the data shown in Figure 9.12 (dots) with the calculated structure of C_{60} superimposed. Contrary to the case with the Q- space scattering, the sharp peaks at low-r come from the C–C correlations on the C_{60} balls themselves, the broad structure at higher-r comes from the *fcc* arrangement of isotropic hollow balls due to the fact the balls are spinning (Thorpe *et al.*, 2002).

The study of disordered carbons has a structural scientific pedigree of the highest order, being studied first by Warren (1934) and later by Rosalind Franklin (1950, 1951) whose role in the discovery of the structure of DNA we referred to in Chapter 3. The work of Warren was on porous 'Carbon blacks' and an example of one of the first PDF analyses of powder data. The study revealed that the materials were made up principally of graphene sheet fragments. The tedious procedure of Fourier transforming data, ca. 1934, prompted Warren to come up with the alternative approach for analyzing data from disordered 2D structures such as these directly in Q-space. Scattering from 2D sheets gives rise to a characteristic asymmetric line-shapes for the Bragg-lines in powder patterns, with a sharp rise and a long tail on the high-angle side, the now called 'Warren line-shape' (Warren, 1941). The data analysis in these early studies was hampered by lack of modern high-flux sources, linear, high-count-rate detectors and no computing. Nonetheless, the amount of information extracted from the scattering is extraordinary. For example, in the Franklin (1950) study of pyrolized polyvinelidene chloride, which forms a particularly disordered carbon, the structure was determined to be made up of fragments of graphene sheets of 16($\pm$ 1) Å stacked together with a layer spacing of 3.70 Å (compared to 3.35 Å for pure graphite); that 65% of the carbon is in the form of graphene sheet fragments, of which 55% is stacked with two or more layers parallel; and that the particles approach each other to a separation of 25 Å. A more complete study of a series of carbons with differing degrees of disorder resulted in a view of the structure of graphitizing and non-graphitizing carbons as shown in Figure 9.14. This picture has a remarkable similarity to that obtained in 1999

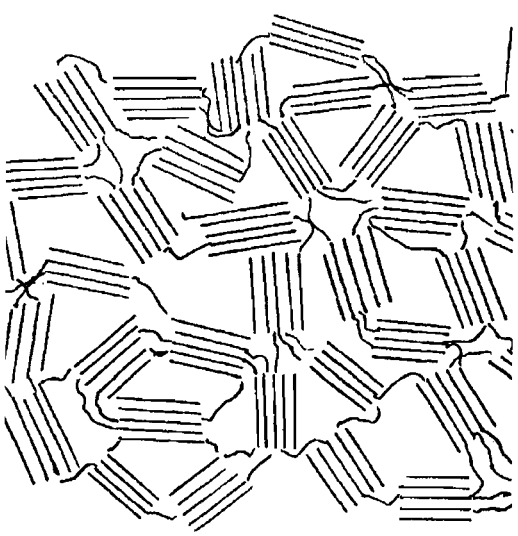

Figure 9.14. Model for highly disordered nanoporous carbon ca. 1950 (Franklin, 1951).

using advanced computer modeling (Acharya *et al.*, 1999), Figure 9.15, from the much wider Q-range neutron data shown in Figure 9.16(b) (Petkov *et al.*, 1999b). The quality in the low-Q region of the 1950 and 1999 data-sets can be compared in Figures 9.16(a) and (b) (note that to convert the x-axis of the Franklin (1950) data to the same units as the Petkov *et al.* (1999b) data it should be multiplied by 2π). The main difference between the data sets clearly comes from the *range* of Q now accessible and this is evident as much higher real-space resolution in the modern PDF shown in Figure 9.17(c). Note that the original PDF of Franklin had terrible contamination from termination ripples (e.g. see the spurious ripple at $r = 1.9$ Å in Figure 9.17(a)) that were eliminated by damping the data, as discussed in Section 5.3.10 and resulting in the PDF in Figure 9.17(b). In the 1999 study the termination ripples in $G(r)$ are minimal *without any data damping* (Figure 9.17(c)), illustrating the importance of measuring data over a wide range of Q. For example, compare the second and third C–C peaks between 2 and 3 Å in Figure 9.17(c). These are completely resolved in Figure 9.17(c), completely unresolved in Figure 9.17(b) and evident as a shoulder (but smaller than the termination ripple at 1.9 Å!) in Figure 9.17(a). The need to collect high-quality data over a wide Q-range cannot be overemphasized.

We now understand that the graphene sheets can be significantly bent by introducing pentagons and this contributes to the loss of structural coherence as well as sheet fragmentation (Figure 9.15). In the more disordered carbons the sheets also can support defects that preserve the network such as higher-membered rings (seven and eight for example).

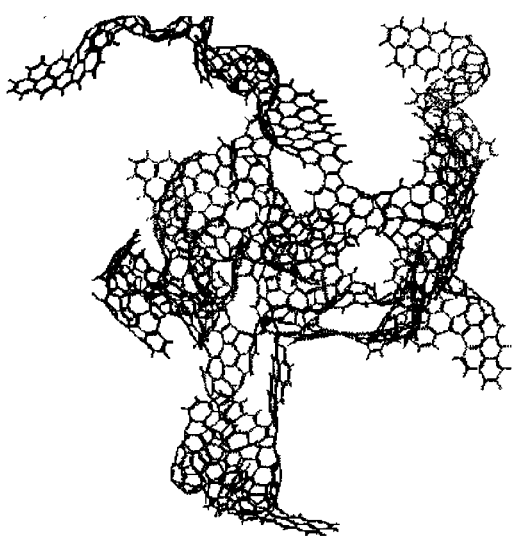

Figure 9.15. Model for highly disordered nanoporous carbon ca. 1999 (Acharya *et al.*, 1999).

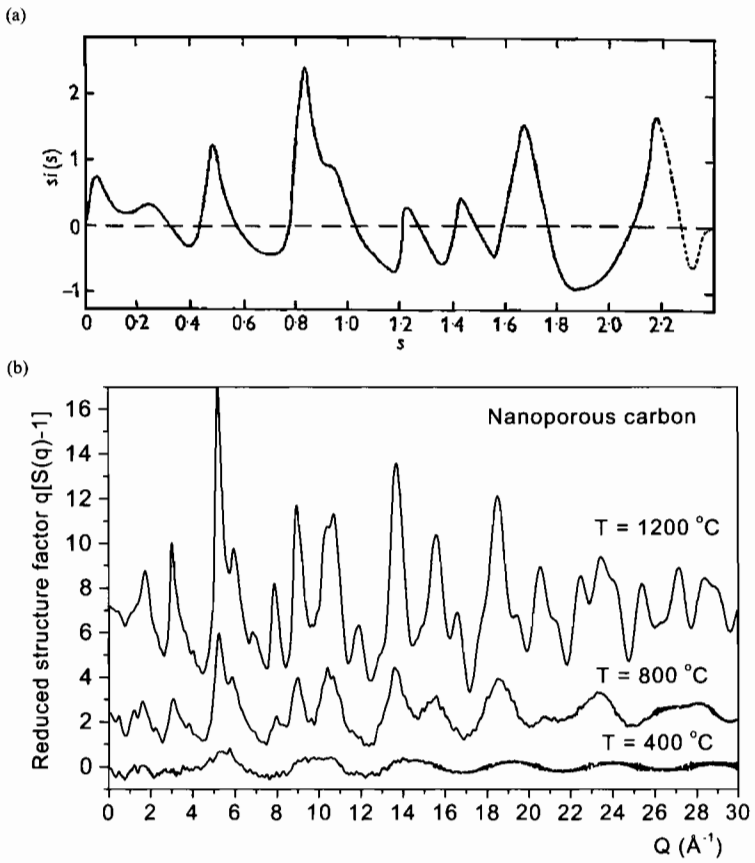

Figure 9.16. Top Panel, structure function from pyrolized polyvinelidene chloride measured in 1950 using laboratory X-rays by Rosalind Franklin (Franklin, 1950). Bottom panel, structure functions from pyrolized polyfurfuryl alcohol, with the pyrolization temperature shown, measured using spallation neutrons in 1999 (Petkov *et al.*, 1999b). Both show the same representation of the data ($Q[S(Q) - 1]$) but the scale on the upper panel should be multiplied by 2π to compare it with the data on the bottom panel. The Q-range of the 1950 data is therefore $0 < Q < 15$ Å^{-1}.

This is apparent because with the higher resolution allowed by a much higher Q_{max} from modern sources the second and third neighbor carbon peaks can be resolved (Figure 9.17(c); Petkov *et al.*, 1999b) where they could not in the Franklin (1950) data (Figure 9.17(b)). Intensity is lost out of the third peak in the more disordered carbons indicating the presence of higher-membered rings. Remarkably, in 2002, 52 years after the Franklin work and 68 years after Warren's pioneering work, we are still struggling to understand the structure of these disordered carbons, which, nonetheless, retain their technological and scientific interest (Petkov *et al.*, 1999b; Claye and Fischer, 1999).

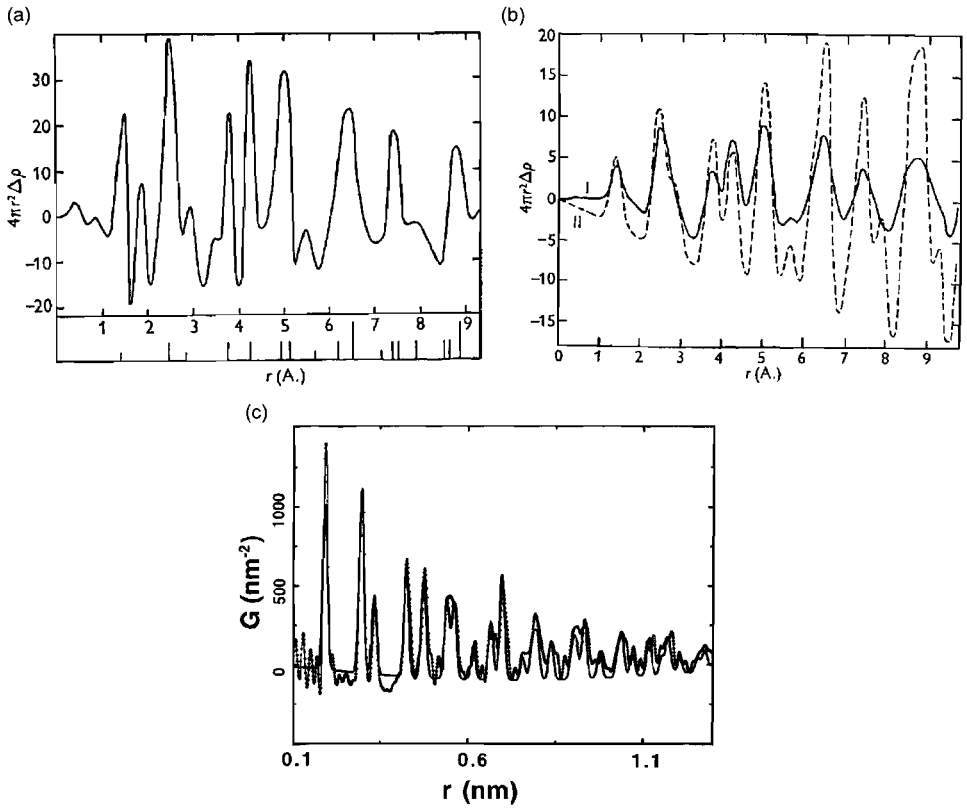

Figure 9.17. (a) PDF of nanoporous carbon from the data shown in Figure 9.16(a). (b) (solid line) PDF from the same data after damping the data to minimize termination ripples. Note the spurious ripple at $r = 1.9$ Å in (a) has disappeared after damping the data (b), but the PDF has become significantly broadened. The dashed line shows the PDF calculated for graphite (Franklin, 1951). (c) PDF from the modern spallation neutron data shown in Figure 9.16(b). This PDF was obtained by direct transform (as were the PDFs in panels (a) and (b)) but without damping. The PDF peaks are sharp, the data high resolution, but the spurious termination ripples are minimal. The amplitude of the data falls off quickly with increasing r because of the nano-scale crystallites (Kane *et al.*, 1996).

9.3.3 Crystalline and nanocrystalline phases of silica

Silica, SiO_2, is a simple binary compound that, nevertheless, exists in many forms from simple cubic crystalline quartz, through complex nanoporous zeolites, to fully amorphous (e.g. see Section 9.2.1). It is made up of networks of corner-shared SiO_4 tetrahedra. The closely related and technologically useful alumino-silicates have some silicon replaced by Al, also in tetrahedral coordination, with a counter-ion providing charge-balance. The PDF has been used to study the high temperature crystalline phases of silica (Tucker *et al.*, 2000, 2001a, 2001b, 2002). Neutron powder diffraction data were collected at 14 temperatures from 20 K to

1073 K from crystalline quartz, traversing the α–β structural phase transition. At this phase transition the Si–O bond shortens, despite the unit cell uniformly expanding on heating as expected. In the β phase an anomalous 180° Si–O–Si bond is also observed. This is evident in Figure 9.18, which shows the measured unit-cell expansion, and the shortening of the average Si–O bond length as the transition is approached from below. What is actually happening is that the oxygen atoms midway between neighboring silicons begin precessing around the line separating the Si neighbors, as shown in Figure 1.11. The actual, local, Si–O bond smoothly increases in length over the entire temperature range, as directly measured from the position of the first peak in the neutron PDFs (Figure 9.19). Detailed RMC refinements of the structure have been carried out. The resulting RMC models show instantaneous snapshots of the structure of the tetrahedral network in the two phases (Figure 9.20). When the local configurations are averaged into a single unit cell, the crystallographic results are recovered (Tucker *et al.*, 2000, 2001a). The RMC refined models can be analyzed to obtain information such as the bond-angle distribution functions, as shown in Figure 9.21. From this it is evident

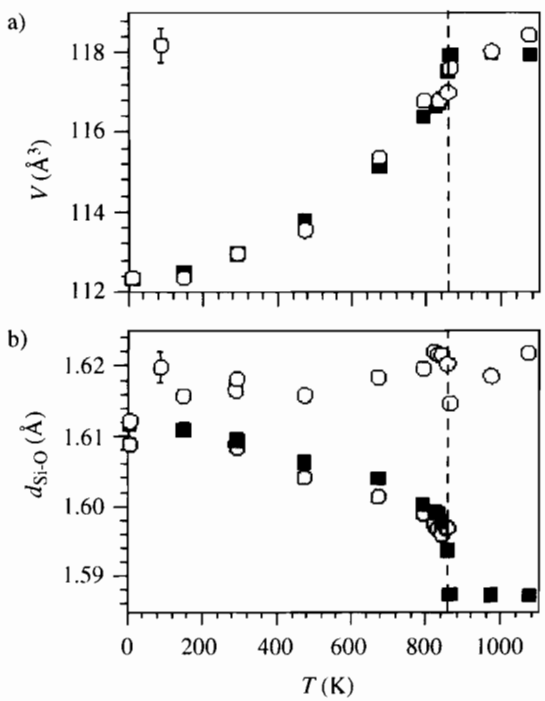

Figure 9.18. Temperature dependence of the (a) unit cell volume, (b) Si–O distance, in quartz. The vertical dashed line shows the phase transition from α to β. In (a) data from the Rietveld refinement and the 17 Å peak in the *PDFs* are given by squares and open circles, respectively. In (b) squares and filled circles represent the average Si–O separation given by Rietveld refinement and the RMC, respectively. The open circles represent the local Si–O bond length obtained from the PDF (Tucker *et al.*, 2000).

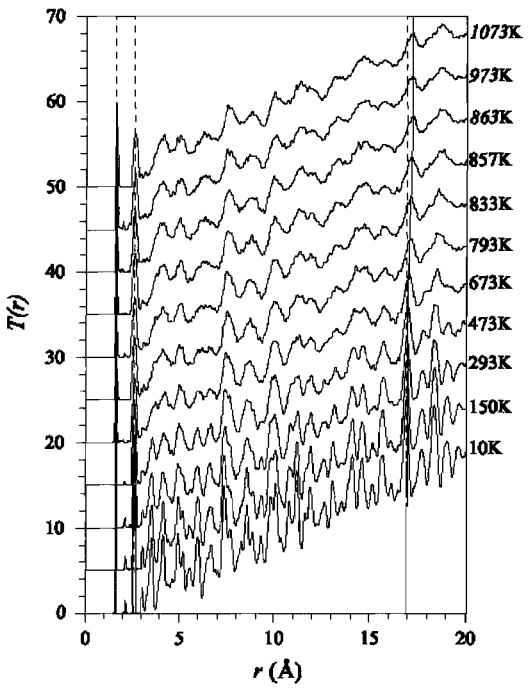

Figure 9.19. Neutron *RDF*'s of quartz over a wide range of temperatures. The dashed lines through the two lowest-*r* peaks follow the temperature evolution of the Si–O and O–O bond distances, and the full line through the peak at around 17 Å follows an interatomic distance that scales with the average linear thermal expansion. The α–β phase transition occurs between the 863 K and 973 K data sets (Tucker *et al.*, 2000).

that a discontinuous change in the Si–Si–Si bond angle distributions occurs at the α–β phase transition. On the other hand, the local structure evolves continuously through the transition (Figure 9.19), reflecting the fact that the network is remaining continuous but the increased thermal energy at high temperature is allowing the oxygen atoms to freely precess.

The results on the quartz were a dramatic confirmation of a rather expected result. In the case of the α–β phase transition in cristobalite, another form of crystalline silica, a similar analysis using PDF analysis resulted in new insight into this phase transition (Tucker *et al.*, 2001b). A plausible model for the β-phase involved it being a microscopic superposition of rotated domains of α-phase. This was not borne out by the analysis that indicates that β–cristobalite is a distinct phase with very distinct local Si–Si–Si bond angle distributions from those of the α-phase. It was also shown that in this phase again the oxygen bridging two silicons is precessing about the Si–Si vector and is not, as is often approximated in crystalline studies, a six-fold multi-welled solution with the oxygens disordering between the six possible sites coming from different α–phase variants. One nice advantage of RMC modeling and refinements is that the resulting configurations can be

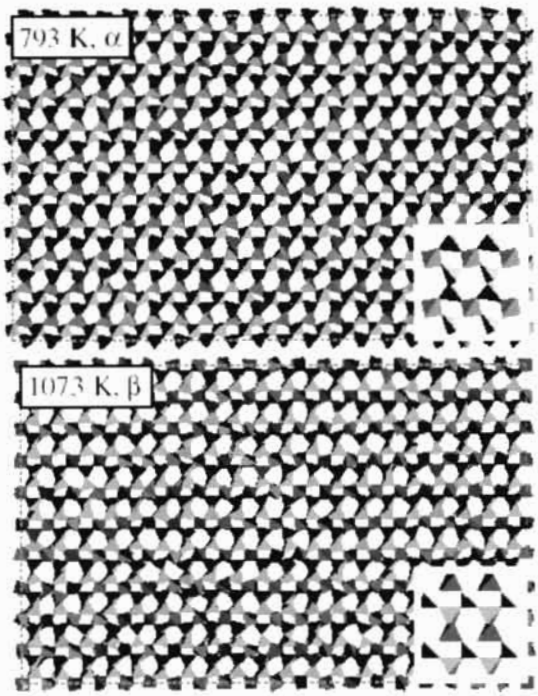

Figure 9.20. Results of RMC refinements. (100) layers of atomic configurations of quartz are shown represented by SiO_4 tetrahedra above and below T_c. The inserts show the 'average' structures obtained by averaging into a single crystallographic unit cell. In this projection the small parallelepiped gaps between tetrahedra become orthogonal in the β-phase, giving a clear representation of the symmetry change at T_c (Tucker *et al.*, 2000).

used to calculate diffuse scattering signatures. This was done in this case and the results compared qualitatively with diffuse scattering from TEM measurements with good results, lending confidence to the RMC-derived solution (Figure 9.22).

As we described above in the section on high-resolution X-ray PDF measurements, amorphous silica and aluminosilicates have also been measured with some success using PDF methods. These silica data were recently compared with silica that forms the walls of disordered nanostructured silica (Pauly *et al.*, 2002). The challenges of measuring the low-density surfactant templated nanoporous silica are significant (most of what is in the beam is empty space!) but it is clearly apparent from these measurements that the average Si–O bond-length in the thin inter-pore walls is longer than in bulk silica.

9.3.4 Crystalline and nanocrystalline MoS_2 and its derivatives

As an example of nanocrystals we consider first the MoS_2 system. Pristine MoS_2 is the key catalyst for the removal of sulfur from crude oil (hydrodesulfurization) (Kanatzidis

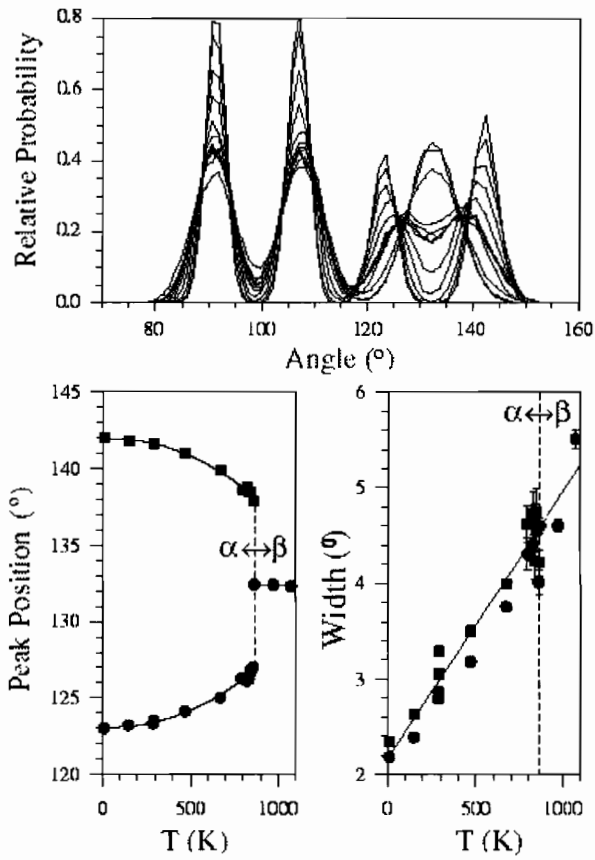

Figure 9.21. The upper plot shows the nearest-neighbor Si–Si–Si angle distribution in quartz. The lower two plots show the temperature-dependence of the positions and widths of the two peaks that coalesce in the β-phase. Note the qualitative change in the Si–Si–Si bond angle distribution around 130° at the transition (Tucker *et al.*, 2000).

et al., 1993). The material is perfectly crystalline and consists of covalently bonded layers of Mo-S_6 trigonal prisms held together by Van der Waals forces. $LiMoS_2$ has Li intercalated between the MoS_2 layers. It is important as a precursor in the preparation of a variety of lamellar nanocomposites (Divigalpitiya *et al.*, 1989). Despite being extensively studied for the last 19 years the structure of $LiMoS_2$ has not been determined. The reason is that, on Li intercalation, pristine MoS_2 is dramatically modified resulting in a product that is too poorly diffracting to allow a structural solution. This leaves unanswered the important question of what exactly happens when MoS_2 gets reduced with lithium.

X-ray powder diffraction data from the MoS_2 and $LiMoS_2$ samples were measured at beamline X7A at NSLS. The reduced structure functions are shown in Figure 9.23 and

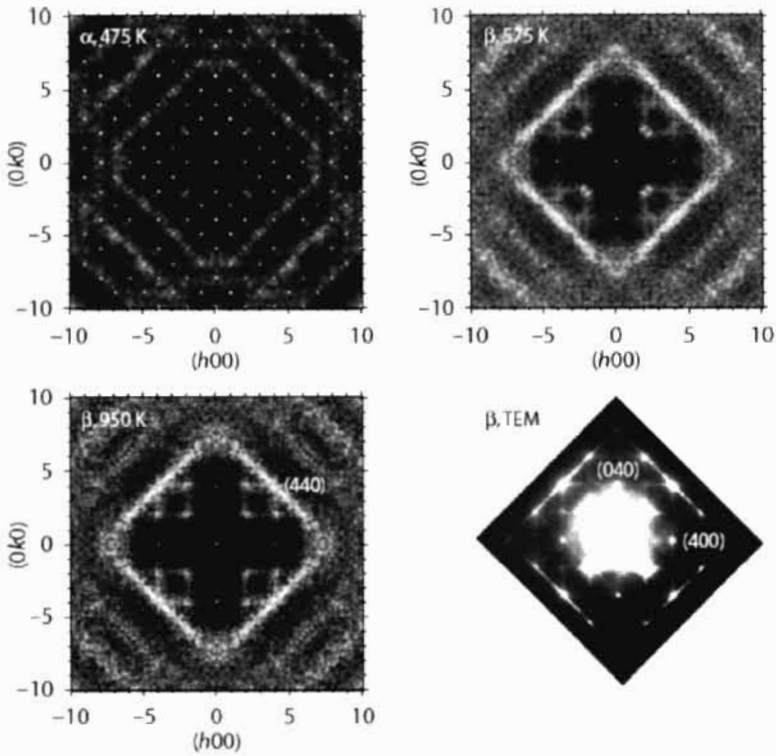

Figure 9.22. Maps of the three-dimensional diffuse scattering from cristobalite, showing the a–b plane in reciprocal space. The single-pixel white spots are the Bragg peaks. The plot in the bottom-right corner shows experimental TEM measurements for β-cristobalite from Hua *et al.* (1988); (Tucker *et al.*, 2001b).

the resulting PDFs in Figure 9.24. Sharp Bragg peaks are present in the $S(Q)$ of MoS_2 up to the maximal Q value of 24 $Å^{-1}$ (Figure 9.23(b), the inset shows the data on an expanded scale). The corresponding $G(r)$ also features sharp peaks reflecting the presence of well-defined coordination spheres in this 'perfectly' crystalline material (Figure 9.24(b)). The inset to Figure 9.24(b) shows $G(r)$ calculated to 5 nm. Clearly, the amplitude of the structural features (the PDF peak: peak amplitude) remains unattenuated over this range as is expected for a long-range ordered material. This is a result of the sharp Bragg-peaks in $S(Q)$ evident in Figure 9.23. The known crystal structure also fit well to the PDF (solid line in the Figure).

The data from the nanocrystallographic $LiMoS_2$ sample serve to illustrate the problem of structure solution from this class of materials. Plenty of structure is evident in the scattering (Figure 9.23(a)) but the peaks are broad and quickly become strongly overlapped. This is especially evident in the inset that can be compared with the data from crystalline MoS_2 in the inset to Figure 9.23(b). Conventional crystallographic methods lose

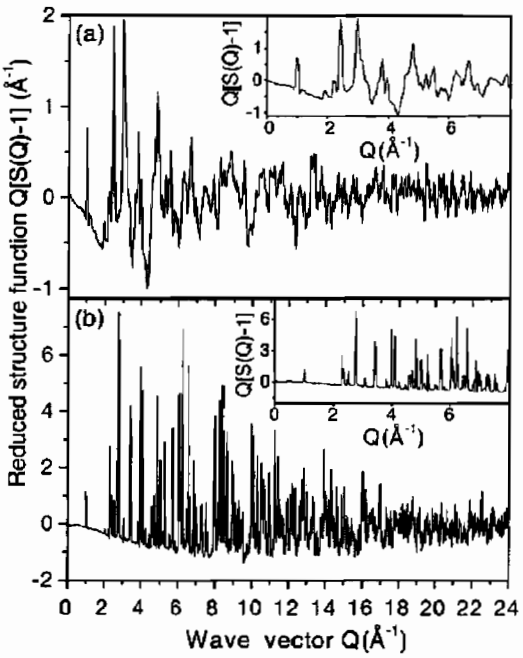

Figure 9.23. Experimental structure functions of (a) $LiMoS_2$ and (b) MoS_2. Note the different intensity scale between (a) and (b). The data are shown in an expanded scale in the insets. Peaks in the nanocrystalline $LiMoS_2$ data are much broader (Petkov *et al.*, 2002a).

their power with data like this, which explains why a full three-dimensional solution of the structure eluded scientists for so long. The Fourier transformed data (Figure 9.24(a)) contain peaks of comparable sharpness to those from the crystalline material (the comparison is even more dramatic in the case of WS_2 described below and shown in Figure 3.3) indicating that the local structure is well defined. On the other hand, features in $G(r)$ die out with increasing r as shown in the inset to Figure 9.24(a), which can be compared to the inset to Figure 9.24(b) from the crystalline material. Oscillations in $G(r)$ have virtually disappeared by 50 Å. The range of the structural coherence is therefore limited which results in the broad peaks in the diffraction pattern.

The relatively sharp features in $G(r)$ allow structural models to be compared to the data and differentiated. A number of structural models were fit to the $LiMoS_2$ data; the best fit of the most successful is also shown as a solid line in Figure 9.24(a). Competing models produced qualitatively poorer fits (Petkov *et al.*, 2002a). The best-fit structural model showed the following. The $Mo-S_2$ layers in $LiMoS_2$ are built of distorted $Mo-S_6$ octahedra. Mo atoms from a single $Mo-S_2$ layer arranged in a regular hexagonal lattice (see Figure 9.25) and are all separated by the same distance of 3.16 Å as in pristine MoS_2. Molybdenum atoms occupy two distinct positions in the triclinic unit cell of $LiMoS_2$

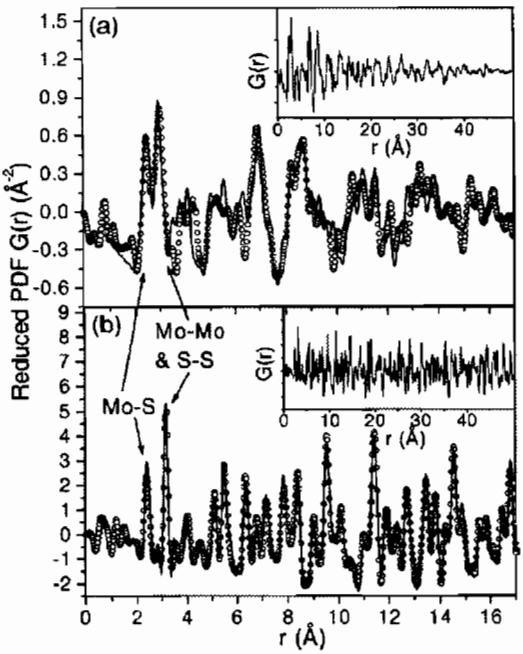

Figure 9.24. PDFs from (a) $LiMoS_2$ and (b) MoS_2 from the data in Figure 9.23 (dots). The experimental data are shown on an extended scale in the insets. Solid lines in the main panel are PDFs calculated from structural models (Petkov *et al.*, 2002a).

(Petkov *et al.*, 2002a) giving rise to short (2.9–3.10 Å) and long (3.44–4.07 Å) Mo–Mo distances. As a result, triangulated diamond chains of short Mo–Mo distances are evident, as shown in Figure 9.25.

The observed distorted structure of Li MoS_2 has an intuitive explanation using simple electron counting arguments. In MoS_2 the molybdenum is in the 4 + state and has 2 d-electrons. It is stable in a prismatic crystal field resulting in a 1-3-1 arrangement of atomic d energy levels. The two electrons both occupy the lowest energy level and are therefore paired. The Mo therefore has non-bonding interactions with its neighboring Mo ions resulting in six equal Mo–Mo distances. When Mo gets reduced by the addition of Li it has 3 d-electrons. The prismatic coordination is destabilized with respect to octahedral coordination that results in triply degenerate t_{2g} and doubly degenerate e_g states. One electron goes into each of the three t_{2g} states that point towards neighboring Mo ions. Each Mo can then form metal-metal bonding interactions with three of its neighboring Mo ions resulting in three shorter (and three longer) Mo–Mo bonds and the diamond like pattern of distortions shown in Figure 9.25(b).

This also explains the zigzag distortion pattern observed in exfoliated-restacked WS_2 (Petkov *et al.*, 2000c). This material is isostructural and chemically very similar to MoS_2.

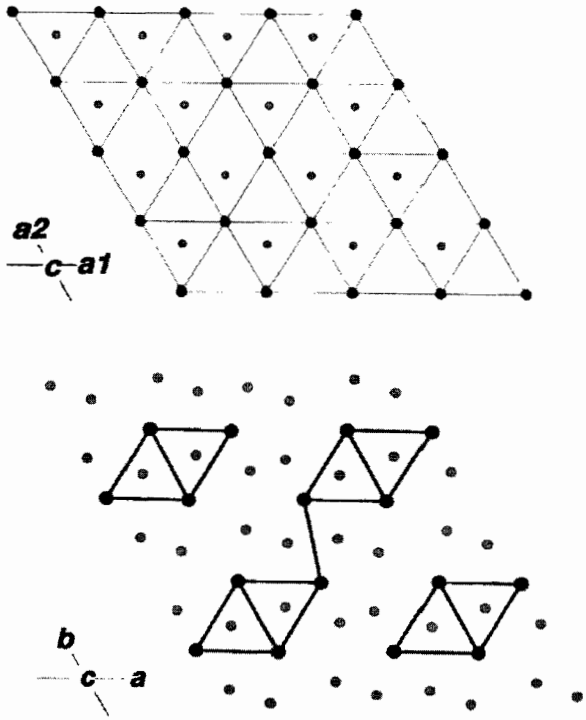

Figure 9.25. Projection down the *c*-axis of the crystal structures of hexagonal MoS_2 (upper) and triclinic $LiMoS_2$ (lower). The large black circles are Mo atoms and the small gray circles are the S atoms. Li atoms are not shown for the sake of clarity. In the $LiMoS_2$ structure the 6 s-neighbor Mo–Mo separations split into 3-long and 3-short (Petkov *et al.*, 2002a).

Lithium can be intercalated to produce $LiWS_2$. The material can then be exfoliated in solution whereby the $(Mo/W)S_2$ layers separate and form a colloid. By changing the chemical conditions the layers can be restacked and the Li washed out. The resulting material is WS_2, chemically identical to the starting material, but significantly modified structurally by the exfoliation-restacking process. The resulting structure is nanocrystalline and metastable, returning to the ground-state structure of pristine $(Mo/W)S_2$ over a period of hours in the case of MoS_2 and weeks for WS_2. The full 3D structure of nanocrystalline WS_2 was solved for the first time by the PDF technique (Petkov *et al.*, 2000c). The structure functions and PDFs of pristine and exfoliated-restacked WS_2 are shown in Figures 9.26 and 3.3, respectively. In Figure 3.3, the low-*r* peaks in the PDF of the nanocrystalline metastable phase are sharp and resolution limited testifying to the well-defined order. However, the extent of the structural order is rather short-range, being already significantly attenuated by 20 Å in this case. The W–W peak at 3 Å in the pristine material splits into

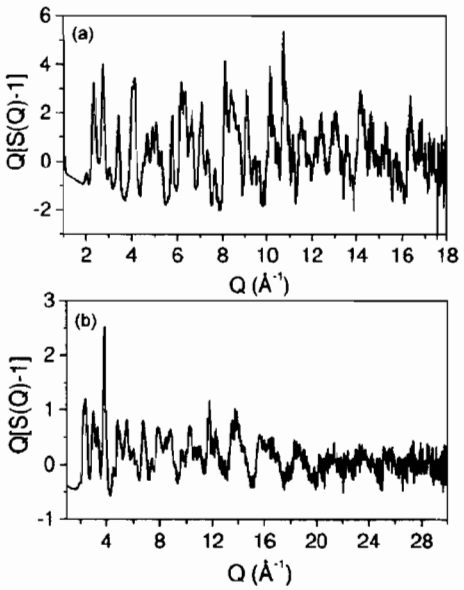

Figure 9.26. Reduced structure functions, measured at X7A of NSLS, of (a) hexagonal pristine WS_2 and (b) exfoliated-restacked WS_2. Note the different Q-ranges for the data due to the data being measured on different instruments (Petkov *et al.*, 2000c).

four peaks (2.77, 2.85, 3.27 and 3.85 Å, Petkov *et al.*, 2000c) resulting in zigzag arrangements of short (~2.8 Å) and long (~3.5 Å) bonds.

In the case of exfoliated-restacked $(Mo/W)S_2$ case the Mo/W is reduced by intercalating Li during the exfoliation process. It therefore transforms into the octahedral coordination of S around Mo similar to reduced $LiMoS_2$. When the Li is removed during restacking the W gets kinetically trapped in its octahedral environment. However, now there are only two electrons instead of three in the t_{2g} states. The W can only bond with two of its W neighbors instead of three and the distortion pattern is a one-dimensional zigzag instead of the triangulated diamonds of $LiMoS_2$.

To summarize, in both Li intercalated and the exfoliated-restacked structures the material forms well-defined 3D-ordered structures that can be described with a rather small unit cell. However, structural coherence of the order is limited to 5 nm or less, apparent as the fall-off in intensity in $G(r)$ with increasing r (Figures 9.24(a) and 3.3(b)). In $S(Q)$ this is apparent as a profound broadening of the 'Bragg-peak' intensity compared to those of the crystalline samples. Note, that despite the broad peaks in $S(Q)$ for the nanocrystalline sample, sharp (resolution limited in the case of WS_2) peaks are evident in $G(r)$, confirming that the structure is locally very well defined though the coherence of the order falls off with increasing-r. This is canonical 'nanocrystalline' behavior.

9.3.5 Crystallographically challenged oxides of molybdenum

As well as the nanocrystalline sulphides of molybdenum described above, oxides of Mo with Mo in the reduced state also present interesting examples of crystallographically challenged materials that benefit from analysis using total scattering methods. Here we describe three examples from the work of Hibble and Hannon (Hibble and Hannon, 2002): $LiMoO_2$ (Hibble *et al.*, 1997a) Li_2MoO_3 (Hibble *et al.*, 1997b; Hibble and Fawcett, 1995) and $LaMo_2O_5$ (Hibble *et al.*, 1998, 1999).

The case of $LiMoO_2$ is directly analogous to the $LiMoS_2$ described above, although in this case the material is not nanocrystalline: it diffracts with clear Bragg-peaks. The structure was solved using crystallographic methods and published (Aleandri and McCarley, 1988). It remained a 'solved structure' for almost 10 years before the PDF of the material was checked. This immediately showed that the published structure was wholly inadequate, as shown in Figure 9.27 (top panel). An alternative model was

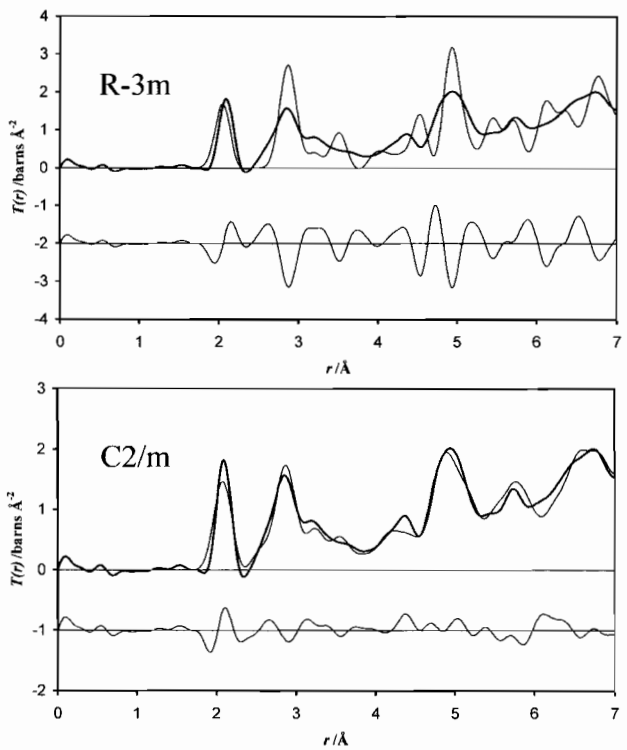

Figure 9.27. Neutron PDF (in the form of the radial distribution function, $R(r)$ (designated $T(r)$ in the figure) of $LiMoO_2$ (thick line) compared with two models: (top panel) published crystallographic model (Aleandri and McCarley, 1988) and model determined using both Rietveld refinement and PDF data as inputs (Hibble *et al.*, 1997a).

proposed that fit both the PDF data and the powder diffraction profile (Hibble *et al.*, 1997a). Interestingly the original rhombohedral model of Aleandri and McCarley (1988) had Mo sitting in a high symmetry position with six second neighbor Mo atoms at equal distances of 2.865 Å. The new model, which accounts also for the PDF data, has short and long Mo–Mo bonds indicating the existence of metal-metal bonding as expected in analogy with the $LiMoS_2$ example above. There are presumably more 'solved' structures in the literature that would benefit from this kind of analysis!

Another similar example is that of Li_2MoO_3 whose structure was solved first by James and Goodenough (1988) whose structural solution proved less than adequate when compared to PDF data. Again, short and long Mo-Mo bonds were missed in the original structural model that became immediately apparent when compared to the neutron PDF data (Hibble *et al.*, 1997b). This is a particularly nice example where multiple techniques were used to get to the bottom of the problem, there being an XAFS study that indicated the presence of short and long Mo–Mo bonds and the full structural solution then being made on neutron powder data that were fit using conventional Rietveld refinement and PDF methods.

The last example is particularly interesting since the structural solution that took into account the PDF data also indicated what had gone wrong with the original structural solution. In the case of $LaMo_2O_5$ the single crystal structure was always known to be problematic since it yielded a solution containing atoms that approached each other too closely (Hibble *et al.*, 1998, 1999). The single crystal structure, in space group $P6_3/mmc$, also gave poor agreement with the PDF. Two more physical structures were found that agreed rather well with the PDF. These were somewhat distorted from the single crystal structure and were described in lower symmetry sub-groups of the parent structure ($P\text{-}3m$ and $P6_3mc$). Furthermore, the two models had very similar short-range order up to around 10 Å. This suggested that perhaps both variants are actually present in the material intergrown into each other. The material is therefore twinned on a nanometer lengthscale over which the crystallographic measurements (including powder diffraction in this case) averages resulting in a crystallographically correct, but physically meaningless, structural solution. Again, comparing models with PDF data was central in sorting out this complicated situation. The resulting solutions also resulted in interesting and somewhat unexpected (though reasonable) structural motifs of Mo–O clusters and an interestingly triangulated Mo–Mo bonded network (Hibble *et al.*, 1998, 1999).

9.3.6 $V_2O_5{\cdot}n(H_2O)$ xerogel

Another important example of nanocrystalline materials is $V_2O_5{\cdot}n(H_2O)$ xerogel. This material has fascinated researchers in the decades since its discovery because of its exotic open nanoporous structure with many potential applications (Livage, 1991; Livage *et al.*, 2000). Despite decades of extensive experiments with $V_2O_5{\cdot}n\,H_2O$ its 3D atomic structure

has not been determined in detail. The reason is that the xerogel exists only as ribbon-like particles about 10 nm wide and 1 μm long. Being such a poorly crystalline solid the xerogel exhibits a diffraction pattern without any Bragg peaks making it impossible to determine the 3D atomic structure by traditional crystallographic techniques. Instead the diffraction pattern consists of a rather small number of quite sharp features, indicating intermediate range order, and a pronounced diffuse component, as we have discussed, characteristic of nanocrystalline materials. Again, the PDF method allowed straightforward testing and refinement of 3D structural models allowing a solution of the nanocrystal structure.

The structure functions for crystalline V_2O_5 and the $V_2O_5{\cdot}n\,H_2O$ xerogel are shown in Figure 9.28 and the resulting PDFs are shown in Figure 9.29 (Petkov *et al.*, 2002b). The diffraction patterns are characteristic for crystals and nanocrystals, respectively, with extensive Bragg peaks in the case of V_2O_5 and well-defined but relatively broad features in the xerogel. Features are also evident at low-Q in the xerogel coming from the appearance of nanoporous channels in the structure. Again characteristics are the PDFs. The crystalline

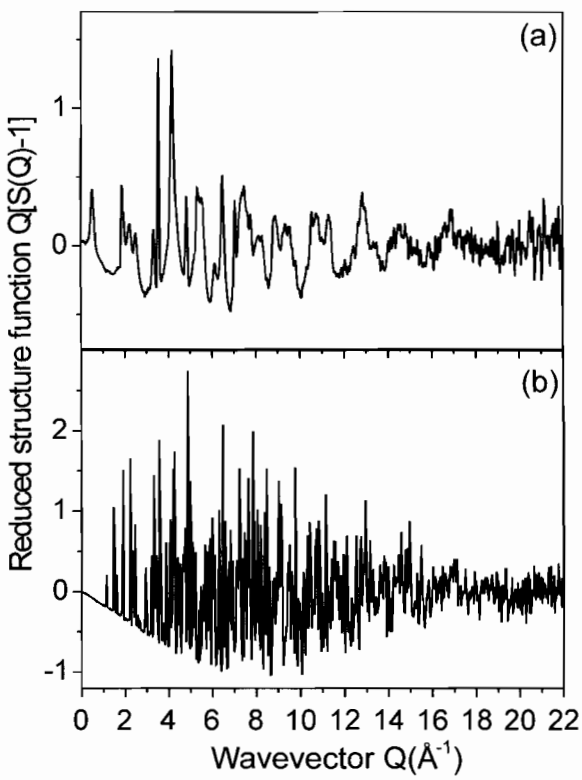

Figure 9.28. Reduced structure functions, $Q[S(Q) - 1]$, of (a) $V_2O_5{\cdot}n\,H_2O$ xerogel and (b) crystalline V_2O_5, collected at beamline X7A, NSLS (Petkov *et al.*, 2002b).

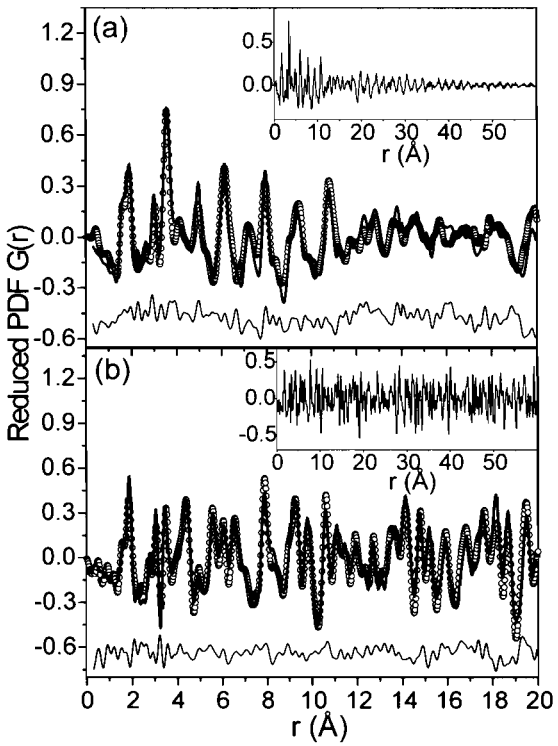

Figure 9.29. Experimental (circles) and fitted (solid line) PDFs for (a) $V_2O_5{\cdot}nH_2O$ xerogel and (b) crystalline V_2O_5. The residual difference is shown in the lower part. The experimental data are shown over longer range in the insets to emphasize the nanocrystalline nature of the xerogel (inset in (a)) (Petkov *et al.*, 2002b).

material has sharp, well-defined PDF-peaks that extend indefinitely in-r. The peaks in the nanocrystalline xerogel are also sharp, especially below 12 Å (about which more later), but the peaks are gradually attenuated with increasing r as highlighted in the insets to Figure 9.29.

Modeling the nanocrystalline $G(r)$ revealed the following (Petkov *et al.*, 2002b). In contrast to crystalline V_2O_5, which is an ordered assembly of single layers of VO_5 units, the gel is a stack of bi-layers of similar VO_5 units with water molecules residing between the bi-layers with the distance of closest approach between the bi-layers being 11.5 Å. In addition to the regular VO_5 a sixth oxygen atom occupies what would be the coordination site opposite to that of the 'capping' oxygen but at a much longer distance of $\sim$2.5 Å.

Sharp decreases in the structural coherence (the amplitude of features in the PDF) are apparent at around 11.5 and 23 Å (e.g. see Figure 9.29(a)). Such a slight but persistent loss of structural coherence repeatedly occurring at distances close to the (bi-layer)–(bi-layer) separation suggests that bi-layers in $V_2O_5{\cdot}nH_2O$ are not stacked in perfect registry

indicating the presence of inter-bilayer stacking disorder. Poorly stacked layers can be mimicked in the PDF by artificially enlarging the atomic thermal factors in the out-of-plane direction, an approach that proved quite successful in modeling the turbostratic disorder in pyrolitic graphite (Kane *et al.*, 1996; Petkov *et al.*, 1999b). The modified model yielded the PDF shown in Figure 9.29(a) as a solid line. The observation of turbostratic disorder in these xerogels is in contrast to the considerable layer–layer correlation occurring in 'restacked' WS_2 and $LiMoS_2$ discussed above. However, it is similar, and probably has a similar origin, to that observed in the pyrolitic graphite that we described above. In that case it is believed to be coming largely from curvature of the graphene sheets. In the case of these xerogels the relatively long, narrow ribbons are known from TEM measurements to be highly curved and tangled which is possible if the bilayers remain in contact but are allowed to slide incoherently over one another.

9.3.7 Nanoclusters intercalated in host materials

Nanoporous materials are important for their ability to store and sieve individual molecules (Brus, 1986). Their large surface area also makes them important as hosts for catalysts. For example, one of the most important catalysts in petroleum cracking is nanoporous zeolite. Nanoporous materials are also being sought for containing hydrogen and lithium for fuel cell and battery applications. There is also fundamental scientific interest in the behavior of materials under confinement, for example, how confinement modifies phase transitions such as melting or superfluid onset (Chan *et al.*, 1988; Porto and Parpia, 1995; Sprague *et al.*, 1995). The practice of making materials with atomic scale holes, and filling them with things, will be around for some time to come. Obviously, it is important to be able to study the material intercalated in the pores. Spectroscopy is very useful in this regard, including NMR and inelastic neutron scattering. However, a prerequisite in having a quantitative understanding of the behavior of materials is to know the structure. We would like to know the structure of materials intercalated into nanopores. The PDF can be very useful because periodicity of the structure is not a prerequisite and so the intercalates need not be long-range ordered, which in general they are not. By using a differential technique such as anomalous X-ray scattering (e.g. see Price and Saboungi, 1998), neutron isotope-exchange, or simply subtracting the scattered intensity from an empty host sample (i.e. considering the host as a sample container and carrying out corrections as outlined in chapter 5!), it is possible to extract the local structure in the vicinity of an intercalated atom or molecule. Because of signal-to-noise problems, this process is relatively in its infancy. However, a number of studies show that the approach is feasible. The structure of Se and CsSe and RbSe clusters intercalated in zeolite Y was solved using anomalous X-ray diffraction (Armand *et al.*, 1997). Also, the position and orientation of $CHCl_3$ in the supercages of NaY zeolite was determined by a hydrogen-deuterium isotope substitution experiment coupled with neutron PDF analysis (Eckert

et al., 2002). By subtracting the scattering from an empty zeolite host it was also possible to study Cs intercalated into the zeolite ITQ-4 (Petkov *et al.*, 2002c).

Based on spectroscopic measurements Cs intercalated into ITQ-4 was thought to be the first room-temperature stable electride material, but no direct structural evidence was available to support this (Dye, 1997). Electrides are interesting low-dimensional correlated electron materials. Ionic solids such as CsCl have a lattice of Cs^+ ions with charge balance provided by Cl^- counter-ions. Alternatively, charged Cs^+ can also be stabilized in solution. In this case, it is stabilized by becoming solvated by polarizable molecules. Electrides are at the interface of these extremes. An ionic lattice forms of alkali cations such as Cs^+ in a polarizable porous solid host analogous to the case of ions in solution. The counter-ions providing charge balance in the electrides are simply the donated electrons. In electrides the donated-electron density has been shown to be confined within cavities and channels in the matrix (Dye, 1997; Allan *et al.*, 1990; Singh *et al.*, 1993; Kaplan *et al.*, 1994). It behaves like a low-density correlated electron gas where the dimensionality of the electron gas and its electronic and magnetic properties are determined by the topology of the cavities in the host matrix (Dye, 1997). X-ray PDF measurements showed that, indeed, the intercalated Cs was in the Cs^+ state verifying that this is indeed an electride material. Furthermore the Cs^+ ions arrange in zigzag chains in the pores of the zeolites host. The pores in the ITQ-4 are narrower than most zeolites (7 Å) and have an undulating 1D topology as shown in Figure 9.30(a). The scattering from the zeolites with and without loading is shown in Figure 9.31(a) and (b) and the resulting PDFs in Figure 9.32(c).

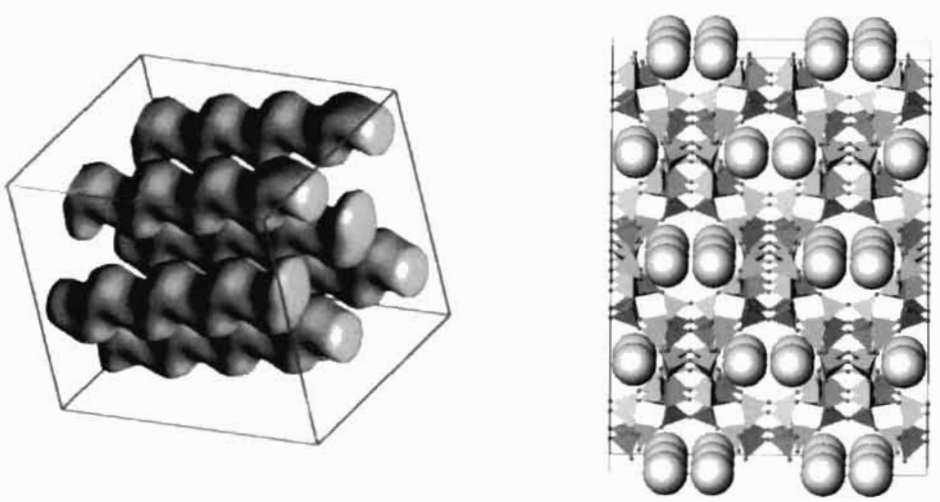

Figure 9.30. (left) representation of the pore topology in the zeolite ITQ-4 (right). Structural model of the Cs^+ ions intercalated in the pores of the zeolites host as determined using differential PDF methods (Petkov *et al.*, 2002c).

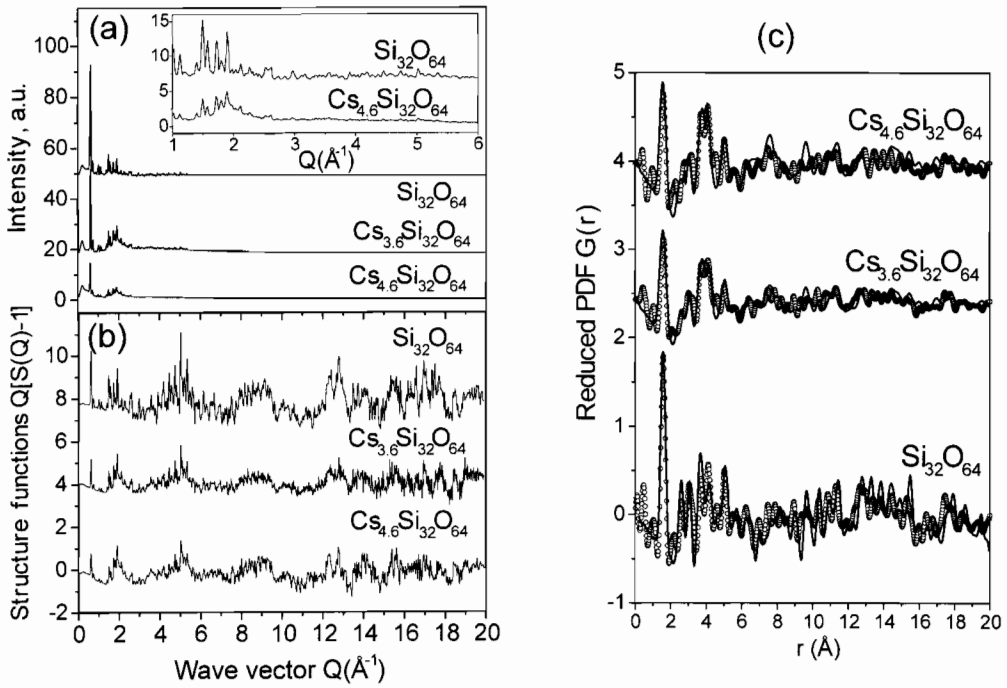

Figure 9.31. (a) raw X-ray powder diffraction data from bare ITQ-4 silica zeolites (top curves in each panel) and Cs loaded electride materials with two different Cs loadings (lower curves). Data were collected at room temperature using beamline X7A at NSLS. (b) Same data converted to the reduced structure function ready for Fourier transformation. Note the reproducible structural features at high-Q that are not immediately evident in the raw data. (c) PDFs from the data in (a) and (b). Dots are the measured data and solid lines are from the structural models. Note the strong increase in intensity of the feature around 4 Å (Petkov *et al.*, 2002).

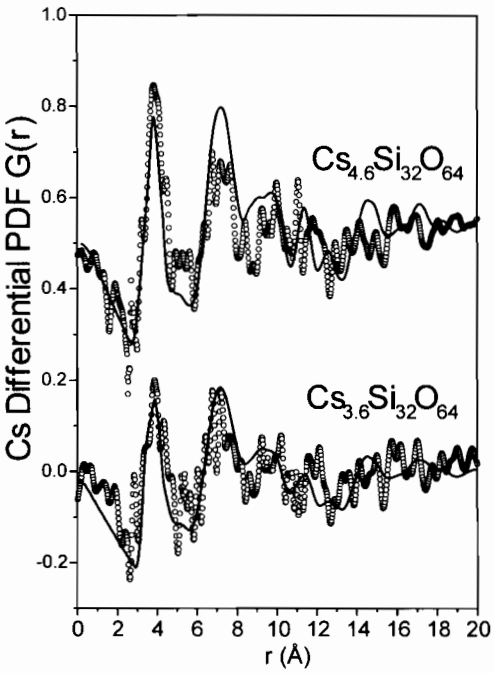

Figure 9.32. Differential PDFs obtained by subtracting the scattering from the zeolite host (dots). Solid lines are calculated PDFs from models fit to both the differential and total PDFs. The models are the same except for taking into account the Cs loading. The only successful models involved Cs^+ indicating that the intercalated Cs is ionized in this material (Petkov *et al.*, 2002c).

Significant new peaks are evident in the PDFs of the Cs loaded zeolites around 4 Å. This is even more apparent in the Cs differential PDFs shown in Figure 9.31. Both the total and differential PDFs were fit with models to come up with the proposed structure of zigzag chains of Cs^+ ions in the pores (Petkov *et al.*, 2002c).

9.4. CHEMICAL SHORT-RANGE ORDER

Most PDF studies on crystals to date have concentrated on extracting information about atomic disorder, in the form of atom displacements from their average positions, and indeed the PDF is most sensitive to this. However, information is contained in the PDF about chemical ordering. Chemical *long-range* order results in superlattice Bragg-peaks, for example, as extensively studied in chemical order–disorder transitions such as in Cu_3Au (e.g. see Cowley, 1995). As with the case of disordered carbon, the list of people who have worked on order–disorder phenomena in alloys has a scattering 'hall of fame' ring to it, including Warren, Cowley, Shockley, Lipson, Guinier, Krivoglaz and Moss

(Warren, 1990; Krivoglaz, 1969, 1996; Cowley, 1995). Above the ordering transition short-range ordering of the chemical species persists and can be studied using diffuse scattering (Cowley, 1950; Moss, 1964). This is still today a topic of great interest in non-stoichiometric compounds such as doped semiconductors, semiconductor alloys and oxides such as high-T_c cuprates where chemical short-range order (CSRO) can significantly modify the properties. It is interesting to know whether this information can be extracted from the PDF and this has been investigated recently (Proffen, 2000; Proffen *et al.*, 2002). In this study data were first simulated and the CSRO information was extracted successfully from the simulated data using a reverse Monte-Carlo approach (Proffen, 2000).

This has also been successfully demonstrated in real data from the Cu_3Au system (Proffen *et al.*, 2002). In this case X-ray PDFs from fully ordered Cu_3Au, and a disordered compound quenched from high temperature, were compared. There are significant differences between both the raw data (Figure 9.33) and the PDFs (Figure 9.34) between

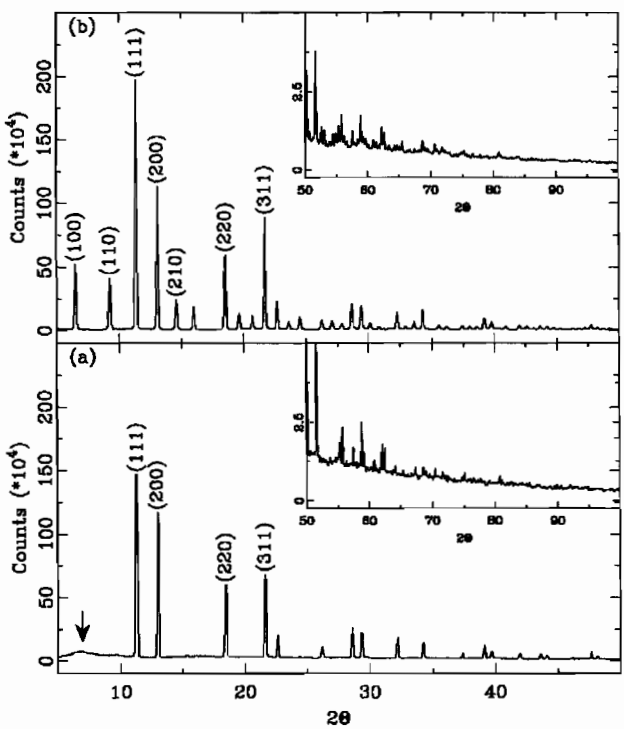

Figure 9.33. X-ray powder diffraction data from ordered (top) and disordered (bottom) samples of Cu_3Au. Superlattice peaks are clearly visible in the chemically ordered sample. Some diffuse scattering, presumably originating from CSRO is evident in the 'disordered' sample below $2\theta = 10°$ (Proffen *et al.*, 2002).

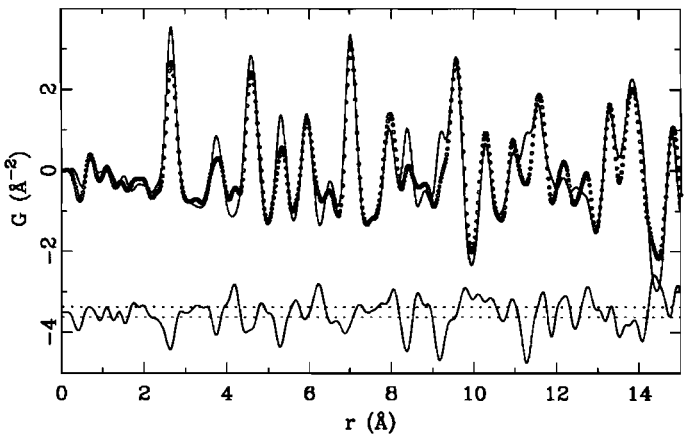

Figure 9.34. Experimental PDFs from disordered (circles) and ordered (solid line) Cu_3Au. The difference is given below as solid line. The estimated experimental uncertainty is marked by horizontal broken lines (Proffen *et al.*, 2002).

the ordered and disordered compounds as expected. As is clear from Eq. 3.5, in the PDF chemical ordering is manifest as changes in the peak intensities since the peak intensities are weighted by the atomic scattering factors of the pairs involved. This is evident in Figure 9.34. Simple least-squares refinement using PDFFIT allowed the ordered and disordered compounds to be distinguished. However, a reverse Monte-Carlo refinement of the data from the disordered material indicated that some short-range order persisted.

In the ordered sample the CSRO parameters gave values exactly as expected for an ordered sample and persisted out indefinitely in r, as they should because the order is long-ranged. In the case of the disordered sample the CSRO parameters were not zero, the values for a random alloy, but deviated from zero in the sense that suggested that the same ordering scheme as seen in the ordered sample was persisting locally in the disordered sample. The non-zero CSRO parameters died out with increasing r and became insignificant around the 6th nearest neighbor. In this case, the residual order is probably the result of an imperfect quench rather than short-range order persisting above the ordering transition (the samples were quenched from 1200 K and the ordering transition is at 667 K). Nonetheless, it indicates that short-range order information can be extracted from the PDF. One thing that is apparent is that the signal of the CSRO in the PDF is rather weak. This is illustrated in Figure 9.35 which shows the calculated PDF from the fully random model and that with the mild CSRO refined to the disordered model. The difference curve, which has been multiplied by $3\times$, shows the difference that is rather small: obtaining high-quality data is especially important in these studies.

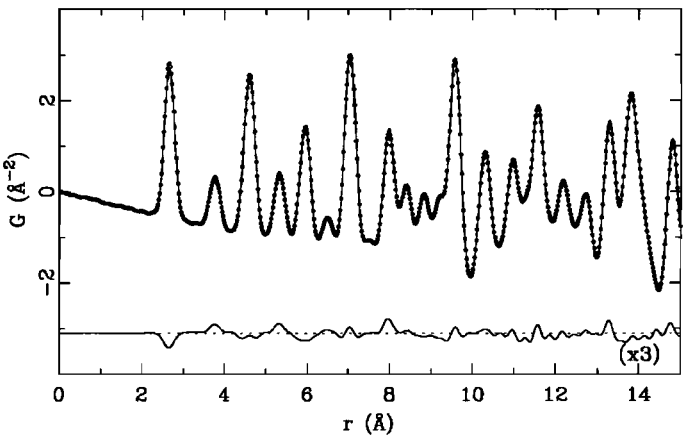

Figure 9.35. Calculated PDFs of the starting (solid line) and resulting structure (circles) of Cu_3Au from the RMC refinement that allows for chemical short-range order to exist in the 'disordered' sample. The difference between both PDFs is enlarged by a factor of three and shown below the curves (Proffen *et al.*, 2002).

REFERENCES

Acharya, M., Strano, M.S., Mathews, J.P., Billinge, S.J.L., Petkov, V., Subramoney, S. & Foley, H.C. (1999) *Phil. Mag. B*, **79**, 1499.

Aleandri, L.E. & McCarley, R.E. (1988) *Inorg. Chem.*, **27**, 1041.

Alivisatos, A.P. (1996) *J. Phys. Chem.*, **100**, 13226.

Allan, G., DeBacker, M.G., Lannoo, M. & Lefebre, (1990) *J. Europhys. Lett.*, **11**, 49.

Armand, P., Saboungi, M.-L., Price, D.L., Iton, L., Cramer, C. & Grimsditch, M. (1997) *Phys. Rev. Lett.*, **79**, 2061.

Bethune, D.S., *et al.* (1993) *Nature*, **363**, 605.

Brus, L.E. (1986) *J. Phys. Chem.*, **90**, 2555.

Chan, M.H.W., Blum, K.I., Murphy, S.Q., Wong, G.K.S. & Reppy, J.D. (1988) *Phys. Rev. Lett.*, **61**, 1950.

Cheetham, A.K., Fender, B.E.F. & Cooper, M.J. (1971) *J. Phys. C: Solid State Phys.*, **4**, 3107.

Claye, A. & Fischer, J.E. (1999) *Electrochim. Acta*, **45**, 107.

Copley, J.R.D., Neumann, D.A., Cappelletti, R.L. & Kamitakahara, W.A. (1992) *J. Phys. Chem.*, **53**, 1353.

Cowley, J.M. (1950) *J. Appl. Phys.*, **21**, 24.

Cowley, J.M. (1995) in *Diffraction Physics*, Elsevier, Amsterdam.

Damay, P. & Leclercq, F. (1994) *Phys. Rev. B*, **49**, 7790.

David, W.I.F., Ibberson, R.M., Matthewman, J.C., Prassides, K., Dennis, T.S.J., Hare, J.P., Kroto, H.W., Taylor, R. & Walton, D.M.R. (1991) *Nature*, **353**, 147.

Divigalpitiya, W.M.R., Frindt, R.F. & Morrison, S.R. (1989) *Science*, **246**, 369.

Dmowski, W., Egami, T., Swider-Lyons, K.E., Love, C.T. & Rolison, D.R., (2002) *J. Phys. Chem. B*, **106**, 12677.

Dresselhaus, M.S., Dresselhaus, G. & Eklund, P.C. (1996) in *Science of Fullerenes and Carbon Nanotubes*, Academic Press, New York.

Dye, J.L. (1997) *Inorg. Chem.*, **36**, 3816.
Eckert, J., Draznieks, C.M. & Cheetham, A.K. (2002) *J. Am. Chem. Soc.*, **124**, 170.
Egami, T., Dmowski, W. & Brezny, R. (1997) *SAE Publication* **970461**; (1998) *SAE 1997 Trans.*, **106**, *J. Fuels Lubricants*, Sec. 4, 98.
Franklin, R.E. (1950) *Acta Crystallogr.*, **3**, 107.
Franklin, R.E. (1951) *Proc. R. Soc. London A*, **209**, 196.
Heiney, P.A., Fischer, J.E., McGhie, A.R., Romanow, W.J., Denenstein, A.M., McAuley, J.P., Smith, A.B., III & Cox, D.E. (1991) *Phys. Rev. Lett.*, **66**, 2911.
Hibble, S.J. & Fawcett, I.D. (1995) *Inorg. Chem.*, **34**, 500.
Hibble, S.J. & Hannon, A.C. (2002) in *From Semiconductors to Proteins: Beyond the Average Structure*, Eds. Billinge, S.J.L. & Thorpe M.F., Kluwer/Plenum, New York, p. 129.
Hibble, S.J., Fawcett, I.D. & Hannon, A.C. (1997a) *Inorg. Chem.*, **36**, 1749.
Hibble, S.J., Fawcett, I.D. & Hannon, A.C. (1997b) *Acta Crystallogr.*, **53**, 604.
Hibble, S.J., Cooper, S.P., Hannon, A.C., Patat, S. & McCarroll, W.H. (1998) *Inorg. Chem.*, **37**, 6839.
Hibble, S.J., Cooper, S.P., Patat, S. & Hannon, A.C. (1999) *Acta Crystallogr. B*, **55**, 683.
Hu, R.Z., Egami, T., Li, F. & Lannin, J.S. (1992) *Phys. Rev. B*, **45**, 9517.
Hua, G.L., Welberry, T.R., Withers, R.L. & Thompson, J.G. (1988) *J. Appl. Crystallogr.*, **21**, 458.
Hutchings, M.T., Clausen, K., Dickens, M.H., Hayes, W., Kjems, J.K., Schnabel, P.G. & Smith, C. (1984) *J. Phys. C: Solid State Phys.*, **17**, 3903.
Iijima, S. & Ichihashi, T. (1993) *Nature*, **363**, 603.
James, A.C.W.P. & Goodenough, J.B. (1988) *J. Solid State Chem.*, **76**, 87.
Jeong, I.-K., Mohiuddin-Jacobs, F., Petkov, V., Billinge, S.J.L. & Kycia, S. (2001) *Phys. Rev. B.*, **63**, 205202.
Kanatzidis, M.G., Bissesssur, R. & DeGroot, D.C. (1993) *Chem. Mater.*, **5**, 595.
Kane, M.S., Goellner, J.F., Foley, H.C., DiFrancesco, R.G., Billinge, S.J.L. & Allard, L.F. (1996) *Chem. Mater.*, **8**, 2159.
Kaplan, T.A., Rencsok, R. & Harrison, J.F. (1994) *Phys. Rev. B*, **50**, 8054.
Krivoglaz, M.A. (1969) in *Theory of X-Ray and Thermal-Neutron Scattering by Real Crystals*, Plenum, New York.
Krivoglaz, M.A. (1996) in *Diffuse Scattering of X-rays and Neutrons by Fluctuations*, Springer, Berlin.
Leclercq, F., Damay, P., Foukani, M., Chieux, P., Bellissent-Funel, M.C., Rassat, A. & Fabre, C. (1993) *Phys. Rev. B*, **48**, 2748.
Li, F., Ramage, D., Lannin, J.S. & Conceicao, (1991) *J. Phys. Rev. B*, **44**, 13167.
Livage, (1991) *J. Chem. Mater.*, **3**, 578.
Livage, J., Pelletier, O. & Davidson, P. (2000) *J. Sol-Gel Sci. Technol.*, **19**, 275.
Mamontov, E. & Egami, T. (2000) *J. Phys. Chem. Solids*, **61**, 1345.
Mamontov, E., Egami, T., Brezny, R., Koranne, M., Juskelis, M. & Tyagi, S. (2000) *J. Phys. Chem. B*, **104**, 11110.
Mikkelson, J.C. & Boyce, J.B. (1982) *Phys. Rev. Lett.*, **49**, 1412.
Moss, S.C. (1964) *J. Appl. Phys.*, **35**, 3547.
Neild, V.M. & Keen, D.A. (2001) in *Diffuse Neutron Scattering from Crystalline Materials*, Oxford Science Publications, Oxford.
Pauly, T.R., Petkov, V., Liu, Y., Billinge, S.J.L. & Pinnavaia, T.J. (2002) *J. Am. Chem.*, **124**, 97.
Peterson, P.F., Proffen, Th., Jeong, I.-K., Billinge, S.J.L., Choi, K.-S., Kanatzidis, M.G. & Radaelli, P.G. (2001) *Phys. Rev. B*, **63**, 165211.

Petkov, V. & Billinge, S.J.L. (2002) in *From Semiconductors to Proteins: Beyond the Average Structure*, Eds. Billinge, S.J.L. & Thorpe M.F., Kluwer/Plenum, New York, p 153.

Petkov, V., Jeong, I.-K., Chung, J.S., Thorpe, M.F., Kycia, S. & Billinge, S.J.L. (1999a) *Phys. Rev. Lett.*, **83**, 4089.

Petkov, V., DiFrancesco, R.G., Billinge, S.J.L., Acharya, M. & Foley, H.C. (1999b) *Phil. Mag. B*, **79**, 1519.

Petkov, V., Jeong, I.-K., Mohiuddin-Jacobs, F., Proffen, Th. & Billinge, S.J.L. (2000a) *J. Appl. Phys.*, **88**, 665.

Petkov, V., Billinge, S.J.L., Shastri, S.D. & Himmel, B. (2000b) *Phys. Rev. Lett.*, **85**, 3436.

Petkov, V., Billinge, S.J.L., Heising, J. & Kanatzidis, M.G. (2000c) *J. Am. Chem. Soc.*, **122**, 11572.

Petkov, V., Billinge, S.J.L., Larson, P., Mahanti, S.D., Vogt, T., Rangan, K.K. & Kanatzidis, M.G. (2002a) *Phys. Rev. B*, **65**, 092105.

Petkov, V., Trikalitis, P.N., Bozin, E.S., Billinge, S.J.L., Vogt, T. & Kanatzidis, M.G. (2002b) *J. Am. Chem. Soc.*, **124**, 10157.

Petkov, V., Billinge, S.J.L., Vogt, T., Ichimura, A.S. & Dye, J.L. (2002c) *Phys. Rev. Lett.*, **89**, 075502.

Pintschovius, L. (1998) *Phase Transit.*, **67**, 295.

Porto, J.V. & Parpia, J.M. (1995) *Phys. Rev. Lett.*, **74**, 4667.

Price, D.-L. & Saboungi, M-L. (1998) in *Local Structure from Diffraction*, Eds. Billinge, S.J.L. & Thorpe M.F., Plenum Press, New York, p. 1.

Proffen, Th. (2000) *Z. Kristallogr.*, **215**, 661.

Proffen, Th., Petkov, V., Billinge, S.J.L. & Vogt, T. (2002) *Z. Kristallogr.*, **217**, 47.

Saito, R., Dresselhaus, M.S. & Dresselhaus, G. (1998) in *Physical Properties of Carbon Nanotubes*, Imperial College Press, London.

Singh, D.J., Krakauer, H., Haas, C. & Pickett, W.E. (1993) *Nature*, **365**, 39.

Soper, A.K., David, W.I.F., Sivia, D.S., Dennis, T.J.S., Hare, P. & Prassides, K. (1992) *J. Phys: Condens. Matter*, **4**, 6087.

Sprague, D.T., Haard, T.M., Kycia, J.B., Rand, M.R., Lee, Y., Hamot, P.J. & Halperin, W.P. (1995) *Phys. Rev. Lett.*, **75**, 661.

Thorpe, M.F., Levashov, V.A., Lei, M. & Billinge, S.J.L. (2002) in *From Semiconductors to Proteins: Beyond the Average Structure*, Eds. Billinge, S.J.L. & Thorpe M.F., Kluwer/Plenum, New York, p. 105.

Tucker, M.G., Dove, M.T. & Keen, D.A. (2000) *J. Phys. Condens. Matter*, **12**, L723.

Tucker, M.G., Keen, D.A. & Dove, M.T. (2001a) *Mineral. Mag.*, **65**, 489.

Tucker, M.G., Squires, M.D., Dove, M.T. & Keen, D.A. (2001b) *J. Phys. Condens. Matter*, **13**, 403.

Tucker, M.G., Dove, M.T. & Keen, D.A. (2002) in *From Semiconductors to Proteins: Beyond the Average Structure*, Eds. Billinge, S.J.L. & Thorpe M.F., Kluwer/Plenum, New York, p. 85.

Warren, B.E. (1934) *J. Chem. Phys.*, **2**, 551.

Warren, B.E. (1941) *Phys. Rev.*, **9**, 693.

Warren, B.E. (1990) in *X-ray Diffraction*, Dover, New York.

Whetten, R.L., Khoury, J.T., Alvarez, M.M., Murthy, S., Vezmar, I., Wang, Z.L., Stephens, P.W., Cleveland, C.L., Luedtke, W.D. & Landman, U. (1996) *Adv. Mater.*, **8**, 426.

This Page Intentionally Left Blank

Chapter 10

Local Structure of Systems with Competing Interactions

This Page Intentionally Left Blank

Chapter 10
Local Structure of Systems with Competing Interactions

10.1. MIXED FERROELECTRIC OXIDES

As we mentioned in Chapter 1, in many modern functional materials responses to external stimuli are maximized by the use of competing interactions, which result in complex local structures. These local structures are quite often directly related to the desirable properties, making it important to study and understand them. The competing interactions produce complex internal structures primarily through a local feedback effect, as we will see in this chapter. A secondary, but important, factor is the effect of disorder. The competing forces are quite often adjusted chemically, by alloying two or more constituent compounds. An example is the high-temperature superconductor $La_{2-x}Sr_xCuO_4$ that is hole-doped by randomly replacing La^{3+} with Sr^{2+}. This alloying effect introduces atomic level chemical disorder. While this chemical disorder itself is usually unimportant, it triggers the competing forces to create complex local structures and pin local patterns so that the whole structure does not have the lattice periodicity. For this reason these alloy solids are rich in complexity at various length scales, down to the nanometer scale, even when they appear to maintain long-range order in the structure. In this chapter we discuss three representative cases that are of current interest, namely, ferroelectric mixed-oxides, manganites that exhibit colossal magnetoresistive phenomenon, and superconducting cuprates.

10.1.1 PZT, $Pb(Zr_{1-x}Ti_x)O_3$

Starting with PZ discussed in Chapter 8, replacing small amounts of Zr by Ti produces PZT, $Pb(Zr_{1-x}Ti_x)O_3$. This brings about dramatic changes in the structure and dielectric properties. While PZ is antiferroelectric PZT is strongly ferroelectric for $x > 0.05$, and the symmetry of the structure changes from orthorhombic to rhombohedral (Jaffe *et al.*, 1971). PZT is widely used as a ferroelectric or piezoelectric material, in various applications, typically in actuators and sensors. It is usually assumed that Ti drives the system to ferroelectricity, since Ti is more ferroelectrically polarizing. However, it is rather surprising to see such a small amount of additive Ti creating dramatic changes in the whole of the oxide structure and properties. For only 5% of Ti to drive the structure of PZT to ferroelectricity, PZ itself must have some tendency toward ferroelectricity. For instance, $SrTiO_3$ (STO) has a high dielectric constant, and is almost ferroelectric. This is understood as a case of quantum paraelectricity in which the weak ferroelectricity is suppressed because of the diverging zero-point oscillations (Samara, 1971). Adding a small amount of

ferroelectric impurities to STO drives the system to ferroelectricity (Mitsui and Westphal, 1961). However, PZ is *strongly antiferroelectric* (AFE) with the Neel temperature of 511 K. How can only 5% of Ti kill such strong AFE?

The pulsed neutron PDF gave a clear answer to this simple question. As shown in Figure 10.1 the PDF of $Pb(Zr_{0.9}Ti_{0.1})O_3$ (PZT 90/10) is very similar to the PDF of PZ in the range up to 5 Å, in spite of large differences in the average structure (Egami *et al.*, 1997). Of course differences are large at larger distances, reflecting the difference in the long-range structure. This implies that upon addition of Ti the local structure of Zr does not change much. This is understandable since both Zr and Ti are 4 + ions, and replacing Zr by Ti does not change the Madelung energy too much. Instead, what Ti does is to change the way the local structural units are arranged by altering the connectivity condition of the local units. The ZrO_6 octahedra are rotated around the ⟨110⟩ axes in PZ as mentioned above, while the Ti^{4+} ion is small, and does not result in a local rotation. Consequently, Ti disrupts the connectivity of the local rotations so that the axis of rotation can change. Indeed, while the octahedra are rotated around ⟨111⟩ in the rhombohedral phase of PZT according to the average structure, locally the rotation axis is still close to ⟨110⟩ even in PZT (Teslic *et al.*, 1997). The direction of the rotation axis changes randomly at the Ti ion, for instance from [110] to [101], thus on average the rotation axis appears to be ⟨111⟩. Such a rearrangement of local units, actually, is most commonly observed during phase transformations in many oxide compounds, as we will discuss also in Chapter 11.

The change in the local rotation directly alters the AFE order. The origin of the AFE in PZ is the ionic size effect as we discussed in Chapter 8. Because Zr^{4+} ions are relatively

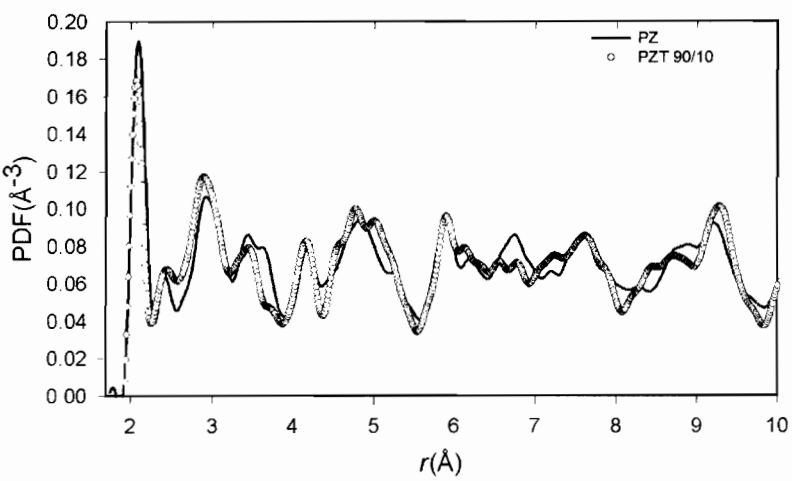

Figure 10.1. PDF of PZ, $PbZrO_3$, compared to that of PZT(90/10), $Pb(Zr_{0.9}Ti_{0.1})O_3$. Note the similarity below $r \sim 5$ Å despite the different average structures (orthorhombic and rhombohedral, respectively) (Egami *et al.*, 1997).

large (0.72 Å, Shannon, 1976), the tolerance factor of PZ is 0.973. This leads to a buckling of the Zr–O–Zr bond and a rotation of the ZrO_6 octahedra. Since rotation of one octahedron results in the rotation of the neighboring octahedra in the opposite sense rotation results in doubling of the unit cell. In particular, it produces oxygen displacements with AFE order, which leads to AFE ordering of the Pb polarization. This chain of rotations can be broken by a small cation such as Ti^{4+}. Furthermore Pb polarization in PZ has ferroelectric fluctuations along the z-axis (Teslic and Egami, 1998). While the x- and y-polarizations have an AFE ordering, the z-axis polarization can develop ferroelectricity due to impurities such as Ti^{4+}. Thus FE and AFE are not incompatible in complex systems, and can locally coexist. The main difference is that the long-range part of the AFE coupling is elastic in nature, while the FE is an electronic phenomenon associated with the long-range dipolar field and covalency.

10.1.2 Relaxor ferroelectric PMN, $Pb(Mg_{1/3}Nb_{2/3})O_3$

Ferroelectric materials have strong dielectric and piezoelectric responses that can be used in various applications. However, the strong response is limited to the vicinity of the transition (Curie) temperature, T_C, and is strongly temperature dependent. This presents a major problem in applications. On the other hand a class of materials called relaxor ferroelectrics show(s) much milder temperature dependence, and are very widely used in a number of applications. Relaxor ferroelectrics show a diffuse, gradual ferroelectric transition and frequency dependent dielectric response. The dependence of the dielectric response on frequency and temperature is very much like that of the mechanical or dielectric response of a glass, hence the origin of the name relaxor ferroelectric. The mechanism of relaxor ferroelectricity is obviously related to disorder, but its details are still controversial, as will be discussed below and in the next Chapter.

A prototypical relaxor ferroelectric is $Pb(Mg_{1/3}Nb_{2/3})O_3$ (PMN). In this compound the element of disorder is introduced by the occupation of the B-site by two ions with different valences (Mg^{2+} and Nb^{5+}) and sizes (0.72 Å for Mg^{2+} and 0.64 Å for Nb^{5+}). Interestingly the initial explanation of relaxor behavior in PMN went in the opposite direction by seeking order rather than disorder. Broad superlattice diffraction peaks were found at the 1/2[111] type reciprocal lattice positions by electron diffraction indicating some ordering that doubled the lattice periodicity in the [111] direction (Husson *et al.*, 1988). In other words, the B-site ions form two sub-lattices as in the NaCl structure. It was proposed that Mg^{2+} and Nb^{5+} occupy each of these sub-lattices. But then local charge neutrality is violated, since the average charge of the A-site has to be +4, because Pb is divalent in this compound, while the average valence of Mg^{+2} and Nb^{+5} is +3.5. Consequently, it was argued, the ordered domain will not grow in size, resulting in nano-domains that are surrounded by a Nb rich matrix. Since these nano-domains are dielectrically separated, they are polarized randomly, and the glassy relaxor behavior is created.

However, this scenario has many problems. First of all, the charged domains of nanometer size would have a huge electrostatic energy. Secondly this picture was developed to explain the relaxor behavior of hetero-valent PMN, while the relaxor behavior is observed also in the homo-valent PZT, when a small amount of Pb is replaced by La, $(Pb_{1-x}La_x)(Zr_{1-y}Ti_y)O_3$ (PLZT), and this scenario fails to explain it. In this scenario the Nb concentration is different in the ordered domain and the rest. The ordered domain has less Nb than average, while the disordered matrix is Nb rich. Such a strong inhomogeneity of Nb distribution should be observable by the small angle scattering, while the measurement did not show such inhomogeneity (Egami *et al.*, 1997). More importantly, recent work (Akbas and Davies, 1997) demonstrated in a very similar system, $(Pb(Mg_{1/3}Ta_{2/3})O_3)_{0.9}(PbZrO_3)_{0.1}$ (PMT-PZ), relaxor behavior persists even when the chemical ordering extends to a macroscopic scale (micron-size). This proves finally that the nano-domains are totally irrelevant to the relaxor behavior. The diffraction study of this system (Dmowski *et al.*, 2000) showed that the 1:1 ordering into the NaCl superlattice is made of Ta^{5+} in one sublattice and the other in the other sublattice, and macroscopically there is no charge imbalance.

The local structure of PMN determined by the pulsed neutron PDF method is very different from the PDF expected for the average crystal structure as shown in Figure 10.2 (Egami *et al.*, 1991). Crystallographically PMN has the structure of a nearly cubic simple perovskite, with a very slight rhombohedral distortion (note the rhombohedral distortion does not change the shape of the BO_6 octahedron). However, the measured PDF reveals significant deviations of the local structure from the average structure. Not only are the PDF peaks broader, but there are peaks in the measured PDF that do not correspond to the peaks in the perovskite PDF. In particular there is a strong peak in the measured PDF at 2.45 Å.

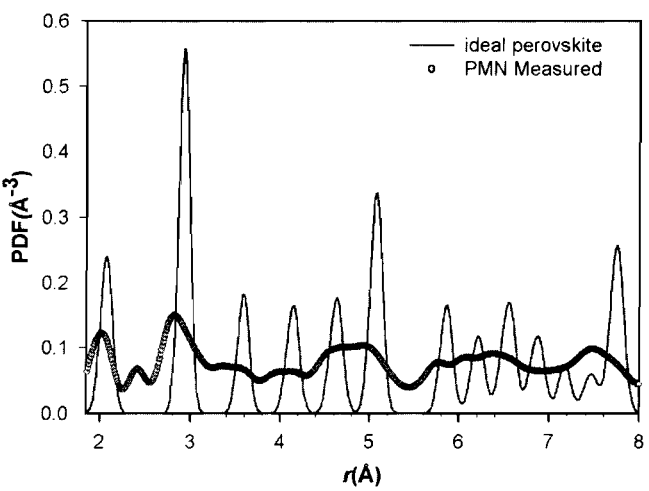

Figure 10.2. Pulsed neutron PDF of PMN, $Pb(Mg_{1/3}Nb_{2/3})O_3$, compared to the PDF calculated for the ideal perovskite structure found crystallographically for PMN (Egami *et al.*, 1991).

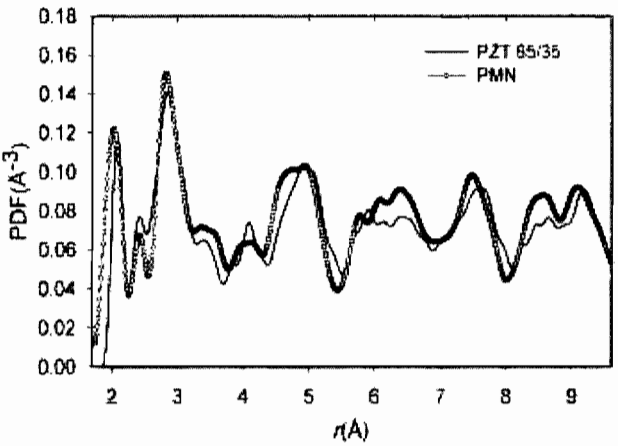

Figure 10.3. PDF of PMN and PZT(65/35). Note the strong similarity despite the different average structures (Egami *et al.*, 1998).

It turned out that the PDF of PMN is surprisingly similar to the PDF of PZT, as shown in Figure 10.3, in spite of the difference in the crystal structure. Both PZT and PMN feature the 2.45 Å peak (Egami *et al.*, 1997). Since the PDF of PZT is similar to the PDF of PZ as shown in Figure 10.1, we can trace the origin of the 2.45 Å peak to PZ, and find that it is produced by the short Pb–O bonds due to lone pair electrons as we discussed earlier. Thus the peak at 2.45 Å indicates the local polarization of the PbO_{12} cluster (Figure 8.11). This leads to an idea that a simple picture may describe the dielectric behavior of Pb containing perovskite based ferroelectrics based upon the interacting PbO_{12} dipoles (Egami *et al.*, 1998). This subject will be discussed in Chapter 11.

10.2. COLOSSAL MAGNETORESISTANCE (CMR) MANGANITES

10.2.1 Colossal magnetoresistance phenomenon

Magnetoresistance (MR) in metals is usually small, with $\Delta\rho/\rho$ of the order of 0.1–1% per Tesla. Recently metallic multi-layered thin films such as Fe/Cr were found to show much larger magnetoresistance ($\Delta\rho/\rho \sim 0.1$–$0.5\ T^{-1}$) and the phenomenon was named '*giant magnetoresistance*' (Parkin, 1995). Since these films can modulate electric current by a magnetic field, they are also called '*spin valves*', and are now beginning to be used in magnetic recording heads and other devices. It was then recognized that the metal-insulator transition in oxides could be used in similar applications. In particular many of the manganite compounds $(R_{1-x}A_x)_{n+1}Mn_nO_{3n+1}$ (R = La, Pr, or Nd, A = Sr, Ba, Ca or Pb) are insulating in the paramagnetic phase but metallic in the ferromagnetic phase

(Ramirez, 1997). Thus, by applying a magnetic field an insulator-to-metal (IM) transition can be induced. Since the magnitude of the change in resistance in terms of $-\Delta\rho/\rho(H)$ can be as large as 10^4, or 10^6%, this phenomenon was coined 'colossal magnetoresistance (CMR)' (Jin *et al.*, 1994).

The basic behaviors of the manganites were discovered already half a century ago (Jonker and Van Santen, 1950; Van Santen and Jonker, 1950), and the electronic mechanism to produce a ferromagnetic metallic phase was discussed by Zener (1951), Goodenough (1955), Hasegawa and Anderson (1955), and DeGennes (1960) in terms of the double-exchange (DE) mechanism. The magnetic interaction most commonly found in insulating oxides of transition metals (TM) is the antiferromagnetic (AFM) *super-exchange* (SE) interaction. Indeed the parent phase of the CMR manganites, $LaMnO_3$, is an AFM insulator. If a hole is introduced in the AFM insulator, it is usually localized, since moving a hole in the AFM matrix will produce parallel spin configurations, which is energetically unfavorable. This state is called the *spin-polaron*, or *magnetic polaron*. However, the kinetic energy of the doped hole is reduced when it is not confined to one TM–O orbital, but is shared in the TM–O–TM bond. Note that in classical mechanics, itinerant particles have a higher kinetic energy. However, quantum-mechanically localizing an electron necessitates squeezing the wavefunction in a small space, creating a large spatial variation, which is proportional to the momentum. Thus *delocalization* results in the reduction in the kinetic energy. For electrons to be mobile, the spins on the TM ions have to be parallel. However, this also increases the kinetic energy, since twice as many electrons occupy one spin band. Thus if the energy gain due to delocalization is greater than the energy loss due to spin polarization, spins turn parallel and electrons become mobile. This is the DE interaction. If enough holes are doped into the system, they become delocalized, converting the whole system into a ferromagnetic metal.

Recently, however, Millis *et al.* (1995) pointed out that the DE interaction is insufficient to explain the details of the CMR behavior. In particular the DE model fails to explain the high electrical resistivity of the paramagnetic phase. They suggested that a strong electron-lattice interaction provides the missing resistivity via *lattice-polaron* formation. A lattice-polaron is a charge carrier that is trapped in the elastic deformation it created. The simplest form of a lattice-polaron is an electron in the lattice of positive ions that are attracted to the electron (Figure 10.4). The attracted positive ions form a cluster of excess positive charge that traps the electron there. In perovskites, however, the situation is slightly more complex, since both cations and anions form the lattice. The doped holes attract cations but repel anions. In manganites the polarons are directly related to the Jahn–Teller distortion discussed in Section 8.1.4. Various direct and indirect experimental methods have been mobilized to detect the polarons, and successfully confirmed the presence of spin-lattice polarons as reviewed in Egami and Louca (2000). The PDF analysis played a major role in this process, and also provided further insight into the physics of CMR (Billinge *et al.*, 1996; Louca *et al.*, 1997).

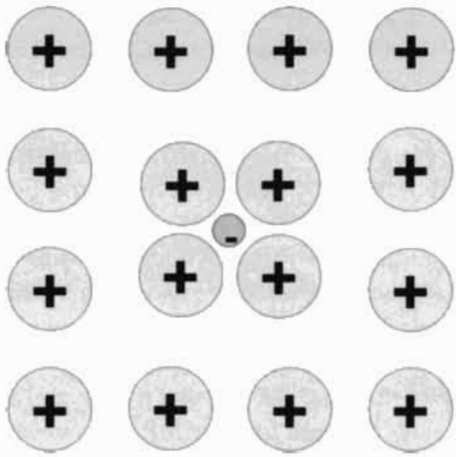

Figure 10.4. Schematic picture of a lattice-polaron. The charge carrier (in this case an electron) localizes in the lattice producing a localized region of negative charge. The system lowers its overall energy by polarizing the surrounding lattice of positive ions.

An even more recent realization has been that these materials are electronically microscopically (and sometimes macroscopically) inhomogeneous. This is discussed in greater detail in Section 11.4. PDF analysis had a role to play here too by identifying a coexistence of localized polaronic and delocalized metallic states coexisting over wide ranges of temperature and composition, even deep in the ferromagnetic metallic phase where it was widely thought that the charges were delocalized and the material a homogenous metal (Louca and Egami, 1999; Billinge *et al.*, 2000). In these two studies the results were interpreted slightly differently, in the one case in terms of polarons growing in size and percolating (Louca and Egami, 1999), in the other a nano-scale phase separation into metallic and small-polaron insulating domains that change their relative concentration, again percolating at the metal-insulator phase transition. Also, the systems studied were different: $La_{1-x}Sr_xMnO_3$ and $La_{1-x}Ca_xMnO_3$, respectively. However, the data are consistent and the message is clear: these materials are electronically inhomogeneous as is now rather well established (Section 11.4).

In semiconductors a small amount of dopant ($\sim 10^{-6}$, Itoh *et al.*, 1996 and references therein) is able to induce a transition from an insulator to a metal. In the CMR manganites, because of the formation of the spin-lattice polarons, the doped charge carriers are localized up to a high doping density of about 17%. At this charge concentration charge carriers become delocalized rather suddenly producing the insulator-to-metal (IM) transition. Before touching upon the issues related to this transition, which will be discussed in Chapter 11, let us review the information provided through the PDF studies on the perovskites and the layered manganite compounds.

10.2.2 Perovskite, $La_{1-x}A_xMnO_3$ (A = Ca, Sr, Ba, Pb)

In $La_{1-x}A_xMnO_3$ the replacement of trivalent La by a divalent ion such as A = Ca, Sr, Ba and Pb reduces the effective valence of Mn, or equivalently introduces holes to the Mn–O band. If the doped hole is localized on the Mn^{3+}, a JT ion, it becomes, at least nominally, Mn^{4+}, (a non-JT ion). The exact state of the localized hole is an interesting problem by itself. With increased hole doping the JT distortion in the average crystal structure quickly becomes smaller, and disappears at about a doping level of $x = 0.17$, and the structure becomes rhombohedral (Urushibara *et al.*, 1995). At 50 % doping, many of the manganites, such as $La_{1/2}Ca_{1/2}MnO_3$, exhibit charge ordering, and become insulating. When the doping exceeds 50% the system remains a charge ordered antiferromagnetic insulator.

In mixed-ion oxides such as $La_{1-x}A_xMnO_3$ the local structure is expected to deviate from the average because of the ionic size difference between La and A. However, such deviations are only indirectly important for the CMR phenomenon. Local deviations that are central to the CMR phenomenon are those due to polaron formation. The local structure of this system was studied by the XAFS method by several groups (Booth *et al.*, 1996; Tyson *et al.*, 1996; Lanzara *et al.*, 1998). The XAFS experiment, however, suffers from the problem of intrinsic peak broadening of the PDF due to the form factor of electron scattering and the lifetime effect of photoelectrons as discussed in Appendix 3.4. Consequently the split in the Mn–O bond distances due to the JT distortion can be detected only by modeling. This introduces ambiguity that is model dependent. As a result the amount of split reported by the XAFS measurement varied widely, from 0.1 Å (Booth *et al.*, 1996) to 0.5 Å (Tyson *et al.*, 1996). Nonetheless, the results of the XAFS studies on the Mn–O distances should be semi-quantitatively correct.

More direct observations of local distortion due to polarons were made by using the pulsed neutron PDF method by Billinge *et al.* (1996) and Louca *et al.* (1997). As we discussed in Chapters 1 and 8, in $LaMnO_3$ the MnO_6 octahedra are Jahn–Teller (JT) distorted (Figure 1.8). This should be compared to the MnO_6 octahedra in $CaMnO_3$, which does not have JT distortion, since in this compound Mn is tetravalent (4 +) and has no electron in the e_g orbital.

Billinge *et al.* (1996) studied the variation of the pulsed neutron PDF with temperature for $La_{1-x}Ca_xMnO_3$, and noted that the peak height at 2.75 Å changes anomalously with temperature as shown in Figure 1.10. Below T_C the height of this peak rises much more quickly with decreasing temperature for the samples with $x = 0.21$ and 0.25, than expected from the normal thermal effect. This peak in part includes the O–O distances in the MnO_6 octahedra. Without the JT distortion each octahedron has 12 O–O bonds that are 2.75 Å long, while with the JT distortion 8 of them become 3.0 Å long. Consequently the PDF peak height at 2.75 Å is reduced when there are local JT distortions. Thus the results are consistent with having polarons involving JT distortions above T_C that disappear below T_C.

Direct evidence for this picture came from modeling the data. The changes in the local structure as the sample passes through T_C were observed by taking a difference between

the PDFs measured just above and just below the transition. The structural changes are significant compared to the errors on the data as is evident in Figure 6.6. These structural changes were well reproduced by a simple one-parameter model in which one-in-four sites, presumed to be the Mn^{4+} polaron sites, were distorted by an isotropic 'breathing mode' collapse of 0.12 Å compared to the undistorted structure evident in the metallic phase. Because of the connectivity of the MnO_6 octahedra this distortion also results in a JT distortion appearing on the sites neighboring the 4 + site. This model is shown schematically in Figures 6.6 and 10.5. Thus, in this model the insulating phase is found to be made up of JT distorted Mn^{3+} sites and single-site Mn^{4+} polarons whereas the ferromagnetic metallic phase is undistorted. The modeling was carried out at a doping level of $x = 0.25$ where the sample becomes significantly delocalized at low temperature (Billinge *et al.*, 1996). As we discussed above, at lower dopings the localized polaronic and delocalized metallic domains coexist even at low-T. Nonetheless, the PDF provided direct structural evidence for the lattice-polarons involving JT distortions envisaged by Millis *et al.* (1995). These can be thought of as 'anti-JT' polarons since on the Mn^{4+} site where the doped hole is localized, the local JT distortion is destroyed and the octahedron becomes isotropic. A representation of the polarons residing in the perovskite lattice is shown in Figure 10.5.

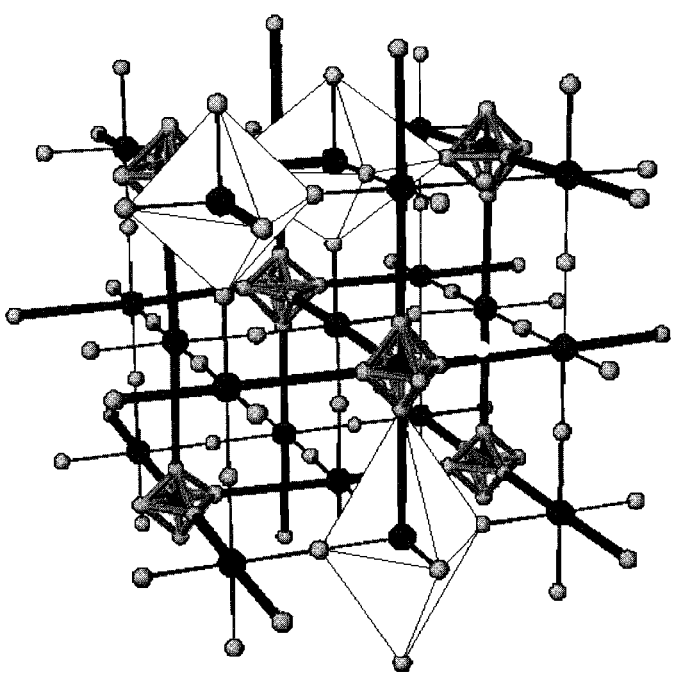

Figure 10.5. Model of locally ordered polarons that polarize the Jahn–Teller distorted orbitals of neighboring octahedra. The size of the distortions is exaggerated for clarity (Billinge *et al.*, 2000).

Louca *et al.* (1997, 1999) focused on the first Mn–O peak of (La,Sr)MnO_3. The first negative peak of the PDF of $LaMnO_3$ (Figure 1.8) is a doublet with a peak at 1.97 Å and at ~2.17 Å, indicating the JT distortion. The average crystallographic JT distortion decreases rapidly with increasing x and disappears at $x > 0.17$. However, the positions of these first two sub-peaks of the PDF are nearly independent of x, as shown in Figure 10.6. Thus *locally* the JT distortion remains unchanged in magnitude, while the *average* JT distortion decreases sharply with composition. In particular the local JT distortions are found to persist even in the metallic rhombohedral phase where all the Mn–O distances are equal in the crystal structure as shown in Figure 6.2 (though with doping, lattice strain quickly causes them to become unresolved). This discrepancy between the local and average structure can be explained only with the non-collinear local JT distortions. If the local JT distortions are randomly oriented in all x, y, and z directions with equal proportions, the local distortions cancel each other and the total JT distortion is absent. This directional randomization happens quickly with doping because of the isotropic orbital-polarizing effect of the Mn^{4+} polarons themselves. To lower the lattice strain of forming a small polaron the orbitals on neighboring Mn^{3+} sites tend to orient themselves such that the long-bonds point towards the small Mn^{4+} octahedron (Billinge *et al.*, 1996, 2000). In this way, the decreasing JT distortion in the average structure can be explained by the gradual loss of JT orbital order with whole concentration.

While hole doping does not change the Mn–O peak positions, doping modifies the peak intensity. The JT distorted MnO_6 octahedron of Mn^{3+} has four short (~1.97 Å) and two

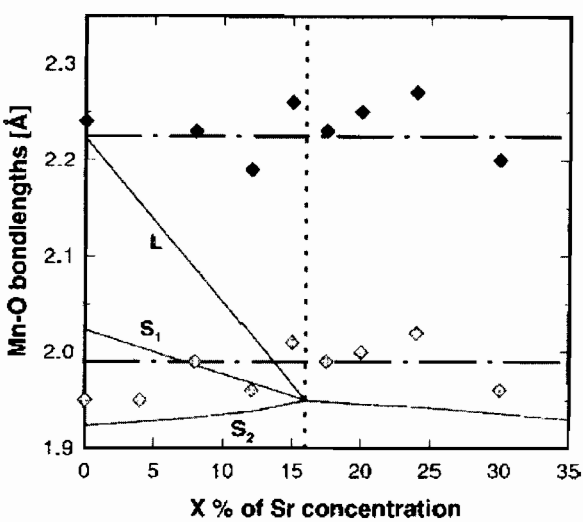

Figure 10.6. The positions of the first two sub-peaks of the PDF for $La_{1-x}Sr_xMnO_3$ as a function of x at $T = 10$ K, compared to the Mn–O bond lengths determined from the crystal structure (Louca *et al.*, 1997).

long (~2.2 Å) Mn–O bonds, while that of Mn^{4+} without the JT distortion has 6 short Mn–O bonds. Thus by counting the number of short bonds per Mn ion the number of Mn sites with JT distortion can be determined. This can be done by integrating the first sub-peak of the PDF (Section 6.2.2.2) to obtain the number of close O neighbors of Mn, N_{Mn-O}. The second sub-peak may partially overlap with the La–O peak at 2.56 Å, and its area cannot be reliably assessed. $N_{Mn-O} = 4$ corresponds to fully JT distorted state as in $LaMnO_3$, and 6 to completely undistorted state as in $SrMnO_3$. It is useful to express N_{Mn-O} in terms of the fraction of the Mn sites without local JT distortion, $\eta = (N_{Mn-O} - 4)/2$. Since the Mn^{4+} ion without local JT distortion is likely to be metallic, η can be considered to represent the metallic volume fraction. The value of η increases from 0 for $x = 0$, but the rate of decrease is temperature dependent. As shown in Figure 6.2 at room temperature the data lie near the straight line connecting $\eta = 0$ for $x = 0$ and 1 for $x = 1$ (small polaron line), representing the mixture of Mn^{3+} and Mn^{4+}. In other words above T_C the charge is localized on one Mn site, forming a small single-site polaron representing Mn^{4+}.

At $T = 10$ K, however, the data of η are well above the small polaron line. It extrapolates to 1 at $x \sim 0.32$, with the slope about three times of the small polaron line. This result can be interpreted such that, at low temperature, each hole kills the JT distortion at three Mn sites; a polaron is extended over about three sites. This could be a consequence of antiferromagnetic spin correlation. If three spins are antiferromagnetically coupled ($\uparrow \downarrow \uparrow$) by flipping the central spin they will become ferromagnetically aligned ($\uparrow \uparrow \uparrow$), allowing a hole to move easily through the three sites. Thus a polaron would become extended over three sites.

Another interpretation is that the sample is phase separating on the nanometer length-scale into coexisting undistorted metallic and JT distorted insulating phases (which, interestingly, may have the same concentration of doped charges) with the metallic component growing on increasing doping. The MnO_6 octahedra in the ferromagnetic metallic phase have six shorter bonds that would account for the fact that η is increasing faster than the small-polaron line (Billinge *et al.*, 2000). This behavior is illustrated in Figure 10.7 that shows the phase diagram of $La_{1-x}Ca_xMnO_3$ with X-ray PDFs of the Mn–O near-neighbor peaks superposed. In the polaronic insulating regions at low doping, and at high-temperature in the higher doped region, short and long bonds are clearly apparent (the peak is a doublet). However, even in the metallic region (low-T high doping region) the peak also has a doublet structure except at the lowest temperatures and highest dopings.

As the temperature is increased η decreases continuously as shown in Figure 10.8. This implies that the total volume over which the local JT distortion is suppressed becomes reduced, as polarons become more localized or as the metallic component is destroyed. The PDF peak height at 2.75 Å follows this closely, since it also quantifies the same thing (Figures 1.10 and 10.8).

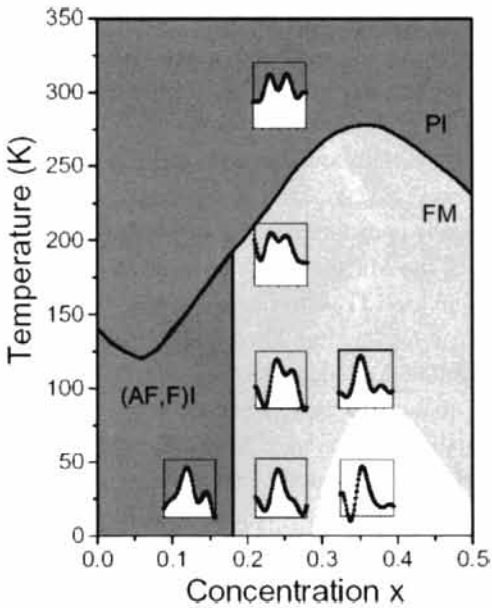

Figure 10.7. Schematic phase diagram for $La_{1-x}Ca_xMnO_3$. 'I' and 'M' refer to insulating and metallic, respectively, and 'P', 'F' and 'AF' to paramagnetic, ferromagnetic and antiferromagnetic. Superimposed on the figure are the low-r X-ray PDF peaks showing the nearest neighbor Mn–O bonds. In the insulating phases the JT long-bond is clearly apparent. There is no JT-long bond deep in the FM phase that is not JT distorted. However, the long-bond gradually appears as the MI boundary is approached. The fully localized polaronic phases have dark shading. The light shading indicates the region where localized and delocalized phases coexist and the white region indicates homogeneous FM phase. The boundaries between the shaded regions are diffuse and continuous and are meant to be suggestive only (Billinge *et al.*, 2000).

10.2.3 Layered manganite, $(La_{1-x}Sr_xMnO_3)_n(SrO)$

Among the perovskite related layered manganites, $(La/A)_{n+1}Mn_nO_{3n+1}$, known as the Ruddlesden–Popper phases (Ruddlesden and Popper, 1958), the $n = 2$ and $n = \infty$ (perovskite) compounds show the CMR phenomenon, while the $n = 1$ compound is insulating (Moritomo *et al.*, 1995; Mitchell *et al.*, 1997). The two-layered ($n = 2$) manganite, $La_{2-2x}Sr_{1+2x}Mn_2O_7$, or $(La_{1-x}Sr_xMnO_3)_2SrO$, is made of two layers of perovskite structure and a single layer of SrO fluorite structure. The perovskite layer has an almost cubic structure, and shows a very small average JT distortion that changes with temperature and composition (Mitchell *et al.*, 1997). This appears to suggest that the JT distortion is not important for the CMR behavior, and a very different mechanism is at work. However, the pulsed neutron PDF determined by Louca *et al.* (1998) shows that locally the MnO_6 octahedra are JT distorted, in a way very similar to the perovskite manganites. Figure 10.9 compares the PDF of the two-layered compound with that of a perovskite, $LaMnO_3$. The shape of the Mn–O peak is very similar between the two.

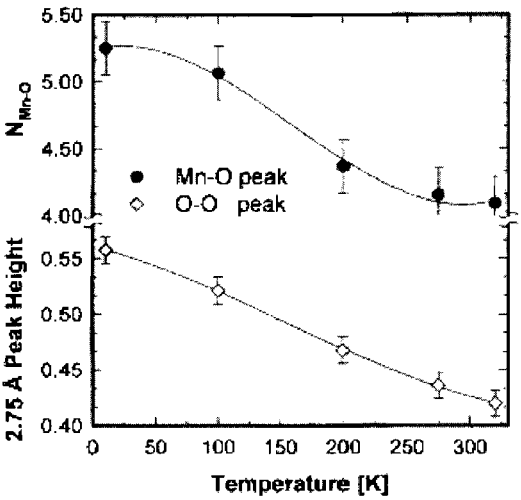

Figure 10.8. Temperature dependence of the number of short Mn–O bonds per Mn site (above) and the PDF peak height at 2.75 Å (below) for $La_{0.825}Sr_{0.175}MnO_3$ (Louca and Egami, 1999).

In particular the presence of local long Mn–O bonds is evident even for the layered compound. Thus it is presumed that the nature of the polarons in the layered compounds is the same as that in perovskites, and polarons are the anti-JT polarons.

The temperature dependence of N_{Mn-O} determined in the same way as in the perovskite is shown in Figure 10.10. Unlike perovskites, however, it changes completely smoothly through T_C (= 117 K), and instead shows anomalous changes around

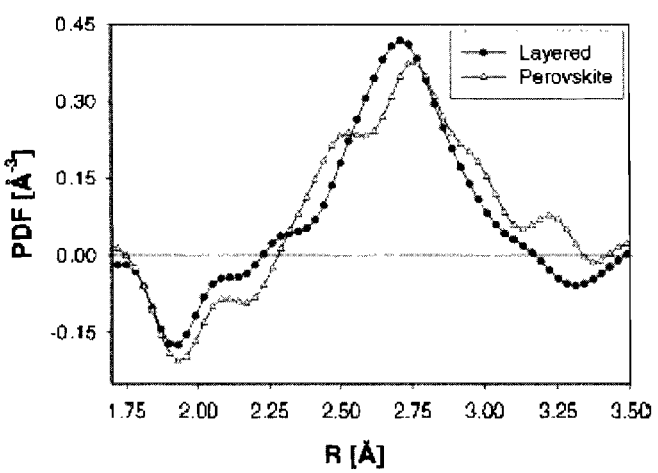

Figure 10.9. The PDF of $La_{1.6}Sr_{1.4}Mn_2O_7$ compared to the PDF of $LaMnO_3$. In order to compare the intensity of the Mn–O peak correctly the PDFs are multiplied through $\langle b^2 \rangle$ (Louca *et al.*, 1998).

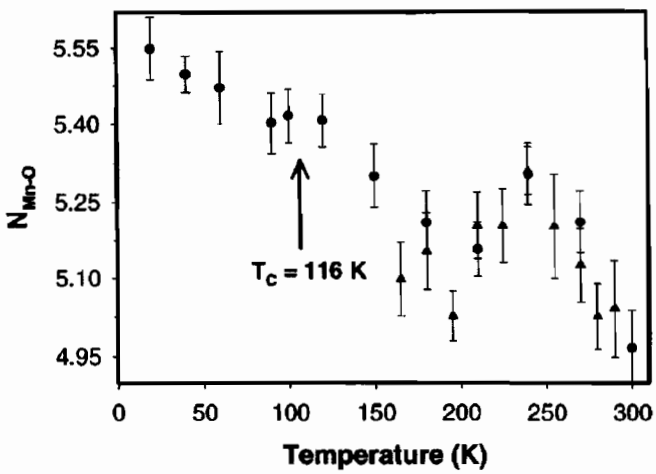

Figure 10.10. Temperature dependence of the number of short Mn–O bonds in $La_{1.6}Sr_{1.4}Mn_2O_7$ (Louca *et al.*, 1998). Note that the data are continuous through T_C (= 117 K).

250 K. The measurement of spin excitation indicates that the magnitude of the exchange constant within the perovskite layer is similar to that in the three-dimensional perovskite. This suggests that strong two-dimensional ferromagnetic correlation develops well above T_C. It is thus possible that the conduction paths made of Mn sites without the local JT distortion are already formed above T_C but shows no overall metallic conduction because of the poor c-axis conduction. The temperature of 250 K, which is similar to the T_C of the three-dimensional perovskite, may signal the onset of such two-dimensional ferromagnetic correlations.

The local structure of CMR manganites determined by the PDF method as discussed here is very different from the one suggested by the crystal structure. At the atomic scale, the real structure in many cases is very heterogeneous, with one local structure being different from another, in the same solid. The subject, however, is much deeper and very rich. In particular, charge distribution is suspected to be inhomogeneous at the atomic scale even in nominally metallic phases. It is most likely that charge inhomogeneity is an integral part of the complex phenomena caused by competing interactions.

10.3. SUPERCONDUCTING CUPRATES

10.3.1 Introduction

Many similarities exist between the manganites and the high-temperature superconducting cuprates. The interesting properties of the manganites arise from competing electronic,

magnetic and lattice interactions. It now appears clear that a similar balance exists in the cuprates, though the role of the lattice has taken much longer to be recognized since the structural effects are much smaller and more subtle in these systems. In many respects, the lessons learned from the manganites have made the interpretation of data in the cuprates, especially from relatively new techniques like PDF analysis, clearer. Many of the ideas that have been described above relating to the structural and electronic effects of heavily doped perovskite transition metal oxides carry over to the cuprates; phase transitions due to structural misfit, disorder due to chemical doping, a structural response to charge doping and mixed valency, and so on. The PDF technique has had a role to play in studying the role of these effects on the properties, though because of the smaller structural responses, the picture is still less clear and work is ongoing. There is an enormous body of work amounting to many tens of thousands of papers on high T_C cuprates. Here we simply summarize some of the contributions that the PDF has made in this area.

10.3.2 Structural transitions in $La_{2-x}(Sr,Ba)_xCuO_4$

Like the perovskite manganites, the CuO_6 octahedra forming the CuO_2 planes in this system become buckled due a mismatch between the rocksalt LaO_2 layer and the copper–oxygen planes. The symmetry of this buckling in undoped La_2CuO_4 is orthorhombic (*Bmab*) up to $T_O \sim 500$ K, and above this temperature the symmetry is tetragonal (*I4/mmm*) (Jorgensen *et al.*, 1988). The value of T_O depends on oxygen stoichiometry (Johnston *et al.*, 1987). In the orthorhombic phase the local CuO_6 octahedra are tilted around the [110] axis. This is a typical case of the effect of tolerance factor discussed above. The tolerance factor in this compound is 0.979, resulting in a compressive stress in the CuO_2 plane and an expansion in the LaO layer. To relieve these stresses the CuO_6 octahedra are tilted, resulting in the orthorhombic structure.

Replacing some of the La with larger Sr ions eases the stresses, and T_O decreases with increasing Sr content (Fleming *et al.*, 1987). At 21% of Sr the orthorhombic distortion in the crystal structure disappears. The tilts disappear due to a relaxation of the mismatch since both the LaO_2 layer expands due to the incorporation of larger Sr or Ba ions and the CuO_2 planes contract because doped copper (nominally Cu^{3+}) makes shorter bonds with oxygen. At low temperature in the Sr doped system the local tilts, measured using the PDF, also decrease their amplitude with doping following the average structure supporting this general picture (Bozin *et al.*, 1999) as shown in Figure 10.11. Above 20% doping small residual tilts of $\sim 2°$ remain in the local structure, probably due to the disordering effect of the Sr dopants. This is also supported by the fact that the residual tilt amplitudes in the Ba doped system are larger which is expected since Ba is a much larger ion than Sr.

The average octahedral tilts also decrease with increasing temperature and this was interpreted in the same terms. In this case the argument is that the thermal expansivity of the LaO_2 layer is greater than that of the CuO_2 planes and at some temperature the misfit

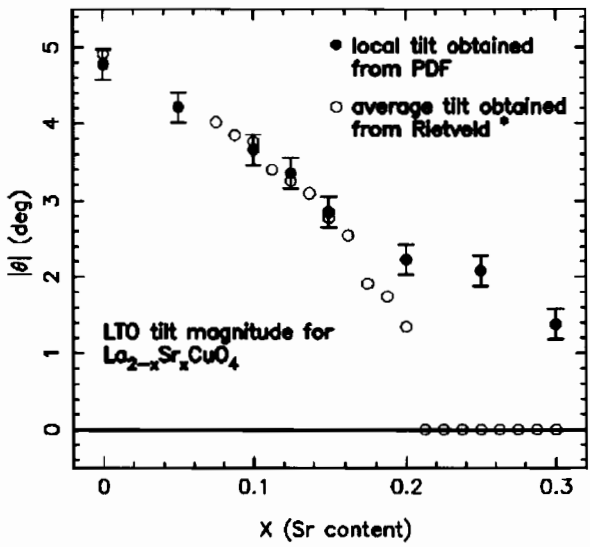

Figure 10.11. Comparison of local octahedral tilt angle measured from the PDF at 10 K (filled circles) with average tilt angle determined using Rietveld (open circles). The local and average tilts agree excellently except in the high doping region where significant local tilts persist despite the disappearance of the average tilts. Residual tilts are presumably due to dopant ion disorder (Bozin *et al.*, 1999).

disappears. Whilst this may be partially true, the PDF technique indicates that significant local tilt amplitude survives at high-temperature in the tetragonal phase where the average tilts are zero. The tilts are thus becoming dynamic above the transition temperature with the octahedra precessing around the average *c*-axis in analogy with the crystalline silica described in Section 9.3.3 (Egami *et al.*, 1988; Sendyka *et al.*, 1992; Bozin *et al.*, 1999).

10.3.3 Octahedral tilts are coupled to doped charges

Through the pioneering observation of charge stripes by Tranquada *et al.* (1995) in $La_{2-x-y}Nd_ySr_xCuO_4$ we now know that doped charges are strongly coupled to the octahedral tilts. In this system, and in related $La_{2-x}Ba_xCuO_4$, doped holes form into long-range ordered stripes separating undoped regions of antiferromagnetic spin order. This effect is only seen when the octahedral tilts have ⟨100⟩ symmetry, i.e. the tilt axis lies along the copper–oxygen bond. This is different from the ⟨110⟩ tilts in the undoped end member. There are a number of possible reasons for this, but before exploring them it is worth emphasizing the main point that *doped holes are coupled to the lattice* otherwise they would not express a preference for the octahedral tilt direction! One reason for the preference for ⟨100⟩ tilts is simply that these tilts have the same symmetry as the stripes and the formation of the stripes drives the structure into this symmetry. A topological analysis has been carried out by Bozin *et al.* (unpublished) based on the well-established

assumption that doping holes into the CuO_2 plane shortens the Cu–O bond. In this case a localized doped hole will locally destroy a tilt. This introduces a defect into the overall tilt structure. It can be shown by topological considerations that in a background of ⟨110⟩ symmetry tilts this defect causes the plane to break up into domains of ⟨110⟩ order with different orientations of the ordering vector (Figure 10.12(a)). Introducing a second such defect is equally costly. In the case of ⟨100⟩ tilts the doped hole defect generates a line defect in the tilt background, which can accommodate further doped holes at no additional cost. Thus, there appears to be a natural tendency for doped holes to create locally ⟨100⟩ tilt structures. These only order over long-range and become observable if the charges freeze into a static, long-range ordered stripe phase, e.g. in $La_{2-x}Ba_xCuO_4$ and $La_{2-x-y}Nd_ySr_xCuO_4$ at 1/8 doping. PDF data show that the local

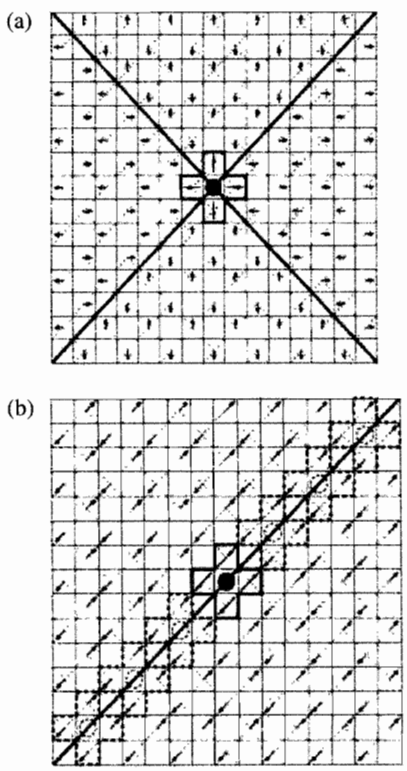

Figure 10.12. Topological models of the tilt disorder when an untilted defect (due to a doped hole, indicated by a filled circle) is placed into a background of (a) ⟨110⟩ 'LTO' tilts and (b) ⟨100⟩ 'LTT' tilts. Note that in the LTT case, the untilted octahedron results in a line-defect whereas in the LTO case the plane breaks up into rotated domains of LTO order. Only in the LTT case untilted octahedra can further be accommodated without energy cost (indicated by dashed lines). There is thus a natural stripe formation tendency for doped holes in the ⟨100⟩ 'LTT' tilted phase (Bozin and Billinge, unpublished).

structure in the doped lanthanum cuprates (though not the undoped end member, Bozin *et al.*, 1999) is consistent with the presence of local tilt amplitude and directional disorder as expected from this picture (Figure 1.7) (Billinge *et al.*, 1994; Bozin *et al.*, 1999).

Similar doped-hole induced changes to the local structure may also hold the key to a long-standing controversy about possible disorder of apical oxygen atoms in $YBa_2Cu_3O_{6+\delta}$ (Gutmann *et al.*, 2000). Again the doped holes shorten the Cu–O bond, but in this case the copper is not sitting on a center of symmetry and the structure responds by shifting the Copper towards its apical oxygen neighbor. Inhomogeneous doping will thus lead to a distribution of copper positions, consistent with modeling of PDF data (Gutmann *et al.*, 2000), and possibly explaining the observation of two Cu-apical oxygen bond distance in XAFS data (Conradson *et al.*, 1990).

10.3.4 Dynamic charge stripes and inhomogeneous doping

The role of charge stripes to the superconducting phenomenon is tantalizing but controversial. This is discussed in greater detail in Section 11.6. One of the outstanding questions is whether charge stripes exist in superconducting samples (and indeed in the superconducting state). There is at least circumstantial evidence for this from the observation of incommensurate spin fluctuation peaks as well as from a number of different spectroscopic measurements. What is lacking is direct structural evidence. Because the stripes are fluctuating they are not visible in the average structure, though their signature should be present in the local structure. Evidence for them has been found using the arguments that we made above. Doping shortens the Cu–O bond. A charge stripe is a highly doped region separating an undoped region. In the presence of charge stripes therefore there should coexist locally short and long Cu–O bonds, similar to what was observed in the manganites. The difficulty is that, the difference between the short and long bonds in the manganites was 0.2 Å, whereas in the cuprates it is closer to 0.02 Å, 10 × smaller. This is certainly beyond the resolution of an XAFS or PDF measurement whose resolutions are limited, in the best possible circumstances, by thermal and zero-point motion to around 0.1 Å. Nonetheless, a search was made in a series of $La_{2-x}Sr_xCuO_4$ samples and a peak broadening of the nearest neighbor Cu–O peak was observed that increased with doping. In fact, the peak width in the PDF of $La_{2-x}Sr_xCuO_4$ increases with x initially, and then decreases beyond $x = 0.15$, mimicking T_C itself, as shown in Figure 1.6. Both the peak broadening and the intermediate range structure could be described well in terms of mixing two phases, one for $x = 0$ and the other for $x = 0.25$. Since the $x = 0$ phase must be insulating and the $x = 0.25$ phase must be metallic, this result indicates that the charge distribution in cuprates is not homogeneous. This conclusion is consistent with recent phonon measurements that also suggest that the charge state in cuprates is inhomogeneous (McQueeney *et al.*, 1999; Petrov *et al.*, 2000). The misfit strain that builds up due to the short bonds in the charge stripe and the long bonds in the intervening region

also provides an elastic mechanism for breaking up the stripes and preventing them from becoming static and long-range ordered, except in special cases such as $La_{2-x-y}Nd_ySr_xCuO_4$ and $La_{2-x}Ba_xCuO_4$, where significant structural compliance exists in the form of large amplitude tilts coming from the misfitting dopant ions (Billinge and Duxbury, 2001, 2002). This is discussed in greater detail in the next chapter.

These results are remarkable in that they suggest that the local structure of cuprates is *inhomogeneous in the superconducting state*. For a long time disorder has been considered to be detrimental to superconductivity. In cuprates, however, local disorder appears not only to be compatible with superconductivity but even to enhance it (Egami and Billinge, 1996). At this moment theoretical developments are not sufficient to allow satisfactory interpretation of these observations, even though many models have been proposed. What is clear is that the high-temperature superconductivity is an unusual phenomenon, very different from the BCS superconductivity which is well understood, and the knowledge of the local structure might facilitate its understanding.

REFERENCES

Akbas, M. & Davies, P.K. (1997) *Commun. Amer. Ceram. Soc.*, **80**, 2933.

Billinge, S.J.L., Kwei, G.H. & Takagi, H. (1994) *Phys. Rev. Lett.*, **72**, 2282.

Billinge, S.J.L., DiFrancesco, R.G., Kwei, G.H., Neumeier, J.J. & Thompson, J.D. (1996) *Phys. Rev. Lett.*, **77**, 715.

Billinge, S.J.L., Proffen, Th., Petkov, V., Sarrao, J.L. & Kycia, S. (2000) *Phys. Rev. B*, **62**, 1203.

Billinge, S.J.L. & Duxbury, P.M (2001) cond-mat/0108338.

Billinge, S.J.L. & Duxbury, P.M. (2002) *Int. J. Mod. Phys.*, to be published.

Booth, C.H., Bridges, F., Snyder, G.J. & Geballe, T.H. (1996) *Phys. Rev. B*, **54**, R15606.

Bozin, E.S., Billinge, S.J.L., Kwei, G.H. & Takagi, H. (1999) *Phys. Rev. B*, **59**, 4445.

Conradson, S.D., Raistrick, I.D. & Bishop, A.R. (1990) *Science*, **248**, 1394.

DeGennes, P.G. (1960) *Phys. Rev.*, **118**, 141.

Dmowski, W., Akbas, M.K., Davies, P.K. & Egami, T. (2000) *J. Phys. Chem. Solids*, **61**, 229.

Egami, T. & Billinge, S.J.L. (1996) in *Physical Properties of High Temperature Superconductors V*, Ed. Ginsberg, D.M., World Scientific, Singapore, p. 265.

Egami, T., Dmowski, W., Jorgensen, J.D., Hinks, D.G., Capone, D.W., II, Segre, C.U., Zhang, K., Bose, S.M. & Tyagi, S.D. (1988) *Rev. Solid State Sci.*, **1**, 247; also in *High T_c Superconductors III*, eds. Bose, S.M. & Tyagi, S.D., World Scientific, Singapore, p. 101.

Egami, T., Rosenfeld, H.D., Toby, B.H. & Bhalla, A. (1991) *Ferroelectrics*, **120**, 11.

Egami, T., Teslic, S., Dmowski, W., Viehland, D. & Vakhrushev, S. (1997) *Ferroelectrics*, **199**, 103.

Egami, T., Dmowski, W., Akbas, M. & Davies, P.K. (1998) *AIP Conf. Proc.*, **436**, 1.

Egami, T. & Louca, D. (2000) *J. Superconductivity: Inc. Novel Magnetism*, **13**, 247.

Fleming, R.M., Batlogg, B., Cava, R.J. & Rietman, E.A. (1987) *Phys. Rev. B*, **35**, 7191.

Goodenough, J.B. (1955) *Phys. Rev.*, **100**, 564.

Gutmann, M., Billinge, S.J.L., Brosha, E.L. & Kwei, G.H. (2000) *Phys. Rev. B*, **61**, 11762.

Hasegawa, T. & Anderson, P.W. (1955) *Phys. Rev.*, **100**, 675.

Husson, E., Chubb, M. & Morell, A. (1988) *Mater. Res. Bull.*, **23**, 357.

Itoh, K.M., Haller, E.E., Beeman, J.W., Hansen, W.L., Emes, J., Reichertz, L.A., Kreysa, E., Shutt, T., Cummings, A., Stockwell, W., Sadoulet, B., Muto, J., Farmer, J.W. & Ozhogin, V.I. (1996) *Phys. Rev. Lett.*, **77**, 4058.

Jaffe, B., Cook, W.R. & Jaffe, H. (1971) in *Piezoelectric Ceramics*, Academic Press, London.

Jin, T., Tiefel, H., McCormack, M., Fastnacht, R.A., Ramesh, R. & Chen, L.H. (1994) *Science*, **264**, 413.

Johnston, D.C., Stokes, J.P., Goshorn, D.P. & Lewandowski, J.T. (1987) *Phys. Rev. B*, **36**, 4007.

Jonker, G.H. & Van Santen, J.H. (1950) *Physica*, **16**, 337.

Jorgensen, J.D., Dabrowski, B., Pei, S., Hinks, D.G., Soderholm, L., Morosin, B., Schirber, J.E., Venturini, E.L. & Ginley, D.S. (1988) *Phys. Rev. B*, **38**, 11337.

Lanzara, A., Saini, N.L., Brunelli, M., Natali, F., Bianconi, A., Radaelli, P.G. & Cheong, S.-W. (1998) *Phys. Rev. Lett.*, **81**, 878.

Louca, D., Egami, T., Brosha, E.L., Röder, H. & Bishop, A.R. (1997) *Phys. Rev. B*, **56**, R8475.

Louca, D., Kwei, G.H. & Mitchell, J.F. (1998) *Phys. Rev. Lett.*, **80**, 3811.

Louca, D. & Egami, T. (1999) *Phys. Rev. B*, **59**, 6193.

McQueeney, R.J., Petrov, Y., Egami, T., Yethiraj, M., Shirane, G. & Endoh, Y. (1999) *Phys. Rev. Lett.*, **82**, 628.

Millis, A.J., Littlewood, P.B. & Shairman, B.I. (1995) *Phys. Rev. Lett.*, **74**, 5144.

Mitchell, J.F., Argyriou, D.N., Jorgensen, J.D., Hinks, D.G., Potter, C.D. & Bader, S.D. (1997) *Phys. Rev. B*, **55**, 63.

Mitsui, T. & Westphal, W.B. (1961) *Phys. Rev.*, **124**, 1354.

Moritomo, Y., Tomioka, Y., Asamitsu, A., Tokura, Y. & Matsui, Y. (1995) *Phys. Rev. B*, **51**, 3297.

Parkin, S.P.P. (1995) *Annual Rev. Mater. Sci.*, **25**, 357.

Petrov, Y., Egami, T., McQueeney, R.J., Yethiraj, M., Mook, H.A. & Dogan, F (2000) cond-mat/0003414.

Ramirez, A.P. (1997) *J. Phys: Cond. Matter*, **9**, 8171.

Ruddlesden, S.N. & Popper, P. (1958) *Acta Cryst.*, **11**, 54.

Samara, G.A. (1971) *Phys. Rev. Lett.*, **27**, 103.

Sendyka, T.R., Egami, T., Hunter, B.A., Jorgensen, J.D., Hinks, D.G. & Mitchell, A.W. (1992) in *Lattice Effects in High T_c Superconductors*, Eds. Bar-Yam, Y., Egami, T., Mustre-de Leon, J. & Bishop, A.R., World Scientific, Singapore, p. 111.

Shannon, R.D. (1976) *Acta Crystalogr. A*, **32**, 751.

Teslic, S. & Egami, T. (1998) *Acta Crystalogr. B*, **54**, 750.

Teslic, S., Egami, T. & Viehland, D. (1997) *Ferroelectrics*, **194**, 271.

Tranquada, J.M., Sternlieb, B.J., Axe, J.D., Nakamura, Y. & Uchida, S. (1995) *Nature*, **375**, 561.

Tyson, T.A., Mustre de Leon, J., Conradson, S.D., Bishop, A.R., Neumeier, J.J. & Zang, J. (1996) *Phys. Rev. B*, **53**, 13985.

Urushibara, A., Moritomo, Y., Arima, T., Asamitsu, A., Kido, G. & Tokura, Y. (1995) *Phys. Rev. B*, **51**, 14103.

Van Santen, J.H. & Jonker, G.H. (1950) *Physica*, **16**, 599.

Zener, C. (1951) *Phys. Rev.* 81, 440.

Chapter 11

Phase Transitions

This Page Intentionally Left Blank

Chapter 11
Phase Transitions

11.1. LOCAL CORRELATIONS AND PHASE TRANSITIONS

The subject of phase transitions is central to materials science and condensed-matter physics. This is partly because phase transitions bring about changes in properties that are often drastic and sometimes useful, but also because the phenomenon itself is singular and fascinating. A good example is the ferroelectric phase transition. As has been discussed for PT in Section 8.1.3, below the ferroelectric Curie temperature, T_C, a ferroelectric crystal has an electric dipole moment and none above. Actually, even below T_C a large crystal has no macroscopic polarization until an electric field is applied, since it has many ferroelectric domains with antiparallel polarizations. But within the domain the solid is uniformly polarized. In terms of crystallography a crystal is centrosymmetric above T_C, but loses centrosymmetry below. This transition represents a major qualitative change of the nature of the crystal.

Since phase transitions produce a change in the long-range order and macroscopic properties, they are usually studied from the global, long-range, point of view. For instance, the second-order phase transition is characterized by the correlation length diverging at the transition. The success of the renormalization group theory (Wilson, 1975) comes from making exact connections between the local interactions and the large length-scale fluctuations. Thus it may appear that the PDF method that describes only the local correlations is not the right tool to study this phenomenon at all. However, as we will see below PDF studies provide knowledge of important microscopic interactions that the measurement of the long-range order parameters cannot reveal. At the same time we have to caution that it can cause unwanted confusion unless the results are interpreted correctly.

For instance, the PDF method is an excellent technique to study ferroelectricity since a local polarization produces different cation–anion bond distances. This can be seen as splitting of the metal–oxygen PDF peak in ferroelectric metal oxides. As an example, the PDFs of ferroelectric $BaTiO_3$ and $PbTiO_3$ (PT) were shown in Figures 8.5 and 8.6. The splitting of the Ti–O distance in Figure 8.6 indicates a strong ferroelectric polarization of Ti within the TiO_6 octahedron. However, if one measures the PDF of such a material through the ferroelectric phase transition, the PDF often appears almost unchanged as shown in Figure 11.1 (we saw this too in $BaTiO_3$, Figure 8.5, and silica at the α–β phase transition, Section 9.3.3 and Figure 9.19). What is going on? One interpretation, which is quite often made, is that the crystal retains the local atomic scale polarization even above T_C, and the phase transition is of the order–disorder type, as was discussed in connection with $BaTiO_3$ (Section 8.1.2). This conclusion appears to be in conflict with the popular

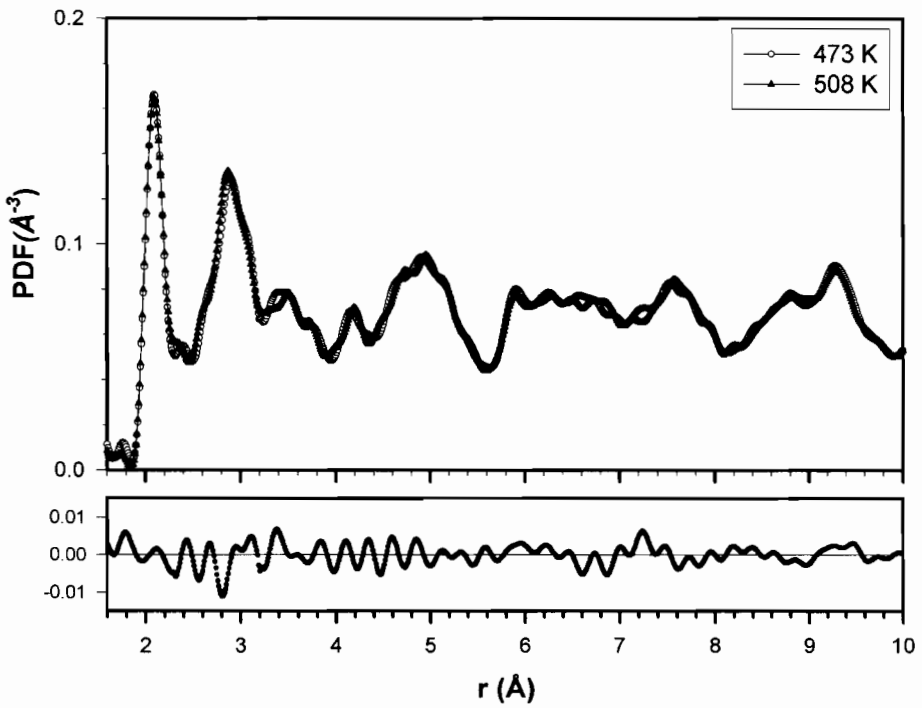

Figure 11.1. Pulsed neutron PDF of PT at $T = 508$ and 473 K, above and below the ferroelectric phase transition temperature (above), and difference (below) (Teslic and Egami, 1998).

view that the ferroelectric phase transition occurs because of soft-phonons, as explained below. How can we reconcile these two apparently opposing views? In order to resolve this conflict we have to understand the dynamics and spatial correlation associated with the ferroelectric phase transition.

The first point to be considered is the dynamics of the phase transition and the phonon soft-mode. The ferroelectric soft-mode is the transverse optical (TO) mode in which cations are out of phase with anions. When the mode with $q = 0$ (infinite wavelength) becomes static, cations will be displaced in one direction while anions are displaced in the other resulting in long-range ferroelectricity. The mode becomes static when its frequency becomes zero and this is the origin of the name 'soft-mode'. As the temperature is lowered towards the phase transition, the frequency of this particular $q = 0$ phonon mode gradually decreases (the 'spring' soften) until it reaches zero at the phase transition. The soft-mode theory provides a very natural description of the ferroelectric transition.

A more general description of second-order phase transitions is given by the Landau–Devonshire theory (Landau and Lifshitz, 1958; Salje, 1990; Gonzalo, 1991). In terms of the ferroelectric order parameter, ϕ, the free energy near the phase transition can be

expressed up to the fourth order in ϕ as

$$G = G_0 + A\phi^2 + B\phi^4 + \cdots \tag{11.1}$$

The free energy is minimized when $\partial G/\partial \phi = 0$, i.e.

$$2A\phi + 4B\phi^3 = 0 \tag{11.2}$$

Thus,

$$\phi = \sqrt{\frac{-A}{2B}} \tag{11.3}$$

The order parameter, ϕ, is zero above the transition and finite below it, going continuously to zero at the transition. Thus, at T_C, $A = 0$ and below T_C, $A < 0$. In the mean-field approximation, A is linear with T:

$$A = A_0(T - T_C) \tag{11.4}$$

Ferroelectric materials are piezoelectric so that the ferroelectric polarization is coupled to the elastic strain. The coupled system can then be described by

$$G = G_0 + A\phi^2 + B\phi^4 - \Gamma\phi\varepsilon + \frac{D}{2}\varepsilon^2 \tag{11.5}$$

where ε is the strain, Γ is the coupling constant, and D is the elastic constant. Elastic strain is a tensorial property, but for simplicity it is presented as a scalar here. By minimizing G with respect to ε, we obtain

$$\phi = \frac{D}{\Gamma}\varepsilon \tag{11.6}$$

Thus Eq. 11.5 becomes

$$G = G_0 + D\left[\frac{AD}{\Gamma^2} - \frac{1}{2}\right]\varepsilon^2 + \frac{BD^4}{\Gamma^4}\varepsilon^4 \tag{11.7}$$

which is minimum at

$$\varepsilon_0 = \frac{D}{\Gamma}\sqrt{\frac{A_0(T - T_C^*)}{2B}}, \qquad T_C^* = T_C + \frac{\Gamma^2}{2A_0D} \tag{11.8}$$

indicating that the critical temperature is shifted from T_C to T_C^* due to the piezoelectric coupling. Expanding G around the minimum, we obtain

$$G = G_M + \frac{D^*}{2}\mathrm{d}\varepsilon^2 + \cdots, \qquad D^* = \frac{2A_0D^2}{\Gamma^2}(T_C^* - T) \tag{11.9}$$

Thus the effective, or renormalized, elastic constant, D^*, vanishes at T_C^*, and the phonon mode associated with polarization, usually the TO mode, becomes zero in energy TO mode.

Now it is important to be reminded that the spallation-neutron PDF method has a natural dynamic window estimated to be 10–20 meV. If the energy of the soft-phonon mode enters this window because of mode softening, the lattice displacements slow down (critical slowing-down), and appear static to neutrons (Figure 11.1). This is why, with the neutron PDF, the atomic polarization appears to persist above T_C. Another point is that the correlation length of the ferroelectric polarization becomes longer as the temperature approaches T_C, so that from the local perspective long-range order appears to exist even when it is not static and infinite in range. For these reasons, from the viewpoint of the PDF, atomic polarizations appear to exist well above T_C. However, this is not inconsistent with the soft-mode theory. From the point of view of the critical phenomena, the dynamics of the PDF measurement is too fast, and the length-scale too small, to capture the critical fluctuations near T_C. As we noted at the onset the PDF method is not the method of choice if one tries to measure the critical fluctuations. On the other hand, the PDF method offers other interesting insights into the phenomenon, as we discuss below.

11.2. PHASE TRANSITIONS IN COMPLEX MATERIALS

11.2.1 Hierarchy of atomic bonds

Since the strength of an atomic bond varies a lot from one species to another, in complex materials involving a large number of atoms the atomic bonds often have a natural hierarchy, and organize themselves into groups of strongly bound atoms. For instance, in oxides the bond between a metal and oxygen (M–O) is a strong covalent bond, while the metal–metal (M–M) interaction is weaker and ionic. The energy scale of the M–O bond is of the order of eV, thus too large to be influenced by thermal energy, except for some cases such as the Jahn–Teller distortion in manganites and cobaltates. Thus the local unit, such as BO_6 in the perovskites, behaves as a molecular unit. This is why the nearest neighbor local structure in solids appears to change so little with temperature, and often even through phase transitions. On the other hand, the energy scale of the interaction between these units is comparable to the thermal energy. What changes with temperature, therefore, is usually the second and third neighbor structure, determined by the interaction among the local units. Consequently, the order in the intermediate distances (3–10 Å) holds the key to understanding the properties. The PDF method has a unique strength in probing such distances, as has been demonstrated for the case of mixed ferroelectric oxides. The XAFS method gives the distance to the nearest neighbor, but information about further neighbors quickly diminishes. Electron microscopy provides some information of the local structure, but only after averaging over the thickness of the sample.

11.2.2 Effect of disorder

In second-order transitions described by Eq. 11.1 the order parameter is spatially homogeneous, and changes continuously as a function of temperature. However, elements of disorder, such as chemical compositional disorder due to alloying, tend to make the transition spatially inhomogeneous and diffuse. This is understandable since disorder produces the 'local transition temperature' to be distributed, although a very small amount of disorder would not make a difference. The question is how much disorder the system can tolerate before the transition becomes diffuse. Depending on the strength and length scale of the disorder, either the critical fluctuations can smear the effect of disorder (weak disorder), or on the other hand the disorder can smear out the transition (strong disorder). The well-known Harris criterion states that the critical exponent of the specific heat is negative in the first case and positive in the second (Harris, 1974).

The PDF provides interesting insight on this problem. An example of the correlation smearing disorder is the case of mixed-cations in ferroelectric systems resulting in the relaxor ferroelectric transition discussed in Chapter 10. For instance, relaxor behavior is observed in PZT when some Pb is replaced with La. As shown in Figure 11.2 the PDF does not show marked changes even when the relaxor behavior sets in and ferroelectricity is destroyed. Replacing Zr with Ti already introduces disorder so that PZT is already strongly disordered. Additional disorder due to La brings about the relaxor behavior, which is why the amount of La necessary to induce the relaxor behavior decreases with the increasing Ti content. The mechanism of relaxor behavior is discussed below.

11.2.3 Non-linearity and first-order transitions

Another factor that can destroy the second-order transition is a strong non-linearity of the interaction. A simple example is the theory of melting by Born (1939). While the applicability of this particular theory to this phenomenon is highly questionable (Tallon, 1984; Egami, 1997), it nicely illustrates the point. Let us consider the Hamiltonian of a harmonic oscillator with a higher order non-linear term,

$$H = \hbar\omega a^{+}a - \lambda a^{+}a^{+}aa \tag{11.10}$$

where a and a^{+} are phonon annihilation and creation operators, and $\lambda > 0$. The equation of motion for this system is

$$[a, H] = \hbar\omega a - 2\lambda a^{+}aa \tag{11.11}$$

which, in the random-phase approximation, becomes

$$[a, H] = \hbar\omega a - 4\lambda\langle a^{+}a\rangle a = \hbar\omega' a \tag{11.12}$$

where ω' is the renormalized frequency. Thus, the phonon softening is proportional to the phonon density. Self-consistency requires

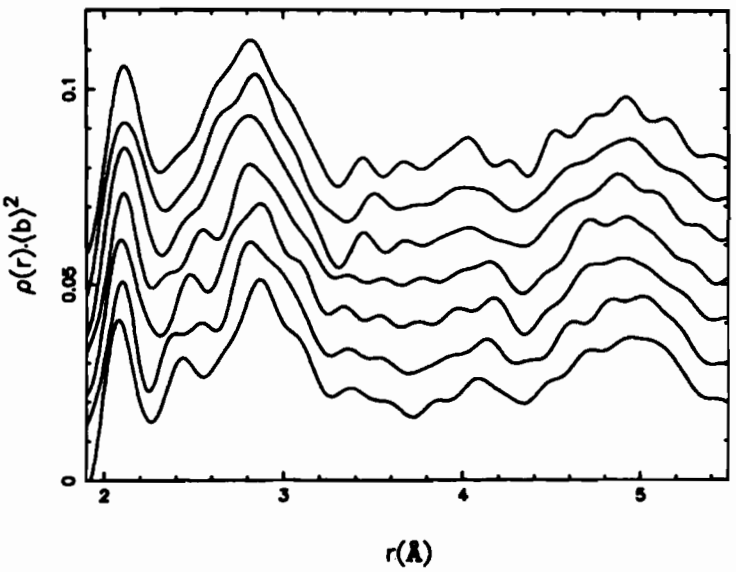

Figure 11.2. PDF of PLZT, $(Pb_{1-3/2x}Lx_x)(Zr_{1-y}Ti_y)O_3$, for various La contents (Teslic *et al.*, 1994). Little change happens in the PDF even though the dielectric behavior changes markedly.

$$\langle a^+ a \rangle = \frac{1}{e^{\hbar\omega'/kT} - 1} \tag{11.13}$$

By solving these equations iteratively the temperature dependence of the phonon frequency can be calculated. At a certain temperature a catastrophic softening takes place resulting in the first-order transition. There is a feedback mechanism in this system: the average phonon occupancy, $\langle a^+ a \rangle$, increases as ω' decreases (Eq. 11.13), but ω' itself decreases with increasing $\langle a^+ a \rangle$ (Eq. 11.12). An easy way to see the catastrophic behavior at a critical value of ω' is to use a high-temperature approximation for Eq. 11.13,

$$\langle a^+ a \rangle \approx \frac{kT}{\hbar\omega'} \tag{11.14}$$

Then from Eq. 11.12,

$$\omega' = \omega - \frac{4\lambda kT}{\hbar^2 \omega'} \tag{11.15}$$

and

$$\omega' = \frac{\omega}{2} \pm \sqrt{\left(\frac{\omega}{2}\right)^2 - \frac{4\lambda kT}{\hbar^2}} \tag{11.16}$$

The critical temperature is given by

$$T_C = \frac{\hbar^2 \omega^2}{16k\lambda} \tag{11.17}$$

where ω' discontinuously jumps from $\omega/2$ to zero.

First-order transitions result in a macroscopic or microscopic phase separation. Global properties such as conductivity are then determined by percolation of the different phases. It is possible to use the PDF analysis in a direct way to determine the state of microsegregation and the nature of the phase transition. For instance, the spatial correlation length of ionic displacements can be determined by modeling the PDF, up to about 30 Å at present, and possibly up to larger distances with greater computing power. In the homogeneous second-order transition the correlation length diverges at the transition, while in disordered systems it remains finite, and the transition occurs through percolation. An example is the metal–insulator transition in CMR oxides discussed below. Both theoretical and experimental evidences are accumulating supporting the idea of phase-separation in certain cases.

11.3. PHASE TRANSITIONS IN SYSTEMS WITH COMPETING INTERACTIONS I: RELAXOR FERROELECTRICITY

11.3.1 Origin of spin-glass behavior

Let us go back to the subject of relaxor ferroelectricity introduced in Chapter 10 and discuss its microscopic mechanism. As we discussed there the origin of the relaxor behavior in the proto-typical relaxor, PMN, was attributed in the beginning to the local ionic ordering with charge imbalance. This idea, however, has been shown to be invalid, and other mechanisms based upon an atomic interaction have been proposed.

The phenomenon of relaxor ferroelectricity has many similarities to disordered magnetic systems; spin glasses in particular (Viehland *et al.*, 1992). Thus, we should first briefly review spin-glass behavior before discussing relaxor ferroelectricity. A spin glass is produced by three mechanisms, namely random exchange, random field and random anisotropy. In all cases the second element with randomness is introduced which is in conflict with uniform ferromagnetism.

11.3.1.1 Random exchange. In a typical, 'Heisenberg', magnetic system, magnet, local spins interact via the Heisenberg exchange interaction

$$H = -\sum_{i,j} J_{ij} \mathbf{S}_i \cdot \mathbf{S}_j \tag{11.18}$$

When J is uniformly positive ferromagnetism results, since parallel spins minimize the energy. But if the exchange interaction turns negative for a particular bond, it will disturb

the local spin configuration. If enough local exchange interactions turn negative, the long-range ferromagnetic order becomes no longer stable, and the system collapses into a spin glass (Sherrington and Kirkpatrick, 1975). A typical phase diagram is shown in Figure 11.3.

11.3.1.2 Random field. If a local field with random direction is applied on each spin, the Hamiltonian becomes

$$H = -\sum_{i,j} J_{ij}\mathbf{S}_i\cdot\mathbf{S}_j - \mu g \sum_i \mathbf{H}_i\cdot\mathbf{S}_i \tag{11.19}$$

Imry and Ma (1975) have shown that for an order parameter with continuous symmetry (such as the Heisenberg magnet) the ordered state is unstable against any random field in dimensions less than four. The question is then how large the correlation is compared to the sample size. If the magnitude of the applied field is comparable to the exchange field the direction of the spins vary strongly from site to site, resulting in the spin-glass state.

11.3.1.3 Random anisotropy. Spins interact with the lattice through the spin–orbit coupling and the crystal-field gradient. The lattice tries to orient the spin in a specific direction. Such a force can be described in terms of the local anisotropy energy,

$$E_a = \sum_i \sum_{\ell,m} B_\ell^m Y_\ell^m(\mathbf{S}_i/S) \tag{11.20}$$

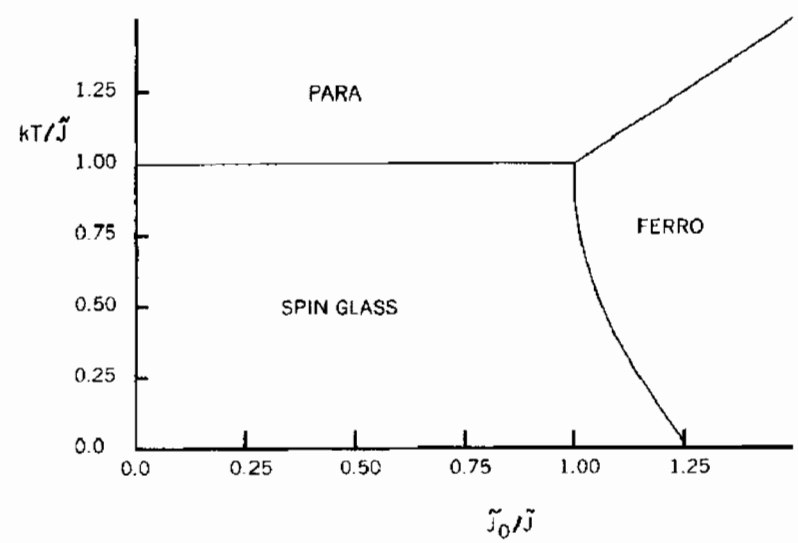

Figure 11.3. The phase diagram of a spin-glass ferromagnet, an analogue for the mixed FE–AFE system (Sherrington and Kirkpatrick, 1975).

where $Y_\ell^m(\mathbf{S}/S)$ are the spherical harmonics. If the local easy axis, along which the anisotropy energy is minimum, is not uniform the collinear spin state is unstable. In this case as well ferromagnetism is unstable no matter how small the anisotropy is (Alben *et al.*, 1978; Pelcovits *et al.*, 1978). However, there is a fairly well-defined threshold below which the behavior is indistinguishable from a ferromagnet.

The total Hamiltonian, i.e. the sum of the exchange Hamiltonian (Eq. 11.18) and the anisotropy energy (Eq. 11.20) may be further simplified by rotating the local axis in the direction of the easy spin polarization, and retaining only the $\ell = 2$, $m = 0$ term. The total Hamiltonian is called the Harris–Plischke–Zuckermann (HPZ) Hamiltonian (Harris *et al.*, 1973). The behavior of the system described by the HPZ Hamiltonian is now well understood. The critical parameter is the ratio between the average values of the Heisenberg exchange constant J_{ij} and the local parameter $B(r_i)$, B/J. Theoretically, the system described by this Hamiltonian is always a spin glass; however, the magnetic correlation length ξ strongly depends upon the B/J ratio (Chi and Egami, 1979). Up to a critical value of B/J ξ is so large that the system behaves like a regular ferromagnet. As the value of B is increased the system crosses over to a non-ergodic spin glass.

11.3.2 Mechanism of Relaxor Ferroelectricity

By analogy to spin glasses ferroelectricity can be destroyed and a spin glass-like relaxor state can prevail if an element, or elements, that compete against ferroelectricity are introduced randomly with sufficient strength. We will first examine the dielectric equivalents of three mechanisms that destroy ferromagnetism.

11.3.2.1 Antiferroelectric interaction. An antiferroelectric (AFE) interaction usually originates from the rotation of the local units, such as BO_6 tetrahedra discussed in Chapters 8 and 10. Because of connectivity through oxygen, the rotation of one BO_6 in one sense induces the rotation of the neighboring BO_6 in the opposite sense. This produces AFE of oxygen displacements, which usually induces an AFE displacement of A cations as well. The rotation of BO_6 octahedra occurs because of the tolerance factor being less than unity. To accommodate small A site ions BO_6 octahedra are rotated to reduce the B–B distance. Thus AFE occurs for large B-site ions such as Zr. The competition between the AFE and FE interactions can bring about the relaxor behavior (Chen *et al.*, 1996).

11.3.2.2 Random field. The local polarization can be tilted away from ferroelectricity by a local electric field. The most natural origin of the local field is the presence of heterogeneous ions, such as Nb^{5+} and Mg^{2+} in PMN. Theories based upon this idea were developed by Klemann and his associates (Westphal *et al.*, 1992). In their theory the local variable is not the atomic-level polarization, but the polarization in the polar nano-domain.

11.3.2.3 Random anisotropy. Random occupation of the B-site by different ions in PMN produces another local force equivalent to the local anisotropy that could produce the relaxor behavior (Egami, 1999). This is particularly applicable to the energetics of the local orientation of the Pb polarization. As shown in Chapter 10 Pb^{2+} ion is always strongly off-centered in the PbO_{12} cluster due to the lone-pair electrons, forming a strong local dipole. These dipoles are not free to rotate, since the off-centering of Pb in the O_{12} cage is produced by the displacement of oxygen ions rather than the displacement of Pb ions, thus the rotation and distortion of the BO_6 octahedra are intimately connected to the Pb polarization. Consequently, the Pb dipoles can interact elastically through these B-site ions. Also the compositional make-up of the B-site around Pb and the configuration of the BO_6 octahedra determine the most likely direction of the Pb polarization. The magnitude of the dipolar moment is estimated to be $p = 1.6 \times 10^{-19}$ C Å, corresponding to a very significant polarization of $P = 0.22$ C/m^2, even assuming a Pb valence of +2. The value of p will be larger if we use the correct Born effective charge.

The local moments, p, interact with each other via various fields. We may describe this system by an effective Hamiltonian,

$$H_c = \sum_{i,j} J(\mathbf{r}_{ij}) \sum_{\ell,m} Q_\ell^m(\mathbf{P}_i) Q_\ell^{-m}(\mathbf{P}_j) \tag{11.21}$$

where $\mathbf{P}_i$ is the local polarization of the ith Pb ion, $Q_\ell^m(\mathbf{P}_i)$ are the spherical harmonic equivalents of $\mathbf{P}_i$, for instance $Q_2^0(P) = 1/2[3P_z^2 - P_2]$, etc. The $\ell = 1$ term describes the pseudo-dipolar interaction due to the electric dipolar fields and hybridization fields through ferroelectrically active B-site elements. The $\ell = 2$ term corresponds to the quadrupolar interaction due to strain fields. The local dipolar moments interact also with the lattice, since the rotation of the local moments requires displacements of oxygen ions that are coupled to the B-site cations. This dipole–lattice interaction may be described by the local anisotropy Hamiltonian,

$$H_a = \sum_i B_\ell^m(\mathbf{r}_{ij}) Q_\ell^m(\mathbf{P}_i) \tag{11.22}$$

The $\ell = 1$ term describes the local electric field, while the $\ell = 2$ term does the steric or elastic field that tends to confine $\mathbf{P}$ along one direction which may be called the easy axis. In PMN, each Pb ion has about 3 Mg^{2+} neighbors and 5 Nb^{5+} neighbors. The electric field due to these heterogeneous charges cannot be expressed by a single electric field such as Eq. 11.19, but requires a tensorial description of Eq. 11.22. The dielectric properties of the interacting Pb dipoles should be described by the total Hamiltonian which is the sum of Eqs. 11.21 and 11.22, which is equivalent to the HPZ Hamiltonian for spin glass discussed above.

11.4. PHASE TRANSITIONS IN SYSTEMS WITH COMPETING INTERACTIONS II: CMR MANGANITES

11.4.1 Charge localization in CMR manganites

As we discussed in Chapter 10, the colossal magnetoresistance (CMR) phenomenon occurs when the applied field delocalizes charge carriers. This is possible when polarons that localize charge carriers are barely stable, and can be destroyed by the applied field. Thus the central question is the stability of the polarons. We will now turn to this question and demonstrate how the knowledge of the local structure helps to elucidate the stability of polarons and the CMR phenomenon. While the CMR phenomenon in manganites is complex, involving magnetism and orbital ordering, in this discussion we focus on the electron–lattice interaction alone to simplify the argument. Within this scope, the stability of lattice polarons is dictated by the competition between the kinetic energy that tends to *delocalize* the carrier and the electron–lattice coupling and spin correlations that tend to *localize* it (Millis *et al.*, 1995, 1996, Röder *et al.*, 1996). The relevant terms to describe the electron–lattice interaction due to the Jahn–Teller (JT) effect are given by

$$H^{\mathrm{JT}} = -g\sum_i q_i n_i + \frac{K}{2}\sum_i q_i^2 \tag{11.23}$$

where q_i is the ionic displacement parameter and n_i is the excess charge density of the ith ion that causes the JT effect; g characterizes the strength of the electron–lattice coupling and K is the elastic modulus. Minimizing H^{JT} with respect to q gives the JT displacement, $\langle q\rangle$, and the JT energy, E_{JT},

$$\langle q\rangle = \frac{g\langle n\rangle}{K}, \qquad E_{\mathrm{JT}} = -\frac{\langle H^{\mathrm{JT}}\rangle_0}{N} = \frac{g^2\langle n\rangle^2}{2K} \tag{11.24}$$

Now let us consider creating a single-site polaron, such as Mn^{4+}, by eliminating the JT distortion from one site. The energy cost, however, is not just E_{JT}, since deforming one lattice site creates a long-range stress field around it. Rewriting Eq. 11.23,

$$H^{\mathrm{JT}} = \sum_i \left[\frac{K}{2}\left(q_i - \frac{gn_i}{K}\right)^2 - \frac{g^2 n_i^2}{2K}\right] \tag{11.25}$$

If we assume $n_i = 0$ only at the site k and equal to $\langle n\rangle$ elsewhere, the energy will be

$$\langle H^{\mathrm{JT}}\rangle_{\mathrm{p}} = \frac{K}{2}q_k^2 + \sum_{i\neq k}\left[\frac{K'}{2}u_i^2 - E_{\mathrm{JT}}\right] \tag{11.26}$$

where $u = q - \langle q \rangle$. We thus obtain the anti-JT polaron energy

$$E_p = \langle H^{JT} \rangle_p - \langle H^{JT} \rangle_0 = \frac{K}{2}(\langle q \rangle^2 + q_k^2) + \frac{K'}{2}\sum_{i \neq k} u_i^2$$

$$= \left[1 + \frac{q_k^2}{\langle q \rangle^2} + \frac{K'}{K}\sum_{i \neq k} \frac{u_i^2}{\langle q \rangle^2} \right] \frac{K}{2}\langle q \rangle^2 = RE_{JT} \tag{11.27}$$

where K' is not necessarily equal to K, depending on the mode of accommodation of the local strain. Since q_k and q_i are all proportional to $\langle q \rangle$, the renormalization factor, R, is independent of $\langle q \rangle$, and depends only upon the local structure. This point is usually unnoticed or neglected, but becomes important later in the discussion of the ionic size effect. The polaron energy competes against the electron kinetic energy

$$H^{DE} = -t \sum_{\langle i,j \rangle \sigma} \sigma_{ij}(c_{i\sigma}^{+} c_{j\sigma} + c_{j\sigma}^{+} c_{i\sigma}) \tag{11.28}$$

where summation is made for the interacting neighbors, σ denotes spin, and σ_{ij} describes the spin correlation between ith and jth spins which is proportional to $\cos(\theta/2)$, where θ is the angle of the spins $\mathbf{S}_i$ and $\mathbf{S}_j$ make. The critical parameter for polaron formation is (Millis *et al.*, 1996; Röder *et al.*, 1996)

$$\lambda = \frac{g^2}{RKt\langle \cos(\theta/2) \rangle} \tag{11.29}$$

By simulation, it is known that there is a critical value, λ_C, for polaron stability, so that when $\lambda > \lambda_C$, polarons are stable. As temperature is raised spins become more disordered, so that $\langle \cos(\theta/2) \rangle$ decreases, increasing the value of λ. This stabilizes polarons, and increases the resistivity rapidly near T_C, resulting in the CMR phenomenon.

11.4.2 Ionic size effects

The CMR effect depends not only on temperature, but also on the ionic size of the A-site ion. As shown in Figure 11.4 (Hwang *et al.*, 1995) when the average A-site ionic radius $\langle r_A \rangle$ is large the system is metallic. If the ionic radius is reduced, keeping the charge concentration constant, resistivity increases and the Curie temperature decreases beyond a certain radius, and eventually the system becomes insulating in spite of the high charge density. Thus the polaron stability strongly depends upon $\langle r_A \rangle$. Conventional thinking on this effect is to focus on the structure dependence of the electron hopping, **t**, through the bending of the Mn–O–Mn bond. As the Mn–O–Mn bond is bent the Mn–O hybridization decreases because the Mn-d orbital and the O-p orbital overlap less effectively. However, actually this effect is too small to account for the observed change (Radaelli *et al.*, 1997a; Fernandez-Baca *et al.*, 1998; Dzero *et al.*, 2000).

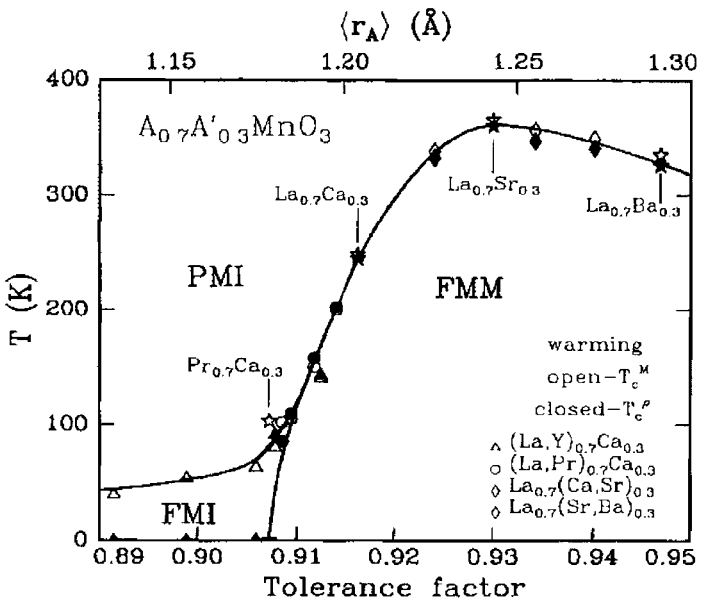

Figure 11.4. The ferromagnetic Curie temperature of $A_{0.7}A'_{0.3}MnO_3$ system as a function of the average A-site radius, $\langle r_A \rangle$ (Hwang *et al.*, 1995). When $\langle r_A \rangle$ is small T_C is low and the system is insulating, while when it is large T_C is high and the system is metallic. The CMR behavior is observed at the crossover region.

On the other hand, the effective elastic constant can also be structure dependent, and in our view this is much more important (Egami and Louca, 1999, 2002; Louca *et al.*, 2001). The dependence of the elastic constant K itself on the ionic radius of the A-site ion is small. However, the polaron formation energy is renormalized by the long-range stress field around it and the renormalization factor R depends upon the structure. As shown below when the radius of the A-site ion is large the value of R is nearly 1.5, but at a certain critical size it becomes reduced to unity.

When $LaMnO_3$ is doped with a divalent ion, thus with a hole, an anti-JT polaron is created as shown above. At the polaron site, the two long Mn–O bonds of the JT-distorted MnO_6 octahedron are shortened to become two short Mn–O bonds. If the Mn–O–Mn bond is straight, this local bond contraction produces tensile strains in the bonds nearby, where Mn–O bonds have to be stretched (*longitudinal* accommodation, Figure 11.5(a)). Thus local contraction of the Mn–O bond creates a long-range stress field. According to the continuum mechanics theory of Eshelby (1957), the total elastic energy is about 3/2 of that without the long-range stress field. Consequently, the effective coupling constant, Eq. 11.29, is nearly halved (Egami and Louca, 2002). On the other hand, if the Mn–O–Mn bond is strongly buckled, the local bond contraction can be accommodated by

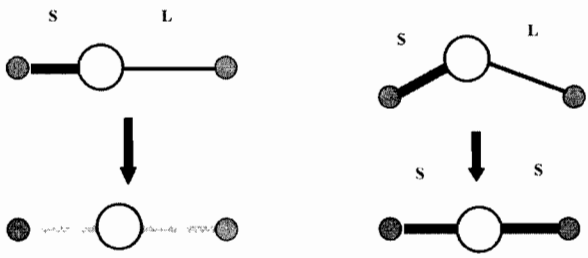

Figure 11.5. (a) Longitudinal accommodation of the strain to eliminate the JT distortion locally when the Mn–O–Mn bond is straight. This results in a long-range strain developing. (b) Transverse accommodation when the Mn–O–Mn bond is buckled. In this case the bond shortening can be accomplished without a long-range strain developing (Egami and Louca, 1999).

straightening the buckled bond (*transverse* accommodation, Figure 11.5(b)). In this case, the local contraction of the Mn–O bond is screened by the transverse oxygen mode and does not propagate to the next Mn site. Thus the renormalization is essentially absent ($R = 1$). Consequently, the effective coupling constant λ changes by nearly a factor of two depending on the ionic size, and becomes much reduced as the size of the A-site ion is reduced. When $\langle r_A \rangle$ is smaller than 1.20 Å the value of λ is large enough to stabilize polarons and the system is insulating. If $\langle r_A \rangle$ is larger, the value of λ is reduced to a half and polarons will not form, resulting in a metallic state. A similar argument was used successfully in explaining the polarons in linear chain compounds that show a Peierls distortion (Batistik *et al.*, 1993).

The condition for the crossover from longitudinal to transverse accommodation can be readily derived based upon the knowledge of the local structure. In $LaMnO_3$, the Mn–O–Mn bond in the plane is made of a combination of long and short Mn–O bonds. When a polaron is created, the long bond becomes a short bond, and the Mn–O–Mn bond is made of two short Mn–O bonds. The lattice has to be able to accommodate this shortened Mn–O–Mn bond. In other words the critical condition is

$$R_{\mathrm{Mn-Mn}} = 2R_{\mathrm{Mn-O}}(S) \tag{11.30}$$

where $R_{\mathrm{Mn-Mn}}$ is the Mn–Mn distance, and $R_{\mathrm{Mn-O}}(S)$ is the short Mn–O bond length. These values are determined from the PDF of $A_{1-x}A'_xMnO_3$ as shown in Figure 11.6. This yielded the critical condition

$$\langle r_A \rangle_{\mathrm{crit}} = 1.20 \text{ Å} \tag{11.31}$$

for the nine-coordinated ionic radius (Egami and Louca, 1999, 2002).

If the radius of the A-site ion is smaller than the critical value equation 11.31, the polaron becomes stable, and the system becomes insulating. While polarons are theoretically mobile, in this system they are pinned, or Anderson-localized, by chemical inhomogeneity due to mixing of different ions, and polaronic system is usually an insulator.

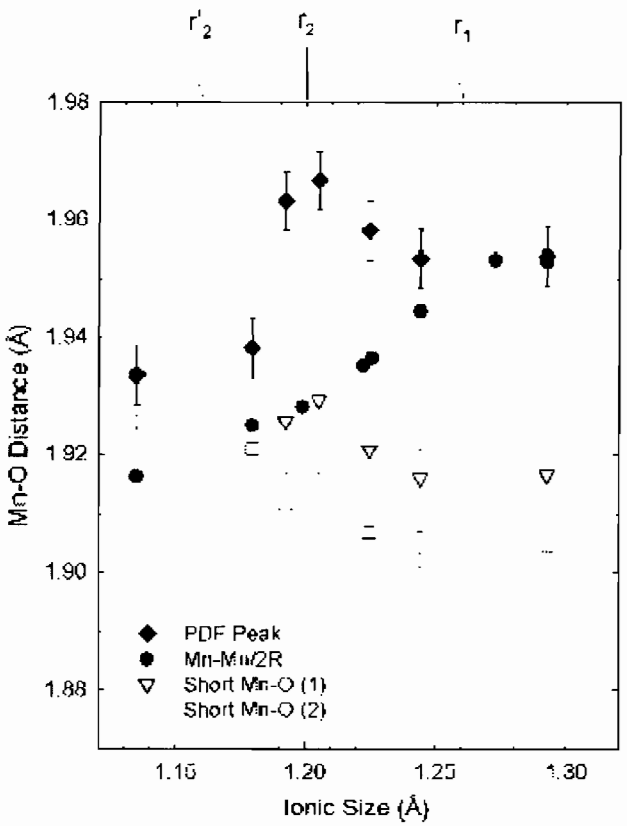

Figure 11.6. The short Mn–O distances measured from the PDF compared to one-half of the Mn–Mn distance, as a function of the A-site ionic radius (Egami and Louca, 2002).

In the crossover regime, the polarons are marginally stable and are influenced easily by external factors such as the applied magnetic field, producing the CMR phenomenon.

It should be noted that this argument on the critical ionic size requires no adjustable parameter, and the value is obtained directly from the observed Mn–O bond length. The prevailing theory based upon the band narrowing, on the other hand, cannot give the ionic size that corresponds to the critical value of λ without numerical calculations. Thus, there is no particular physical importance to the ionic size that produces the crossover, and high accuracy of calculation would have been required to produce agreement with experiment. The mechanism discussed above is basically geometrical, thus robust and does not require calculations of electronic structure.

The discussion so far assumed hole doping into $LaMnO_3$. If we start from the other side, $A^{2+}Mn^{4+}O_3$, and replace A^{2+} with a trivalent ion, the situation is very different. In this

case we are doping an electron that produces a local JT distortion and a JT-polaron in the matrix that is free of the JT distortion. The local JT distortion *increases* the Mn–O bond length locally, which can be accommodated by buckling the Mn–O–Mn bond. Thus a JT polaron is always stable, and the system is always an insulator for $x > 0.5$. This results in the asymmetry between the hole doping and electron doping. Stable polarons in $x \geq 0.5$ often order, forming a polaron lattice.

The dependence of polaron stability on the ionic size and charge density can be summarized in the phase diagram shown in Figure 11.7 (Egami and Louca, 1999). At small doping levels of holes, the system is insulating up to a percolation concentration as discussed later. The CMR phenomenon is observed in the crossover region indicated in the diagram. This phase diagram is in excellent agreement with the experimental phase diagram by Ramirez (1997), if we note that the radius of La (1.22 Å in Figure 11.8) corresponds to the covalent radius of 1.7 Å.

Another phenomenon worth mentioning here is the isotope effect (Zhao *et al.*, 1996). It is particularly interesting that the sample with ^{18}O has a lower T_C than that with ^{16}O, and the difference increases with a decreasing A-site ionic size. The dependence on the size of the A-site ion may be explained in the following way. Usually ^{18}O has a smaller vibrational amplitude than ^{16}O does, since the phonon amplitude is proportional to $1/\sqrt{M}$. Thus the

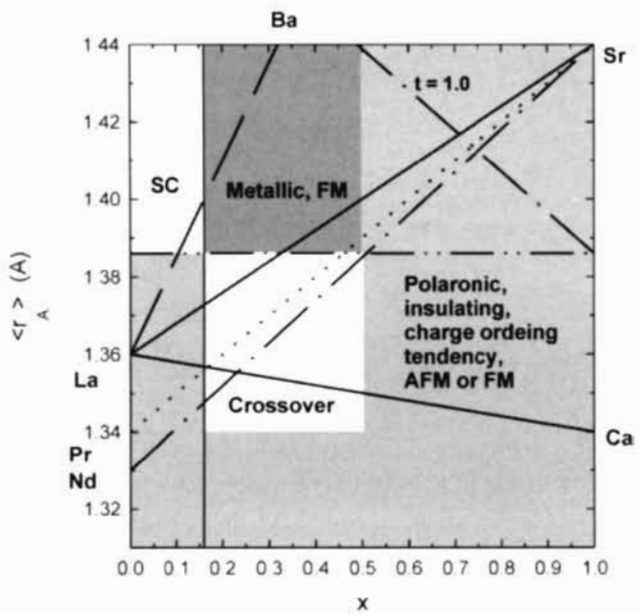

Figure 11.7. Phase diagram of the ionic radius of the A-site ion vs. the concentration of the divalent ion, x. The CMR behavior is observed in the crossover regime where polarons are marginally stable and are influenced easily by external forces (Egami and Louca, 1999).

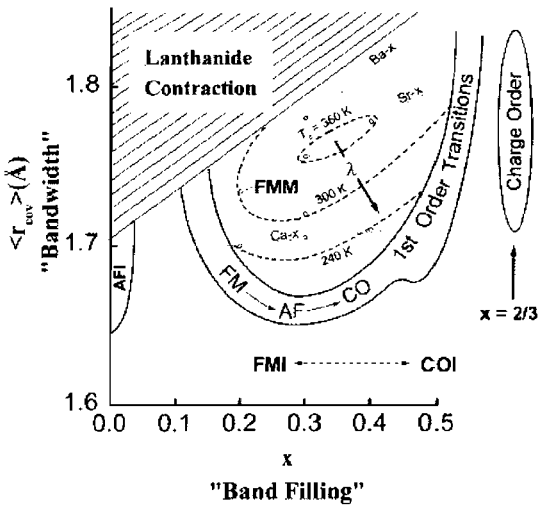

Figure 11.8. The experimentally determined diagram of T_C as a function of the 'covalent radius' representing $\langle r_A \rangle$ and the hole density, x (Ramirez, 1997). This phase diagram corresponds well to Figure 15 if the vertical axis is rescaled so that the position of La (1.34 Å in Figure 15 and 1.7 Å in Figure 16) is adjusted accordingly.

zero-point vibrational amplitude $\langle u^2 \rangle$ of oxygen is reduced, reducing both the Cu–O and A–O distances due to the anharmonic effect. But, since the Cu–O bond is much stiffer, the change in the A–O distance is greater, increasing the buckling of the Mn–O–Mn bond. This will increase the stability of the polarons in the line of argument above, resulting in the suppression of T_C. The effect is more pronounced if the A-site ionic radius is close to the critical value. This will explain the dependence of the isotope effect on the ionic radius. This provides further evidence of the polaron stabilization mechanism through bond bending.

11.5. LATTICE INVOLVEMENT IN THE METAL–INSULATOR TRANSITION AND THE CMR EFFECT

11.5.1 Metal–insulator transition as a function of charge density at low temperatures

As shown in Figure 6.2, the data for the fraction of Mn sites with local JT distortion, η, as a function of doping, x, are continuous through the M–I transition. The value of η is only about 0.5 at the M–I transition, and remains non-zero even in the metallic phase up to $x \sim 0.32$. A similar result was obtained recently also for the La–Ca system (Billinge *et al.*, 2000). These data appear to indicate that the polarons survive in the metallic phase close to the MI transition boundary (Figure 10.7). This, however, is a very strange notion since the tendency of localization by forming polarons and metallic conductivity are not mutually

compatible. Usually, the high dielectric constant of the metallic phase reduces the polaron binding energy and delocalizes the carriers.

A *percolative* picture emerges from these results (Egami, 1996; Egami *et al.*, 1997; Louca *et al.*, 1997; Egami and Louca, 2000). As the density of polarons is increased, they start to become in contact. If the polarons are single-site polarons, charges will remain localized even if two polarons are in contact because of the high coulomb repulsion to place two carriers on the same site (Hubbard, 1963). However, if the polarons are more extended over several sites, as is the case for (La/Sr)MnO_3, the coulomb repulsion between two carriers is small and charge carriers will become mobile within the connected network of the polarons. If the size of the network of the connected polarons reaches a macroscopic scale, metallic conduction commences by percolation. At the M–I transition the number of short Mn–O bonds is about five, as shown in Figure 6.2, indicating that the volume fraction of the undistorted, metallic sites is 50%. This is consistent with the percolation in a two-dimensional square lattice (Zallen, 1983). The percolative nature of M–I transition was discussed very extensively for doped semiconductors by Phillips (1997, 1998). The power law for the concentration dependence of conductivity is given by $\sigma \approx (x - x_{crit})^{1/2}$ (Itoh *et al.*, 1996 and references therein). Phillips (1997, 1998) has derived this relationship and demonstrated its fundamental importance to the conductivity, possibly even superconductivity, of complex electron systems. Indeed the data for (La,Sr)MnO_3 (Urushibara *et al.*, 1995) follow this law quite well as shown in Figure 11.9.

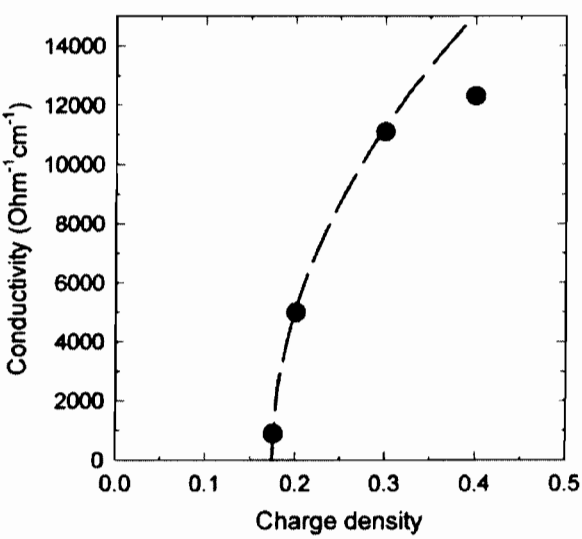

Figure 11.9. Low temperature conductivity of $La_{1-x}Sr_xMnO_3$ from Urushibara *et al.* (1995) plotted vs. charge density (or doping). The solid curve is the fit by $\alpha(x - x_c)^{1/2}$.

In this picture, the carriers in the connected pathways are not localized, but flow through the metallic channels within which the JT distortion is locally suppressed. In-between the metallic channels, however, the JT distortion is locally alive, the charge density is low, and conductivity is very low. We may call these regions 'insulating' islands. This proposal was strongly criticized in the beginning since it differed from the commonly accepted notion of total carrier delocalization. However, within a few years theoretical works arrived at this picture of phase segregation as well (Gor'kov and Kresin, 1998; Yunoki *et al.*, 1998a,b; Moreo *et al.*, 1999). In addition, a similar 'two-fluid' model was proposed by analyzing the transport data (Jaime *et al.*, 1998). The picture of percolative MI transition is now very widely accepted (Fäth *et al.*, 1999; Uehara *et al.*, 1999). The magnetic coupling within the insulating islands could either be antiferromagnetic or ferromagnetic, depending upon the presence of local orbital ordering. If the orbital moments are ordered in the zigzag manner as in the layers of $LaMnO_3$, the superexchange interaction is ferromagnetic. Since the metallic samples are fully magnetized at low temperatures, ferromagnetic interaction appears to win over the antiferromagnetic interaction.

This percolative picture explains various observations quite well, such as the antiferromagnetic fluctuation near T_C (Perring *et al.*, 1997), strong spin wave softening and damping (Lynn *et al.*, 1997; Hwang *et al.*, 1998), relatively low conductivity (Urushibara *et al.*, 1995), smeared Fermi edge (Dessau *et al.*, 1998), and small thermopower (Zhou *et al.*, 1996). In particular, the ARPES studies show that the electronic dispersion is well defined only up to about 1 eV below the Fermi level, and near the Fermi level it becomes totally smeared (Dessau *et al.*, 1998). This smearing could be evidence of scattering by the split e_g levels. Where the JT distortion is locally present, the e_g level should be locally split and the potential locally lowered by $\Delta/2 = 0.7$ eV. This distortion will scatter electrons within $\Delta/2$ from the Fermi surface, as is observed.

11.5.2 Metal–insulator transition at T_C

The pulsed neutron PDF revealed the fundamental difference in the local lattice behavior near T_C between the perovskites and the layered compounds. In the perovskites η changes sharply at T_C indicating a rapid change in the volume of the metallic conducting phase (Figures 1.10 and 10.8). The magnetic transition is achieved by a catastrophic collapse of polarons into a metallic volume, indicating that the nature of the transition is of first-order. On the other hand, in the layered compound, η changes smoothly through T_C (Figure 10.10), just as in the case of the metal-insulator transition as a function of x (Figure 6.2). The magnetic transition is achieved by coherence of spin and local JT distortion, or in other words orbital ordering, while the metallic volume changes continuously. This is indicative of a second-order transition.

11.5.2.1 Perovskite. As temperature is decreased through T_C in the perovskite, the fraction of the volume in which the JT distortion is suppressed, η is increased sharply as

shown in Figure 10.8. This increase must be indicating partial, but not total, delocalization of the carriers through the DE interaction. Indeed, an increase in conductivity is accompanied by the increase in η as indicated in Figure 1.10 in terms of the PDF peak height at 2.75 Å. Thus, it is expected that the parts of the sample without the local JT distortion are metallic and ferromagnetic since the DE interaction should be dominant there. The sharp change in the conducting volume at T_C must be indicative of a first-order phase transition, as suggested by the temperature dependence of the magnetization (Ramirez, 1997). However, the value of η remains less than unity, except at $T = 0$ for x greater than ~ 0.3 for $La_{1-x}(Sr,Ca)_xMnO_3$ (Figure 6.2 and 10.7, Louca and Egami, 1999; Billinge *et al.*,2000), leading to a two-phase picture and the percolative view of the transport phenomena. This approach can explain the transport data qualitatively rather well (Mayr *et al.*, 2001). Details of the morphology of the two-phases require a separate discussion given below.

11.5.2.2 Layered compounds. The temperature dependence of η through T_C of the perovskite is in strong contrast to that of the layered compound $La_{1.4}Sr_{1.6}Mn_2O_7$ (Figures 1.10 and 10.8). In $La_{1.4}Sr_{1.6}Mn_2O_7$, the metallic volume changes smoothly through T_C while the lattice constant undergoes a discontinuous change. Such a behavior is typical of an order/disorder-type second-order ferroelastic phase transition in which the local units of distortion that are randomly oriented at high temperatures become aligned at T_C (Salje, 1990). At high temperatures (>250 K), the axis of distortion of MnO_6 octahedra is randomly oriented, and carriers appear to be in the single-site polaronic state. Below 250 K carriers could become more delocalized, resulting in two-dimensional local metallic islands, although there are controversies about the transport data. The presence of strong in-plane spin correlation above T_C and the absence of its divergence at T_C support this view (Osborn *et al.*, 1998). These islands are not fully connected, and c-axis conduction is very poor. Consequently, conductivity is low even in the $a-b$ plane. At T_C, the local JT distortions (orbital moments) start to align along the c-axis, and three-dimensional metallic conduction commences. For that reason it is likely that the driving force for this transition is not only the spin correlations, but also the orbital ordering.

It is not quite clear whether the local JT distortion in the layered compounds is the same as in the perovskite, producing an elongated octahedron with four short and two long Mn–O bonds, or different, resulting in a pyramid with five short and one long M–O bonds. The axial symmetry of the layered compounds appears to prefer the second. However, the magnitude of the local JT distortion is as large as the one in the perovskite. Note that the total JT distortion in the crystal structure is an order of magnitude smaller than the local JT distortion even at low temperatures. As was discussed above this implies that the local JT distortions are nearly randomly oriented. Almost 2/3 of the local JT distortions are in the plane, with the distortion along the c-axis slightly exceeding 1/3. Thus the total

symmetry is not as important as it might appear, and it is most likely that the local chemistry produces an environment very similar to that in the perovskite, with two long and four short M–O bonds around an Mn^{3+} ion. In this scenario, the local M–I transition within the plane takes place around 250 K where the number of short Mn–O bonds is about 5.0 (Figure 10.10), which is consistent with the density of the JT-distorted sites at T_C for the perovskite as shown in Figure 6.2. Thus the transition around 250 K must be percolative, while the transition at T_C is due to the three-dimensional ordering of the spin and orbital moment.

11.5.3 Spatial distribution of charge carriers in the metallic state

As we have shown above, the metallic state just above the critical charge density for the M–I transition is in a two-phase state. It is not clear, however, how these two phases are mixed in space. One extreme is macroscopic phase separation (PS) that happens when the attraction between the charges is strong. The attractive interaction originates from the elastic interaction to ease the local elastic strain due to the local JT distortion, and the DE interaction to reduce the kinetic energy. However, the price to pay for charge segregation is the hefty electrostatic energy. When the attractive interaction overcomes the repulsive force PS would occur. The other extreme is the charge ordered (CO) state. Modeling the PDF in the medium range suggests that the size of the charged region is of the order of 15 Å. Growing beyond this size would cost too much electrostatic energy.

In Figure 11.10 the PDF of $La_{0.8}Sr_{0.2}MnO_3$ [20%] is compared to that of $La_{0.6}Sr_{0.4}MnO_3$ [40%] at $T = 10$ K (Egami and Louca, 2000). Here the r-axis of the 40% sample is scaled by 0.6% so that the lattice constants of the two samples match. At $T = 10$ K the 40% sample is metallic without JT distortion whereas some local JT distortions are left in the 20% sample. Indeed the PDF of the 40% sample is very close to the PDF calculated for the average crystal structure, while that of the 20% sample deviates considerably from the PDF of the average structure. The two experimental PDFs in Figure 11.10 differ considerably at short distances, while the difference becomes smaller beyond about 15 Å, and falls to the level of the noise. This observation implies that the local JT distortions in the 20% sample are uncorrelated in orientation and magnitude beyond $3 \sim 4$ times the lattice constant, a. Should the phase segregation exist this length-scale of 15 Å must be the correlation length of the two phases. For three-dimensional correlations, this correlation domain includes only $30 \sim 60$ Mn ions, and in two-dimensions only 15 Mn ions. Such an object can barely be called a phase. This result suggests that the large-scale charge segregation is highly unlikely in this system, mainly because of electrostatic repulsion. On the other hand, the correlation length of 15 Å is not short either, suggesting that the polarons self-organize themselves locally to some extent. For instance, the strong correlation at 5.5 Å ($= \sqrt{2}a$) indicates a local short-range ordering of orbital moments in the 20% sample. It is also interesting to note that the correlation length of 15 Å is close to the periodicity of

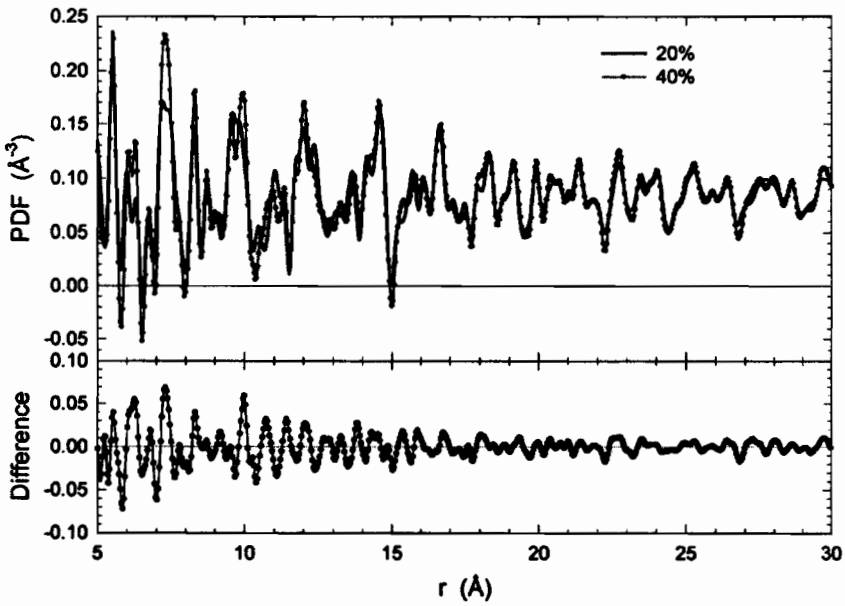

Figure 11.10. The PDF of $La_{1-x}Sr_xMnO_3$ ($x = 0.2$, 0.4) determined by pulsed neutron scattering. The r-axis of the PDF of 40% sample is scaled by 0.6% so that the lattice constants match. The difference after scaling (below) shows that the two structures are very similar in the length-scale larger than 15 Å. Thus, the local JT distortions in the 20% sample are uncorrelated beyond 15 Å, suggesting that the charge correlation length may be of the order of 15 Å (Egami and Louca, 2000).

the charge stripes expected for this composition. It is possible that the charges are ordered in the short range into local stripes.

11.5.4 Charge ordering

The charge-ordered (CO) state has been observed for various rational values of x, typically for $x \geq 0.5$ (Ramirez *et al.*, 1996; Cheong and Hwang, 1999). Polaron stability is an important issue for this phenomenon as well, since bare electrons do not become ordered to form the Wigner lattice unless the density is very low and temperature extremely low. Only the heavy dressing of electrons by phonons, forming polarons, increases the effective mass sufficiently so that they can become ordered. Thus the CO state should be considered as a polaron lattice, where polarons are ordered in a periodic manner. The fact that both PS and CO state occur in the same phase diagram indicates that the repulsive and attractive forces among the charge carriers are very close in strength, and almost balanced. It should be noted, however, that in real samples the degree of charge ordering is less than perfect, possibly disturbed by the distribution of La and Ca ions. Thus, the distortion of the MnO_6 octahedra in the average structure (Radaelli *et al.*, 1997b) can be much smaller than that of the real local structure. The PDF measurement (Louca, 2001) suggests the magnitude

of the JT distortion is again as large as in the undoped $LaMnO_3$. The CO state can be disrupted by the application of electric or magnetic fields resulting in a metallic state (Asamitsu *et al.*, 1995), indicating that the CO state is only marginally stable.

The configuration of orbital moments at $x = 0.5$ includes alternating long–short and short–short Mn–O bond combinations; and for this pattern to be stable, the short–short Mn–O bond combination has to be either free of strain or bent, but not in tension. This agrees with the crossover condition above (Eq. 11.31) and suggests that charge ordering at $x = 0.5$ will not take place when $\langle r_A \rangle$ is larger than $\langle r_A \rangle_{CR}$. However, where the value of $\langle r_A \rangle$ is reduced below this value, charge ordering will take place, localizing the carriers and depressing or eliminating T_C. Where the value of x is close to 0.5, apparently charges still can order locally, thus pulling down T_C. This tendency is clearly shown in the experimental result of Figure 11.11 (Tomioka *et al.*, 1997). Thus, a theory of a finer scale has to be developed to account for the actual values of T_C within the crossover regime in Figure 11.7.

11.6. PHASE TRANSITION IN SYSTEMS WITH COMPETING INTERACTIONS III: HIGH-T_C CUPRATES

11.6.1 Suppression of superconductivity at charge density of 1/8

The phase diagram of $La_{2-x}Ba_xCuO_4$ has an anomaly at $x = 1/8$, where T_C sharply nose dives to zero. A similar, and clearer, behavior is observed for $La_{2-x-y}Nd_ySr_xCuO_4$

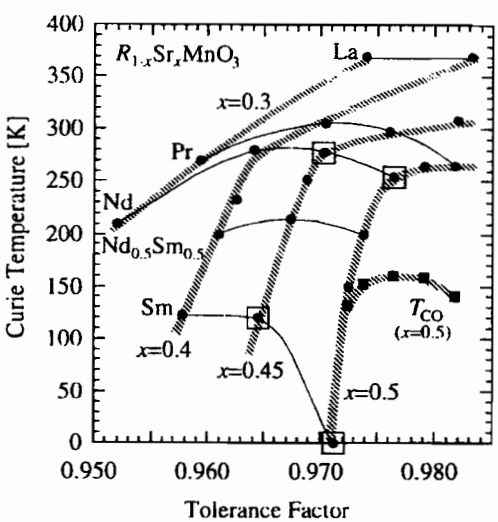

Figure 11.11. Curie temperature of $R_{1-x}Sr_xMnO_3$ system as a function of the A-site atomic size expressed in terms of the tolerance factor. At $x = 0.5$ as the size decreases T_C is quickly suppressed below $t = 0.976$ ($Nd_{0.5}Sr_{0.5}MnO_3$) which corresponds to $\langle r_A \rangle = 1.384$ Å in our definition (XII coordination) (Tomioka *et al.*, 1997).

($y = 0.4$). When T_C is suppressed around $x = 1/8$ both magnetic and lattice satellite peaks were observed around the Bragg peaks, indicating that the spin and charge structure has been modulated (Tranquada *et al.*, 1995). The magnetic periodicity determined from the position of the satellites is $8a$, while the charge periodicity is $4a$. The magnetic satellites are observed around the 1/2[110] point in reciprocal space, while the charge (lattice) satellites appear at the 1/2[100] point. Tranquada *et al.*, (1995) suggested that the structural modulation takes the form of the spin–lattice stripes. In this model the charge stripes run along the [100] direction at every fourth lattice spacing (Figure 11.12). The charge stripe is also an antiphase domain boundary in the antiferromagnetic order, as predicted by Zaanen and Gunnarson (1989), so that the magnetic periodicity is twice the charge periodicity: 8 lattice spacings. Charges have strong one-dimensional characters in this phase as revealed by the Hall effect measurement (Noda *et al.*, 1999) and photoemission (Zhou *et al.*, 1999). The stripes are non-superconducting but semiconducting.

One of the requirements for the stripes to appear is the so-called low-temperature tetragonal (LTT) phase, clearly indicating the role of the lattice. In the orthorhombic phase the CuO_6 octahedra are tilted around the [110] axis, while in the LTT phase they are tilted

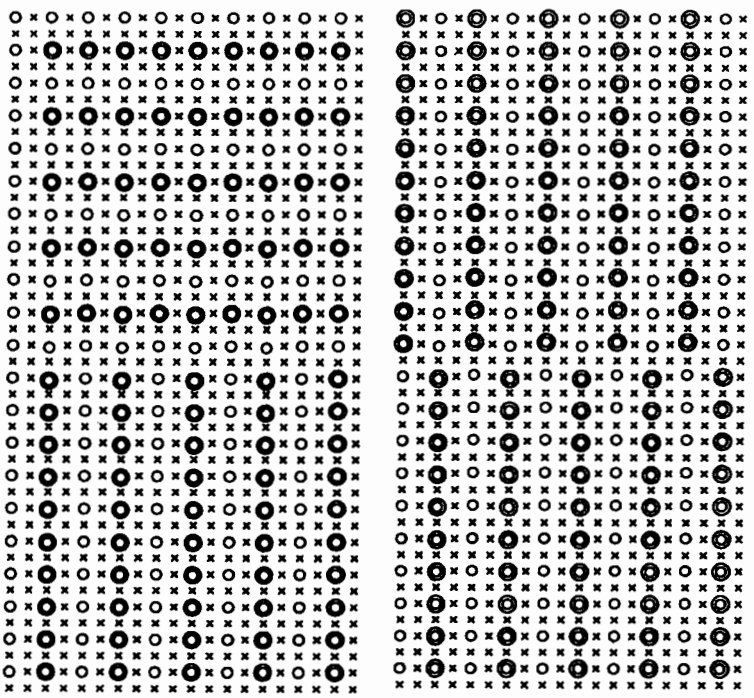

Figure 11.12. Examples of domain structures made of broken charge stripes stabilized by the lattice misfit strain energy. Circles and crosses indicate the positions of copper atoms in the CuO_2 plane, the double circles indicate charges localized on copper sites forming into stripes (Billinge and Duxbury, 2001).

around the [100] axis. Apparently, the [100] tilt stabilizes the [100] charge stripes as we discussed in Section 10.3.3. The charge stripes could be considered as one-dimensional array of polarons. Indeed the condition to stabilize the stripes appears to strongly resemble those to stabilize polarons in CMR manganites. If the Cu–O–Cu bond is buckled beyond a certain angle, about 3.6° in LSCO (Büchner *et al.*, 1994) and 5.5° for YBCO (Chmaissem *et al.*, 1999) superconductivity disappears. Thus the stripe phase and superconductivity compete against each other (Tranquada *et al.*, 1997). Just as stable polarons resulted in the insulating state for the manganites, stable stripes result in non-superconducting state for cuprates. Furthermore, as marginal stability of polarons was required for the CMR effect, marginal stability of stripes may be a prerequisite for superconductivity (Egami, 2000; Egami and Louca, 2002).

The observation of the spin–charge stripes was extremely important in proving the suspected microscopic phase separation can really happen in cuprates and we should not be just thinking in terms of a homogeneous electron state. Since this is such a remarkable breakthrough, many have postulated that the dynamic stripe state can produce the superconductivity itself through dynamic stripes, or in terms of stripe defects such as stripe edge dislocations (Kivelson *et al.*, 1998; Zaanen, 2000). This requires the stripes to be broken, not ordered over long range. Interestingly, the lattice may have a role to play in breaking up the stripes because of the electron–lattice coupling described above. As we described in Sections. 10.3.3 and 10.3.4 the doped charges shorten the Cu–O bond. If the doped charges form into stripes with undoped material in between a misfit stress therefore builds up at the interface. As the stripe gets longer this stress increases until the energy cost to add an additional hole exceeds the energy gain from the hole joining the stripe. This leads to a stripe breakup length that depends on the ratio of the energy of the stripe dislocation to the misfit stress energy (Billinge and Duxbury, 2001, 2002). The broken stripes form a nano-scale ferroelastic domain structure, as shown in Figure 11.12 much the same as the tweed structures seen in martensitic alloys (Shenoy *et al.*, 1999). The domain size depends on the misfit strain that may explain the difference in T_C between different cuprate systems as discussed in Billinge and Duxbury (2001, 2002).

Whilst the presence of nanoscale structural and charge inhomogeneities is strongly suggested the actual presence of dynamic charge stripes in the superconducting state is not confirmed. In fact the relevant charge fluctuation may not be the dynamic stripe state ($q = \pi/2$). Recent phonon measurements (McQueeney *et al.*, 1999; Egami *et al.* 1999; Petrov *et al.*, 2000) suggest that dynamic short-range Peierls charge fluctuation with the $2a$ periodicity ($q = \pi$) may be present in the superconducting LSCO and YBCO. Occurrence of such Peierls instability is only reasonable, since, after all, the system is a doped Mott insulator with a nearly half-filled band. Indeed calculations suggested such a possibility (Sachdev and Read, 1991; Sachdev, 2000; Röder *et al.*, 1993; Ishihara *et al.*, 1997; Petrov and Egami, 1998). It is possible that the competition between the Peierls state and the stripe state is preventing either from developing into the long-range order, and that is important

to superconductivity, since long-range charge order (CDW) will suppress superconductivity (Egami *et al.*, 1999).

11.6.2 Role of the Lattice in high-temperature superconductivity

Various unusual local lattice dynamics have been observed for cuprates that exhibit high-temperature superconductivity (Egami and Billinge, 1994, 1996). Since high-temperature superconductivity is a highly unusual phenomenon, it is not surprising that unusual behaviors are observed, but the question whether this indicates the significant role of the lattice or not is controversial. The conventional thinking on the origin of the high-temperature superconductivity in cuprates is that it is purely an electronic phenomenon involving spins, and the lattice (phonon) has little to do with it (Anderson, 1997). In this view all the lattice related phenomena are just the consequences of superconductivity with a short coherence length, and they are irrelevant to the mechanism. Indeed it is practically impossible that the conventional phonon mechanism (BCS theory) results in high-temperature superconductivity.

However, the BCS mechanism is not the only way phonons become involved in superconductivity. In systems with strongly correlated electrons the electron–phonon coupling also affects the spin systems, and there are possibilities of various synergies involving spin, charge and lattice. For instance, recent calculations (Piekarz and Egami, 2003) suggests that phonon-induced charge transfer (Egami *et al.*, 1993) can be spin-polarized in strongly correlated electron systems, resulting in unconventional electron-phonon coupling. This could lead to synergetic effect of phonon, charge and spin, and could contribute to unusally strong pairing in the cuprates. While the details need to be studied further it is clear that opportunities exist for phonons to be involved in superconductivity in cuprates in unconventional ways. The PDF method played no small part in bringing the role of the lattice on high-temperature superconductivity under a spotlight.

REFERENCES

Alben, R., Becker, J.J. & Chi, M.C. (1978) *J. Appl. Phys.*, **49**, 1653.

Anderson, P.W. (1997) in *Theory of Superconductivity in the High-T_C Cuprates*, Princeton University Press, Princeton.

Asamitsu, A., Moritomo, Y., Tomioka, A., Arima, T. & Tokura, Y. (1995) *Nature (London)*, **373**, 407.

Batistik, I., Huang, X.Z., Bishop, A.R. & Saxena, A. (1993) *Phys. Rev. B*, **48**, 6065.

Billinge, S.J.L. & Duxbury, P.M. (2001) cond-mat/0108338.

Billinge, S.J.L. & Duxbury, P.M. (2002) *Int. J. Mod. Phys.*, to be published.

Billinge, S.J.L., Proffen, Th., Petkov, V., Sarrao, J.L. & Kycia, S. (2000) *Phys. Rev. B*, **62**, 1203.

Born, M. (1939) *J. Chem. Phys.*, **7**, 591.

Büchner, B., Breuer, M., Freimuth, A. & Kampf, A.P. (1994) *Phys. Rev. Lett.*, **73**, 1841.

Chen, I.-W., Li, P. & Wang, Y. (1996) *J. Phys. Chem. Solids*, **57**, 1525.

Cheong, S.-W. & Hwang, H.Y. (1999) in *Colossal Magnetoresistance Oxides*, Ed. Tokura, Y., Gordon & Breach, London.
Chi, M.C. & Egami, T. (1979) *J. Appl. Phys.*, **50**, 1651.
Chmaissem, O., Jorgensen, J.D., Short, S., Knizhnik, A., Eckstein, Y. & Shaked, H. (1999) *Nature (London)*, **397**, 45.
Dessau, D.S., Saitoh, T., Park, C.-H., Shen, Z.-X., Villela, P., Hamada, N., Morimoto, Y. & Tokura, Y. (1998) *Phys. Rev. Lett.*, **81**, 192.
Dzero, M.O., Gor'kov, L.P. & Kresin, V.Z. (2000) *Eur.Phys. J.*, **14**, 459.
Egami, T. (1996) *J. Low Temp. Phys.*, **105**, 791.
Egami, T. (1997) *Mater. Sci. Eng. A*, **226–228**, 261.
Egami, T. (1999) *Ferroelectrics*, **222**, 163.
Egami, T. (2000) *AIP Conf. Proc.*, in press.
Egami, T. & Billinge, S.J.L. (1994) *Prog. Mater. Sci.*, **38**, 359.
Egami, T. & Billinge, S.J.L. (1996) in *Physical Properties of High Temperature Superconductors V*, Ed. Ginsberg, D., World Scientific, Singapore, p. 265.
Egami, T. & Louca, D. (1999) *J. Supercond.*, **12**, 23.
Egami, T. & Louca, D. (2000) *J. Supercond.*, **13**, 247.
Egami, T. & Louca, D. (2002) *Phys. Rev. B*, **65**, 094422.
Egami, T., Ishihara, S. & Tachiki, M. (1993) *Science*, **55**, 3163.
Egami, T., Louca, D. & McQueeney, R.J. (1997) *J. Supercond.*, **10**, 323.
Egami, T., McQueeney, R.J., Petrov, Y., Yethiraj, M., Shirane, G. & Endoh, Y. (1999) *AIP Conf. Proc.*, **483**, 231.
Eshelby, J.D. (1957) *Proc. Roy. Soc. A*, **241**, 376.
Fäth, M., Freisem, S., Menovsky, A.A., Tomioka, Y., Aarts, J. & Mydosh, J.A. (1999) *Science*, **285**, 1540.
Fernandez-Baca, J.A., Dai, P., Hwang, H.Y., Kloc, C. & Cheong, S.-W. (1998) *Phys. Rev. Lett.*, **80**, 4012.
Gonzalo, J.A. (1991) in *Effective Field Approach to Phase Transitions and Some Applications to Ferroelectrics*, World Scientific, Singapore.
Gor'kov, L.P. & Kresin, V.Z. (1998) *JETP Lett.*, **67**, 985.
Harris, A.B. (1974) *J. Phys. C: Solid State Phys.*, **7**, 1671.
Harris, R., Plischke, M. & Zuckermann, M.I. (1973) *Phys. Rev. Lett.*, **31**, 160.
Hubbard, J. (1963) *Proc. R. Soc. A*, **276**, 238.
Hubbard, J. (1963) *Proc. R. Soc. A*, **277**, 237.
Hwang, H.Y., Cheong, S.-W., Radaelli, P.G., Marezio, M. & Batlogg, B. (1995) *Phys. Rev. Lett.*, **75**, 914.
Hwang, H.Y., Dai, P., Cheong, S.-W., Aeppli, G., Tennant, D.A. & Mook, H.A. (1998) *Phys. Rev. Lett.*, **80**, 1316.
Imry, Y. & Ma, S.-K. (1975) *Phys. Rev. Lett.*, **35**, 1399.
Ishihara, S., Egami, T. & Tachiki, M. (1997) *Phys. Rev. B*, **55**, 3163.
Itoh, K.M., Haller, E.E., Beeman, J.W., Hansen, W.L., Emes, J., Reichertz, L.A., Kreysa, E., Shutt, T., Cummings, A., Stockwell, W., Sadoulet, B., Muto, J., Farmer, J.W. & Ozhogin, V.I. (1996) *Phys. Rev. Lett.*, **77**, 4058.
Jaime, M., Lin, P., Salamon, M.B. & Han, P.D. (1998) *Phys. Rev. B*, **58**, R5901.
Kivelson, S.A., Fradkin, E. & Emery, V.J. (1998) *Nature (London)*, **393**, 550.
Landau, L.D. & Lifshitz, E.M. (1958) *Statistical Physics*, Addison-Wesley, Reading.
Louca, D (2001) unpublished.

Louca, D., Egami, T., Brosha, E.L., Röder, H. & Bishop, A.R. (1997) *Phys. Rev. B*, **56**, R8475.
Louca, D. & Egami, T. (1999) *Phys. Rev. B*, **59**, 6193.
Louca, D., Egami, T., Dmowski, W. & Mitchell, J.F. (2001) *Phys. Rev. B*, **64**, R180403.
Lynn, J.W., Erwin, R.W., Borchers, J.A., Santoro, A., Huang, Q., Peng, J.-L. & Greene, R.L. (1997) *J. Appl. Phys.*, **81**, 5488.
McQueeney, R.J., Petrov, Y., Egami, T., Yethiraj, M., Shirane, G. & Endoh, Y. (1999) *Phys. Rev. Lett.*, **82**, 628.
Mayr, M., Moreo, A., Vergés, J.A., Arispe, J., Feiguin, A. & Dagotto, E. (2001) *Phys. Rev. Lett.*, **86**, 135.
Millis, A.J., Littlewood, P.B. & Shairman, B.I. (1995) *Phys. Rev. Lett.*, **74**, 5144.
Millis, A.J., Shraiman, B.I. & Mueller, R. (1996) *Phys. Rev. Lett.*, **77**, 175.
Moreo, A., Yunoki, S. & Dagotto, E. (1999) *Science*, **283**, 2034.
Noda, T., Eisaki, H. & Uchida, S. (1999) *Science*, **286**, 265.
Osborn, R., Rosenkranz, S., Argyriou, D.N., Vasiliu-Doloc, L., Lynn, J.W., Sinha, S.K., Mitchell, J.F., Gray, K.E. & Bader, S.D. (1998) *Phys. Rev. Lett.*, **81**, 3964.
Pelcovits, R.A., Pytte, E. & Rudnick, J. (1978) *Phys. Rev. Lett.*, **40**, 476.
Perring, T.G., Aeppli, G., Hayden, S.M., Carter, S.A., Remeika, J.P. & Cheong, S.-W. (1997) *Phys. Rev. Lett.*, **78**, 3197.
Petrov, Y. & Egami, T. (1998) *Phys. Rev. B*, **58**, 9485.
Petrov, Y. & Egami, T. (1999) cond-mat/9912449.
Petrov, Y., Egami, T., McQueeney, R.J., Yethiraj, M., Mook, H.A. & Dogan, F. (2000) cond-mat/0003414.
Phillips, J.C. (1997) *Proc. Natl Acad. Sci. USA*, **94**, 10528.
Phillips, J.C. (1998) *Proc. Natl Acad. Sci. USA*, **95**, 7264.
Piekarz, P. & Egami, T. (2003) *unpublished.*
Radaelli, P.G., Iannone, G., Marezio, M., Hwang, H.Y., Cheong, S.-W., Jorgensen, J.D. & Argyriou, D.N. (1997a) *Phys. Rev. B*, **56**, 8265.
Radaelli, P.G., Cox, D.E., Marezio, M. & Cheong, S.-W. (1997b) *Phys. Rev. B*, **55**, 3015.
Ramirez, A.P. (1997) *J. Phys: Condens. Matter*, **9**, 8171.
Ramirez, A.P., Schiffer, P., Cheong, S.-W., Chen, C.H., Bao, W., Palstra, T.M., Zegarski, B., Gammel, P.L. & Bishop, D.J. (1996) *Phys. Rev. Lett.*, **76**, 3188.
Röder, H., Bishop, A.R. & Gammel, J.T. (1993) *Phys. Rev. Lett.*, **70**, 3498.
Röder, H., Zang, J. & Bishop, A.R. (1996) *Phys. Rev. Lett.*, **76**, 1356.
Sachdev, S. (2000) *Science*, **288**, 475.
Sachdev, S. & Read, N. (1991) *Int. J. Mod. Phys. B*, **5**, 219.
Salje, E.K.H. (1990) in *Phase Transitions in Ferroelastic and Co-elastic Crystals*, Cambridge University Press, Cambridge.
Shenoy, S.R., Lookman, T., Saxena, A. & Bishop, A.R. (1999) *Phys. Rev. B*, **60**, R12537.
Sherrington, D. & Kirkpatrick, S. (1975) *Phys. Rev. Lett.*, **35**, 1792.
Tallon, J.L. (1984) *J. Phys. Chem. Solids*, **41**, 837.
Teslic, S. & Egami, T. (1998) *Acta Crystallogr. B*, **54**, 750.
Teslic, S., Egami, T. & Viehland, D. (1996) *J. Phys. Chem. Solids*, **57**, 1537.
Tomioka, A., Kuwahara, H., Asamitsu, A., Kasai, M. & Tokura, Y. (1997) *Appl. Phys. Lett.*, **70**, 3609.
Tranquada, J.M., Sternlieb, B.J., Axe, J.D., Nakamura, Y. & Uchida, S. (1995) *Nature (London)*, **375**, 561.

Tranquada, J.M., Axe, J.D., Ichikawa, N., Nakamura, Y., Uchida, S. & Nachumi, B. (1997) *Phys. Rev. B*, **54**, 7489.

Uehara, M., Mori, S., Chen, C.H. & Cheong, S.-W. (1999) *Nature (London)*, **399**, 560.

Urushibara, A., Moritomo, Y., Arima, T., Asamitsu, A., Kido, G. & Tokura, Y. (1995) *Phys. Rev. B*, **51**, 14103.

Viehland, D., Li, J.E., Jang, S.J., Cross, L.E. & Wuttig, M. (1992) *Phys. Rev. B*, **46**, 8013.

Westphal, V., Kleemann, W. & Glinchuk, M.D. (1992) *Phys. Rev. Lett.*, **68**, 847.

Wilson, K. (1975) *Rev. Mod. Phys.*, **47**, 773.

Yunoki, S., Hu, J., Malvezzi, A.L., Moreo, A., Furukawa, N. & Dagotto, E. (1998a) *Phys. Rev. Lett.*, **80**, 845.

Yunoki, S., Moreo, A. & Dagotto, E. (1998b) *Phys. Rev. Lett.*, **81**, 5612.

Zaanen, J. (2000) *Nature (London)*, **404**, 714.

Zaanen, J. & Gunnarson, O. (1989) *Phys. Rev. B*, **40**, 7391.

Zallen, R. (1983) in *The Physics of Amorphous Solids*, Wiley, New York.

Zhao, G.-M., Conder, K., Keller, H. & Müller, K.A. (1996) *Nature (London)*, **381**, 676.

Zhou, J.-S., Archibald, W. & Goodenough, J.B. (1996) *Nature (London)*, **381**, 770.

Zhou, X.J., Bogdanov, P., Keller, S.A., Noda, T., Eisaki, H., Uchida, S., Hussain, Z. & Shen, Z.-X. (1999) *Science*, **286**, 269.

This Page Intentionally Left Blank

Chapter 12

Concluding Remarks

This Page Intentionally Left Blank

Chapter 12
Concluding Remarks

For a long time since the development of the X-ray diffraction technique in the early 20th century determining the atomic structure of a solid has meant determining the crystal structure, by carrying out a diffraction measurement and analyzing the data with crystallographic methods. If one occasionally ran into a glass, the structure would be termed "amorphous", i.e. structureless, and the analysis would be practically abandoned there. However, sophistication in materials development brought about a major class of materials that are neither perfectly crystalline nor totally amorphous. Such a material, a crystallographically challenged material, would fall right into the gap of the existing techniques of structural analysis. And yet the details of the atomic structure usually have profound effects on their properties. In this book we discussed how to determine the structure of such a complex material, mainly borrowing from the method of structural analysis for glasses and liquids. Compared to glasses and liquids, however, the systems have much stronger local atomic order. In order to characterize such short- and medium-range order quantitatively the data have to be collected with high accuracy and the analysis has to be carried out with great care. But when it is executed properly the power of the method is quite substantial.

The purpose of this book is to introduce the readers to the technique of PDF analysis of amorphous and crystalline materials by starting from scratch and getting into some practical details. Since many of us are familiar with the conventional methods of crystal structural analysis that is done in reciprocal space, the notion of using the PDF method for the structural study of a crystal may appear strange in the beginning. Actually the PDF is a much more intuitive way to characterize the structure than in reciprocal space, particularly because we, at least most of us, live in real space! It simply represents the bond lengths and other interatomic distances, and by combining these distances in three-dimensions the total structure can be reconstructed.

An important factor that differentiates the PDF method from conventional methods is the inclusion of diffuse scattering. The presence of diffuse scattering in the data may not be obvious, particularly for the powder diffraction data. But it is always present, at least in the form of thermal diffuse scattering. In the case when the crystal lattice is not perfect additional diffuse scattering is produced by the defects, and it provides important information regarding the nature and spatial distribution of the defects. In some crystals, such as the crystals with polarons, these defects arise not because of lattice imperfections but due to the interaction of the lattice with electrons. These defects are intrinsic, rather than extrinsic. In this book, we included some examples of complex oxides with competing

interactions in which local lattice deviations are caused by these interactions. These complex oxides represent the class of modern materials of technological importance because of their outstanding properties. These properties are intimately connected with the local deviations in the lattice, and characterizing these local structures is a crucial step in understanding these complex materials.

The importance of the local structure is well recognized in some fields, particularly in the XAFS community. However, because of the technical limitations that the XAFS method provides the knowledge of only the nearest neighbors, the local structure usually implies the structure defined by the nearest neighbors. On the other hand the intermediate or nano-scale structure is equally important in determining the properties of the system. The PDF method is a unique probe that provides the information on such intermediate-range structure. While the measurement and the data analysis of this method are more complex than those for the XAFS technique, with proper training anyone can practice this method. Our hope is that this book will spark interests in this method and will play a role of introductory document into the field of the local structural research using the PDF method. By presenting data analysis equations in some detail we hope too that it will become a point of reference on the subject, though these technical Chapters and Appendices may make grueling reading.

As more pulsed neutron and synchrotron radiation sources are constructed the opportunity to practice this method is growing rapidly. We hope this method will impact wide ranges of materials research fields, from condensed-matter physics and solid-state-chemistry to biology and biomedical materials science.

Index

This Page Intentionally Left Blank